frontiers | Research Topics

Methods in head and neck cancer

Edited by
Thomas Gander and Lorenz Kadletz-Wanke

Published in
Frontiers in Oncology

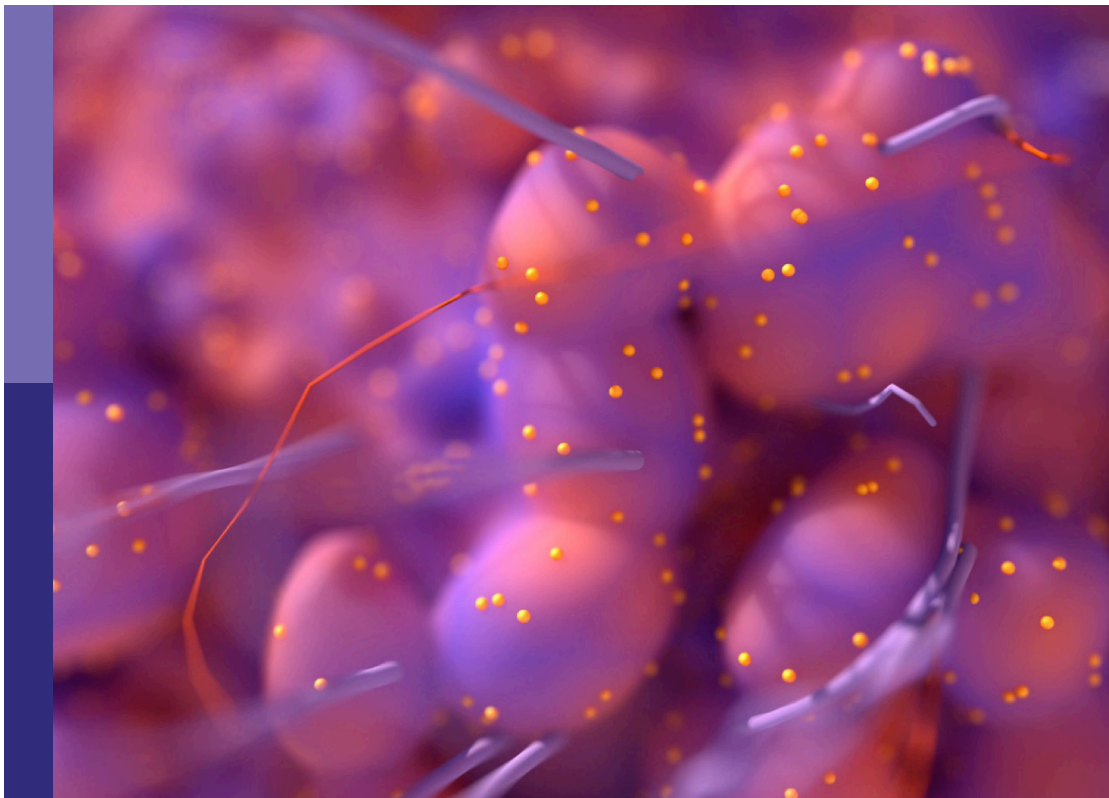

ISSN 1664-8714
ISBN 978-2-8325-4830-1
DOI 10.3389/978-2-8325-4830-1

About Frontiers

Frontiers is more than just an open access publisher of scholarly articles: it is a pioneering approach to the world of academia, radically improving the way scholarly research is managed. The grand vision of Frontiers is a world where all people have an equal opportunity to seek, share and generate knowledge. Frontiers provides immediate and permanent online open access to all its publications, but this alone is not enough to realize our grand goals.

Frontiers journal series

The Frontiers journal series is a multi-tier and interdisciplinary set of open-access, online journals, promising a paradigm shift from the current review, selection and dissemination processes in academic publishing. All Frontiers journals are driven by researchers for researchers; therefore, they constitute a service to the scholarly community. At the same time, the *Frontiers journal series* operates on a revolutionary invention, the tiered publishing system, initially addressing specific communities of scholars, and gradually climbing up to broader public understanding, thus serving the interests of the lay society, too.

Dedication to quality

Each Frontiers article is a landmark of the highest quality, thanks to genuinely collaborative interactions between authors and review editors, who include some of the world's best academicians. Research must be certified by peers before entering a stream of knowledge that may eventually reach the public - and shape society; therefore, Frontiers only applies the most rigorous and unbiased reviews. Frontiers revolutionizes research publishing by freely delivering the most outstanding research, evaluated with no bias from both the academic and social point of view. By applying the most advanced information technologies, Frontiers is catapulting scholarly publishing into a new generation.

What are Frontiers Research Topics?

Frontiers Research Topics are very popular trademarks of the *Frontiers journals series*: they are collections of at least ten articles, all centered on a particular subject. With their unique mix of varied contributions from Original Research to Review Articles, Frontiers Research Topics unify the most influential researchers, the latest key findings and historical advances in a hot research area.

Find out more on how to host your own Frontiers Research Topic or contribute to one as an author by contacting the Frontiers editorial office: frontiersin.org/about/contact

Methods in head and neck cancer

Topic editors

Thomas Gander — University Hospital Zürich, Switzerland

Lorenz Kadletz-Wanke — Medical University of Vienna, Austria

Citation

Gander, T., Kadletz-Wanke, L., eds. (2024). *Methods in head and neck cancer*. Lausanne: Frontiers Media SA. doi: 10.3389/978-2-8325-4830-1

Table of contents

frontiers | Frontiers in Oncology

TYPE Review
PUBLISHED 03 August 2022
DOI 10.3389/fonc.2022.960340

OPEN ACCESS

EDITED BY
Thomas Gander,
University Hospital Zürich, Switzerland

REVIEWED BY
Max M. Gong,
Trine University, United States
Franz Rödel,
University Hospital Frankfurt, Germany

*CORRESPONDENCE
Maryam Tabrizian
maryam.tabrizian@mcgill.ca
Nicole Y. K. Li-Jessen
nicole.li@mcgill.ca

SPECIALTY SECTION
This article was submitted to Head and Neck Cancer, a section of the journal Frontiers in Oncology

RECEIVED 02 June 2022
ACCEPTED 29 June 2022
PUBLISHED 03 August 2022

CITATION
Moya-Garcia CR, Okuyama H, Sadeghi N, Li J, Tabrizian M and Li-Jessen NYK (2022) *In vitro* models for head and neck cancer: Current status and future perspective. *Front. Oncol.* 12:960340. doi: 10.3389/fonc.2022.960340

In vitro models for head and neck cancer: Current status and future perspective

Christian R. Moya-Garcia[1], Hideaki Okuyama[2,3], Nader Sadeghi[4,5], Jianyu Li[1,6], Maryam Tabrizian[1,7]* and Nicole Y. K. Li-Jessen[1,2,4,5]*

[1]Department of Biomedical Engineering, McGill University, Montreal, QC, Canada, [2]School of Communication Sciences and Disorders, McGill University, Montreal, QC, Canada, [3]Department of Otolaryngology – Head & Neck Surgery, Kyoto University, Kyoto, Japan, [4]Department of Otolaryngology – Head and Neck Surgery, McGill University, Montreal, QC, Canada, [5]Research Institute of McGill University Health Center, McGill University, Montreal, QC, Canada, [6]Department of Mechanical Engineering, McGill University, Montreal, QC, Canada, [7]Faculty of Dental Medicine and Oral Health Sciences, McGill University, Montreal, QC, Canada

The 5-year overall survival rate remains approximately 50% for head and neck (H&N) cancer patients, even though new cancer drugs have been approved for clinical use since 2016. Cancer drug studies are now moving toward the use of three-dimensional culture models for better emulating the unique tumor microenvironment (TME) and better predicting *in vivo* response to cancer treatments. Distinctive TME features, such as tumor geometry, heterogenous cellularity, and hypoxic cues, notably affect tissue aggressiveness and drug resistance. However, these features have not been fully incorporated into *in vitro* H&N cancer models. This review paper aims to provide a scholarly assessment of the designs, contributions, and limitations of *in vitro* models in H&N cancer drug research. We first review the TME features of H&N cancer that are most relevant to *in vitro* drug evaluation. We then evaluate a selection of advanced culture models, namely, spheroids, organotypic models, and microfluidic chips, in their applications for H&N cancer drug research. Lastly, we propose future opportunities of *in vitro* H&N cancer research in the prospects of high-throughput drug screening and patient-specific drug evaluation.

KEYWORDS

head and neck cancer, tumor micoenvironment, 3D cancer models, spheroids, organotypic models, microfluidic devices, drug screening

Abbreviations: 2D, two dimensional; 3D, three dimensional; 5-FU, 5-fluorouracil; CCL-2, C–C motif chemokine ligand 2; ECM, extracellular matrix; EGFR, epithelial growth factor receptor; EMT, epithelial–mesenchymal transition; FDA, Food and Drug Administration; H&N, head and neck; HGF, hepatocyte growth factor; HPV, human papillomavirus; HTS, high-throughput drug screening; IL, interleukin; LTS, low-throughput drug screening; MDSC, myeloid-derived suppressor cell; MEK, mitogen-activated protein kinase; MMP, metalloproteinase; mTOR, mammalian target of rapamycin; PD-1, programmed cell death 1; PDO, patient-derived organoid; PDX, patient-derived xenograft; R&D, research and development; TGF, transforming growth factor; TME, tumor microenvironment; UV, ultraviolet; VEGF, vascular epithelial growth factor.

Introduction

Cancer drug research and development (R&D) are considered as one of the most expensive expenditures among drug development as compared to that of all other diseases (1). The global spending on oncology drugs reached $164 billion in 2020 and an estimated $269 billion by 2025 even as annual growth rates ease to approximately 10% (2). Mailankody and Prasad from National Cancer Institutes in the United States critically pointed out that new cancer drugs may not necessarily help to increase the survival rate in cancer patients despite the expensive investments in cancer drug R&D (3). In 2016, the Food and Drug Administration (FDA) approved the chemotherapy drug hydroxyurea for the treatment of locally advanced head and neck (H&N) cancer as well as the immunotherapy drugs pembrolizumab and nivolumab for recurrent/metastatic H&N cancer (4). Since, the role of these three drugs in the H&N cancer primary treatment has not been properly elucidated, the 5-year overall survival of H&N cancer patients remains less than 50% (5) with 30% of them experiencing cancer relapse and resistance to treatment (6).

The R&D pipeline for new drug discoveries starts with *in vitro* models, followed by preclinical/animal testing and clinical trials. *In vitro* platforms often represent a first milestone to reach the evaluation of drug cytotoxicity, dose, resistance, and sensitivity as well as the identification of the target molecular mechanisms of prognostic markers (7). Specific to cancer drug screening and discovery, *in vitro* models are often designed to mimic the tumor microenvironment (TME) of interest (8, 9). For instance, an overexpression of epithelial growth factor receptors (EGFRs) were noted in almost 90% of patients with H&N tumors (10, 11). To reflect this environment, in one of the very early *in vitro* studies with H&N squamous cell carcinoma cultures collected from larynx, retromolar trigone, cervical lymph node, and the floor of mouth, the inhibition of the EGFR was assessed by incorporating two anti-EGFR monoclonal antibodies (MAbs 425 and 528) based on *in vitro* models (12). Cell viability results showed that the two anti-EGFR antibodies reduced cancer cell growth by up to 97% compared to healthy mucosal epithelial cells after a 5-day exposure. Further, *in vitro* and *in vivo* studies on monoclonal antibodies against EGFR led to the discovery of cetuximab, which was approved by the FDA for colon cancer treatment in 2004 and in 2011 for the treatment of recurrent/metastatic H&N cancer (13).

The recent evolution of *in vitro* cancer models has been focused on emulating the tissue-specific TME as much as possible to recapitulate drug resistance and uptake in specific tumor tissues. Advances in spheroid/organoid bioengineering and their culturing methods, as well as microfluidic technologies, are harnessed to enable physiologically and clinically relevant *in vitro* cancer models. Distinctive TME features, namely, three-dimensional (3D) tumor geometry, heterogeneous cell populations, and fenestrated tumor vasculature, have been incorporated into *in vitro* models, such as breast (14), lung (15), and liver (16) cancers. However, tissue-specific TME features have not been fully applied to *in vitro* H&N cancer model designs, which might explain the slow advancement of effective drug discovery and longitudinal drug evaluation for H&N cancers.

To survey the current implementation of 3D *in vitro* models for H&N cancer, we performed a search for original research papers published on The National Center for Biotechnology Information (NCBI) PubMed® between January 2017 and April 2022 using the following combined terms, namely, "*head and neck cancer*," "*spheroid*," "*organoid*," "*microfluidic*," and "*organotypic*" (Figure 1). The search generated 71 research studies. Spheroid cultures (34%; N = 24) and scaffold models (22%; N = 16) were the two most common 3D culture models in H&N cancer research.

To understand the uptake of 3D *in vitro* models for H&N cancer drug discovery, a search was performed on the original studies of 12 common cancers including H&N (17) published on NCBI PubMed® between January 2017 and April 2022 using the following combined terms: "*in vitro*", "*drug discovery*", "*breast*", "*lung*", "*colorectal*", "*glioblastoma*", "*prostate*", "*melanoma*", "*lymphoma*", "*pancreatic*", "*cervical*", "*head and neck*", "*thyroid*", "*oral*", "*laryngeal*", "*bladder*", "*renal*", and "*cancer*". The search generated 489 results. Among the 12 organs searched, approximately 27.6% (N = 135) were related to breast cancer while only 2.2% (N = 11) were associated with H&N cancer. Further search on drug discovery–related publication for H&N cancer showed that only 3 out of the 11 results used 3D *in vitro* models. In other words, approximately 4.2% [(3 out of 11)/71] of 3D *in vitro* models were applied in the study of cancer drug discovery. The aforesaid statement described the need for more H&N cancer research using advanced 3D *in vitro* models instead of conventional 2D cultures for developing new anticancer drugs.

In this paper, we review the unique TME characteristics in H&N cancers and their relevance to the tumor tissue aggressiveness and drug resistance. We present the design principles of *in vitro* models to mimic key TME features relevant to H&N cancer. We then report on several state-of-the-art culturing models, namely, spheroids, 3D scaffolds, organotypic models, and microfluidic devices that have contributed to the H&N cancer therapeutic R&D. Finally, we provide a perspective on more reproducible and robust *in vitro* H&N cancer models for high-throughput drug screening and patient-specific drug development.

Tumor microenvironment in head and neck cancers

A typical TME in H&N cancer is heterogeneously composed of neoplastic cells, endothelial cells, and fibroblasts, as well as tumor-infiltrating immune cells from the mucosae of the oral,

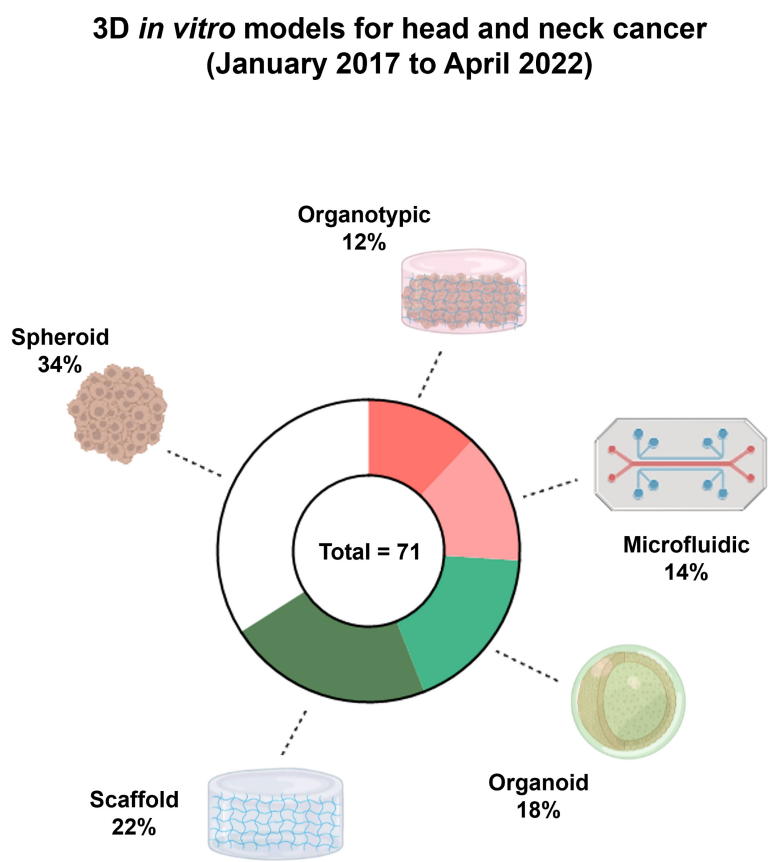

FIGURE 1
Culturing models in head and neck (H&N) cancers. Pie graph of published articles between 2017 and 2022 using the NCBI PubMed®. Related publications of three-dimensional (3D) *in vitro* models in H&N cancer with spheroids being the most abundant type of culture model. Figure created with BioRender.com and GraphPad Prism 9.3.1.

nasal and paranasal cavities, larynx, and pharynx (6, 17) (Figure 2). Approximately 90% of H&N cancer cells are considered as squamous cell carcinomas (6, 18). The H&N carcinomas present an air–liquid interface conformation since the apical TME is in contact with the air from the cavity lumen whereas the basal TME interacts with blood (6, 18, 19). In particular, these fish scale–like/squamous epithelial neoplastic cells exhibit an aggressive abnormal cell proliferation crossing the boundaries of surrounding cells in concert with endothelial cells and fibroblasts (18). Extracellular matrix (ECM) proteins as collagen, elastin, fibronectin, and laminin provide a structural support that plays a part in cell adhesion and migration in the TME of H&N (19).

H&N squamous cell carcinomas may present oncogenes associated with human papillomavirus (HPV) infection (18, 20), largely p16 followed by p18 genes (20). A classification of H&N squamous cell carcinoma relies on the presence of HPV-associated oncogenes that are normally referred to as HPV^+ or HPV^- H&N cancer (20). In particular, the mutation and down- or upregulation of molecular mechanisms such as PI3K/Akt/mTOR (mammalian target of rapamycin), TP53, NOTCH, EGFR, JAK/STAT, Ras/MEK/ERK, and MET pathways are found to be associated with the progression of H&N squamous cell carcinoma (20) (Figure 2D). For example, the PI3K/Akt/mTOR pathway is upregulated in more than 90% of H&N squamous cell carcinomas, resulting in an increased resistance to chemotherapy and radiotherapy and cancer progression (21).

Similar to other cancer progressions, in H&N cancer, epithelial, mesothelial, and endothelial cells shift from a basal to mesenchymal phenotype that allows these cells to acquire mobility and protect tumor cells from anoikis, a programmed cell death (19). These phenomena are commonly known as epithelial, mesothelial, and endothelial mesenchymal transitions, respectively. Cancer-associated fibroblasts may differentiate from resident fibroblasts and from epithelial, mesothelial, and

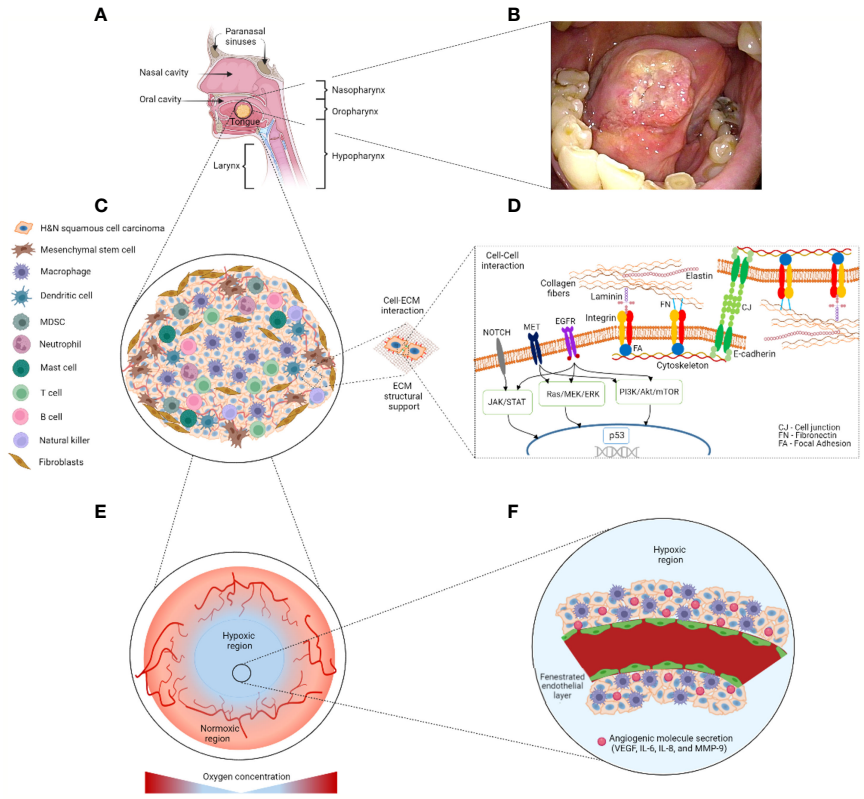

FIGURE 2
Schematic representation of the potential tumor location and tumor microenvironment (TME) in H&N cancer. **(A)** H&N cancer may be found at oral, nasal, and paranasal cavities, larynx, and pharynx anatomical sites. **(B)** Clinical image of stage 2 tongue cancer (<4 cm) provided by Drs. Yo Kishimoto and Hideaki Okuyama's research team at the Kyoto University Hospital with patient's consent. **(C)** Heterogeneous cell populations are resided within an H&N squamous cell carcinoma. Stromal cells including mesenchymal stem cells and fibroblasts are commonly found in the outer layer of the tumorous body. Tumor-infiltrating immune cells including macrophages and T cells among others are found within the tumor. **(D)** The extracellular matrix provides structural support and biochemical cues to the TME *via* cell−cell/−ECM interactions. Mutation of pathways PI3K/Akt/mTOR, TP53, NOTCH, EGFR, JAK/STAT, Ras/MEK/ERK, and MET relate to H&N cancer development. **(E)** The hypoxic region is located at the center of the tumor, which is characterized by aberrant vasculature. **(F)** This fenestrated vasculature hampers the proper supply of nutrients, oxygen, and therapeutics. ECM, extracellular matrix; IL, interleukin; MDSC, myeloid-derived suppressor cell; MMP, metalloproteinase; VEGF, vascular epithelial growth factor. Figure created with BioRender.com.

endothelial cells during respective mesenchymal transitions. Cancer-associated fibroblasts play important roles in tumor growth and maintenance through secreting autocrine and paracrine signaling molecules such as IL-1α, IL-1β, IL-6, IL-33, HGF, VEGF, TNF-α, TGF-β, CCL-2, CXCL-12, CXCR-4, MMP-2, and Snail (17, 19, 22). Cancer-associated fibroblasts in concert with endothelial cells secrete EGF that enhances tumorous motility and stemness (23, 24). In addition, stromal cells such as fibroblasts produce ECM proteins (e.g., collagen, elastin, and fibronectin) that create the fibrous architectural conformation of the tumorous body (19, 25). This structural fibrous network contributes to cell adhesion, cell proliferation, and cell migration, which, in turn, leads to tumor progression and reduced response to treatment (18, 19, 25).

Specific to the H&N cancer, the TME aggressiveness and resistance to treatment are linked to two primary mechanisms, namely, the dysregulation of the immune system and tumor hypoxia (20). With respect to the dysregulated immune system, a plethora of immune cells including T cells (cytotoxic and regulatory phenotypes), B cells, natural killers, tumor-associated macrophages (anti- and pro-tumor phenotypes), tumor-associated neutrophils, myeloid-derived suppressor cells, and mast cells are found within the TME of H&N tumors (6, 26). Checkpoint markers, including programmed cell death 1 (PD-1) and its ligand PD-L1, were found upregulated on exhausted T cells and myeloid-derived suppressor cells in the H&N TME (6). As a result, two PD-1 inhibitor drugs, pembrolizumab and nivolumab, were developed and approved for H&N cancer treatment in 2016, for unresectable and cisplatin-resistant recurrent/metastatic H&N cancer (4, 27, 28).

Tumor hypoxia is another well-recognized factor contributing to the aggressive tumor behavior and drug

resistance in H&N cancer (19, 20, 29). The fenestrated tumor vessels result in aberrant tumor blood flow to the underperfused areas of the solid tumor (Figures 2E, F). In particular, oxygen, nutrients, and drugs are restricted to reach the cells in certain tumor areas, leading to some high-level hypoxic regions within the TME (18, 20). Pro-tumor/anti-inflammatory macrophages are reported to secrete excessive angiogenic cytokines such as VEGF, IL-6, IL-8, CCL-2, and MMP-9, which results in aberrant angiogenesis and the hypoxic H&N-specific TME *in vitro* and *in vivo* (6, 17, 18, 30, 31).

Design principles of *in vitro* head and neck cancer models

Like many other *in vitro* models mimicking the TME, a representative *in vitro* H&N tumor model is expected to sufficiently recapitulate: (I) a 3D tumor-like geometry for cell–cell and cell–ECM interactions; (II) the heterogeneous cell types such as squamous cell carcinomas, stromal, and immune cells in the TME; and (III) the aberrant and fenestrated vasculature for the high-level hypoxic TME (Figure 2). These principles are further elaborated in the following paragraphs.

Three-dimensional tumor geometry

Tumors are 3D sphere-like solid structures with unique physical and biochemical boundaries, in which they need to be considered for cancer drug screening and evaluation. First, the physical geometry of the tumor affects drug disposition, diffusion, and absorption (32–34). For instance, the flat two-dimensional (2D) monolayer geometry exposes the drug application to the entire cell monolayer, making the cells more susceptible to the applied drug compared to that of 3D geometry (35, 36). Advanced *in vitro* cancer models have incorporated 3D spherical geometries to make the drug diffusion and uptake by cellular targets more similar to the *in vivo* settings of solid H&N tumors. Second, the 3D tumor geometry is a key parameter in the organization of cell membrane receptors and the remodeling of ECM constituents, which, in turn, modulate autocrine and paracrine signaling mechanisms in the TME. For example, E-cadherin adhesion proteins were found to be upregulated in 12 individual spheroid cultures made from each H&N cancer cell line (FaDu, HLaC78, Hep-2, Hep-2-Tax, HLaC79, HLaC79-Tax, HPaC79, HSmC78, CAL-27, PE/CA-PJ41, SCC4, HNO210) but not in any of the corresponding 2D monolayer controls (32). As such, 3D sphere-like culture models, as of spheroids, are essential to emulate the physical and biochemical characteristics of the solid tumor shape in the evaluation of cell–cell/–ECM crosstalk and pharmacokinetics of cancer drugs (32, 33).

Heterogeneous cell types

Recently, multicellular *in vitro* models have been developed for lung (37), breast (38), and pancreatic (39) cancer research. Such model is particularly useful to study the crosstalk between cells in response to cancer drugs. For example, a triple coculture pancreatic model was developed to create a hetero-, multicellular tumor spheroid consisting of pancreatic cancer cells, fibroblasts, and endothelial cells for the investigation of the TME response to chemotherapy (39). To mimic the heterogenous TME in H&N cancer, cell lines such as CAL-27, CAL-33, Detroit 562, Hep2, Hep3, FaDu, SCC-4, UM-SCC-3, UM-SCC-4, and UM-SCC-17A, among others, are widely used in *in vitro* 2D and 3D H&N cancer models (40).

Being able to model a heterogeneous cell population *in vitro* is key to understand the complex interactions of cancer, stromal, and immune cells, and their collective response to the testing drugs within the TME (Figures 2C, D). For instance, a cisplatin sensitivity study used a simple 2D transwell system with Boyen's chambers to coculture patient-derived CAFs and pharyngeal cancer cell lines (FaDu and Detroit 562) (41). Clonogenic survival and gene inspection showed that CAFs notably affected the colony-forming and cisplatin-sensitizing capabilities of pharyngeal cancer cells through the paracrine signaling of VEGFA, PGE2S, COX2, EGFR, and NANOG. As 2D transwell systems can incorporate two cell types at most, enhancing the complexity of *in vitro* models is a necessary step to better mimic the 3D tumor cell heterogeneity in H&N and other tumors. However, one major challenge of multicellular coculture models is the cross-contamination of culture media (42). To address this challenge, microfluidic platforms can be used to compartmentalize heterogeneous cell populations within the same culture platform (43, 44). One plausible strategy is to culture individual cell populations in separate compartments sharing a constantly irrigated channel with cultured media. The shared media will then contain paracrine factor secretion aiding the multicellular interactions of the individual cellular compartments.

Hypoxic environment and fenestrated vasculature

Tumor hypoxia is a notable factor of avascular solid tumor cores and micrometastases in cancer development (45). The TME of H&N cancer may have regions with oxygen levels as low as <5 mmHg at hypoxic sites (46). Fenestrated vasculature in hypoxic niches leads to vessel leakage, which limits an effective supply of oxygen, nutrients, and therapeutics to the tumor core. Hypoxic cues, namely, oxygen deprivation and irregular irrigation, are thus two key parameters to be considered in the design of effective *in vitro* H&N cancer models (Figures 2E, F).

Regarding oxygen deprivation, hypoxic gradients can be created by utilizing 3D *in vitro* culture geometry (47) or hypoxic culture chambers with microfluidics (48). For instance, spheroid cultures have been created to generate three geometrical regions with distinctive hypoxic gradients, namely, (I) an outer high-oxygen/nutrient-proliferative region, (II) a middle medium-oxygen/nutrient senescence region, and (III) a low-oxygen/nutrient necrotic region found in the spheroid core (36, 45).

Concerning irregular irrigation, static cultures do not translate the capillary supply as of *in vivo* systems (49). To this end, microfluidic technologies hold great promises to mimic the irregular blood supply of tumors by precisely controlling and monitoring the flow rate of media (ranging in microliters per minute) with integrated microchannels and a sensing element into the culturing platform (50). Hypoxic profiles can also be tuned by integrating spheroid models into microfluidic platforms. The cellular uptake of chemotherapy drugs can then be imaged along specific hypoxic gradients with real-time microscopy (51).

Advanced *in vitro* models for head and neck cancer drug screening and evaluation

The most common evaluation platform for drug development in H&N cancer is conventional 2D *in vitro* models thus far due to their low cost, high reproducibility, and potential coculture capability (52). However, 2D *in vitro* models are unable to (I) mimic the physical geometry of tumor, (II) avoid the cross-contamination of culture media in multicellular models, and (III) mimic the oxygen deprivation and irregular irrigation of the hypoxia region, which are key factors in the evaluation of tumor progression, chemoresistance, and treatment response (35, 36, 52). Advanced *in vitro* systems, including spheroids, 3D scaffolds, and microfluidic devices, have thus been developed to overcome these barriers (53). Although the application of these culture platforms to model H&N cancer microenvironment and its drug discovery is still in its infancy, recent research on H&N cancer has been using 3D *in vitro* models to advance the growing need of these systems for clinical translation (Figure 3).

Spheroid models

Spheroids are functional aggregations of cells that are generally formed *via* forced floating aggregation, hanging drop, or organotypic hydrogel embedment methods (52). The forced floating aggregation methods are most commonly used in H&N cancer models (32–34, 54–57) (Table 1, Figure 4). The forced floating method is to use low-attachment well-plates that hinder the cell–substrate interaction and promote cell self-aggregation. In addition, hanging drop and hydrogel embedment methods were also used to fabricate H&N cancer spheroids. The hanging drop methodology is to place a drop of cell suspension on the underside of culture plates that cells can aggregate and form spheroids at the drop tip (58, 59). For the organotypic hydrogel embedment approach, cell suspensions are pipetted into an ECM-based

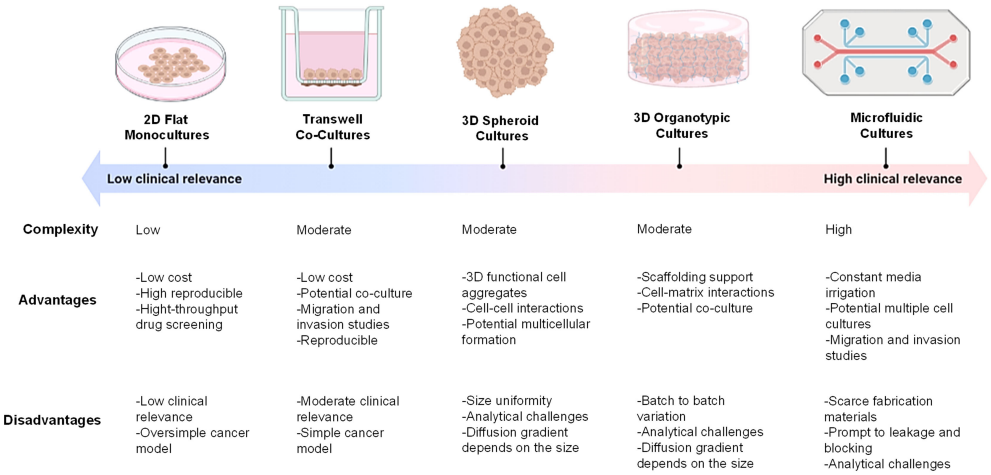

FIGURE 3
Common *in vitro* cancer models. Two-dimensional (2D) flat monolayer cell cultures grown on plastic or glass surfaces. Transwell systems with Boyden's chamber inserts for cellular cocultures. 3D spheroid-based systems by forced aggregation of cells into a 3D construct. 3D organotypic systems by culturing cells within a matrix such as a hydrogel. Microfluidic-based culture systems by culturing cells within a microchannel with fluid circulation. Figure created with BioRender.com.

hydrogel for cellular support, self-assembly, and spheroid formation (60, 61).

With the introduction of spheroid H&N models, researchers were able to better decipher the epithelial–mesenchymal transition (EMT) mechanism under a hypoxic environment with or without cancer drugs (62). For example, Melissaridou et al. (33) compared 2D and 3D cell cultures from five H&N squamous cell carcinoma–derived cell lines in their expression of EMT and stemness markers as well as response to cetuximab and cisplatin drugs. EMT-associated and stem cell markers including CDH1, NANOG, and SOX2 were upregulated in 3D spheroid groups but not in 2D monolayer controls. In addition, the spheroid groups showed increased resistance to cisplatin and cetuximab treatments compared to 2D monolayer cultures. Essid et al. (48) developed spheroids from a human tongue cell line to investigate the relationship between EMT and hypoxia. These spheroids were grown in hypoxic chambers subjected to 1% O_2 for 30 days. Results showed an increased mRNA expression in E-cadherin and N-cadherin as well as carbonic anhydrase 9, a hypoxic marker, in the spheroid hypoxic cores.

To further investigate the effect of hypoxia on the treatment response in H&N cancers (Figure 4), Basheer et al. (47) analyzed protein expression on five H&N cancer cell lines under normoxia and hypoxia in both OSC-19 spheroid cultures and monolayer controls using Western blot, flow cytometry, and immunofluorescence staining. The protein expression of CCR7, a chemokine receptor associated with hypoxia, was found significantly higher in the hypoxic core of the spheroid cultures compared to monolayer and normoxic controls. All in all, previously mentioned results pointed to the importance of tumor-like geometries as presented in spheroid models for the evaluation of drug sensitivity and cytotoxicity.

Future prospects

New 3D bioprinting techniques such as inkjet-based, pressure-assisted, and laser-assisted approaches (63) hold new promises for fabricating complex organotypic tumor spheroids in terms of cellularity and architecture (64). To fabricate multicellular spheroids, bioprinting allows the layer-by-layer precise assembly of 3D biological constructs. Synthetic polymers (e.g., polycaprolactone) and naturally derived polymers (e.g., alginate) are commonly used as bioinks to resemble the tissue-specific ECM (65, 66). Bioinks can also be printed with multiple cell types (squamous cell carcinomas, CAFs, and pro-tumor macrophages of H&N tumors) by using pressure-assisted and laser-assisted printing approaches (63). The incorporation of cancer stem cells may further mirror the aggressive H&N TME (55, 67) in the bioprinted construct due to the self-renewal and differentiation capabilities of these cell types. In addition, physiological cues such as 3D tumor geometry, cell heterogeneity, and normoxic-to-hypoxic strata can thus be recreated to induce cel–cell/–ECM interactions as expected in the H&N TME (68).

TABLE 1 Spheroid models in head and neck (H&N) cancer research.

Author	Aim	Drug Stimulant	Culture Model Design and Components				Analytic Outputs	Main Findings
			Single vs. Multicellular Cultures	Primary vs. Cell Lines	2D vs. 3D Geometry	Hypoxic Cues		
Schmidt et al. (32)	To compare the effect of 2D and 3D culture methods regarding gene expression in terms of cell junctions, cell adhesion, cell cycle, and metabolism	NS	Single	**Primary:** NS **Cell lines:** - FaDu -HLaC78 -Hep-2 -Hep-2-Tax -HLaC79 -HLaC79-Tax -HPaC79 -HSmC78 -CAL-27 -PE/CA-PJ41 -SCC4 -HNO210	**2D:** Monolayer control **3D:** Forced floating method	NS	-RNA extraction -RNA quality control -Microarray analysis -Real-time PCR -Scanning electron microscopy	-Spheroid tight formation was dependent on the upregulation of E-cadherin (cell adhesion) and downregulation of Ki67 (cell proliferation) in comparison to monolayer controls

(Continued)

TABLE 1 Continued

Author	Aim	Drug Stimulant	Culture Model Design and Components				Analytic Outputs	Main Findings
			Single vs. Multicellular Cultures	Primary vs. Cell Lines	2D vs. 3D Geometry	Hypoxic Cues		
Melissaridou et al. (33)	To compare the effect of 2D and 3D culture methods on cell proliferation, response to anticancer drugs, and EMT profiles	-Cetuximab -Cisplatin	Single	**Primary:** NS **Cell lines:** -LK0858B -LK0902 -LK0917 -LK1108 -LK1122	**2D:** Monolayer control **3D:** Forced floating method	NS	-Clonogenic assay -Tunel staining -CellTiter 96® Proliferation Assay -Western blotting -RT-qPCR	-Spheroids presented a cancer stem cell-like phenotype (upregulation of EMT-associated proteins). -Drug effects were significantly different on spheroids compared to monolayer control.
Azharuddin et al. (34)	To compare the effect of 2D and 3D culture methods regarding chemoresistance	-Cisplatin -Doxorubicin -Methotrexate	Tri-culture (cancer cells)	**Primary:** NS **Cell lines:** -LK0902 -LK0917 -LK1108	**2D:** Monolayer control **3D:** Forced floating method	NS	-CellTiter 96® Proliferation Assay -Live-cell imaging calcein-AM -Ros DCFDA assay -Flow cytometry	-Drug vulnerability and potential chemoresistance was predicted by analyzing efflux pump (ABC pump) activities. -Comparative response of multidrug resistance, drug efflux capability, and reactive oxygen species on treated cells.
Essid et al. (48)	To compare the effect of 2D and 3D culture methods on EMT, cancer stem cell, and hypoxia markers	Hypoxia 1% O_2 chamber (monolayer)	Single	**Primary:** NS **Cell lines:** -CAL-33	**2D:** Monolayer control **3D:** Forced floating method	✓	-Clonogenic assay -Western blotting -Immunofluorescence staining -RT-PCR	-Serum in media was reported to revert EMT, cancer stem cell, and hypoxia phenotype. -Spheroids cultured under hypoxia (1% O_2) showed increased carbonic anhydrase IX, vimentin, N-cadherin, glioma-associated oncogene homolog 1, and decreased E-cadherin.
Basheer et al. (47)	To compare the effect of hypoxic and normoxic culture methods on HIF-1α–CCR7 correlation	Hypoxia, low O_2 or $CoCl_2$ to cell culture medium	Multicellular	**Primary:** NS **Cell lines:** -OSC-19 -FaDu -SCC-4 -A-253 -Detroit-562	**2D:** Monolayer control **3D:** Spheroid formation Not specified	✓	-Immunofluorescence staining -Immunoblotting -Flow cytometry	-HIF-1α expression (hypoxia) was associated with the expression of CCR7 (migration marker). -Correlation between HIF-1 α and CCR7 was noted in early histological xenograft cancer samples
Hagemann et al. (54)	To compare 2D and 3D methods as chemotherapy and radiotherapy testing platforms	-Cisplatin -5-FU -2-Gy radiation	Single	**Primary:** -Tumor biopsy from H&N squamous cell carcinoma **Cell lines:** -CAL-27 -FaDu -PiCa	**2D:** Monolayer control **3D:** -Forced floating and -Hanging drop methods	NS	-WST-8 assay -ELISA	-Forced floating method was reported to be safer and more reliable than the hanging drop method. -Proof-of-concept data concerning spheroids as a therapy screening platform. -Spheroid growth was reduced after chemoradiation treatment. Significant negative impact was noted with the cisplatin + radiation treatment compared to cisplatin alone.

(Continued)

TABLE 1 Continued

Author	Aim	Drug Stimulant	Culture Model Design and Components				Analytic Outputs	Main Findings
			Single vs. Multicellular Cultures	Primary vs. Cell Lines	2D vs. 3D Geometry	Hypoxic Cues		
Goričan et al. (55)	To evaluate a 3D model as a therapy testing platform	All-trans retinoic acid (ATRA)	Single	**Primary:** NS **Cell lines:** -FaDu	**2D:** NS **3D:** Forced floating method	NS	-Immunofluorescence staining -qPCR -Flow cytometry -Western blotting -HTS	-A new cancer stem cell–enriched spheroid model adaptable for HTS of anticancer stem cell compounds -ATRA treatment was reported to reduce cancer stem cell markers.
Magan et al. (56)	To evaluate a 3D model as chemotherapy and immunotherapy testing platforms	-Cisplatin -Cetuximab	Two-culture	**Primary:** Patient-derived cancer-associated fibroblasts **Cell lines:** -LK0902 -LK0917 -LK1108	**2D:** NS **3D:** Forced floating method		-Immunofluorescence staining -TUNEL assay -RT-qPCR - CellTiter 96® Proliferation Assay	-Cancer-associated fibroblasts increased cancer cell proliferation and EGFR expression in cocultured tumor spheroid -EGFR-overexpressed spheroids showed increased response toward cetuximab after 72-h exposure -Ki67 overexpression was noted in tumor cells treated with cisplatin for 72 h
Kochanek et al. (57)	To evaluate a 3D model as a chemotherapy testing platform	-Doxorubicin	Single	**Primary:** NS **Cell lines:** -FaDu -CAL-27 -CAL-33 -OSC-19 -Detroit-562 -BIRC-56 -PCI-13 -PCI-52 -UM-SCC-1 UM-22B -SCC-9 -HET-1A	**2D:** NS **3D:** Forced floating method	NS	-Immunofluorescence staining -Widefield microscopy -LIVE/DEAD staining -Proliferation assay -Mitochondrial mass and membrane potential assay	-Cells at the outer layer of the spheroid showed higher drug uptake compared to cores after 1-day exposure -Spheroid morphology was altered after 1-day drug exposure

NS, not studied.

Further, a multi- and heterogeneous-layer geometry of the tumor spheroids can be bioprinted by implementing cell-laden bioink deposition with zone-specific techniques, for example, by varying pore-size and interconnectivity (63, 66, 69). As a result, each layer of the organotypic spheroid can have individual TME cell populations and ECM compositions to better mimic hypoxic niches within the tumor-like *in vitro* models (63). Within the 3D organotypic models, organoids that are specific 3D cell–embedded models consisting of stem or patient-specific cells and ECM constituents in the form of a multilayer geometry are very desirable H&N TME models (70). The future perspective of organoids is further discussed in the Future Outlook section.

Organotypic models

Organotypic models provide intracellular communication between cells embedded in ECM-based scaffolds (71–74) (Figure 5). A 3D scaffold-based *in vitro* model aims at recapitulating the native tissue's ECM microenvironment in terms of mechanical stability and structural architecture in the

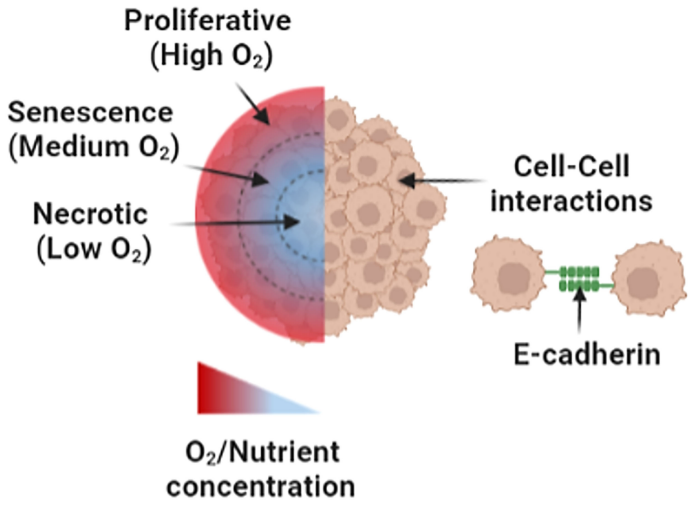

FIGURE 4
An illustration of spheroid culture model. Hypoxic gradients within spheroid cultures comprise an outer high-oxygen/nutrient region, a middle medium-oxygen/nutrient region, and a low-oxygen/nutrient region. In addition, cell–cell interactions take place in the spheroid model *via* functional cell aggregation and E-cadherin binding. Figure created with BioRender.com.

support of cell signaling, migration, survival, and growth (75). The materials used to make biological scaffolds are mostly obtained from natural or synthetic polymers, often in aqueous form. To convert the aqueous materials to a gel-like scaffold, crosslinking methods such as UV radiation, enzymatic reactions, and temperature changes have been adopted for sol–gel transitions in most *in vitro* cancer model developments (76).

To date, organotypic H&N models comprise the use of patient-derived H&N squamous cells together with decellularized extracellular matrix (dECM) (77–80) or synthetic ECM substitutes (60, 61, 81–83) as the most common constituent materials (Table 2). In particular, dECM scaffolds are often selected for cancer modeling, owing to their retained bioactive molecules (e.g., collagen, proteoglycans, and glycoproteins) (75) to support H&N cancer and TME cells for organoid formation. In addition, synthetic ECM substitutes such as the commercially available Matrigel®, which is derived from mice sarcoma (84), are also used for fabricating organotypic

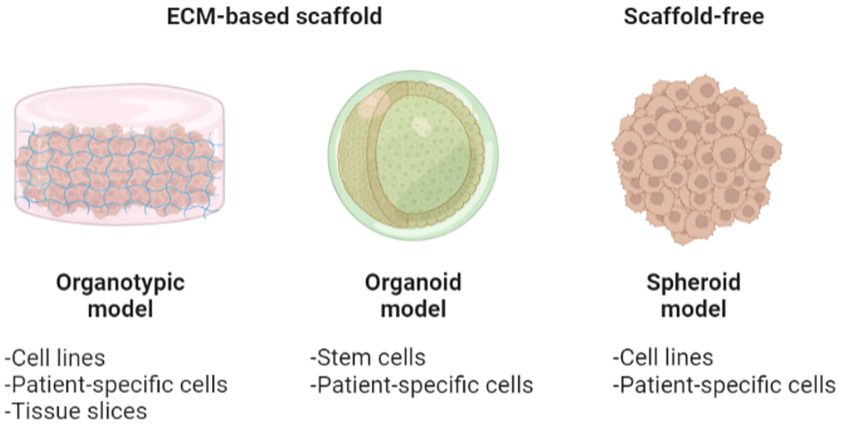

FIGURE 5
An illustration of organotypic culture models. Organotypic models provide cell–cell/ECM interactions within the culture model. Organotypic models are 3D *in vitro* platforms comprising the embedment of disaggregated cells/tissues in ECM-based scaffolds. Particularly, organoids are those organotypic models derived specifically from stem or patient-specific cells. Spheroids may be fabricated using one or multiple conventional cell lines or patient-derived cells, with or without the use of ECM-based embedment. Figure created with BioRender.com.

TABLE 2 Organotypic models in H&N cancer research.

Author	Aim	Drug Stimulant	Culture Model Design and Components				Analytic Outputs	Main Findings
			Single vs. Multicellular Cultures	Primary vs. Cell Lines	2D vs. 3D Geometry	Hypoxic Cues		
Tanaka et al. (60)	To compare 2D vs. 3D methods as a chemotherapy sensitivity platform	-Cisplatin -Docetaxel	Single	**Primary:** -Tumor biopsy from H&N squamous cell carcinoma **Cell lines:** -MDA-HN2016-2 -MDA-HN2016-18 -MDA-HN2016-21	**2D:** Monolayer control **3D:** Forced floating method and then transferred into Matrigel®	NS	-DNA extraction -STR profiling -Western blotting -Clonogenic assay	-Patient-derived organotypic models were useful as testing platforms for chemotherapy agents. -Seven 2D cell lines and 13 organoid cell lines produced after this study -Obtained cell lines presented chemoresistance cues as a tissue source
Driehuis et al. (61)	To compare 2D vs. 3D methods as a photodynamic therapy testing platform	Photosensitizer (binds EGFR) for photodynamic therapy	Single	**Primary:** -Tumor biopsy from H&N squamous cell carcinoma **Cell lines:** - UM-SCC-14C -CRL-1555 -human cervical carcinoma cell line HeLa (CCL-2) -human embryonal kidney cell line HEK293T (CRL-3216)	**2D:** Monolayer control **3D:** Basement Membrane Extract type 2 (an ECM mimetic agent) in media	NS	-qPCR -Flow cytometry -Immunofluorescence staining -PDT assay	-Patient-derived organotypic model had similar EGFR expression as a tissue source. -These models were useful as testing platforms for EGFR-targeted therapy.
Zhao et al. (77)	To compare 2D vs. 3D methods as chemotherapy screening and a regenerative platform	Cisplatin	Single	**Primary:** -Patient-derived tongue squamous cell carcinoma and cancer-associated fibroblasts **Cell lines:** -CAL-27	**2D:** Monolayer control 3D: Decellularized tongue extracellular matrix From mice, pig, and rat collagen I/ Matrigel® matrix	NS	-Immunohistochemistry and immunofluorescence staining -Scanning electron microscopy -Transmission electron microscopy -Atomic force microscopy -DNA quantification -Proteomic analysis -MTT assay -Scratch assay	-3D scaffold derived from tongue squamous cell carcinoma as *in vitro* culture support and migration -3D ECM-like platform for drug testing -Mouse-derived dECM scaffold showed increased cell adhesion, survival, and differentiation compared to control -Cisplatin exposure data showed the heterogeneity of cisplatin response within the muscle and basal layers of the mouse-derived dECM scaffold *via* cell cytotoxicity and caspase 8

(Continued)

TABLE 2 Continued

Author	Aim	Drug Stimulant	Culture Model Design and Components				Analytic Outputs	Main Findings
			Single vs. Multicellular Cultures	Primary vs. Cell Lines	2D vs. 3D Geometry	Hypoxic Cues		
								positive staining compared to monolayer control.
Burghartz et al. (78)	To compare 2D vs. 3D methods as *in vitro* support model	NS	Single	**Primary:** Human salivary gland epithelial cells **Cell lines:** -CAL-27	**2D:** Monolayer control **3D:** Decellularized porcine jejunum matrix	NS	-Immunofluorescence staining -Scanning electron microscopy -Transmission electron microscopy -Amylase Assay Kit -RT-PCR	-3D ECM-like platform for potential radiotherapy use -Gene expression of α-amylase was higher in 3D mono- and coculture compared to 2D monoculture
Ayuso et al. (79)	To compare 2D vs. 3D methods as dual drug-screening platform	-AZD8055 (mTOR inhibitor) -Cetuximab (Erbitux)	Two-culture	**Primary:** -Patient-derived cancer-associated fibroblasts **Cell lines:** -UM-SCC-1 -UM-SCC-47	**2D:** Monolayer control **3D:** Spheroid hanging drop (cultured without fibroblasts) 3D collagen hydrogel (cultured without fibroblasts)	NS	- CellTiter 96® Proliferation Assay -Immunofluorescence staining	-3D ECM-like platform as coculture setup for drug testing and EGFR pathway analysis -Cell cytotoxicity data showed higher drug resistance response in the coculture (1.4-fold increase) and 3D culture groups (2.6-fold increase) compared to 2D monocultures
Tuomainen et al. (80)	To compare 2D vs. 3D methods as a drug-screening platform	-EGFR (gefitinib, erlotinib, cetuximab, canertinib, and afatinib) -MEK (trametinib, TAK-733, selumetinib, refametinib, pimasertib, and binimetinib) -mTOR (temsirolimus, sirolimus, ridaforolimus, PF-04691502, omipalisib, everolimus, dactolisib, and apitolisib)	Single	**Primary:** NS **Cell lines:** -UT-SCC-8 -UT-SCC-14 -UT-SCC-24A -UT-SCC-24B -UT-SCC-28 -UT-SCC-42A -UT-SCC-42B -UT-SCC-40 -UT-SCC-44 -UT-SCC-73 -UT-SCC-81 -T-SCC-106A	**2D:** Monolayer control **3D:** Matrigel® and a leiomyoma-derived matrix "Myogel"	NS	-Drug sensitivity and resistance testing - CellTiter 96® Proliferation Assay -Meta-analysis of Clinical Data -Immunoblot analysis	-3D ECM-like platform for drug testing and pathway analyses -Cells seeded in Myogels showed significantly lower EGFR and MEK inhibition activity -Cells seeded in both scaffolds showed a low mTOR inhibition activity in most of the cell lines
Young et al. (81)	To compare 2D vs. 3D methods as radiotherapy-screening platform	5 or 10 Gray	Two-culture	**Primary:** -Patient-derived Cancer-associated fibroblasts **Cell lines:** -CAL-27	**2D:** Monolayer control **3D:** Tissue Roll for the Analysis of Cellular Environment	✓	-MTT assay -Immunofluorescence staining -Hypoxia (EF5) staining -Live/Dead staining -Cell migration -Clonogenic assay	-3D ECM-like platform as coculture setup for radiotherapy and hypoxia analysis -Increased cell migration and invasion of tumor-stroma cocultures within the layers of the tissue roll

(Continued)

TABLE 2 Continued

Author	Aim	Drug Stimulant	Culture Model Design and Components				Analytic Outputs	Main Findings
			Single vs. Multicellular Cultures	Primary vs. Cell Lines	2D vs. 3D Geometry	Hypoxic Cues		
					and Response (TRACER) construct a collagen gel and cellulose scaffold			construct -No significant radiation resistance of tumor-stroma cocultures within the layers of the tissue roll construct
Lee et al. (82)	To compare 2D vs 3D methods as chemotherapy testing platform	-Cisplatin -Docetaxel	Two-culture	**Primary:** -Tumor biopsy/ explants from H&N squamous cell carcinoma **Cell lines:** -NS	**2D:** Monolayer control **3D:** Dissociated epithelial cells seeded on a mixture of solidified fibrin glue and tumor explants	✓	-Cell counting kit-8 (CCK-8) -LIVE/DEAD assay using -LOX-1 a hypoxia probe	-Tumor explants were reported to present hypoxic cues, and drug screening sensitivity -Tumor explants in fibrin matrix survived over 10 days while those explants without the matrix survived less than 8 days
Engelmann et al. (83)	To compare HPV-associated organotypic explants as radiotherapy testing platform	2 Gray	Multicellular	**Primary:** -Tumor biopsy/ explants from H&N squamous cell carcinoma **Cell lines:** -NS	**2D:** NS **3D:** Dermal equivalents from viscose fiber fabric embedded with fibroblast for ECM production H&N squamous cell carcinoma as tissue slices	NS	-H&E staining -Immunohistochemical staining -Immunofluorescence staining -PCR -Motility and invasiveness analysis -Cell viability, proliferation, and apoptosis assays	-3D ECM-like platform for radiotherapy use -Radioresistant tumor cells and morphological variations were noted after 5-day fractionated irradiation exposure -Tumor slices/explants in dermal equivalents remained viable for up to 21-day cultures

NS, not studied.

H&N cancer models (60, 77, 80). However, Matrigel® is reported with single-batch variations that cause a significant concern on mechanical inconsistency, especially in fabricating reproducible organoids even when using the same batch of the product (84).

In an effort of developing patient-specific organotypic models, Tanaka et al. (60) combined an epithelial cell sheet, the Matrigel®, and individual squamous cell carcinomas derived from 43 biopsies of H&N cancer patients. The organotypic models were subjected to the exposure of cisplatin and docetaxel for eight consecutive days (60). Results showed that these models displayed a patient-specific chemoresistant response. For example, the MDA-HN-2C organoid group developed resistance to cisplatin and docetaxel, corresponding to that of the individual patient donor with recurrent H&N cancer. In addition, the organoid-like models showed increased resistance to both drugs in comparison to that of 2D monolayer controls. The proposed patient-derived organoid (PDO) platform served a notable step toward the application of predicting patient-specific H&N drug sensitivity *in vitro*.

One advancement of the cancer organotypic model is to approximate the heterogeneity of tissue strata as seen in the tumor architecture. For instance, in H&N tumor, tissue strata mostly comprise squamous epithelia, basal strata, stroma, and lamina propria. Zhao et al. (77) investigated whether the tissue sources of dECM would result in a specific stratum architecture of the scaffold that might, in turn, affect the drug response of cancer cells. Mouse, rat, and pig tongue tissue samples were decellularized and used to fabricate scaffolds with patient-specific cancer-associated fibroblasts and CAL-27 cells. Hematoxylin & eosin staining, scanning electron microscopy, and transmission electron microscopy showed a similar histological stratum architecture of the three dECM scaffolds. Further investigation using a mouse dECM scaffold showed that the elastic modulus of mouse dECM scaffolds was comparable to that of native mouse tongue tissue (0.503 MPa vs. 0.567 MPa).

Compared to monolayer non-scaffold controls, mouse-derived dECM scaffolds showed improved cell adhesion, proliferation, and survival after 14 and 28 days of cultures in the absence of drug exposure. After a 2-day exposure of cisplatin, an apoptotic marker, namely, caspase 8, showed distinctive staining patterns across the strata of mouse-derived dECM scaffolds. For instance, cancer cells at the muscle fiber layer of the scaffold expressed stronger caspase 8 expression than those at the basal layer of the scaffold, possibly owing to the drug-penetration gradients.

Aside from the evaluation of dECM sources, Ayuso et al. (79) compared 3 culture models, namely, (I) 2D monolayer cocultures with primary cancer-associated fibroblasts and H&N cancer cell lines (UM-SCC-1 and UM-SCC-47), (II) 3D collagen hydrogel scaffolds seeded with H&N cancer cells, and (III) 3D H&N cancer cell spheroids of their responses to cetuximab and an mTOR inhibitor. Cell cytotoxicity results indicated a stronger drug resistance response in the coculture (1.4-fold increase) and 3D culture groups (2.6-fold increase) compared to 2D monocultures. No statistical comparison was reported between the two 3D culture groups. Nevertheless, the differentiated drug resistance between the 2D and the 3D culture groups may be associated with the geometry-induced drug impediment.

High-throughput screening (HTS) with organotypic models is one critical advancement of scaffold models for immune-oncology and drug discovery (85). Using 384-well plates, Tuomainen et al. (80) evaluated the effect of 19 immunotherapy drugs on 12 H&N cancer cell lines seeded within 3D scaffolds inserted in those plates. The 19 immuno-drugs were inhibitors of 5 EGFR (gefitinib, erlotinib, cetuximab/erbitux, canertinib, and afatinib), 6 MEK (trametinib, TAK-733, selumetinib, refametinib, pimasertib, and binimetinib), and 8 mTOR (temsirolimus, sirolimus, ridaforolimus, PF-04691502, omipalisib, everolimus, dactolisib, and apitolisib). The testing scaffolds included Matrigel® and human-derived leiomyoma referred to as Myogel. Compared to Matrigel®, cells embedded in Myogels showed significantly lower EGFR and MEK inhibition activity after 72 h of drug inspection. Normalized HTS drug response profiles consisted of four activity levels based on a drug-sensitivity score (DSS) and artificial cutoff points: inactive DSS < 5, low 5 ≥ DSS < 10, moderate 10 ≥ DSS < 15, and high DSS ≥ 15 (80). Overall, a low activity of mTOR inhibitors was consistently found in most of the cell lines from both Matrigel® and Myogel scaffold models. Results from this study provided early evidence of the reliability and predictability of using HTS organoid platforms in the evaluation of cancer therapeutics.

In addition to chemotherapy drug–related studies, Young et al. (81) developed a 3D tissue construct of a collagen and cellulose tissue roll scaffold "TRACER" for radiation therapy screening. The FaDu cell line and primary cancer–associated fibroblasts, stromal cells, were transfected with green fluorescent protein and mCherry, respectively. Both cells were seeded into the cellulose layer (cancer-associated fibroblasts in layer 1 and FaDu in layer 3) with or without a central collagen/agarose layer to separate the coculture. The cell-seeded TRACER was rolled onto an acrylic core placed into custom-made 50-ml Falcon tubes and then subjected to 5- or 10-Gray radial arc radiations. Clonogenic results indicated that no radioprotective behavior from the CAFs was observed in the cocultures regardless of the presence of the central layer after 24-h culture. In a separate study, x-ray radiation (0–15 Gray) was found to downregulate HeLa cancer cell proliferation, cell viability, vinculin, and α-tubulin expression in 2% agarose hydrogels with 250 μm of diameter compared to 2D flat counterparts (86). Although results from these two radiation studies were not fully corroborated, 3D tissue constructs with cocultures showed the potentials of elucidating epithelial–stromal interactions of tumor response to radiation exposure.

Future prospects

Organotypic models have demonstrated great possibilities for approximating the TME and supporting the HTS cancer drug platform. Several technical challenges remain to adapt the organotypic models to fulfill the two aforesaid promises. Organotypic fabrication is complex, especially considering the scaffold embedment that influences the therapeutic response based on the scaffold's composition and network (87). For instance, these models have not been fully designed to incorporate the irrigation features of tumor modeling. One possibility is to place the scaffolds into microfluidic channels to recapitulate the constant irrigation features of native tumor or healthy tissues with bioprinting and electrospinning techniques (88). Electrolyte-assisted electrospinning can further help to fabricate nanofibrous membranes through electrostatic forces to draw charged threads of dissolved polymers to a grounded electrolyte solution (89). These nanofiber membranes can be located inside microfluidic channels for tissue-engineered scaffolds (89). By integrating electrospinning and microfluidic technologies, scaffold-based models can better meet the functionality of continuous monitoring and irrigation of cancer therapeutics.

Microfluidic platforms

Microfluidic platforms are micromanufactured devices with interconnected chambers, membranes, and grooves that share low volumes of fluids (Figure 6), which have been widely applied for *in vitro* modeling such as organ-on-a-chip models (49, 90–95) and point-of-care systems (96). In cancer research, microfluidic platforms are mostly fabricated using lithography and surface micromatching techniques with polydimethylsiloxane, silicon, glass, polycarbonate, and polymethylmethacrylate as main materials (49, 91–93, 97–99). Flow mechanisms can be

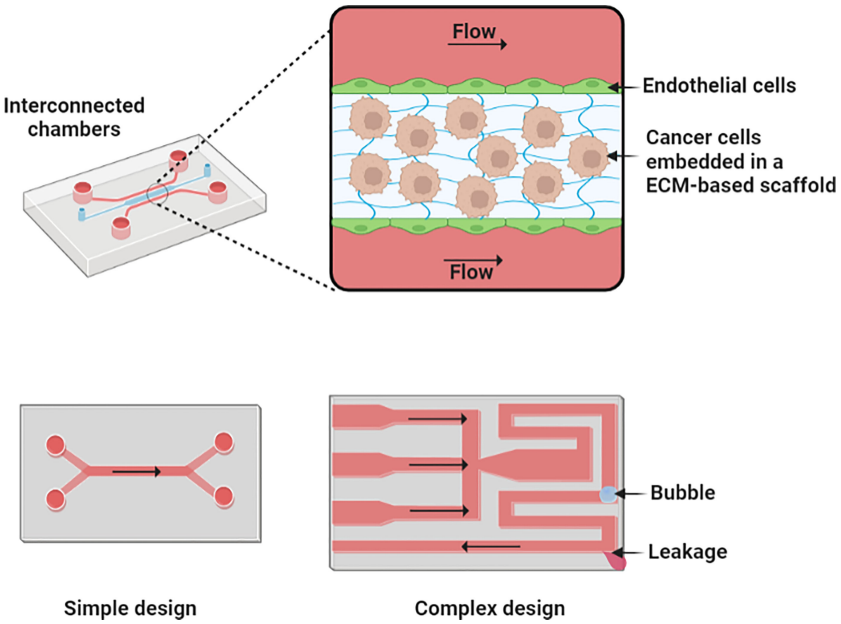

FIGURE 6
An illustration of microfluidic culture models. Microfluidic devices comprise the interconnection of chambers and grooves sharing low volumes of liquids. A more complex design with more channels and chambers can enhance its physiological representation but may also increase the chance of challenges as bubble blocking and liquid leakage. Figure created with BioRender.com.

implemented through a passive or an active approach within the microfluidic device. Passive flow can be driven by gravity, hydrostatic pressure, surface tension, or osmotic pumps (93). Active flow mechanism, which is commonly used in H&N microfluidic devices, involves the use of peristaltic (2 µl/min to 10 L/min), syringes (0.012 nl/min to 0.3 L/min), and pressure-driven pumps (nl/min to ml/min) (49, 91, 93, 96–100).

Microfluidic platforms support simultaneous compartmentalization of multiple cancer cell populations with constant culture media irrigation (90). This compartmentalization with dynamic flow features allows for the programmatic control and real-time monitoring of cancer cell–vasculature interplay through the interconnected cellular compartments of the platform (49, 91, 101). Most chemotherapy drugs are also delivered intravenously that flow dynamically through blood vessels to the tumor vasculature and extravascular tissues (102). The dynamic flow feature of microfluidic devices can thus resemble the transportation of intravenous systemic treatment and help to evaluate its pharmacokinetics in a more precise, controllable manner. Chemotherapy drugs, such as paclitaxel, cisplatin, and 5-fluorouracil, have been tested with microfluidic devices in H&N cancer research (Table 3).

The first microfluidic device for H&N cancer drug screening was designed by Hattersley et al. *via* lithography in polydimethylsiloxane and a syringe pump (49). Primary H&N squamous cell carcinoma biopsies (~3-mm^3 size) placed in the microfluidic device equipped with a syringe pump were exposed to cisplatin and 5-flourouracil continuous flow up to 7 days. Results showed decreases in cell viability and proliferation on drug-exposed groups compared to unexposed controls. In addition, the sandwich ELISA results of cytochrome c, a key compound in cell apoptosis, were found higher in the culture media in the treated groups compared to untreated controls. This study represented an important step of evaluating the personalized treatment of patient's tumor biopsies under constant drug irrigation.

Riley et al. (91) further advanced the design of microfluidic platforms for personalized H&N drug screening. This platform was fabricated with two polyether–ether–ketone support plates, a silicone gasket as a tissue well, and a syringe pump. Such platform was applied to evaluate the effect of a combined JNK inhibitor and etoposide drug treatment on thyroid cancer biopsies (~5-mm diameter) from 23 individual patients. After 4 days of drug exposure, increased cell death was found in the thyroid cancer biopsy group compared to the unexposed group although no patient-specific drug responses were observed in this study.

Interconnected compartmentalization strategies within microfluidic devices for H&N cancer modeling were first implemented by Jin et al. (103). Their microfluidic platforms were made of two layers of polydimethylsiloxane interconnected by a porous polycarbonate membrane and flow applied *via* a double syringe pump. This membrane allowed the nutrient/drug exchange between the top chamber

TABLE 3 Microfluidic Devices in H&N Cancer Research.

Author	Aim	Drug Stimulant	Culture Model Design and Components				Analytic Outputs	Main Findings
			Single vs. Multicellular Cultures	Primary vs. Cell Lines	2D vs. 3D Geometry	Hypoxic Cues		
Hattersley et al. (49)	A dynamic culture method as chemotherapy screening platform	-5-FU -Cisplatin	Single	**Primary:** Patient-derived H&N squamous cell carcinoma **Cell lines:** -NS	**2D:** Unexposed control Dynamic flow **3D:** Multimicro channels Dynamic flow Syringe pump	NS	-H&E staining -Lactose dehydrogenase release -WST-1 metabolism -Trypan blue -Cytochrome C analysis	-Preclinical model for personalized medicine and testing -H&E staining showed the retention of multilayer tissue strata -Combination therapy presented higher levels of cytochrome C compared to untreated control
Riley et al. (91)	A dynamic culture method as drug screening platform	-Etoposide (topoisomerase II inhibitor) -SP600125 (JNK inhibitor)	Single	**Primary:** Human thyroid tissue samples **Cell lines:** -NS	**2D:** Unexposed control Dynamic flow **3D:** Tissue chamber Dynamic flow Syringe pump	NS	-Hematoxylin and eosin -Flow cytometry -Trypan blue -Immunohistochemistry staining -Functional analysis - Lactose dehydrogenase release -TUNEL assay -Immunoblot analysis	-Preclinical model for personalized medicine and testing -H&E staining showed the retention of multilayer tissue strata -Thyroid biopsies were considered functional due to the production of T4 during the culture period -Increased apoptosis on thyroid samples after the perfusion of both drugs in comparison to untreated control
Al-Samadi et al. (92)	A dynamic culture method as drug screening platform	-PDL1 antibody -IDO1 inhibitor	Single	**Primary:** Primary H&N squamous cell carcinomas, T cells, B cells, NK cells, monocytes, and dendritic cells **Cell lines:** -HSC-3	**2D:** Unexposed control Dynamic flow **3D:** Chambers coated with ECM substitute Dynamic flow Unspecified pump	NS	-Migration assay -Immunofluorescence staining - CellTiter 96® Proliferation Assay -Cell Trace kit	-Preclinical organotypic model for personalized medicine and testing -IDO 1 inhibitor influences immune cell migration to cancer cells -Therapy response was reported to be patient dependent
Bower et al. (94)	A dynamic culture method as maintenance platform	NS	Single	**Primary:** Human biopsies of laryngeal, oropharyngeal, or oral cavity tumors staged at T2–T4 **Cell lines:** -NS	**2D:** Unexposed control Dynamic flow **3D:** Biopsy chamber Dynamic flow Syringe pump	NS	-H&E staining -Trypan blue -Flow cytometry -MTS proliferation assay	-Patient-derived samples were viable for 48 h after placement in the microfluidic chip -No significance difference concerning the average proliferation of samples pre- and postcultured in the chip
Lugo-Cintrón et al. (95)	A dynamic culture method as	NS	Two-culture	**Primary:** Human tubular lymphatic	**2D:** Unexposed control	NS	-H&E staining -Immunofluorescence staining	-Preclinical organotypic model for personalized medicine and testing

(Continued)

TABLE 3 Continued

Author	Aim	Drug Stimulant	Culture Model Design and Components				Analytic Outputs	Main Findings
			Single vs. Multicellular Cultures	Primary vs. Cell Lines	2D vs. 3D Geometry	Hypoxic Cues		
	angiogenesis platform			vessels and cancer-associated fibroblasts **Cell lines:** -HLEC2500 -HOrF2640	Dynamic flow **3D:** Collagen hydrogel adhesion chamber Dynamic flow Syringe pump		-Immunohistochemistry staining -Proliferation assay -Migration and permeability assay -RT-qPCR -Multiphoton microscopy	-Cancer-associated fibroblasts increased the gene expression of prolymphangiogenic factors in the lymphatic-like vessels
Sharafeldin et al. (96)	A dynamic culture method as biomarker detection platform	NS	Single	**Primary:** NS **Cell lines:** -HN12 -HN13 -HN30 -CAL-27	**2D:** Subtract biomarker control signal **3D:** Sonic-assisted chemical lysis chambers Dynamic flow peristaltic micropump	NS	-Biomarker quantification (desmoglein 3, VEGF-A, VEGF-C, β-Tub)	-Biomarker detection model for cancer metastasis diagnostic -Limit of detection was below 0.20 fg/ml of the analyzed analyte in 20-min evaluation
Jin et al. (103)	A dynamic culture method as a chemotherapy screening platform	-Paclitaxel -Cisplatin -5-FU	Two-culture	**Primary:** Patient-derived tumor cells from squamous cell carcinoma and salivary gland adenoid cystic carcinoma **Cell lines:** -ACC-M -UM-SCC-6 -HUVEC	**2D:** NS **3D:** Transwell-like channels -Bottom chambers coated with an ECM substitute Dynamic flow Double syringe pump	NS	-Hoechst 33342 and propidium iodide -Immunofluorescence staining	-Preclinical organotypic model for personalized medicine and testing -High concentration of drugs did not provide a therapeutic effect as HUVEC cells were killed. A lower concentration was recommended to provide a therapy to kill cancer cells (over 50% apoptosis) and low HUVEC cytotoxicity (over 50% viability) -Therapy response was reported to be patient dependent concerning different low drug concentrations

NS, not studied.

of endothelial cells Human umbilical vein endothelial cells (HUVEC) and the bottom chamber of cancer spheroids (103). To further optimize the device design, bubble trappers were proposed to facilitate continuous laminar flows and avoid chamber blockings in synchronous drug delivery, which is known prone to the bubble generation within microfluidic devices. This platform was also designed to emulate the tumor perivasculature by using concentration gradient chambers. These chambers comprised two drug inlets with six downstream channels for parallel drug gradient formation connected to the HUVEC culture chambers. Patient-specific or human salivary adenoid cystic carcinoma (ACC-M cell line) were used to fabricate cancer spheroids. Cell spheroids were subjected to parallel drug exposure mimicking the dual treatment of cisplatin/paclitaxel or cisplatin/5-fluorouracil *via* the two-drug inlet synchronous application. After a 24-h parallel exposure of combined drug treatments, cell viability ACC-M spheroids (ACC-2 group) showed higher sensitivity

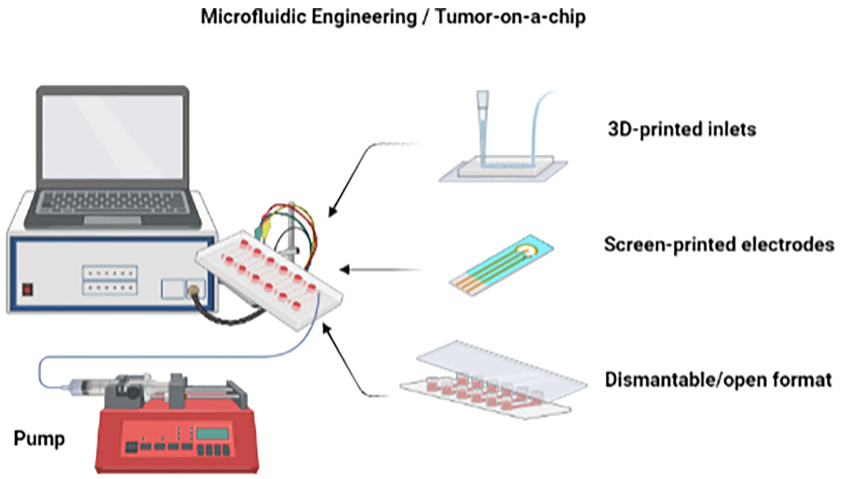

FIGURE 7
Advances in microfluidic technology. Microfluidic devices as tumor-on-a-chip may incorporate 3D-printed components and a dismantable/open format. Figure created with BioRender.com.

(i.e., more cell death) to cisplatin/5-fluorouracil treatment whereas patient-specific spheroids (SCC-1 group) were more sensitive to cisplatin/paclitaxel treatment.

Future prospects

H&N cancer drug studies with microfluidic models emphasized the importance of using patient-derived biopsies from oral cavity, pharynx, larynx, lymph nodes, and thyroid for patient-specific prediction of drug response (49, 91, 94), echoing those as in the review of organoid models. Patient-derived tissue biopsies preserve key cellular heterogeneity and geometry of the tumor, which are important variables for drug screenings. However, the use of tissue/tumor biopsies for microfluidic platforms is hampered by the technical challenge of on-chip imaging and off-chip analysis (104). Milliscale tissues as tumor biopsies usually give raise to culture challenge concerning the complex tissue preservation during long-term culture times (105). Fortunately, advances in microfluidic platforms make the long-term culture of thick tissue samples possible with an effective nutrient and oxygen supply through a dynamic flow of culture medium (49, 91). In particular, pump-free microfluidic devices were shown to be able to maintain 2-mm human organotypic models for a 75-day continuous culture of human brain organoids (106).

Other advances in microfluidic technology, such as dismantable/open and droplet-based formats, also facilitate the development of tumor-on-a-chip devices (104) (Figure 7). The dismantable/open-layer feature of microfluidic platforms allows for the direct retrieval of the analyzed samples by taking apart the top layer of the device (104). Cultured materials can then be easily accessible for off-chip analysis as the histological staining of biopsies and biopsy-like tissues. The fabrication of tumor-on-a-chip platforms can be complicated due to the necessity of having a microscale cell culture environment and chamber flow interconnection, which often requires high manual skill sets. The use of 3D printing for creating the on-chip microcomponents such as chambers, membranes, and grooves is therefore a very wise option to save labor and costs compared to conventional lithography and polydimethylsiloxane molding (107–111).

Lastly, combined chemotherapy drugs, namely, cisplatin and docetaxel, have already been tested as a tumor reduction strategy in HPV^+ oropharynx cancer patients (112). The multicompartments of microfluidic devices can be harnessed for screening multiple therapeutics in parallel, mimicking various combinations of cancer drug treatments like dual chemotherapy drugs or even the combination of chemoradiotherapy (105).

Future outlook

The development of multicellular tumor spheroid systems that are compatible for preclinical studies, as HTS drug screening (113), is one important milestone of advancing personalized cancer medicine (114). As a result, PDOs became increasingly used to preserve part of the structural features and genome, epitome, transcriptome, proteome, and metabolome information of an individual's H&N tumorigenesis for anticancer drug studies (115–117). Certain challenges such as suboptimal reproducibility and high manufacturing costs are well-known barriers with advanced culturing systems. In

particular, the development of microfluidic devices requires specialized microfabrication and operation skills. Below, we further present specific challenges with PDOs in their adaptation for HTS with respect to their sourcing, fabrication, and culturing life span (Figure 8).

Overcoming the limited source of patient-derived organoids

Tumor tissue biopsies are needed from cancer patients to generate PDOs, but the source is often limited and unpredictable with clinical samples (Figure 8A). Fortunately, PDOs can be replicated and cryopreserved in specialized facilities, known as living biobanks, without losing cell-type specificity (87, 118). For example, intraductal papillary mucinous neoplasms were collected from patients with pancreatic cancer (119). The tumor tissues were first digested with a proteolytic enzyme for cell retrieval. The recovered cancer cells were then seeded in Matrigel® and stored as PDOs in a living biobank (119). The gene analysis data of key markers KRAS, PTEN, PIK3CA, GNAS, RNF43, and BRAF showed a similar expression between PDO and the patient's tumor tissue biopsy, which confirmed the preservation of patient samples' genome in living biobanks.

The stock of PDOs from living biobanks can be further expanded with the method of patient-derived xenografts (PDXs) (120–122). A PDX is to first insert PDOs in animals and then amplify the PDOs within the host. The derived PDXs (i.e., cloned PDOs) are then cryopreserved and stored in living biobanks, preserving cell–cell interactions as those of parent tumor. Of note, the genome copy number alterations of PDX-expanded PDOs may change after extensive passaging due to possible host reactions to the implant (123–125). As such, if a high passage (>P10) is used in treatment, caution needs to be exercised as PDOs and PDX-expanded PDOs may display a differentiated response to drug therapeutics. Furthermore, PDX models are time consuming and expensive, the engraftment efficiencies may be different among the TME types, and finally, the immune response cannot be properly evaluated due to the immunodeficiency of host strains (126). As a result, additional cancer model strategies are thus required.

Patient-derived organoids from cancer and healthy stem cells

In addition to tissue biopsies, organoids can be grown from cancer or healthy stem cells (115, 116, 120, 123, 127–133) although their use in cancer research is still in its infancy (128, 133–135). PDOs from cancer stem cells possess metastatic, chemotherapy, and radiotherapy resistance features, while healthy stem cells do not present those intrinsic characteristics (133, 136). At the same time, cancer stem cells are criticized of their limited clonal heterogeneity (133). A plethora of cancer-associated markers such as CD133, CD44, ABCG2, aldehyde dehydrogenase, octamer binding transcriptional factor 4, SOX2, and NANOG have been reported in cancer stem cells (134, 135, 137). However, marker expression does not necessarily translate into a cancer stem cell phenotype without transplantation assays (138). These assays are necessary to verify and characterize the tumor-initiating and -regenerating capabilities of such cells on implanted hosts.

Conversely, healthy adult stem cells like mesenchymal stem cells (139) and induced pluripotent stem cells (140) are another option of PDOs in cancer research. Human-induced pluripotent stem cells from healthy adults were proposed to generate PDOs for liver cancer studies (140). For instance, induced pluripotent stem cell reprogramming from human fibroblasts was successfully directed toward a hepatic endoderm-like phenotype *via* differentiation media containing activin A, bFGF, and BMP4 after 8 days of exposure (141). Then, the exposure of differentiation media with NOTCH activator agents to generate liver tumoroids or NOTCH inhibitors for liver organoids was performed after 2–3 weeks (140). The aforesaid methodology could be adjusted, following the generation protocol of vocal fold mucosae from human-induced pluripotent cells (142). At that point, the PDO fabrication protocol for H&N cancer may implement the

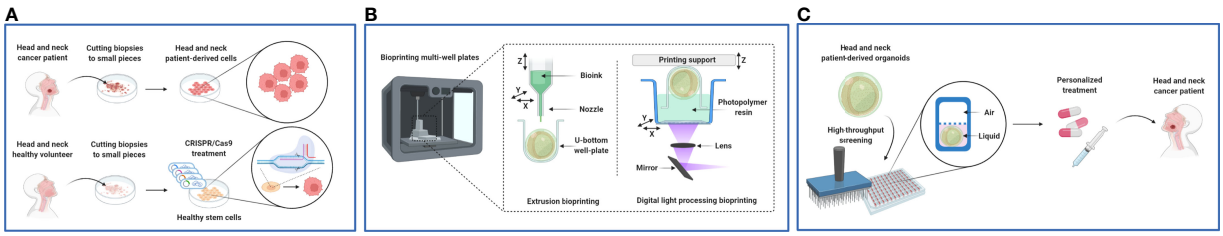

FIGURE 8
Future outlook of *in vitro* H&N cancer patient-derived organoid (PDO) models. **(A)** Sourcing of H&N PDO models using the tumor biopsies of cancer patients and CRISPR DNA–modified healthy cells. **(B)** Fabrication of H&N PDO models using bioprinting. **(C)** H&N PDO model life span used as air–liquid interface in HTS for personalized medicine purposes. Figure created with BioRender.com.

upregulation of Snail, the downregulator of epithelial markers and the upregulator of mesenchymal markers (143), and exposure to FGFs to generate stratified squamous epithelia (139, 144).

In more detail, induced pluripotent stem cell–based cancer modeling can be used as follows (145): (I) genetic alterations can be engineered into normal human-induced pluripotent stem cells using transcription activator-like effector nucleases (TALENs) or CRISPR/Cas9 (146). These stem- derived cells with engineered cancer-associated mutations can be used to acquire the initial cancer molecular events to then emulate cancer progression (145). (II) Induced pluripotent stem cells can be used to reprogram patient-specific somatic cells with cancer predisposition syndromes such as Li–Fraumeni syndrome (147). (III) Induced pluripotent stem cells can be engineered as cancer-specific cells by targeting tumor suppressors such as SMAD4, Rb/P16, BRCA1, CDKN1A, and CDKN2A (145). The previously mentioned stem cell strategies may help advance PDO research on H&N cancer.

Lastly, human embryonic stem cells were implemented as organoids for metastatic brain cancer modeling using induced pluripotency stem cell strategy (148). However, the use of embryonic stem cells possess ethical concern, low immune compatibility and potential rejection after clinical transplantation (149). Nevertheless, continuous *in vitro* validation such as phenotype analysis is warranted to ensure the safe use of healthy stem cells as PDO models for cancer research.

Patient-derived organoids from CRISPR/Cas9 DNA-modified healthy cells

CRISPR/Cas9 transgenesis technology has been proposed to genetically modify healthy biopsies into PDOs (115, 116, 120, 123). The technology of CRISPR/Cas9, simply put, involves activating/silencing a specific gene of target (Figure 8A). CRISPR/Cas9-mediated genome editing comprises the implementation of two components: (I) single-effector Cas9 protein to allow double-stranded breaks in the target DNA and (II) a single-guide RNA to guide the Cas9 complex to the targeted genomic zone (150, 151). The CRISPR/Cas9 technology has already been used to fabricate human oncogenic organoids from healthy liver by editing PTEN/TP53 and from healthy colon by targeting APC/SMAD4/TP53/K ras/PIK3CA (152). Interestingly, human pluripotent stem cells can gain CRISPR/Cas9-mutated p53 with a critical functional evaluation of p53 to avoid double-strand break toxicities dependent on p53/TP53 (153). Furthermore, wild-type human gastric organoid cell lines with ARID1A, an early-stage gastric cancer marker, as a single mutant target has been modified through CRISPR/Cas9 technology (154). In H&N cancer, gene editing may target the EGFR/PI3K/Akt/mTOR pathway for oncogenic organotypic fabrication.

One known limitation with CRISPR/Cas9 technology is related to the low specificities to the target genes (150, 152). For instance, the off-target effect is often observed at a rate ≥50% in RNA-guided endonuclease-induced mutations in unintended target zones (150, 155). *In silico* libraries as the sgDesigner tool can be used to optimize the design of novel plasmids by including both the single- guide RNA and the target site that was not used before (150). In addition, implementing Cas9 variants such as Cas9 nickase has also been used to induce single-stranded breaks combined with a single-guide RNA in order to produce double-stranded DNA breaks at the desired location (150).

Overcoming the fabrication complexity of patient-derived organoids

Organotypic models provide a superior potential in patient-specific cellular heterogeneity, molecular phenotypes, tissue–stratum architecture, and geometry (156). Bioprinting may help fabricate PDO fabrication in a more precise and automated manner compared to conventional PDO production. Specifically, the layer-by-layer strategy of bioprinting can help to generate spatial-specific cell distribution and ECM architecture in PDO fabrication (Figure 8B). This strategy is empowered by inkjet/extrusion, laser-assisted, and stereolithography bioprinting methods (120, 157–159). For example, a 3D digital light processing bioprinting/HTS study was conducted to bioprint hepatocellular carcinomas and HUVECs in 96-well plates (160). The bioprinted gelatin methacryloyl (GelMa)–based construct had the dimensions of 2.4 mm × 2.4 mm × 250 μm, highlighting the spatial precision of Digital light processing bioprinting (DLP) technology required for HTS.

Digital light processing bioprinting technology has enhanced the resolution (~10 times) of bioprinted PDOs, which has been one notable barrier with nozzle extrusion (159–162). In addition, digital light processing bioprinting offers a shear stress–free advantage over extrusion bioprinting by reducing potential cell damage during organotypic assembly (66, 158, 162). This shear stress–free printing method achieves a cell viability of ≥90% within the 3D-printed construct, whereas that of extrusion bioprinting is 40%–80% (66). Concerning multiple gradients in the printed assembly, digital light processing bioprinting presents a dynamic gradient tunability needed for proper recapitulation of complex anatomical structures compared to that of extrusion bioprinting (163). In addition, a low amount of bioink waste is found while changing the gradients using digital light processing bioprinting combined with microfluidic technology (163). Digital light bioprinting also allows to swiftly produce photopolymerized 3D constructs *via* a projected light (66, 160–162) (Figure 8B).

Typically speaking, the resolution of digital light processing bioprinting meets the need of organoid bioprinting (158, 159, 161).

For instance, the resolution for inkjet/extrusion and laser-assisted bioprinting is ~50–500 μm and ~100 μm, respectively, while digital light processing bioprinting can achieve as high as 50-μm resolution (161, 162, 164). In general, digital light processing bioprinting take up to 40 min to entirely bioprint a 96-well plate (160) at the speed of 0.5–15 mm/s (164). Extrusion bioprinting has been reported to have longer fabrication times, 10–50 μm/s (165), because of the interaction between the bioink viscoelasticity and the extrusion nozzle size (166, 167). Given that the resolution necessary for the cell-laden tumor organotypic models is below 100 μm (161), the high-resolution capability of digital light processing bioprinting will allow precise fabrication of H&N PDO models without comprising the time cost. The increased resolution of 3D-printed organ-on-a-chip can also benefit the development of HTS platforms down the road (168).

The challenges of digital light processing bioprinting are the scarce number of photoinitiators such as Eosin Y, Irgacure 819, and lithium phenyl-2,4,6-trimethylbenzoylphosphinate (160, 164) and photo-crosslinking resins like GelMA, methacryloyl hyaluronic acid, and poly(ethylene glycol) diacrylate (159, 162, 164). A deficient concentration of photoinitiators within the construct provokes poor mechanical properties affecting the desired resolution and cell viability (159, 162). Because of that deficiency, proper standardization to balance the photoinitiator and resin concentrations will need to be carried out to achieve the reported cell viability ≥90% (66) and high resolution ≤50 μm (159, 162, 164). Another hurdle of digital light processing bioprinting is the limited incorporation of multiple materials within the 3D cell–based construct (159, 162, 164). However, digital light processing bioprinting can incorporate a multimaterial structure combined with microfluidics to print multiple bioinks (163). Taken into consideration the bioink component accessibility, nozzle extrusion bioprinting remains the most popular bioprinting method for bioprinting (159, 167, 169).

Overcoming the long-term culturing of patient-derived organoids

Microfluidic chips allow the long-term culture of sizable biological micro-/milliscale samples such as PDOs with effective nutrient/waste exchange *via* the dynamic liquid flow within the chip (109). Recent airway-on-a-chip microfluidic platforms, especially those with air–liquid interface feature (170–173), are particularly suitable and adapted for H&N cancer modeling given that the H&N squamous cell carcinomas are constantly exposed to air. However, most airway-on-a-chip devices need pumps to perfuse air and liquid through the air–liquid interface channels, respectively (171–174). This pump requirement presents a critical challenge for the adaption of HTS arrays. To date, non-microfluidic air–liquid interface platforms may incorporate up to 96 individual Transwell plates (175), whereas microfluidic-based air–liquid interface systems are able to integrate up to 64 individual chambers at most (176). None of these are truly considered as high throughput, in which HTS is commonly known as testing hundreds of samples on one array.

That said, one most recent microfluidic platform, developed by Bircsak et al. (177), allowed to house tumor organoids cultures up to 200 individual chambers. This device comprised the use of a multiplexer fluid control, a perfusion rocker platform, and culture chambers overlayed by the three-lane fluid channels. One of the analyses of this liver-on-a-chip platform was to study the drug metabolism of five drugs: phenacetin, coumarin, diclofenac, terfenadine, and phenolphthalein. Adopting such a microfluidic platform with air–liquid interface and pump-free features will present a great leap of advancing in *in vitro* H&N cancer modeling for high-throughput drug screening (**Figure 8C**). Accomplishing the combination of human multiorgan-on-chips (178) and high-throughput testing could benefit personalized anti-cancer therapy screening and discovery to boot (179).

Conclusion

Geometry, multicellularity, and constant irrigation are key features for developing H&N-specific *in vitro* models for drug screening and discovery. Organotypic multicellular spheroid and organoid cultures are highly applicable to approximate cancer-specific TME by mirroring desired geometry and cell–cell/–ECM interactions as presented *in vivo* tumor tissues. Organotypic models can be further combined with microfluidic devices to evaluate the crosstalk between cells and barriers to the mass transport of oxygen, nutrients, and drug therapeutics. Ultimate *in vitro* H&N models can be achieved by incorporating PDOs, air–liquid interface, and high-throughput readouts for *de novo* oncology drug discovery and evaluation. The adoption of such a tumor-on-a-chip platform is expected to minimize the need of animal models and reduce the chance of failures in clinical trials for translational research.

Authors contributions

CM-G: Conceptualization, visualization, writing-original draft, reviewing and editing. NL-J: Conceptualization, visualization, writing-original draft, reviewing and editing, supervision, funding acquisition. MT: Conceptualization, visualization, writing-original draft, reviewing and editing, supervision. HO: visualization, writing-reviewing and editing. NS: writing-reviewing and editing. JL: writing-reviewing and editing. All authors contributed to the article and approved the submitted version.

Funding

This study was supported by the National Sciences and Engineering Research Council of Canada (RGPIN-2018–03843 and ALLRP 548623-19; PI: N.L.-J.), Canada Research Chair research stipend (J.Y.L., M.T., N.L.-J.) and the National Institutes of Health (R01 DC-018577-01A1). The presented content is solely the responsibility of the authors and does not necessarily represent the official views of the above funding agencies.

Acknowledgments

We thank Dr.S. Yo Kishimoto and HO's team for their work in obtaining permission for the clinical figure.

Conflict of interest

The authors declare that the research was conducted in the absence of any commercial or financial relationships that could be construed as a potential conflict of interest.

Publisher's note

References

1. Wouters OJ, McKee M, Luyten J. Estimated research and development investment needed to bring a new medicine to market, 2009-2018. *JAMA J Am Med Assoc* (2020) 323(9):844–53. doi: 10.1001/jama.2020.1166

2. IQVIA Institute for Human Data Science. *Global trends in r & d: Overview through 2021*. Available at: https://www.iqvia.com/insights/the-iqvia-institute/reports/global-trends-in-r-and-d-2022.

3. Mailankody S, Prasad V. Five years of cancer drug approvals: Innovation, efficacy, and costs. *JAMA Oncol* (2015) 1(4):539–40. doi: 10.1001/jamaoncol.2015.0373

4. National Cancer Institute. *Drugs approved for head and neck cancer*. National Cancer Institute (2021) National Institutes of Health, Maryland, USA. p. 1. Available at: http://www.cancer.gov/about-cancer/treatment/drugs/head-neck.

5. Kowalski LP, Coletta RD, Salo T, Maschietto M, Chojniak R, Lima JM, et al. Head and neck cancer: Emerging concepts in biomarker discovery and opportunities for clinical translation. *Clin Transl Med* (2020) 10(7):3–7. doi: 10.1002/ctm2.209

6. Chen SMY, Krinsky AL, Woolaver RA, Wang X, Chen Z, Wang JH. Tumor immune microenvironment in head and neck cancers. *Mol Carcinog* (2020) 59 (7):766–74. doi: 10.1002/mc.23162

7. Jafri MA, Kalamegam G, Abbas M, Al-Kaff M, Ahmed F, Bakhashab S, et al. Deciphering the association of cytokines, chemokines, and growth factors in chondrogenic differentiation of human bone marrow mesenchymal stem cells using an ex vivo osteochondral culture system. *Front Cell Dev Biol* (2020) 7. doi: 10.3389/fcell.2019.00380

8. Croston GE. The utility of target-based discovery. *Expert Opin Drug Discov* (2017) 12(5):427–9. doi: 10.1080/17460441.2017.1308351

9. Moffat JG, Vincent F, Lee JA, Eder J, Prunotto M. Opportunities and challenges in phenotypic drug discovery: An industry perspective. *Nat Rev Drug Discov* (2017) 16(8):531–43. doi: 10.1038/nrd.2017.111

10. Leemans CR, Braakhuis BJM, Brakenhoff RH. The molecular biology of head and neck cancer. *Nat Rev Cancer* (2011) 11(1):9–22. doi: 10.1038/nrc2982

11. Kalyankrishna S, Grandis JR. Epidermal growth factor receptor biology in head and neck cancer. *J Clin Oncol* (2006) 24(17):2666–72. doi: 10.1200/JCO.2005.04.8306

12. Grandis JR, Chakraborty A, Melhem MF, Zeng Q, Tweardy DJ. Inhibition of epidermal growth factor receptor gene expression and function decreases proliferation of head and neck squamous carcinoma but not normal mucosal epithelial cells. *Oncogene* (1997) 15(4):409–16. doi: 10.1038/sj.onc.1201188

13. Cramer JD, Burtness B, Le QT, Ferris RL. The changing therapeutic landscape of head and neck cancer. *Nat Rev Clin Oncol* (2019) 16(11):669–83. doi: 10.1038/s41571-019-0227-z

14. Bahcecioglu G, Basara G, Ellis BW, Ren X, Zorlutuna P. Breast cancer models: Engineering the tumor microenvironment. *Acta Biomater* (2020) 106:1–21. doi: 10.1016/j.actbio.2020.02.006

15. Kim M, Mun H, Sung CO, Cho EJ, Jeon HJ, Chun SM, et al. Patient-derived lung cancer organoids as *in vitro* cancer models for therapeutic screening. *Nat Commun* (2019) 10(1):1–15. doi: 10.1038/s41467-019-11867-6

16. Broutier L, Mastrogiovanni G, Verstegen MMA, Francies HE, Gavarró LM, Bradshaw CR, et al. Human primary liver cancer-derived organoid cultures for disease modeling and drug screening. *Nat Med* (2017) 23(12):1424–35. doi: 10.1038/nm.4438

17. Utispan K, Koontongkaew S. Fibroblasts and macrophages: Key players in the head and neck cancer microenvironment. *J Oral Biosci* (2017) 59(1):23–30. doi: 10.1016/j.job.2016.11.002

18. Curry JM, Sprandio J, Cognetti D, Luginbuhl A, Bar-Ad V, Pribitkin E, et al. Tumor microenvironment in head and neck squamous cell carcinoma. *Semin Oncol* (2014) 41(2):217–34. doi: 10.1053/j.seminoncol.2014.03.003

19. Peltanova B, Raudenska M, Masarik M. Effect of tumor microenvironment on pathogenesis of the head and neck squamous cell carcinoma: A systematic review. *Mol Cancer* (2019) 18(1):1–24. doi: 10.1186/s12943-019-0983-5

20. Alsahafi E, Begg K, Amelio I, Raulf N, Lucarelli P, Sauter T, et al. Clinical update on head and neck cancer: molecular biology and ongoing challenges. *Cell Death Dis* (2019) 10(8):1–17. doi: 10.1038/s41419-019-1769-9

21. Marquard FE, Jücker M. PI3K/AKT/mTOR signaling as a molecular target in head and neck cancer. *Biochem Pharmacol* (2020) 172:113729. doi: 10.1016/j.bcp.2019.113729

22. Fujii N, Shomori K, Shiomi T, Nakabayashi M, Takeda C, Ryoke K, et al. Cancer-associated fibroblasts and CD163-positive macrophages in oral squamous cell carcinoma: Their clinicopathological and prognostic significance. *J Oral Pathol Med* (2012) 41(6):444–51. doi: 10.1111/j.1600-0714.2012.01127.x

23. Zhang Z, Dong Z, Lauxen IS, Filho MSA, Nör JE. Endothelial cell-secreted EGF induces epithelial to mesenchymal transition and endows head and neck cancer cells with stem-like phenotype. *Cancer Res* (2014) 74(10):2869–81. doi: 10.1158/0008-5472.CAN-13-2032

24. Álvarez-Teijeiro S, García-Inclán C, Villaronga MÁ, Casado P, Hermida-Prado F, Granda-Díaz R, et al. Factors secreted by cancer-associated fibroblasts that sustain cancer stem properties in head and neck squamous carcinoma cells as potential therapeutic targets. *Cancers (Basel)* (2018) 10(9):334. doi: 10.3390/cancers10090334

25. Saint A, Van Obberghen-Schilling E. The role of the tumor matrix environment in progression of head and neck cancer. *Curr Opin Oncol* (2021) 33(3):168–74. doi: 10.1097/CCO.0000000000000730

26. Zhang X, Shi M, Chen T, Zhang B. Characterization of the immune cell infiltration landscape in head and neck squamous cell carcinoma to aid immunotherapy. *Mol Ther Nucleic Acids* (2020) 22:298–309. doi: 10.1016/j.omtn.2020.08.030

27. Pai SI, Zandberg DP, Strome SE. The role of antagonists of the PD-1:PD-L1/PD-L2 axis in head and neck cancer treatment. *Oral Oncol* (2016) 61:152–8. doi: 10.1016/j.oraloncology.2016.08.001

28. Larkins E, Blumenthal GM, Yuan W, He K, Sridhara R, Subramaniam S, et al. FDA Approval summary: Pembrolizumab for the treatment of recurrent or metastatic head and neck squamous cell carcinoma with disease progression on or after platinum-containing chemotherapy. *Oncologist* (2017) 22(7):873–8. doi: 10.1634/theoncologist.2016-0496

29. Curry JM, Sprandio J, Cognetti D, Luginbuhl A, Bar-Ad V, Pribitkin E, et al. Tumor microenvironment in head and neck squamous cell carcinoma. *Semin Oncol* (2014) 41(2):217–34. doi: 10.1053/j.seminoncol.2014.03.003

30. Schmieder A, Michel J, Schönhaar K, Goerdt S, Schledzewski K. Differentiation and gene expression profile of tumor-associated macrophages. *Semin Cancer Biol* (2012) 22(4):289–97. doi: 10.1016/j.semcancer.2012.02.002

31. Li B, Ren M, Zhou X, Han Q, Cheng L. Targeting tumor-associated macrophages in head and neck squamous cell carcinoma. *Oral Oncol* (2020) 106:104723. doi: 10.1016/j.oraloncology.2020.104723

32. Schmidt M, Scholz CJ, Polednik C, Roller J. Spheroid-based 3-dimensional culture models: Gene expression and functionality in head and neck cancer. *Oncol Rep* (2016) 35(4):2431–40. doi: 10.3892/or.2016.4581

33. Melissaridou S, Wiechec E, Magan M, Jain MV, Chung MK, Farnebo L, et al. The effect of 2D and 3D cell cultures on treatment response, EMT profile and stem cell features in head and neck cancer 11 medical and health sciences 1112 oncology and carcinogenesis. *Cancer Cell Int* (2019) 19(1):1–10. doi: 10.1186/s12935-019-0733-1

34. Azharuddin M, Roberg K, Dhara AK, Jain MV, Darcy P, Hinkula J, et al. Dissecting multi drug resistance in head and neck cancer cells using multicellular tumor spheroids. *Sci Rep* (2019) 9(1):1–12. doi: 10.1038/s41598-019-56273-6

35. Langhans SA. Three-dimensional *in vitro* cell culture models in drug discovery and drug repositioning. *Front Pharmacol* (2018) 9:1–14. doi: 10.3389/fphar.2018.00006

36. Pinto B, Henriques AC, Silva PMA, Bousbaa H. Three-dimensional spheroids as *in vitro* preclinical models for cancer research. *Pharmaceutics* (2020) 12(12):1–38. doi: 10.3390/pharmaceutics12121186

37. Lamichhane SP, Arya N, Kohler E, Xiang S, Christensen J, Shastri VP. Recapitulating epithelial tumor microenvironment *in vitro* using three dimensional tri-culture of human epithelial, endothelial, and mesenchymal cells. *BMC Cancer* (2016) 16(1):1–12. doi: 10.1186/s12885-016-2634-1

38. Nash CE, Mavria G, Baxter EW, Holliday DL, Tomlinson DC, Treanor D, et al. Development and characterisation of a 3D multi-cellular *in vitro* model of normal human breast: A tool for cancer initiation studies. *Oncotarget* (2015) 6 (15):13731–41. doi: 10.18632/oncotarget.3803

39. Lazzari G, Nicolas V, Matsusaki M, Akashi M, Couvreur P, Mura S. Multicellular spheroid based on a triple co-culture: A novel 3D model to mimic pancreatic tumor complexity. *Acta Biomater* (2018) 78:296–307. doi: 10.1016/j.actbio.2018.08.008

40. Lin CJ, Grandis JR, Carey TE, Gollin SM, Whiteside TL, Koch WM, et al. Head and neck squamous cell carcinoma cell lines: established models and rationale for selection. *Head Neck J Sci Spec Head Neck* (2007) 29(2):163–88. doi: 10.1002/hed.20478

41. Peltanova B, Liskova M, Gumulec J, Raudenska M, Polanska HH, Vaculovic T, et al. Sensitivity to cisplatin in head and neck cancer cells is significantly affected by patient-derived cancer-associated fibroblasts. *Int J Mol Sci* (2021) 22(4):1–13. doi: 10.3390/ijms22041912

42. Vis MAM, Ito K, Hofmann S. Impact of culture medium on cellular interactions in *in vitro* Co-culture systems. *Front Bioeng Biotechnol* (2020) 8:1–8. doi: 10.3389/fbioe.2020.00911

43. Materne EM, Maschmeyer I, Lorenz AK, Horland R, Schimek KMS, Busek M, et al. The multi-organ chip - a microfluidic platform for long-term multi-tissue coculture. *J Vis Exp* (2015) 2015(98):1–11. doi: 10.3791/52526

44. De Vitis E, La Pesa V, Gervaso F, Romano A, Quattrini A, Gigli G, et al. A microfabricated multi-compartment device for neuron and schwann cell differentiation. *Sci Rep* (2021) 11(1):1–12. doi: 10.1038/s41598-021-86300-4

45. Rodrigues J, Heinrich MA, Teixeira LM, Prakash J. 3D *In vitro* model (R) evolution: Unveiling tumor–stroma interactions. *Trends Cancer* (2021) 7(3):249–64. doi: 10.1016/j.trecan.2020.10.009

46. Joseph JP, Harishankar MK, Pillai AA, Devi A. Hypoxia induced EMT: A review on the mechanism of tumor progression and metastasis in OSCC. *Oral Oncol* (2018) 80:23–32. doi: 10.1016/j.oraloncology.2018.03.004

47. Basheer HA, Pakanavicius E, Cooper PA, Shnyder SD, Martin L, Hunter KD, et al. Hypoxia modulates CCR7 expression in head and neck cancers. *Oral Oncol* (2018) 80:64–73. doi: 10.1016/j.oraloncology.2018.03.014

48. Essid N, Chambard JC, Elgaaïed AB. Induction of epithelial-mesenchymal transition (EMT) and Gli1 expression in head and neck squamous cell carcinoma (HNSCC) spheroid cultures. *Bosn J Basic Med Sci* (2018) 18(4):336–46. doi: 10.17305/bjbms.2018.3243

49. Hattersley SM, Sylvester DC, Dyer CE, Stafford ND, Haswell SJ, Greenman J. A microfluidic system for testing the responses of head and neck squamous cell carcinoma tissue biopsies to treatment with chemotherapy drugs. *Ann BioMed Eng* (2012) 40(6):1277–88. doi: 10.1007/s10439-011-0428-9

50. Orcheston-Findlay L, Hashemi A, Garrill A, Nock V. A microfluidic gradient generator to simulate the oxygen microenvironment in cancer cell culture. *Microelectron Eng* (2018) 195:107–13. doi: 10.1016/j.mee.2018.04.011

51. Grist SM, Nasseri SS, Laplatine L, Schmok JC, Yao D, Hua J, et al. Long-term monitoring in a microfluidic system to study tumour spheroid response to chronic and cycling hypoxia. *Sci Rep* (2019) 9(1):1–13. doi: 10.1038/s41598-019-54001-8

52. Costa EC, Moreira AF, de Melo-Diogo D, Gaspar VM, Carvalho MP, Correia IJ. 3D tumor spheroids: an overview on the tools and techniques used for their analysis. *Biotechnol Adv* (2016) 34(8):1427–41. doi: 10.1016/j.biotechadv.2016.11.002

53. Pozzi S, Scomparin A, Israeli Dangoor S, Rodriguez Ajamil D, Ofek P, Neufeld L, et al. Meet me halfway: Are *in vitro* 3D cancer models on the way to replace *in vivo* models for nanomedicine development? *Adv Drug Deliv Rev* (2021) 175:113760. doi: 10.1016/j.addr.2021.04.001

54. Hagemann J, Jacobi C, Gstoettner S, Welz C, Schwenk-Zieger S, Stauber R, et al. Therapy testing in a spheroid-based 3D cell culture model for head and neck squamous cell carcinoma. *J Vis Exp* (2018) 2018(134):1–8. doi: 10.3791/57012

55. Goričan L, Gole B, Potočnik U. Head and neck cancer stem cell-enriched spheroid model for anticancer compound screening. *Cells* (2020) 9(7):1707. doi: 10.3390/cells9071707

56. Magan M, Wiechec E, Roberg K. CAFs affect the proliferation and treatment response of head and neck cancer spheroids during co-culturing in a unique *in vitro* model. *Cancer Cell Int* (2020) 20(1):1–11. doi: 10.1186/s12935-020-01718-6

57. Kochanek SJ, Close DA, Johnston PA. High content screening characterization of head and neck squamous cell carcinoma multicellular tumor spheroid cultures generated in 384-well ultra-low attachment plates to screen for better cancer drug leads. *Assay Drug Dev Technol* (2019) 17(1):17–36. doi: 10.1089/adt.2018.896

58. Hagemann J, Jacobi C, Hahn M, Schmid V, Welz C, Schwenk-Zieger S, et al. Spheroid-based 3D cell cultures enable personalized therapy testing and drug discovery in head and neck cancer. *Anticancer Res* (2017) 37(5):2201–10. doi: 10.21873/anticanres.11555

59. Santi M, Mapanao AK, Cappello V, Voliani V. Production of 3D tumor models of head and neck squamous cell carcinomas for nanotheranostics assessment. *ACS Biomater Sci Eng* (2020) 6(9):4862–9. doi: 10.1021/acsbiomaterials.0c00617

60. Tanaka N, Osman AA, Takahashi Y, Lindemann A, Patel AA, Zhao M, et al. Head and neck cancer organoids established by modification of the CTOS method can be used to predict *in vivo* drug sensitivity. *Oral Oncol* (2018) 87:49–57. doi: 10.1016/j.oraloncology.2018.10.018

61. Driehuis E, Spelier S, Beltrán Hernández I, de Bree R, M. Willems S, Clevers H, et al. Patient-derived head and neck cancer organoids recapitulate EGFR expression levels of respective tissues and are responsive to EGFR-targeted photodynamic therapy. *J Clin Med* (2019) 8(11):1880. doi: 10.3390/jcm8111880

62. Jung AR, Jung CH, Noh JK, Lee YC, Eun YG. Epithelial-mesenchymal transition gene signature is associated with prognosis and tumor microenvironment in head and neck squamous cell carcinoma. *Sci Rep* (2020) 10 (1):1–11. doi: 10.1038/s41598-020-60707-x

63. Li J, Chen M, Fan X, Zhou H. Recent advances in bioprinting techniques: Approaches, applications and future prospects. *J Transl Med* (2016) 14(1):1–15. doi: 10.1186/s12967-016-1028-0

64. Kitaeva KV, Rutland CS, Rizvanov AA, Solovyeva VV. Cell culture based *in vitro* test systems for anticancer drug screening. *Front Bioeng Biotechnol* (2020) 8:1–9. doi: 10.3389/fbioe.2020.00322

65. Skardal A, Atala A. Biomaterials for integration with 3-d bioprinting. *Ann BioMed Eng* (2015) 43(3):730–46. doi: 10.1007/s10439-014-1207-1

66. Tiwari AP, Thorat ND, Pricl S, Patil RM, Rohiwal S, Townley H. Bioink: a 3D-bioprinting tool for anticancer drug discovery and cancer management. *Drug Discovery Today* (2021) 26(7):1574–90. doi: 10.1016/j.drudis.2021.03.010

67. Affolter A, Lammert A, Kern J, Scherl C, Rotter N. Precision medicine gains momentum: Novel 3D models and stem cell-based approaches in head and neck cancer. *Front Cell Dev Biol* (2021) 9:1–27. doi: 10.3389/fcell.2021.666515

68. Almela T, Tayebi L, Moharamzadeh K. 3D bioprinting for *in vitro* models of oral cancer: Toward development and validation. *Bioprinting* (2021) 22:e00132. doi: 10.1016/j.bprint.2021.e00132

69. Daly AC, Davidson MD, Burdick JA. 3D bioprinting of high cell-density heterogeneous tissue models through spheroid fusion within self-healing hydrogels. *Nat Commun* (2021) 12(1):1–13. doi: 10.1038/s41467-021-21029-2

70. Chakraborty S, DePalma TJ, Skardal A. Increasing accuracy of *In vitro* cancer models: Engineering stromal complexity into tumor organoid platforms. *Adv NanoBiomed Res* (2021) 2100061:2100061. doi: 10.1002/anbr.202100061

71. Jacobi N, Seeboeck R, Hofmann E, Schweiger H, Smolinska V, Mohr T, et al. Organotypic three-dimensional cancer cell cultures mirror drug responses *in vivo*: Lessons learned from the inhibition of EGFR signaling. *Oncotarget* (2017) 8 (64):107423–40. doi: 10.18632/oncotarget.22475

72. Watters KM, Bajwa P, Kenny HA. Organotypic 3D models of the ovarian cancer tumor microenvironment. *Cancers (Basel)* (2018) 10(8):1–10. doi: 10.3390/cancers10080265

73. De Gregorio V, Urciuolo F, Netti PA, Imparato G. *In vitro* organotypic systems to model tumor microenvironment in human papillomavirus (HPV)-related cancers. *Cancers (Basel)* (2020) 12(5):1150. doi: 10.3390/cancers12051150

74. Suryaprakash RTC, Kujan O, Shearston K, Farah CS. Three-dimensional cell culture models to investigate oral carcinogenesis: A scoping review. *Int J Mol Sci* (2020) 21(24):1–17. doi: 10.3390/ijms21249520

75. Ferreira LP, Gaspar VM, Mano JF. Decellularized extracellular matrix for bioengineering physiomimetic 3D *in vitro* tumor models. *Trends Biotechnol* (2020) 38(12):1397–414. doi: 10.1016/j.tibtech.2020.04.006

76. Nele V, Wojciechowski JP, Armstrong JPK, Stevens MM. Tailoring gelation mechanisms for advanced hydrogel applications. *Adv Funct Mater* (2020) 30 (42):2002759. doi: 10.1002/adfm.202002759

77. Zhao L, Huang L, Yu S, Zheng J, Wang H, Zhang Y. Decellularized tongue tissue as an *in vitro* model for studying tongue cancer and tongue regeneration. *Acta Biomater* (2017) 58:122–35. doi: 10.1016/j.actbio.2017.05.062

78. Burghartz M, Lennartz S, Schweinlin M, Hagen R, Kleinsasser N, Hackenberg S, et al. Development of human salivary gland-like tissue *In vitro*. *Tissue Eng Part A* (2018) 24(3–4):301–9. doi: 10.1089/ten.tea.2016.0466

79. Ayuso JM, Vitek R, Swick AD, Skala MC, Wisinski KB, Kimple RJ, et al. Effects of culture method on response to EGFR therapy in head and neck squamous cell carcinoma cells. *Sci Rep* (2019) 9(1):1–9. doi: 10.1038/s41598-019-48764-3

80. Tuomainen K, Al-Samadi A, Potdar S, Turunen L, Turunen M, Karhemo PR, et al. Human tumor–derived matrix improves the predictability of head and neck cancer drug testing. *Cancers (Basel)* (2020) 12(1):1–15. doi: 10.3390/cancers12010092

81. Young M, Rodenhizer D, Dean T, D'Arcangelo E, Xu B, Ailles L, et al. A TRACER 3D Co-culture tumour model for head and neck cancer. *Biomaterials* (2018) 164:54–69. doi: 10.1016/j.biomaterials.2018.01.038

82. Lee J, You JH, Shin D, Roh JL. Ex vivo culture of head and neck cancer explants in cell sheet for testing chemotherapeutic sensitivity. *J Cancer Res Clin Oncol* (2020) 146(10):2497–507. doi: 10.1007/s00432-020-03306-7

83. Engelmann L, Thierauf J, Laureano NK, Stark HJ, Prigge ES, Horn D, et al. Organotypic co-cultures as a novel 3d model for head and neck squamous cell carcinoma. *Cancers (Basel)* (2020) 12(8):1–20. doi: 10.3390/cancers12082330

84. Aisenbrey EA, Murphy WL. Synthetic alternatives to matrigel. *Nat Rev Mater* (2020) 5(7):539–51. doi: 10.1038/s41578-020-0199-8

85. Sivakumar R, Chan M, Shin JS, Nishida-Aoki N, Kenerson HL, Elemento O, et al. Organotypic tumor slice cultures provide a versatile platform for immuno-oncology and drug discovery. *Oncoimmunology* (2019) 8(12):e1670019. doi: 10.1080/2162402X.2019.1670019

86. Qiu Y, Ning D, Zhang P, Curly S, Qiao Y, Ma L, et al. Three-dimensional microtissues as an *in vitro* model for personalized radiation therapy. *Analyst* (2017) 142(19):3605–12. doi: 10.1039/C7AN00794A

87. Gilazieva Z, Ponomarev A, Rutland C, Rizvanov A, Solovyeva V. Promising applications of tumor spheroids and organoids for personalized medicine. *Cancers (Basel)* (2020) 12(10):1–19. doi: 10.3390/cancers12102727

88. Akther F, Little P, Li Z, Nguyen NT, Ta HT. Hydrogels as artificial matrices for cell seeding in microfluidic devices. *RSC Adv* (2020) 10(71):43682–703. doi: 10.1039/D0RA08566A

89. Giannitelli SM, Costantini M, Basoli F, Trombetta M, Rainer A. Electrospinning and microfluidics: An integrated approach for tissue engineering and cancer. In: *Electrofluidodynamic technologies (EFDTs) for biomaterials and medical devices: Principles and advances*. Università Campus Bio-Medico di Roma, Rome, Italy: Elsevier Ltd (2018). p. 139–155 p. doi: 10.1016/B978-0-08-101745-6.00008-6

90. Fitzgerald AA, Li E, Weiner LM. 3D culture systems for exploring cancer immunology. *Cancers (Basel)* (2021) 13(1):1–19. doi: 10.3390/cancers13010056

91. Riley A, Green V, Cheah R, McKenzie G, Karsai L, England J, et al. A novel microfluidic device capable of maintaining functional thyroid carcinoma specimens ex vivo provides a new drug screening platform. *BMC Cancer* (2019) 19(1):1–13. doi: 10.1186/s12885-019-5465-z

92. Al-Samadi A, Poor B, Tuomainen K, Liu V, Hyytiäinen A, Suleymanova I, et al. *In vitro* humanized 3D microfluidic chip for testing personalized immunotherapeutics for head and neck cancer patients. *Exp Cell Res* (2019) 383 (2):111508. doi: 10.1016/j.yexcr.2019.111508

93. Duzagac F, Saorin G, Memeo L, Canzonieri V, Rizzolio F. Microfluidic organoids-on-a-chip: Quantum leap in cancer research. *Cancers (Basel)* (2021) 13 (4):1–35. doi: 10.3390/cancers13040737

94. Bower R, Green VL, Kuvshinova E, Kuvshinov D, Karsai L, Crank ST, et al. Maintenance of head and neck tumor on-chip: Gateway to personalized treatment? *Futur Sci OA* (2017) 3(2):FSO174. doi: 10.4155/fsoa-2016-0089

95. Lugo-Cintrón KM, Ayuso JM, Humayun M, Gong MM, Kerr SC, Ponik SM, et al. Primary head and neck tumour-derived fibroblasts promote lymphangiogenesis in a lymphatic organotypic Co-culture model. *EBioMedicine* (2021) 73:103634. doi: 10.1016/j.ebiom.2021.103634

96. Sharafeldin M, Chen T, Ozkaya GU, Choudhary D, Molinolo AA, Gutkind JS, et al. Detecting cancer metastasis and accompanying protein biomarkers at single cell levels using a 3D-printed microfluidic immunoarray. *Biosens Bioelectron* (2021) 171:112681. doi: 10.1016/j.bios.2020.112681

97. Xie H, Appelt JW, Jenkins RW. Going with the flow: Modeling the tumor microenvironment using microfluidic technology. *Cancers (Basel)* (2021) 13(23):1–26. doi: 10.3390/cancers13236052

98. Yang Y, Wang H. Microfluidic technologies for head and neck cancer: from single-cell analysis to tumor-on-a-chip. In: *Early detection and treatment of head & neck cancers* (2021) Springer. p. 43–62.

99. Akgönüllü S, Bakhshpour M, Pişkin AK, Denizli A. Microfluidic systems for cancer diagnosis and applications. *Micromachines* (2021) 12(11):1349. doi: 10.3390/mi12111349

100. Roh JL, Park JY, Kim EH, Jang HJ, Kwon M. Activation of mitochondrial oxidation by PDK2 inhibition reverses cisplatin resistance in head and neck cancer. *Cancer Lett* (2016) 371(1):20–9. doi: 10.1016/j.canlet.2015.11.023

101. Shang M, Soon RH, Lim CT, Khoo BL, Han J. Microfluidic modelling of the tumor microenvironment for anti-cancer drug development. *Lab Chip* (2019) 19(3):369–86. doi: 10.1039/C8LC00970H

102. Dewhirst MW, Secomb TW. Transport of drugs from blood vessels to tumour tissue. *Nat Rev Cancer* (2017) 17(12):738–50. doi: 10.1038/nrc.2017.93

103. Jin D, Ma X, Luo Y, Fang S, Xie Z, Li X, et al. Application of a microfluidic-based perivascular tumor model for testing drug sensitivity in head and neck cancers and toxicity in endothelium. *RSC Adv* (2016) 6(35):29598–607. doi: 10.1039/C6RA01456A

104. Bērziņa S, Harrison A, Taly V, Xiao W. Technological advances in tumor-on-chip technology: From bench to bedside. *Cancers (Basel)* (2021) 13(16):4192. doi: 10.3390/cancers13164192

105. Eduati F, Utharala R, Madhavan D, Neumann UP, Longerich T, Cramer T, et al. A microfluidics platform for combinatorial drug screening on cancer biopsies. *Nat Commun* (2018) 9(1):1–13. doi: 10.1038/s41467-018-04919-w

106. Cho AN, Jin Y, An Y, Kim J, Choi YS, Lee JS, et al. Microfluidic device with brain extracellular matrix promotes structural and functional maturation of human brain organoids. *Nat Commun* (2021) 12(1):1–23. doi: 10.1038/s41467-021-24775-5

107. Kim SK, Kim YH, Park S, Cho SW. Organoid engineering with microfluidics and biomaterials for liver, lung disease, and cancer modeling. *Acta Biomater* (2021) 132:37–51. doi: 10.1016/j.actbio.2021.03.002

108. Velasco V, Shariati SA, Esfandyarpour R. Microtechnology-based methods for organoid models. *Microsystems Nanoeng* (2020) 6(1):1–13. doi: 10.1038/s41378-020-00185-3

109. Kurth F, Györvary E, Heub S, Ledroit D, Paoletti S, Renggli K, et al. Organs-on-a-chip engineering. In: *Organ-on-a-chip* Academic Press (2020). pp. 47–130.

110. Serex L, Bertsch A, Renaud P. Microfluidics: A new layer of control for extrusion-based 3D printing. *Micromachines* (2018) 9(2):86. doi: 10.3390/mi9020086

111. Bhattacharjee N, Urrios A, Kang S, Folch A. The upcoming 3D-printing revolution in microfluidics. *Lab Chip* (2016) 16(10):1720–42. doi: 10.1039/C6LC00163G

112. Sadeghi N, Khalife S, Mascarella MA, Ramanakumar AV, Richardson K, Joshi AS, et al. Pathologic response to neoadjuvant chemotherapy in HPV-associated oropharynx cancer. *Head Neck* (2020) 42(3):417–25. doi: 10.1002/hed.26022

113. Calpe B, Kovacs WJ. High-throughput screening in multicellular spheroids for target discovery in the tumor microenvironment. *Expert Opin Drug Discov* (2020) 15(8):955–67. doi: 10.1080/17460441.2020.1756769

114. Han SJ, Kwon S, Kim KS. Challenges of applying multicellular tumor spheroids in preclinical phase. *Cancer Cell Int* (2021) 21(1):1–19. doi: 10.1186/s12935-021-01853-8

115. Veninga V, Voest EE. Tumor organoids: Opportunities and challenges to guide precision medicine. *Cancer Cell* (2021) 39(9):1190–201. doi: 10.1016/j.ccell.2021.07.020

116. Wensink GE, Elias SG, Mullenders J, Koopman M, Boj SF, Kranenburg OW, et al. Patient-derived organoids as a predictive biomarker for treatment response in cancer patients. *NPJ Precis Oncol* (2021) 5(1):1–13. doi: 10.1038/s41698-021-00168-1

117. Signati L, Allevi R, Piccotti F, Albasini S, Villani L, Sevieri M, et al. Ultrastructural analysis of breast cancer patient-derived organoids. *Cancer Cell Int* (2021) 21(1):1–13. doi: 10.1186/s12935-021-02135-z

118. Gunti S, Hoke ATK, Vu KP, London NR. Organoid and spheroid tumor models: Techniques and applications. *Cancers (Basel)* (2021) 13(4):1–18. doi: 10.3390/cancers13040874

119. Beato F, Reverón D, Dezsi KB, Ortiz A, Johnson JO, Chen DT, et al. Establishing a living biobank of patient-derived organoids of intraductal papillary mucinous neoplasms of the pancreas. *Lab Investig* (2021) 101(2):204–17. doi: 10.1038/s41374-020-00494-1

120. Qu J, Kalyani FS, Liu L, Cheng T, Chen L. Tumor organoids: synergistic applications, current challenges, and future prospects in cancer therapy. *Cancer Commun* (2021) 41(12):1–23. doi: 10.1002/cac2.12224

121. Nero C, Vizzielli G, Lorusso D, Cesari E, Daniele G, Loverro M, et al. Patient-derived organoids and high grade serous ovarian cancer: from disease modeling to personalized medicine. *J Exp Clin Cancer Res* (2021) 40(1):1–14. doi: 10.1186/s13046-021-01917-7

122. Takahashi N, Higa A, Hiyama G, Tamura H, Hoshi H, Dobashi Y, et al. Construction of *in vitro* patient-derived tumor models to evaluate anticancer agents and cancer immunotherapy. *Oncol Lett* (2021) 21(5):1–12. doi: 10.3892/ol.2021.12667

123. Rae C, Amato F, Braconi C. Patient-derived organoids as a model for cancer drug discovery. *Int J Mol Sci* (2021) 22(7):3483. doi: 10.3390/ijms22073483

124. Karakasheva TA, Kijima T, Shimonosono M, Maekawa H, Sahu V, Gabre JT, et al. Generation and characterization of patient-derived head and neck, oral, and esophageal cancer organoids. *Curr Protoc Stem Cell Biol* (2020) 53(1):1–27. doi: 10.1002/cpsc.109

125. Ben-David U, Ha G, Tseng YY, Greenwald NF, Oh C, Shih J, et al. Patient-derived xenografts undergo murine-specific tumor evolution. *Nat Genet* (2017) 49 (11):1567–75. doi: 10.1038/ng.3967

126. Murayama T, Gotoh N. Patient-derived xenograft models of breast cancer and their application. *Cells* (2019) 8(6):621. doi: 10.3390/cells8060621

127. Crespo M, Vilar E, Tsai SY, Chang K, Amin S, Srinivasan T, et al. Colonic organoids derived from human induced pluripotent stem cells for modeling colorectal cancer and drug testing. *Nat Med* (2017) 23(7):878–84. doi: 10.1038/nm.4355

128. Azar J, Bahmad HF, Daher D, Moubarak MM, Hadadeh O, Monzer A, et al. The use of stem cell-derived organoids in disease modeling: An update. *Int J Mol Sci* (2021) 22(14):7667. doi: 10.3390/ijms22147667

129. Kim EJ, Kang KH, Ju JH. Crispr-cas9: A promising tool for gene editing on induced pluripotent stem cells. *Korean J Intern Med* (2017) 32(1):42–61. doi: 10.3904/kjim.2016.198

130. Matano M, Date S, Shimokawa M, Takano A, Fujii M, Ohta Y, et al. Modeling colorectal cancer using CRISPR-Cas9-mediated engineering of human intestinal organoids. *Nat Med* (2015) 21(3):256–62. doi: 10.1038/nm.3802

131. De Masi C, Spitalieri P, Murdocca M, Novelli G, Sangiuolo F. Application of CRISPR/Cas9 to human-induced pluripotent stem cells: From gene editing to drug discovery. *Hum Genomics* (2020) 14(1):1–12. doi: 10.1186/s40246-020-00276-2

132. Huang L, Holtzinger A, Jagan I, Begora M, Lohse I, Ngai N, et al. Ductal pancreatic cancer modeling and drug screening using human pluripotent stem cell- and patient-derived tumor organoids. *Nat Med* (2015) 21(11):1364–71. doi: 10.1038/nm.3973

133. Pernik MN, Bird CE, Traylor JI, Shi DD, Richardson TE, McBrayer SK, et al. Patient-derived cancer organoids for precision oncology treatment. *J Pers Med* (2021) 11(5):423. doi: 10.3390/jpm11050423

134. Chen D, Wang C-Y. Targeting cancer stem cells in squamous cell carcinoma. *Precis Clin Med* (2019) 2(3):152–65. doi: 10.1093/pcmedi/pbz016

135. Mohan A, Raj Rajan R, Mohan G, Kollenchery Puthenveettil P, Maliekal TT. Markers and reporters to reveal the hierarchy in heterogeneous cancer stem cells. *Front Cell Dev Biol* (2021) 9. doi: 10.3389/fcell.2021.668851

136. Ukai S, Honma R, Sakamoto N, Yamamoto Y, Pham QT, Harada K, et al. Molecular biological analysis of 5-FU-resistant gastric cancer organoids; KHDRBS3 contributes to the attainment of features of cancer stem cell. *Oncogene* (2020) 39(50):7265–78. doi: 10.1038/s41388-020-01492-9

137. Yang L, Shi P, Zhao G, Xu J, Peng W, Zhang J, et al. Targeting cancer stem cell pathways for cancer therapy. In: *Signal transduction and targeted therapy*, vol. Vol. 5. Springer US (2020). doi: 10.1038/s41392-020-0110-5

138. Tang DG. Understanding cancer stem cell heterogeneity and plasticity. *Cell Res* (2012) 22(3):457–72. doi: 10.1038/cr.2012.13

139. Spencer H, Moshkbouymatin N, Webb WR, Joshi A, D'Souza A. Update on the role of emerging stem cell technology in head and neck medicine. *Head Neck* (2021) 43(6):1928–38. doi: 10.1002/hed.26674

140. Nguyen R, Da Won Bae S, Qiao L, George J. Developing liver organoids from induced pluripotent stem cells (iPSCs): An alternative source of organoid generation for liver cancer research. *Cancer Lett* (2021) 508:13–7. doi: 10.1016/j.canlet.2021.03.017

141. Takebe T, Zhang RR, Koike H, Kimura M, Yoshizawa E, Enomura M, et al. Generation of a vascularized and functional human liver from an iPSC-derived organ bud transplant. *Nat Protoc* (2014) 9(2):396–409. doi: 10.1038/nprot.2014.020

142. Lungova V, Thibeault S. Developmental derivation of vocal fold mucosa from human induced pluripotent stem cells. *Protocolexchange* (2019), 1:1–14. doi: 10.21203/rs.2.12611/v1

143. Ota I, Masui T, Kurihara M, Yook JI, Mikami S, Kimura T, et al. Snail-induced EMT promotes cancer stem cell-like properties in head and neck cancer cells. *Oncol Rep* (2016) 35(1):261–6. doi: 10.3892/or.2015.4348

144. Lungova V, Chen X, Wang Z, Kendziorski C, Thibeault SL. Human induced pluripotent stem cell-derived vocal fold mucosa mimics development and responses to smoke exposure. *Nat Commun* (2019) 10(1):1–16. doi: 10.1038/s41467-019-12069-w

145. Zhang M, Vandana JJ, Lacko L, Chen S. Modeling cancer progression using human pluripotent stem cell-derived cells and organoids. *Stem Cell Res* (2020) 49:102063. doi: 10.1016/j.scr.2020.102063

146. Pu J, Frescas D, Zhang B, Feng J. Utilization of TALEN and CRISPR/Cas9 technologies for gene targeting and modification. *Exp Biol Med* (2015) 240 (8):1065–70. doi: 10.1177/1535370215584932

147. Lee DF, Su J, Kim HS, Chang B, Papatsenko D, Zhao R, et al. Modeling familial cancer with induced pluripotent stem cells. *Cell* (2015) 161(2):240–54. doi: 10.1016/j.cell.2015.02.045

148. Choe MS, Kim JS, Yeo HC, Bae CM, Han HJ, Baek K, et al. A simple metastatic brain cancer model using human embryonic stem cell-derived cerebral organoids. *FASEB J* (2020) 34(12):16464–75. doi: 10.1096/fj.202000372R

149. Ho BX, Pek NMQ, Soh BS. Disease modeling using 3D organoids derived from human induced pluripotent stem cells. *Int J Mol Sci* (2018) 19(4):936. doi: 10.3390/ijms19040936

150. Uddin F, Rudin CM, Sen T. CRISPR gene therapy: Applications, limitations, and implications for the future. *Front Oncol* (2020) 10. doi: 10.3389/fonc.2020.01387

151. Asmamaw M. Biologics: Targets and therapy mechanism and applications of CRISPR / cas-9-Mediated genome editing. *Biologics: Targets & Therap* (2021) 15:353–61. doi: 10.2147/BTT.S326422

152. Ramakrishna G, Babu PE, Singh R, Trehanpati N. Application of CRISPR-Cas9 based gene editing to study the pathogenesis of colon and liver cancer using organoids. *Hepatol Int* (2021) 15(6):1309–17. doi: 10.1007/s12072-021-10237-z

153. Ihry RJ, Worringer KA, Salick MR, Frias E, Ho D, Theriault K, et al. P53 inhibits CRISPR-Cas9 engineering in human pluripotent stem cells. *Nat Med* (2018) 24(7):939–46. doi: 10.1038/s41591-018-0050-6

154. Lo YH, Kolahi KS, Du Y, Chang CY, Krokhotin A, Nair A, et al. A crispr/cas9-engineered arid1a-deficient human gastric cancer organoid model reveals essential and nonessential modes of oncogenic transformation. *Cancer Discovery* (2021) 11(6):1562–81. doi: 10.1158/2159-8290.CD-20-1109

155. Zhang XH, Tee LY, Wang XG, Huang QS, Yang SH. Off-target effects in CRISPR/Cas9-mediated genome engineering. *Mol Ther Nucleic Acids* (2015) 4(11): e264. doi: 10.1038/mtna.2015.37

156. Zanoni M, Cortesi M, Zamagni A, Arienti C, Pignatta S, Tesei A. Modeling neoplastic disease with spheroids and organoids. *J Haematol Oncol* (2020) 0:1–15. doi: 10.1186/s13045-020-00931-0

157. Brassard JA, Nikolaev M, Hübscher T, Hofer M, Lutolf MP. Recapitulating macro-scale tissue self-organization through organoid bioprinting. *Nat Mater* (2021) 20(1):22–9. doi: 10.1038/s41563-020-00803-5

158. Daly AC, Prendergast ME, Hughes AJ, Burdick JA. Bioprinting for the biologist. *Cell* (2021) 184(1):18–32. doi: 10.1016/j.cell.2020.12.002

159. Sun W, Starly B, Daly AC, Burdick JA, Groll J, Skeldon G, et al. The bioprinting roadmap. *Biofabrication* (2020) 12(2):022002. doi: 10.1088/1758-5090/ab5158

160. Hwang HH, You S, Ma X, Kwe L, Victorine G, Lawrence N, et al. High throughput direct 3D bioprinting in multiwell plates. *Biofabrication* (2021) 13 (2):025007. doi: 10.1088/1758-5090/ab89ca

161. Li J, Parra-Cantu C, Wang Z, Zhang YS. Improving bioprinted volumetric tumor microenvironments *in vitro*. *Trends Cancer* (2020) 6(9):745–56. doi: 10.1016/j.trecan.2020.06.002

162. Huh JT, Moon YW, Park J, Atala A, Yoo JJ, Lee SJ. Combinations of photoinitiator and UV absorber for cell-based digital light processing (DLP) bioprinting. *Biofabrication* (2021) 13(3):034103. doi: 10.1088/1758-5090/abfd7a

163. Wang M, Li W, Mille LS, Ching T, Luo Z, Tang G, et al. Digital light processing based bioprinting with composable gradients. *Adv Mater* (2022) 34 (1):2107038. doi: 10.1002/adma.202107038

164. Goodarzi Hosseinabadi H, Dogan E, Miri AK, Ionov L. Digital light processing bioprinting advances for microtissue models. *ACS Biomater Sci Eng* (2022) 8(4):1381–95. doi: 10.1021/acsbiomaterials.1c01509

165. Arslan-Yildiz A, El Assal R, Chen P, Guven S, Inci F, Demirci U. Towards artificial tissue models: Past, present, and future of 3D bioprinting. *Biofabrication* (2016) 8(1):014103. doi: 10.1088/1758-5090/8/1/014103

166. Lee B, Kim S, Ko J, Lee SR, Kim Y, Park S, et al. 3D micromesh-based hybrid bioprinting: multidimensional liquid patterning for 3D microtissue engineering. *NPG Asia Mater* (2022) 14(1):1–10. doi: 10.1038/s41427-022-00355-x

167. Suntornnond R, Tan EYS, An J, Chua CK. A mathematical model on the resolution of extrusion bioprinting for the development of new bioinks. *Mater (Basel)* (2016) 9(9):756. doi: 10.3390/ma9090756

168. Cui P, Wang S. Application of microfluidic chip technology in pharmaceutical analysis: A review. *J Pharm Anal* (2019) 9(4):238–47. doi: 10.1016/j.jpha.2018.12.001

169. Betancourt N, Chen X. Review of extrusion-based multi-material bioprinting processes. *Bioprinting* (2022) 25:e00189. doi: 10.1016/j.bprint.2021.e00189

170. Park JY, Ryu H, Lee B, Ha DH, Ahn M, Kim S, et al. Development of a functional airway-on-a-chip by 3D cell printing. *Biofabrication* (2019) 11 (1):015002. doi: 10.1088/1758-5090/aae545

171. Si L, Bai H, Rodas M, Cao W, Oh CY, Jiang A, et al. A human-airway-on-a-chip for the rapid identification of candidate antiviral therapeutics and prophylactics. *Nat BioMed Eng* (2021) 5(8):815–29. doi: 10.1038/s41551-021-00718-9

172. Si L, Prantil-Baun R, Benam KH, Bai H, Rodas M, Burt M, et al. Discovery of influenza drug resistance mutations and host therapeutic targets using a human airway chip. *BioRxiv* (2019) 685552. doi: 10.1101/685552

173. Benam KH, Villenave R, Lucchesi C, Varone A, Hubeau C, Lee HH, et al. Small airway-on-a-chip enables analysis of human lung inflammation and drug responses *in vitro*. *Nat Methods* (2016) 13(2):151–7. doi: 10.1038/nmeth.3697

174. Shrestha J, Ryan ST, Mills O, Zhand S, Razavi Bazaz S, Hansbro PM, et al. A 3D-printed microfluidic platform for simulating the effects of CPAP on the nasal epithelium. *Biofabrication* (2021) 13(3):035028. doi: 10.1088/1758-5090/abe4c1

175. Bluhmki T, Bitzer S, Gindele JA, Schruf E, Kiechle T, Webster M, et al. Development of a miniaturized 96-transwell air–liquid interface human small airway epithelial model. *Sci Rep* (2020) 10(1):1–14. doi: 10.1038/s41598-020-69948-2

176. Jung O, Tung YT, Sim E, Chen YC, Lee E, Ferrer M, et al. Development of human-derived, three-dimensional respiratory epithelial tissue constructs with perfusable microvasculature on a high-throughput microfluidics screening platform. *Biofabrication* (2022) 14(2):025012. doi: 10.1088/1758-5090/ac32a5

177. Schuster B, Junkin M, Kashaf SS, Romero-Calvo I, Kirby K, Matthews J, et al. Automated microfluidic platform for dynamic and combinatorial drug screening of tumor organoids. *Nat Commun* (2020) 11(1):1–12. doi: 10.1038/s41467-020-19058-4

178. Ingber DE. Human organs-on-chips for disease modelling, drug development and personalized medicine. *Nat Rev Genet* (2022) 0123456789. doi: 10.1038/s41576-022-00466-9

179. Zuchowska A, Skorupska S. Multi-organ-on-chip approach in cancer research. *Organs-on-a-Chip* (2022) 4:100014. doi: 10.1016/j.ooc.2021.100014

frontiers | Frontiers in Oncology

TYPE Methods
PUBLISHED 30 August 2022
DOI 10.3389/fonc.2022.950228

OPEN ACCESS

EDITED BY
Marta Cavagnaro,
Sapienza University of Rome, Italy

REVIEWED BY
LI Ping Sun,
Tongji University, China
Nguyen Minh Duc,
Pham Ngoc Thach University of Medicine, Vietnam

*CORRESPONDENCE
Chunyang Zhou
cyzhounscmc@163.com
Man Lu
nscmcphdcyjq@163.com

SPECIALTY SECTION
This article was submitted to Head and Neck Cancer, a section of the journal Frontiers in Oncology

RECEIVED 22 May 2022
ACCEPTED 08 July 2022
PUBLISHED 30 August 2022

CITATION
Yang J, Guo W, Huang R, Xu Z, Zhou C and Lu M (2022) Ultrasound-guided microwave ablation in the treatment of early-stage tongue cancer.
Front. Oncol. 12:950228.
doi: 10.3389/fonc.2022.950228

Ultrasound-guided microwave ablation in the treatment of early-stage tongue cancer

Jianquan Yang[1,2], Wen Guo[3], Rong Huang[3], Zhengmin Xu[3], Chunyang Zhou[3*] and Man Lu[1,2*]

[1]The School of Medicine, University of Electronic Science and Technology of China, Chengdu, China, [2]Department of Ultrasound Medical Center, Sichuan Cancer Hospital and Institute, Sichuan Cancer Center, School of Medicine, University of Electronic Science and Technology of China, Chengdu, China, [3]Institute of Materia Medica, North Sichuan Medical College, Nanchong, China

Background: Tongue cancer is a common malignant tumor of the head and neck. Its treatment methods include surgery, radiotherapy, and chemotherapy. However, these treatments have serious side effects and poor cosmetic effect, so it is urgent to find new treatment methods. We pioneered the use of microwave ablation (MWA) in the treatment of early tongue cancer and achieved good results.

Case Presentation: A 67-year-old woman (Han nationality) was admitted to the hospital because of progressive aggravation of tongue pain. She had a history of tongue pain of more than 1 year. Pathological biopsy showed squamous cell carcinoma; following this, radical operation of the tongue cancer was planned. The preoperative examination showed thyroid occupation in the upper mediastinum region compressing the airway; hence, the risk of general anesthesia was high. Consent was obtained from the patient and her family. Ultrasound-guided MWA was successfully performed under the lingual nerve block. The patient was followed for 1 year. She recovered well with no dysphagia and unclear articulation symptoms, and the cosmetic effect was excellent.

Conclusion: To our knowledge, this is the first case of using MWA for the treatment of early-stage tongue cancer (ESTC). Ultrasound-guided MWA may be used for ESTC that can completely ablate the tumor and retain the function of the tongue, further improving the quality of life of the patient. However, it is only a case report and needs more research to verify the use of MWA in ESTC.

KEYWORDS

ultrasound, microwave ablation, early-stage, tongue cancer, treatment

Introduction

Oral cancer is considered one of the most common malignant tumors of the head and neck. Recent statistical data on oral cancer have shown it to be increasing year by year and accounting for about 4% (1); tongue cancer accounts for a large proportion of oral cancers. Surgery is considered one of the major treatments for tongue cancer, while patients with advanced stage need postoperative radiotherapy and chemotherapy. The major drawback of radical resection of tongue cancer is trauma, which in turn affects the patient's daily life. This adversely affects vital functions of patients such as swallowing, chewing, and speaking. Treatments such as postoperative radiotherapy and chemotherapy will further aggravate these side effects. The 5-year survival rate of these patients is found to be 50%–60% (2), while there is no significant improvement of the survival rate in the past 10 years (3). It is urgent to find new treatments to improve the prognosis of patients with tongue cancers.

With the progress of modern imaging technology, microwave ablation (MWA) has been applied in the treatment of a variety of solid tumors, such as liver cancer, thyroid papillary carcinoma. MWA has been proven to be safe, effective, and minimally invasive (4–6). However, the use of MWA in the treatment of tongue cancer, especially in early-stage tongue cancer (ESTC), has not been reported elsewhere. Herein, we report a case of ultrasound-guided MWA in the treatment of ESTC.

Case presentation

A 67-year-old woman (Han nationality) was admitted to the hospital because of progressive aggravation of tongue pain. She had a history of tongue pain of more than 1 year. Pathological biopsy showed squamous cell carcinoma; following this, radical operation of the tongue cancer was planned. The preoperative examination showed thyroid occupation in the upper mediastinum region compressing the airway; hence, the risk of general anesthesia was high. The doctor convinced them of the issue and advised them to undergo MWA; as a result, consent was given by the patient and family members.

Preoperative examination

There was no abnormality in the blood routine, liver and kidney function, blood coagulation, and ECG. The Ultrasound was performed using Philips EPIQ 7 ultrasound system (10 MHz endocavitary transducer, Bothell, WA, USA) to discover the belly of the right tongue. The tongue was rough, and ulcerative changes of about 0.6 cm in diameter were also observed at about 1 cm from the root of the tongue; there was no obvious tenderness or bleeding by touch (Figure 1A).

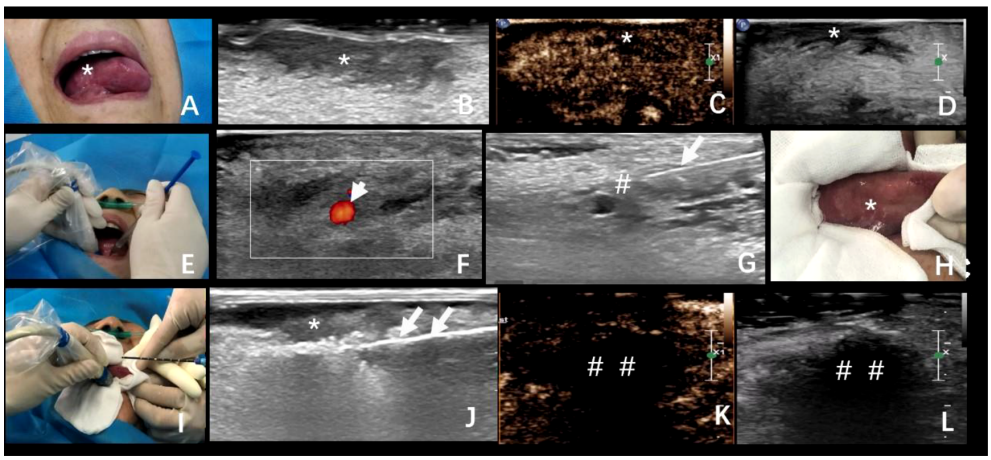

FIGURE 1
(A) A 67-year-old woman with progressive aggravation of tongue pain, and her lesion was confirmed in pathology as squamous cell carcinoma. **(A, B)** Tumor location and ultrasonic image. **(C, D)** Preoperative contrast-enhanced ultrasonography of the tumor. **(E–G)** The process of lingual nerve block guided by ultrasound. **(H)** Protection of the surrounding mucosa before ablation. **(I, J)** The process of ultrasound-guided microwave ablation. The double arrowhead: the ablation needle. **(K, L)** The area of ablation showed no enhancement in the arterial phase and venous phase after ablation. *The exact location of the tumor; #lingual nerve block area; long arrow: puncture needle; ##The area of ablation. Short arrow: Lingual artery; Long arrow: Puncture needle; The double arrowhead: The ablation needle.

Ablation process

The consent was obtained from the patient and her family; the ablation was performed on 20 April 2020. The operation procedure was performed by the doctor with 10 years of experience in interventional ultrasound. First of all, the puncture path was confirmed by traditional and contrast-enhanced ultrasound; this showed low enhancement in the arterial phase and venous phase of the lesion (Figures 1B–D). Further with appropriate sterilization, the patient was given local anesthesia *via* the lingual nerve block with a mixture of 2% lidocaine and ropivacaine (2 ml) (Figures 1E–G). Moreover, during the procedure, critical care has been taken to protect the oral mucosa and normal tongue tissue by ice physiological saline bag (normal saline, 50 ml) with soaked sterile gauze (Figure 1H). Then, the microwave antenna (22G) (model: KY-2450A-1, Kangyou Medical, Nanjing, China) was advanced to the predetermined position in the target hypoechoic nodule by ultrasound guidance. The ablation needle was inserted into the tongue, and the ablation was expanded from the base of the low echo mass to the shallow surface. The output power was 30 W during the procedure (Figures 1I, J), and the operation time lasted for about 10 min. Contrast-enhanced ultrasound showed no enhancement in the arterial phase and venous phase after ablation by injection of 2.4 ml sulfur hexafluoride (Figures 1K, L). After ablation, the gasification range exceeded the boundary of the mass by 1.5 cm. The score of numeric rating scale (NRS) intraoperatively was 0, and 8 h after ablation, the score was 3. Soon afterward, the patient reported to be relieved of pain after ice compress, and there was no symptom of fever or difficulty in chewing.

Postoperative follow-up

Four days after ablation, a scab was formed in the ablation area that was light brown in color (Figure 2A). One week later, the crust fell off with bleeding and hemostasis outside the hospital (Figure 2B). Three weeks later, the crust completely peeled off with mucous membrane growth (Figure 2C). Two months later, scars were formed in the ablation area, with no restriction of tongue movement and difficulty in chewing (Figure 2D). Further follow-up using contrast-enhanced ultrasound in the ablation area revealed slow and low enhancement in the arterial phase and equal enhancement in the venous phase (Figures 2E–G). In order to verify the complete

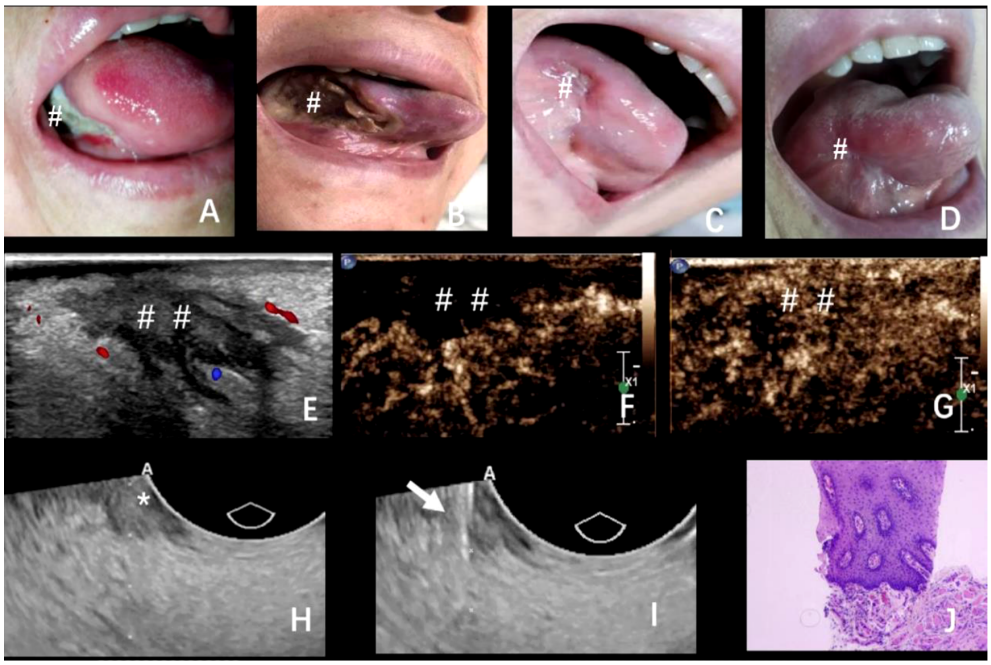

FIGURE 2
(A–D) The changes in the ablation area after the operation at 4, 7, and 21 days and 2 months; **(E–G)** 2 months after the operation, ultrasound examination showed that the ablation area showed patchy low echo, clear boundary, irregular shape, and punctate blood flow signal. Contrast-enhanced ultrasound showed that the ablation area showed slow and low enhancement in the arterial phase and equal enhancement in the venous phase; **(H, I)** Puncture biopsy of different parts of hypoechoic area under the guidance of intracavitary ultrasound; **(J)** Pathological biopsy showed that no cancer cells were found in the ablation area. The arrow: Puncture biopsy needle; * and #The exact location of the lesions; ##The area of ablation.

ablation of the tumor, we used intraluminal ultrasound-guided puncture biopsy in different parts of the hypoechoic area (Figures 2H, I). Moreover, the pathological biopsy showed no cancer cells in the ablation area (Figure 2J). Six months (Figure 3A) and 1 year later (Figure 3B), the patient recovered well after ablation, with no restriction of tongue movement and chewing.

Discussion

Tongue cancer as a common oral malignant tumor, due to the lack of specific clinical symptoms in the early stage, is difficult to distinguish from oral benign diseases. Most of them are diagnosed in the advanced or late stage. It is also noted that the 5-year survival rate of these patients is always less than 60%. Therefore, it is urge to find a new treatment strategy to increase the efficiency in early diagnosis and improve survival time.

CT and MRI are common examination methods for oral diseases, especially tumors, but some early-stage cases and some oral metal foreign bodies cannot be diagnosed qualitatively (7). As a routine imaging examination, ultrasound imaging plays an important role in the staging and restaging of head and neck tumors (8, 9). However, ultrasound images are not much efficient to diagnose the deep position of the oropharynx and floor of the mouth by body surface scanning. In our previous research, the intraluminal probe (frequency 10 MHz) was used to display the tumor location, and puncture biopsy was carried out under the guidance of ultrasound, which improved the positive rate of tumor diagnosis (10). Hence, in this case, we had used intracavitary ultrasound probe, which can clearly show the tumor location and boundary, providing images for tumor ablation.

Surgery is considered the main treatment in tongue cancer patients, while patients with advanced stage undergo postoperative radiotherapy and chemotherapy (11, 12). Radical resection of tongue cancer causes great trauma to the patients and changes the normal anatomical structure and reduces the quality of life of the patients. Moreover, postoperative radiotherapy will further aggravate the patients' speaking and chewing. As a minimally invasive treatment, MWA has the same survival time compared with surgery in hepatocellular carcinoma, especially with diameters less than 3 cm. MWA was also performed in thyroid papillary carcinoma, and the result showed a better therapeutic and cosmetic effect (13–15). In this patient, because of her thyroid occupation, general anesthesia could not be performed. In lingual soft tissue anesthesia, the most commonly used technique is inferior alveolar nerve block, which can induce potential complications such as nerve injury, occlusion, facial nerve paralysis. Some researchers have proven that lingual nerve block is better than inferior alveolar block in oral disease, which can reduce the incidence of abnormal sensation of the lingual nerve and difficulty in mouth opening (16). Therefore, in this case, we used lingual nerve block to anesthetize. After anesthesia, the ablation process was performed successfully and no obvious pain in the process of ablation.

Radical resection of the tongue cancer is the main treatment of tongue cancer, but after the operation, it will seriously affect the patients' functions of speaking and chewing and significantly decrease the quality of life of the patients. At the same time, postoperative radiotherapy will further aggravate the patients' speaking and swallowing function (17–19). As a minimally invasive treatment, MWA not only kills the tumor but also retains the integrity of organs and improve the cosmetic effect. In this case, moderate pain occurred within 8 h after the operation and relieved after ice compress. During the postoperative follow-up, we found that scab was formed gradually in the ablation area. One month later, a scar was formed in the ablation area, and there were no symptoms of dysphagia and unclear articulation. In early-stage liver cancer, MWA is carried out for those patients who cannot tolerate surgery. Studies have also shown that there is no difference in overall survival time in patients who have undergone MWA or radical surgery (20). However, patients undergoing ablation have a higher local recurrence rate (21), which may be related to the enhancement of invasiveness of residual tumor cells caused by incomplete ablation (22). Two months later, complete ablation was confirmed by puncture biopsy, and the curative effect was evaluated as complete remission (CR). Hence, this case implied that MWA may be safe and effective in the treatment of ESTC.

To our knowledge, this is the first case to explore the use of MWA in the treatment of ESTC. There are a few shortcomings: first, it is a case report; second, the patient's follow-up time was short. In order to use MWA in the treatment of tongue cancer, multicenter large-sample studies are needed in order prove its efficacy and safety.

Conclusion

Ultrasound-guided MWA may be used for ESTC, which can completely ablate the tumor and retain the function of the tongue, further improving the quality of life of the patient. However, it is only a case report and needs more research to verify the use of MWA in ESTC.

FIGURE 3
(A, B) The changes in the ablation area after the operation at 6 months **(A)** and 1 year **(B)**. #The exact location of the lesions.

Data availability statement

The raw data supporting the conclusions of this article will be made available by the authors, without undue reservation.

Ethics statement

The studies involving human participants were reviewed and approved by the Ethics Committee of Sichuan Cancer Hospital. The patients/participants provided their written informed consent to participate in this study. Written informed consent was obtained from the individual(s) for the publication of any potentially identifiable images or data included in this article.

Author contributions

JY, WG and RH carried out the concepts, design, data acquisition, data analysis and manuscript preparation. ZX provided assistance for data acquisition, data analysis. CZ and ML performed manuscript review. All authors contributed to the article and approved the submitted version.

Funding

This study was supported by funds from National Key Research and Development Program (NO. 2019YFE0196700); Sichuan Medical Association Project (No. S19012).

Conflict of interest

The authors declare that the research was conducted in the absence of any commercial or financial relationships that could be construed as a potential conflict of interest.

Publisher's note

All claims expressed in this article are solely those of the authors and do not necessarily represent those of their affiliated organizations, or those of the publisher, the editors and the reviewers. Any product that may be evaluated in this article, or claim that may be made by its manufacturer, is not guaranteed or endorsed by the publisher.

References

1. Siegel R, Miller K, Goding Sauer A, Fedewa S, Butterly L, Anderson J, et al. Colorectal cancer statistics, 2020. *CA Cancer J Clin* (2020) 70(3):145–64. doi: 10.3322/caac.21601

2. Brouwer AF, Eisenberg MC, Meza R. Case studies of gastric, lung, and oral cancer connect etiologic agent prevalence to cancer incidence. *Cancer Res* (2018) 78 (12):3386–96. doi: 10.1158/0008-5472.Can-17-3467

3. Zeng H, Chen W, Zheng R, Zhang S, Ji JS, Zou X, et al. Changing cancer survival in China during 2003-15: a pooled analysis of 17 population-based cancer registries. *Lancet Glob Health* (2018) 6(5):e555–67. doi: 10.1016/s2214-109x(18) 30127-x

4. Chi J, Ding M, Shi Y, Wang T, Cui D, Tang X, et al. Comparison study of computed tomography-guided radiofrequency and microwave ablation for

pulmonary tumors: A retrospective, case-controlled observational study. *Thorac Cancer* (2018) 9(10):1241–8. doi: 10.1111/1759-7714.12822

5. Liang P, Dong B, Yu X, Yu D, Wang Y, Feng L, et al. Prognostic factors for survival in patients with hepatocellular carcinoma after percutaneous microwave ablation. *Radiology* (2005) 235(1):299–307. doi: 10.1148/radiol.2351031944

6. Chu KF, Dupuy DE. Thermal ablation of tumours: biological mechanisms and advances in therapy. *Nat Rev Cancer* (2014) 14(3):199–208. doi: 10.1038/nrc3672

7. Künzel J, Strieth S, Wirth G, Bozzato A. Ultrasound in the re-staging of cervical metastases after chemoradiotherapy for head and neck cancer. *Ultraschall Med* (2018) 39(6):659–66. doi: 10.1055/a-0573-0908

8. Lin CM, Wang CP, Chen CN, Lin CY, Li TY, Chou CH, et al. The application of ultrasound in detecting lymph nodal recurrence in the treated neck of head and neck cancer patients. *Sci Rep* (2017) 7(1):3958. doi: 10.1038/s41598-017-04039-3

9. Kajanti M, Holsti LR, Holsti P. Radical surgery and postoperative split-course radiotherapy in squamous cell carcinoma of the mobile tongue: factors influencing local control and the time to recurrence. *Radiother Oncol* (1991) 22(3):174–9. doi: 10.1016/0167-8140(91)90021-8

10. Wei T, Lu M, Wang L, Jiang Z, Wu M, Li J, et al. Contrast-enhanced ultrasound guided transoral core needle biopsy: A novel, safe and well-tolerated procedure for obtaining high-quality tissue in patients with oral cancer. *Ultrasound Med Biol* (2020) 46(12):3210–7. doi: 10.1016/j.ultrasmedbio.2020.09.001

11. Minamiyama S, Mitsudo K, Hayashi Y, Iida M, Iwai T, Nakashima H, et al. Retrograde superselective intra-arterial chemotherapy and daily concurrent radiotherapy for T2-4N0 tongue cancer: Control of occult neck metastasis. *Oral Surg Oral Med Oral Pathol Oral Radiol* (2017) 124(1):16–23. doi: 10.1016/j.oooo.2017.02.004

12. Christopherson K, Morris CG, Kirwan JM, Amdur RJ, Dziegielewski PT, Boyce BJ, et al. Radiotherapy alone or combined with chemotherapy for base of tongue squamous cell carcinoma. *Laryngoscope* (2017) 127(7):1589–94. doi: 10.1002/lary.26460

13. Yue WW, Qi L, Wang DD, Yu SJ, Wang XJ, Xu HX, et al. US-Guided microwave ablation of low-risk papillary thyroid microcarcinoma: Longer-term results of a prospective study. *J Clin Endocrinol Metab* (2020) 105(6):1791–800. doi: 10.1210/clinem/dgaa128

14. Cui T, Jin C, Jiao D, Teng D, Sui G. Safety and efficacy of microwave ablation for benign thyroid nodules and papillary thyroid microcarcinomas: A systematic review and meta-analysis. *Eur J Radiol* (2019) 118:58–64. doi: 10.1016/j.ejrad.2019.06.027

15. Song Z, Liu T, Chen J, Ge C, Zhao F, Zhu M, et al. HIF-1α-induced RIT1 promotes liver cancer growth and metastasis and its deficiency increases sensitivity to sorafenib. *Cancer Lett* (2019) 460:96–107. doi: 10.1016/j.canlet.2019.06.016

16. Balasubramanian S, Paneerselvam E, Guruprasad T, Pathumai M, Abraham S, Krishnakumar Raja VB. Efficacy of exclusive lingual nerve block versus conventional inferior alveolar nerve block in achieving lingual soft-tissue anesthesia. *Ann Maxillofac Surg* (2017) 7(2):250–5. doi: 10.4103/ams.ams_65_17

17. Elfring T, Boliek CA, Winget M, Paulsen C, Seikaly H, Rieger JM. The relationship between lingual and hypoglossal nerve function and quality of life in head and neck cancer. *J Oral Rehabil* (2014) 41(2):133–40. doi: 10.1111/joor.12116

18. Jamal N, Erman A, Chhetri DK. Transoral partial epiglottidectomy to treat dysphagia in post-treatment head and neck cancer patients: a preliminary report. *Laryngoscope* (2014) 124(3):665–71. doi: 10.1002/lary.24278

19. Shin YS, Koh YW, Kim SH, Jeong JH, Ahn S, Hong HJ, et al. Radiotherapy deteriorates postoperative functional outcome after partial glossectomy with free flap reconstruction. *J Oral Maxillofac Surg* (2012) 70(1):216–20. doi: 10.1016/j.joms.2011.04.014

20. Fang Y, Chen W, Liang X, Li D, Lou H, Chen R, et al. Comparison of long-term effectiveness and complications of radiofrequency ablation with hepatectomy for small hepatocellular carcinoma. *J Gastroenterol Hepatol* (2014) 29(1):193–200. doi: 10.1111/jgh.12441

21. Lee HW, Lee JM, Yoon JH, Kim YJ, Park JW, Park SJ, et al. A prospective randomized study comparing radiofrequency ablation and hepatic resection for hepatocellular carcinoma. *Ann Surg Treat Res* (2018) 94(2):74–82. doi: 10.4174/astr.2018.94.2.74

22. Rozenblum N, Zeira E, Scaiewicz V, Bulvik B, Gourevitch S, Yotvat H, et al. Oncogenesis: An "Off-target" effect of radiofrequency ablation. *Radiology* (2015) 276(2):426–32. doi: 10.1148/radiol.2015141695

frontiers | Frontiers in Oncology

TYPE Review
PUBLISHED 29 September 2022
DOI 10.3389/fonc.2022.994172

OPEN ACCESS

EDITED BY
Lorenz Kadletz-Wanke,
Medical University of Vienna, Austria

REVIEWED BY
Dharmendra Kumar Yadav,
Gachon University, South Korea
Saskia Preissner,
Charité Universitätsmedizin Berlin, Germany
Mojgan Alaeddini,
Tehran University of Medical Sciences, Iran

*CORRESPONDENCE
Fei Tan
iatrologist@163.com

†These authors have contributed equally to this work

SPECIALTY SECTION
This article was submitted to Head and Neck Cancer, a section of the journal Frontiers in Oncology

RECEIVED 14 July 2022
ACCEPTED 25 August 2022
PUBLISHED 29 September 2022

CITATION
Li X, Rui X, Li D, Wang Y and Tan F (2022) Plasma oncology: Adjuvant therapy for head and neck cancer using cold atmospheric plasma. *Front. Oncol.* 12:994172. doi: 10.3389/fonc.2022.994172

Plasma oncology: Adjuvant therapy for head and neck cancer using cold atmospheric plasma

Xuran Li[1†], Xiaoqing Rui[2†], Danni Li[1], Yanhong Wang[1] and Fei Tan[1,3,4*]

[1]Shanghai Fourth People's Hospital, and School of Medicine, Tongji University, Shanghai, China, [2]Shanghai East Hospital, Shanghai, China, [3]Department of Surgery, The Royal College of Surgeons in Ireland, Dublin, Ireland, [4]Department of Surgery, The Royal College of Surgeons of England, London, United Kingdom

The worldwide incidence of head and neck cancer (HNC) exceeds half a million cases annually, and up to half of the patients with HNC present with advanced disease. Surgical resection remains the mainstay of treatment for many HNCs, although radiation therapy, chemotherapy, targeted therapy, and immunotherapy might contribute to individual patient's treatment plan. Irrespective of which modality is chosen, disease prognosis remains suboptimal, especially for higher staging tumors. Cold atmospheric plasma (CAP) has recently demonstrated a substantial anti-tumor effect. After a thorough literature search, we provide a comprehensive review depicting the oncological potential of CAP in HNC treatment. We discovered that CAP applies to almost all categories of HNC, including upper aerodigestive tract cancers, head and neck glandular cancers and skin cancers. In addition, CAP is truly versatile, as it can be applied not only directly for superficial or luminal tumors but also indirectly for deep solid organ tumors. Most importantly, CAP can work collaboratively with existing clinical oncotherapies with synergistic effect. After our attempts to elaborate the conceivable molecular mechanism of CAP's anti-neoplastic effect for HNC, we provide a brief synopsis of recent clinical and preclinical trials emphasizing CAP's applicability in head and neck oncology. In conclusion, we have enunciated our vision of plasma oncology using CAP for near future HNC treatment.

KEYWORDS

cold atmospheric plasma, plasma medicine, head and neck cancer, clinical application, plasma oncology

1 Introduction

1.1 Head and neck cancer and its treatment

Head and neck cancer (HNC) was the seventh most common cancer worldwide and comprise of tumors affecting the upper aerodigestive tract (1, 2). HNC encompasses three categories: the upper aerodigestive tract cancers (oral cavity, nasal cavity, paranasal sinuses, pharynx, and larynx), head and neck glandular cancers (thyroid gland and salivary gland), and head and neck skin cancers. Many head and neck cancers arise from mucosal epithelial cells in the oral cavity, pharynx, and larynx, and the most common histological type is squamous cell carcinoma (SCC) (3). The mainstay treatment paradigm for HNC includes surgery, radiotherapy, and chemotherapy including platinums, taxanes, antimetabolic agents, and DNA damaging agents (4–6) (Table 1). In addition, the immune checkpoint inhibitors, pembrolizumab and nivolumab, have been approved by the FDA for the treatment of cisplatin-refractory recurrent or metastatic head and neck squamous cell carcinoma (HNSCC) (15, 16). Despite receiving these therapies, more than 65% of patients with advanced HNSCC have recurrence or metastasis, and only half of the patients remain alive after five years (17). In addition, advanced HNC is often accompanied by complications and treatment side effects, such as severe infection and persistent tumor ulcers, which further reduce the patients' quality of life. Therefore, there is a great need to explore more treatment modalities for controlling HNC.

1.2 Cold atmospheric plasma

Plasma, the fourth state of matter, has been widely used in industry in the past few decades. Cold atmospheric plasma (CAP) is a partially ionized gas that is generated under atmospheric pressure at room temperature (18). It has been adopted in the medical field because of its host-friendly low temperature. The cold atmospheric plasma can be generated by various technologies. Piezoelectric direct discharge (PDD) is a new technology which is based on the resonant piezoelectric transformer (RPT) principle (19). Compared to the traditional corona discharge (CD) and dielectric barrier discharge (DBD) technology, PDD is more versatile using different excitation structures. The Piezobrush® compact handheld plasma devices, PZ2 and PZ3, are based on PDD technology. In order to improve the potential of CAP, argon (Ar), helium (He), oxygen (O_2), nitrogen (N_2), air, and two or more of them can be utilized to generate CAP.

1.3 CAP's anti-neoplastic effect

The potential contributors by which CAP inhibits cancer development include long-lived and short-lived reactive species, charged particles, pressure gradients, and changes in electromagnetic fields. CAP produces a large number of reactive oxygen species (ROS) and reactive nitrogen species (RNS), which impact tumor cells by increasing their oxidative stress. The RONS could be classified into interconverting long-lived and short-lived reactive species. The short-lived particles include singlet oxygen ($^1O_2$), hydroxyl radicals ($^{\bullet}OH$), superoxide anions (O_2^-), and peroxynitrite ($ONOO^-$). The $^1O_2$ is a highly active molecule that is involved in the apoptosis process and produces cytotoxic chemicals. The O_2^- is also highly reactive and can increase the oxidative stress that the tumor cells are exposed to. The hydroxyl radicals were extremely reactive oxidizing species, which contribute to the oxidation of lipid, nuclide and protein, resulting in cell death. On the other hand, the long-lived particles compromise hydrogen peroxide (H_2O_2), nitrite (HNO_2/NO_2^-), and nitrate (HNO_3/NO_3^-). The effect of the long-lived RONS generated by CAP has been described in the plasma-activated medium (PAM) treatment (Figure 1).

TABLE 1 Commonly used chemotherapeutic drugs for head and neck cancer.

Drug type	Subtype	Commercial drugs	Combined with CAP	Refs
Chemotherapy	Platinum	Cisplatin	Y	(7)
		Carboplatin	NA	(8)
	Taxane	Paclitaxel	NA	(6)
		Docetaxel	NA	(9)
	Antimetabolic agents	Fluorouracil	NA	(10)
		Methotrexate	NA	(11)
		Hydroxyurea	NA	(12)
	DNA damaging agents	Bleomycin sulfate	NA	(4)
Immunotherapy	PD-1 antibodies	Nivolumab	Y	(13)
		Pembrolizumab	NA	(15)
Targeted therapy	EGFR antibodies	Cetuximab	Y	(14)

(EGFR, epidermal growth factor receptor; PD-1, programmed cell death protein 1; Y, yes; NA, not applicable).

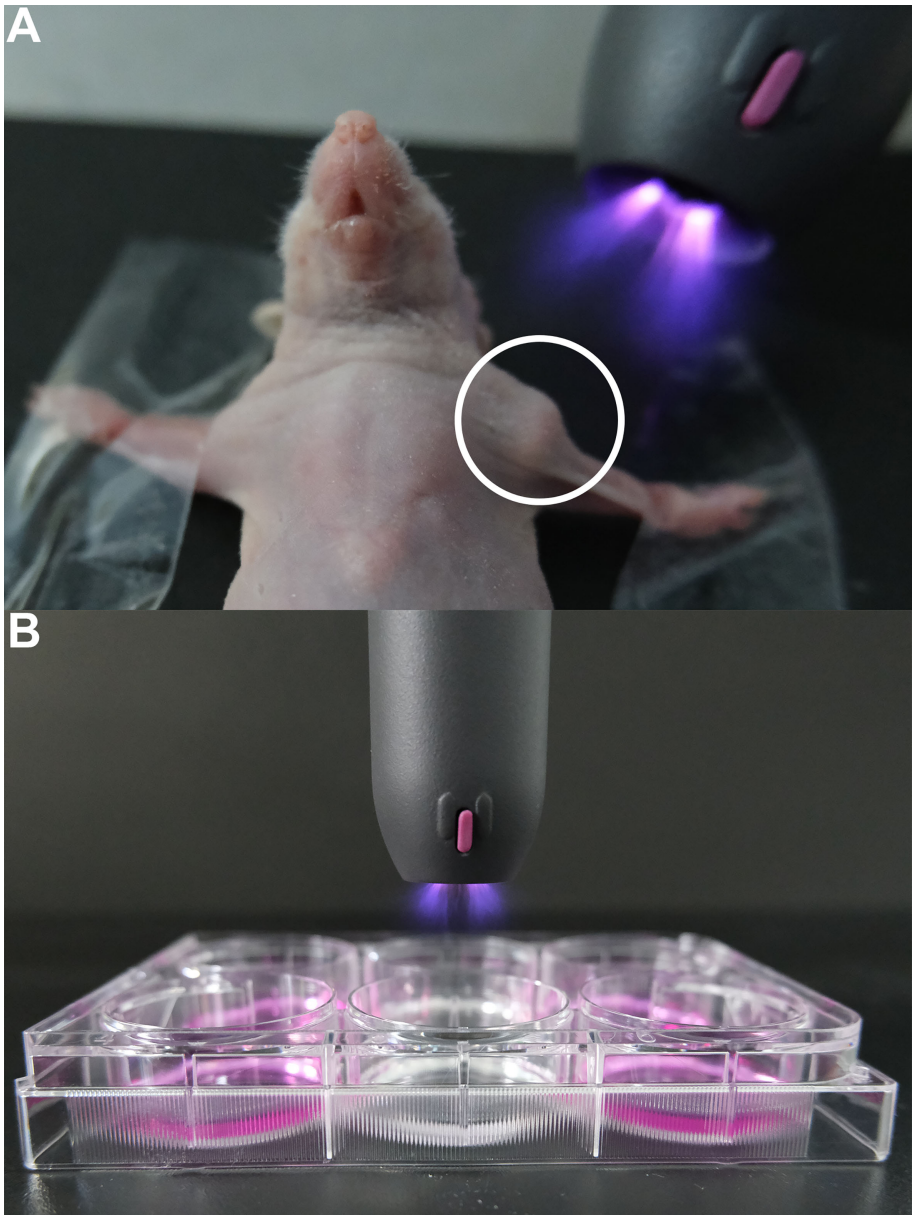

FIGURE 1
Examples of the direct and indirect applications of CAP in HNC plasma oncology. The portable Piezobrush CAP system is used for illustration. **(A)** Direct treatment of human tumor CDX model using CAP (the circle highlights the implanted tumor in an immunodeficient mouse). **(B)** Indirect treatment of HNC cell culture in various media. (CAP, cold atmospheric plasma; CDX, cell line-derived xenograft; HNC, head and neck cancer).

The H_2O_2 entered tumor cells as a secondary messenger for triggering signaling cascades. The NO_2^- and NO_3^- enhance the anti-tumor effect of CAP by generating short-lived $ONOO^-$. In addition, the oxidative stress caused by CAP also modifies the amino acids of proteins, contributing to structure distortion and dysfunction of these proteins (20).

Physical factors are also essential components of CAP. One recent study suggested that magnetic field can induce the activation of cancer cells, rendering them more susceptible to ROS (21). In addition, other physical species produced by CAP include highly energetic photons in the ultraviolet. They can impact energy transport and break chemical bonds in cancer

cells (22). During this process, some proteins and DNA of cells may absorb this energy and turn abnormal. These highly energetic photons can even induce photolysis in liquid, thus producing •OH radicals (23).

1.4 Potential of CAP in HNC treatment

Recently, the potential application of CAP in HNC treatment has increasingly raised attention. Unlike other applications of CAP, such as antimicrobial management and promoting wound healing (24), the applications of CAP in HNC treatment aim at microscopically killing the tumor cells and macroscopically alleviating the tumor-associated symptoms. In order to elucidate the underlying mechanism and demonstrate the therapeutic effect of CAP in HNC treatment, we designed this review with twofold implications, bridging the gap between plasma biotechnology (Table 2) and clinical oncology (Table 3). Horizontally, we discussed HNCs that apply to CAP treatment, based on their anatomical subsites. Vertically, we interpreted the molecular mechanisms of CAP therapy for each subtype of HNCs (Figure 2). Finally, we provided a summary of the latest examples of successful preclinical and clinical trials using adjuvant CAP therapy.

2 Methods

2.1 Literature review process

The PubMed database, Web of Science and Google Scholar were used to search the scientific literature for current researches

TABLE 2 Overview of studies on CAP treatment in head and neck cancer.

Category of cancer	Subtype	Test model	Synopsis	Refs
Head and neck upper aerodigestive tract cancers	SCC	JHU-022, JHU-028, JHU-029 and SCC25 cells	CAP selectively eliminates HNSCC cell lines through non-apoptotic mechanisms, with minimal effect on normal oral epithelial cell lines	(25)
		HSC-2, SCC-15 cells	CAP induces EGFR dysfunction in EGFR-overexpressing oral SCC *via* NO radicals	(26)
		MSKQLL1, SCC1483 cells	among 3 gases, N_2 CAP inhibited cell migration and invasion most potently *via* decreased FAK & MMP	(27)
		FaDu, SNU1041and SNU899 cells, mice	CAP induces apoptosis of HNC cells through a mechanism involving MAPK-dependent mitochondrial ROS	(28)
		SNU1041, SNU1076 and SCC25 cells	PAM induces HNC cell death *via* the upregulation of ATF4/CHOP activity by damaging mitochondria through excessive mtROS accumulation	(29)
		MSK QLL1, SCC1483, SCC15 and SCC25 cells	CAP induced OSCC cell apoptosis through a mechanism involving DNA damage and triggering of sub-G1 arrest *via* the ATM/p53 pathway	(30)
		FaDu, SCC15, SCC-QLL1, SCC1483 andHN6 cells	PAM inhibits tumor progression by increasing the MUL1 level and reducing p-AKT level	(31)
		KYSE-30 cells	CAP induces genotoxicity and cytotoxicity in cancer cells	(32)
		SCC25 cells	the killing efficiency of CAP in the presence of EGFR antibody conjugated GNP is amplified about 18 times	(33)
		SCC25 cells	PD-L1 antibody + GNP + CAP significantly increased the number of dead cancer cells	(13)
		MSKQLL1, SCCQLL1, HN6, SCC25, SCC15, Cal27 and SCC1483 cells	A combination of CAP and cetuximab shows inhibited invasion and migration *via* NF-κB signaling in cetuximab-resistant OSCC cells	(14)
		SCC-15 cells	The synergy of cisplatin & CAP reduces the required dosage of chemotherapy	(34)
Head and neck glandular cancers	thyroid gland cancer	SNU80 cells	The altered antioxidant system stimulates CAP-induced cell death	(35)
		BHP10-3 andTPC1 cells	CAP inhibits cell invasion *via* cytoskeletal modulation and altered MMP-2/-9/uPA activity	(36)
		BCPAP, HTh7, KTC2, 8505C, and FRO-Luc cells	activation of EGR1/GADD45α by CAP mediates thyroid cancer cell death	(37)
		HTH83, U-HTH 7, and SW1763 cells	CAP induces apoptosis in anaplastic thyroid cancer cell lines *via* the JNK signaling pathway and p38 MAPK-dependent ROS	(38)
	parotid gland cancer	HN9 cells	CAP induces apoptosis in HN9 cells	(28)
Head and neck skin cancers	melanoma	A375 cells	combined therapy using PpIX-loaded polymersome-mediated PDT and CAP	(39)
		G-361 cells, mice		(40)

(Continued)

TABLE 2 Continued

Category of cancer	Subtype	Test model	Synopsis	Refs
			CAP & SN synergistically inhibit mitochondrial function *via* the HGF/c-MET signalling pathway	
		G-361 cells	CAP & SN activate autophagy by activating PI3K/mTOR and EGFR pathways	(41)
		L929 cells, mice	both CAP monotherapy and combination with chemotherapy significantly decreased tumor growth	(42)
		Mel Juso cell line	The synergy between CAP-induced RONS and acidic conditions promotes anti-cancer effects	(43)
		A375 and A875 cells	CAP increases Sestrin2 expression and further activates Fas *via* the MAPK signaling pathway	(44)
		SK-Mel-147 cells	CAP inhibits migration and disorganizes the actin cytoskeleton through multiple signaling pathways, using transcriptomic analysis	(45)
		Mel Im cell line	CAP changes the amino acid composition of the cell culture medium and affects the anti-tumor mechanism	(46)
	BCC	TE354T cells	PAM induces apoptosis *via* MAPK signalling pathway	(47)

(ATF4, activating transcription factor 4; ATM, ataxia telangiectasia-mutated gene; BCC, basal cell carcinoma; CAP, cold atmospheric plasma; CHOP, C/EBP homologous protein; c-MET, c-mesenchymal-epithelial transition factor; ECT, electrochemotherapy; EGFR, epidermal growth factor receptor; EGR1, early growth response 1; FAK, focal adhesion kinase; GNP, gold nanoparticles; HGF, hepatocyte growth factor; HNC, head and neck cancer; HNSCC, head and neck squamous cell carcinoma; JNK, c- Jun N-terminal kinase; MAPK, mitogen-activated protein kinase; MCT, multi cellular tumor spheroids; MMP, matrix metalloproteinase; mtROS, mitochondrial reactive oxygen species; mTOR, mammalian target of rapamycin; MUL1, mitochondrial E3 ubiquitin protein ligase1; N_2, nitrogen; NO, nitric oxide; O_2, oxygen; OSCC, oral squamous cell carcinoma; PAM, plasma-activated medium; PDT, photodynamic therapy; PI3K, phosphatidylinositol 3 kinase; PpIX, protoporphyrin IX; PD-L1, programmed death-ligand 1; ROS, reactive oxygen species; RNS, reactive nitrogen species; SCC, squamous cell carcinoma; SMD, surface micro discharging; SN, silymarin).

related to CAP and HNC. The search terms included "head and neck neoplasm OR HNSCC OR HNC" and "cold atmospheric plasma", "cold plasma", "non-thermal atmospheric plasma", "plasma medicine". The final search included CAP-related articles published between 2011 and 2022. These include *in vitro* studies, preclinical studies, and clinical studies.

3 CAP's treatment for head and neck upper aerodigestive tract cancers

The upper aerodigestive tract (ADT) consists of several subsites in the head and neck, serving respiratory and swallowing functions. These include the oral cavity, nasal cavity, paranasal sinuses, pharynx, and larynx. Ninety percent of the head and neck ADT malignant tumors are histologically squamous cell carcinoma (SCC) (54). The incidence of HNSCC is approximately 600,000 cases per year worldwide (55, 56).

3.1 CAP selectively eliminates cancer cells

The oncotherapy using CAP demonstrates selectivity to cancer cells over adjacent healthy cells. Yan et al. conducted a study comparing cancer cells with normal cells and found that CAP showed strong selectivity in most of the chosen cancer cell lines (57). There are multiple reasons for the selectivity of CAP treatment in HNSCC.

3.1.1 Cell cycle factor for CAP's selectivity

CAP's selectivity to HNSCC cells may be related to cell cycle manipulation. It is well known that tumor cells proliferate rapidly, meaning a faster progression of the cell cycle with a high proportion of cells in the S phase. This may render cancer cells more vulnerable to plasma treatment (58). Compared to tumor cells, normal cells at the end of differentiation are rarely in the phase of division. Although data suggested that CAP treatment affects all phases of the cell cycle, the response of cells to CAP treatment varies depending on the phase distribution of the cell cycle. Interestingly, tracer assay and γH2A.X expression study have shown that cells in the S phase were more sensitive to CAP treatment.

3.1.2 Cell membrane factor for CAP's selectivity

There are many differences between tumor cells and normal cells in terms of cell membrane structure. The first difference in the cell membrane is the expression of aquaporin, a protein which is usually more abundant in tumor cells. These proteins function as a selective filter which could facilitate the transportation of small molecules, such as CO_2, NO, and reactive oxygen species (ROS). Recent experiments have shown that increased expression of aquaporin could lead to increased concentration of intracellular ROS concentration, which contributes to the high level of oxidative stress (59). In addition, reduced cholesterol content in tumor cells renders the cell membrane incapable of providing a barrier against the entry of reactive species, such as H_2O_2 (60). Considering the

TABLE 3 Recent preclinical and clinical trials of CAP treatment in head and neck cancer.

Category of cancer	No. of pts	Tumor location & subunits	Staging	Symptomatic improvement	Tumor suppression	Side effects	Refs
Head and neck upper aerodigestive tract cancers (SCC and adenocarcinoma)	12	floor of mouth (n = 5), hypopharynx (n = 1), tonguebase (n= 1), upper jaw (n= 2), lower jaw (n= 3)	T3/4	decreased microbial load, odor, and pain (6/12)	partial remission (4/12)	bad taste, pain, exhaustion, edema, and bleeding	(48)
	21	head and neck	T3/4	vascular stimulation or a contraction of tumor ulceration (4/12)	increased cell apoptosis in CAP-treated tissues	bad taste, pain, sialorrhea, exhaustion, edema, and bleeding	(49)
	2	neck	T3/4	improved microcirculation (2/2) and postoperative wound healing (2/2)	N/A	N/A	(50)
	6	oropharynx	T4	reduced odor and pain (5/6)	partial remission (2/6)	pain, sialorrhea, dry mouth, exhaustion, edema, and bleeding	(51)
	10	mouth (n = 5), cheek (n = 2), tongue (n = 1), retromolar region (n = 1), maxillary sinus (n = 1, adenocarcinoma)	T4	N/A	increased cell apoptosis in CAP-treated tissues	N/A	(52)
Head and neck skin cancers (melanoma)	6	metastatic cutaneous melanoma	T4	decreased secretion of inflammatory cytokines (1/3)	increased cell apoptosis in CAP-treated tissues	N/A	(53)

(CAP, cold atmospheric plasma; pts, patients; SCC, squamous cell carcinoma; N/A, Not available).

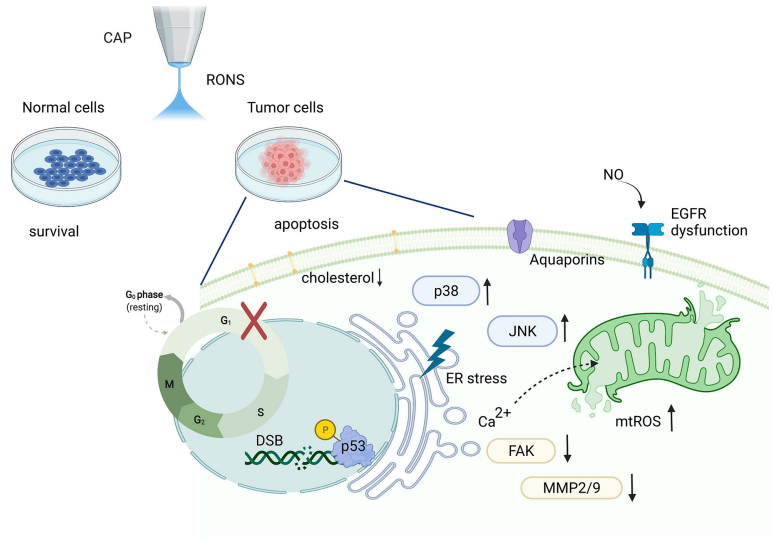

FIGURE 2
Schematics of CAP treatment of HNSCC cells and the potential underlying molecular mechanism. CAP demonstrates selectivity to cancer cells sparing adjacent healthy cells. In addition, CAP treatment induces a series of DNA damage and mitochondrial dysfunction in cancer cells. Moreover, CAP activates several tumor progression-associated signalling pathways, such as the p53 and MAPK signalling pathways. (CAP, cold atmospheric plasma; DSB, DNA double-stranded breakage; EGFR, epidermal growth factor receptor; ER, endoplasmic reticulum; FAK, focal adhesion kinase; MAPK, mitogen-activated protein kinases; MMP, matrix metalloproteinase; mtROS, mitochondrial reactive oxygen species; NO, nitric oxide; JNK, Jun N-terminal kinase; RONS, reactive oxygen and nitrogen species).

high levels of preexisting ROS in cancer cells, additional ROS introduced by CAP could lead to a tipping of the balance with detrimental results.

3.1.3 Cellular receptor factor for CAP's selectivity

The epidermal growth factor receptor (EGFR) plays a vital role in the upper ADT mucosal cells and regulates the cell cycle, cell proliferation, and transformation. It is well known that EGFR is overexpressed in HNSCC cells. Lee et al. reported that the selective killing effect of CAP in oral SCC is associated with NO-induced dysfunction of EGFR (26). Moreover, pretreatment using NO scavenger rescued the dysfunction of the EGFR and the following killing effect.

Irrespective of the contributing factors mentioned above, CAP application could still selectively damage HNSCC cell lines with little effect on normal oral cell lines, in a non-apoptosis-inducing way. Guerrero-preston et al. applied CAP treatment on four HNSCC cell lines (JHU-029, JHU-028, JHU-022, SCC25) and two normal oral mucosa epithelial cell lines (OKF6 and NOKsi) (25). Due to the short duration of CAP treatment, significant apoptosis was not observed in either type of cells. They revealed that CAP selectively impaired HNSCC cell viability in a dose-dependent manner by MTT assays, and the viability of normal cells remained virtually unchanged.

3.2 CAP affects major cellular processes during cancer progression

In general, CAP reduces cell viability, inhibits cell migration, and induces apoptosis in tumor cells (61). There are several underlying molecular mechanisms that may lead to the above changes in tumor cell behavior. These include DNA damage, mitochondrial dysfunction, and other processes.

3.2.1 DNA damage caused by CAP treatment

CAP causes a series of DNA damage in HNSCC cells. The main components of CAP are not only RONS but also charged particles, UV radiation, and electromagnetic fields (62). Previous studies have proven that all these components are associated with DNA damage (63–65). Chang et al. uncovered that the CAP treatment induced DNA double-strand breakage (DSB) and triggered sub-G1 arrest in oral SCC (OSCC) cells (30). Although the cell cycle can be arrested to allow for the repair of DNA damage, but if the damage is overwhelming and beyond repair, apoptosis will be induced. Large-scale image analysis has found that S phase-gathering cells were more susceptible to DNA damage than either G1 or G2 phase-gathering cells. Tumor cells happen to be mostly in the S phase due to their dividing nature. These results confirm that CAP induces DNA damage, particularly in cancer cells (32, 66).

3.2.2 Mitochondrial dysfunction caused by CAP treatment

HNSCC cells exhibit reduced mitochondrial function and elevated numbers of disrupted mitochondria after CAP treatment. Specifically, an RNA sequencing analysis revealed that the mitochondrial oxidative phosphorylation-related genes tended to be down-regulated after CAP irradiation (29). Further experiments not only confirmed the accumulation of mitochondrial reactive oxygen species (mtROS) but also revealed that this was associated with ATF4/CHOP regulation using transcriptomic analysis. In addition, an increased level of RONS induced by CAP triggered endoplasmic reticulum stress, leading to a calcium influx into mitochondria. As a result, the excess calcium overwhelms the oxidative phosphorylation of mitochondria, decreases mitochondrial membrane potential, and induces mitochondria-related apoptosis.

3.3 CAP activates various signaling pathways in cancer cells

Several tumor progression-associated signaling pathways are activated during CAP treatment. These include, but are not limited to, p53, mitogen-activated protein kinases (MAPK), and other signaling pathways, depending on the mode of plasma treatment.

3.3.1 The p53 signaling pathway is activated after CAP treatment

Under normal circumstances, p53 remains inactivated with a low expression level. When there is DNA damage, it could rapidly activate p53 through upregulation of the ATM gene (67). The activated p53 triggers its downstream effectors, which regulate cell cycle checkpoint and apoptosis (68). Similarly, the ATM/p53 signaling pathway plays an important role in the CAP-induced apoptosis in OSCC. After CAP treatment, the DNA damage triggered the activation of ATM, which led to the phosphorylation of p53. If the DNA damage is severe and cannot be repaired, the Ser 46 of p53 could be phosphorylated by ATM, and apoptosis ensued (30). In addition, indirect treatment using PAM also exerted similar anti-tumor effects to direct CAP treatment. Agene expression analysis showed that p53 pathway-related genes were also highly activated in OSCC cells treated by PAM (69).

3.3.2 The MAPK signaling pathway is activated after CAP treatment

The MAPK signaling pathway is involved in cancer cell proliferation, inflammation, differentiation, migration and apoptosis (70). The main branching nodes of MAPK signaling pathway comprise of extracellular signal-related kinases (ERK1/2), Jun amino-terminal kinases (JNK), and p38 (71). Previous studies suggested that activation of ERK promotes cell proliferation, whereas that of JNK and p38 facilitates cell apoptosis (72). In FaDu cells (from hypopharyngeal SCC), CAP induced increased level of mtROS and apoptosis *via* the MAPK signaling pathway (28). In this study, increased levels of p-p38 and p-JNK were detected after CAP treatment. Blocking the activation of JNK and p38 using inhibitors rescued CAP-induced apoptosis and reduced mitochondrial damage.

3.3.3 Other signaling pathways activated by CAP treatment

During direct CAP treatment of OSCC, tumor cell migration and invasion were inhibited through decreased focal adhesion kinase (FAK) expression and reduced matrix metalloproteinases (MMP2/9) activity (27). In comparison, indirect plasma treatment using PAM induced SCC cell detachment from multi-cellular tumor spheroids (MCTS) in a dose-dependent manner (73). After multiple treatments using PAM, inhibition of cell growth was observed in MCTS, and cell death in 2D cell cultures, respectively. Furthermore, PAM inhibited tumor progression by enhancing the expression of MUL1 and decreasing that of p-AKT in a xenograft tumor model (31).

3.4 CAP provides synergy with other oncotherapies

CAP, when combined with other oncotherapy, has the potential of manifesting synergistic effect. These trialed cancer treatments are mostly chemotherapy, targeted therapy, and immunotherapy.

3.4.1 CAP combined with chemotherapy

Chemotherapy has been used as an anti-HNC treatment for a long time, but its success is not without side effects. Lee et al. reported that the combination of CAP treatment and chemotherapy proved synergistic (34). Their study discovered that this combinatorial treatment could increase the anti-tumor efficacy while reducing the required dosage of chemotherapy medication. This treatment mode greatly reduced the chance of normal cells being mistakenly killed by chemotherapy drugs.

3.4.2 CAP combined with targeted therapy

As mentioned in section 3.1.3, EGFR is overexpressed or constitutively remains activated in HNC. Therefore, blocking EGFR has been regarded as one of the most promising targets for HNC treatment. CAP combined with EGFR antibody-conjugated gold nanoparticles (GNPs) showed high selectivity to tumor cells. It also amplified the anti-neoplastic effect about 18 times compared to plasma treatment in the absence of conjugates (33). Although EGFR has been one of the main molecular targets, only 10–20% of patients with HNSCC are sensitive to anti-EGFR therapy (74). Therefore, a strategy to overcome the resistance to EGFR treatment is clinically required. Cetuximab, a commonly used targeting agent, exerts its anti-tumor effect by competitively binding to EGFR. It is known that cetuximab with chemotherapy as a first-line treatment prolongs survival in HNCs. Interestingly, the combination of CAP and cetuximab showed inhibited invasion and migration in cetuximab-resistant OSCC cells (14). Further experiments revealed that this combination attenuated tumor invasion and migration *via* the NF-κB signaling pathway.

3.4.3 CAP combined with immunotherapy

Programmed cell death protein 1 (PD-1) is an immune-inhibitory receptor expressed by T cells, and is involved in various physiological responses, such as infection, cancer and immune homeostasis. PD-L1, the ligand for PD1, is highly expressed in many cancers, including HNCs. Thus, blocking the PD-1/PD-L1 interaction by antibodies could inhibit tumor progression (75). In Park's latest innovative study, the combination of CAP and immunotherapy showed a synergistic effect (13). They collectively applied CAP and GNP- conjugated PD-L1 antibodies in OSCC cells. This combinatorial treatment significantly increased the number of apoptotic cells when compared to the monotherapy groups.

4 CAP's treatment for head and neck glandular cancers

4.1 Thyroid gland cancers

Located near the base of the neck, the thyroid is a large endocrine gland that produces and releases thyroid hormone. Thyroid cancer is the fifth most common cancer in women in the USA (76). Histologically, there are five types of thyroid cancer: papillary, follicular, medullary, anaplastic thyroid cancer, and thyroid lymphoma. Some subtype of thyroid cancer, especially anaplastic thyroid cancer, has a very poor prognosis and high mortality rate. Despite conventional treatments, such as surgery and radioactive iodine therapy, there is an urgent need for novel adjunctive therapies in cases of surgically challenging thyroid cancer.

4.1.1 CAP's selectivity for thyroid cancer cells

Just like CAP's selectivity for SCC cells during HNC treatment (section 2.1), CAP is also selective for thyroid

cancer cells. Kuashik et al. reported that the increased ROS in thyroid cancer cells, which were introduced by CAP, could contribute to cell apoptosis *via* alterations in GSH/GSSG ratio, NADP+/NADPH ratio, and total antioxidant activity (35). In addition, plasma decreased the metabolic viability and colony formation of thyroid cancer cells. These findings suggest a promising elimination of thyroid cancer cells by CAP irradiation while sparing normal healthy cells.

4.1.2 Potential molecular mechanism of CAP's selectivity

Further studies elucidated the molecular mechanism underlying CAP's therapeutic effect on thyroid cancer. Jung et al. advised that CAP treatment in the form of PAM upregulated the gene expression of early growth response 1 (EGR1), which in turn increased the level of DNA damage-inducible 45α (GADD45A) through direct binding to its promoter (37). In their xenograft mouse tumor model, PAM inhibited thyroid cancer progression also by elevating EGR1 levels. In a different study, CAP inhibited the invasion and metastasis of thyroid papillary cancer cells by decreasing the expression of MMP2/MMP9 and uPA (36). This inhibitory effect was also accomplished by rearranging the cytoskeleton, which was regulated by the FAK/Src complex (36). These findings revealed that CAP could be a novel approach for locally invasive and metastatic thyroid cancers.

4.2 Salivary gland cancers

Major salivary glands, such as the parotid gland and submandibular gland, are both located in the head and neck region. Salivary gland cancer constitutes only 3% of all HNCs, and most salivary gland tumors arise in the parotid gland (77). Recent studies have shown that parotid gland carcinoma cells were also sensitive to CAP treatment. Consistent with the findings in HNSCC cells, treatment using CAP resulted in increased apoptosis of HN9, which is a cell line established from an undifferentiated cancer of the parotid gland (28). However, no studies have been conducted to investigate the specific mechanism of the above results. It is interesting to see whether CAP's anti-neoplastic effect on parotid tumor cells shares a similar mechanism as previously mentioned in CAP's treatment in head and neck upper ADT SCC (section 2).

5 CAP's treatment for head and neck skin cancers

Common head and neck skin cancers include basal cell carcinoma (BCC), SCC, and malignant melanoma, in decreasing order of disease prevalence (78). One way to explore CAP's treatment for head and neck skin SCC might be to draw on the experience of successful application of CAP on upper ADT SCC (section 2), as they share histological commonalities. Between melanoma and BCC, the former attracts more attention than the latter.

5.1 Malignant melanoma

Melanoma is a malignant tumor that originates from skin melanocytes. Melanoma accounts for only 3% of the entire skin cancer but is responsible for 65% of the skin cancer-related deaths (79). This is mainly because melanoma is more likely to metastasize early with a higher tumor staging, compared to other types of skin cancers. In the advanced stage of melanomas, surgery and chemotherapy provide limited efficacy, leading to a poor five-year survival rate (80). In addition, resistance to chemotherapy is also a challenging problem in the clinical management of melanoma (81). Fortunately, CAP has proven a versatile tool in effectively treating melanoma.

5.1.1 CAP selectively kills melanoma cells

Previous studies have shown that different types of tumor cells have different sensitivity to RONS, leading to treatment sensitivity. Unlike pancreatic cancer cells, melanoma cell lines, such as SK-MEL-28, A375, MaMel86a, and 501-MEL, are sensitive to CAP treatment (82). Interestingly, the cystine-glutamate antiporter xCT (SLC7A11) gene is upregulated in melanoma cell lines which are resistant to CAP treatment. Therefore, we can use SLC7A11 as a screening marker before CAP treatment, aiming to evaluate whether the patient is suitable for CAP treatment.

5.1.2 Managing melanoma using direct CAP treatment

CAP's versatility in melanoma treatment is manifested in three aspects: direct exposure, indirect treatment, and collaboration with other oncotherapies. The molecular mechanism of each mode will be discussed below. When CAP is applied directly, low doses of plasma could induce senescence in melanoma cells, whereas high doses lead to DNA damage in tumor cells, thus promoting the induction of the sub-G1 phase and increasing apoptosis (83). In another study, it found that cell surface receptor Fas, which is related to the extrinsic apoptosis pathway, participated in the CAP-induced apoptosis in melanoma cell lines (44). This process was triggered by Sestrin2 which was manipulated by CAP. The overexpression of Sestrin2 activated the MAPK signaling pathway, and subsequently increased the level of Fas and Fas ligand. In addition to cancer cell apoptosis, cell migration and adhesion in the melanoma cell lines can also be suppressed by CAP (45). Inhibition of tumor metastasis continues to be one of the main

therapeutic objectives in oncology. In this study, CAP reduced tumor cell motility and colony formation without significantly affecting cell metabolism and cell cycle progression.

Further to the above *in vitro* results, CAP's anti-neoplastic effect was validated *in vivo*. After melanoma was induced in nude mice, the tumor volume was significantly decreased in CAP-treated groups in a dose-dependent manner (84). Most previous cancer studies have focused on the role of ROS as the main physicochemical component of CAP. However, it is well known that CAP contains far more biologically active ingredients than ROS. A genome-wide analysis found that non-ROS constituents were also responsible for the inhibition of tumor cell growth by regulating PTGER3 and HSPA6 (85). Therefore, we suspect that the anti-melanoma effect of CAP is the collective result of various components of plasma.

5.1.3 Managing melanoma using indirect CAP treatment

In addition to direct CAP irradiation, indirect CAP treatment in the form of PAM also demonstrates comparable anti-tumor efficacy in melanoma cells. RONS are described as the primary components accounting for the anti-tumor effect of CAP, and rich and long-lived RONS have been found in PAM (86). On one hand, the modification of amino acids by RONS in PAM may lead to protein inactivation or activation, hence triggering anti-tumor signaling pathways (46). On the other hand, CAP could cause acidification of water and media. Meanwhile, the Ca^{2+} influx induced by CAP in melanoma cells was more prominent in acidic conditions than in physiological conditions. Moreover, CAP induced NO production which caused protein nitrification in melanoma cells under CAP-induced acidic condition (43). In summary, although direct CAP treatment is more efficient, especially for superficial cancer, PAM still has unique advantages. For example, PAM can eliminate deep space tumors and locoregional metastasis by injection, which are not normally accessible by direct CAP irradiation.

5.1.4 CAP combined with other oncotherapy for melanoma

Combining CAP with existing anti-cancer therapies is also a potential treatment option for melanoma. In Alimohammadi's study, it was found that CAP induced higher lipid peroxidation and NO production in B16 melanoma cells than in normal cells. In addition, CAP combined with chemotherapy (dacarbazine) lead to improved tumor control in mice with melanoma (42). In a parallel study, Daeschlein et al. found that CAP treatment alone showed a significantly delayed tumor growth, although less effective than electrochemotherapy (ECT). But when CAP was combined with ECT, they improved the survival of mice while reducing the dosage of ECT (87). Therefore, this type of joint therapy offers an alternative for patients who cannot tolerate ECT alone.

As previously mentioned, synergy existed between CAP and nanomedicine in HNSCC treatment (section 2). This synergy also applies to melanoma treatment. In Adhikari's study, CAP combined with silymarin nanoemulsion (SN) destroyed mitochondrial membrane integrity and reduced ATP production in melanoma cells (41). Moreover, the downregulation of the PI3K/AKT/mTOR survival pathway and RAS/MEK transcriptional pathway were also observed in the co-treatment group. These data confirmed that CAP and SN together could activate autophagy in melanoma cells. Further study by the same group discovered that CAP and SN synergistically inhibit human melanoma tumorigenesis by blocking the HGF/c-MET downstream pathway (40).

5.2 Basal cell carcinoma

BCC is a slow-growing, locally aggressive malignant epidermal skin tumor with a high incidence in Caucasians (88). Ultraviolet radiation exposure is generally considered to be the main cause of BCC. BCC occurs mainly in the body areas which are exposed to sunlight, most commonly in the head and neck (80% of all cases) (89). Unlike the large number of studies devoted to CAP treatment for melanoma, the number of experiments on BCC treatment using CAP is very limited. In one study by Yang et al., PAM was produced by CAP irradiation of Dulbecco's modified eagle medium (DMEM) and phosphate-buffered saline (PBS) and used on BCC cells (47). The TE354T BCC cells were cultured with PAM and showed decreased viability and increased apoptosis. Further investigations identified changes in the MAPK and TNF signaling pathways which contributed to PAM-induced apoptosis in BCC cells.

6 Recent preclinical and clinical trials in CAP oncology

A series of clinical trials have revealed that CAP has tremendous therapeutic potential for HNCs. This is partially because of CAP's distinct technical advantages. Some of the most common cancers, such as those arising from solid organs (lung and liver) and gastrointestinal tracts (colorectum and stomach), are anatomically deep. This poses real challenges for direct CAP treatment. In comparison, most cancers in the head and neck should be accessible by CAP, as they are either superficial (skin cancers), subcutaneous (thyroid and parotid glands), or reachable through upper ADT (oral cavity, pharynx, and larynx). Nowadays, surgery is still the mainstay treatment modality for many HNCs. Fortunately, CAP serves as a versatile tool throughout the entire peri-operative period. However, due to the diversity in tumor type, location, and stage, the optimal timing of CAP's participation varies.

6.1 CAP is applied as a preoperative sensitizer

CAP can be used in HNC treatment before surgical resection. Preoperative CAP treatment can induce apoptosis of tumor cells, reduce tumor volume, and decrease the difficulty of surgery. Schuster et al. devised an ingenious experiment in which nine patients with advanced HNC were treated with CAP first, followed by radical surgical resection two weeks later (49). The pathological analysis showed that apoptotic cells appeared more frequently in CAP-treated tissue than in untreated areas. This is coupled with clinically visible tumor surface response. Another clinical study exposed human cutaneous melanoma tissue to CAP (53). The authors identified an increased level of apoptosis and alleviated inflammatory response after CAP treatment.

6.2 CAP is applied as an intraoperative assistant

CAP can potentially be used during surgical operations for HNCs as a future-proof standard. Surgeons could use plasma jet intuitively like a hand-held instrument, either in a stand-alone fashion or attached to any common surgical equipment, e.g., scalpel or monopolar diathermy. For surgically challenging tumors, such as cancer near vital structures, e.g., carotid artery, vagus nerve, skull bases and meninges, CAP can be applied intraoperatively owing to its non-thermal nature. This not only avoids damaging the above tissues but also induces cancer cell apoptosis. Hasse et al. treated tissue samples surgically obtained from patients with stage T4 HNC (52). CAP treatment of tumor tissue induced more apoptotic cells than in healthy tissues that were accompanied by elevated extracellular cytochrome C levels.

6.3 CAP is applied as a postoperative adjunct

CAP can be used after surgical resection of HNC. Cancer-related symptoms or treatment-associated complications can still be debilitating even after extensive management, especially in palliative HNC patients. CAP is bactericidal and can reduce microbial contamination in heavily infected tumor ulcers, which is often seen in patients with advanced HNC (49). In addition, CAP can promote microcirculation and further facilitate the healing of chronic cancer ulcers (50). Metelmann et al. noticed that most patients afflicted with advanced HNSCC reported a decreased need for analgesics, reduction of typical fetid odor, and wound healing of infected ulcerations after CAP treatment (48). Their subsequent cohort reported that CAP-treated patients with locally advanced (T4) HNC received not only the aforementioned benefits but also improved social function and positive emotional affect (51).

7 Limitations of CAP treatment

Although CAP has proven to be a promising head and neck treatment as discussed above, there are also limitations to its application due to its safety profile. Due to the complexity of CAP components, overtreatment with plasma is likely to cause undesired side effects.

For example, the formation of free radicals by plasma raises a concern regarding its potential side effects on HNC patients. In a retrospective analysis of 20 patients suffering from locally advanced HNC who received palliative CAP treatment, there were no severe side effects observed, certainly no life-threatening ones (90). The reported issues were mostly mild reactions, uneasiness, and discomfort, which were tolerated by most patients. These include bad taste, exhaustion, collateral edema, and minimal hemorrhage (51).

Technological limitation also hindered the application of CAP equipment in the clinical treatment of otolaryngology head and neck surgery. Although many portable CAP generators have been developed, they are still unable to be carried into the existing surgical instrument. Due to the special anatomical structure of the head and neck, CAP will have greater potential for clinical application if it can be combined with existing therapeutic instruments such as nasal endoscopy.

8 Conclusion

Plasma oncology using CAP has been gaining increasing attention in HNC treatment, owing to CAP's several advantages. Firstly, CAP is a comprehensive therapy covering the entire disease spectrum of HNC, including upper ADT cancers, glandular cancers, and head and neck skin cancers. Secondly, CAP demonstrates excellent technical versatility, as it can be used either directly as superficial irradiation or indirectly in the form of PAM, each with distinct advantages. Thirdly, CAP serves as a multimodal treatment for HNCs, as it can not only work independently but also collaborate with other existing oncotherapies, such as chemotherapy, targeted therapy, and immunotherapy. Microscopically, CAP affects various cellular events, such as cell apoptosis and cell invasion, through several potential molecular mechanisms, such as the p53 and MAPK signaling pathways. Macroscopically, CAP has manifested great potential in recent clinical trials, which is best exemplified by its participation during the entire perioperative period and management of post-treatment cancer-related complications.

Fortunately, CAP oncotherapy did not excel at the price of causing severe side effects to the HNC patients. It is still considered a safe and patient-friendly treatment modality. Overall, CAP oncotherapy has significantly strengthened the arsenal for fighting HNCs.

Author contributions

FT: Conceptualization, methodology, validation, formal analysis, resources, data curation, writing, supervision, project administration, funding acquisition. XL: Formal analysis, resources, data curation, writing, visualization. XR: conceptualization, methodology, formal analysis, resources. DL: Software, resources, visualization. YW: Resources, supervision. All authors contributed to the article and approved the submitted version.

Funding

This work is sponsored by the Fundamental Research Funds for the Central Universities and Tongji University Affiliated Shanghai Fourth People's Hospital Startup Research Funding.

Acknowledgments

The authors wish to thank Relyon Plasma GmbH (Regensburg, Germany) for providing the handheld CAP device, Piezobrush PZ2, used Figure 1. Figure 2 was created with BioRender.com.

Conflict of interest

The authors declare that the research was conducted in the absence of any commercial or financial relationships that could be construed as a potential conflict of interest.

Publisher's note

All claims expressed in this article are solely those of the authors and do not necessarily represent those of their affiliated organizations, or those of the publisher, the editors and the reviewers. Any product that may be evaluated in this article, or claim that may be made by its manufacturer, is not guaranteed or endorsed by the publisher.

References

1. Bray F, Ferlay J, Soerjomataram I, Siegel RL, Torre LA, Jemal A. Global cancer statistics 2018: GLOBOCAN estimates of incidence and mortality worldwide for 36 cancers in 185 countries. *CA Cancer J Clin* (2018) 68:394–424. doi: 10.3322/caac.21492

2. Siegel RL, Miller KD. Cancer statistics, 2021. *CA: Cancer J Clin* (2021) 71:7–33. doi: 10.3322/caac.21654

3. Mody MD, Rocco JW, Yom SS, Haddad RI, Saba NF. Head and neck cancer. *Lancet (London England)* (2021) 398:2289–99. doi: 10.1016/S0140-6736(21)01550-6

4. Bone RC, Byfield JE, Feren AP, Seagren SL. Bleomycin: its utilization in the treatment of head and neck cancer. *Laryngoscope* (1979) 89:224–33. doi: 10.1288/00005537-197902000-00005

5. Noronha V, Joshi A, Patil VM, Agarwal J, Ghosh-Laskar S, Budrukkar A, et al. Once-a-Week versus once-Every-3-Weeks cisplatin chemoradiation for locally advanced head and neck cancer: A phase III randomized noninferiority trial. *J Clin Oncol* (2018) 36:1064–72. doi: 10.1200/JCO.2017.74.9457

6. Hitt R, Irigoyen A, Cortes-Funes H, Grau JJ, García-Sáenz JA, Cruz-Hernandez JJ. Phase II study of the combination of cetuximab and weekly paclitaxel in the first-line treatment of patients with recurrent and/or metastatic squamous cell carcinoma of head and neck. *Ann Oncol* (2012) 23:1016–22. doi: 10.1093/annonc/mdr367

7. Brunner TF, Probst FA, Troeltzsch M, Schwenk-Zieger S, Zimmermann JL, Morfill G, et al. Primary cold atmospheric plasma combined with low dose cisplatin as a possible adjuvant combination therapy for HNSCC cells-an in-vitro study. *Head Face Med* (2022) 18:21. doi: 10.1186/s13005-022-00322-5

8. Vermorken JB, Mesia R, Rivera F, Remenar E, Kawecki A, Rottey S, et al. Platinum-based chemotherapy plus cetuximab in head and neck cancer. *N Engl J Med* (2008) 359:1116–27. doi: 10.1056/NEJMoa0802656

9. Cohen EEW, Soulières D, Le Tourneau C, Dinis J, Licitra L, Ahn MJ, et al. Pembrolizumab versus methotrexate, docetaxel, or cetuximab for recurrent or metastatic head-and-neck squamous cell carcinoma (KEYNOTE-040): A randomised, open-label, phase 3 study. *Lancet (London England)* (2019) 393:156–67. doi: 10.1016/S0140-6736(18)31999-8

10. Posner MR, Hershock DM, Blajman CR, Mickiewicz E, Winquist E, Gorbounova V, et al. Cisplatin and fluorouracil alone or with docetaxel in head and neck cancer. *N Engl J Med* (2007) 357:1705–15. doi: 10.1056/NEJMoa070956

11. Browman GP, Goodyear MD, Levine MN, Russell R, Archibald SD, Young JE. Modulation of the antitumor effect of methotrexate by low-dose leucovorin in squamous cell head and neck cancer: A randomized placebo-controlled clinical trial. *J Clin Oncol* (1990) 8:203–8. doi: 10.1200/JCO.1990.8.2.203

12. Argiris A, Haraf DJ, Kies MS, Vokes EE. Intensive concurrent chemoradiotherapy for head and neck cancer with 5-fluorouracil- and hydroxyurea-based regimens: Reversing a pattern of failure. *Oncologist* (2003) 8:350–60. doi: 10.1634/theoncologist.8-4-350

13. Park J, Jang Y-S, Choi J-H, Ryu M, Kim G-C, Byun J-H, et al. Anticancer efficacy of nonthermal plasma therapy combined with PD-L1 antibody conjugated gold nanoparticles on oral squamous cell carcinoma. *Appl Sci* (2021) 11:4559. doi: 10.3390/app11104559

14. Chang JW, Kang SU, Shin YS, Seo SJ, Kim YS, Yang SS, et al. Combination of NTP with cetuximab inhibited invasion/migration of cetuximab-resistant OSCC cells: Involvement of NF-κB signaling. *Sci Rep* (2015) 5:18208. doi: 10.1038/srep18208

15. Burtness B, Harrington KJ, Greil R, Soulières D, Tahara M, de Castro GJr., et al. Pembrolizumab alone or with chemotherapy versus cetuximab with chemotherapy for recurrent or metastatic squamous cell carcinoma of the head and neck (KEYNOTE-048): A randomised, open-label, phase 3 study. *Lancet (London England)* (2019) 394:1915–28. doi: 10.1016/S0140-6736(19)32591-7

16. Ferris RL, Blumenschein GJr., Fayette J, Guigay J, Colevas AD, Licitra L, et al. Nivolumab for recurrent squamous-cell carcinoma of the head and neck. *N Engl J Med* (2016) 375:1856–67. doi: 10.1056/NEJMoa1602252

17. Chow LQM. Head and neck cancer. *N Engl J Med* (2020) 382:60–72. doi: 10.1056/NEJMra1715715

18. Tan F, Fang Y, Zhu L, Al-Rubeai M. Controlling stem cell fate using cold atmospheric plasma. *Stem Cell Res Ther* (2020) 11:368. doi: 10.1186/s13287-020-01886-2

19. Korzec D, Hoppenthaler F, Nettesheim S. Piezoelectric direct discharge: Devices and applications. *Plasma* (2021) 4:1–41. doi: 10.3390/plasma4010001

20. Attri P, Park J-H, De Backer J, Kim M, Yun J-H, Heo Y, et al. Structural modification of NADPH oxidase activator (Noxa 1) by oxidative stress: An experimental and computational study. *Int J Biol Macromolecules* (2020) 163:2405–14. doi: 10.1016/j.ijbiomac.2020.09.120

21. Xu W, Yan D, Sun J, Chen J, Yao X, Sherman JH, et al. The activation of cancer cells by a nanosecond-pulsed magnetic field generator. *J Phys D: Appl Phys* (2020) 53:125401. doi: 10.1088/1361-6463/ab62c1

22. Golda J, Biskup B, Layes V, Winzer T, Benedikt J. Vacuum ultraviolet spectroscopy of cold atmospheric pressure plasma jets. *Plasma Processes Polymers* (2020) 17:1900216. doi: 10.1002/ppap.201900216

23. Hefny MM, Pattyn C, Lukes P, Benedikt J. Atmospheric plasma generates oxygen atoms as oxidizing species in aqueous solutions. *J Phys D: Appl Phys* (2016) 49:404002. doi: 10.1088/0022-3727/49/40/404002

24. Tan F, Rui X, Xiang X, Yu Z, Al-Rubeai M. Multimodal treatment combining cold atmospheric plasma and acidic fibroblast growth factor for multi-tissue regeneration. *FASEB J Off Publ Fed Am Societies Exp Biol* (2021) 35: e21442. doi: 10.1096/fj.202002611R

25. Guerrero-Preston R, Ogawa T, Uemura M, Shumulinsky G, Valle BL, Pirini F, et al. Cold atmospheric plasma treatment selectively targets head and neck squamous cell carcinoma cells. *Int J Mol Med* (2014) 34:941–6. doi: 10.3892/ijmm.2014.1849

26. Lee JH, Om JY, Kim YH, Kim KM, Choi EH, Kim KN. Selective killing effects of cold atmospheric pressure plasma with NO induced dysfunction of epidermal growth factor receptor in oral squamous cell carcinoma. *PloS One* (2016) 11:e0150279. doi: 10.1371/journal.pone.0150279

27. Kang SU, Seo SJ, Kim YS, Shin YS, Koh YW, Lee CM, et al. Comparative effects of non-thermal atmospheric pressure plasma on migration and invasion in oral squamous cell cancer, by gas type. *Yonsei Med J* (2017) 58:272–81. doi: 10.3349/ymj.2017.58.2.272

28. Kang SU, Cho JH, Chang JW, Shin YS, Kim KI, Park JK, et al. Nonthermal plasma induces head and neck cancer cell death: the potential involvement of mitogen-activated protein kinase-dependent mitochondrial reactive oxygen species. *Cell Death Dis* (2014) 5:e1056. doi: 10.1038/cddis.2014.33

29. Oh C, Won HR, Kang WS, Kim DW, Jung SN, Im MA, et al. Head and neck cancer cell death due to mitochondrial damage induced by reactive oxygen species from nonthermal plasma-activated media: Based on transcriptomic analysis. *Oxid Med Cell Longevity* (2021) 2021:9951712. doi: 10.1155/2021/9951712

30. Chang JW, Kang SU, Shin YS, Kim KI, Seo SJ, Yang SS, et al. Non-thermal atmospheric pressure plasma induces apoptosis in oral cavity squamous cell carcinoma: Involvement of DNA-damage-triggering sub-G(1) arrest *via* the ATM/p53 pathway. *Arch Biochem Biophys* (2014) 545:133–40. doi: 10.1016/j.abb.2014.01.022

31. Kim SY, Kim HJ, Kang SU, Kim YE, Park JK, Shin YS, et al. Non-thermal plasma induces AKT degradation through turn-on the MUL1 E3 ligase in head and neck cancer. *Oncotarget* (2015) 6:33382–96. doi: 10.18632/oncotarget.5407

32. Estarabadi H, Atyabi SA, Tavakkoli S, Noormohammadi Z, Gholami MR, Ghiaseddin A, et al. Cold atmospheric plasma induced genotoxicity and cytotoxicity in esophageal cancer cells. *Mol Biol Rep* (2021) 48:1323–33. doi: 10.1007/s11033-021-06178-3

33. Kim G, Park SR, Kim GC, Lee JK. Targeted cancer treatment using anti-EGFR and -TFR antibody-conjugated gold nanoparticles stimulated by nonthermal air plasma. *Plasma Med* (2011) 1:45–54. doi: 10.1615/PlasmaMed.v1.i1.40

34. Lee CM, Jeong YI, Kook MS, Kim BH. Combinatorial effect of cold atmosphere plasma (CAP) and the anticancer drug cisplatin on oral squamous cell cancer therapy. *Int J Mol Sci* (2020) 21:7646. doi: 10.3390/ijms21207646

35. Kaushik NK, Kaushik N, Park D, Choi EH. Altered antioxidant system stimulates dielectric barrier discharge plasma-induced cell death for solid tumor cell treatment. *PloS One* (2014) 9:e103349. doi: 10.1371/journal.pone.0103349

36. Chang JW, Kang SU, Shin YS, Kim KI, Seo SJ, Yang SS, et al. Non-thermal atmospheric pressure plasma inhibits thyroid papillary cancer cell invasion *via* cytoskeletal modulation, altered MMP-2/-9/uPA activity. *PloS One* (2014) 9: e92198. doi: 10.1371/journal.pone.0092198

37. Jung SN, Oh C, Chang JW. EGR1/GADD45α activation by ROS of non-thermal plasma mediates cell death in thyroid carcinoma. *Cancers (Basel)* (2021) 13:351. doi: 10.3390/cancers13020351

38. Lee SY, Kang SU, Kim KI, Kang S, Shin YS, Chang JW, et al. Nonthermal plasma induces apoptosis in ATC cells: involvement of JNK and p38 MAPK-dependent ROS. *Yonsei Med J* (2014) 55:1640–7. doi: 10.3349/ymj.2014.55.6.1640

39. Wang M, Geilich BM, Keidar M, Webster TJ. Killing malignant melanoma cells with protoporphyrin IX-loaded polymersome-mediated photodynamic therapy and cold atmospheric plasma. *Int J Nanomedicine* (2017) 12:4117–27. doi: 10.2147/IJN.S129266

40. Adhikari M, Kaushik N, Ghimire B, Adhikari B, Baboota S, Al-Khedhairy AA, et al. Cold atmospheric plasma and silymarin nanoemulsion synergistically inhibits human melanoma tumorigenesis *via* targeting HGF/c-MET downstream pathway. *Cell Commun Signal* (2019) 17:52. doi: 10.1186/s12964-019-0360-4

41. Adhikari M, Adhikari B, Ghimire B. Cold atmospheric plasma and silymarin nanoemulsion activate autophagy in human melanoma cells. *Int J Mol Sci* (2020) 21:1939. doi: 10.3390/ijms21061939

42. Alimohammadi M, Golpur M. Cold atmospheric plasma is a potent tool to improve chemotherapy in melanoma *In vitro* and *In vivo*. *Biomolecules* (2020) 10:1011. doi: 10.3390/biom10071011

43. Schneider C, Gebhardt L, Arndt S, Karrer S, Zimmermann JL, Fischer MJM, et al. Acidification is an essential process of cold atmospheric plasma and promotes the anti-cancer effect on malignant melanoma cells. *Cancers (Basel)* (2019) 11:671. doi: 10.3390/cancers11050671

44. Xia J, Zeng W, Xia Y, Wang B, Xu D, Liu D, et al. Cold atmospheric plasma induces apoptosis of melanoma cells *via* Sestrin2-mediated nitric oxide synthase signaling. *J Biophotonics* (2019) 12:e201800046. doi: 10.1002/jbio.201800046

45. Schmidt A, Bekeschus S, von Woedtke T, Hasse S. Cell migration and adhesion of a human melanoma cell line is decreased by cold plasma treatment. *Clin Plasma Med* (2015) 3:24–31. doi: 10.1016/j.cpme.2015.05.003

46. Arndt S, Fadil F. Cold atmospheric plasma changes the amino acid composition of solutions and influences the anti-tumor effect on melanoma cells. *Int J Mol Sci* (2021) 22:7886. doi: 10.3390/ijms22157886

47. Yang X, Yang C, Wang L, Cao Z, Wang Y, Cheng C, et al. Inhibition of basal cell carcinoma cells by cold atmospheric plasmaactivated solution and differential gene expression analysis. *Int J Oncol* (2020) 56:1262–73. doi: 10.3892/ijo.2020.5009

48. Metelmann H-R, Nedrelow DS, Seebauer C, Schuster M, von Woedtke T, Weltmann K-D, et al. Head and neck cancer treatment and physical plasma. *Clin Plasma Med* (2015) 3:17–23. doi: 10.1016/j.cpme.2015.02.001

49. Schuster M, Seebauer C, Rutkowski R, Hauschild A, Podmelle F, Metelmann C, et al. Visible tumor surface response to physical plasma and apoptotic cell kill in head and neck cancer. *J Cranio-Maxillo-Facial Surg* (2016) 44:1445–52. doi: 10.1016/j.jcms.2016.07.001

50. Rutkowski R, Schuster M, Unger J, Seebauer C, Metelmann HR, Woedtke T, et al. Hyperspectral imaging for *in vivo* monitoring of cold atmospheric plasma effects on microcirculation in treatment of head and neck cancer and wound healing. *Clin Plasma Med* (2017) 7-8:52–7. doi: 10.1016/j.cpme.2017.09.002

51. Metelmann H-R, Seebauer C, Miller V, Fridman A, Bauer G, Graves DB, et al. Clinical experience with cold plasma in the treatment of locally advanced head and neck cancer. *Clin Plasma Med* (2018) 9:6–13. doi: 10.1016/j.cpme.2017.09.001

52. Hasse S, Seebauer C, Wende K, Schmidt A, Metelmann H-R, von Woedtke T, et al. Cold argon plasma as adjuvant tumour therapy on progressive head and neck cancer: A preclinical study. *Appl Sci* (2019) 9:2061. doi: 10.3390/app9102061

53. Bekeschus S, Moritz J, Helfrich I, Boeckmann L, Weltmann K-D, Emmert S, et al. Ex vivo exposure of human melanoma tissue to cold physical plasma elicits apoptosis and modulates inflammation. *Appl Sci* (2020) 10:1971. doi: 10.3390/app10061971

54. Sanderson RJ, Ironside JA. Squamous cell carcinomas of the head and neck. *BMJ* (2002) 325:822–7. doi: 10.1136/bmj.325.7368.822

55. Braakhuis BJ, Brakenhoff RH, Leemans CR. Treatment choice for locally advanced head and neck cancers on the basis of risk factors: biological risk factors. *Ann Oncol* (2012) 23(Supplement 10):x173–7. doi: 10.1093/annonc/mds299

56. Johnson DE, Burtness B, Leemans CR, Lui VWY, Bauman JE, Grandis JR. Head and neck squamous cell carcinoma. *Nat Rev Dis Primers* (2020) 6:92. doi: 10.1038/s41572-020-00224-3

57. Yan D, Talbot A, Nourmohammadi N, Sherman JH, Cheng X, Keidar M. Toward understanding the selective anticancer capacity of cold atmospheric plasma–a model based on aquaporins (Review). *Biointerphases* (2015) 10:040801. doi: 10.1116/1.4938020

58. Volotskova O, Hawley TS, Stepp MA, Keidar M. Targeting the cancer cell cycle by cold atmospheric plasma. *Sci Rep* (2012) 2:636. doi: 10.1038/srep00636

59. Miller EW, Dickinson BC, Chang CJ. Aquaporin-3 mediates hydrogen peroxide uptake to regulate downstream intracellular signaling. *Proc Natl Acad Sci USA* (2010) 107:15681–6. doi: 10.1073/pnas.1005776107

60. Van der Paal J, Neyts EC. Effect of lipid peroxidation on membrane permeability of cancer and normal cells subjected to oxidative stress. *Chem Sci* (2016) 7:489–98. doi: 10.1039/C5SC02311D

61. Welz C, Emmert S, Canis M, Becker S, Baumeister P, Shimizu T, et al. Cold atmospheric plasma: A promising complementary therapy for squamous head and neck cancer. *PloS One* (2015) 10:e0141827. doi: 10.1371/journal.pone.0141827

62. Tan F, Fang Y, Zhu L, Al-Rubeai M. Cold atmospheric plasma as an interface biotechnology for enhancing surgical implants. *Crit Rev Biotechnol* (2021) 41:425–40. doi: 10.1080/07388551.2020.1853671

63. Panagopoulos DJ. Comparing DNA damage induced by mobile telephony and other types of man-made electromagnetic fields. *Mutat Res Rev Mutat Res* (2019) 781:53–62. doi: 10.1016/j.mrrev.2019.03.003

64. Van den Heuvel F. A closed parameterization of DNA-damage by charged particles, as a function of energy - a geometrical approach. *PloS One* (2014) 9: e110333. doi: 10.1371/journal.pone.0110333

65. Mullenders LHF. Solar UV damage to cellular DNA: from mechanisms to biological effects. *Photochem Photobiol Sci* (2018) 17:1842–52. doi: 10.1039/C8PP00182K

66. Han X, Kapaldo J. Large-Scale image analysis for investigating spatio-temporal changes in nuclear DNA damage caused by nitrogen atmospheric pressure plasma jets. *Int J Mol Sci* (2020) 21:4127. doi: 10.3390/ijms21114127

67. Cheng Q, Chen J. Mechanism of p53 stabilization by ATM after DNA damage. *Cell Cycle* (2010) 9:472–8. doi: 10.4161/cc.9.3.10556

68. Sachweh MCC, Drummond CJ, Higgins M, Campbell J, Laín S. Incompatible effects of p53 and HDAC inhibition on p21 expression and cell cycle progression. *Cell Death Dis* (2013) 4:e533. doi: 10.1038/cddis.2013.61

69. Shi L, Yu L, Zou F, Hu H, Liu K, Lin Z. Gene expression profiling and functional analysis reveals that p53 pathway-related gene expression is highly activated in cancer cells treated by cold atmospheric plasma-activated medium. *PeerJ* (2017) 5:e3751. doi: 10.7717/peerj.3751

70. Soleimani A, Rahmani F, Saeedi N, Ghaffarian R, Khazaei M, Ferns GA, et al. The potential role of regulatory microRNAs of RAS/MAPK signaling pathway in the pathogenesis of colorectal cancer. *J Biophotonics* (2019) 120:19245–53. doi: 10.1002/jcb.29268

71. Guo YJ, Pan WW, Liu SB, Shen ZF, Xu Y, Hu LL. ERK/MAPK signalling pathway and tumorigenesis. *Exp Ther Med* (2020) 19:1997–2007. doi: 10.3892/etm.2020.8454

72. Sun Y, Liu WZ, Liu T, Feng X, Yang N, Zhou HF. Signaling pathway of MAPK/ERK in cell proliferation, differentiation, migration, senescence and apoptosis. *J Recept Signal Transduction Res* (2015) 35:600–4. doi: 10.3109/10799893.2015.1030412

73. Chauvin J, Judee F, Merbahi N, Vicendo P. Effects of plasma activated medium on head and neck FaDu cancerous cells: Comparison of 3D and 2D response. *Anti-cancer Agents Medicinal Chem* (2018) 18:776–83. doi: 10.2174/1871520617666170801111055

74. Boeckx C, Op de Beeck K, Wouters A, Deschoolmeester V, Limame R, Zwaenepoel K, et al. Overcoming cetuximab resistance in HNSCC: The role of AURKB and DUSP proteins. *Cancer Lett* (2014) 354:365–77. doi: 10.1016/j.canlet.2014.08.039

75. Dong H, Strome SE, Salomao DR, Tamura H, Hirano F, Flies DB, et al. Tumor-associated B7-H1 promotes T-cell apoptosis: A potential mechanism of immune evasion. *Nat Med* (2002) 8:793–800. doi: 10.1038/nm730

76. Cabanillas ME, McFadden DG, Durante C. Thyroid cancer. *Lancet (London England)* (2016) 388:2783–95. doi: 10.1016/S0140-6736(16)30172-6

77. Gandolfi MM, Slattery W3rd. Parotid gland tumors and the facial nerve. *Otolaryngol Clin N Am* (2016) 49:425–34. doi: 10.1016/j.otc.2015.12.001

78. Linares MA, Zakaria A, Nizran P. Skin cancer. *Prim Care* (2015) 42:645–59. doi: 10.1016/j.pop.2015.07.006

79. Pavri SN, Clune J, Ariyan S, Narayan D. Malignant melanoma: Beyond the basics. *Plast Reconstr Surg* (2016) 138:330e–40e. doi: 10.1097/PRS.0000000000002367

80. Siegel R, Ma J, Zou Z, Jemal A. Cancer statistics, 2014. *CA Cancer J Clin* (2014) 64:9–29. doi: 10.3322/caac.21208

81. MacKie RM, Hauschild A, Eggermont AM. Epidemiology of invasive cutaneous melanoma. *Ann Oncol* (2009) 20(Supplement 6):vi1–7. doi: 10.1093/annonc/mdp252

82. Bekeschus S, Eisenmann S, Sagwal SK, Bodnar Y, Moritz J, Poschkamp B, et al. xCT (SLC7A11) expression confers intrinsic resistance to physical plasma treatment in tumor cells. *Redox Biol* (2020) 30:101423. doi: 10.1016/j.redox.2019.101423

83. Arndt S, Wacker E, Li YF, Shimizu T, Thomas HM, Morfill GE, et al. Cold atmospheric plasma, a new strategy to induce senescence in melanoma cells. *Exp Dermatol* (2013) 22:284–9. doi: 10.1111/exd.12127

84. Binenbaum Y, Ben-David G, Gil Z, Slutsker YZ, Ryzhkov MA, Felsteiner J, et al. Cold atmospheric plasma, created at the tip of an elongated flexible capillary using low electric current, can slow the progression of melanoma. *PloS One* (2017) 12:e0169457. doi: 10.1371/journal.pone.0169457

85. Ji HW, Kim H, Kim HW, Yun SH, Park JE, Choi EH, et al. Genome-wide comparison of the target genes of the reactive oxygen species and non-reactive oxygen species constituents of cold atmospheric plasma in cancer cells. *Cancers (Basel)* (2020) 12:2640. doi: 10.3390/cancers12092640

86. Cheng YJ, Lin CK, Chen CY, Chien PC, Chuan HH, Ho CC, et al. Plasma-activated medium as adjuvant therapy for lung cancer with malignant pleural effusion. *Sci Rep* (2020) 10:18154. doi: 10.1038/s41598-020-75214-2

87. Daeschlein G, Scholz S, Lutze S, Arnold A, von Podewils S, Kiefer T, et al. Comparison between cold plasma, electrochemotherapy and combined therapy in a melanoma mouse model. *Exp Dermatol* (2013) 22:582–6. doi: 10.1111/exd.12201

88. Di Stefani A, Chimenti S. Basal cell carcinoma: Clinical and pathological features. *G Ital Dermatol Venereol* (2015) 150:385–91.

89. Rubin AI, Chen EH, Ratner D. Basal-cell carcinoma. *N Engl J Med* (2005) 353:2262–9. doi: 10.1056/NEJMra044151

90. Schuster M, Rutkowski R, Hauschild A, Shojaei RK, von Woedtke T, Rana A, et al. Side effects in cold plasma treatment of advanced oral cancer–clinical data and biological interpretation. *Clin Plasma Med* (2018) 10:9–15. doi: 10.1016/j.cpme.2018.04.001

frontiers | Frontiers in Oncology

TYPE Original Research
PUBLISHED 20 October 2022
DOI 10.3389/fonc.2022.1013410

OPEN ACCESS

EDITED BY
Lorenz Kadletz-Wanke,
Medical University of Vienna, Austria

REVIEWED BY
Fei Tan,
Tongji University, China
Salvatore Sorrenti,
Sapienza University of Rome, Italy

*CORRESPONDENCE
Shuhang Xu
shuhangxu@163.com
Fangsen Xiao
xfs888@163.com

†These authors have contributed equally to this work and share first authorship

SPECIALTY SECTION
This article was submitted to Head and Neck Cancer, a section of the journal Frontiers in Oncology

RECEIVED 07 August 2022
ACCEPTED 06 October 2022
PUBLISHED 20 October 2022

CITATION
Yang J, Sun Y, Li X, Zhao Y, Han X, Chen G, Ding W, Li R, Wang J, Xiao F, Liu C and Xu S (2022) Diagnostic performance of six ultrasound-based risk stratification systems in thyroid follicular neoplasm: A retrospective multi-center study.
Front. Oncol. 12:1013410.
doi: 10.3389/fonc.2022.1013410

Diagnostic performance of six ultrasound-based risk stratification systems in thyroid follicular neoplasm: A retrospective multi-center study

Jingjing Yang[1†], Yu Sun[1,2†], Xingjia Li[1,3], Yueting Zhao[1], Xue Han[1], Guofang Chen[1,3], Wenbo Ding[4], Ruiping Li[5], Jianhua Wang[6], Fangsen Xiao[7*], Chao Liu[1,3] and Shuhang Xu[1*]

[1]Endocrine and Diabetes Center, Affiliated Hospital of Integrated Traditional Chinese and Western Medicine, Jiangsu Province Academy of Traditional Chinese Medicine, Nanjing University of Chinese Medicine, Nanjing, China, [2]Department of Endocrinology and Metabolism, The Affiliated Suqian Hospital of Xuzhou Medical University, Suqian, China, [3]Key Laboratory of Traditional Chinese Medicine (TCM) Syndrome and Treatment of Yingbing of State Administration of Traditional Chinese Medicine, Jiangsu Province Academy of Traditional Chinese Medicine, Nanjing, China, [4]Department of Ultrasound, Affiliated Hospital of Integrated Traditional Chinese and Western Medicine, Nanjing University of Chinese Medicine, Nanjing, China, [5]Department of Pathology, Affiliated Hospital of Integrated Traditional Chinese and Western Medicine, Nanjing University of Chinese Medicine, Nanjing, China, [6]Department of General Surgery, Affiliated Hospital of Integrated Traditional Chinese and Western Medicine, Nanjing University of Chinese Medicine, Nanjing, China, [7]Department of Endocrinology and Diabetes, The First Affiliated Hospital of Xiamen University, School of Medicine, Xiamen University, Xiamen, China

This study aimed to compare the diagnostic performances of six commonly used ultrasound-based risk stratification systems for distinguishing follicular thyroid adenoma (FTA) from follicular thyroid carcinoma (FTC), including the American Thyroid Association Sonographic Pattern System (ATASPS), ultrasound classification systems proposed by American Association of Clinical Endocrinologists, American College of Endocrinology, and Associazione Medici Endocrinology (AACE/ACE/AME), Korean thyroid imaging reporting and data system (K-TIRADS), European Thyroid Association for the imaging reporting and data system (EU-TIRADS), American College of Radiology for the imaging reporting and data system (ACR-TIRADS), and 2020 Chinese Guidelines for Ultrasound Malignancy Risk Stratification of Thyroid Nodules (C-TIRADS). A total of 225 FTA or FTC patients were retrospectively analyzed, involving 251 thyroid nodules diagnosed by postoperative pathological examinations in three centers from January 2013 to October 2021. The diagnostic performances of six ultrasound-based risk stratification systems for distinguishing FTA from FTC were assessed by plotting the receiver operating characteristic (ROC) curves and compared at different cut-off values. A total of 205 (81.67%) cases of FTA and 46 (18.33%) cases of FTC were involved in the present study. Compared with those of FTA, FTC presented more typical ultrasound features of solid component, hypoechoic, irregular margin and sonographic halo (all $P<0.001$). There were no significant differences in ultrasound features of calcification, shape and comet-tail artifacts between

cases of FTA and FTC. There was a significant difference in the category of thyroid nodules assessed by the six ultrasound-based risk stratification systems (P<0.001). The areas under the curve (AUCs) of ATASPS, AACE/ACE/AME, K-TIRADS, EU-TIRADS, ACR-TIRADS and C-TIRADS in distinguishing FTA from FTC were 0.645, 0.729, 0.766, 0.635, 0.783 and 0.798, respectively. Our study demonstrated that all the six ultrasound-based risk stratification systems present potential in the differential diagnosis of FTA and FTC. Specifically, C-TIRADS exerts the best diagnostic performance among the Chinese patients. ATASPS possesses a high sensitivity, while K-TIRADS possesses a high specificity in distinguishing FTA from FTC.

KEYWORDS

Thyroid nodule, Follicular neoplasm, Thyroid Imaging Reporting and Data System, Follicular adenoma, Thyroid follicular carcinoma

Introduction

Follicular neoplasm (FN), a type of thyroid carcinoma of follicular epithelial origin that lacks the features of papillary thyroid carcinoma (PTC), has a pathology involving follicular thyroid adenoma (FTA), follicular thyroid carcinoma (FTC), follicular variant papillary thyroid carcinoma (FVPTC) and other follicular lesions (1). In addition to PTC, FTC is the most-common differentiated thyroid cancer, accounting for 10-15% of thyroid carcinomas (2). Pathological confirmation of tumor capsule invasion and/or vascular invasion in surgically resected specimen is the only diagnostic criterion for FTC. However, the fine needle aspiration cytology (FNAC) and core needle biopsy (CNB) cannot provide a panoramic view of the entire fibrous capsule and vascular invasion, thus restricting their application in the diagnosis of FN (3, 4). Preoperative differential diagnosis of benign and malignant FN remains challenging in clinical practice.

Thyroid ultrasound is a preferred tool for thyroid nodule examination. A growing number of thyroid nodules have been detected by ultrasonography. To standardize the evaluation of malignant thyroid nodules, various clinical societies have developed ultrasound-based systems to stratify malignant risks (5). Based on the Thyroid Imaging Reporting and Data System (TIRADS) proposed by Horvath et al. (6), several "pattern-based" systems and "score-based" systems have been established. The former includes the ATASPS (American Thyroid Association Sonographic Pattern System), K-TIRADS (Korean Society of Thyroid Radiology), AACE/ACE/AME (American College of Endocrinology, and Associazione Medici Endocrinologi Medical), K-TIRADS (Korean Society of Thyroid Radiology), and EU-TIRADS (European Thyroid Association). The latter is represented by ACR-TIRADS (American College of Radiology) and C-TIRADS (2020 Chinese Guidelines for Ultrasound Malignancy Risk Stratification of Thyroid Nodules). Meanwhile, contrast-enhanced ultrasound (CEUS) has been introduced to evaluate thyroid parenchyma, but it is debatable whether CEUS can improve the diagnostic accuracy of ultrasound imaging reporting systems at present (7). The accuracy of artificial intelligence tools in characterizing thyroid nodules and cancers remains controversial (8). Therefore, ultrasound risk stratification systems are still the main tool for thyroid nodule examination.

The ultrasound characteristics suspected by the abovementioned systems are related to PTC, including the solid component, hypoechoic appearance, irregular margin, microcalcification, and taller-than-wide (9). Ultrasound findings of hypoechoic appearance, punctate microcalcification, indistinct or irregular margin, taller-than-wide, and increased intranodular blood flow may help establish the diagnosis of FTC (10). However, ultrasound characteristics of FTC and FTA may substantially overlap, typically manifested as a solitary, smooth margin, homogeneously isechoic or hypoechoic nodule with a peripheral halo, parallel orientation to the skin surface, and no lymph node enlargement (1). In addition, there is a significant difference in the incidence between PTC and FTC. The Surveillance, Epidemiology, and Results Program (SEER) data from 1974 to 2013 revealed that the incidence of PTC and FTC increased by an average of 4.4% and 0.6% per year, respectively (11). Trimboli et al. (12) showed that the vast majority (88.9%-99.6%) of malignant tumor specimens reported by the ultrasound-based risk stratification system were diagnosed as PTC. Therefore, whether the existing ultrasound-based risk stratification systems are suitable for the diagnosis of FN remains controversial, and current clinical data on their diagnostic potential are inconsistent (13–15).

The present multi-center retrospective study aimed to compare the diagnostic performances of ATASPS, AACE/ACE/AME, K-TIRADS, EU-TIRADS, ACR-TIRADS and C-

TIRADS in distinguishing FTA from FTC, thus providing references for preoperative diagnosis of FN.

Materials and methods

Subjects

A total of 225 FTA or FTC patients postoperatively diagnosed in the Affiliated Hospital of Integrated Traditional Chinese and Western Medicine of Nanjing University of Chinese Medicine (Nanjing, China), the First Affiliated Hospital of Xiamen University (Xiamen, China), and Suqian People's Hospital (Suqian, China) from January 2013 to October 2021 were retrospectively analyzed, based on their clinical data, thyroid ultrasound reports and postoperative pathological data (Figure 1).

Exclusion criteria: (i) Clinical data were incomplete; ultrasound elasticity imaging data or postoperative pathological data were unable to be assessed by ATASPS, AACE/ACE/AME, K-TIRADS, EU-TIRADS, ACR-TIRADS and C-TIRADS; (ii) Pathological results were inconsistent with clinical data or ultrasound results.

Ultrasound examination

Ultrasonography examinations were performed by three sonographers in three centers equipped with using the Hi Vision Preirus ultrasound machine. All sonographers had more than 5 years of experience in superficial organ ultrasound diagnosis, and were specialized in differential diagnosis of thyroid diseases. Thyroid nodules were assessed based on the following ultrasound features: maximum diameter (cm); component (solid, mixed solid and cystic, or cystic); echogenicity (hyperechoic, isoechoic, hypoechoic, or markedly hypoechoic); margin (smooth, or irregular); calcification (absent, microcalcification, macrocalcification, or peripheral calcification); shape (wider-than-tall or taller-than-wide); presence of halo and comet-tail artifacts; suspected invasion of neck lymph nodes and extrathyroid invasion.

All thyroid nodules were retrospectively assessed by the ATASPS, AACE/ACE/AME, K-TIRADS, EU-TIRADS, ACR-TIRADS and C-TIRADS (5, 16–20). Based on the conventional assessment, the former four classified thyroid nodules into the following categories: benign, very low suspicion or low suspicion, intermediate suspicion and high suspicion (5, 16, 18, 20). ACR-TIRADS and C-TIRADS assessed thyroid nodules by grading the typical ultrasound characteristics and calculating the total scores (17, 19). Notably, a total of 13 cases of FTA and 9 cases of FTC, which were assessed by ATASPS, did not belong to any category.

Statistical analysis

Continuous measurement data that were normally distributed (e.g., age, diameter of thyroid nodules) were expressed as $\bar{x}$ s, and compared by the paired t-test. Enumeration data (e.g., sex, ultrasound characteristics, thyroid nodule category) were expressed as percentage, and compared by the Chi-square test. ROC curves were plotted with the sensitivity and specificity as the ordinate and abscissa, respectively, in which the postoperative pathology served as the gold standard. The AUC was calculated based on the binomial distribution of the category of thyroid nodules

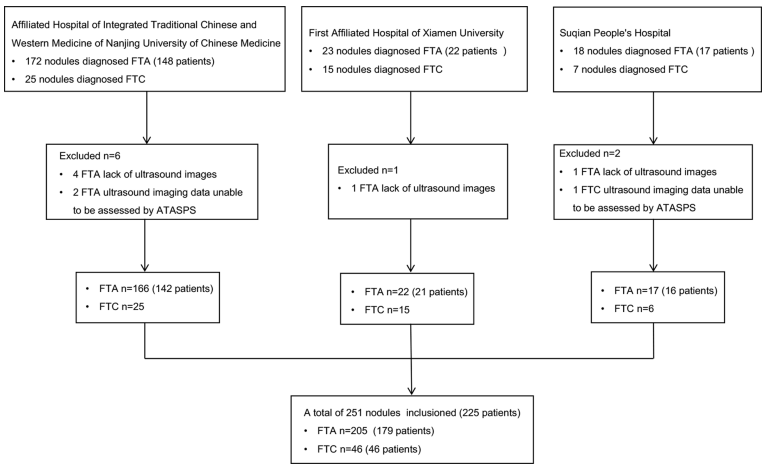

FIGURE 1
Flowchart summarizing the patient inclusion process.

assessed by the six systems. Moreover, the Youden index, cut-off value, sensitivity, specificity, positive predictive value (PPV) and negative predictive value (NPV) were calculated. $P<0.05$ was considered as statistically significant.

Results

Baseline characteristics

A total of 225 patients (251 thyroid nodules) were included in the present study, including 179 FTA patients (205 nodules) and 46 FTC patients (46 nodules). There were 42 male and 137 female FTA patients, and 12 male and 34 female FTC patients. No significant differences in the age and the maximum diameter of thyroid nodules were detected between FTA and FTC patients (Table 1). The ratio of FTA or FTC in females was significantly higher than that in males.

Ultrasound characteristics and malignancy rates of thyroid nodules

Most of included thyroid nodules presented typical ultrasound characteristics of solid components (44.22%), hyperechoic/isoechoic appearance (80.88%), regular margin (83.67%), non-calcification (88.44%) and wider-than-tall (98.41%) (Table 2). The incidences of solid (34.14% vs. 89.13%, $P<0.001$), hypoechoic (16.10% vs. 30.44%, $P=0.007$), irregular margin (4.88% vs. 28.26%, $P<0.001$) and presence of halo (15.61% vs. 36.96%, $P<0.001$) in cases of FTA were significantly lower than those in cases of FTC (Figure 2). No significant differences in the incidences of calcification ($P=0.936$), shape of thyroid nodules ($P=0.099$) and the presence of comet-tail artifacts ($P=0.915$) were found between FTA and FTC.

The malignancy rate of all solid thyroid nodules (36.94%) was significantly higher than that of predominately solid (7.01%) or predominately cystic ones (1.75%), and that of markedly hypoechoic (100%) or hypoechoic thyroid nodules (29.78%) was significantly higher than that of hyperechoic/isoechoic nodules (15.27%). Thyroid nodules with irregular margins showed a significantly high malignancy rate than those with regular margins (76.74% vs. 6.25%). The malignancy rate of thyroid nodules with tall-than-wider shape was significantly higher than that of the remaining (50.00% vs. 17.81%). Moreover, a significantly higher malignancy rate was detected in thyroid nodules with halos than in those lacking halos (34.69% vs. 14.36%).

Malignancy rates of thyroid nodules categorized by ultrasound-based risk stratification systems

There was a significant difference in the category of thyroid nodules assessed by the six ultrasound-based risk stratification systems (all $P<0.001$, Table 3). In detail, 40.49%, 42.44%, 43.90%, 79.20%, 56.59% and 49.27% of FTA were considered as benign, moderately suspicious, K-TR3, EU-TR3, ACR-TR2 and C-TR3 assessed by ATASPS, AACE/ACE/AME, K-TIRADS, EU-TIRADS, ACR-TIRADS and C-TIRADS, respectively. Among them, the highest malignancy rate was detected in thyroid nodules with K-TR5 (66.67%), followed by C-TR4C (55.56%).

Diagnostic performances of six ultrasound-based risk stratification systems in distinguishing FTA from FTC

The diagnostic performances of six ultrasound-based risk stratification systems for distinguishing FTA from FTC were assessed by plotting the ROC curves. The AUCs of ATASPS, AACE/ACE/AME, K-TIRADS, EU-TIRADS, ACR-TIRADS and C-TIRADS in distinguishing FTA from FTC were 0.645, 0.729, 0.766, 0.635, 0.783 and 0.798, respectively (Figure 3, all $P<0.05$). Based on the Youden index, the optimal cut-off of ATASPS, AACE/ACE/AME, K-TIRADS, EU-TIRADS, ACR-

TABLE 1 Baseline characteristics of FTA and FTC patients.

	Pathology of thyroid nodules		Total	*P* value
	FTA	FTC		
Thyroid nodules (n, %)	205 (81.67)	46 (18.33)	251	
Case number (n, %)	179 (79.56)	46 (20.44)	225	
Age (years)	47.99 ± 13.63	48.20 ± 16.25		0.932
Sex (n, %)				
Male	42 (23.46)	12 (26.09)		
Female	137 (76.54)	34 (73.91)		
Thyroid nodule diameter (cm)	3.27 ± 1.66	3.30 ± 1.71		0.896

FTA, follicular thyroid adenoma; FTC, follicular thyroid carcinoma.

TABLE 2 Ultrasound characteristics of FTA and FTC, and the malignancy rate.

Ultrasound characteristics	Pathology		Total	Malignancy rate (%)	*P* value
	FTA n=205	FTC n=46			
Component					<0.001
Solid	70 (34.14)	41 (89.13)	111 (44.22)	36.94	
Cystic	83 (40.49)	0	83 (33.07)	0	
Mixed solid and cystic	52 (25.37)	5 (10.87)	57 (22.71)	8.77	
Echogenicity					0.007
Markedly hypoechoic	0 (0)	1 (2.17)	1 (0.40)	100	
Hypoechoic	33 (16.10)	14 (30.44)	47 (18.73)	29.78	
Isoechoic/hyperechoic	172 (83.90)	31 (67.39)	203 (80.88)	15.27	
Margin					<0.001
Irregular	10 (4.88)	13 (28.26)	208 (82.87)	6.25	
Regular	195 (95.12)	33 (71.74)	43 (17.13)	76.74	
Calcification					0.936
Microcalcification	11 (5.37)	3 (6.52)	14 (5.58)	21.43	
Macrocalcification	12 (5.85)	3 (6.52)	15 (5.98)	20.00	
Absent	182 (88.78)	40 (86.96)	222 (88.44)	18.01	
Shape					0.099
Taller-than-wide	2 (0.6)	2 (4.35)	4 (1.59)	50.00	
Wider-than-tall	203 (99.4)	44 (95.65)	247 (98.41)	17.81	
Comet-tail artifact					
Detected	5 (2.44)	1 (2.17)	6 (2.41)	16.67	0.915
Not detected	200 (97.56)	45 (97.82)	245 (97.59)	18.37	
Halo					<0.001
Detected	32 (15.61)	17 (36.96)	49 (19.52)	34.69	
Not detected	173 (84.39)	29 (63.04)	202 (80.48)	14.36	

FTA, follicular thyroid adenoma; FTC, follicular thyroid carcinoma.

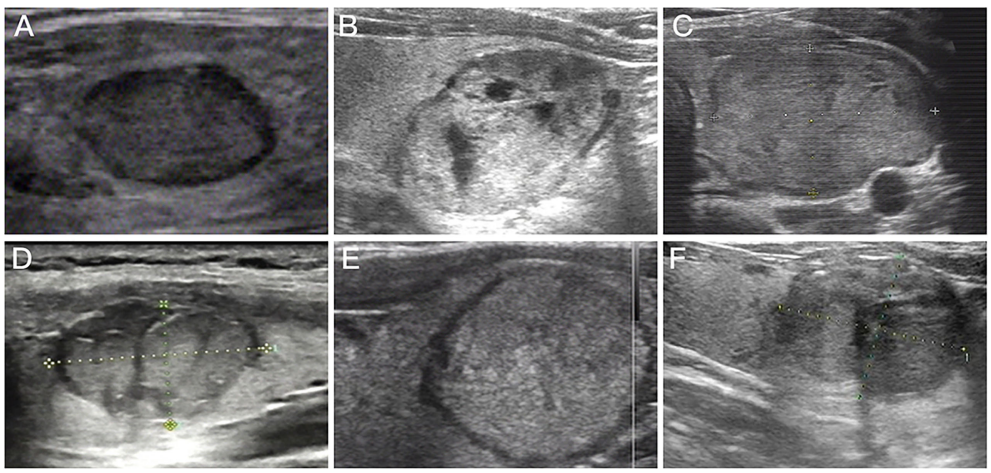

FIGURE 2
Preoperative ultrasound images for follicular thyroid adenoma and follicular thyroid carcinoma. **(A)** Preoperative ultrasound image of nodule with regular margin diagnosed as follicular thyroid adenoma; **(B)** Mixed nodule that postoperative pathological diagnosis was follicular thyroid adenoma; **(C)** Preoperative ultrasound image of isoechoic nodule diagnosed as follicular thyroid adenoma; **(D)** Preoperative ultrasound image of nodule with irregular margin diagnosed as follicular thyroid carcinoma; **(E)** Purely solid nodule that postoperative pathological diagnosis was follicular thyroid carcinoma; **(F)** Preoperative ultrasound image of hypoechoic nodule diagnosed as follicular thyroid carcinoma.

TABLE 3 Malignancy rate of thyroid nodules assessed by the six ultrasound-based risk stratification systems.

	Pathology		Malignancy rate (%)	
	Benign thyroid nodules n=205	Malignant thyroid nodules n=46		*P* value
ATASPS				<0.001
Benign	83 (40.49)	1 (2.17)	1.19	
Very low suspicion	43 (20.98)	1 (2.17)	2.27	
Low suspicion	48 (23.41)	22 (47.83)	31.43	
Intermediate suspicion	15 (7.32)	10 (21.74)	40	
High suspicion	3 (1.46)	3 (6.52)	50	
Nonclassifiable group	13 (6.34)	9 (19.57)	40.9	
AACE/ACE/AME				<0.001
Low	76 (37.07)	0	0	
Intermediate	87 (42.44)	24 (52.17)	21.62	
High suspicion	42 (20.49)	22 (47.82)	34.38	
K-TIRADS				<0.001
Benign (K-TR2)	81 (39.51)	0	0	
Low suspicion (K-TR3)	90 (43.90)	26 (56.52)	22.41	
Intermediate suspicion (K-TR4)	30 (14.63)	12 (26.09)	28.57	
High suspicion (K-TR5)	4 (1.95)	8 (17.39)	66.67	
EU-TIRADS				
Benign (EU-TR2)	0	0	0	<0.001
Low risk (EU-TR3)	162 (79.02)	24 (52.18)	12.9	
Intermediate risk (EU-TR4)	22 (10.73)	6 (13.04)	21.43	
High risk (EU-TR5)	21 (10.25)	16 (34.78)	43.24	
ACR-TIRADS				
Benign (ACR-TR1)	0	0	0	<0.001
Not suspicious (ACR-TR2)	116 (56.59)	2 (4.35)	1.7	
Mildly suspicious (ACR-TR3)	45 (21.95)	23 (50.00)	33.82	
Moderately suspicious (ACR-TR4)	37 (18.05)	15 (32.61)	28.85	
Highly suspicious (ACR-TR5)	7 (3.41)	6 (13.04)	46.15	
C-TIRADS				<0.001
C-TR2	0	0	0	
C-TR3	101 (49.27)	4 (8.69)	3.81	
C-TR4A	72 (35.12)	22 (47.83)	23.4	
C-TR4B	24 (11.71)	10 (21.74)	29.41	
C-TR4C	8 (3.90)	10 (21.74)	55.56	
C-TR5	0	0	0	

FTA, follicular thyroid adenoma; FTC, follicular thyroid carcinoma; 2 ATASPS, The American Thyroid Association Sonographic Pattern System; AACE/ACE/AME, American Association of Clinical Endocrinologists, American College of Endocrinology, and Associazione Medici Endocrinology; K-TIRADS, Korean thyroid imaging reporting and data system; EU-TIRADS, European Thyroid Association for the imaging reporting and data system; ACR-TIRADS, American College of Radiology for the imaging reporting and data system; C-TIRADS, 2020 Chinese Guidelines for Ultrasound Malignancy Risk Stratification of Thyroid Nodules.

TIRADS and C-TIRADS in distinguishing FTA from FTC was low suspicion, intermediate-risk, K-TR4, EU-TR5, ACR-TR3 and C-TR4A, respectively. In particular, the largest AUC was detected in C-TIRADS (0.798; 95%CI, 0.743-0.862), with sensitivity, specificity, PPV and NPV of 94.59% (95%CI, 81.85-99.34), 52.62% (95%CI, 45.38-59.81), 27.86% (95%CI, 24.59-31.36) and 98.17% (95%CI, 92.24-99.57), respectively. No significant difference in AUC was detected among the six ultrasound-based risk stratification systems. The highest sensitivity and specificity were achieved by the ATASPS (97.30%; 95%CI, 85.89-99.98) and K-TIRADS (97.92%; 95%CI, 94.81-99.48), respectively (Table 4).

Discussion

The diagnosis of FTC depends upon pathological confirmation of tumor capsular invasion and/or vascular invasion. Nevertheless, conventional tools for assessing thyroid nodules like ultrasonography, FNAC and CNB are unable to

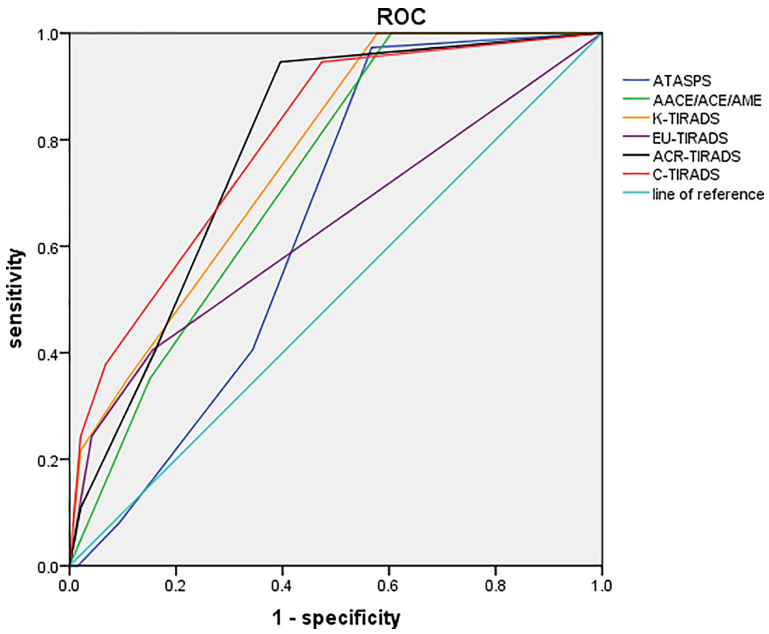

FIGURE 3
ROC curves of the six ultrasound-based risk stratification systems for distinguishing FTA from FTC. ROC, receiver operating characteristic; FTA, follicular thyroid adenoma; FTC, follicular thyroid carcinoma; ATASPS, The American Thyroid Association Sonographic Pattern System; AACE/ACE/AME, American Association of Clinical Endocrinologists, American College of Endocrinology, and Associazione Medici Endocrinology; K-TIRADS, Korean thyroid imaging reporting and data system; EU-TIRADS, European Thyroid Association for the imaging reporting and data system; ACR-TIRADS, American College of Radiology for the imaging reporting and data system; C-TIRADS, 2020 Chinese Guidelines for Ultrasound Malignancy Risk Stratification of Thyroid Nodules.

visualize these invasions, thereby discounting their diagnostic potential (21). Therefore, preoperative differential diagnosis of benign and malignant FN remains challenging. It is reported that the incidences of FTC and Hürthle cell carcinoma (HHC) from 1974 to 2013 remained stable (0.5-0.6% and 1.1-1.6%, respectively) in males and females, or even presented a decreasing trend (22). Englum et al. (23) have demonstrated that the male gender, black people, tumor size increase and distant metastasis are predictive factors for the diagnosis of FTC. In addition, as patients' age increased from 45 years, patients were more likely to be diagnosed with FTC. In the present study, there were no significant differences in the sex, mean age and thyroid nodule size between FTC and FTA patients. Therefore, the potential of age and sex in predicting benign or malignant FN remains to be further analyzed.

High-resolution ultrasonography of thyroid nodules is of great significance in the screening, diagnosis, preoperative evaluation, and postoperative follow-up (24, 25). In the

TABLE 4 The diagnostic performance of 2015 ATA, AACE/ACE/AME, K-TIRADS, EU-TIRADS, ACR-TIRADS and C-TIRADS.

	Cut-off	Sensitivity (%, 95%CI)	Specificity (%, 95%CI)	PPV (%, 95%CI)	NPV (%, 95%CI)	AUC
ATASPS	Low suspicion	97.30 (85.89-99.98)	43.23 (36.17-50.64)	24.81 (22.49-27.46)	98.83 (92.34-99.82)	0.645 (0.573-0.716)
AACE/ACE/AME	Intermediate suspicion	93.85 (91.73-99.91)	39.58 (32.64-46.91)	24.28 (22.18-26.35)	99.31 (95.21-99.98)	0.729 (0.667-0.790)
K-TIRADS	K-TR4	21.62 (9.29-38.27)	97.92 (94.81-99.48)	66.73 (38.82-86.37)	86.69 (84.59-88.53)	0.766 (0.707-0825)
EU-TIRADS	EU-TR5	24.32 (11.82-41.25)	95.83 (92.01-98.27)	52.93 (31.77-73.24)	86.83 (84.51-88.86)	0.635 (0.547-0.723)
ACR-TIRADS	ACR-TR3	94.59 (81.85-99.34)	60.42 (53.18-67.42)	31.55 (27.63-35.89)	98.32 (93.76-99.65)	0.783 (0.702-0.847)
C-TIRADS	C-TR4A	94.59 (81.85-99.34)	52.62 (45.38-59.81)	27.86 (24.59-31.36)	98.17 (92.24-99.57)	0.798 (0.743-0.862)

CI, confidence interval; PPV, positive predictive value; NPV, negative predictive value; AUC, area under the curve; 2015 ATA, the 2015 American Thyroid Association management guidelines for adult patients with thyroid nodules and differentiated thyroid cancer; AACE/ACE/AME, American Association of Clinical Endocrinologists, American College of Endocrinology, and Associazione Medici Endocrinology; K-TIRADS, Korean thyroid imaging reporting and data system; EU-TIRADS, European Thyroid Association for the imaging reporting and data system; ACR-TIRADS, American College of Radiology for the imaging reporting and data system; C-TIRADS, 2020 Chinese Guidelines for Ultrasound Malignancy Risk Stratification of Thyroid Nodules.

present study, we compared the ultrasound characteristics of FTA and FTC patients, involving 251 thyroid nodules. Only 5 FTC were mixed cystic and solid thyroid nodules, and most of the rest only were solid nodules; 34.13% and 40.49% cases of FTA were solid and cystic, respectively, and the remaining were mixed solid and cystic; 30.73% of FTA cases were postoperatively diagnosed as follicular adenoma with cystic lesions or hemorrhage. Mixed cystic and solid thyroid nodules are mainly caused by the degeneration of benign thyroid nodules, including cystic degeneration, hemorrhage, necrosis, etc. Only a small number of thyroid nodules contain epithelial tissues, and the malignancy rate of mixed cystic and solid thyroid nodules ranges 5.4-11.1% (26, 27). FTC is solid in most cases, closely linked with the angiogenesis during the process of tumor cell formation and growth. It is reported that the vascular endothelial growth factor-2 (VEGFR2) signaling pathway acts to promote the pathological angiogenesis during tumor cell generation and hyperplasia (28). Asghar et al. (29) have revealed that stromal interaction molecule 1 (STIM1) is significantly upregulated in thyroid tumor tissues than in normal thyroid tissues, the expression level of which is higher in FTC than in PTC. Moreover, knockdown of STIM1 results in the downregulation of VEGFR2 in FTC cells *in vitro*.

Compared with FTA, FTC mainly manifested the following ultrasound characteristics, including solid component, hypoechoic appearance, irregular margin and the presence of halo. Sillery et al. (30) have demonstrated that the sonographic features of FTA are similar to those of FTC, but larger lesion size, lack of a sonographic halo, hypoechoic, and absence of cystic change are conducive to the diagnosis of FTC. The EU-TIRADS proposes that interrupted peripheral macrocalcifications, a thick halo, or lack of a halo would increase the malignancy risk, while a thin halo indicates a benign thyroid nodule (18). Li et al. (31) have suggested that an intermittent or uninterrupted irregular halo, hypoechoic or markedly hypoechoic, and solid component are independent risk factors for FTC. In the present study, there were 30 and 2 cases of FTA with a thin and a thick halo, respectively, while 14 and 3 cases of FTC presented a thin and a thick halo, respectively. No significant difference in the incidence of thin/thick halo was detected between FTA and FTC patients (P=0.326). Collectively, ultrasound characteristics of FTC were mainly characterized as solid component, hypoechoic appearance, and irregular margin. Moreover, the ultrasound characteristics of a sonographic halo should be further analyzed.

Microcalcification used to be considered as a classical sign of malignant thyroid tumors, while coarse calcification or macrocalcification is more commonly detected in benign nodules. Kuo et al. (32) have suggested that calcification on the ultrasound image is an independent factor for predicting FTC. Therefore, it is believed that calcification contributes to distinguishing FTC from FTA. Our study showed that the malignancy rate of thyroid nodules with microcalcification was slightly higher than those with macrocalcification (21.43% vs. 18.01%), while no significant difference in the calcification type was detected between FTA and FTC. A total of 11 cases of cystic or mixed solid and cystic FTA presented microcalcification, and among them, 8 cases represented the comet-tail artifacts. However, comet-tail artifacts were not detected in 3 cases of FTC with solid nodules. Hyperechoic along with comet-tail artifacts in thyroid nodules with cystic components are highly suggestive of benignity (5, 33). In addition to the calcification, echogenic foci also suggest the concentrated colloid, which is the manifestation of benign cystic thyroid nodules. Notably, echogenic foci with comet-tail artifacts are not the absolute predictor of benign thyroid nodules. Wu et al. (34) have argued that echogenic foci with comet-tail artifacts in cystic components are the predictor of benign thyroid nodules, while those in solid components are not an absolute predictor of benign thyroid nodules. Therefore, punctate echogenic foci with comet-tail artifacts contribute to distinguishing benign thyroid nodules from malignant ones. The diagnostic potential of microcalcification in FTC, however, remains unclear.

Based on the Youden index, the optimal cut-off values of ATASPS, AACE/ACE/AME, K-TIRADS, EU-TIRADS, ACR-TIRADS and C-TIRADS in distinguishing FTA from FTC were low suspicion pattern, moderately suspicious, K-TR4, EU-TR5, ACR-TR3 and C-TR4A, respectively. Castellana et al. (14) have categorized 45 cases of FTC using 7 ultrasound-based risk stratification systems. When they were classified in 7 US RSSs, the prevalent classes were intermediate risk by AACE/ACE/AME (53%), TR4 by ACR-TIRADS (60%), U4 by BTA (50%), K-TIRADS 4 by K-TIRADS (53%) and TIRADS 4A by TIRADS (75%). Moreover, AACE/ACE/AME, ACR-TIRADS, ATA, EU-TIRADS and TIRADS missed 1 case of FTC (16%) and K-TIRADS did not miss any case based on the cut-off value of moderate suspicion. Our data showed that the specificity of K-TIRADS in diagnosing FTC was remarkably higher than that of other systems.

Existing data on the evaluation of FN using different ultrasound-based risk stratification systems are inconsistent. Here, the AUCs of diagnosing FTC by the six ultrasound-based risk stratification systems ranged from 0.635 to 0.798 (P<0.05). Lin et al. (15) have reported that the AUC of K-TIRADS, EU-TIRADS, ACR-TIRADS, C-TIRADS, ACEE and ATA in diagnosing FTC based on the cut-off value of moderate or highly suspicion is disappointing (AUC=0.511-0.611, P<0.05). Liu et al. (35) have revealed the acceptable performance of ATA (AUC=0.744, P<0.001) and ACR-TIRADS (AUC=0.744, P<0.001) in distinguishing benign FN from malignant ones. Hamour et al. (36) have shown that the standardized use of TI-RADS and educational initiatives increases the clinical value of TI-RADS. Notably, most cases of FTC can be preoperatively identified by current ultrasound-based risk stratification systems and subjected to FNAC, because the lesion size is considered as the indicator for FNAC (14). Given that some cases of FTC are non-highly suspicious and difficult to be identified by cytological evaluation,

follow-up ultrasonography is recommended for thyroid nodules with uncertain cytological findings.

Several limitations in this study should be noted. First of all, it was a retrospective study involving surgically treated patients after thyroid lobectomy or total thyroidectomy, which may result in the selection bias and increased malignancy rate of thyroid nodules. Second, it was a multi-center study that may cause differences related to investigators at different institutions. Prospective studies with a larger sample size are needed to analyze other suspicious factors for diagnosing malignant thyroid nodules in the future.

Taken together, all the six ultrasound-based risk stratification systems display favorable diagnostic potential for FN. Among them, C-TIRAD presents the best diagnostic performance, followed by ACR-TIRADS, K-TIRADS, AACE/ACE/AME and ATASPS. In addition, ATASPS and K-TIRADS pose the highest sensitivity and specificity in distinguishing FTA from FTC, respectively.

Data availability statement

The raw data supporting the conclusions of this article will be made available by the authors, without undue reservation.

Ethics statement

The studies involving human participants were reviewed and approved by the ethics committee of the Jiangsu Province Academy of Traditional Chinese Medicine. Written informed consent for participation was not required for this study in accordance with the national legislation and the institutional requirements.

Author contributions

JY, FX, and SX developed the research questionnaire and wrote the protocol for this study. JY, FX, and YS were responsible for data collection and analysis. XL, GC, WD, and RL participated the diagnosis. JW were the operators for surgery. YZ and XH were responsible for the perioperative management. SX, FX, and CL interpreted the results. JY and YS wrote the article. SX and CL revised it critically for important intellectual content. All authors agreed to take responsibility for the integrity of the data and the accuracy of the data analysis. All authors contributed to the article and approved the submitted version.

Funding

This work was granted by the Key Research and Development Plan (Social Development) of Jiangsu Province, BE2020726, Medical Scientific Research Foundation of Jiangsu Province of China (Surface project), M2020102, Research and Practice Innovation Project of Nanjing University of Chinese Medicine, SJCX21_0752.

Conflict of interest

The authors declare that the research was conducted in the absence of any commercial or financial relationships that could be construed as a potential conflict of interest.

Publisher's note

All claims expressed in this article are solely those of the authors and do not necessarily represent those of their affiliated organizations, or those of the publisher, the editors and the reviewers. Any product that may be evaluated in this article, or claim that may be made by its manufacturer, is not guaranteed or endorsed by the publisher.

References

1. Grani G, Lamartina L, Durante C, Filetti S, Cooper DS. Follicular thyroid cancer and hurthle cell carcinoma: challenges in diagnosis, treatment, and clinical management. *Lancet Diabetes Endocrinol* (2018) 6:500–14. doi: 10.1016/S2213-8587(17)30325-X

2. Dralle H, Machens A, Basa J, Fatourechi V, Franceschi S, Hay ID, et al. Follicular cell-derived thyroid cancer. *Nat Rev Dis Primers* (2015) 1:15077. doi: 10.1038/nrdp.2015.77

3. Choi YJ, Baek JH, Suh CH, Shim WH, Jeong B, Kim JK, et al. Core-needle biopsy versus repeat fine-needle aspiration for thyroid nodules initially read as atypia/follicular lesion of undetermined significance. *Head Neck* (2017) 39:361–9. doi: 10.1002/hed.24597

4. VandenBussche CJ, Olson MT, Adams C, Ali SZ. Cytotechnologist performance for screening microfollicular atypia in indeterminate thyroid fine-needle aspirates. *Acta Cytol* (2014) 58:432–8. doi: 10.1159/000367882

5. Zhou J, Yin L, Wei X, Zhang S, Song Y, Luo B, et al. 2020 Chinese guidelines for ultrasound malignancy risk stratification of thyroid nodules: the c-TIRADS. *Endocrine* (2020) 70:256–79. doi: 10.1007/s12020-020-02441-y

6. Horvath E, Majlis S, Rossi R, Franco C, Niedmann JP, Castro A, et al. An ultrasonogram reporting system for thyroid nodules stratifying cancer risk for clinical management. *J Clin Endocrinol Metab* (2009) 94:1748–51. doi: 10.1210/jc.2008-1724

7. Sorrenti S, Dolcetti V, Fresilli D, Del Gaudio G, Pacini P, Huang P, et al. The role of CEUS in the evaluation of thyroid cancer: From diagnosis to local staging. *J Clin Med 10* (2021) 10:4559. doi: 10.3390/jcm10194559

8. Sorrenti S, Dolcetti V, Radzina M, Bellini MI, Frezza F, Munir K, et al. Artificial intelligence for thyroid nodule characterization: Where are we standing? *Cancers (Basel)* (2022) 14:3357. doi: 10.3390/cancers14143357

9. Nam SY, Shin JH, Han BK, Ko EY, Ko ES, Hahn SY, et al. Preoperative ultrasonographic features of papillary thyroid carcinoma predict biological behavior. *J Clin Endocrinol Metab* (2013) 98:1476–82. doi: 10.1210/jc.2012-4072

10. McHenry CR, Phitayakorn R. Follicular adenoma and carcinoma of the thyroid gland. *Oncologist* (2011) 16:585–93. doi: 10.1634/theoncologist.2010-0405

11. La Vecchia C, Malvezzi M, Bosetti C, Garavello W, Bertuccio P, Levi F, et al. Thyroid cancer mortality and incidence: a global overview. *Int J Cancer* (2015) 136:2187–95. doi: 10.1002/ijc.29251

12. Trimboli P, Castellana M, Piccardo A, Romanelli F, Grani G, Giovanella L, et al. The ultrasound risk stratification systems for thyroid nodule have been evaluated against papillary carcinoma. a meta-analysis. *Rev Endocr Metab Disord* (2021) 22:453–60. doi: 10.1007/s11154-020-09592-3

13. Park JW, Kim DW, Kim D, Baek JW, Lee YJ, Baek HJ. Korean Thyroid imaging reporting and data system features of follicular thyroid adenoma and carcinoma: a single-center study. *Ultrasonography* (2017) 36:349–54. doi: 10.14366/usg.17020

14. Castellana M, Piccardo A, Virili C, Scappaticcio L, Grani G, Durante C, et al. Can ultrasound systems for risk stratification of thyroid nodules identify follicular carcinoma? *Cancer Cytopathol* (2020) 128:250–9. doi: 10.1002/cncy.22235

15. Lin Y, Lai S, Wang P, Li J, Chen Z, Wang L, et al. Performance of current ultrasound-based malignancy risk stratification systems for thyroid nodules in patients with follicular neoplasms. *Eur Radiol* (2022) 32:3617–30. doi: 10.1007/s00330-021-08450-3

16. Shin JH, Baek JH, Chung J, Ha EJ, Kim JH, Lee YH, et al. Ultrasonography diagnosis and imaging-based management of thyroid nodules: Revised Korean society of thyroid radiology consensus statement and recommendations. *Korean J Radiol* (2016) 17:370–95. doi: 10.3348/kjr.2016.17.3.370

17. Tessler FN, Middleton WD, Grant EG, Hoang JK, Berland LL, Teefey SA, et al. Reporting and data system (TI-RADS): White paper of the ACR TI-RADS committee. *J Am Coll Radiol* (2017) 14:587–95. doi: 10.1016/j.jacr.2017.01.046

18. Russ G, Bonnema SJ, Erdogan MF, Durante C, Ngu R, Leenhardt L. European Thyroid association guidelines for ultrasound malignancy risk stratification of thyroid nodules in adults: The EU-TIRADS. *Eur Thyroid J* (2017) 6:225–37. doi: 10.1159/000478927

19. Haugen BR, Alexander EK, Bible KC, Doherty GM, Mandel SJ, Nikiforov YE, et al. 2015 American thyroid association management guidelines for adult patients with thyroid nodules and differentiated thyroid cancer: The American thyroid association guidelines task force on thyroid nodules and differentiated thyroid cancer. *Thyroid* (2016) 26:1–133. doi: 10.1089/thy.2015.0020

20. Gharib H, Papini E, Garber JR, Duick DS, Harrell RM, Hegedus L, et al. American Association of clinical endocrinologists, American college of endocrinology, and associazione Medici endocrinologi medical guidelines for clinical practice for the diagnosis and management of thyroid nodules–2016 update. *Endocr Pract* (2016) 22:622–39. doi: 10.4158/EP161208.GL

21. Daniels GH. Follicular thyroid carcinoma: A perspective. *Thyroid* (2018) 28:1229–42. doi: 10.1089/thy.2018.0306

22. Lim H, Devesa SS, Sosa JA, Check D, Kitahara CM. Trends in thyroid cancer incidence and mortality in the united states, 1974-2013. *JAMA* (2017) 317:1338–48. doi: 10.1001/jama.2017.2719

23. Englum BR, Pura J, Reed SD, Roman SA, Sosa JA, Scheri RP. A bedside risk calculator to preoperatively distinguish follicular thyroid carcinoma from follicular variant of papillary thyroid carcinoma. *World J Surg* (2015) 39:2928–34. doi: 10.1007/s00268-015-3192-4

24. Yoo J, Ahn HS, Kim SJ, Park SH, Seo M, Chong S. Evaluation of diagnostic performance of screening thyroid ultrasonography and imaging findings of screening-detected thyroid cancer. *Cancer Res Treat* (2018) 50:11–8. doi: 10.4143/crt.2016.600

25. Ahn HS, Lee JB, Seo M, Park SH, Choi BI. Distinguishing benign from malignant thyroid nodules using thyroid ultrasonography: utility of adding superb microvascular imaging and elastography. *Radiol Med* (2018) 123:260–70. doi: 10.1007/s11547-017-0839-2

26. Lee MJ, Kim EK, Kwak JY, Kim MJ. Partially cystic thyroid nodules on ultrasound: probability of malignancy and sonographic differentiation. *Thyroid* (2009) 19:341–6. doi: 10.1089/thy.2008.0250

27. Garcia-Pascual L, Barahona MJ, Balsells M, del Pozo C, Anglada-Barcelo J, Casalots-Casado J, et al. Complex thyroid nodules with nondiagnostic fine needle aspiration cytology: histopathologic outcomes and comparison of the cytologic variants (cystic vs. acellular). *Endocrine* (2011) 39:33–40. doi: 10.1007/s12020-010-9409-2

28. Jang JY, Choi SY, Park I, Park DY, Choe K, Kim P, et al. VEGFR2 but not VEGFR3 governs integrity and remodeling of thyroid angiofollicular unit in normal state and during goitrogenesis. *EMBO Mol Med* (2017) 9:750–69. doi: 10.15252/emmm.201607341

29. Asghar MY, Lassila T, Paatero I, Nguyen VD, Kronqvist P, Zhang J, et al. Stromal interaction molecule 1 (STIM1) knock down attenuates invasion and proliferation and enhances the expression of thyroid-specific proteins in human follicular thyroid cancer cells. *Cell Mol Life Sci* (2021) 78:5827–46. doi: 10.1007/s00018-021-03880-0

30. Sillery JC, Reading CC, Charboneau JW, Henrichsen TL, Hay ID, Mandrekar JN. Thyroid follicular carcinoma: sonographic features of 50 cases. *AJR Am J Roentgenol* (2010) 194:44–54. doi: 10.2214/AJR.09.3195

31. Li W, Song Q, Lan Y, Li J, Zhang Y, Yan L, et al. The value of sonography in distinguishing follicular thyroid carcinoma from adenoma. *Cancer Manag Res* (2021) 13:3991–4002. doi: 10.2147/CMAR.S307166

32. Kuo TC, Wu MH, Chen KY, Hsieh MS, Chen A, Chen CN. Ultrasonographic features for differentiating follicular thyroid carcinoma and follicular adenoma. *Asian J Surg* (2020) 43:339–46. doi: 10.1016/j.asjsur.2019.04.016

33. Malhi H, Beland MD, Cen SY, Allgood E, Daley K, Martin SE, et al. Echogenic foci in thyroid nodules: significance of posterior acoustic artifacts. *AJR Am J Roentgenol* (2014) 203:1310–6. doi: 10.2214/AJR.13.11934

34. Wu H, Zhang B, Li J, Liu Q, Zhao T. Echogenic foci with comet-tail artifact in resected thyroid nodules: Not an absolute predictor of benign disease. *PloS One* (2018) 13:e0191505. doi: 10.1371/journal.pone.0191505

35. Liu BJ, Zhang YF, Zhao CK, Wang HX, Li MX, Xu HX. Conventional ultrasound characteristics, TI-RADS category and shear wave speed measurement between follicular adenoma and follicular thyroid carcinoma. *Clin Hemorheol Microcirc* (2020) 75:291–301. doi: 10.3233/CH-190750

36. Hamour AF, Yang W, Lee JJW, Wu V, Ziai H, Singh P, et al. Association of the implementation of a standardized thyroid ultrasonography reporting program with documentation of nodule characteristics. *JAMA Otolaryngol Head Neck Surg* (2021) 147:343–9. doi: 10.1001/jamaoto.2020.5233

frontiers | Frontiers in Oncology

TYPE Original Research
PUBLISHED 08 November 2022
DOI 10.3389/fonc.2022.1012724

OPEN ACCESS

EDITED BY
Lorenz Kadletz-Wanke,
Medical University of Vienna, Austria

REVIEWED BY
Salvatore Sorrenti,
Department of Surgical Sciences,
Sapienza University of Rome, Italy
Fajin Dong,
Jinan University, China

*CORRESPONDENCE
Jiawei Tian
jwtian2004@163.com
Yanyan Yu
yy.yu@szu.edu.cn

†These authors have contributed equally to this work

SPECIALTY SECTION
This article was submitted to Head and Neck Cancer, a section of the journal Frontiers in Oncology

RECEIVED 05 August 2022
ACCEPTED 18 October 2022
PUBLISHED 08 November 2022

CITATION
Tao Y, Yu Y, Wu T, Xu X, Dai Q, Kong H, Zhang L, Yu W, Leng X, Qiu W and Tian J (2022) Deep learning for the diagnosis of suspicious thyroid nodules based on multimodal ultrasound images. *Front. Oncol.* 12:1012724. doi: 10.3389/fonc.2022.1012724

Deep learning for the diagnosis of suspicious thyroid nodules based on multimodal ultrasound images

Yi Tao[1†], Yanyan Yu[2*†], Tong Wu[1], Xiangli Xu[3], Quan Dai[1], Hanqing Kong[1], Lei Zhang[1], Weidong Yu[1], Xiaoping Leng[1], Weibao Qiu[4] and Jiawei Tian[1*]

[1]Department of Ultrasound, The Second Affiliated Hospital of Harbin Medical University, Harbin, China, [2]The National-Regional Key Technology Engineering Laboratory for Medical Ultrasound, Guangdong Key Laboratory for Biomedical Measurements and Ultrasound Imaging, School of Biomedical Engineering, Health Science Center, Shenzhen University, Shenzhen, China, [3]Department of Ultrasound, The Second Hospital of Harbin, Harbin, China, [4]Shenzhen Key Laboratory of Ultrasound Imaging and Therapy, Paul C. Lauterbur Research Center for Biomedical Imaging, Shenzhen Institutes of Advanced Technology, Chinese Academy of Sciences, Shenzhen, China

Objectives: This study aimed to differentially diagnose thyroid nodules (TNs) of Thyroid Imaging Reporting and Data System (TI-RADS) 3–5 categories using a deep learning (DL) model based on multimodal ultrasound (US) images and explore its auxiliary role for radiologists with varying degrees of experience.

Methods: Preoperative multimodal US images of 1,138 TNs of TI-RADS 3–5 categories were randomly divided into a training set (n = 728), a validation set (n = 182), and a test set (n = 228) in a 4:1:1.25 ratio. Grayscale US (GSU), color Doppler flow imaging (CDFI), strain elastography (SE), and region of interest mask (Mask) images were acquired in both transverse and longitudinal sections, all of which were confirmed by pathology. In this study, fivefold cross-validation was used to evaluate the performance of the proposed DL model. The diagnostic performance of the mature DL model and radiologists in the test set was compared, and whether DL could assist radiologists in improving diagnostic performance was verified. Specificity, sensitivity, accuracy, positive predictive value, negative predictive value, and area under the receiver operating characteristics curves (AUC) were obtained.

Results: The AUCs of DL in the differentiation of TNs were 0.858 based on (GSU + SE), 0.909 based on (GSU + CDFI), 0.906 based on (GSU + CDFI + SE), and 0.881 based (GSU + Mask), which were superior to that of 0.825-based single GSU (p = 0.014, p< 0.001, p< 0.001, and p = 0.002, respectively). The highest AUC of 0.928 was achieved by DL based on (G + C + E + M)US, the highest specificity of 89.5% was achieved by (G + C + E)US, and the highest accuracy of 86.2% and sensitivity of 86.9% were achieved by DL based on (G + C + M)US. With DL assistance, the AUC of junior radiologists increased from 0.720 to 0.796 (p< 0.001), which was slightly higher than that of senior

radiologists without DL assistance (0.796 vs. 0.794, $p > 0.05$). Senior radiologists with DL assistance exhibited higher accuracy and comparable AUC than that of DL based on GSU (83.4% vs. 78.9%, $p = 0.041$; 0.822 vs. 0.825, $p = 0.512$). However, the AUC of DL based on multimodal US images was significantly higher than that based on visual diagnosis by radiologists ($p< 0.05$).

Conclusion: The DL models based on multimodal US images showed exceptional performance in the differential diagnosis of suspicious TNs, effectively increased the diagnostic efficacy of TN evaluations by junior radiologists, and provided an objective assessment for the clinical and surgical management phases that follow.

KEYWORDS

thyroid nodule, deep learning, multimodal, ultrasound, diagnosis

1 Introduction

Thyroid cancer has become the most common endocrine malignancy, with an increasing incidence of approximately 7%–15% annually (1, 2). Ultrasound (US) is widely used as a first-line screening tool for the clinical examination of thyroid lesions, with the advantages of no exposure to radiation, real-time dynamic imaging, and simplicity of procedure (1, 3). Multiple versions of the Thyroid Imaging Reporting and Data System (TI-RADS) have been proposed for US imaging to standardize and improve the diagnostic consistency and accuracy of thyroid lesions, and each risk stratification system has its advantages (1, 3–6).

Nevertheless, US diagnosis of thyroid nodules (TNs) is subjective to a certain extent. Various diagnostic results of US evaluation of TNs were obtained from different observers, especially less-experienced radiologists, who showed relatively lower accuracy. In previous studies, moderate variability in the interobserver agreement was found among different TI-RADS scores (7). There was fair agreement in margin, echotexture, and echogenicity (k = 0.34, 0.26, and 0.34, respectively) for interobserver variability (8–10). Clinically, there is a wide range of malignant risks (approximately 2%–90%) and some overlapping US features for the TNs of TI-RADS 3–5 categories; therefore, it was difficult for radiologists to accurately differentiate between benign and malignant TNs (11–13), resulting in overdiagnosis or misdiagnosis.

Fine-needle aspiration (FNA) is a relatively effective method for the preoperative diagnosis of TNs (14). The radiologists assess the malignant probability of TNs and then recommend patients for FNA or US follow-up according to TI-RADS. However, FNA is an invasive procedure with some possible complications, such as bleeding, and FNA results are also dependent on the size, composition of TNs, and skills of radiologists. Moreover, approximately 20% of the FNA results were rendered inconclusive, which led to uncertainty in the next course of clinical treatment (15–17). The development of artificial intelligence (AI) technology has shown great potential in reducing the influence of subjectivity and improving the consistency of diagnosis.

In the past two decades, machine-learning methods have been used in TN characterization, which is usually known as "radiomics" (18, 19). Radiomics can automatically extract features in the region of interest (ROI), which tends to be difficult to discern with the naked eye. It should be noted that high-throughput features extracted by radiomics from the ROI are easily affected by the segmentation strategy and imaging parameters. Deep learning (DL) is a machine-learning concept that has shown strong capability in medical image characterization and outperforms traditional machine-learning methods. With the help of artificial neural networks, DL has been widely applied to differentiate breast, thyroid, and liver lesions with good performance (20–22). However, radiologists cannot be completely replaced with AI technology. It is crucial to integrate DL methods into clinical practice; therefore, they can aid radiologists in diagnosis, evaluation, and decision-making (23). In this study, the diagnostic performances of junior and senior radiologists with and without a DL assistant were compared.

Most previous studies using DL for the diagnosis of TNs have concentrated on grayscale US (GSU) imaging. However, beyond conventional GSU, some new US technologies such as color Doppler flow imaging (CDFI), elastography, and contrast-enhanced ultrasonography are commonly used to assist in the

diagnosis of GSU for TNs, which have been proven to improve the diagnostic accuracy in the clinical evaluation (13, 24, 25). This indicated that the features of blood flow and hardness also played an important role in thyroid US diagnosis. Therefore, in our study, new DL models based on multimodal US imaging were proposed to explore their application value in improving the diagnostic accuracy of suspicious thyroid lesions and the role of auxiliary diagnosis for radiologists.

2 Materials and methods

2.1 Patients

This retrospective study was approved by the Ethics Committee of The Second Affiliated Hospital of Harbin Medical University, and the requirement for informed consent was waived (approval number KY2021-152). Consecutive patients who had undergone thyroid surgery at The Second Affiliated Hospital of Harbin Medical University between September 9, 2020, and June 6, 2021, were enrolled. The inclusion criteria of the enrolled patients were as follows: lesions with (1) complete or high-quality transverse and longitudinal section images (2), complete surgical records and pathological results (3), no preoperative operation such as FNA and ablation or surgical treatment of TNs, and (4) US examination in our hospital within 1 week before surgery. Finally, 1,138 TNs of TI-RADS 3–5 categories from 781 patients were included in the study. The postoperative pathological results were used as the gold standard. The mean diagnostic age of patients was 47.74 ± 10.60 years (range, 21–79 years). According to the pathological results, there were 550 (48.33%) malignant and 588 (51.67%) benign TNs. The workflow of the selection is shown in Figure 1.

2.2 Ultrasound image acquisition and analysis

Preoperative thyroid US examinations were performed by two radiologists with 10 years of experience (Q.D. and H.K.) using a US device (Hitachi HI VISION Avius, Hitachi Medical Corporation, Tokyo, Japan) equipped with a 5- to 13-MHz linear probe. According to the Chinese TI-RADS (C-TIRADS) issued by the Chinese Society of Ultrasound in Medicine in 2020, thyroid scanning and imaging parameter adjustments were guided and completed (6). The GSU, CDFI, and strain elastography (SE) images of the TNs were acquired in transverse and longitudinal sections, which showed obvious characteristics and were saved in BMP format.

The ultrasonographic features were evaluated for all 1,138 TNs in our study. To maintain consistency, the images were independently analyzed by two experienced radiologists (L.Z. and W.Y.) in a double-blind manner, and results were obtained through consultation by consensus when discrepancies arose. GSU features, including the maximum diameter, position, echotexture, echogenicity, composition, orientation, margin, punctate echogenic foci, halo, and posterior features, were evaluated visually according to the C-TIRADS. CDFI could indicate tumor blood flow characteristics using the vascular

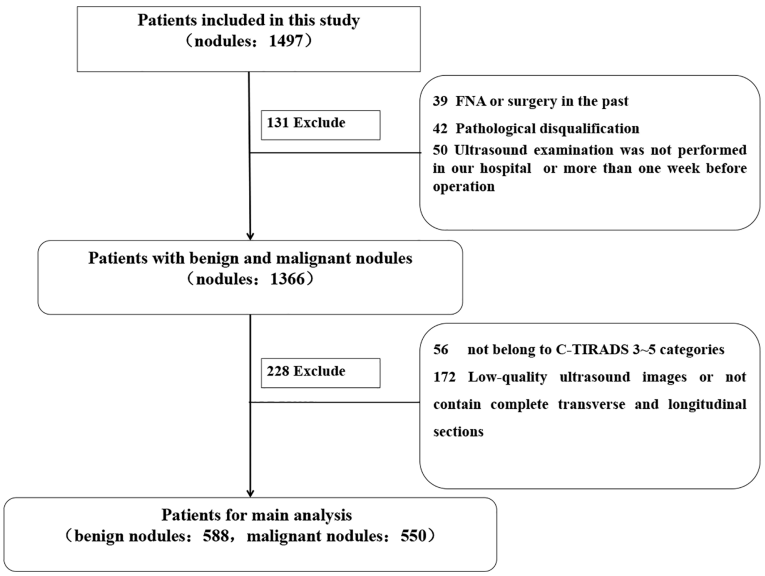

FIGURE 1
Flowchart of enrolling patients with thyroid nodules.

distribution pattern and Adler grade (0–3) standards (26). Tumor tissue hardness was evaluated on a scale of 1–4 according to the Asteria standard by SE (27).

2.3 Construction of deep learning

2.3.1 Pretreatment of multimodal and double-view ultrasound images

Four modalities of TN images were included in our research: GSU, CDFI, SE, and ROI mask (Mask) images. Each modal image was captured from both horizontal and vertical perspectives. The multimodal and double-view US images of a TN in the right lobe of a 65-year-old female patient with pathologically proven papillary carcinoma are illustrated in Figure 2. The Masks of the TNs were manually segmented using ImageJ (version 1.48, National Institutes of Health, USA) by two radiologists (Q.D. and Y.T.). The total data set was separated into training, validation, and test data sets, with a ratio of 4:1:1.25.

2.3.2 Deep residual learning with attention block

Deep networks can extract more abstract information from low-level feature maps, which enables them to perform better than shallow networks. The residue strategy provides a skip connection to solve the degradation problem, making it possible to train a very deep network. To make full use of the multimodal image features, ResNet-50 (28) was used as the backbone for feature extraction in our method. In the ResNet-50, there is one convolutional layer and 16 residual blocks. For the essential composition of ResNet-50, a residual block is defined as follows:

$$y = x + F(x, W) \tag{1}$$

where x and y denote the input and output feature maps of the residual block, respectively. F refers to the residual function, which is learned by stacked convolutional layers with different kernel sizes in the residual block. The right side of the equation is obtained by feedforward neural networks with skip connections, which allow gradients to propagate through the networks.

All available multimodal images were preprocessed to a size of $224 \times 224 \times 3$ pixels, where 224 denotes the width and height and 3 denotes the channels of images. The training and validation data sets were randomly divided into five parts for fivefold cross-validation. Multimodal US images of the same patient were sent to the training, validation, or testing data set as one sample. During the training process, the parameters of the modal were optimized by forward and backward propagation computing until the prediction reached a high accuracy related to the ground truth. The feedforward process can be mathematically expressed as follows:

$$h_l = R_l(W_l * h_{l-1} + b_l) \tag{2}$$

where l denotes the number of layers. h_l represents the output feature map of the l layer with h_{l-1} as the input. W and b denote the weights and biases of the convolutional filter bank, respectively. R is a rectified linear activation (ReLU) function. In back propagation, the parameters of the network are updated by optimizing the following binary cross-entropy loss.

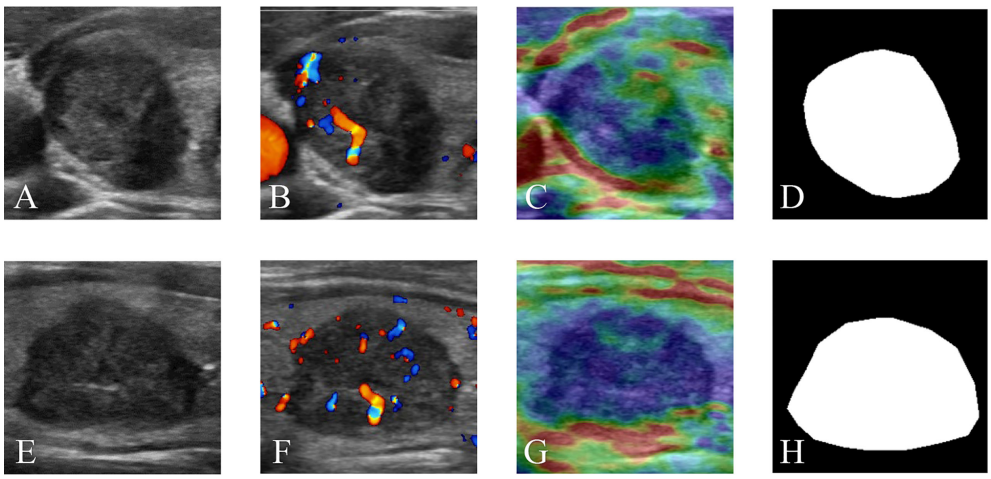

FIGURE 2
Multimodal ultrasound images of a thyroid nodule in the right lobe of a 65-year-old female patient with a pathologically proven papillary carcinoma. **(A)** GSU, **(B)** CDFI, **(C)** SE, and **(D)** Mask ultrasound images in transverse section. **(E)** GSU, **(F)** CDFI, **(G)** SE, and **(H)** Mask ultrasound images in longitudinal section. GSU, grayscale ultrasound; CDFI, color Doppler flow imaging; SE, strain elastography; Mask, region of interest mask.

Because of the low contrast and small area of TNs in thyroid US images, it is necessary to obtain effective feature information. However, the key channels and spatial position of the lesion cannot be identified because the information obtained by the convolution operation with the kernel in ResNet is local and may fail to capture effective features from the global image. To solve this problem, we combined the convolutional bottleneck attention module (29) and ResNet-50 to learn the weights for our feature maps (Figure 3). Two attention units were inserted before the first and after the last residual block to obtain abstract features from both the higher and lower layers, as shown in Figure 3A. There are two types of attention mechanisms in the attention unit: spatial attention and channel attention, as shown in Figure 3B. Channel-wise attention was used to select features that could calculate the strongest channel-wise activation values. Spatial attention performs average pooling and max pooling along the channel axis on the feature map to obtain the activated feature map with a local receptive field in the spatial dimension. To complement channel attention, spatial attention was applied to find the informative region for the input feature map in the spatial dimension.

2.3.3 Implementation

To establish the DL model, we used 588 benign and 550 malignant TNs with multimodal and double-view images as the data set. Furthermore, fivefold cross-validation was applied to the data sets.

To evaluate the performance of the four types of sonography in thyroid cancer diagnosis, we performed experiments with multimodal inputs (i.e., GSU, CDFI, SE, and Mask). The four streams in Figure 4 correspond to the four modalities. All four modalities (Figure 4), as well as one or multiple modalities of the same patient, were taken as the inputs. Popular ResNet-50 was used as the feature extraction backbone (Figure 3A). The features obtained by multiple network streams from the different modalities and views were averaged and then applied to fully connected layers to predict the classification result. In our experiments, each network stream had its own independent parameters.

The framework was implemented on a Dell-T7920 workstation equipped with an NVIDIA GeForce RTX3090 GPU and 64 GB of memory. The Adam optimization algorithm for minibatch gradient descent was used for training with a batch size of 32. The learning rate was initially set to 0.00001 and reduced by 0.1 every 30 epochs. A pretrained model was used for parameter initialization. The models with the smallest loss values within 100 training epochs were selected as the final models to generate classification results. We set the same epochs for training every modal, including the double- and single-view modes.

2.4 Comparing the diagnosis of the deep learning model and radiologists

In this section, we investigate the diagnostic performance of the DL models and radiologists using 228 cases from the test set. According to a survey, the diagnostic accuracy of radiologists

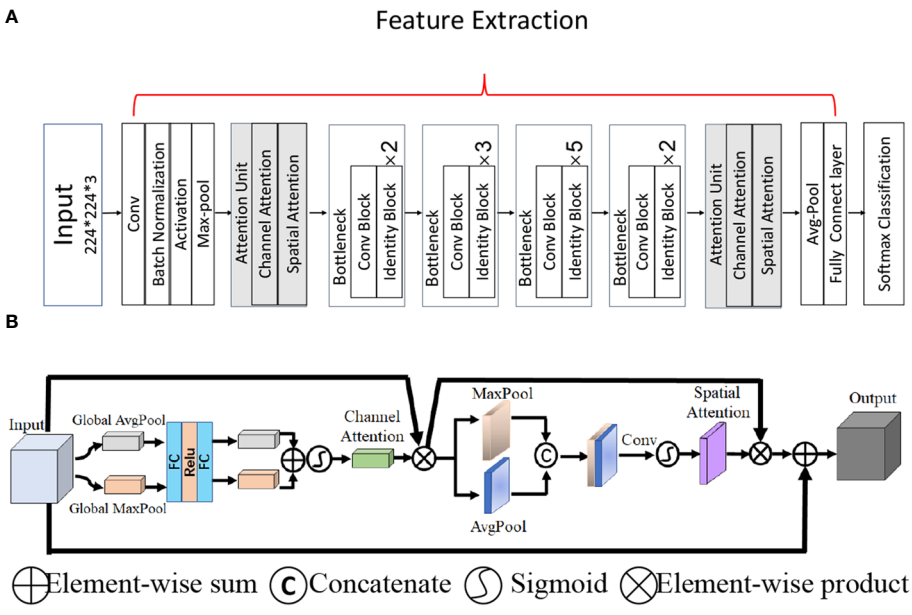

FIGURE 3
The overall network architecture. **(A)** Architecture of the backbone network ResNet-50 with two attention units. **(B)** The attention unit.

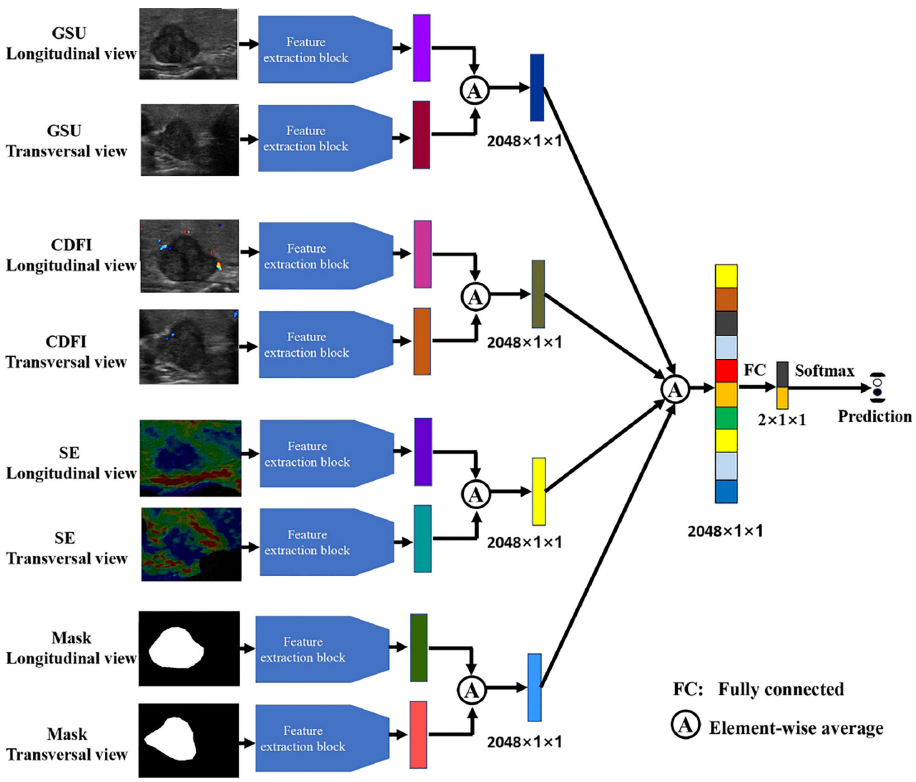

FIGURE 4
The illustration of multimodality inputs and feature fusion.

increased when they classified the final category into either dichotomous prediction or malignant risk (9). In our study, radiologists diagnosed TNs of the test set based on multimodal US images, and the results were compared with those of the DL method. Five senior radiologists with 5–10 years of experience and five junior radiologists with 1–3 years of experience independently evaluated the TNs and were blinded the diagnosis to the postoperative pathological results. The radiologist then performed a second diagnosis based on the results of the DL and arrived at the final diagnosis. The diagnostic performance of the radiologist alone and in combination with DL assistance was compared.

2.5 Statistical analysis

R software (version 1.8) and MedCalc (version 11.2, Ostend, Belgium) were used to analyze the data. The data set was randomly divided into five non-overlapping groups, whereas there was no data intersection for the same subject for each group. After fivefold cross-validation, the accuracy, sensitivity, specificity, positive predictive value (PPV), negative predictive value (NPV), and area under the receiver operating characteristics curves (AUC) were obtained to evaluate the performance of the presented DL model in the test set. The Delong test results in terms of the AUC for the test data set were introduced to evaluate the statistical difference between DL based on different combined US images and radiologists with variable levels. A 95% confidence interval was used to estimate the range of these evaluation values; p-values of less than 0.05 (two-tailed) were considered statistically significant.

3 Results

3.1 General and ultrasonic characteristic analysis

Among the 781 patients, 135 (17.29%) were men and 646 (82.71%) were women. The mean diagnostic age of the patients was 45.92 ± 10.18 years (range, 22–67 years) for men and 48.11 ± 10.66 years (range, 21–79 years) for women. The average size of malignant TNs (12.5 ± 7.40 mm) was significantly larger than that of benign TNs (9.70 ± 6.40 mm) ($p< 0.001$) (Table 1).

The US characteristics of the 1,138 TNs were statistically analyzed, and the results are listed in Table 1. Except for

10.3389/fonc.2022.1012724

TABLE 1 Comparing the characteristics of benign and malignant thyroid nodules.

Characteristics	All nodules (n = 1138) n (%)	Benign (n = 588) n (%)	Malignant (n = 550) n (%)	*p*
Size(mm)				< 0.001
Mean ± SD	11.2 ± 7.1	12.5 ± 7.4	9.7 ± 6.4	
(Range)	(3.0–59.0)	(3.0–44.5)	(3.0–59.0)	
Position 1				0.001
Left lobe	533 (46.84)	295 (50.17)	238 (43.27)	
Right lobe	585 (51.41)	290 (49.32)	295 (53.64)	
Isthmus	20 (1.76)	3 (0.51)	17 (3.09)	
Position 2				0.001
Upper region	250 (21.97)	117 (19.90)	133 (24.18)	
Mid region	478 (42.00)	264 (44.90)	214 (38.91)	
Lower region	390 (34.27)	204 (34.69)	186 (33.82)	
Isthmus	20 (1.76)	3 (0.51)	17 (3.09)	
Position 3				0.005
Shallow side	364 (31.99)	196 (33.33)	168 (30.55)	
Mid side	347 (30.49)	171 (29.08)	176 (32.00)	
Deep side	407 (35.76)	218 (37.07)	189 (34.36)	
Isthmus	20 (1.76)	3 (0.51)	17 (3.09)	
Echotexture				0.604
Homogeneous	113 (9.92)	61(10.40)	52(9.50)	
Heterogeneous	1025 (90.10)	527(89.60)	498(90.50)	
Echogenicity				< 0.001
Isoechoic or hyperechoic	359 (31.55)	307 (52.21)	52 (9.45)	
Hypoechoic	671 (58.96)	259 (44.05)	412 (74.91)	
Markedly hypoechoic	108 (9.49)	22 (3.74)	86 (15.64)	
Composition				< 0.001
Predominantly solid	142 (12.48)	131 (22.28)	11 (2.00)	
solid	996 (87.52)	457 (77.72)	539 (98.00)	
Orientation				< 0.001
Parallel	589 (51.76)	451 (76.70)	138 (25.09)	
Vertical	549 (48.24)	137 (23.30)	412 (74.91)	
Punctate echogenic foci				< 0.001
No punctate echogenic foci	872 (76.63)	523 (88.95)	349 (63.45)	
Punctate echogenic foci of undetermined significance	70 (6.15)	21 (3.57)	49 (8.91)	
Microcalcifications	196 (17.22)	44 (7.48)	152 (27.64)	
Margin				< 0.001
Circumscribed	473 (41.56)	354 (60.20)	119 (21.64)	
Ill-defined	88 (7.73)	61 (10.37)	27 (4.91)	
Irregular or extrathyroidal extension	577 (50.70)	173 (29.42)	404 (73.45)	
Halo				< 0.001
Absent	954 (83.83)	504 (85.71)	450 (81.82)	
Complete	53 (4.66)	38 (6.46)	15 (2.73)	
Incomplete	131 (11.51)	46 (7.82)	85 (15.45)	
Posterior features				< 0.001
No posterior features	932 (81.90)	530 (90.14)	402 (73.09)	
Enhancement	46 (4.04)	26 (4.42)	20 (3.64)	
Shadowing	160 (14.06)	32 (5.44)	128 (23.27)	
Vascular distribution pattern				0.004

(Continued)

TABLE 1 Continued

Characteristics	All nodules (n = 1138) n (%)	Benign (n = 588) n (%)	Malignant (n = 550) n (%)	*p*
Avascularity	171 (15.03)	70 (11.90)	101 (18.36)	
Peripheral vascularity	643 (56.50)	330 (56.12)	313 (56.91)	
Mainly central vascularity	121 (10.63)	71 (12.07)	50 (9.09)	
Mixed vascularity	203 (17.84)	117 (19.90)	86 (15.64)	
Adler grade				< 0.001
0	119 (10.46)	50 (8.50)	69 (12.55)	
1	385 (33.83)	166 (28.23)	219 (39.82)	
2–3	634 (55.71)	372 (63.27)	262 (47.64)	
Elastography score				< 0.001
2	559 (49.12)	386 (65.65)	173 (31.45)	
3	495 (43.50)	186 (31.63)	309 (56.18)	
4	84 (7.38)	16 (2.72)	68 (12.36)	
C-TIRADS				< 0.001
3	110 (9.67)	108 (18.37)	2 (0.36)	
4a	255 (22.41)	219 (37.24)	36 (6.55)	
4b	320 (28.12)	159 (27.04)	161 (29.27)	
4c	360 (31.63)	93 (15.82)	267 (48.55)	
5	93 (8.17)	9 (1.53)	84 (15.27)	

echotexture (p = 0.649), the risk features of GSU were significantly different between malignant and benign nodules (p< 0.05). We found some significantly different US features in the vascular distribution pattern, Adler grading, and Asteria standard in this study (p< 0.05).

3.2 Diagnostic performance of deep learning models

The performances of the various DL models for differentiating TNs are summarized in Table 2 and Figure 5. In our study, a total of eight DL models were established based on multimodal US imaging. We found that the feature fusion of images from both transverse and longitudinal sections could achieve better performance than that from a single section (Supplementary Text S1).

The AUCs of DL using multimodal US imaging (0.909 based on [G + C]US, 0.858 based on [G + E]US, and 0.906 based on [G + C + E]US) outperformed those of GSU imaging alone (0.825) (p = 0.014, p< 0.001, and p< 0.001, respectively). There was a statistically significant difference in the diagnosis between the (G + C)US and (G + E)US images (0.909 vs. 0.858, p = 0.001). However, the AUC of the DL model based on (G + C + E)US exhibited an excellent performance similar to that based on (G + C)US (0.906 vs. 0.909, p = 0.294), which were both markedly better than DL based on (G + E)US (0.906 vs. 0.858, p = 0.002; 0.909 vs. 0.858, p = 0.001, respectively). In addition, the accuracy, specificity, PPV, and NPV of DL based on (G + C + E)US were better than those of (G + C)US; however, only the PPV was statistically significant (87.8% vs. 85.2%, p = 0.045; Supplementary Text S2).

Furthermore, after adding the Mask feature, the diagnostic performance was obviously better than that of GSU alone (0.881 vs. 0.825, p = 0.002), and the AUCs of (G + C)US, (G + E)US, and (G + C + E)US were also increased (0.918 vs. 0.909, 0.889 vs. 0.858, 0.928 vs. 0.906), but without statistical differences (p = 0.57, p = 0.22, and p = 0.28; Table 2). The highest accuracy of 86.2%, sensitivity of 86.9%, and PPV of 87.8 were achieved by the DL model based on (G + C + M)US, and the highest specificity of 89.5% and NPV of 87.7% were achieved based on (G + C + E)US. The DL model using (G + C + E + M)US images achieved the best performance (AUC of 0.928), with an increase of 10.3% compared with that using a single GSU (p< 0.001).

3.3 Deep learning performance compared with radiologists

The diagnostic performance of radiologists with different levels of experience in differentiating malignant from benign TNs is shown in Table 3 and Figure 6. When independently evaluating the TNs without DL assistance, the diagnosis of senior radiologists showed higher accuracy, specificity, and AUC than that of juniors (80.6% vs. 72.7%, p = 0.008; 81.7% vs. 72.0%, p = 0.018; 0.794 vs. 0.720, p = 0.002, respectively). The

TABLE 2 Comparing the deep learning diagnostic performance based on multimodal ultrasound images.

Models	Accuracy %	Sensitivity %	Specificity %	PPV %	NPV %	AUC
G	78.9 (76.7–81.1)	77.5 (74.3–80.7)	80.3 (78.5–82.1)	78.6 (76.6–80.6)	79.3 (76.8–81.8)	0.825 (0.815–0.835)
G + C	83.8 (82.1–85.5)*	80.4 (76.5–84.3)	86.9 (86.0–87.8)**	85.2 (84.5–85.9)**	82.7 (80.0–85.4)	0.909 (0.894–0.924)**
G + E	81.8 (79.0–84.6)	75.5 (69.7–81.3)	87.6 (85.9–89.3)**	85.0 (83.2–86.8)*	79.5 (75.6–83.4)	0.858 (0.844–0.872)*
G + C + E	84.8 (82.3–87.3)*	79.8 (73.1–86.5)	89.5 (87.0–92.0)**	87.8 (85.8–89.8)**	83.0 (78.7–87.3)	0.906 (0.895–0.917)**
G + M	82.4 (81.7–83.1)*	82.9 (81.5–84.3)*	81.9 (80.8–83.0)	81.0 (80.1–81.9)	83.7 (82.6–84.8)*	0.881 (0.870–0.892)*
G + C + M	86.2 (84.4–88.0)*	86.9 (82.9–90.9)*	85.6 (84.5–86.7)*	84.9 (84.0–85.8)**	87.7 (84.5–90.9)*	0.918 (0.906–0.930)**
G + E + M	82.5 (80.5–84.5)*	82 (79.2–84.8)	82.9 (80.4–85.4)	81.7 (79.5–83.9)	83.2 (80.9–85.5)	0.889 (0.880–0.898)*
G + C + E + M	86.1 (85.5–86.7)**	84.7 (83.6–85.8)*	87.5 (86.3–88.7)**	86.3 (85.2–87.4)**	86.0 (85.2–86.8)*	0.928 (0.921–0.935)**
p_1	0.264	0.208	0.501	0.889	0.220	0.001†
p_2	0.145	0.362	0.254	0.083	0.274	0.002†
p_3	0.504	0.894	0.099	0.045†	0.929	0.294
p_4	0.020†	0.017†	0.196	0.061	0.014†	0.002†
p_5	0.099	0.050	0.087	0.655	0.051	0.570
p_6	0.685	0.083	0.013	0.051	0.143	0.215
p_7	0.342	0.193	0.193	0.255	0.205	0.284

Data in parentheses have 95% confidence intervals.
US, ultrasound; G, grayscale ultrasound; C, color Doppler flow imaging; E, strain elastography; M, region of interest mask; AUC, area under the receiver operator characteristic curve; PPV, positive predictive value; NPV, negative predictive value.
p_1 = G + C vs. G + E, p_2 = G + E vs. G + C + E, p_3 = G + C vs. G + C + E, p_4 = G vs. G + M, p_5 = G + C vs. G + C + M, p_6 = G + E vs. G + E + M, p_7 = G + C + E vs. G + C + E + M.
The accuracy, sensitivity, specificity, PPV, NPV, and AUC of the DL-based multimodality was statistically compared to those of the DL-based single GSU.
*p< 0.05. **p<0.001. †p-Values for statistical significance (<0.05).

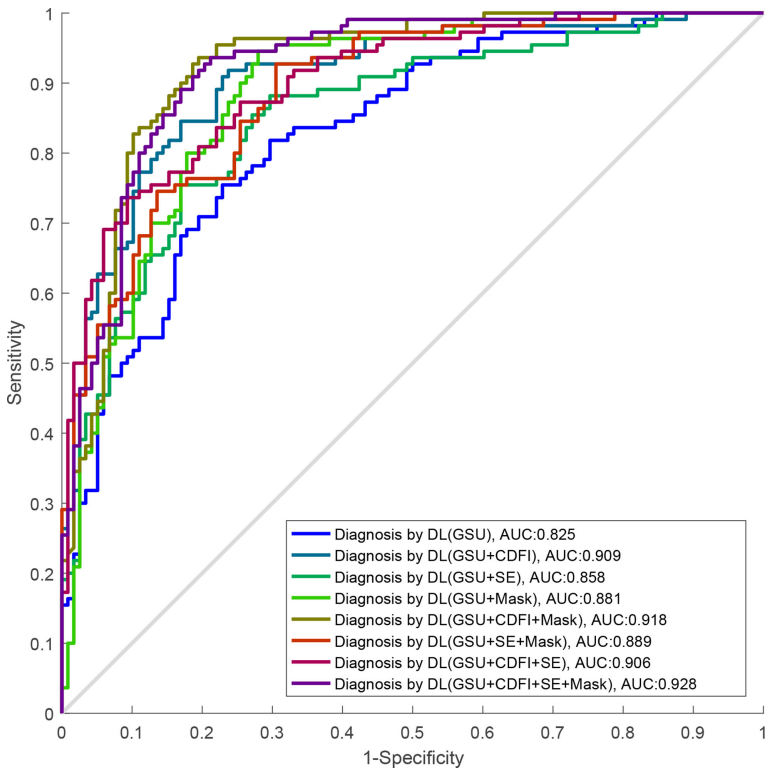

FIGURE 5
The ROC curves of DL-based single GSU and multimodality. ROC, receiver operating characteristics; DL, deep learning; GSU, gray-scale ultrasound.

TABLE 3 The diagnostic performance of deep learning (DL), radiologists alone, and DL-assisted radiologists.

Radiologists	Accuracy %	Sensitivity %	Specificity %	PPV %	NPV %	AUC
First diagnosis without DL assistance						
Senior	80.6 (77.2–84.0)*	79.5 (75.2–83.8)	81.7 (76.4–87.0)*	80.5 (75.7–85.3)*	81.1 (77.7–84.5)*	0.794 (0.758–0.830)*
Junior	72.7 (70.8–74.6)	73.5 (70.5–76.5)	72.0 (69.8–74.2)	71.0 (69.2–72.8)	74.5 (72.2–76.8)	0.720 (0.702–0.738)
Second diagnosis with DL assistance						
Senior	83.4 (80.9–85.9)**	82.9 (79.0–86.8)**	83.9 (80.0–87.8)**	82.9 (79.5–86.3)**	84.2 (81.2–87.2)**	0.822 (0.793–0.851)**
Junior	80.2 (79.2–81.2)**	80.9 (77.9–83.9)*	79.5 (78.0–81.0)*	78.6 (77.7–79.5)**	81.8 (79.7–83.9)*	0.796 (0.786–0.806)**
p_1	0.285	0.315	0.571	0.490	0.269	0.141
p_2	0.070	0.489	0.099	0.066	0.290	0.465
p_3	0.041†	0.081	0.177	0.083	0.054	0.512
p_4	0.856	0.411	0.208	0.290	0.532	0.019†
p_5	0.491	0.465	0.059	0.060	0.677	0.027†
p_6	0.106	0.446	0.158	0.131	0.319	0.010†

Data in parentheses have 95% confidence intervals.
US, ultrasound; G, grayscale ultrasound; C, color Doppler flow imaging; E, strain elastography; M, region of interest mask; AUC, area under the receiver operator characteristic curve; PPV, positive predictive value; NPV, negative predictive value.
p_1 = (senior diagnosis standalone vs. senior diagnosis with DL assistance), p_2 = (junior diagnosis with DL assistance vs. senior diagnosis with DL assistance), p_3 = (senior diagnosis with DL assistance vs. DL diagnosis [GSU], p_4 = (senior diagnosis with DL assistance vs. DL diagnosis [G + C]), p_6 = (senior diagnosis with DL assistance vs. DL diagnosis [G + C + E]), p_6 = (senior diagnosis with DL assistance vs. DL diagnosis [G + C + E + M]).
The accuracy, sensitivity, specificity, PPV, NPV, and AUC were statistically compared with those of junior radiologists in the first diagnosis without DL assistance.
*p< 0.05. **p< 0.001. †p-Values for statistical significance (<0.05).

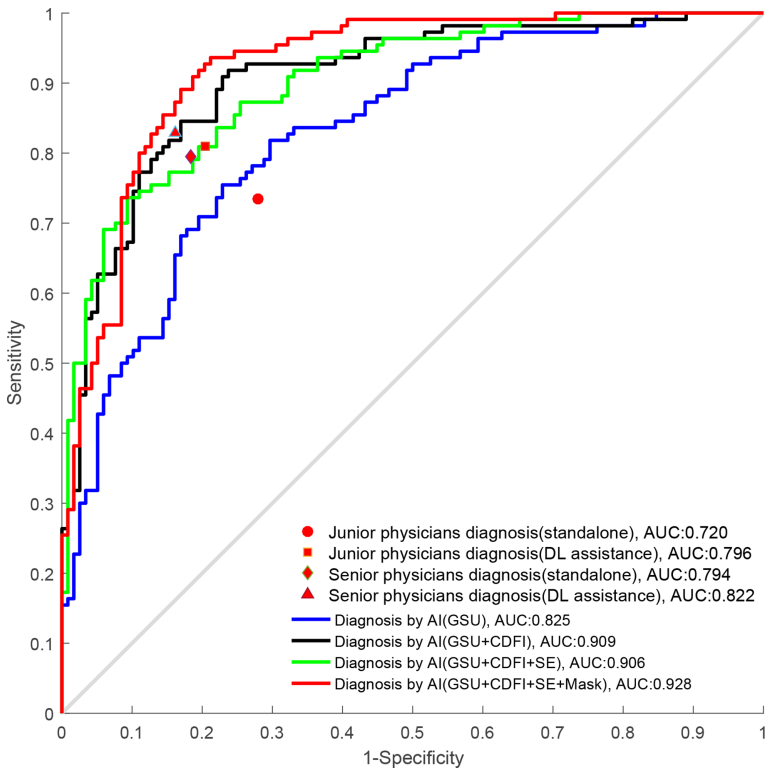

FIGURE 6
The ROC curves of DL and radiologists with different degrees of experience. ROC, receiver operating characteristics; DL, deep learning.

sensitivity (79.5%) of US diagnosis by senior radiologists was also better than that (73.5%) of junior radiologists ($p = 0.079$).

When the DL method was added for the second diagnosis in the test set, the diagnostic performance of junior radiologists significantly increased from 0.720 to 0.796 ($p< 0.001$). The AUC of the junior radiologists in the second diagnosis was similar to that of the first diagnosis by senior radiologists (0.796 vs. 0.794) but was considered inferior (0.796 vs. 0.822), and the differences were not statistically significant ($p > 0.05$). Moreover, the DL model also had a certain auxiliary diagnostic effect and could slightly improve the diagnostic performance of senior radiologists in terms of accuracy (from 80.6% to 83.4%), which was higher than that of DL based on GSU (83.4% vs. 78.9%, $p = 0.041$). However, the AUC of senior radiologists with DL assistance was only comparable to that of DL based on a single GSU (0.822 vs. 0.825, $p = 0.512$) and significantly less than that of DL based on multimodal US images (0.822 vs. 0.858–0.928, $p< 0.05$).

4 Discussion

Thyroid cancer has recently become one of the most common malignancies in Chinese women (2). US was the first choice for the examination of thyroid lesions, and TNs were diagnosed on US imaging by radiologists according to TI-RADS. Each guideline has its strengths and weaknesses; for example, the American Thyroid Association 2015 guideline showed better diagnostic efficiency in evaluating TNs >1 cm, the TIRADS issued by the American College of Radiology in 2017 had more advantages in reducing unnecessary biopsy operations, and TNs were well diagnosed by radiologists according to C-TIRADS, achieving a higher performance (6–8). However, the diagnostic results were susceptible to operator dependency, probe, and US equipment variability. FNA is a comparatively accurate method for differentiating TNs preoperatively, but it was reported that approximately 20% of FNA samples obtained had ambiguous results (15–17). AI not only solves the complex problem of the US risk stratification system but also reduces intra- and interobserver variability in US diagnosis (23, 30).

Nevertheless, most applications of DL in the diagnosis of TNs have been conducted based on single GSU imaging or single-view sections, limiting access to image information to a certain extent (21, 31–33). In addition to GSU, radiologists also referred to CDFI and elastography for obtaining the blood flow and hardness information of TNs to assist the GSU diagnosis clinically and make a diagnosis after a comprehensive analysis. In terms of the statistical analysis in our study, a higher elastic score was markedly correlated with malignant TNs, confirming that malignant TNs tend to be hard. The differences in vascular distribution pattern and Adler grade were statistically significant in TNs, and malignant TNs tended to be less or lacked blood flow. In addition, many studies have verified the effectiveness of combined or multimodal US imaging in the differentiation of TNs visually (11, 13, 24, 25). Therefore, based on multimodal US images of TNs obtained from transverse and longitudinal sections, new DL models were used to distinguish benign from malignant TNs in our study.

In our study, the diagnostic performance of GSU (0.825) was comparable to that of previous studies (AUC of 0.788 and 0.829) (32, 33). However, the DL models using combined or multimodal US images achieved a better performance (0.858–0.928) than those using GSU alone (0.825) ($p< 0.05$). Notably, the AUC of the DL model based on GSU alone was also greatly improved after adding CDFI (0.825 vs. 0.909, $p< 0.001$). In a related study, Baig et al. quantified the regional blood flow indices of TNs, and the diagnostic accuracy of GSU features was increased from 58.6% to 79.3% when combined with CDFI ($p< 0.05$) (34). The DL models in our study provided consistent and repeatable results and outperformed conventional machine learning-based methods with a specificity of 86.9%, a PPV of 85.2%, and an accuracy of 83.8%. As for the improvement in diagnostic efficiency after adding CDFI, we found that it may be due to the attention mechanism algorithm applied in this study, which could obtain richer and more objective features that were previously unrecognized visually by learning the information of CDFI images autonomously. We also demonstrated that SE imaging helped improve the diagnosis of DL based on GSU (0.825 vs. 0.858, $p< 0.05$). However, the AUC of the DL model based on (G + E)US was markedly less than that based on (G + C)US (0.858 vs. 0.909, $p = 0.001$). Additionally, there were no significant differences between (G + C + E)US and (G + C)US (0.906 vs. 0.909, $p = 0.294$). Therefore, our study confirmed that CDFI played a more substantial role in distinguishing TNs than SE in our study, and the less obvious advantages of SE may be associated with the subjectivity of the collecting process of SE images.

Adding a Mask containing the contour information of the TNs was found to help improve the diagnostic performance of DL models based on GSU (from 0.825 to 0.881), (G + C)US (from 0.909 to 0.918), (G + E)US (from 0.858 to 0.889), and (G + C + E)US (from 0.906 to 0.928), indicating that effective delineation of the nodular boundaries in US images played an important role in characterizing TNs. The best AUC of 0.928 was achieved by DL using (G + C + E + M)US. The highest specificity (89.5%) and PPV (87.8%) were achieved by DL based on (G + C + E)US, which could play a primary role in avoiding overdiagnosis and helping reduce unnecessary biopsies for the diagnosis of TNs, whereas the highest sensitivity (86.9%) and NPV (87.7%) of great clinical significance for screening out malignant TNs and avoiding misdiagnosis were achieved by DL based on (G + C + M)US. In summary, the performance of DL models based on multimodal US imaging was superior to that based on a single GSU, which supports our assumption that multimodal US could provide more comprehensive and effective information for TN diagnosis.

In clinical practice, US diagnosis by radiologists cannot be completely replaced by AI technology, and a final diagnosis should be made by radiologists. Therefore, we compared the performance of the DL method for differentiating TNs with that of visual diagnosis by radiologists and further explored the auxiliary role of DL for radiologists' diagnosis. Compared with the first diagnosis of TNs visually by junior radiologists, there was a significant improvement in the second diagnosis with DL assistance (0.720 vs. 0.796, $p< 0.001$), which could be comparable to that of the seniors in the first diagnosis (0.796 vs. 0.794, $p > 0.05$). Moreover, the DL method could also provide an auxiliary diagnosis for senior radiologists in terms of accuracy (from 80.6% to 83.4%), which was superior to DL based on GSU alone (83.4% vs. 78.9%, $p = 0.041$). It has been proven that DL can assist clinical radiologists in improving diagnostic ability and increasing confidence, especially for juniors with less experience. In a study by Peng et al. (35), the DL-assisted method also improved the AUC of radiologists in diagnosing TNs from 0.837 to 0.875 ($p< 0.001$).

Nevertheless, there were no significant diagnostic differences with and without DL assistance for senior radiologists (0.794 vs. 0.822, $p = 0.141$). It seems that DL-aided diagnosis was less effective for senior than junior radiologists, which may be related to the fact that senior radiologists were more likely to rely on their own clinical experience. Our analysis may also be due to the fact that, by using DL models, we sacrificed interpretability for robust and complex imaging features with greater generalizability. Furthermore, DL technology obtained results based on features that were learned and extracted independently rather than on predefined handcrafted features, where the process was abstract and incomprehensible, leading to distrust by the radiologists. To resolve the visualization of DL learning and decision processes, Kim et al. (36) applied Grad-CAM to generate output images overlaid with heat maps to achieve visual interpretability. Meanwhile, Zhou et al. (20) found that the adjacent parenchyma of TNs is critical for classification by visual interpretability of DL.

By comparing the radiologists' and DL's diagnostic efficacy, we found that senior radiologists with DL assistance only had a diagnosis comparable to the DL model based on GSU in terms of AUC (0.822 vs. 0.825, $p = 0.512$), which could not be compared with the diagnosis based on multimodal US imaging (0.822 vs. 0.858–0.928, $p< 0.05$), effectively demonstrating the excellent clinical value of the DL method, especially for multimodal US imaging, with potential for further development and application. Radiologists may be affected by fatigue and other factors in daily work, whereas AI can run on its own and has the characteristics of indefatigability with stable and high diagnostic efficiency.

Our study has several advantages. To our knowledge, this is the first study in which the attention mechanism-guided residual network was used to construct a variety of DL models based on different US imaging combinations. The objects in our study were TNs of the C-TIRADS 3–5 categories, which are more suitable for clinical diagnosis difficulties and extend the scope of clinical application. We have verified that DL models based on multimodal US can assist radiologists in improving diagnostic performance, especially for those with less experience, and postoperative pathological results were used as the gold standard for statistical analysis in this study, which was more objective than the studies using cytological pathological results (20, 31). Our case set included relatively more samples and achieved a balance between benign and malignant TNs, which could effectively reduce the diagnostic bias compared with a previous study (18).

This study had some limitations. First, the main limitation of our study was that the data were retrospectively derived from a single center, and additional external validation or multicenter studies are needed to refine our study. Second, the images in this study were static images stored in a compressed format, which may have led to some potential image features not being mined. Therefore, dynamic images or raw radiofrequency signals should be included in future studies. Third, the visualization of the DL proposed in this study was not achieved. Visualization of the DL process could be conducted to make the results more reliable in subsequent studies. More technologies could be included, such as shear wave elastography, superb microvascular imaging, and contrast-enhanced US.

In conclusion, the DL model based on multimodal US images can achieve a high diagnostic value in the differential diagnosis of benign and malignant TNs of C-TIRADS 3–5 categories, aid second-opinion provision, and improve the diagnostic ability for radiologists, which is of great significance for clinical decision-making.

Data availability statement

The original contributions presented in the study are included in the article/Supplementary Material. Further inquiries can be directed to the corresponding authors.

Ethics statement

The studies involving human participants were reviewed and approved by the Ethics Committee of the Second Affiliated Hospital of Harbin Medical University. Written informed consent for participation was not required for this study in accordance with the national legislation and the institutional requirements.

Author contributions

YY and JT conceived and designed the study. YT, QD, and HK collected the clinical and image data and performed image preprocessing. YT, LZ, and WY analyzed and evaluated the

ultrasonographic features of thyroid nodules. YY and WQ provided a deep learning algorithm and built the models. YY analyzed the image data and performed statistical analysis. YT, YY, and TW wrote the manuscript. JT, XX, and XL reviewed and edited the manuscript. All authors have contributed to the manuscript and approved the submitted version.

Funding

This work was supported by the National Key R&D Program of China (2018YFA0701400), the Shenzhen Universities Stabilization Support Program (20200812144239001), the National Nature Science Foundation Grants of China (12174267, 62022086, 11874382, and 81827802), the Shenzhen Foundation (JCYJ20200109114237902, SGDX2020110309400200, and ZDSYS201802061806314), CAS research projects (KFJ-PTXM-012 and 2011DP173015), the Natural Science Foundation of Guangdong Province (2022A1515011343, 2020B1111130002, and 2020B1212060051), and the Youth Innovation Promotion Association (CAS 2018391).

Acknowledgments

We would like to thank the ultrasound doctors in the Department of Ultrasound, The Second Affiliated Hospital of Harbin Medical University, Harbin, for participating in the diagnosis of thyroid nodules.

Conflict of interest

The authors declare that the research was conducted in the absence of any commercial or financial relationships that could be construed as a potential conflict of interest.

Publisher's note

Supplementary material

The Supplementary Material for this article can be found online at: https://www.frontiersin.org/articles/10.3389/fonc.2022.1012724/full#supplementary-material

References

1. Haugen BR, Alexander EK, Bible KC, Doherty GM, Mandel SJ, Nikiforov YE, et al. American Thyroid association management guidelines for adult patients with thyroid nodules and differentiated thyroid cancer the American thyroid association guidelines task force on thyroid nodules and differentiated thyroid cancer. *Thyroid* (2016) 26:1–133. doi: 10.1089/thy.2015.0020

2. Chen W, Zheng R, Baade PD, Zhang S, Zeng H, Bray F, et al. Cancer statistics in China, 2015. *CA Cancer J Clin* (2016) 66:115–32. doi: 10.3322/caac.21338

3. Pacini F, Castagna MG, Brilli L, Pentheroudakis GGrp EGW. Thyroid cancer: ESMO clinical practice guidelines for diagnosis, treatment and follow-up. *Ann Oncol* (2012) 23:110–9. doi: 10.1093/annonc/mds230

4. Kwak JY, Han KH, Yoon JH, Moon HJ, Son EJ, Park SH, et al. Thyroid imaging reporting and data system for US features of nodules: A step in establishing better stratification of cancer risk. *Radiology* (2011) 260:892–9. doi: 10.1148/radiol.11110206

5. Tessler FN, Middleton WD, Grant EG, Hoang JK, Berland LL, Teefey SA, et al. ACR thyroid imaging, reporting and data system (TI-RADS): White paper of the ACR TI-RADS committee. *J Am Coll Radiol* (2017) 14:587–95. doi: 10.1016/j.jacr.2017.01.046

6. Zhou J, Song Y, Zhan W, Wei X, Zhang S, Zhang R, et al. Thyroid imaging reporting and data system (TIRADS) for ultrasound features of nodules: Multicentric retrospective study in China. *Endocrine* (2021) 72:157–70. doi: 10.1007/s12020-020-02442-x

7. Liu H, Ma AL, Zhou YS, Yang DH, Ruan JL, Liu XD, et al. Variability in the interpretation of grey-scale ultrasound features in assessing thyroid nodules: A systematic review and meta-analysis. *Eur J Radiol* (2020) 129:109050. doi: 10.1016/j.ejrad.2020.109050

8. Choi SH, Kim EK, Kwak JY, Kim MJ, Son EJ. Interobserver and intraobserver variations in ultrasound assessment of thyroid nodules. *Thyroid* (2010) 20:167–72. doi: 10.1089/thy.2008.0354

9. Park CS, Kim SH, Jung SL, Kang BJ, Kim JY, Choi JJ, et al. Observer variability in the sonographic evaluation of thyroid nodules. *J Clin Ultrasound* (2010) 38:287–93. doi: 10.1002/jcu.20689

10. Lee HJ, Yoon DY, Seo YL, Kim JH, Baek S, Lim KJ, et al. Intraobserver and interobserver variability in ultrasound measurements of thyroid nodules. *J Ultrasound Med* (2018) 37:173–8. doi: 10.1002/jum.14316

11. Chaigneau E, Russ G, Royer B, Bigorgne C, Bienvenu-Perrard M, Rouxel A, et al. TIRADS score is of limited clinical value for risk stratification of indeterminate cytological results. *Eur J Endocrinol* (2018) 179:13–20. doi: 10.1530/EJE-18-0078

12. Seo H, Na DG, Kim JH, Kim KW, Yoon JW. Ultrasound-based risk stratification for malignancy in thyroid nodules: A four-tier categorization system. *Eur Radiol* (2015) 25:2153–62. doi: 10.1007/s00330-015-3621-7

13. Pei SF, Cong SZ, Zhang B, Liang CH, Zhang L, Liu JJ, et al. Diagnostic value of multimodal ultrasound imaging in differentiating benign and malignant TI-RADS category 4 nodules. *Int J Clin Oncol* (2019) 24:632–9. doi: 10.1007/s10147-019-01397-y

14. Ha EJ, Na DG, Baek JH, Sung JY, Kim JH, Kang SY. US Fine-needle aspiration biopsy for thyroid malignancy: Diagnostic performance of seven society guidelines applied to 2000 thyroid nodules. *Radiology* (2018) 287:893–900. doi: 10.1148/radiol.2018171074

15. Singh Ospina N, Brito JP, Maraka S, Espinosa de Ycaza AE, Rodriguez-Gutierrez R, Gionfriddo MR, et al. Diagnostic accuracy of ultrasound-guided fine needle aspiration biopsy for thyroid malignancy: Systematic review and meta-analysis. *Endocrine* (2016) 53:651–61. doi: 10.1007/s12020-016-0921-x

16. Theoharis CGA, Schofield KM, Hammers L, Udelsman R, Chhieng DC. The Bethesda thyroid fine-needle aspiration classification system: Year 1 at an academic institution. *Thyroid* (2009) 19:1215–23. doi: 10.1089/thy.2009.0155

17. Mathur A, Weng J, Moses W, Steinberg SM, Rahbari R, Kitano M, et al. A prospective study evaluating the accuracy of using combined clinical factors and candidate diagnostic markers to refine the accuracy of thyroid fine needle aspiration biopsy. *Surgery* (2010) 148:1170–6. doi: 10.1016/j.surg.2010.09.025

18. Liu Z, Zhong SB, Liu Q, Xie CX, Dai YZ, Peng C, et al. Thyroid nodule recognition using a joint convolutional neural network with information fusion of ultrasound images and radiofrequency data. *Eur Radiol* (2021) 31:5001–11. doi: 10.1007/s00330-020-07585-z

19. Wang K, Lu X, Zhou H, Gao Y, Zheng J, Tong M, et al. Deep learning radiomics of shear wave elastography significantly improved diagnostic performance for assessing liver fibrosis in chronic hepatitis b: A prospective multicentre study. *Gut* (2019) 68:729–41. doi: 10.1136/gutjnl-2018-316204

20. Zhou H, Jin YH, Dai L, Zhang MW, Qiu YQ, Wang K, et al. Differential diagnosis of benign and malignant thyroid nodules using deep learning radiomics of thyroid ultrasound images. *Eur J Radiol* (2020) 127:108992. doi: 10.1016/j.ejrad.2020.108992

21. Kwon SW, Choi IJ, Kang JY, Jang WI, Lee GH, Lee MC. Ultrasonographic thyroid nodule classification using a deep convolutional neural network with surgical pathology. *J Digit Imaging* (2020) 33:1202–8. doi: 10.1007/s10278-020-00362-w

22. Akkus Z, Cai J, Boonrod A, Zeinoddini A, Weston AD, Philbrick KA, et al. A survey of deep-learning applications in ultrasound: Artificial intelligence-powered ultrasound for improving clinical workflow. *J Am Coll Radiol* (2019) 16:1318–28. doi: 10.1016/j.jacr.2019.06.004

23. Sorrenti S, Dolcetti V, Radzina M, Bellini MI, Frezza F, Munir K, et al. Artificial intelligence for thyroid nodule characterization: Where are we standing? *Cancers* (2022) 14(14). doi: 10.3390/cancers14143357

24. Colakoglu B, Yildirim D, Alis D, Ucar G, Samanci C, Ustabasioglu FE, et al. Elastography in distinguishing benign from malignant thyroid nodules. *J Clin Imag Sci* (2016) 6:51. doi: 10.4103/2156-7514.197074

25. Sorrenti S, Dolcetti V, Fresilli D, Del Gaudio G, Pacini P, Huang PT, et al. The role of CEUS in the evaluation of thyroid cancer: From diagnosis to local staging. *J Clin Med* (2021) 10(19). doi: 10.3390/jcm10194559

26. Adler DD, Carson PL, Rubin JM, Quinn-Reid D. Doppler Ultrasound color flow imaging in the study of breast cancer: Preliminary findings. *Ultrasound Med Biol* (1990) 16:553–9. doi: 10.1016/0301-5629(90)90020-d

27. Asteria C, Giovanardi A, Pizzocaro A, Cozzaglio L, Morabito A, Somalvico F, et al. US-Elastography in the differential diagnosis of benign and malignant thyroid nodules. *Thyroid* (2008) 18:523–31. doi: 10.1089/thy.2007.0323

28. He KM, Zhang XY, Ren SQ, Sun JIeee. (2016). Deep residual learning for image recognition, in: *2016 IEEE Conference on Computer Vision and Pattern Recognition (CVPR)* (Seattle, WA) 27-30. doi: 10.1109/cvpr.2016.90

29. Woo SH, Park J, Lee JY, Kweon IS eds. (2018). CBAM: convolutional block attention module, in: *Lecture Notes in Computer Science*. (Munich, Germany: 15th Eur Conference on Computer Vision (ECCV)) (2018):3–19. doi: 10.1007/978-3-030-01234-2_1

30. Ha EJ, Baek JH, Na DG. Risk stratification of thyroid nodules on ultrasonography: Current status and perspectives. *Thyroid* (2017) 27:1463–8. doi: 10.1089/thy.2016.0654

31. Li XC, Zhang S, Zhang Q, Wei X, Pan Y, Zhao J, et al. Diagnosis of thyroid cancer using deep convolutional neural network models applied to sonographic images: A retrospective, multicohort, diagnostic study. *Lancet Oncol* (2019) 20:193–201. doi: 10.1016/S1470-2045(18)30762-9

32. Wu GG, Lv WZ, Yin R, Xu JW, Yan YJ, Chen RX, et al. Deep learning based on ACR TI-RADS can improve the differential diagnosis of thyroid nodules. *Front Oncol* (2021) 11:575166. doi: 10.3389/fonc.2021.575166

33. Zhang YC, Wu Q, Chen YT, Wang Y. A clinical assessment of an ultrasound computer-aided diagnosis system in differentiating thyroid nodules with radiologists of different diagnostic experience. *Front Oncol* (2020) 10:557169. doi: 10.3389/fonc.2020.557169

34. Baig FN, van Lunenburg JTJV, Liu SYW, Yip SP, Law HKW, Ying M. Computer-aided assessment of regional vascularity of thyroid nodules for prediction of malignancy. *Sci Rep* (2017) 7:14350. doi: 10.1038/s41598-017-14432-7

35. Peng S, Liu YH, Lv WM, Liu LZ, Zhou Q, Yang H, et al. Deep learning-based artificial intelligence model to assist thyroid nodule diagnosis and management: A multicentre diagnostic study. *Lancet Digit Health* (2021) 3:e250–9. doi: 10.1016/S2589-7500(21)00041-8

36. Kim YJ, Choi Y, Hur SJ, Park KS, Kim HJ, Seo M, et al. Deep convolutional neural network for classification of thyroid nodules on ultrasound: Comparison of the diagnostic performance with that of radiologists. *Eur J Radiol* (2022) 152:110335. doi: 10.1016/j.ejrad.2022.110335

frontiers | Frontiers in Oncology

TYPE Original Research
PUBLISHED 08 December 2022
DOI 10.3389/fonc.2022.1047010

OPEN ACCESS

EDITED BY
Lorenz Kadletz-Wanke,
Medical University of Vienna, Austria

REVIEWED BY
Wei Han,
Nanjing University, China
Dawei Jiang,
Huazhong University of Science and Technology, China

*CORRESPONDENCE
Yue Chen
chenyue5523@126.com
Ya Liu
1935221414@qq.com

†These authors have contributed equally to this work and share first authorship

SPECIALTY SECTION
This article was submitted to Head and Neck Cancer, a section of the journal Frontiers in Oncology

RECEIVED 17 September 2022
ACCEPTED 21 November 2022
PUBLISHED 08 December 2022

CITATION
Ding H, Liang J, Qiu L, Xu T, Cai L, Wan Q, Wang L, Liu Y and Chen Y (2022) Prospective comparison of ^{68}Ga-FAPI-04 and ^{18}F-FDG PET/CT for tumor staging in nasopharyngeal carcinoma. *Front. Oncol.* 12:1047010. doi: 10.3389/fonc.2022.1047010

Prospective comparison of ^{68}Ga-FAPI-04 and ^{18}F-FDG PET/CT for tumor staging in nasopharyngeal carcinoma

Haoyuan Ding[1,2,3,4†], Juan Liang[5†], Lin Qiu[2,3,4], Tingting Xu[2,3,4], Liang Cai[2,3,4], Qiang Wan[2,3,4], Li Wang[2,3,4], Ya Liu[2,3,4*] and Yue Chen[1,2,3,4*]

[1]Jinan University, Guangzhou, Guangdong, China, [2]Department of Nuclear Medicine, The Affiliated Hospital of Southwest Medical University, Luzhou, Sichuan, China, [3]Nuclear Medicine and Molecular Imaging Key Laboratory of Sichuan Province, Luzhou, Sichuan, China, [4]Institute of Nuclear Medicine, Southwest Medical University, Luzhou, Sichuan, China, [5]Department of Ultrasound, The Affiliated Hospital of Southwest Medical University, Luzhou, Sichuan, China

Purpose: To explore the difference in the effectiveness of gallium-68 fibroblast activation protein inhibitor (^{68}Ga-FAPI-04) PET/CT and fluorine-18 fluorodeoxyglucose (^{18}F-FDG) PET/CT for the initial staging of patients with nasopharyngeal carcinoma (NPC).

Methods: The Affiliated Hospital of Southwest Medical University hosted this single-center prospective investigation (Clinical Trials registration No.ChiCTR2100044131) between March 2020 and September 2021. Within a week, all subjects underwent MR scans, ^{68}Ga-FAPI-04 PET/CT, and ^{18}F-FDG PET/CT in order. The effectiveness of medical staging employing ^{68}Ga-FAPI-04 and ^{18}F-FDG PET/CT was compared.

Results: Twenty-eight patients with primary NPC were evaluated (mean age53 ± 11 years). ^{68}Ga-FAPI-04 PET/CT indicated an elevated recognition rate for diagnosing primary tumors (28/28 [100%] vs. 27/28 [96%]) and lymph node metastases (263/285 [92%] vs. 228/285 [80%]), but a lower detection rate for distant metastases (5/7 [71%] vs. 7/7 [100%]) compared with ^{18}F-FDG PET/CT. A significant association between the maximum standard uptake value (SUVmax) of ^{18}F-FDG PET and ^{68}Ga-FAPI-04 PET was found in the primary cancers ($r = 0.691$, $p < 0.001$). In comparison to ^{18}F-FDG PET/CT, ^{68}Ga-FAPI-04 PET/CT upstaged the T stage in five patients while downstaging the N stage in seven patients. ^{68}Ga-FAPI-04 PET/CT corrected the overall staging of five patients on^{18}F-FDG PET/CT.

Conclusion: ^{68}Ga-FAPI-04 PET/CT is preferable to ^{18}F-FDG PET/CT for NPC staging in terms of the detection efficiency for primary tumors and lymph node metastasis. This is especially true when evaluating the primary cancer and any spread to contiguous tissues. It is possible to improve the staging assessment of NPC by using ^{68}Ga-FAPI-04 PET/CT in conjunction with ^{18}F-FDG PET/CT.

10.3389/fonc.2022.1047010

KEYWORDS

^{18}F-FDG, ^{68}Ga-FAPI-04, PET/CT, nasopharyngeal carcinoma, tumor staging

Introduction

Nasopharyngeal carcinoma (NPC) is a prevalent epithelial malignancy; its incidence is related to ethnicity and regional distribution. People in East and Southeast Asia, especially in Fujian and Guangdong areas of China, have a high incidence of NPC (1). In 2020, a survey of 185 countries determined that NPC was newly diagnosed in 133,354 patients and resulted in almost 80,000 fatalities (2). NPC tends to infiltrate locally early and typically involves regional nodes (3). Patients with terminal disease often develop distant metastases (4); thus, early and correct staging of NPC is critical for enhancing the individuals' quality of life and treatment outcomes (5).

As the first-choice imaging method for NPC, MR is excellent for showing adjacent soft tissue infiltration, skull base bone and intracranial invasion, and retropharyngeal lymph node involvement (6). The National Comprehensive Cancer Network currently recommends fluorine-18 fluorodeoxyglucose (^{18}F-FDG) PET/CT as a well-proven imaging strategy for NPC management (7), with elevated accuracy and sensitivity for identifying lymph nodes and distant metastases (8, 9). ^{18}F-FDG reveals the glucose metabolism of abnormalities. Owing to the high physiological glucose utilization in healthy brain tissues and the lesser soft tissue resolution of PET/CT compared to that of MR, the precision of ^{18}F-FDG PET/CT for the T staging of NPC is insufficient, mainly for the description of the skull base and intracranial invasion (10, 11).

Gallium-68-labeled fibroblast activation protein inhibitor (^{68}Ga-FAPI) is a recently developed cancer tracer. It indicates the degree of fibroblast activation protein (FAP) expression (12–14). Cancer-associated fibroblasts overexpress FAP in most epithelial cancers, including NPC, whereas its expression is modest in most healthy tissues and organs. PET/CT using ^{68}Ga-FAPI-04 reveals tumors and metastases in various malignant tumors, such as head and neck cancers, with strong tracer uptake in lesions (13–15). ^{68}Ga-FAPI has a greater target to background ratio than ^{18}F-FDG (16). Furthermore, prior research have demonstrated that ^{68}Ga-FAPI-04 PET/CT is an effective investigative approach for NPC, especially for the assessment of the primary cancer and any spread to contiguous tissues (17, 18).

Therefore, we carried out a prospective investigation to explore the difference in the effectiveness of ^{18}F-FDG PET/CT and ^{68}Ga-FAPI-04 PET/CT in discovering primary tumor, nodal, and distant metastases in patients with NPC.

Materials and methods

Participants

Between March 2020 and September 2021, the affiliated hospital of Southwest Medical University provided access to this prospective medical trial. The research protocol was approved by both the China Clinical Trials Registry and the Clinical Research Ethics Committee at the previously mentioned hospital (Clinical Trials registration No.ChiCTR2100044131; Ethics Committee approval No.2020035). All individuals gave their written permission after being fully informed. Within seven days, all individuals completed MR scans, ^{68}Ga-FAPI-04 PET/CT, and ^{18}F-FDG PET/CT in order. The acquisition interval between ^{68}Ga-FAPI-04 PET/CT and ^{18}F-FDG PET/CT was at least one day. The criteria for inclusion were: (a) individuals with *de novo* histopathologically given a diagnosis NPC; (b) subjects participated who had not received antitumor therapy before the evaluation; (c) individuals with cancer who chose to undergo paired ^{18}F-FDG along with ^{68}Ga-FAPI-04 PET/CT tests to stage their disease; and (d) subjects who agreed to follow the protocol procedures, gave their written informed consent, and gave their signatures. The following is a list of the conditions for exclusion: (a) individuals with contraindications for the exams, (b) people with additional primary cancers at the time of the testing, and (c) individuals who began therapy prior to the completion of the three tests.

^{18}F-FDG and ^{68}Ga-FAPI-04 preparation

^{18}F-FDG was formed utilizing normal procedures and a coincident ^{18}F-FDG synthesizing form (FDG-N, PET Science & Technology). DOTA-FAPI-04 was acquired from MedChemExpress LLC. As previously mentioned (19), radiolabeling and purifying of ^{68}Ga-FAPI-04 were conducted. The radiochemical purity of ^{68}Ga-FAPI-04 and ^{18}F-FDG exceeded 95%, and the finished radiopharmaceuticals were sterile and devoid of pyrogens.

Imaging acquisition

Before undergoing the ^{18}F-FDG PET/CT evaluation, the subjects abstained from food and drink for at least six hours to ensure that their blood glucose levels were within the accepted values (3.9–6.1 mmol/L). However, there was no need to make any preparations in order to take the ^{68}Ga-FAPI-04 PET/CT test. The doses of ^{68}Ga-FAPI-04 and ^{18}F-FDG that were administered *via* intravenous injection were 3.7 and 1.85 MBq/kg, respectively (19, 20). Following a tracer injection, participants got a PET/CT scan (uMI780, United Imaging Healthcare) 40–60 mins later. All scans were conducted in accordance with a previously outlined technique (21, 22), and the resulting data were provided to a post-processing workstation (Version R002, uWS-MI, United Imaging Healthcare). The PET data were recreated with the help of an algorithm called sorted subset anticipation maximization (two iterations and 20 subsets). Evaluations of the nasopharynx and the cervical area employing contrast-enhanced (CE) MR were carried out using head and neck coils on 1.5-T MR scanners (Achieva 1.5T, Philips, Amsterdam, the Netherlands). We acquired the MR images, containing axial T1-weighted fast spin-echo images immediately before injection of contrast. (repetition time [TR] = 450 ms; echo time [TE] = 15 ms, flip angle = 90°, field of view [FOV] =232 mm × 232 mm, slice thickness = 5 mm, spacing between slices = 1 mm), axial T2-weighted fast spin-echo images (TR = 3,575 ms, TE = 80 ms, flip angle = 90°, FOV =232 mm × 232 mm, slice thickness = 5 mm, spacing between slices = 1 mm), and axial and coronal T2-weighted fat-suppressed spin-echo images (TR = 1,927 ms, TE = 55 ms, flip angle = 90°, FOV =250 mm × 250 mm, slice thickness = 5 mm, spacing between slices = 1 mm). At a rate of 1.5 mL/s, intravenous doses of 0.1 mmol/kg gadopentetate dimeglumine were delivered. Using the exact parameters as the axial T1-weighted fast spin-echo images, the axial T1-weighted fast spin-echo sequence was obtained.

Imaging analysis

Two board-certified nuclear medicine specialists investigated all PET/CT sets of data. To avoid bias, cohort 1 (L.C. and Y.C.) assessed all ^{18}F-FDG PET/CT pictures, while cohort 2 (Y.Z. and L.Q.) reviewed all ^{68}Ga-FAPI-04 PET/CT images. Two board-certified radiologists (D.C. and J.S.) who were blinded to the PET/CT outcomes analyzed the MRI. Investigating any non-physiological uptake employing ^{18}F-FDG or ^{68}Ga-FAPI-04 PET that was higher than the activities of the background blood pool or the activities of the background of the neighboring healthy tissue was the primary focus of the study. On transverse PET scans, regions of interest were outlined for semi-quantitative analysis. The SUVmax was automatically computed to estimate the uptake of ^{18}F-FDG or ^{68}Ga-FAPI-04 in primary cancers, associated lymph nodes, and distant metastases. Clinical staging is based on three different types of images in accordance with the American Joint Committee on Cancer staging system version 8th (23).

Primary lesion evaluation

On PET images, the SUVmax of every primary lesion was recorded. By comparing the radioactivity of the lesion border to that of the nearby healthy tissue, the boundaries were visually evaluated. The border and extent of the invasion were identified if the radioactivity at the border of the injury was significantly greater than that of the nearby healthy tissue. Corresponding CT image was employed to help recognize morphology and localization of the lesions. The extent and border of every lesion were evaluated, and any variation between the three imaging techniques were noted.

Lymph node evaluation

Patients' lymph nodes were categorized into four sections: the retropharyngeal region, the right and left sides of the neck located above the cricoid cartilage inferior edge, and the region below the cricoid cartilage inferior boundary. Employing ^{18}F-FDG and ^{68}Ga-FAPI-04 PET/CT, the quantity of lesions and SUVmax with the greatest pathological tracer buildup were measured for every lymph node area, and the techniques were compared. According radiographic criteria, the MR identification of metastatic lymph nodes located in the cervical region must meet at least one of the following (9): (a) there was extracapsular expansion or necrosis, (b) in the retropharyngeal region, the lowest axial diameter was 5 mm, and in other locations, it was ≥ 10 mm, and (c) there were ≥ 3 lymph nodes of borderline size.

Distant metastasis evaluation

Except for the primary tumor and nodal metastases, any non-physiological uptake above the activities of the background blood pool or the activities of the background of the neighboring healthy tissue on PET/CT, with or without morphological abnormalities, was classified as a possible distant metastasis. Distant metastases were also considered as positive if the signal is different from that of adjacent background tissues on MRI. Lesions with aberrant tracer uptake and MR signals were counted and localized. The SUVmax of each metastatic lesion was also recorded.

Reference standard

Histopathological analysis of the biopsied or resected samples served as the basis for the definitive diagnosis. In accordance with the criteria of the National Comprehensive Cancer Network (7), CE-MR is the gold standard for assessing the cancer and its

invasion of neighboring tissues. Due to technological and ethical constraints, histological verification of all lymph nodes and distant metastases was not achievable. Therefore, the tumor was classified as malignancy based on the confirmation of typical malignant characteristics by multimodal imaging. The duration of the follow-up was over three months. During follow-up following anti-cancer therapies, including chemotherapy, radiation, and/or targeted therapy, a considerable decrease in lesion size was determined to be malignant.

Statistical analyses

All statistical analyses were done by employing SPSS (version 22.0; SPSS Inc.). Categorical data are represented numerically and as a percentage. The expression for continuous variables is the mean standard deviation. Using Spearman's correlation analysis, the relationship between the kind of pathology and the degree of tracer uptake was found. Employing the paired samples t-test, the SUVmax values of the primary and metastatic lesions were compared between ^{18}F-FDG and ^{68}Ga-FAPI-04 PET/CT. The ^{18}F-FDG SUVmax was compared between metastatic and non-metastatic lymph nodes using a t-test for independent samples. Two-tailed p-values of < 0.05 were regarded as statistically significant.

Results

Participant characteristics

This investigation comprised twenty-eight individuals (5 women and 23 men) aged 33–75 years (mean = 53 ± 10 years). ^{68}Ga-FAPI-04 and ^{18}F-FDG PET/CT were well tolerated by all subjects, and no ^{68}Ga-FAPI-04-related side effects were identified. All individuals were newly diagnosed with nasopharyngeal carcinoma, in which two instances were keratinizing squamous cell carcinoma (WHO Type I), eleven patients were non-keratinizing differentiated carcinoma (WHO Type II), and fifteen patients were non-keratinizing undifferentiated carcinoma (WHO Type III). The clinical data is displayed in Table 1.

TABLE 1 Summary of patient basic characteristics.

Characteristics	Value
Number of patients	28
Age (year)	
Mean (average ± standard deviation)	53 ± 11
Range	33-75
Sex	
Female	5
Male	23
Histology, WHO type	
I	2
II	11
III	15

Diagnostic effectiveness of ^{68}Ga-FAPI-04 and ^{18}F-FDG PET/CT for primary tumors

The PET/CT scan utilizing ^{68}Ga-FAPI-04 identified all 28 primary cancers with a detection rate of one hundred percent. ^{18}F-FDG PET/CT revealed 27 of the 28 primary cancers, which is a 96% detection rate. There was no indication of a greater SUVmax value for ^{68}Ga-FAPI-04 PET in the primary malignancies comparing with ^{18}F-FDG PET (12.1 ± 4.9 vs. 11.7 ± 4.6; $p = 0.543$) (Table 2). Additional comparison of the connection between the uptake of the two tracers revealed a substantial relation between the SUVmax values of ^{68}Ga-FAPI-04 and ^{18}F-FDG ($r = 0.69$, $p < 0.001$). Furthermore, there was no relation among the different histopathological kinds and the SUVmax of the two tracers ($p > 0.05$). A visual assessment of the primary lesion invasion was performed using the two tracers (Table 3).

Nasopharyngeal invasion

Both modalities clearly delineated the boundary and extent of tumor invasion, except in one case (Figure 1) of nonkeratinizing differentiated carcinoma that was not detected by ^{18}F-FDG PET. Visual evaluation of nasopharyngeal invasion was similar for the two tracers in 27 participants, but of which two cases were found to be inferior to MR.

Parapharyngeal space invasion

Eighteen participants had parapharyngeal space invasion. The extent of lesions on ^{68}Ga-FAPI-04 PET/CT was larger than that on MR in one of the 18 participants, while there were two cases with a smaller extent and one case with a larger extent on ^{18}F-FDG PET/CT compared with MR. There were 2 and 16, respectively, patients with ^{68}Ga-FAPI-04 who were dominant and equal to ^{18}F-FDG.

Skull base bone invasion

Typically, 11 participants had invasion of the skull base bone. ^{68}Ga-FAPI-04 PET/CT had a 100% (11/11) positive detection rate and showed a tumor extent and border delineation similar to that of MR. The 11 patients discovered by ^{18}F-FDG PET/CT included one false-positive case, while one person with skull base invasion went undetected. In 4 of the 11 participants, ^{68}Ga-FAPI-04 PET/CT showed a greater degree of skull base bone invasion compared to ^{18}F-FDG PET/CT (Figure 2).

TABLE 2 The SUVmax comparison between ^{18}F-FDG and ^{68}Ga-FAPI-04 PET/CT in primary tumor, nodal, and distant metastasis.

Index	Primary tumor	Nodal metastasis	Distant metastasis
^{18}F-FDG PET/CT	11.7 ± 4.6	13.6 ± 5.5	8.3 ± 5.9
^{68}Ga-FAPI PET/CT	12.1 ± 4.9	11.7 ± 5.0	6.6 ± 4.0
p value	0.543	0.133	0.450

TABLE 3 Visual evaluation of tumor invasion using the 3 modalities.

	Detection No.			Visual evaluation				
Lesion Invasion	MR	FDG	FAPI	FDG = FAPI	FDG > FAPI	FDG < FAPI	FDG = MR	FAPI= MR
Nasopharynx	28	27	28	27	0	0	25	25
Parapharyngeal space	18	18	18	16	0	2	15	17
Skull base bone	11	11*	11	7	1	4	7	11
intracalvarium	4	1	4	1	0	3	1	4

*Including 1 false positive case.

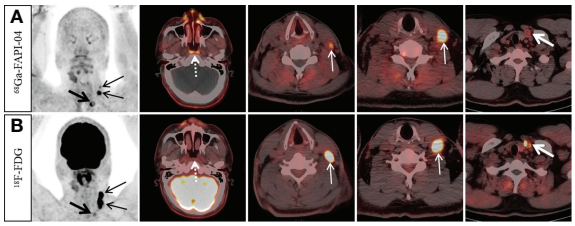

FIGURE 1
A 49-year-old man with nonkeratinizing differentiated carcinoma. ^{68}Ga-FAPI-04 PET/CT showed intensive ^{68}Ga-FAPI-04 uptake in the posterior nasopharyngeal wall (**A**, dotted arrow, SUVmax 3.8), ^{18}F-FDG PET/CT showed no abnormal ^{18}F-FDG uptake in the primary tumor (**B**, dotted arrow). Moreover, ^{68}Ga-FAPI-04 PET/CT reveals higher tracer uptake than ^{18}F-FDG PET/CT in the left supraclavicular lymph node (**A**, thick arrow, SUVmax 9.4 vs. **B**, thick arrow, SUVmax 3.8), but the tracer uptake of left cervical (level III) lymph nodes was lower than that of ^{18}F-FDG PET/CT (**A**, thin arrow, SUVmax, 4.5–11.0 vs. **B**, thin arrow, SUVmax, 17.7–19.4).

Intracranial invasion

Typically, 4 participants had an intracranial invasion. The positive detection rates for ^{68}Ga-FAPI-04 PET/CT along with ^{18}F-FDG PET/CT were, respectively, 100% (4/4) and 25% (1/4) (Figure 2). Owing to the physiological high uptake of ^{18}F-FDG in the brain, both ^{68}Ga-FAPI-04 PET/CT and MR revealed a more precise border of intracranial invasion than ^{18}F-FDG PET/CT.

Diagnostic effectiveness of ^{68}Ga-FAPI-04 and ^{18}F-FDG PET/CT for nodal metastasis

Twenty-seven of the 28 participants (285 lymph nodes) were suspected to have lymph node metastases. For 25/285 lymph nodes, histopathological analysis acted as a reference standard, and for the remaining lymph nodes, morphological analysis and/or follow-up imaging were used. Of the 285 suspected lymph nodes, 234 lymph nodes in 24 participants were considered malignant and 51 lymph nodes were lastly verified as inflammatory. From a total of 285 lymph nodes, ^{68}Ga-FAPI-04 PET/CT recognized 263 (false-positive uptake in 2 lymph nodes and false-negative uptake in 20 lymph nodes). By comparison, 228 lymph nodes were successfully detected by ^{18}F-FDG PET/CT (false-positive uptake in 51 lymph nodes and false-negative uptake in six lymph nodes, Figure 3). MR accurately diagnosed 262 lymph nodes, with two false-positive and twenty-one false-negative lymph nodes, respectively. Only one of the 203 lymph nodes with positive ^{68}Ga-FAPI-04 and ^{18}F-FDG uptake was confirmed to be a false positive. The SUVmax of metastatic lymph nodes was somewhat greater in ^{18}F-FDG than in ^{68}Ga-FAPI-04 (13.6 ± 5.5 vs. 11.7 ± 5.0), but the variation was not substantially significant ($p = 0.133$. Table 2). Significantly greater

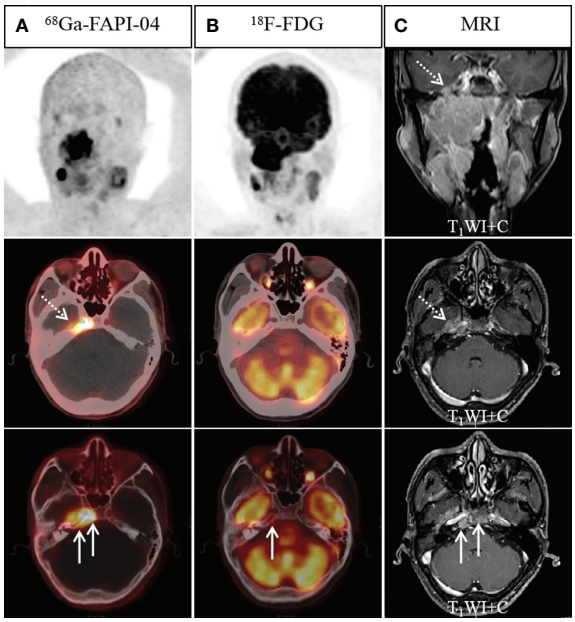

FIGURE 2
A 45-year-old man with nonkeratinizing differentiated carcinoma. Intense ^{68}Ga-FAPI-04 uptake was observed in the left temporal lobe (**A**, dotted arrow), suggesting intracranial invasion, but ^{18}F-FDG PET/CT **(B)** showed no abnormal intracranial ^{18}F-FDG uptake. Moreover, intense ^{68}Ga-FAPI-04 uptake was observed in the occipital and right temporal bone (**A**, solid arrow), while ^{18}F-FDG PET/CT only showed low tracer uptake in the right temporal bone (**B**, solid arrow), which was confirmed by MRI (**C**, solid arrow). ^{68}Ga-FAPI-04 PET/CT revealed more extensive lesions on intracranial and skull base invasion than ^{18}F-FDG PET/CT.

^{18}F-FDG uptake was seen in the metastatic lymph nodes compared to the non-metastatic reactive lymph nodes (13.6 ± 5.5 vs. 3.2 ± 0.7; $p < 0.001$).

Diagnostic effectiveness of ^{68}Ga-FAPI-04 and ^{18}F-FDG PET/CT for distant metastasis

Among the 28 participants, seven distant metastases were found in four participants (including three pulmonary and four bone metastases). All distant metastases were detected by ^{18}F-FDG PET/CT, whereas ^{68}Ga-FAPI-04 uptake was negative in two pulmonary metastases (Figure 4). One individual had concurrent bone and lung metastases. Across all evaluations of distant metastases, the SUVmax of ^{68}Ga-FAPI-04 did not vary significantly from that of ^{18}F-FDG (6.6 ± 4.0 vs. 8.3± 5.9; $p = 0.450$. Table 2).

Variations in tumor staging

The outcomes of the ^{68}Ga-FAPI-04 PET/CT, ^{18}F-FDG PET/CT, and MR imaging were compiled in Table 4, which provides a summary of the cancer staging for each of the 28 subjects. ^{68}Ga-FAPI-04 PET/CT underestimated the number of participants in the N staging and M staging by 1. In contrast, ^{18}F-FDG PET/CT undervalued the T staging in five participants and overestimated the N staging in seven participants. For the overall staging, although ^{68}Ga-FAPI-04 PET/CT underestimated the medical stage of two participants, it correctly upgraded the medical staging of ^{18}F-FDG PET/CT in two participants (from III to IVA) and downgraded the medical staging of ^{18}F-FDG PET/CT in three participants (two from III to I and one from III to II).

Discussion

Accurate staging is vital for NPC management. In our investigation, ^{68}Ga-FAPI-04 PET/CT revealed more recognition efficiency in diagnosing primary cancers (28/28 [100%] vs. 27/28 [96%]) and lymph node metastases (263/285 [92%] vs. 228/285 [80%]) than^{18}F-FDG PET/CT. However, in comparison to the efficacy of ^{18}F-FDG PET/CT in identifying distant metastases, the effectiveness of ^{68}Ga-FAPI-04 PET/CT in this regard was lower (5/7, or 71%), coming in at (7/7, or 100%). The combination of ^{18}F-FDG along with ^{68}Ga-FAPI-04 PET/CT led to consistent staging in 21 of the 28 participants, with a concordance rate of 75% for overall staging. Despite the fact that ^{68}Ga-FAPI-04 PET/CT underestimated the clinical staging in 2/

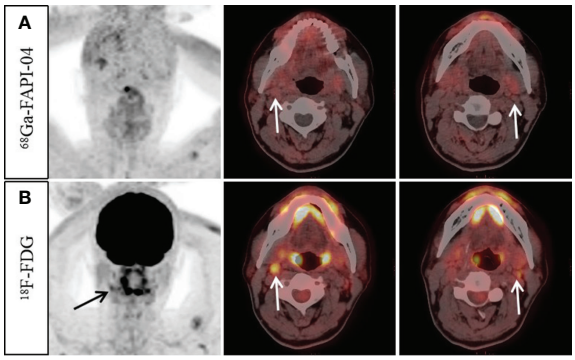

FIGURE 3
A 57-year-old man with nonkeratinizing undifferentiated carcinoma. An increase ^{18}F-FDG uptake was observed in the bilateral cervical (level II) lymph nodes (**B**, arrow, SUVmax 3.3–4.2). However, no abnormal ^{68}Ga-FAPI-04 uptake was observed in the cervical lymph nodes (**A**, arrow). Ultrasound-guided biopsy of the right level II lymph node revealed proliferating lymphoid cells with no signs of metastatic disease. Finally, it was confirmed by follow-up that all the suspected metastatic lymph nodes were reactive.

28 subjects, it corrected the staging of ^{18}F-FDG PET/CT in 5/28 participants. As a consequence of this, we believe that ^{68}Ga-FAPI-04 PET/CT is valuable for NPC diagnosis and staging.

Between the primary tumors' ^{18}F-FDG as well as ^{68}Ga-FAPI-04 uptake, there was no substantial variations. Interestingly, although the imaging principles of the two tracers were different, our study revealed a significant relation between the primary tumor uptake of ^{68}Ga-FAPI-04 and ^{18}F-FDG, which differed from previous reports (17, 18). Raised ^{68}Ga-FAPI-04 uptake in tumors is accompanied by higher glucose metabolism, which is positively correlated with cancer aggressiveness (24, 25). This demonstrates that NPC invasiveness may be predicted employing ^{68}Ga-FAPI-04 imaging. Previous studies have shown that ^{68}Ga-FAPI-04 PET/CT may increase the recognition rate of primary tumors in FDG-negative head and neck tumor (17, 26). In our investigation, ^{18}F-FDG could not detect the primary lesion in one patient with squamous cell carcinoma confirmed by biopsy, whereas ^{68}Ga-FAPI-04 successfully recognized the primary site in the posterior nasopharyngeal wall. This may be due to the superior tumor-to-background ratio of ^{68}Ga-FAPI-04 PET/CT comparing with ^{18}F-FDG, which may enhance the recognition rate of occult NPC.

A high physiological uptake of ^{18}F-FDG in normal brain tissue may lead to an underestimation of the presence or extent of tumor invasion on PET/CT (3, 17, 18). Due to the extra benefit of a low brain background, our results confirmed that ^{68}Ga-FAPI-04 dominates ^{18}F-FDG PET/CT in determining malignancy invasion of the parapharyngeal space, skull base bone, and intracranial areas. At present MR is the standard approach for T staging in NPC (7). However, two participants in our study showed a smaller extent of nasopharyngeal invasion on ^{68}Ga-FAPI-04 PET/CT than on MR, which may be edema and inflammation rather than tumor invasion, resulting in a

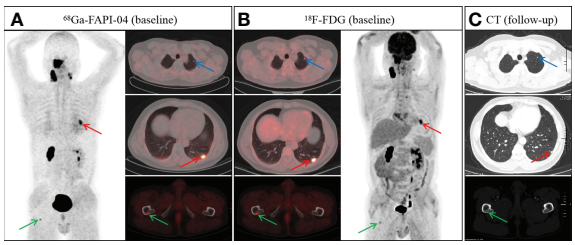

FIGURE 4
A 48-year-old man with nonkeratinizing undifferentiated carcinoma.^{68}Ga-FAPI-04 **(A)** and ^{18}F-FDG PET/CT **(B)** revealed an abnormal nodule in the left lower lobe (**A**, red arrow, SUVmax 4.9 vs. B, red arrow, SUVmax 8.2). However, the nodule in the left upper lobe showed abnormal uptake on ^{18}F-FDG PET/CT (**B**, blue arrow), but not on ^{68}Ga-FAPI-04 PET/CT (**A**, blue arrow). In addition, both ^{68}Ga-FAPI-04 (**A**, green arrow) and ^{18}F-FDG PET/CT (**B**, green arrow) revealed abnormal activity in the right femur. Follow-up CT after two cycles of induction chemotherapy showed a reduction in the volume of pulmonary metastases (**C**, red and blue arrow). Meanwhile, the bone metastasis of the right femur revealed a repair response after treatment, showing osteosclerotic nodule on follow-up CT (**C**, green arrow).

10.3389/fonc.2022.1047010

TABLE 4 Comparison of MR, ^{18}F-FDG, and ^{68}Ga-FAPI-04 PET/CT-based tumor staging (n = 28).

ParticipantNo.	Tumor Stage (FDG-based)	Tumor Stage (FAPI-based)	Tumor Stage (MR-based)	Additional finding (FDG vs FAPI)	Additional finding (FAPI vs FDG)	Staging changes (FAPI vs FDG)
1	III: T1N2M0	I: T1N0M0	I: T1N0M0	None	None	Down
2	III:T3N2M0	IVA: T4N2M0	IVA: T4N2M0	Cervical lymph node	Intracranial involvement	Up
3	IVB: T2N3M1	IVB: T2N3M1	IVA: T2N3M0	Cervical lymph node	None	None
4	IVB: T3N3M1	IVB: T2N2M1	III: T2N2M0	1 pulmonary metastasis	None	None
5	III: T2N2M0	II: T2N1M0	III: T2N2M0	Cervical lymph node	None	Down
6	III: T3N2M0	III: T3N2M0	III: T3N2M0	None	None	None
7	III: T2N2M0	III: T3N1M0	III: T3N1M0	Cervical lymph node	Skull base bone involvement	None
8	III: T3N2M0	III: T3N2M0	III: T3N2M0	None	None	None
9	III: T2N2M0	III: T2N2M0	III: T2N2M0	None	Cervical lymph node	None
10	III: T1N2M0	III: T1N2M0	II: T1N1M0	None	None	None
11	III: T3N1M0	IVA: T4N0M0	IVA: T4N0M0	None	Intracranial involvement	Up
12	III: T3N1M0	III: T3N1M0	III: T3N1M0	None	None	None
13	III: T2N2M0	III: T2N2M0	III: T2N2M0	None	None	None
14	IVA: T1N3M0	IVA: T1N3M0	IVA: T1N3M0	None	None	None
15	II:T1N1M0	II:T1N1M0	II:T1N1M0	None	None	None
16	III: T1N2M0	I: T1N0M0	I: T1N0M0	None	None	Down
17	II:T2N0M0	II:T2N0M0	II:T2N0M0	None	None	None
18	IVA: T4N3M0	IVA: T4N3M0	IVA: T4N3M0	None	Cervical lymph nodes	None
19	III:T1N2M0	III:T1N2M0	III:T1N2M0	None	None	None
20	IVB:T3N2M1	III: T3N2M0	III: T3N2M0	1 pulmonary metastasis	None	Down
21	IVB:T3N3M1	IVB:T4N3M1	IVA: T4N2M0	None	Intracranial involvement	None
22	III:T1N2M0	III:T1N2M0	III:T1N2M0	Cervical lymph node	None	None
23	III:T1N2M0	III:T1N2M0	III:T1N2M0	Cervical lymph node	None	None
24	III: T1N2M0	II:T1N1M0	II:T1N1M0	Cervical lymph node	None	Down
25	II:T2N1M0	II:T2N1M0	II:T2N1M0	None	None	None
26	IVA: T3N3M0	IVA: T3N3M0	IVA: T3N3M0	None	None	None
27	III:T3N2M0	III:T3N1M0	III:T3N1M0	Cervical lymph node	None	None
28	IVA:T0N3M0	IVA: T1N3M0	IVA: T1N3M0	None	Primary lesion	None

positive result on MR (27). Therefore, ^{68}Ga-FAPI-04 PET/CT indicated a greater recognition efficiency than ^{18}F-FDG PET/CT for precise T staging, and it was able to detect the target extent for radiotherapy with a greater degree of precision (17, 18).

Staging of the nodes is essential for the management and prognostication of NPC cases. Because of the high prevalence of inflammatory and reactive hyperplasia in cervical lymph nodes, ^{18}F-FDG PET/CT has been mentioned to have a greater incidence of producing false-positive outcomes when diagnosing lymph node metastasis (28, 29). In our investigation, the quantity of false-positive lymph nodes on ^{18}F-FDG PET/CT was substantially more than that on ^{68}Ga-FAPI-04 PET/CT and MR (^{18}F-FDG, 51/279 vs. ^{68}Ga-FAPI, 2/216 vs. MR, 2/215), which is consistent with the outcomes of prior investigations (28, 29). Utilising ^{68}Ga-FAPI-04 PET/CT, the N staging of the 7 participants was downstaged in comparison to ^{18}F-FDG PET/CT. However, ^{68}Ga-FAPI-04 PET/CT revealed more metastatic lymph nodes without positive tracer uptake than ^{18}F-FDG PET/CT (20/285 [7%] vs. 6/285 [2%]). Moreover, only one was diagnosed as a false positive out of all 203 lymph nodes with double-positive ^{18}F-FDG and ^{68}Ga-FAPI-04 uptake. Previous research has discovered significant correlations between the uptake of ^{18}F-FDG and ^{68}Ga-FAPI-04 in pairs of double-positive lymph nodes (18). Therefore, in assessing lymph node status in NPC patients prior to treatment, it's possible that the specificity of ^{68}Ga-FAPI-04 PET/CT is greater than that of ^{18}F-FDG PET/CT. When used in conjunction with one another, ^{68}Ga-FAPI-04 and ^{18}F-FDG PET/CT imaging have the potential to increase diagnostic precision for lymph node metastasis in NPC cases.

NPC is prone to distant metastasis (4). Prior investigations have shown that ^{68}Ga-FAPI-04 PET/CT has greater sensitivity than ^{18}F-FDG in identifying visceral and bone metastases of various malignant tumors, including NPC, and metastatic lesions showed higher tracer uptake on ^{68}Ga-FAPI-04 PET/CT (15, 17, 18, 21). However, in our investigation, ^{68}Ga-FAPI-04 PET/CT did not have a greater detection efficiency compared to ^{18}F-FDG for distant metastatic lesions in NPC. There were no

substantial variations in the uptake of ^{68}Ga-FAPI and ^{18}F-FDG by metastatic lesions. This is likely due to the small amount of metastatic lesions that were studied (n = 7). In addition to this, the ^{68}Ga-FAPI-04 PET missed both of the patient's pulmonary metastases. Therefore, it is essential to consider false-negative status in pulmonary metastases for M staging when conducting ^{68}Ga-FAPI-04 PET/CT.

Our investigation has some limitations. First, the sample size (n = 28) was small, and the number of distant metastatic lesions was particularly low. Consequently, prospective studies with greater cohorts are necessary, especially for the detection of distant metastasis. The morphologic and/or follow-up imaging data also served as the evaluation criterion in our examination because histological verification was not probable for totally nodal and distant metastases owing to ethical and technical considerations. Potential false-negative lesions were not sufficiently assessed, as imaging evaluation was also employed as a reference for cancer staging,

In summary, our preliminary findings suggest that ^{68}Ga-FAPI-04 has a positive impact on the clinical stage of NPC. Since ^{68}Ga-FAPI-04 PET/CT had better tumor-to-background contrast than ^{18}F-FDG and less false-positive uptake in inflammatory and reactive proliferative lymph nodes, it improved the capability to recognize primary cancer and lymph node metastases, mainly for the assessment of the skull base and intracranial invasion. Nevertheless, when it comes to the detection of distant metastases, ^{68}Ga-FAPI-04 PET/CT does not have an advantage over ^{18}F-FDG PET/CT. The staging assessment of NPC may be improved utilizing ^{68}Ga-FAPI-04 PET/CT in conjunction with ^{18}F-FDG PET/CT.

Data availability statement

The original contributions presented in the study are included in the article/supplementary material. Further inquiries can be directed to the corresponding authors.

Ethics statement

The studies involving human participants were reviewed and approved by The Clinical Research Ethics Committee of the Affiliated Hospital of Southwest Medical University. The patients/participants provided their written informed consent to participate in this study.

Author contributions

HD and JL contributed to the study conception and design. Material preparation and data collection were performed by HD, JL, LQ, TX, LC, QW, LW, YC. HD and YL processed and analysed the data. The first draft of the manuscript was written by HD and JL reviewed and revised the manuscript. All authors contributed to the article and approved the submitted version

Funding

This study was supported in part by the Project of Sichuan Provincial Health Commission, China (Grant 21ZD005).

Acknowledgments

The authors are grateful to the members of Department of Nuclear Medicine, The Affiliated Hospital, Southwest Medical University and Nuclear Medicine and Molecular Imaging Key Laboratory of Sichuan Province for their technical guidance, cooperation and assistance in completing this article.

Conflict of interest

The authors declare that the research was conducted in the absence of any commercial or financial relationships that could be construed as a potential conflict of interest.

Publisher's note

References

1. Chen YP, Chan A, Le QT, Blanchard P, Sun Y, Ma J. Nasopharyngeal carcinoma. *Lancet* (2019) 394(10192):64–80. doi: 10.1016/S0140-6736(19)30956-0

2. Sung H, Ferlay J, Siegel RL, Laversanne M, Soerjomataram I, Jemal A, et al. Global cancer statistics 2020: GLOBOCAN estimates of incidence and mortality worldwide for 36 cancers in 185 countries. *CA Cancer J Clin* (2021) 71(3):209–49. doi: 10.3322/caac.21660

3. Wu HB, Wang QS, Wang MF, Zhen X, Zhou WL, Li HS. Preliminary study of 11C-choline PET/CT for T staging of locally advanced nasopharyngeal carcinoma:

comparison with 18F-FDG PET/CT. *J Nucl Med* (2011) 52(3):341–6. doi: 10.2967/jnumed.110.081190

4. Chiesa F, De Paoli F. Distant metastases from nasopharyngeal cancer. *ORL J Otorhinolaryngol Relat Spec* (2001) 63(4):214–6. doi: 10.1159/000055743

5. Lee AW, Ma BB, Ng WT, Chan AT. Management of nasopharyngeal carcinoma: Current practice and future perspective. *J Clin Oncol* (2015) 33 (29):3356–64. doi: 10.1200/JCO.2015.60.9347

6. Sun XS, Liu SL, Luo MJ, Li XY, Chen QY, Guo SS, et al. The association between the development of radiation therapy, image technology, and chemotherapy, and the survival of patients with nasopharyngeal carcinoma: A cohort study from 1990 to 2012. *Int J Radiat Oncol Biol Phys* (2019) 105(3):581–90. doi: 10.1016/j.ijrobp.2019.06.2549

7. Caudell JJ, Gillison ML, Maghami E, Spencer S, Pfister DG, Adkins D, et al. NCCN guidelines® insights: Head and neck cancers, version 1.2022. *J Natl Compr Canc Netw* (2022) 20(3):224–34. doi: 10.6004/jnccn.2022.0016

8. Yen RF, Chen TH, Ting LL, Tzen KY, Pan MH, Hong RL. Early restaging whole-body (18)F-FDG PET during induction chemotherapy predicts clinical outcome in patients with locoregionally advanced nasopharyngeal carcinoma. *Eur J Nucl Med Mol Imaging* (2005) 32(10):1152–9. doi: 10.1007/s00259-005-1837-5

9. Ng SH, Chan SC, Yen TC, Chang JT, Liao CT, Ko SF, et al. Staging of untreated nasopharyngeal carcinoma with PET/CT: comparison with conventional imaging work-up. *Eur J Nucl Med Mol Imaging* (2009) 36(1):12–22. doi: 10.1007/s00259-008-0918-7

10. King AD, Ma BB, Yau YY, Zee B, Leung SF, Wong JK, et al. The impact of 18F-FDG PET/CT on assessment of nasopharyngeal carcinoma at diagnosis. *Br J Radiol* (2008) 81(964):291–8. doi: 10.1259/bjr/73751469

11. Zhang Y, Chen Y, Huang Z, Zhang L, Wan Q, Lei L. Comparison of 18F-NaF PET/CT and 18F-FDG PET/CT for detection of skull-base invasion and osseous metastases in nasopharyngeal carcinoma. *Contrast Media Mol Imaging* (2018) 2018:8271313. doi: 10.1155/2018/8271313

12. Kratochwil C, Flechsig P, Lindner T, Abderrahim L, Altmann A, Mier W, et al. 68Ga-FAPI PET/CT: Tracer uptake in 28 different kinds of cancer. *J Nucl Med* (2019) 60(6):801–5. doi: 10.2967/jnumed.119.227967

13. Loktev A, Lindner T, Mier W, Debus J, Altmann A, Jäger D, et al. A tumor-imaging method targeting cancer-associated fibroblasts. *J Nucl Med* (2018) 59 (9):1423–9. doi: 10.2967/jnumed.118.210435

14. Giesel FL, Kratochwil C, Lindner T, Marschalek MM, Loktev A, Lehnert W, et al. 68Ga-FAPI PET/CT: Biodistribution and preliminary dosimetry estimate of 2 DOTA-containing FAP-targeting agents in patients with various cancers. *J Nucl Med* (2019) 60(3):386–92. doi: 10.2967/jnumed.118.215913

15. Syed M, Flechsig P, Liermann J, Windisch P, Staudinger F, Akbaba S, et al. Fibroblast activation protein inhibitor (FAPI) PET for diagnostics and advanced targeted radiotherapy in head and neck cancers. *Eur J Nucl Med Mol Imaging* (2020) 47(12):2836–45. doi: 10.1007/s00259-020-04859-y

16. Giesel FL, Kratochwil C, Schlittenhardt J, Dendl K, Eiber M, Staudinger F, et al. Head-to-head intra-individual comparison of biodistribution and tumor uptake of 68Ga-FAPI and 18F-FDG PET/CT in cancer patients. *Eur J Nucl Med Mol Imaging* (2021) 48(13):4377–85. doi: 10.1007/s00259-021-05307-1

17. Zhao L, Pang Y, Zheng H, Han C, Gu J, Sun L, et al. Clinical utility of [68Ga]Ga-labeled fibroblast activation protein inhibitor (FAPI) positron emission tomography/computed tomography for primary staging and recurrence detection in nasopharyngeal carcinoma. *Eur J Nucl Med Mol Imaging* (2021) 48 (11):3606–17. doi: 10.1007/s00259-021-05336-w

18. Qin C, Liu F, Huang J, Ruan W, Liu Q, Gai Y, et al. A head-to-head comparison of 68Ga-DOTA-FAPI-04 and 18F-FDG PET/MR in patients with nasopharyngeal carcinoma: a prospective study. *Eur J Nucl Med Mol Imaging* (2021) 48(10):3228–37. doi: 10.1007/s00259-021-05255-w

19. Lan L, Liu H, Wang Y, Deng J, Peng D, Feng Y, et al. The potential utility of [68 Ga]Ga-DOTA-FAPI-04 as a novel broad-spectrum oncological and non-oncological imaging agent-comparison with [18F]FDG. *Eur J Nucl Med Mol Imaging* (2022) 49(3):963–79. doi: 10.1007/s00259-021-05522-w

20. Lan L, Zhang S, Xu T, Liu H, Wang W, Feng Y, et al. Prospective comparison of 68Ga-FAPI versus 18F-FDG PET/CT for tumor staging in biliary tract cancers. *Radiology* (2022) 304(3):648–57. doi: 10.1148/radiol.213118

21. Chen H, Pang Y, Wu J, Zhao L, Hao B, Wu J, et al. Comparison of [68Ga]Ga-DOTA-FAPI-04 and [18F] FDG PET/CT for the diagnosis of primary and metastatic lesions in patients with various types of cancer. *Eur J Nucl Med Mol Imaging* (2020) 47(8):1820–32. doi: 10.1007/s00259-020-04769-z

22. Chen H, Zhao L, Ruan D, Pang Y, Hao B, Dai Y, et al. Usefulness of [68Ga]Ga-DOTA-FAPI-04 PET/CT in patients presenting with inconclusive [18F]FDG PET/CT findings. *Eur J Nucl Med Mol Imaging* (2021) 48(1):73–86. doi: 10.1007/s00259-020-04940-6

23. Huang SH, O'Sullivan B. Overview of the 8th edition TNM classification for head and neck cancer. *Curr Treat Options Oncol* (2017) 18(7):40. doi: 10.1007/s11864-017-0484-y

24. Chen X, Liu X, Wang L, Zhou W, Zhang Y, Tian Y, et al. Expression of fibroblast activation protein in lung cancer and its correlation with tumor glucose metabolism and histopathology. *Eur J Nucl Med Mol Imaging* (2022) 49(8):2938–48. doi: 10.1007/s00259-022-05754-4

25. Moreno-Ruiz P, Corvigno S, Te Grootenhuis NC, La Fleur L, Backman M, Strell C, et al. Stromal FAP is an independent poor prognosis marker in non-small cell lung adenocarcinoma and associated with p53 mutation. *Lung Cancer* (2021) 155:10–9. doi: 10.1016/j.lungcan.2021.02.028

26. Gu B, Xu X, Zhang J, Ou X, Xia Z, Guan Q, et al. The added value of 68Ga-FAPI-04 PET/CT in patients with head and neck cancer of unknown primary with 18F-FDG negative findings. *J Nucl Med* (2021) 63(6):875–81. doi: 10.2967/jnumed.121.262790

27. van den Brekel MW, Runne RW, Smeele LE, Tiwari RM, Snow GB, Castelijns JA. Assessment of tumour invasion into the mandible: The value of different imaging techniques. *Eur Radiol* (1998) 8(9):1552–7. doi: 10.1007/s003300050585

28. Lee SH, Huh SH, Jin SM, Rho YS, Yoon DY, Park CH. Diagnostic value of only 18F-fluorodeocyglucose positron emission tomography/computed tomography-positive lymph nodes in head and neck squamous cell carcinoma. *Otolaryngol Head Neck Surg* (2012) 147(4):692–8. doi: 10.1177/0194599812443040

29. Shang Q, Zhao L, Pang Y, Yu Y, Chen H. 68Ga-FAPI PET/CT distinguishes the reactive lymph nodes from tumor metastatic lymph nodes in a patient with nasopharyngeal carcinoma. *Clin Nucl Med* (2022) 47(4):367–8. doi: 10.1097/RLU.0000000000003939

frontiers | Frontiers in Oncology

TYPE Original Research
PUBLISHED 20 December 2022
DOI 10.3389/fonc.2022.1068210

OPEN ACCESS

EDITED BY
Lorenz Kadletz-Wanke,
Medical University of Vienna, Austria

REVIEWED BY
Jie Ren,
Third Affiliated Hospital of Sun Yat-sen University, China
Daniele Pironi,
Sapienza University of Rome, Italy

*CORRESPONDENCE
Qiu Xinguang
895909533@163.com

SPECIALTY SECTION
This article was submitted to Head and Neck Cancer, a section of the journal Frontiers in Oncology

RECEIVED 12 October 2022
ACCEPTED 30 November 2022
PUBLISHED 20 December 2022

CITATION
Yi Z, Siyu L, Lijun F, Danhua Z, Jianhua L and Xinguang Q (2022) Efficacy, safety, and controversy of ultrasound-guided radiofrequency ablation in the treatment of T1N0M0 papillary thyroid carcinoma. *Front. Oncol.* 12:1068210. doi: 10.3389/fonc.2022.1068210

Efficacy, safety, and controversy of ultrasound-guided radiofrequency ablation in the treatment of T1N0M0 papillary thyroid carcinoma

Zhang Yi[1], Li Siyu[2], Fu Lijun[1], Zhang Danhua[1], Li Jianhua[1] and Qiu Xinguang[1*]

[1]Department of Thyroid surgery, First Affiliated Hospital of Zhengzhou University, Zhengzhou, China, [2]Physical Examination Center, First Affiliated Hospital of Zhengzhou University, Zhengzhou, China

Objective: To evaluate the safety effect, and controversy on the treatment outcomes of radiofrequency ablation (RFA) for T1N0M0 papillary thyroid carcinoma (PTC).

Materials and methods: This study is assessed the medical records of 142 patients with primary T1N0M0 PTC tumors after RFA between 2014 and 2022. 4 patients underwent delayed surgery (DS) after RFA and 411 T1N0M0 patients underwent DS were recorded. Outcomes were compared between RFA and DS groups after propensity score matching (PSM).

Results: The maximal diameter (MD) and volume (V) increased in months 1 ($P < 0.01$) and reduced after the 6-month follow-up (all $P < 0.01$). The disappearance and disease progression rates were 53.5% and 2.1%, respectively. The complication and disease progression rates had no significant difference between RFA and DS ($P>0.05$). In some cases, the tumors were not fully inactivated after RFA, and the central compartment lymph node (CCLN) were metastasis. The CCLN metastasis rate was 13.4%. MD, V and clustered calcifications were independent risk factors for CCLN metastasis by univariate analysis.

Conclusions: RFA is an effective and safe treatment option in selected patients with solitary T1N0M0 PTC. There are the risks of tumor incompletely ablated and CCLN metastasis.

KEYWORDS

radiofrequency ablation, papillary thyroid carcinoma, ultrasound, lymph node metastasis, delayed surgery

Introduction

Papillary thyroid carcinoma (PTC) is the most common thyroid malignancy with an ever-increasing yearly incidence rate (1, 2). With the development of high-frequency ultrasound (US) and biopsy techniques, more cases of papillary thyroid microcarcinoma (PTMC) are being identified (3, 4). Although there are many controversies regarding the treatment strategy of PTMC without lymph node metastasis (LNM), traditional or endoscopic thyroidectomy remains the primary treatment strategy (5).

The American Thyroid Association guidelines introduced active surveillance (AS), instead of surgery, due to the surgical complications and low risk of metastasis associated with PTC (6–8). Radiofrequency ablation (RFA) has been rapidly promoted as the first-line approach for treating benign thyroid tumors or as a palliative treatment for metastatic lymph nodes in patients with thyroid cancer. RFA provides a new option for these patients because it is minimally invasive, has no impact on aesthetic appearance, and results in less trauma and scanty complications for the patient.

RFA was conceived initially as a way to treat benign thyroid nodules (BTNs) (9, 10) and is more frequently used in treating primary thyroid malignancies (11–13). In 2017, the Korean Radiofrequency Ablation Association published guidelines that proposed thermal ablation as a treatment method for thyroid cancer with LNM and PTMC and provided a basis for using RFA in PTMC (14). The Chinese Medical Doctors' Association and European Thyroid Association successively produced guidelines for the thermal ablation of thyroid tumors (15, 16). Many studies have confirmed that RFA is effective and safe for treating BTNs (17–19) which the incidence of RFA-associated complications, such as dysphonia, hypocalcemia and bleeding, is very low (20–22). Recent several studies have shown that RFA is effective for treating PTMC (23–25). However, studies on the prognosis, safety, and efficacy of RFA in treating T1N0M0 PTC are still insufficient. In addition, current studies mostly explore the efficacy and safety of thermal ablation. However, some potential risks are disregarded, including inadequate tumor inactivation, missed central compartment lymph node (CCLN) metastasis.

Therefore, this study aimed to explore the prognosis, safety, and efficacy of RFA in treating T1N0M0 PTC moreover to analyze risk factors of postoperative recurrence. Some cases underwent delayed surgery (DS) after RFA to evaluate tumor inactivation. Thus, the patients with T1N0M0 disease which is performed DS were selected to assess the proportion and related factors of missed CCLN metastasis. This was done as the results might provide a more impartial evaluation of RFA in patients with T1N0M0 PTC possible can be benefit to patients when they select between RFA and DS.

Materials and methods

This retrospective study was approved by the ethics committee at our respective institutes (Reference No. 2022-KY-0844-001) and the requirement for informed consent was waived. Informed consent was obtained from all patients for the treatment delivered.

The inclusion criteria were (a) maximum diameter (MD) less than 20 mm, (b) puncture biopsy indicating PTC with no invasion and rupture of the thyroid capsule on the preoperative US, (c) no invasion of surrounding tissues or regional lymph nodes, or distant metastasis, (d) ineligibility for or refusal to undergo surgery, and (e) at least 6-month duration of follow-up. Exclusion criteria were (a) multiple PTCs, (b) tumor located in the isthmus of the thyroid, (c) age younger than 18 years or pregnancy, and (d) unavailability of complete follow-up data.

Pre- and postoperative US examinations were performed by expert doctors (more than 5 years of experience) at our hospital's Ultrasound Department. US imaging provided data on tumor location, size (three meridians), and US characteristics of the tumor. The volume was calculated using:

$$V = \pi ABC/6$$

(where V is the volume, A is the MD, and B and C are the other two vertical diameters). The pathology results of preoperative fine-needle aspiration (FNA) indicated PTC presence, while $BRAF^{V600E}$ gene detection was used for auxiliary judgment when necessary. Computed tomography imaging of the neck and chest was performed to detect lymph node and distant metastasis.

The VIVA RF Generator (STARmed, Gyeonggi-do, South Korea) was used in this study. An 18-gauge, modified, monopolar, and internally cooled RFA antenna with a 1-cm active tip and a 7-cm shaft length was used; this was specifically modified for the ablation of thyroid nodules. The patients were asked to remain the supine position, and the shoulder and neck were padded and hyperextended to expose the neck fully. Routine disinfection and towel laying were performed. Lidocaine (2%) was used as the local anesthetic. Under US guidance, an electrode was inserted along the local anesthesia track into the nodule. Fixed ablation was used for small nodules, and multipoint or mobile ablation (moving-shot technique) was used for large nodules with multiple expected movements of the applicator into the target thyroid nodule. The treatment was considered complete when the strong echo range exceeded the original tumor margin by 5 mm (minimum 2 mm). The liquid isolated the recurrent laryngeal nerve (RLN), internal jugular vein, and common carotid artery. The average ablation time was 4.15 ± 1.48min, and compression was applied for 20–30 min postoperatively. Elevations of blood pressure, dysphonia, bleeding, and other complications were monitored.

All patients returned for follow-up US examinations at 1, 3, 6, and 12 months postoperatively, and every 6 months after that. Follow-up data were mainly based on thyroid US. The important indicators were as follows: 1. the size and volume of the lesion, and the percentage of reduction in the volume of the lesion after RFA, 2. the presence of recurrence and metastasis based on puncture biopsy results, when necessary, 3. the scope and morphology of necrosis in the ablation area, and 4.tumor disappearance and complication rate (the standard for image-guided thyroid ablation) (26).

Data analysis was performed using the SPSS software (SPSS for windows 21.0, SPSS, Chicago, IL). Descriptive statistics that are normally distributed are expressed as mean ± standard deviation, and categorical variables are given as frequency and percentage. Propensity score matching (PSM) was performed using the Stata 15.The paired t-test was used to assess differences between pretreatment and posttreatment, and the chi-squared test was used for comparing groups. Univariate analysis and log-rank test were separately used to analyze the factors of CCLN metastasis not identified on US. A value of $P < 0.05$ was considered to define statistically significant differences.

Results

Patient demographic and tumor characteristics

Since August 2014 to October 2022, the total numbers of patients (142) which is included 36 males 106 females respectively, aged 19–81 (mean age, 46.40 ± 14.30 years) underwent US-guided FNA or core-needle biopsy (CNB), and the pathology results were PTC (Figure 1). T1N0M0 PTC refers to a single thyroid nodule with a diameter of less than 2 cm, clear pathological indication, and no LNM. These 142 patients further underwent US-guided RFA. In addition, 411 patients who underwent DS and prophylactic CCLN dissection and whose preoperative US showed T1N0M0 PTC in the same period were selected. 142 cases were selected to compare after propensity score matching (PSM) (Table 1). Some exceptional cases were collected, including 4 patients who underwent DS after RFA.

The curative effects

Postoperative contrast-enhanced (CE) US imaging was performed to ensure that all tumors were completely enhanced by different degrees at the end of ablation. The filling defect at the ablation site of the CE US was an anechoic area, suggesting that the lesion was completely ablated. The ablation range was 2-3 mm larger than the lesion range. The ablation power and range were appropriately reduced at the upper and lower poles, especially for the lesions near important tissues such as RLN, esophagus, blood vessel etc.

The mean MD of the nodules before ablation was 6.37 ± 3.14 mm, and the mean V was 156.65 ± 251.26 mm^3. The MD and V of the ablation low echo area were larger than those of the original tumor at the evaluations performed during months 1 after ablation ($P < 0.001$); this is due to the ablation range having been 2-3 mm larger than the lesion range. The MD and V of the ablation low echo area were less than those of the original tumor at the 6-month and longer follow-up examinations after ablation ($P < 0.001$ for all). The changes are shown in Table 2. The MD and V were significantly reduced at the 6–24-month follow-up, while the

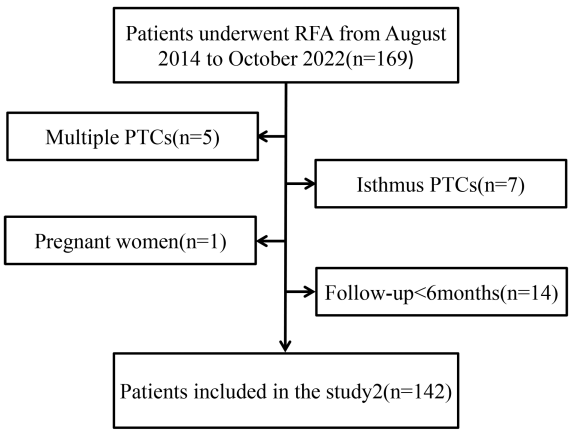

FIGURE 1
Research flowchart. RFA, radiofrequerncy, ablation, PTC, papillary thyroid carcinoma.

TABLE 1 Demographic characteristics of the study population.

Variable	Before PSM		P Value	After PSM		P Value
	RFA(n=142)	DS(n=411)		RFA(n=142)	DS(n=142)	
Age (year)*	46.40 ± 14.30	50.06 ± 9.59	0.005	46.40 ± 14.30	48.84 ± 8.74	0.084
Sex						
Female	106 (74.6)	327 (79.6)	0.221	106 (74.6)	109(76.8)	0.678
Male	36 (25.4)	84 (20.4)		36 (25.4)	33 (23.2)	
Location						
Left/Right	63/79	191/220	0.664	63/79	66/76	0.721
upper/middle/lower	41/46/55	119/103/189	0.186	41/46/55	33/42/67	0.328
deep/middle/shallow	42/71/29	131/211/69	0.606	42/71/29	46/75/21	0.456
Clustered calcifications(-/+)	40/102	149/262	0.080	40/102	41/101	0.895
Hypoechoic(-/+)	10/132	32/379	0.773	10/132	13/129	0.514
Diameter (mm)*	6.37 ± 3.14	7.73 ± 3.48	<0.001	6.37 ± 3.14	6.92 ± 2.91	0.124
Volume (mm^3)*	156.65 ± 251.26	755.82 ± 1 424.97	<0.001	156.65 ± 251.26	194.81 ± 291.35	0.216
Thyroid function						
FT3 (pmol/L)	4.89 ± 0.87	4.83 ± 1.01	0.489	4.89 ± 0.87	4.79 ± 1.02	0.362
FT4 (pmol/L)	12.80 ± 2.90	13.06 ± 3.08	0.380	12.80 ± 2.90	12.71 ± 3.21	0,795
TSH (uIU/ml)	3.31 ± 1.57	3.28 ± 1.57	0.855	3.31 ± 1.57	3.42 ± 1.53	0.547
Time of diagnosis	18.17 ± 14.57	24.60 ± 15.78	<0.001	18.17 ± 14.57	20.75 ± 14.10	0.131

Unless otherwise specified, data are the number of patients. * Data presented as Means ± standard deviation. PSM, propensity score matching. Normal range: FT3 3.28~6.47 pmol/L, FT4 7.90~18.40 pmol/L, TSH 0.56~5.91 uIU/ml.

reduction was minimal after 24 months, which has shown in Figure 2. The tumor disappearance rate was 53.5% (76/142).

The American Joint Committee classifies the T1 PTC into T1a (tumor ≤ 1 cm) and T1b (tumor > 1 cm but ≤ 2 cm). The follow-up data for T1a and T1b PTC are shown in Table 3. The MD and V of T1a of the ablation zone at the 12-month follow-up were less than those for the original tumor (P < 0.001 for both). The changes of MD and V in T1b PTC at the 12-month follow-up were significant (P = 0.003 and P = 0.004, respectively).

The safety and treatment efficacy

The complication rate at the most recent follow-up was 2.8% (4/142), with hematoma and dysphonia. There was no significant difference in the complication rate between RFA and DS in the short term (P = 0.518, Table 4). The disease progression rate after RFA was 2.1% (3/142) in the present study. The disease progression rate after DS was 1.4% (2/142). There was no significant difference in disease

TABLE 2 The changes of mean maximal diameter and volume after ablation over 1 year.

Follow up time	MD (mm)	*P* Value	Volume (mm^3)	*P* Value
Preablation (n=142)	6.37 ± 3.14		156.63 ± 222.69	
Postablation				
1 month (n=142)	11.15 ± 4.78	<0.001	586.79 ± 653.12	<0.001
3 month (n=142)	6.90 ± 3.21	0.031	180.43 ± 246.94	0.173
6 month (n=117)	4.73 ± 1.96	<0.001	58.01 ± 78.22	<0.001
12 month (n=50)	4.13 ± 1.36	<0.001	31.53 ± 35.73	<0.001

Data are means ± standard deviation. P value is preablation vs postablation respectively. MD, maximum diameter.

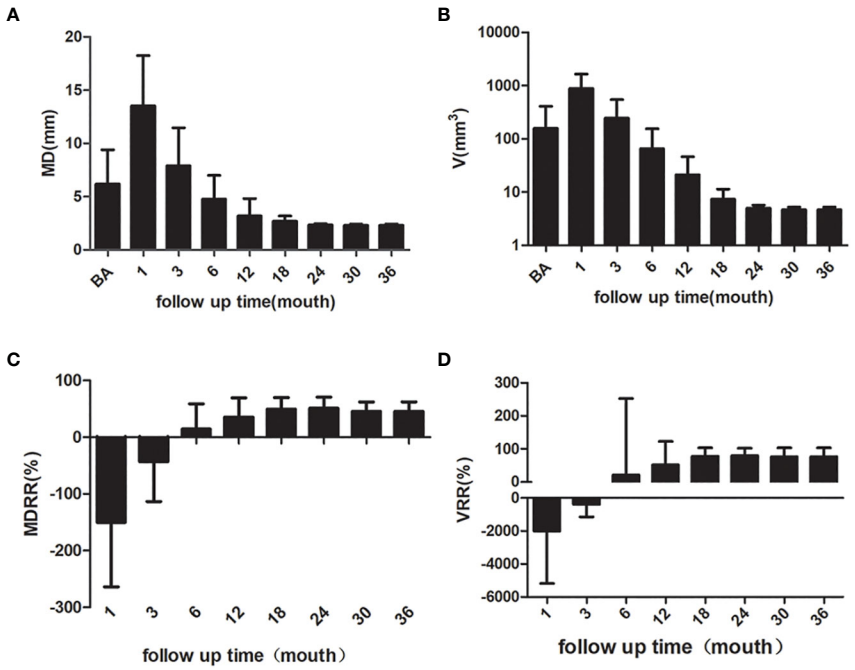

FIGURE 2
The MD, V, MDRR and VRR of the nodules. **(A)** MD of the nodules **(B)** V of the nodules **(C)** MDRR of the nodules **(D)** VRR of the nodules. MD, maximum diameter; V, volume; MDRR, maximal diameter reduction ratio; VRR, volume reduction ratio.

progression rate between RFA and DS in the short term (P =0.652, Table 4).

The four cases that underwent DS after RFA were assessed to understand whether the tumor was completely ablated. All RFA were performed by doctors who had more than 100 procedures. The first patient underwent DS due to enlargement of thyroid nodules 4 years after RFA; the postoperative pathology showed that the ablation region had a new tumor (PTC, MD was 3 mm).

TABLE 3 The comparison of T1a and T1b PTC.

Variable	T1a PTC (n=122)	T1b PTC (n=20)	P
Preablation			
MD (mm)	5.37 ± 1.96	12.39 ± 2.11	< 0.001
Volume (mm^3)	79.89 ± 82.04	624.75 ± 238.05	< 0.001
Postablation			
MD (mm)			
6 month	4.27 ± 1.62	6.98 ± 1.96	< 0.001
12 month	3.81 ± 1.23	5.06 ± 1.34	0.003
Volume (mm^3)			
6 month	39.78 ± 52.31	146.40 ± 116.68	< 0.001
12 month	23.39 ± 22.35	55.30 ± 54.39	0.004
Disappearance rate*	72 (59%)	4 (20%)	0.001
Disease progression*	2 (1.6%)	1 (5%)	0.368

Data are means ± standard deviation. * Data presented as number.
PTC, papillary thyroid carcinoma; MD, maximum diameter.

TABLE 4 The complications and disease progression of RFA and DS.

Variable	RFA (n=142)	DS(n=142)	P
Complication	4	6	0.518
Hematoma	1	1	
Hypocalcemia	0	1	
Dysphonia	3	4	
Disease progression	3	2	0.652
New tumors	1	1	
LNMs	2	1	

Data are expressed as number of findings. RFA, radiofrequency ablation.
DS, delayed surgery; LNM, lymph node metastasis.

The second patient underwent DS because CCLN metastasis was observed 3 months after RFA; the postoperative pathology showed the tumor was not ablated, and there was CCLN metastasis (metastasis/all was 7/9). The remaining 2 patients underwent concomitant RFA and FNA followed by DS as the puncture biopsy results indicated PTC. The pathology suggested that the tumor was completely ablated in one case but not in the other. The US and pathology images are shown in Figure 3.

To calculate the characteristics of CCLN metastasis in T1N0M0 PTC, the data of 142 patients were analyzed who

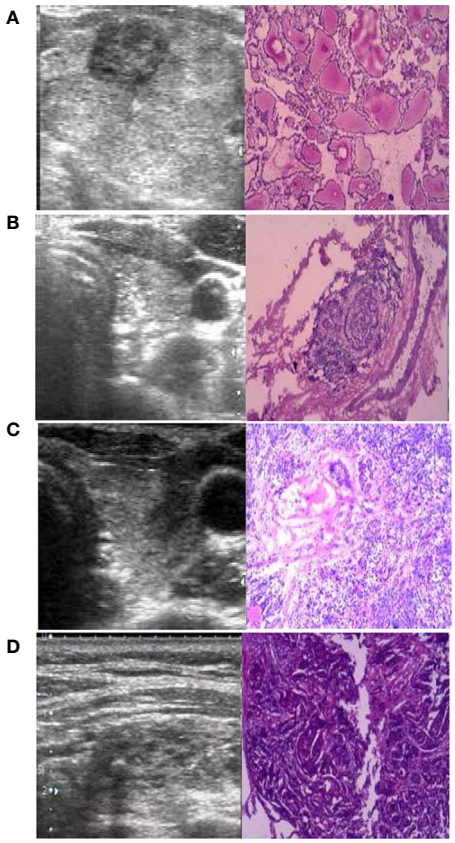

FIGURE 3
The preoperative ultrasound (US) and postoperative pathology (x100). **(A)** The ablation region had a new PTC four years after radiofrequency ablation (RFA). **(B)** The lymph nodes were metastasis (positive/all was 7/9) 3 months after RFA. **(C)** The PTC was not completely ablated 3 months after RFA. **(D)** The PTC was completely ablated 1 months after RFA.

underwent DS and CCLN dissection. The postoperative pathology revealed that the rate of LNM was 13.4% (19/142). The results of the chi-squared test and t-test showed that the independent risk factors for CCLN metastasis were MD, V and clustered calcifications as shown in Table 5.

Discussion

There is still no clear consensus on the optimal management strategy for PTC. The controversy surrounding management approaches includes the choice among open surgery, thermal ablation, and AS. RFA has been rapidly promoted as the first approach for treating benign thyroid tumors or even for the palliative treatment of metastatic lymph nodes in patients with thyroid cancer because it is minimally invasive and has no impact on aesthetic appearance (27). Multiple studies have reported that using RFA for patients with PTMC was safe, effective, and reliable (28, 29). Our study confirmed the safety, efficacy, and reliability of RFA in treating T1N0M0 PTC.

In this study, the tumor disappearance, disease progression, and complication rates of tumors after RFA were 53.5%, 2.1% and 2.8%, respectively. Moreover, our study showed that the tumor disappearance rate of T1N0M0 PTC was lower than the results of a meta-analysis of data from 12 studies (combined n = 1187) that showed the complete disappearance rate of PTMC was 76.2% (30). The reason may be it is required greater range and power when RFA in treat of T1N0M0 PTC. The tumors showed reduction in 12 month both at T1a and T1b groups. RFA is a feasible and effective treatment option in selected patients with T1a and T1b PTC.

The complication rate of this study is similar to result which has shown in studies of PTMC and BTNs. In the terms of RFA complications, dysphonia was the most common and occurred secondary to recurrent thermal injury of the RLN. As RLN edema subsided, the dysphonia was resolved within 6 months. In some previous studies, the dysphonia incidence rate due to DS was 3-4% (31–33), which was insignificantly different to the result in this study (2.8%). Wei et al. (34) reported that there was no difference regarding disease progression and complications between microwave ablation and DS. In this study, the complication rates following RFA were the same as DS (P = 0.518). There were no differences in disease progression between RFA and DS (P = 0.652). To reduce the incidence of thermal injury of the RLN, the surgeon should employ hydro-dissection and accurate puncturing, as well as the ablation time and subsequent release of energy should be reduced. This study observed that the safety and efficacy of RFA in T1N0M0 PTC were favorable when compared with DS.

During the 24-month follow-up examination, we found that RFA was reliable regarding the tumor gradually reduced or disappeared. This study showed favorable results in the medium- and short-term follow-up examinations. Although PTC progresses slowly, several controversial issues cannot be ignored until the long-term follow-up examination results are available or until further research is conducted. However, while there are several studies on the effectiveness of RFA, only a few investigate its limitations, which may mislead doctors or patients into overconfidence about RFA. The most controversial issues of RFA are whether the tumor is entirely necrotic and LNM. Four cases that underwent DS after RFA were analyzed to investigate tumor necrosis, and the results proved that tumor is not removed completely and LNM existed. Sun et al. (35) reported that of 21 patients who underwent surgery after RFA, 33.3% had bilateral cancer and 47.6% had CCLN; similar results (66.7%, 8/12) were reported by Ma et al. (36).Due to the lack of cases, the extent of these situations is unknown.

To explore LNM, we collected clinical data from T1N0M0 PTC patients who had performed DS and CCLN dissection, the same inclusion criteria as RFA. The requirement of RFA make the inclusion criteria different from traditional T1N0M0 PTC. The tumors should be single and located in some distance from the boundary of envelope, trachea, esophagus, recurrent laryngeal

TABLE 5 Univariate analysis of CCLN metastasis in T1N0M0 PTC.

Parameters	CCLN metastasis (+) (n=19)	CCLN metastasis (-) (n=123)	*P*
Age(year)*	46.79 ± 9.69	49.15 ± 8.58	0.274
Sex(Female/Male)	15/4	94/29	0.807
MD (mm)*	9.58 ± 3.58	6.51 ± 2.57	0.002
Volume (mm^3)*	422.71 ± 322.27	159.61 ± 271.02	0.003
Location			
right/lift	13/6	60/63	0.218
upper/middle/lower	6/6/7	27/36/60	0.560
deep/middle/shallow	2/8/9	19/38/66	0.660
Clustered calcifications(-/+)	7/12	96/27	<0.001

Data are the number of patients. *Data presented as Means ± standard deviation and use t test. CCLN, central compartment lymph node; MD, maximum diameter.

nerve. The patients should have no family history, no radiation history. After using PSM to reduce the dimension of the data, the CCLN metastasis rate was 13.4% which significantly lower than traditional T1N0M0 PTC (37, 38). The univariate analysis showed that MD, V, and clustered calcifications correlated significantly with CCLN metastasis. Compared with hypoechoic nodules, clustered calcifications were strongly correlated with CCLN metastasis. In some studies, CCLN metastasis was associated with PTC recurrence rates (39–41). As the risk for recurrence of LNM remains, our study found that patients with smaller-diameter and no cluster calcificationare are more suitable for RFA.

This study found that appropriately expanding the scope of operation, prolonging the operation time, and performing postoperative CE US to ensure complete ablation of lesions can prevent recurrence. RFA should be performed from top to bottom and deep to shallow regions to ensure no omissions. Few patients with CCLN metastasis bear a high risk of recurrence, often undergoing DS after RFA. Doctors should adhere strictly to the indications of RFA and fully inform patients when discussing RFA as an option with PTC patients, as undergoing DS after RFA increases the financial burden of patients and may lead to disease progression. A significant advantage was that DS performed after RFA was reasonably straightforward based on clinical experience; only slight tissue adhesions were found intraoperatively. In addition, our study found that most patients receiving minimally invasive treatments were females aged 18-30 years and patients with jobs that required a high aesthetic appearance. These patients refused to undergo open surgery; thus, RFA may be the appropriate alternative treatment. Open surgery should be considered the primary treatment option for patients who prefer radical treatment over aesthetic appearance and minimally invasive surgery.

This study confirmed the safety and reliability of RFA in treating T1N0M0 PTC. Nonetheless, patient subsets that can and cannot undergo RFA are still not known. Further studies are required to fully predict which groups of patients with thyroid cancer are suitable for RFA and to detect LNM that cannot be detected by color Doppler ultrasound. Furthermore, future studies should answer whether RFA is better than AS and whether it provides the same results and outlook of open surgery, as well as determine which options are available for any remaining residual tumor post-RFA.

Our research had some limitations. First, this was a single-center study. Second, the mean follow-up period in this study was short based on the progression of PTC. Third, this study lacks data regarding the pathology diagnosis of RFA. Lastly, the CCLN metastasis ratio was inferred by pathological results obtained during DS, rather than after RFA.

Conclusions

In conclusion, RFA is a safe and effective treatment for T1N0M0 PTC but is associated with a higher recurrence risk than DS. We found that RFA was associated with fewer postoperative complications and less trauma to the patients, had no impact on aesthetic appearance, and required only local anesthesia. Moreover, RFA is more suitable for females aged 18-30 years, elderly patients or patients with serious other illnesses. However, the incomplete tumor inactivation and LNM make RFA unsuitable to replace open surgery as the primary treatment option. Therefore, the indications of RFA should be carefully considered, and the patients should be fully informed.

Data availability statement

The original contributions presented in the study are included in the article/supplementary material. Further inquiries can be directed to the corresponding author.

Ethics statement

The studies involving human participants were reviewed and approved by the ethical and scientific review board of the First Affiliated Hospital of Zhengzhou University. Written informed consent for participation was not required for this study in accordance with the national legislation and the institutional requirements. Written informed consent was obtained from the individual(s) for the publication of any potentially identifiable images or data included in this article.

Author contributions

ZY, LS, FL, ZD, LJ: Study design and manuscript writing. ZY, LS, FL: Studies selecting and data analysis. ZY, ZD, LJ, QX: Study quality evaluating. ZY, QX: Manuscript revising. All authors have read and approved the final manuscript. All authors contributed to the article and approved the submitted version.

Funding

This work was supported by the key projects of health commission in Henan province under Grant No. 212102310172.

Acknowledgments

We thank all researchers for their support in this study.

Conflict of interest

The authors declare that the research was conducted in the absence of any commercial or financial relationships that could be construed as a potential conflict of interest.

Publisher's note

References

1. Haugen BR, Alexander EK, Bible KC, Doherty GM, Mandel SJ, Nikiforov YE, et al. 2015 American Thyroid association management guidelines for adult patients with thyroid nodules and differentiated thyroid cancer: The American thyroid association guidelines task force on thyroid nodules and differentiated thyroid cancer. *Thyroid* (2016) 26(1):1–133. doi: 10.1089/thy.2015.0020

2. Schlumberger M, Leboulleux S. Current practice in patients with differentiated thyroid cancer. *Nat Rev Endocrinol* (2021) 17(3):176–88. doi: 10.1038/s41574-020-00448-z

3. Davies L, Hoang JK. Thyroid cancer in the USA: Current trends and outstanding questions. *Lancet Diabetes Endocrinol* (2021) 9(1):11–2. doi: 10.1016/s2213-8587(20)30372-7

4. Filetti S, Durante C, Hartl D, Leboulleux S, Locati LD, Newbold K, et al. Thyroid cancer: ESMO clinical practice guidelines for diagnosis, treatment and follow-up. *Ann Oncol* (2019) 30(12):1856–83. doi: 10.1093/annonc/mdz400

5. Tuttle RM. Controversial issues in thyroid cancer management. *J Nucl Med* (2018) 59(8):1187–94. doi: 10.2967/jnumed.117.192559

6. Davies L, Chang CH, Sirovich B, Tuttle RM, Fukushima M, Ito Y, et al. Thyroid cancer active surveillance program retention and adherence in Japan. *JAMA otolaryngology– Head Neck Surg* (2021) 147(1):77–84. doi: 10.1001/jamaoto.2020.4200

7. Lowenstein LM, Basourakos SP, Williams MD, Troncoso P, Gregg JR, Thompson TC, et al. Active surveillance for prostate and thyroid cancers: evolution in clinical paradigms and lessons learned. *Nat Rev Clin Oncol* (2019) 16(3):168–84. doi: 10.1038/s41571-018-0116-x

8. Alexander EK, Doherty GM, Barletta JA. Management of thyroid nodules. *Lancet Diabetes Endocrinol* (2022) 10(7):540–8. doi: 10.1016/s2213-8587(22)00139-5

9. Li N, Huber TC. Radiofrequency ablation for benign thyroid nodules: Radiology in training. *Radiology* (2022), 220116. doi: 10.1148/radiol.220116

10. Tufano RP, Pace-Asciak P, Russell JO, Suárez C, Randolph GW, López F, et al. Update of radiofrequency ablation for treating benign and malignant thyroid nodules. *Future Is Now Front Endocrinol* (2021) 12:698689. doi: 10.3389/fendo.2021.698689

11. Kim HJ, Cho SJ, Baek JH. Comparison of thermal ablation and surgery for low-risk papillary thyroid microcarcinoma: A systematic review and meta-analysis. *Korean J Radiol* (2021) 22(10):1730–41. doi: 10.3348/kjr.2020.1308

12. van Dijk SPJ, Coerts HI, Gunput STG, van Velsen EFS, Medici M, Moelker A, et al. Assessment of radiofrequency ablation for papillary microcarcinoma of the thyroid: A systematic review and meta-analysis. *JAMA Otolaryngology– Head Neck Surg* (2022) 148(4):317–25. doi: 10.1001/jamaoto.2021.4381

13. Cao XJ, Wang SR, Che Y, Liu J, Cong ZB, He JF, et al. Efficacy and safety of thermal ablation for treatment of solitary T1N0M0 papillary thyroid carcinoma: A multicenter retrospective study. *Radiology* (2021) 300(1):209–16. doi: 10.1148/radiol.2021202735

14. Kim JH, Baek JH, Lim HK, Ahn HS, Baek SM, Choi YJ, et al. 2017 Thyroid radiofrequency ablation guideline: Korean society of thyroid radiology. *Korean J Radiol* (2018) 19(4):632–55. doi: 10.3348/kjr.2018.19.4.632

15. Papini E, Monpeyssen H, Frasoldati A, Hegedüs L. 2020 European Thyroid association clinical practice guideline for the use of image-guided ablation in benign thyroid nodules. *Eur Thyroid J* (2020) 9(4):172–85. doi: 10.1159/000508484

16. Xu D, Ge M, Yang A, Cheng R, Sun H, Wang H, et al. Expert consensus workshop report: Guidelines for thermal ablation of thyroid tumors (2019 edition). *J Cancer Res Ther* (2020) 16(5):960–6. doi: 10.4103/jcrt.JCRT_558_19

17. Bernardi S, Palermo A, Grasso RF, Fabris B, Stacul F, Cesareo R. Current status and challenges of US-guided radiofrequency ablation of thyroid nodules in the long term: A systematic review. *Cancers* (2021) 13(11). doi: 10.3390/cancers13112746

18. Kandil E, Omar M, Aboueisha M, Attia AS, Ali KM, Abu Alhuda RF, et al. Efficacy and safety of radiofrequency ablation of thyroid nodules: A multi-institutional prospective cohort study. *Ann Surg* (2022) 276(4):589–96. doi: 10.1097/sla.0000000000005594

19. Lin Y, Shi YP, Tang XY, Ding M, He Y, Li P, et al. Significance of radiofrequency ablation in large solid benign thyroid nodules. *Front Endocrinol* (2022) 13:902484. doi: 10.3389/fendo.2022.902484

20. Kuo JH, Lee JA. The adoption of ultrasound-guided radiofrequency ablation of thyroid nodules in the united states. *Ann Surg* (2021) 273(1):e10–2. doi: 10.1097/sla.0000000000003930

21. Mauri G, Papini E, Bernardi S, Barbaro D, Cesareo R, De Feo P, et al. Image-guided thermal ablation in autonomously functioning thyroid nodules. a retrospective multicenter three-year follow-up study from the Italian minimally invasive treatment of the thyroid (MITT) group. *Eur Radiol* (2022) 32(3):1738–46. doi: 10.1007/s00330-021-08289-8

22. Navin PJ, Thompson SM, Kurup AN, Lee RA, Callstrom MR, Castro MR, et al. Radiofrequency ablation of benign and malignant thyroid nodules. *Radiographics* (2022) 42(6):1812–28. doi: 10.1148/rg.220021

23. Cho SJ, Baek SM, Na DG, Lee KD, Shong YK, Baek JH. Five-year follow-up results of thermal ablation for low-risk papillary thyroid microcarcinomas: systematic review and meta-analysis. *Eur Radiol* (2021) 31(9):6446–56. doi: 10.1007/s00330-021-07808-x

24. Choi Y, Jung SL. Efficacy and safety of thermal ablation techniques for the treatment of primary papillary thyroid microcarcinoma: A systematic review and meta-analysis. *Thyroid* (2020) 30(5):720–31. doi: 10.1089/thy.2019.0707

25. Chung SR, Baek JH, Choi YJ, Sung TY, Song DE, Kim TY, et al. Efficacy of radiofrequency ablation for recurrent thyroid cancer invading the airways. *Eur Radiol* (2021) 31(4):2153–60. doi: 10.1007/s00330-020-07283-w

26. Mauri G, Pacella CM, Papini E, Solbiati L, Goldberg SN, Ahmed M, et al. Image-guided thyroid ablation: Proposal for standardization of terminology and reporting criteria. *Thyroid* (2019) 29(5):611–8. doi: 10.1089/thy.2018.0604

27. Jin H, Fan J, Lu L, Cui M. A propensity score matching study between microwave ablation and radiofrequency ablation in terms of safety and efficacy for benign thyroid nodules treatment. *Front Endocrinol* (2021) 12:584972. doi: 10.3389/fendo.2021.584972

28. van Dijk SPJ, Coerts HI, van Ginhoven TM. Radiofrequency ablation for papillary microcarcinoma of the thyroid-reply. *JAMA Otolaryngology– Head Neck Surg* (2022) 148(7):698–9. doi: 10.1001/jamaoto.2022.1177

29. Yang S, Xu X. Radiofrequency ablation for papillary microcarcinoma of the thyroid. *JAMA otolaryngology– Head Neck surg* (2022) 148(7):698. doi: 10.1001/jamaoto.2022.1174

30. Tong M, Li S, Li Y, Li Y, Feng Y, Che Y. Efficacy and safety of radiofrequency, microwave and laser ablation for treating papillary thyroid microcarcinoma: a systematic review and meta-analysis. *Int J Hyperthermia* (2019) 36(1):1278–86. doi: 10.1080/02656736.2019.1700559

31. Wang TS, Sosa JA. Thyroid surgery for differentiated thyroid cancer - recent advances and future directions. *Nat Rev Endocrinol* (2018) 14(11):670–83. doi: 10.1038/s41574-018-0080-7

32. Cirocchi R, Arezzo A, D'Andrea V, Abraha I, Popivanov GI, Avenia N, et al. Intraoperative neuromonitoring versus visual nerve identification for prevention of recurrent laryngeal nerve injury in adults undergoing thyroid surgery. *Cochrane Database Systematic Rev* (2019) 1(1):Cd012483. doi: 10.1002/14651858.CD012483.pub2

33. Li C, Lopez B, Fligor S, Broekhuis JM, Maeda A, Duncan S, et al. Long-term voice changes after thyroidectomy: Results from a validated survey. *Surgery* (2021) 170(6):1687–91. doi: 10.1016/j.surg.2021.04.060

34. Wei Y, Niu WQ, Zhao ZL, Wu J, Peng LL, Li Y, et al. Microwave ablation versus surgical resection for solitary T1N0M0 papillary thyroid carcinoma. *Radiology* (2022) 304(3):704–13. doi: 10.1148/radiol.212313

35. Sun W, Zhang H, He L, Zhang T, Wang Z, Dong W, et al. Surgery after ultrasound-guided radiofrequency ablation for papillary thyroid carcinoma in 21 patients: A retrospective study from a single center in China. *Med Sci Monit* (2020) 26:e928391. doi: 10.12659/MSM.928391

36. Ma B, Wei W, Xu W, Wang Y, Guan H, Fan J, et al. Surgical confirmation of incomplete treatment for primary papillary thyroid carcinoma by percutaneous

thermal ablation: A retrospective case review and literature review. *Thyroid* (2018) 28(9):1134–42. doi: 10.1089/thy.2017.0558

37. Wang Y, Deng C, Shu X, Yu P, Wang H, Su X, et al. Risk factors and a prediction model of lateral lymph node metastasis in CN0 papillary thyroid carcinoma patients with 1-2 central lymph node metastases. *Front Endocrinol* (2021) 12:716728. doi: 10.3389/fendo.2021.716728

38. Huang C, Cong S, Shang S, Wang M, Zheng H, Wu S, et al. Web-based ultrasonic nomogram predicts preoperative central lymph node metastasis of cN0 papillary thyroid microcarcinoma. *Front Endocrinol* (2021) 12:734900. doi: 10.3389/fendo.2021.734900

39. Yu ST, Ge JN, Sun BH, Wei ZG, Xiao ZZ, Zhang ZC, et al. Lymph node yield in the initial central neck dissection (CND) associated with the risk of recurrence in papillary thyroid cancer: A reoperative CND cohort study. *Oral Oncol* (2021) 123:105567. doi: 10.1016/j.oraloncology.2021.105567

40. Ho AS, Luu M, Shafqat I, Mallen-St Clair J, Chen MM, Chen Y, et al. Predictive impact of metastatic lymph node burden on distant metastasis across papillary thyroid cancer variants. *Thyroid* (2021) 31(10):1549–57. doi: 10.1089/thy.2021.0131

41. Guang Y, He W, Zhang W, Zhang H, Zhang Y, Wan F. Clinical study of ultrasonographic risk factors for central lymph node metastasis of papillary thyroid carcinoma. *Front Endocrinol* (2021) 12:791970. doi: 10.3389/fendo.2021.791970

frontiers | Frontiers in Oncology

TYPE Original Research
PUBLISHED 22 December 2022
DOI 10.3389/fonc.2022.1076548

OPEN ACCESS

EDITED BY
Lorenz Kadletz-Wanke,
Medical University of Vienna, Austria

REVIEWED BY
Fahim Ahmad,
National Cancer Institute at Frederick (NIH), United States
Weidong Dai,
Chinese Academy of Agricultural Sciences, China

*CORRESPONDENCE
Jie Fan
fanjie198903@outlook.com
Shanting Liu
liushanting@163.com
Ruihua Luo
666lrh@sina.com

†These authors have contributed equally to the work

SPECIALTY SECTION
This article was submitted to Head and Neck Cancer, a section of the journal Frontiers in Oncology

RECEIVED 21 October 2022
ACCEPTED 30 November 2022
PUBLISHED 22 December 2022

CITATION
Qin J, Yang Y, Du W, Li G, Wu Y, Luo R, Liu S and Fan J (2022) The potential value of LC-MS non-targeted metabonomics in the diagnosis of follicular thyroid carcinoma. *Front. Oncol.* 12:1076548. doi: 10.3389/fonc.2022.1076548

The potential value of LC-MS non-targeted metabonomics in the diagnosis of follicular thyroid carcinoma

Jiali Qin[1†], Yang Yang[2†], Wei Du[1,3], Gang Li[1], Yao Wu[1], Ruihua Luo[1*], Shanting Liu[1*] and Jie Fan[1*†]

[1]Department of Head Neck and Thyroid Surgery, Affiliated Cancer Hospital of Zhengzhou University, Henan Cancer Hospital, Zhengzhou, Henan, China, [2]Department of Nephrology, The First Affiliated Hospital of Zhengzhou University, Zhengzhou, Henan, China, [3]Department of Anatomy, Zhengzhou University, Zhengzhou, Henan, China

Background: To explore the metabolic differences of follicular thyroid carcinoma (FTC) by metabonomics, to find potential biomarkers for the diagnosis of FTC, and to explore the pathogenesis and diagnosis and treatment strategies of FTC.

Method: The metabonomics of 15 patients with FTC and 15 patients with follicular thyroid nodules(FTN) treated in Henan Cancer Hospital were analyzed by liquid chromatography-mass spectrometry (LC-MS).

Results: The analysis showed that the metabolite profiles of FTC tissues could be well distinguished from those of control tissues, and 6 kinds of lipids were identified respectively, including lysophosphatidic acid(LysoPA) [LysoPA(0:0/18:0),LysoPA(0:0/18:2(9Z,12Z)],LysoPA[20:4(8Z,11Z,14Z,17Z)/0:0)]; phosphatidic acid(PA) [PA(20:3(8Z,11Z,14Z)/0:0),PA(20:4(5Z,8Z,11Z,14Z)/0:0), PA(20:5(5Z,8Z,11Z,14Z,17Z)/0:0)]; lysophosphatidylcholine(LPC) [LPC(18:1), LPC(16:0),LPC[16:1(9Z)/0:0],LPC(17:0),LPC[22:4(7Z,10Z,13Z,16Z),LPC(20:2(11Z,14Z); phosphatidylcholine(PC)(PC(14:0/0:0),PC(16:0/0:0); sphingomyelin (SM) (d18:0/12:0); fatty acid(FA)(18:1(OH3)]. There are 2 kinds of amino acids, including L-glutamate,L-glutamine.There are 3 other metabolites, including retinol,flavin adenine dinucleotide,androsterone glucuronide.Lipid metabolites are the main metabolites in these metabolites.The metabolic pathways related to FTC were analyzed by KEGG and HMDB, and 9 metabolic pathways were found, including 4 amino acid related metabolic pathways, 1 lipid metabolic pathways and 4 other related pathways.

Conclusion: There are significant differences in many metabonomic characteristics between FTC and FTN, suggesting that these metabolites can be used as potential biomarkers. Further study found that LysoPA and its analogues can be used as biomarkers in the early diagnosis of FTC.It may be related to the abnormal metabolism of phospholipase D (PLD), the key enzyme

of LysoPA synthesis caused by RAS pathway. At the same time, it was found that the metabolic pathway of amino acids and lipids was the main metabolic pathway of FTC. The abnormality of LysoPA may be the cause of follicular tumor carcinogenesis caused by lipid metabolic pathway.

KEYWORDS

follicular thyroid carcinoma, metabonomics, lipid metabolites, RAS, LysoPA

1 Introduction

Follicular thyroid tumor mainly include FTC, atypical follicular thyroid adenoma and follicular thyroid adenoma (FTA). FTC is one of the highly differentiated malignant tumors, and its incidence is second only to papillary thyroid carcinoma (PTC). The main reason for its occurrence is the abnormal differentiation of thyroid follicular epithelial cells (1). In 2017, WHO divided FTC into three types: slightly invasive type (only invading the capsule), intracapsular vascular infiltrating type and extensive infiltrating type. Lymph node metastasis in FTC was less common than that in PTC, but distant tissue or organ metastasis was easy to occur (2). At present, there are few studies on the pathogenesis of FTC, and the clinical diagnosis and treatment of FTC are mainly focused on imaging examination, fine needle aspiration cytology and so on.Fine needle aspiration cytology(FNAC) is currently the most accurate method to evaluate the benign and malignant thyroid nodules, but there are still 20% to 30% follicular tumors that cannot be determined by FNAC, and FTC is easily confused with FTA in clinical diagnosis, resulting in misdiagnosis (3). Clinically, there is an urgent need for a highly sensitive, specific, efficient, non-invasive and widely used objective index for the diagnosis of thyroid nodules. Therefore, it is necessary to find a stable and reliable tumor molecular marker to assist the diagnosis of FTC.

Metabolomics is a subject of qualitative and quantitative analysis of low molecular weight metabolites in an organism or cell to monitor the changes of chemical products in living cells. It has significant advantages in the early screening of tumor markers (4). The most commonly used analytical methods in metabonomics are nuclear magnetic resonance and liquid or gas chromatography-tandem mass spectrometry(LC/GC-MS) (5). At present, the application of metabonomics in tumor diagnosis is mainly focused on gastric cancer (6), liver cancer (7), lung cancer (8), breast cancer (9), prostate cancer (10) and so on. Metabonomic studies related to thyroid cancer are mainly focused on thyroid papillary carcinoma.Skorupa (11) analyzed 38 cases of PTC, 32 benign thyroid nodules (BTNs) and 112 non-tumor tissue samples by high-resolution magic angle rotation nuclear magnetic resonance technique. It was found that the levels of alanine and lysine in PTC tissue samples were higher than those in non-tumor lesions, while sphingositol content increased in BTNs. In addition, Aboosb R (12) analyzed thyroid nodule patients (including 19 patients with PTC and 16 patients with nodular goiter) and 20 healthy controls by GC-MS. It was found that there were differences in amino acid metabolism, tricarboxylic acid cycle, fatty acid, purine and pyrimidine metabolism between the two groups. At present, few papers on metabonomics related to FTC have been published. In this study, Liquid chromatography-tandem mass spectrometry (LC-MS) metabonomics was used to detect FTC and FTN tissue samples, to screen differential metabolites, to find abnormal metabolic pathways, to explore the potential biomarkers and pathogenesis of FTC, and to provide basis for early diagnosis and treatment of FTC.

2 Materials and methods

2.1 Study subjects

The subjects were from the patients treated in Henan Cancer Hospital. All the patients in the experimental group were confirmed to be FTC by operation and pathological examination.The experimental group will meet the following items: a). It was confirmed by pathology as FTC;b). No history of other cancers; c). Age ≥ 18 years old; d). No history of blood transfusion; e). No history of taking immunosuppressive drugs. The control group was matched with case frequency according to age and sex. The study was carried out with the informed consent of the subjects.

2.2 Sample preparation

Take 50mg solid sample or 100 μl liquid sample into 1.5ml centrifuge tube, add 400 μ l extract (acetonitrile: methanol = 1:1), after vortex mixing for 30s, extract 30min (5 °C, 40KHz) by low temperature ultrasonic extraction, place the sample at-20°C,

30 min, 4°C, 13000g centrifugal 15min, remove the supernatant, dry with nitrogen, re-dissolve 120 μ l complex solution (acetonitrile: water = 1:1), and extract 5min (5 °C,40KHz), 4°C, 13000g centrifugal 5min, the supernatant was removed to the injection vial with internal intubation for analysis.

2.3 QC samples LC-MS analysis

All the sample metabolites of the same volume were mixed into quality control samples (QC). In the process of instrumental analysis, one QC sample was inserted into every 10 samples to investigate the repeatability of the whole analysis process.

2.4 LC-MS analysis

The instrument platform of this LC-MS analysis is AB SCIEX's UPLC-TripleTOF system of ultra high performance liquid chromatography tandem time of flight mass spectrometry. Chromatographic conditions: 10ul samples were separated by BEH C18 column (100mm × 2.1 mm I.D., 1.8 μ m) and then detected by mass spectrometry. Mobile phase A: water (containing 0.1% formic acid), mobile phase B: acetonitrile/ isopropanol (1pm 1) (containing 0.1% formic acid). Separation gradient: 0-3 min, mobile phase A from linear 95% to 80%, mobile phase B from linear 5% to 20% min, mobile phase A from linear 80% to 5%, mobile phase B linear from 20% to 95% min, mobile phase A linear to 5%, mobile phase B linear to 95%. 13.0-13.1 min, the linearity of mobile phase An increases from 5% to 95%, the linearity of mobile phase B decreases from 95% to 5%, the linearity of mobile phase A maintains 95%, and the linearity of mobile phase B maintains 5%. The flow rate is 0.40 mL/min and the column temperature is 40 °C. Mass spectrometry conditions: the sample mass spectrometry signal was collected in positive and negative ion scanning mode, and the mass scanning range (m/z) was 50-1000. Ion spray voltage, positive ion voltage 5000V, negative ion voltage 4000V, de-cluster voltage 80V, fog 50psi, auxiliary heater 50psi, air curtain gas 30psi, ion source heating temperature 500°C, 20-60V cycle collision energy.

2.5 Data preprocessing and database search

After the completion of the computer, the LC-MS raw data are imported into the metabonomics processing software Progenesis QI (Waters Corporation, Milford, USA) for baseline filtering, peak identification, integration, retention time correction and peak alignment, and finally a data matrix of retention time, mass-to-charge ratio and peak intensity is obtained. The data matrix uses the 80% rule to remove the missing values, that is, to retain at least one group of samples with non-zero values of more than 80%. Then fill the vacancy value (the minimum value in the original matrix). In order to reduce the error caused by sample preparation and instrument instability, the response intensity of the essential spectrum peak of the sample is normalized by the sum normalization method, and the normalized data matrix is obtained.At the same time, the variables with relative standard deviation (RSD) > 30% of QC samples are deleted and logarithmized by log10 to get the final data matrix for follow-up analyses. At the same time, the metabolite information was obtained by matching the mass spectrometry information of MS and MSMS with the metabolic public database HMDB (http://www.hmdb.ca/) and Metlin (https://metlin.scripps.edu/) database. Metabolite identifications were accepted if they could be established on a basis of at least one unique metabolite identified with a high confidence (FDR < 1%). Metabolite abundances were calculated using intensity of all precursors. For each case, normalized abundance by SEQUEST searches for the metabolite. The metabonomics data of a specimen was determined by the metabolite with the largest normalized abundance.

2.6 Analysis of differential metabolites

The preprocessed data is uploaded to Meiji biological cloud platform (https://cloud.majorbio.com) for data analysis. The R software package ropls (Version1.6.2) carries out orthogonal least square discriminant analysis (OPLS-DA), and uses 7 cycles of interactive verification to evaluate the stability of the model. In addition, student's t test and multiple of difference analysis were performed. The selection of significant differential metabolites was based on the variable weight value (VIP) obtained by OPLS-DA model and the p value of student's t test. The metabolites with VIP > 1 and p <0.05 (student's t test) were significant differential metabolites. A total of 11 differential metabolites were screened.

2.7 Bioinformatics analysis

Notes for KEGG access: the metabolic pathways were annotated by KEGG database (https://www.kegg.jp/kegg/pathway.html) to obtain the pathways involved by differential metabolites. KEGG enrichment analysis: the pathway enrichment analysis was carried out by Python software package scipy.stats, and the biological pathway most related to the experimental treatment was obtained by Fisher accurate test. HMDB compound classification: the differential identified metabolites were classified by HMDB compound classification database. IPath metabolic pathway analysis: iPath3.0 (http://pathways.embl.de) was used to visually analyze the metabolic pathways involved in metabolic sets to view the metabolic pathway information of the whole biological system.

3 Results

3.1 Metabolism of FTC and FTN

In this study, LC-MS was used to analyze FTC tissue and FTN tissue control group. A total of 140 metabolites, including lipids, amino acids, carbohydrates, organic acids and esters, were identified and quantified. Cluster heat map analysis of differential metabolites between FTC and control groups showed the differences of 140 metabolites between FTC and FTN groups, and the relative changes of metabolites concentration in different groups (Figure 1). According to the ROC curve (Figure 2), the metabolic spectrum of thyroid tissue shows representative metabolites: lipids, amino acids. A total of 11 metabolites were identified, including 6 kinds of

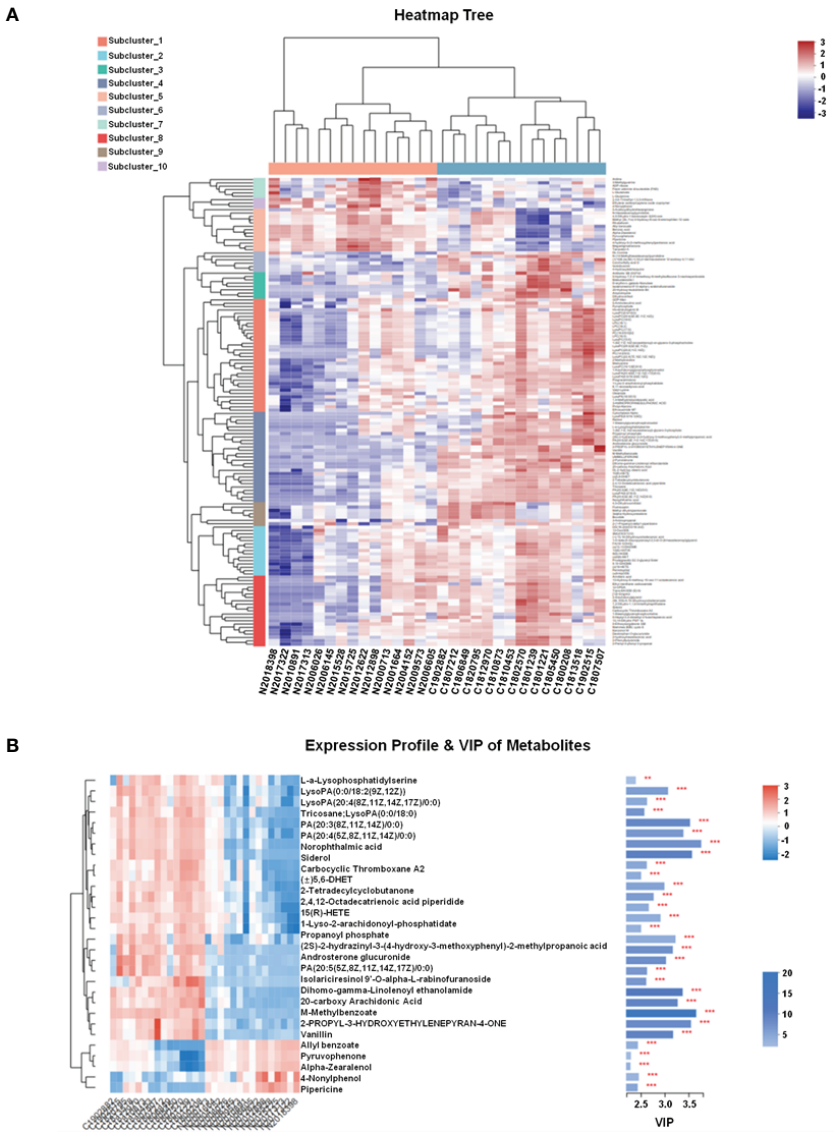

FIGURE 1
FTC and FTN tissue metabolites clustering heat map and VIP diagram. **(A)** FTC and FTN tissue metabolites clustering heat map. **(B)** Metabolite expression profile and VIP diagram. Each column in the Figure represents a sample and each row represents a metabolite. The color in the Figure indicates the relative expression of the metabolite in this group of samples.There is a tree of metabolites clustering on the left and the names of metabolites on the right. The closer the two metabolites branch to each other, the closer their expression is.The tree view of the sample clustering at the top and the name of the sample at the bottom. In the VIP diagram,on the right side is the metabolite VIP bar chart, the bar length represents the contribution of the metabolite to the difference between the two groups, the default is not less than 1, the higher the value, the greater the difference between the two groups.The bar color indicates that there is a significant difference in metabolites between the two groups, that is, the smaller the P_value, the larger the-log10 (P-value) and the darker the color. On the right, **P < 0.01, and ***represents P < 0.001.

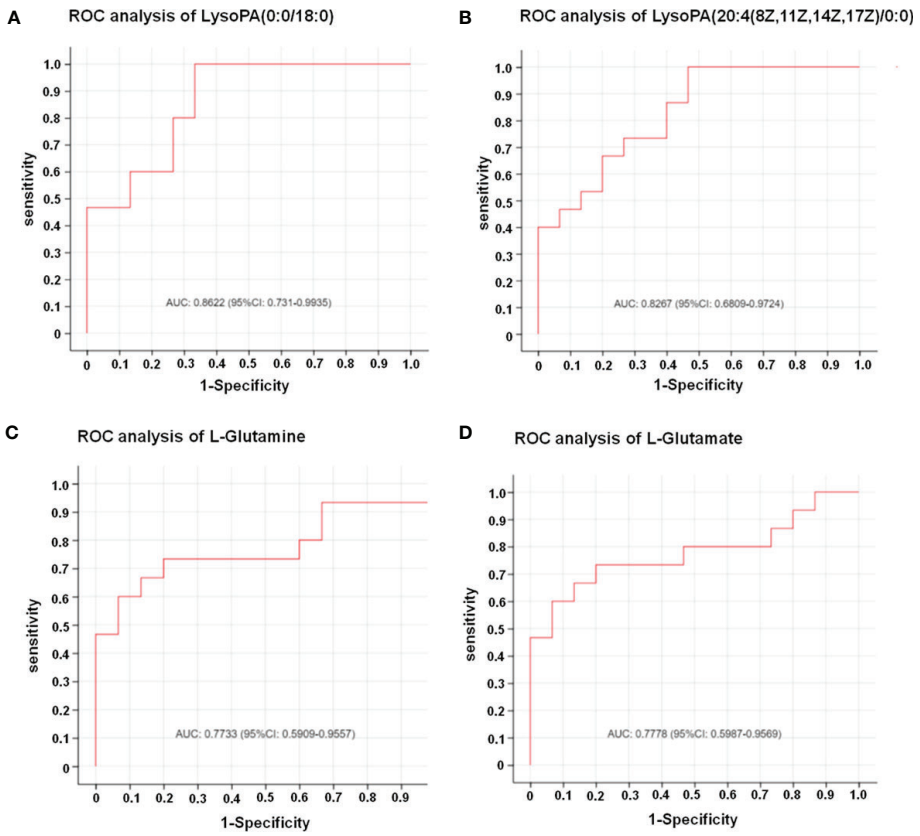

FIGURE 2
The results of ROC analysis showed that the four metabolites had significant diagnostic value for FTC. **(A)** Result of ROC analysis of LysoPA(0:0/18:0). AUC: 0.8622 (95%CI: 0.731-0.9935). **(B)** Result of ROC analysis of LysoPA(20:4(8Z,11Z,14Z,17Z)/0:0)). AUC: 0.8267 (95%CI: 0.6809-0.9724). **(C)** Result of ROC analysis of L-glutamine. AUC: 0.7733 (95%CI: 0.5909-0.9557). **(D)** Result of ROC analysis of L-glutamate. AUC: 0.7778 (95%CI: 0.5987-0.9569). The X axis in the picture is 1-Specificity; Y axis is Sensitivity;The AUC marked in the Figure is the area under the corresponding curve;AUC values are usually between 0.5 and 1.0;When AUC > 0.5, the closer the AUC is to 1, the better the diagnostic effect is; The accuracy of AUC is lower at 0.5-0.7, that of AUC is higher when 0.7-0.9, and that of AUC above 0.9 is extremely high.

lipids, 2 kinds of amino acids and 3 kinds of other metabolites (Table 1). The expression of each metabolite is shown in the box diagram (Figure 3).

3.2 Comparison of metabolites between FTC and FTN

3.2.1 Orthogonal partial least-squares discriminant analysisis used to distinguish between FTC and FTN

In addition, OPLS-DA is carried out, and the OPLS-DA score map filters out the information that has nothing to do with the grouping through orthogonal rotation, so as to better distinguish the differences between groups and improve the efficiency of the model. In the anion mode: the OPLS-DA score map (Figure 4A) shows that there are significant differences in metabolites between the control group and the experimental group, which can be well distinguished. OPLS-DA permutation test (Figure 4A) (R2Y=0.976 and Q2 = 0.863) shows that these models are reliable. In the cation mode: the OPLS-DA score chart (Figure 4B) shows that there are significant differences in metabolites between the control group and the experimental group, which can also be well distinguished.OPLS-DA permutation test (R2Y=0.991 and Q2 = 0.923) shows that these models are reliable (Figure 4B).

3.1.2 VIP diagram analysis is used to distinguish between FTC and FTN

Predictive variable importance (VIP) scores based on the OPLS-DA model indicate the potential metabolites as biomarkers (Figure 1B). Variables with VIP scores greater than 1.5 are considered important to the classification model. The VIP scores of various metabolites were more than 1.5, including LysoPA, PA and so on.

10.3389/fonc.2022.1076548

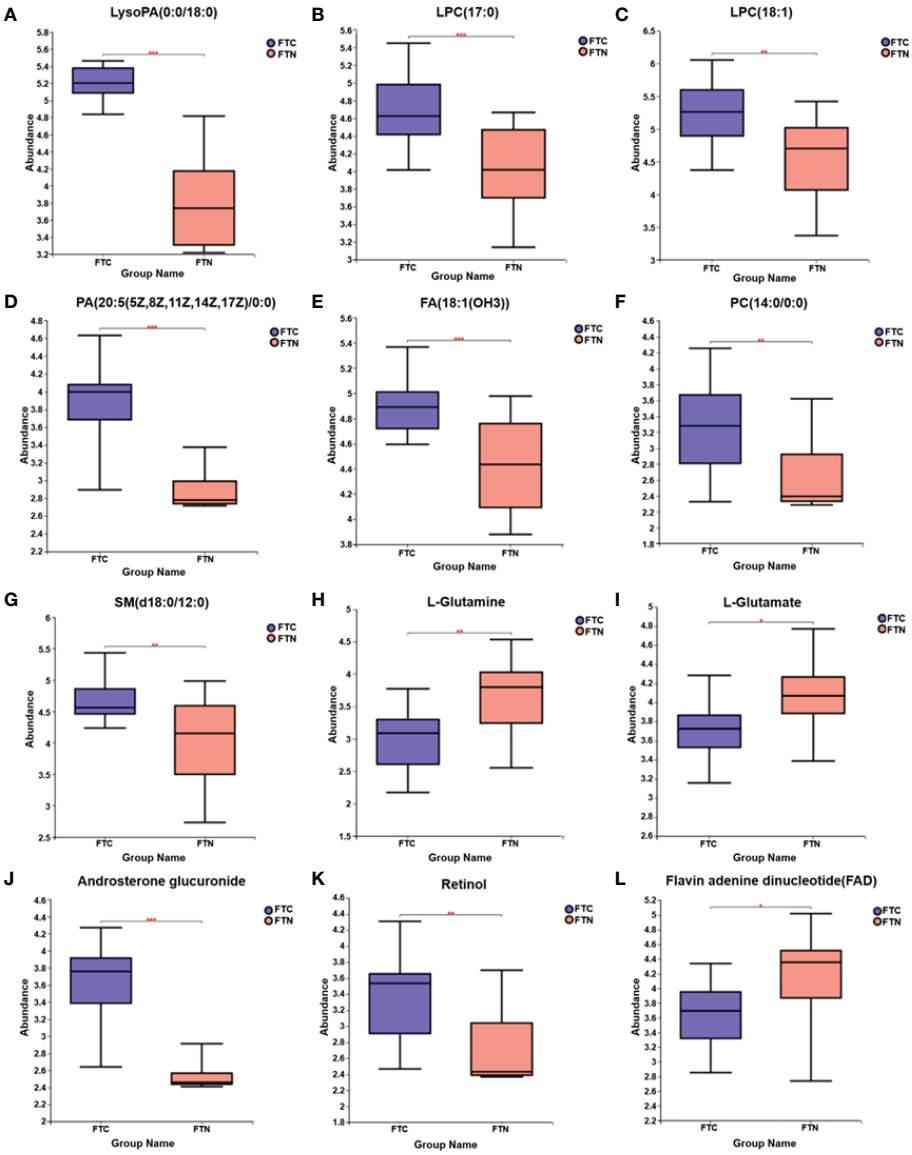

FIGURE 3
Box diagram of medium metabolite distribution for each group of samples. **(A-L)** Box diagrams of LysoPA(0:0/18:0), LPC(17:0), (LPC(18:1), PA (20:5(5Z,8Z,11Z,14Z,17Z)/0:0), FA(18:1(OH3)), PC(14:0/0:0), SM(d18:0/12:0), L-glutamine, L-glutamate, androsterone glucuronide, retinol, flavin adenine dinucleotide distributions in FTC and FTN groups, respectively. The line in the middle of the box represents the median relative abundance of metabolites.The upper and lower bottom of the box are the upper quartile (Q3) and the lower quartile (Q1) of the relative strength of metabolites, respectively.The height of the box reflects the degree of fluctuation of the data to some extent.The upper and lower edges represent the maximum and minimum values of the set of data.The data outside the box can be understood as "outliers" in the data.* represents $P < 0.05$,** represents $P < 0.01$, and *** represents $P < 0.001$.

3.1.3 Volcanogram analysis is used to distinguish FTC from FTN

The point on the right side of the volcano chart indicates that the metabolite is up-regulated and the point on the left side indicates that the metabolite is down-regulated. In the anion model of metabolites, most of the differential metabolites in FTC and FTN groups showed an up-regulation trend, while a few metabolites showed a down-regulation trend (Figure 5A). In the metabolite cation model, most of the differential metabolites in FTC and FTN groups showed an up-regulation trend, while some metabolites showed a down-regulation trend (Figure 5B).

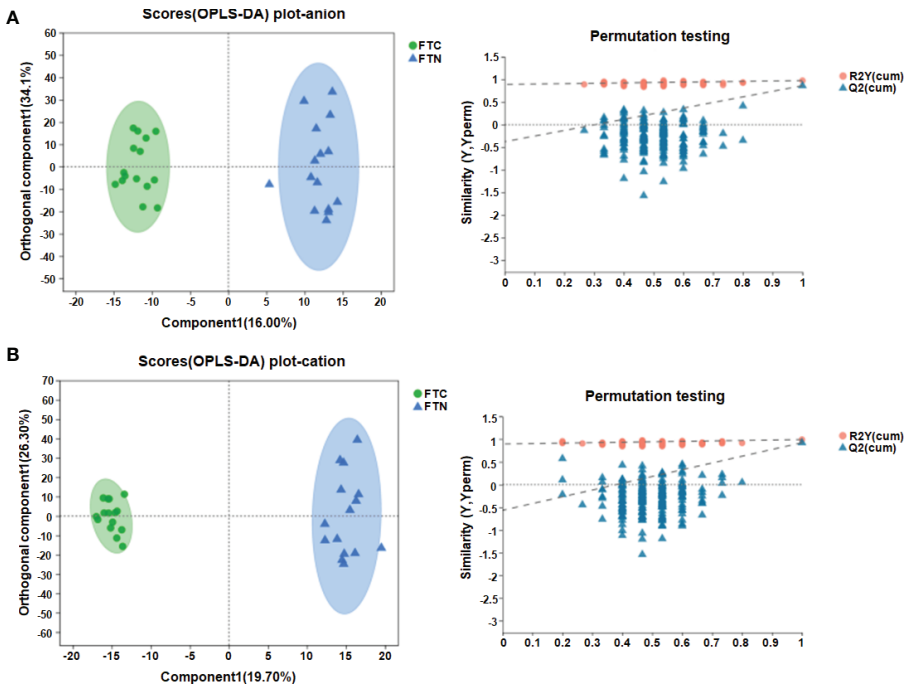

FIGURE 4
OPLS-DA results showed the efficient discriminant of the model. **(A)** OPLS-DA score chart and permutation test(anion mode); **(B)** OPLS-DA score chart and permutation test(cationic mode). The OPLS-DA score chart is often used to directly show the classification effect of the model. In OPLS-DA score chart, the abscissa is the interpretation degree of Comp1's first predicted principal component, and the ordinate is the interpretation degree of orthogonal Comp1's first orthogonal component.In OPLS-DA permutation test, Abscissa represents the permutation retention of permutation test, ordinate indicates the value of R2 (red dot) and Q2 (blue triangle) permutation test, and the two dotted lines represent the regression lines of R2 and Q2 respectively.

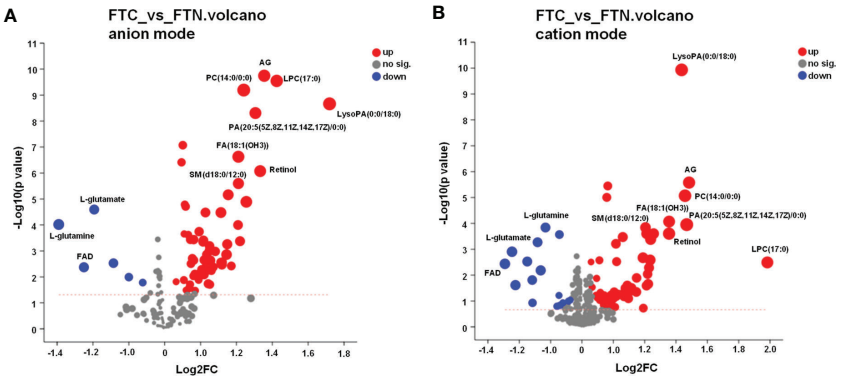

FIGURE 5
Volcano diagram of metabolite in FTC and FTN. **(A)** Volcano diagram of metabolites identified between FTC and FTN in anion mode. **(B)** Volcano diagram of metabolites identified between FTC and FTN in cation mode. Abscissa is the multiple change value of metabolite expression difference between the two groups, namely log2FC, ordinate is the statistical test value of metabolite expression difference, namely-log10 (p_value) value, the higher the value is, the more significant the difference is, and the values of horizontal and vertical coordinates are logarithmized. Each point in the Figure represents a specific metabolite, and the size of the point represents the VIP value. The point on the left is the metabolite of differential down-regulation, and the point on the right is the metabolite of differential up-regulation. The more close to the left and right side and the above point, the more significant the expression difference.

3.3 Metabolic pathways affecting FTC

The metabolic pathways related to FTC and reliable results were analyzed by Kyoto Encyclopedia of Genes and Genomes (KEGG) and human metabolome database(HMDB), and the KEGG metabolic pathways could be divided into six categories (Figure 6A): metabolism, genetic information processing, environmental information processing,cellular processes, organismal systems and human diseases. The results of pathway analysis are shown in Table 2 and Figure 6B, and seven meaningful pathways have been found, including D-glutamine and D-glutamate metabolism, alanine, aspartate and glutamate metabolism, arginine biosynthesis, glycerophospholipid metabolism, glyoxylate and dicarboxylate metabolism, aminoacyl-tRNA biosynthesis and steroid hormone biosynthesis, which were significantly correlated with FTC. In addition, in order to expand the understanding of the metabolic pathways related to FTC, the enrichment analysis module of the metabolic analysis system (Figure 6C) was used to find a number of pathways significantly related to FTC, including two metabolic pathways, including linoleic acid metabolism and glutathione metabolism.

4 Discussion

Thyroid cancer(TC) is one of the malignant tumors with the fastest increasing incidence in the world in recent years (13).

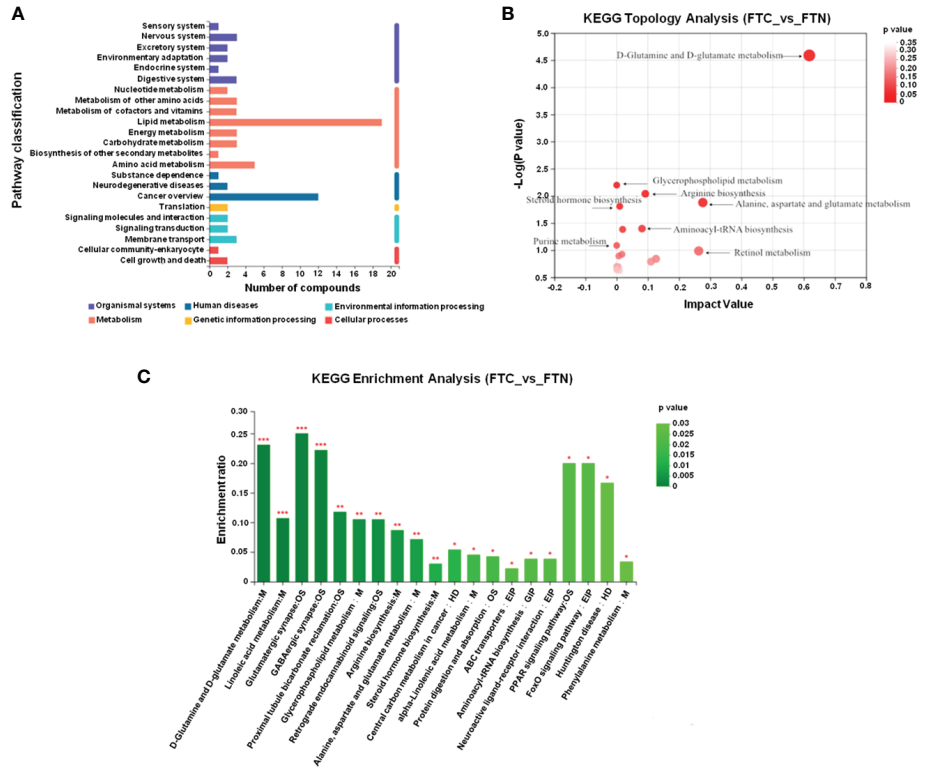

FIGURE 6
Metabolic pathways involved in FTC. **(A)** KEGG pathway analysis shows that abnormal lipid metabolism pathway plays a key role in the formation of FTC. The ordinate is the secondary classification of the KEGG metabolic pathway, and the Abscissa is the number of metabolites annotated to the pathway. KEGG metabolic pathways can be divided into seven categories: Metabolism,Genetic Information Processing,Environmental Information Processing,Cellular Processes,Organismal Systems,Human Disease and Drug Development. **(B)** KEGG Topology Analysis Bubble Diagram. Note: each bubble in the Figure represents a KEGG Pathway pathway; the horizontal axis represents the relative importance of metabolites in the pathway Impact Value; the vertical axis represents the significant enrichment significance of metabolites in the pathway-log10 (Pvalue); the bubble size represents the Impact Value value; the larger the bubble, the greater the importance of the pathway. **(C)** KEGG enrichment analysis(FTC_vs_FTN). Note: Abscissa denotes pathway name, and ordinate denotes enrichment rate, indicating the ratio of the metabolite number enriched in the pathway to the number of background number to pathway. The higher the ratio, the greater the degree of enrichment.The color gradient of the column indicates the significance of enrichment. The darker the default color, the more significant the enrichment of the KEGG term. Pvalue or FDR < 0.001 is marked as ***, Pvalue or FDR < 0.01 is marked as **, Pvalue or FDR < 0.05 is marked as *.

TABLE 1 Differences of characteristic metabolites between experimental group and control group.

Ion mode	Metabolite	VIP_OPLS-DA	VIP_PLS-DA	FC(FTC/FTN)	P	AUC
Neg	LysoPA(0:0/18:0)	3.524	2.948	1.359	6.61E-10	0.862
Neg	LysoPA(0:0/18:2(9Z,12Z))	3.064	2.665	1.331	2.44E-07	0.831
POS	LysoPA(20:4(8Z,11Z,14Z,17Z)/0:0)	2.623	2.304	1.312	4.79E-06	0.827
POS	LPC(18:1)	1.837	1.686	1.155	0.002	0.804
Neg	LPC(16:0)	1.705	1.505	1.120	0.002	0.8
POS	LPC(16:1(9Z)/0:0)	1.467	1.482	1.140	0.014	0.724
Neg	LPC(17:0)	1.982	1.769	1.163	0.0004	0.844
Neg	LPC(22:4(7Z,10Z,13Z,16Z))	1.670	1.502	1.199	0.006	0.773
Neg	LPC(20:2(11Z,14Z))	1.674	1.533	1.208	0.004	0.809
POS	PA(20:3(8Z,11Z,14Z)/0:0)	3.385	2.944	1.472	6.58E-08	0.796
POS	PA(20:4(5Z,8Z,11Z,14Z)/0:0)	3.758	3.284	1.591	1.32E-08	0.782
POS	PA(20:5(5Z,8Z,11Z,14Z,17Z)/0:0)	2.623	2.353	1.333	6.61E-08	0.756
POS	PC(14:0/0:0)	1.684	1.488	1.228	0.003	0.7
POS	PC(16:0/0:0)	1.568	1.436	1.105	0.004	0.687
Neg	FA(18:1(OH3))	1.699	1.524	1.106	0.0004	0.722
POS	SM(d18:0/12:0)	1.743	1.658	1.166	0.005	0.751
Neg	L-Glutamate	1.220	1.191	0.920	0.017	0.778
Neg	L-Glutamine	1.897	1.812	0.821	0.003	0.773
POS	Retinol	1.781	1.593	1.238	0.002	0.722
Neg	Androsterone glucuronide	3.021	2.776	1.422	5.06E-09	0.773
Neg	Flavin adenine dinucleotide	1.479	1.725	0.872	0.01	0.751

(1) Ion mode: the mode of substance detection by mass spectrometer, which mainly includes pos (positive ion mode) and neg (negative ion mode); (2) Metabolite: the name of the metabolite identified; (3) VIP_OPLS-DA: the VIP value of this metabolite in the OPLS-DA model between two groups; (4) FC (Y/ X): the differential expression multiple of the metabolite between the two groups.X, the expression of this metabolite in the control group X; Y, the expression of this metabolite in experimental group Y; X as control; (5) P-value: the result of significance test of the difference of this metabolite between two samples.

With the improvement of living standards, routine physical examination is becoming more and more popular. About 1/5 of adults find thyroid nodules in the physical examination (14). At present, FNAB is the gold standard for the diagnosis of thyroid cancer, but due to insufficient sampling and the difficulty in determining the nature of follicular thyroid tumors, 20% to 30% of thyroid nodules cannot be identified clinically.Of the thyroid nodules of uncertain nature, 10% to 30% were diagnosed as malignant after operation (15, 16). Therefore, it is necessary to have a highly sensitive, specific, efficient, non-invasive and widely used objective index for the diagnosis of thyroid nodules. Metabonomics is a discipline that comprehensively and systematically describes all small molecular metabolites in biological samples. It has obvious advantages in disease diagnosis and research (17, 18).

The main methods of metabolic research include nuclear magnetic resonance (NMR) spectroscopy and mass spectrometry (MS), gas chromatography (GC) and liquid chromatography (LC) and other separation techniques. Nuclear magnetic resonance technology has the advantages of non-selective and non-destructive analysis of samples, low sample consumption, simple sample pretreatment, non-invasive and other advantages, and can be used for the analysis of various body fluids (19). However, its sensitivity and resolution need to be improved, and the required sample concentration is high, so it is impossible to analyze the components with large concentration difference at the same time. Mass spectrometry has wide adaptability, high specificity and sensitivity, but its disadvantage lies in low selectivity and poor ability to identify a large number of spectral peaks. The chromatographic technology has strong separation ability and accurate quantitative analysis, but the ability of qualitative analysis is weak. Liquid chromatography-mass spectrometry can make up for their shortcomings, with good repeatability,

TABLE 2 Pathway analysis of metabolic changes in FTC.

Pathway Desciption	Total	Impact	P_value
D-Glutamine and D-glutamate metabolism	2	0.618	2.58E-05
Alanine, aspartate and glutamate metabolism	2	0.276	0.013
Arginine biosynthesis	2	0.092	0.009
Steroid hormone biosynthesis	2	0.010	0.016
Glycerophospholipid metabolism	10	0.009	0.006
Purine metabolism	2	0	0.082
Aminoacyl-tRNA biosynthesis	2	0.081	0.040
Retinol metabolism	1	0.263	0.103
Glyoxylate and dicarboxylate metabolism	2	0.019	0.041

Note: (1) Pathway Description is the name of the channel; (2) Total: the number of metabolites identified in the pathway; (3) Impact: comprehensive importance score of the path, with a total score of 1; Calculated according to the relative position of metabolites in the pathway; (4) P-value: the result of significance test of the difference of this metabolite between two samples.

high sensitivity, strong qualitative and quantitative ability, and can detect most of the organic molecules in biological samples (20). In this study, 15 cases of FTC and 15 cases of FTN were analyzed by liquid chromatography-mass spectrometry (LC-MS). It was found that there were significant differences in lipids and amino acids between FTC and control tissues. It can be used in the diagnosis of FTC.

The development of thyroid cancer requires the existence of specific conditions under which cell metabolism is reprogrammed to meet its bioenergy and biosynthesis needs and to allow cells to proliferate uncontrolled. Therefore, the low molecular weight metabolites of cancer tissues are significantly different from those of other tissues. Metabonomics technology can accurately detect the differences between these metabolites and find the relative relationship between these metabolites and physiological and pathological changes to diagnose diseases and monitor health. As an important metabolite, lipids participate in the self-assembly of phospholipids to form biofilms and participate in cell differentiation and signal transduction as second messengers. Previous studies (21) have found that the occurrence and development of tumors are closely related to the changes of lipid levels. In this study, our experimental results showed that the level of PA, SM in FTC was significantly increased, and the AUG value was more than 0.7. This may be the capsular infiltration or vascular infiltration of FTC, and the tumor tissue penetrates the capsule, resulting in changes in the composition of the cell membrane. It causes abnormal levels of phospholipids and metabolites related to cell membrane synthesis in the body.

Guo (22) studied the lipid changes of TC and BTN tissue and blood by tissue mass spectrometry and serum lipid spectrum analysis. It was found that the biomarker group composed of phosphatidic acid (PA) (36:3) and sphingomyelin (SM) (34:1) could distinguish between benign and malignant tumors, with an AUC value of 0.961, a sensitivity of 87.8% and a specificity of 92.9%, which was similar to our results. In addition, our study also found that the level of FA, PC is higher than that of FTN, which may be related to the increase of thyrotropin and the corresponding increase of thyroxine synthesis in patients with FTC, resulting in abnormal plasma lipid levels.On the other hand, there are great differences in lipid metabolism between benign and malignant nodules. Circulating free fatty acids are important for energy replenishment, especially when glucose is insufficient. Excessive proliferation of malignant tumor cells, insufficient energy supply of glucose oxidation, energy supply by fat oxidation, which also indirectly leads to abnormal lipids. Guo (23) performed lipid imaging and analysis on tissue samples from six different types of cancer, including 124 cases of TC and 122 controls (healthy subjects and BTN samples). The results showed that the levels of 10 lipids in TC serum changed, including 3 phosphatidylcholines, 6 phosphatidic acids and 1 sphingomyelin, which indicated that there were differences in lipid metabolism between TC and other thyroid tissues.

Interestingly, we found that a variety of lysophosphatidic acid (LysoPA) levels are generally increased in FTC, and LysoPA is produced under physiological and pathophysiological conditions of cells and extracellular fluid. It mediates a variety of cellular responses and activities, including cell proliferation, migration, invasion, cytokine production, reactive oxygen species (ROS) production and cancer cell progression (24). The latest study (25) found that LysoPA can act on specific G protein-coupled receptors and regulate many metabolic processes, such as vascular development, immunity and carcinogenesis. In addition, LysoPA has been found to induce

the characteristics of many cancers, including cellular processes such as proliferation, survival, migration, invasion and neovascularization. So far, LysoPA has been detected in many human body fluids, including plasma (26), serum, cerebrospinal fluid (27), pleural effusion (28) and so on.

LysoPA has two main biosynthetic pathways. First, phosphatidic acid (PA) is formed by the decomposition of phospholipids by phospholipase D (PLD), and then converted by phospholipase A1 or A2 (PLA1 and PLA2) to LysoPA. Second, lysophospholipids are produced by the corresponding phospholipids through PLA1 or PLA2. They are then cut into LysoPA by the action of lysophospholipase D (also known as autophagotoxin (ATX)) (25). Related studies have found that abnormal LysoPA levels are associated with a variety of diseases, including breast cancer (29), ovarian cancer (30) and so on. At present, the source and mechanism of the increase of LysoPA in FTC are not clear. We guess: 1. LysoPA can recognize two kinds of G protein coupled receptors: LysoPA1-3 receptor and LysoPA4-6 receptor, which belong to endothelial gene (EDG) family and non-endothelial gene family respectively.Some studies (31) found that the expression of EDG4 receptor mRNA in FTC increased by 3 times, and had a high affinity for LysoPA, which led to the increase of LysoPA. 2.RAS pathway is the key pathway of FTC (32), and phospholipase D (PLD) is the key enzyme to produce LysoPA. We speculate that the metabolism of RAS protein in RAS pathway is abnormal during follicular thyroid tumor carcinogenesis. It has been found that Ras protein is a key element in the regulation of phospholipase D (PLD) (33). Therefore, the increase of LysoPA in FTC may be due to the abnormal metabolism of Ras protein, which leads to the increase of phospholipase D synthesis and further leads to the increase of LysoPA.3. Lysophospholipids are produced by the corresponding phospholipids through PLA1 or PLA2, and then cut into LysoPA by lysophospholipase D (also known as autophagy toxin (ATX)). The resulting LysoPA is dephosphorylated by phospholipid phosphatase (LPP) and degraded to monoacylglycerol (MAG), or converted to PA by acyltransferase. The increase of LysoPA in FTC may be the result of ATX-LysoPA-LPP axis misalignment. 4. FTC can be diagnosed when follicular thyroid tumor invades blood vessels, capsule and surrounding tissue.LysoPA acts on tissues to produce endothelin and angiogenic factors (vascular endothelial growth factor (VEGF), interleukin (IL)-6, etc.), which can be used as paracrine growth factors of malignant cells. The increase of LysoPA in FTC may be caused by tumor invasion of surrounding blood vessels and tissues. These results suggest that the different expression of LysoPA in different tissues may provide a non-invasive, simple and accurate method for the diagnosis of FTC.

The characteristics of low molecular weight metabolites in tumor tissues are significantly different from those in other tissues. These metabolite characteristics can be expressed in two ways:1. The concentration of low molecular weight metabolites is constantly changing at each stage of tumor tissue progression, and these differential metabolites can be detected by metabonomics to diagnose diseases. 2. There are also many changes in metabolic pathways involved in each stage of tumor tissue progression. After annotating KEGG and HMDB and analyzing their pathways and enrichment, we found that important metabolic pathways are related to FTC. The changes of amino acids in FTC mainly include L-glutamate and L-glutamine. The KEGG pathways involved in L-glutamate and L-glutamine include D-glutamine and D-glutamate metabolism, alanine, aspartic acid and glutamate metabolism, arginine biosynthesis, glutathione metabolism and so on. Recently, Gu (34) studied 33 patients with TC and 137 healthy controls by amino acid analyzer. It was found that the levels of threonine and arginine in TC samples were higher, while those of aspartic acid, glutamic acid and proline were lower. Shen (35) and other researchers identified 31 metabolites by comparing the sera of 37 patients with distant metastasis of TC with those of 40 patients with BTN. They are related to glucose, amino acids, lipids, vitamins metabolism and diet/intestinal microbiota interaction. Pathway analysis shows that alanine, aspartic acid and glutamate metabolism and inositol phosphate metabolism are the most related pathways. These findings all support our results. Therefore, the increase of L-glutamate and L-glutamine in thyroid tissue should be noticed, as they may be new tumor markers of FTC. At present, the mechanism of changes in amino acid metabolic pathways related to FTC is still unclear, but it has been found that there are many related metabolic pathways, with the deepening of research, more amino acid metabolic pathways may be found. Another type of KEGG pathway we found is related to lipids, which is glycerol phospholipid metabolic pathway, which involves metabolites such as PC, PA, SM, FA, LysoPA and so on. Miccoli (36) analyzed 28 cases of thyroid papillary carcinoma, 40 cases of thyroid follicular lesions and 4 cases of benign nodules by high resolution magic angle rotation NMR. It was found that benign and malignant tumors could be distinguished by metabonomics. Choline and lipid metabolism were abnormal in malignant samples (thyroid papillary carcinoma and FTC). This is similar to our findings, and we speculate that abnormal LysoPA may be the cause of follicular tumor carcinogenesis caused by lipid metabolic pathway. In addition, KEGG pathways involved in FTC also include Glyoxylate and dicarboxylate metabolism, Aminoacyl-tRNA biosynthesis, Steroid hormone biosynthesis,Linoleic acid metabolism. There are few studies on these pathways related to thyroid cancer, and a large number of sample studies are still needed to confirm their exact relationship.

Conclusion

In short, there are significant differences in a variety of metabonomic characteristics between FTC and FTN, suggesting

that these metabolites can be used as potential biomarkers. At the same time, our study found that LysoPA has a very strong diagnostic ability for FTC, which may be related to the abnormal metabolism of phospholipase D (PLD), the key enzyme of LysoPA synthesis caused by RAS pathway. In addition, LysoPA can be detected in a variety of human body fluids, which has the potential to be used in clinic, but it still needs a large number of experiments to confirm. We also found that Amino acid metabolic pathway and lipid-related metabolic pathway may be the key pathways of follicular tumor carcinogenesis, which need to be further studied to explore its potential mechanism and its role in the development of FTC.This study provides new insights into the diagnosis of FTC by studying the differences of related metabolites and abnormal metabolic pathways of FTC, and explores the potential biomarkers of FTC, which has great potential in the diagnosis and treatment of FTC.

Data availability statement

The original contributions presented in the study are included in the article/Supplementary Material. Further inquiries can be directed to the corresponding author.

Ethics statement

Our study was approved by the Institutional Ethics Committee of the Henan Cancer Hospital. All participants signed informed consent to medical research before the initial treatment, and all experiments were performed in accordance with the relevant guidelines and regulations.

Author contributions

JF and JQ: conceptualization and original draft; JF and YY: data curation and methodology; JQ, JF and YY: manuscript review and editing; JF, DW and JQ: software; SL and RL: investigation; YW and GL: project administration; JF, RL and SL: supervision, validation, and visualization. All authors contributed to the article and approved the submitted version.

Funding

This research was supported by the National Natural Science Foundation of China (8157110152). Project of Science and Technology in Science and Technology Department of Henan Province (212102310125) and Joint construction project of medical science and technology in Henan Province (LHGJ20200186) and Project of Education Department of Henan Province (22A320018).

Acknowledgments

We would like to thank Dr. Zhang He for providing assistance with the images included in this manuscript.

Conflict of interest

The authors declare that the research was conducted in the absence of any commercial or financial relationships that could be construed as a potential conflict of interest.

Publisher's note

Supplementary material

The Supplementary Material for this article can be found online at: https://www.frontiersin.org/articles/10.3389/fonc.2022.1076548/full#supplementary-material

References

1. Wenter V, Albert NL, Unterrainer M, Ahmaddy F, Ilhan H, Jellinek A, et al. Clinical impact of follicular oncocytic (Hürthle cell) carcinoma in comparison with corresponding classical follicular thyroid carcinoma. *Eur J Nucl Med Mol Imaging.* (2021) 48(2):449–60. doi: 10.1007/s00259-020-04952-2

2. Lloyd RV, Osamura RY, Klöppel G, Rosai J. *WHO classification of tumours: pathology and genetics of tumours of endocrine organs. 4th ed.* Lyon: IARC Press (2017).

3. Cooper DS, Doherty GM, Haugen BR, Hauger BR, Kloos RT, Lee SL, et al. Revised American thyroid association manage ment guidelines for patients with thyroid nodules and differentia ted thyroid cancer. *Thyroid* (2009) 19(11):11674214.

4. Pearson H. Meet the human metabolome. *Nature.* (2007) 446(7131):8. doi: 10.1038/446008a

5. Abooshahab R, Gholami M, Sanoie M, Azizi F, Hedayati M. Advances in metabolomics of thyroid cancer diagnosis and metabolic regulation. *Endocrine.* (2019) 65(1):1–14. doi: 10.1007/s12020-019-01904-1

6. Kwon HN, Lee H, Park JW, Kim YH, Park S, Kim JJ, et al. Screening for early gastric cancer using a noninvasive urine metabolomics approach. *Cancers (Basel)* (2020) 12(10):2904. doi: 10.3390/cancers12102904

7. Casadei-Gardini A, Del Coco L, Marisi G, Conti F, Rovesti G, Ulivi P, et al. 1H-NMR based serum metabolomics highlights different specific biomarkers between early and advanced hepatocellular carcinoma stages. *Cancers (Basel)* (2020) 12(1):241.

8. Ghini V, Laera L, Fantechi B, Monte FD, Benelli M, McCartney A, et al. Metabolomics to assess response to immune checkpoint inhibitors in patients with non-small-cell lung cancer. *Cancers (Basel)* (2020) 12(12):3574.

9. Sun C, Wang F, Zhang Y, Yu J, Wang X. Mass spectrometry imaging-based metabolomics to visualize the spatially resolved reprogramming of carnitine metabolism in breast cancer. *Theranostics* (2020) 10(16):7070–82.

10. Qu F, Gu Y, Wang Q, He M, Zhou F, Sun J, et al. Metabolomic profiling to evaluate the efficacy of proxalutamide, a novel androgen receptor antagonist, in prostate cancer cells. *Invest New Drugs* (2020) 38(5):1292–302.

11. Skorupa A, Ciszek M, Chmielik E, Boguszewicz Ł, Oczko-Wojciechowska M, Kowalska M, et al. Shared and unique metabolic features of the malignant and benign thyroid lesions determined with use of 1H HR MAS NMR spectroscopy. *Sci Rep* (2021) 11(1):1344.

12. Abooshahab R, Hooshmand K, Razavi SA, Gholami M, Sanoie M, Hedayati M. Plasma metabolic profiling of human thyroid nodules by gas chromatography-mass spectrometry (GC-MS)-Based untargeted metabolomics. *Front Cell Dev Biol* (2020) 8:385. doi: 10.3389/fcell.2020.00385

13. Wiltshire JJ, Drake TM, Uttley L, Balasubramanian SP. Systematic review of trends in the incidence rates of thyroid cancer. *Thyroid.* (2016) 26(11):1541–52. doi: 10.1089/thy.2016.0100

14. Liu X, Sun J, Fang W, Xu Y, Zhu Z, Liu Y. Current iodine nutrition status and morbidity of thyroid nodules in mainland China in the past 20 years. *Biol Trace Elem Res* (2021) 199(12):4387–95. doi: 10.1007/s12011-020-02565-2

15. Navas-Carrillo D, Rodriguez JM, Montoro-García S, Orenes-Piñero E. High-resolution proteomics and metabolomics in thyroid cancer: Deciphering novel biomarkers. *Crit Rev Clin Lab Sci* (2017) 54(7-8):446–57. doi: 10.1080/10408363.2017.1394266

16. Matsuura D, Yuan A, Wang L, Ranganath R, Adilbay D, Harries V, et al. Follicular and hurthle cell carcinoma: Comparison of clinicopathological features and clinical outcomes. *Thyroid.* (2022) 32(3):245–54. doi: 10.1089/thy.2021.0424

17. Giera M, Branco Dos Santos F, Siuzdak G. Metabolite-induced protein expression guided by metabolomics and systems biology. *Cell Metab* (2018) 27 (2):270–2. doi: 10.1016/j.cmet.2018.01.002

18. Bauermeister A, Mannochio-Russo H, Costa-Lotufo LV, Jarmusch AK, Dorrestein PC. Mass spectrometry-based metabolomics in microbiome investigations. *Nat Rev Microbiol* (2022) 20(3):143–60. doi: 10.1038/s41579-021-00621-9

19. Seo JW, Han K, Lee J, Kim EK, Moon HJ, Yoon JH, et al. Application of metabolomics in prediction of lymph node metastasis in papillary thyroid carcinoma. *PloS One* (2018) 13(3):e0193883. doi: 10.1371/journal.pone.0193883

20. Wojakowska A, Chekan M, Widlak P, Pietrowska M. Application of metabolomics in thyroid cancer research. *Int J Endocrinol* (2015) 2015:258763. doi: 10.1155/2015/258763

21. Bian X, Liu R, Meng Y, Xing D, Xu D, Lu Z. Lipid metabolism and cancer. *J Exp Med* (2021) 218(1):1–17. doi: 10.1084/jem.20201606

22. Guo S, Qiu L, Wang Y, Qin X, Liu H, He M, et al. Tissue imaging and serum lipidomic profiling for screening potential biomarkers of thyroid tumors by matrix-assisted laser desorption/ionization-Fourier transform ion cyclotron resonance mass spectrometry. *Anal Bioanal Chem* (2014) 406(18):4357–70. doi: 10.1007/s00216-014-7846-0

23. Guo S, Wang Y, Zhou D, Li Z. Significantly increased monounsaturated lipids relative to polyunsaturated lipids in six types of cancer microenvironment are observed by mass spectrometry imaging. *Sci Rep* (2014) 4:5959. doi: 10.1038/srep05959

24. Mills GB, Moolenaar WH. The emerging role of lysophosphatidic acid in cancer. *Nat Rev Cancer.* (2003) 3(8):582–91. doi: 10.1038/nrc1143

25. Liu W, Hopkins AM, Hou J. The development of modulators for lysophosphatidic acid receptors: A comprehensive review. *Bioorg Chem* (2021) 117:105386. doi: 10.1016/j.bioorg.2021.105386

26. Xu Y, Shen Z, Wiper DW, Wu M, Morton RE, Elson P, et al. Lysophosphatidic acid as a potential biomarker for ovarian and other gynecologic cancers. *JAMA.* (1998) 280(8):719–23. doi: 10.1001/jama.280.8.719

27. Jiang D, Ju W, Wu X, Zhan X. Elevated lysophosphatidic acid levels in the serum and cerebrospinal fluid in patients with multiple sclerosis: therapeutic response and clinical implication. *Neurol Res* (2018) 40(5):335–9. doi: 10.1080/01616412.2018.1446256

28. Bai CQ, Yao YW, Liu CH, Zhang H, Xu XB, Zeng JL, et al. Diagnostic and prognostic significance of lysophosphatidic acid in malignant pleural effusions. *J Thorac Dis* (2014) 6(5):483–90.

29. Zhang Q, Yang X, Wang Q, Zhang Y, Gao P, Li Z, et al. "Modeling-prediction" strategy for deep profiling of lysophosphatidic acids by liquid chromatography-mass spectrometry: Exploration biomarkers of breast cancer. *J Chromatogr A.* (2020) 1634:461634.

30. Gendaszewska-Darmach E. Lysophosphatidic acids, cyclic phosphatidic acids and autotaxin as promising targets in therapies of cancer and other diseases. *Acta Biochim Pol* (2008) 55(2):227–40. doi: 10.18388/abp.2008_3070

31. Schulte KM, Beyer A, Köhrer K, Oberhäuser S, Röher HD. Lysophosphatidic acid, a novel lipid growth factor for human thyroid cells: over-expression of the high-affinity receptor edg4 in differentiated thyroid cancer. *Int J Cancer.* (2001) 92(2):249–56. doi: 10.1002/1097-0215(200102)9999:9999<::AID-IJC1166>3.0.CO;2-D

32. An JH, Song KH, Kim SK, Park KS, Yoo YB, Yang JH, et al. RAS mutations in indeterminate thyroid nodules are predictive of the follicular variant of papillary thyroid carcinoma. *Clin Endocrinol (Oxf).* (2015) 82(5):760–6. doi: 10.1111/cen.12579

33. Lucas L, Penalva V, Ramírez de Molina A, Del Peso L, Lacal JC. Modulation of phospholipase d by ras proteins mediated by its effectors ral-GDS, PI3K and raf-1. *Int J Oncol* (2002) 21(3):477–85. doi: 10.3892/ijo.21.3.477

34. Gu Y, Chen T, Fu S, Sun X, Wang L, Wang J, et al. Perioperative dynamics and significance of amino acid profiles in patients with cancer. *J Transl Med* (2015) 13:35. doi: 10.1186/s12967-015-0408-1

35. Shen CT, Zhang Y, Liu YM, Yin S, Zhang XY, Wei WJ, et al. A distinct serum metabolic signature of distant metastatic papillary thyroid carcinoma. *Clin Endocrinol (Oxf).* (2017) 87(6):844–52. doi: 10.1111/cen.13437

36. Miccoli P, Torregrossa L, Shintu L, Magalhaes A, Chandran J, Tintaru A, et al. Metabolomics approach to thyroid nodules: a high-resolution magic-angle spinning nuclear magnetic resonance-based study[J]. *Surgery* (2012) 152(6):1118–24. doi: 10.1016/j.surg.2012.08.037

frontiers | Frontiers in Oncology

TYPE Original Research
PUBLISHED 12 January 2023
DOI 10.3389/fonc.2022.972215

OPEN ACCESS

EDITED BY
Thomas Gander,
University Hospital Zürich, Switzerland

REVIEWED BY
Andrea Santarelli,
Marche Polytechnic University, Italy
Hao Li,
Wuhan University, China

*CORRESPONDENCE
Xiao-Tang Yang
yangxt210@126.com
Pei-Feng He
hepeifeng2006@126.com
Feng Li
lifenglover@sina.com

†These authors have contributed equally to this work and share first authorship

SPECIALTY SECTION
This article was submitted to Head and Neck Cancer, a section of the journal Frontiers in Oncology

RECEIVED 18 June 2022
ACCEPTED 22 December 2022
PUBLISHED 12 January 2023

CITATION
Han F, Wang H-Z, Chang M-J, Hu Y-T, Liang L-Z, Li S, Liu F, He P-F, Yang X-T and Li F (2023) Development and validation of a GRGPI model for predicting the prognostic and treatment outcomes in head and neck squamous cell carcinoma. *Front. Oncol.* 12:972215. doi: 10.3389/fonc.2022.972215

Development and validation of a GRGPI model for predicting the prognostic and treatment outcomes in head and neck squamous cell carcinoma

Fei Han[1†], Hong-Zhi Wang[2†], Min-Jing Chang[3,4†], Yu-Ting Hu[3], Li-Zhong Liang[3], Shuai Li[3], Feng Liu[1], Pei-Feng He[5*], Xiao-Tang Yang[6*] and Feng Li[7*]

[1]Department of Head and Neck Surgery, Shanxi Province Tumor Hospital, Shanxi Hospital Affiliated to Cancer Hospital, Chinese Academy of Medical Sciences, Affiliated Tumor Hospital of Shanxi Medical University, Taiyuan, China, [2]Department of Anesthesiology, Shanxi Province Tumor Hospital, Shanxi Hospital Affiliated to Cancer Hospital, Chinese Academy of Medical Sciences, Affiliated Tumor Hospital of Shanxi Medical University, Taiyuan, China, [3]Ministry of Education, Key Laboratory of Cellular Physiology at Shanxi Medical University, Taiyuan, China, [4]Shanxi Key Laboratory of Big Data for Clinical Decision, Shanxi Medical University, Taiyuan, China, [5]Medical Data Sciences, Shanxi Medical University, Taiyuan, China, [6]Department of Radiology, Shanxi Province Tumor Hospital, Shanxi Hospital Affiliated to Cancer Hospital, Chinese Academy of Medical Sciences, Affiliated Tumor Hospital of Shanxi Medical University, Taiyuan, China, [7]Department of Cell biology, Shanxi Province Tumor Hospital, Shanxi Hospital Affiliated to Cancer Hospital, Chinese Academy of Medical Sciences, Affiliated Tumor Hospital of Shanxi Medical University, Taiyuan, China

Background: Head and neck squamous cell carcinoma (HNSCC) is among the most lethal and most prevalent malignant tumors. Glycolysis affects tumor growth, invasion, chemotherapy resistance, and the tumor microenvironment. Therefore, we aimed at identifying a glycolysis-related prognostic model for HNSCC and to analyze its relationship with tumor immune cell infiltrations.

Methods: The mRNA and clinical data were obtained from The Cancer Genome Atlas (TCGA), while glycolysis-related genes were obtained from the Molecular Signature Database (MSigDB). Bioinformatics analysis included Univariate cox and least absolute shrinkage and selection operator (LASSO) analyses to select optimal prognosis-related genes for constructing glycolysis-related gene prognostic index(GRGPI), as well as a nomogram for overall survival (OS) evaluation. GRGPI was validated using the Gene Expression Omnibus (GEO) database. A predictive nomogram was established based on the stepwise multivariate regression model. The immune status of GRGPI-defined subgroups was analyzed, and high and low immune groups were characterized. Prognostic effects of immune checkpoint inhibitor (ICI) treatment and chemotherapy were investigated by Tumor Immune Dysfunction and Exclusion (TIDE) scores and half inhibitory concentration (IC50) value. Reverse transcription-quantitative PCR (RT-qPCR) was utilized to validate the model by analyzing the mRNA expression levels of the

prognostic glycolysis-related genes in HNSCC tissues and adjacent non-tumorous tissues.

Results: Five glycolysis-related genes were used to construct GRGPI. The GRGPI and the nomogram model exhibited robust validity in prognostic prediction. Clinical correlation analysis revealed positive correlations between the risk score used to construct the GRGPI model and the clinical stage. Immune checkpoint analysis revealed that the risk model was associated with immune checkpoint-related biomarkers. Immune microenvironment and immune status analysis exhibited a strong correlation between risk score and infiltrating immune cells. Gene set enrichment analysis (GSEA) pathway enrichment analysis showed typical immune pathways. Furthermore, the GRGPIdel showed excellent predictive performance in ICI treatment and drug sensitivity analysis. RT-qPCR showed that compared with adjacent non-tumorous tissues, the expressions of five genes were significantly up-regulated in HNSCC tissues.

Conclusion: The model we constructed can not only be used as an important indicator for predicting the prognosis of patients but also had an important guiding role for clinical treatment.

KEYWORDS

prediction, glycolysis prognosis model, head and neck squamos cell carcinoma, immune microenviroment, chemothearapeutic responses

1 Introduction

HNSCC is a heterogeneous epithelial tumor that includes nasopharyngeal, oropharyngeal, hypopharyngeal, and laryngeal cancers. The risk factors for HNSCC include long-term alcohol exposure, smoking, betel nut chewing, chronic oral trauma, and HPV infections (1). The complexity of its etiology is a major contributor to HNSCC heterogeneity. Surgical, radiotherapy-chemotherapy, targeted therapy and immunotherapy approaches have been developed to treat HNSCC patients. However, HNSCC is associated with poor prognostic outcomes, and its 5-year OS rate is 50% (2). Therefore, there is a need to establish viable markers for the clinical prophetic prediction of HNSCC.

Recent studies have evaluated metabolic changes in tumor cells. The Warburg effect, the most prevalent and widely studied metabolic change in cancer cells, explains that under aerobic conditions, tumor tissues metabolize approximately tenfold more glucose to lactate in a given time than normal tissues, enhanced glucose uptake by tumor cells, and inhibited glucose oxidation in adjacent tissues (3). During glycolysis, glucose is converted to lactate, and cancer cells gain maximum energy. Molecular imaging revealed markedly increased glycolysis levels in HNSCC (4–6), a metabolic phenotype typical of aggressive tumor growth. This metabolic change increases glucose uptake and lactate production, affecting cell growth, proliferation, angiogenesis, and invasion (7). Overall, the oncogenic regulation of glycolysis emphasizes the biological significance of tumor glycolysis in HNSCC patients, demonstrating that targeting glycolysis remains potentially effective for clinical relevance and therapeutic intervention (8, 9). In addition, researchers have suggested that glycolysis in HNSCC is associated with alterations in oncogenes and tumor suppressor genes (10). Akt, the serine/threonine kinase, an oncogene that boosts cancer growth (11), has been proven to activate aerobic glycolysis significantly, leading to cancer cells dependent on glycolysis for survival (12). Notably, screening and identification of biological markers predicting prognosis in HNSCC by using broad glycolysis-related gene expression profiles have enormous potentially clinical relevance in targeting glycolysis for cancer therapy.

Premalignant cells frequently metastasize but are spontaneously eliminated by the immune system before developing aggressive tumors, thereby preventing tumor transformation. Thus, there is an interaction between the cancerous tissue and the immune suppressive network within the tumor microenvironment (TME). Changes in peripheral blood immune cell pool and activity are also associated with tumors (13, 14). The immune system plays a key

role in carcinogenesis, development, and progression of HNSCC, where immune cell infiltration is diverse and heterogeneous. The immune system is controlled by immune checkpoint pathways that typically remain self-tolerant and limit collateral tissue damage during inflammation. Upregulated TIM-3 (15), OX40 (16), and IDO1 expressions in tumor-infiltrating lymphocytes suggest a rationale for the therapeutic targeting of these molecules. Targeting these checkpoints has led to breakthroughs in cancer immunotherapy. Immunotherapy, which activates the host's natural defense system to identify and eliminate tumor cells, has emerged as a practical therapeutic approach. We analyzed tumor-infiltrating immune cells, immune checkpoints, and immune pathways. Our findings have clinical implications for developing personalized immunotherapeutic strategies to improve treatment outcomes for HNSCC patients.

2 Method and materials

2.1 Gene set enrichment analysis

GSEA was performed using the GSEA software (version 4.2.3) (https://www.gsea-msigdb.org/gsea/downloads.jsp) with the MSigDB glycolysis-related pathway gene sets, which contain 1320 gene sets. Pathways with $p < 0.05$ and FDR < 0.05 were considered significantly enriched.

2.2 Data collection and acquisition of glycolysis-related genes

The HNSCC gene expression data (RNA-Seq) and the corresponding clinical data (including age, gender, stage, grade, smoking, alcohol, HPV, survival time, and survival status) were downloaded from the TCGA database (https://portal.gdc.cancer.gov) and GEO dataset (https://www.ncbi.nlm.nih.gov/geo/). Used as a training cohort, the inclusion criteria for TCGA-HNSCC were: HNSCC samples with complete somatic mutation data and clinical information (457 retrieved HNSCC samples with single nucleotide polymorphism(SNP) data were analyzed), with 462 HNSCC samples and 32 adjacent non-tumor tissue samples included. The glycolysis-related gene dataset was downloaded from MSigDB. Expression characteristics of glycolysis-related genes were obtained from the MSigDB (https://www.gsea-msigdb.org/gsea/msigdb/index.jsp).

2.3 Identification of differential glycolysis-related genes

Using $|\log FC| > 1$ and $p < 0.05$ as thresholds, differentially expressed genes between HNSCC samples and adjacent non-tumor tissue samples were evaluated using the Wilcoxon test in the limma package. Then, differentially expressed glycolysis-related genes were selected from all differentially expressed genes (DEGs) and displayed on a Venn diagram.

2.4 Identification and validation of a glycolysis-related gene signature

Survival-associated differentially expressed glycolytic genes were identified *via* univariate Cox regression and Lasso regression analyses, after which a polygenic prognostic risk model was constructed. Based on the median risk score of the TCGA training set as the cutoff, HNSCC patients were assigned into high- and low-risk groups. Clustering effects of Principal Component Analysis (PCA) dimensionality reduction revealed significant differences between the groups. Kaplan-Meier survival curves, time-dependent receiver operating characteristic (ROC) curves, and risk score distributions for OS prediction were evaluated to verify the prognostic significance of risk scores. Similar to the training set approach, the GEO cohort was used as an independent validation set to assess the generality and reliability of the prognostic risk model.

2.5 Construction of the nomogram

Independent prognostic factors in HNSCC patients were determined by univariate and multivariate Cox regression analysis. Both TCGA training set and GEO validation set were used to construct a nomogram for predicting the 1-year, 3-year, and 5-year survival outcomes of HNSCC patients. Consistency between actual survival rates and nomogram-predicted rates was tested *via* a calibration curve. In addition, decision curves were used to assess the reliability of risk scores and clinical stage.

2.6 Analysis of tumor immune microenvironment

The "Cell Type Identification by Estimating Relative Subsets of RNA Transcripts (CIBERSORT)"was used to assess immune cell infiltrations. The immune, stromal, and ESTIMATE (Estimation of STromal and Immune cells in MAlignant Tumors using Expression data) scores for each sample were calculated using the ESTIMATE algorithm. Correlations between the GRGPI score and those scores were determined by Spearman correlation analysis.

2.7 Assessment of tumor mutation burden

The tumor mutation data was obtained from the cBioPortal database. The tumor mutation burden (TMB) for all samples

was calculated using "maftools" in R. Based on median TMB values, HNSCC samples were assigned into high TMB and low TMB groups. A total of 16360 genes involved in developing SNP in 457 samples were obtained by MusigCV (running under the linux system), and the top ten were screened using q<0.05 as the cut-off. Correlations between the prognosis for HNSCC patients with GRGPI and TMB were determined by Kaplan-Meier survival curves in R.

2.8 Analysis of drug sensitivity

To assess the clinical applicability of the established model, pRRophetic was used to calculate the IC50 of HNSCC chemotherapeutic drugs.

2.9 Statistical analysis

The R software (version 4.1.1) was used for statistical analyses. Differentially expressed genes between tumor and adjacent normal tissues were compared by the Wilcoxon test. Survival-associated differentially expressed glycolytic genes were identified by univariate Cox and Lasso regression analyses. Then, Kaplan-Meier survival curves were plotted. Univariate COX and multivariate COX regression analyses were performed to determine the independent prognostic factors for OS. The predictive ability of the model was assessed by KM survival curves and ROC curves. Correlation tests were conducted by Spearman correlation analyses. Categorical data were compared by the chi-square test. $p \leq 0.05$ was the threshold for statistical significance. The flow chart of our study is shown in Figure 1.

2.10 Reverse transcription-quantitative PCR

All HNSCC and adjacent non-tumorous tissue samples were collected from 10 patients in the Shanxi Province Cancer Hospital. Extraction of total RNA from HNSCC tissues and adjacent non-tumor tissues was performed by the TRIzol reagent (Invitrogen, CA, USA). cDNA synthesis from the extracted RNA was performed by PrimeScriptTM RT Master Mix (RR036B, Takara). We use Quantitative PCR to analyze the mRNA expression levels of the prognostic glycolysis-related genes by GoTaq® qPCR Master Mix (Promega, A6001). The RT-qPCR was utilized in the ABI Vii7 Sequence detection system (ABI, USA). The PCR reaction system and conditions were according to the manufacturer's instructions. Gene expression levels of STC1, STC2, AURKA, P4HA1, and PLOD2 were calculated using the 2-ΔΔCT method.

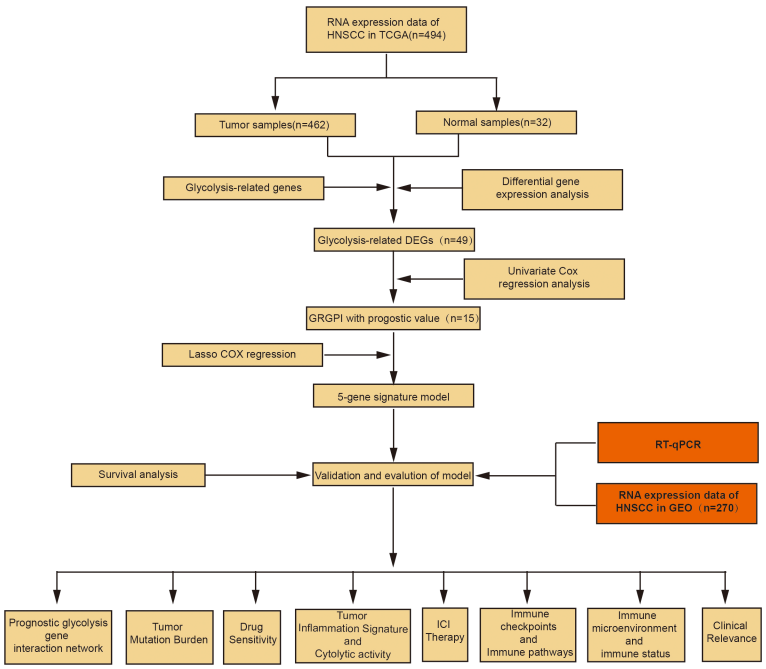

FIGURE 1
Flow chart of the study process.

3 Results

3.1 GSEA

Based on KEGG, REACTOME and HALLMARK gene sets, GSEA was performed to reveal potential differences between HNSCC and control groups. These pathways are associated with glycolysis, implying that glycolysis plays an essential role in HNSCC (Supplementary Figures 1A–C).

3.2 Identification of glycolysis-related DEGs

A total of 1695 differentially expressed genes (DEGs) (149 upregulated and 119 downregulated genes) in the TCGA training cohort were identified by Wilcoxon signed-rank test and visualized using volcano plots (Figure 2A) and heatmaps (Figure 2B). Then, 49 glycolysis-related genes were extracted from the DEGs (Figure 2C).

3.3 Construction of glycolysis-related gene signature for predicting patient outcomes

Through univariate Cox regression analysis, 15 prognosis glycolytic genes were established to be closely associated with survival outcomes of HNSCC patients (Figure 3A). The 15 OS-related genes may be collinear rather than independent. LASSO Cox regression analysis was performed to determine the real OS-affecting factors, and finally, a prognostic panel consisting of five glycolysis-related genes was established. The risk score was calculated as: Riskscore=0.021*AURKA+0.099*P4HA1 +0.015*PLOD2+0.031*STC1+0.163*STC2. (Figure 3B, C). Based on this gene signature, all patients were assigned to high (n=231) and low-risk (n=231) subgroups using the risk score median as the threshold. Risk scores, survival scores, and heatmap of prognostic glycolytic gene expressions among the low-risk and high-risk patients are presented in Figure 3D. Based on expressions of these five hub genes, dimensionality reduction was performed in all patients and presented with methods of t-distributed stochastic neighbor embedding (t-SNE), suggesting that different risk subgroups show significant discrete tendencies directly in the two-dimensional plane (Figure 3E). Kaplan-Meier survival curves revealed that high-risk score patients had significantly worse OS outcomes than low-risk score patients. The area under the curve (AUC) analysis for HNSCC patients at 1-year, 3-year, and 5-year revealed respective OS rates of 0.622, 0.649, and 0.614, demonstrating the optimal predictive performance of GRGPI (Figures 3F, G). Finally, the year with the largest AUC value is shown in the RMST plot (Figure 3H).

3.4 Verification of the five gene signature using the validation cohort

Given that the predictive potential of GRGPI in different datasets is misty into account, GSE65858 was used as the independent validation set. Based on the above risk scores, patients were assigned to low-risk (n=140) and high-risk (n=130) groups (Figure 4A). Findings from t-SNE and KM survival analyses of the GEO validation set were consistent with the results of the TCGA training cohort (Figures 4B, C). The AUC values for ROC curves accurately revealed the predictive performance of the prognostic risk model, with the largest AUC value year shown as an RMST plot (Figures 4D, E).

3.5 Independent prognostic, predictive value of risk scores and construction of the nomogram

In this study, the risk score, gender, smoking, and clinical stage were established to be independent prognostic factors in HNSCC patients, and they were used to construct subsequent

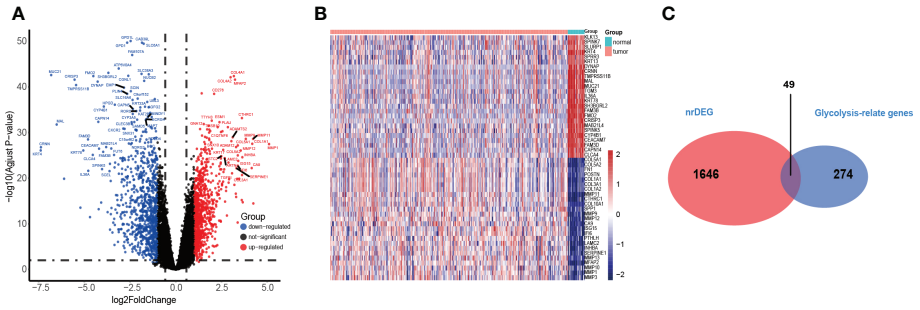

FIGURE 2
Identification of the HNSC-related DEGS in TCGA. **(A, B)** The volcano and heatmap plot showed differentially expressed genes between tumor and adjacent normal tissue. **(C)** Venn diagram showed glycolysis-relate differentially expressed genes between tumor and adjacent normal tissue.

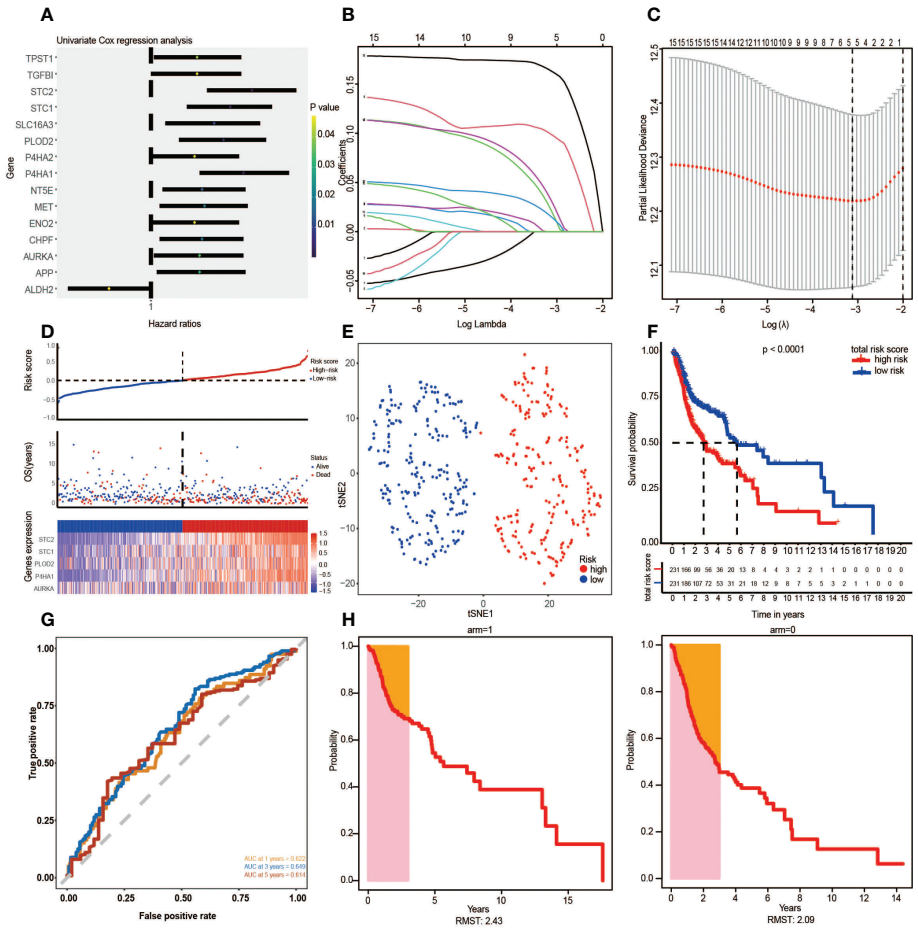

FIGURE 3
The Glycolysis-Related Gene Signature on the training cohort was constructed to predict patient outcomes. **(A)** Univariate Cox regression analysis yielded 15 prognosis-associated differentially expressed glycolysis-related genes. **(B, C)** LASSO regression analysis identified the five prognostic genes. **(D)** The TCGA risk score, survival time, survival status, and expression of the five-gene signature. **(E)** t-SNE cluster showed groups with high and low-risk scores. **(F)** Kaplan-Meier survival curve analysis for HNSCC patients divided into high-risk and low-risk groups. **(G)** Time-independent ROC curve of a risk score for prediction of 1-year, 3-year, and 5-year overall survival outcomes. **(H)** RMST plot for the TCGA training set.

nomograms (Figure 5A). Nomograms were used to predict the 1-year, 3-year, and 5-year survival probabilities of HNSCC patients (Figure 5B). Moreover, a calibration curve was constructed to assess the agreement between nomogram predictions and actual survival outcomes (Figure 5C). The actual and predicted survival rates at 1-year, 3-year, and 5-year were well matched, indicating that the nomogram has a good predictive performance. A decision curve (DCA) was used to assess the reliability of the risk score. It was observed that Model1 (Stage) was close to the extreme curve, while Model2 (RiskScore) was significantly higher than the extreme curve (Figure 5D).

The above analyses were also performed on the GEO validation set to verify the robustness of the model (Figure 6A). Unlike the TCGA training set, univariate and multivariate Cox regression analyses revealed that in the GEO validation set, only risk score and clinical stage were independent prognostic factors for HNSCC patients. Therefore, a nomogram integrating risk scores and clinical stages was constructed to predict the 1-year, 3-year, and 5-year survival probabilities of HNSCC patients (Figure 6B). Findings from the calibration curve were consistent with those of the TCGA training set (Figure 6C).

3.6 Clinical relevance form

Based on the relationship between high and low-risk groups and clinical stages in the TCGA training set, a clinical correlation table was prepared. It was established that about 60% of patients in the low-risk group were in locations I/II, while 76% of patients in the high-risk group were in stages III/IV (Supplementary

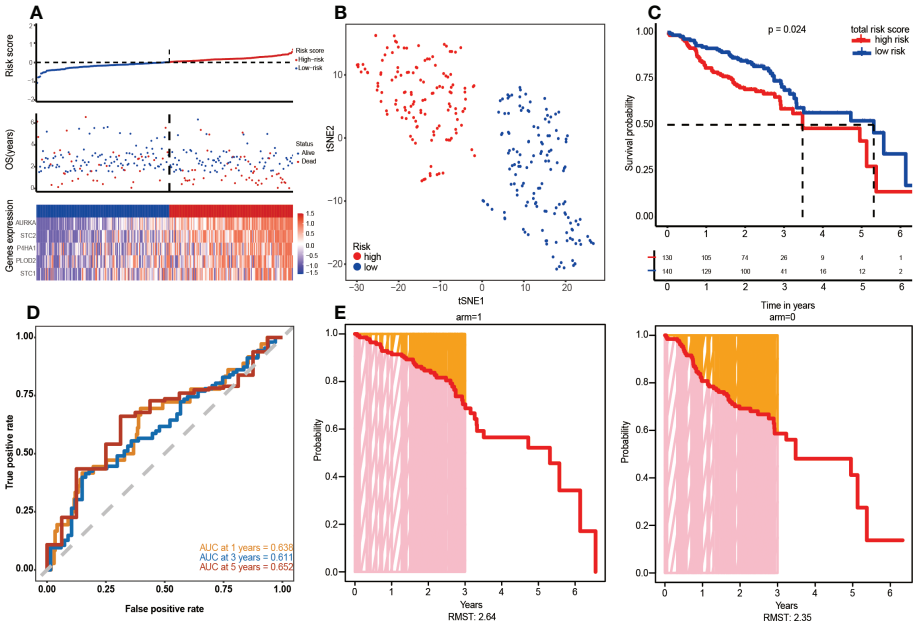

FIGURE 4
Verification of the five-gene signature in the validation cohort (GSE65858). **(A)** Risk map of patients based on risk score heatmap of survival status and risk gene expression profiles of individual HNSCC patients. **(B)** t-SNE grouping cluster. **(C)** Kaplan–Meier curves according to the five-gene signature. Log-rank tests were performed to determine the p values. **(D)** ROC curve and AUC values of five-gene feature classification in GEO. **(E)** RMST plot for the GEO testing set.

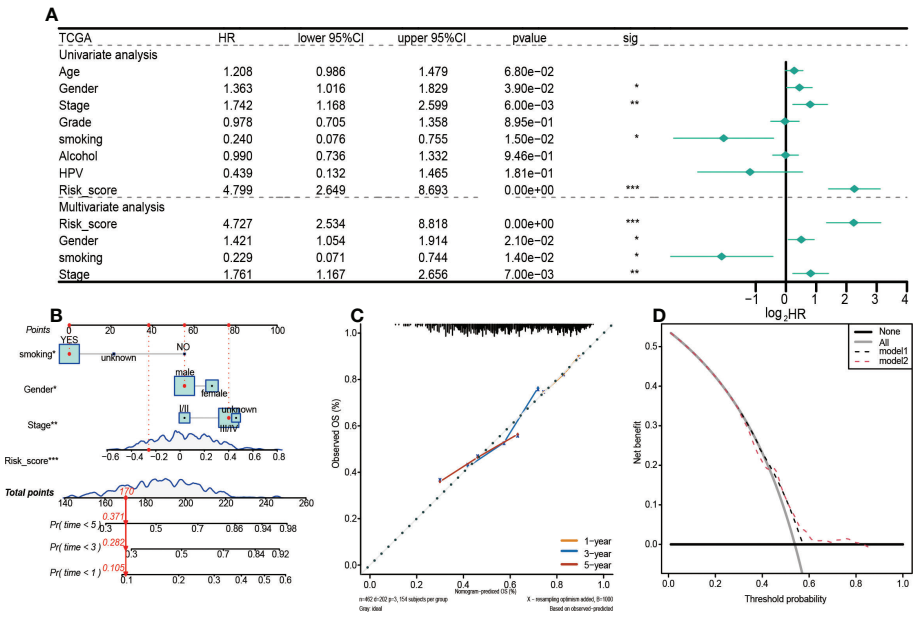

FIGURE 5
Prognostic values of the 5-gene signature model in the TCGA training set. **(A)** Results of univariate and multivariate Cox regression analyses regarding OS. **(B)** Nomogram for prediction of 1-year, 3-year, and 5-year survival probabilities of HNSCC patients. **(C)** Calibration curve for assessing the agreement between nomogram predicted and actual survival outcomes. **(D)** Assessment of the reliability of risk scores by DCA (decision curve). (*p < 0.05, **p < 0.01, ***p < 0.001).

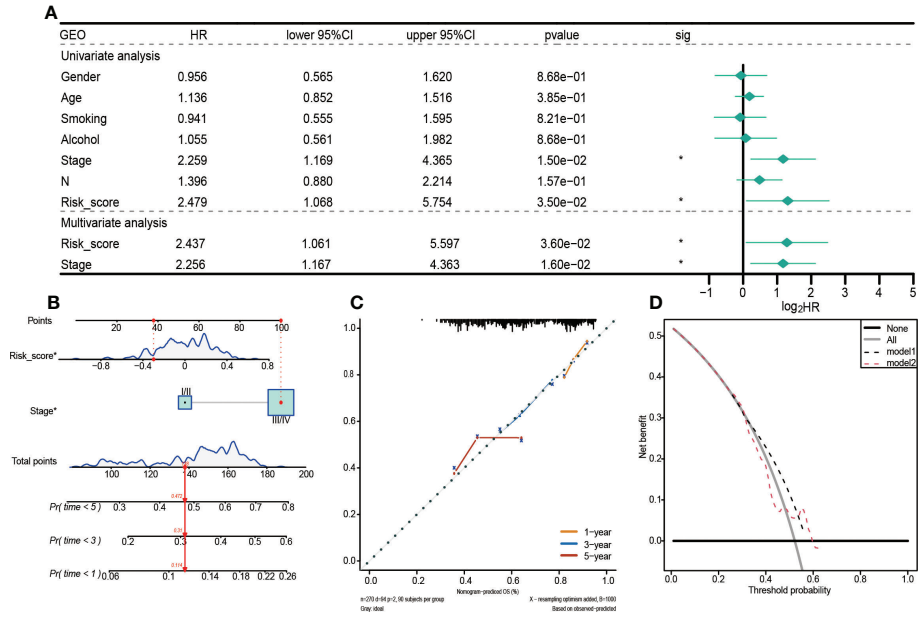

FIGURE 6
Prognostic values of the 5-gene signature model in the GEO set. **(A)**Univariate and multivariate Cox regression analysis to investigate the independence of risk models among clinicopathological factors. **(B)** Nomogram for predicting the 1-year, 3-year, and 5-year survival probabilities of HNSCC patients. **(C)** Calibration curve for assessing the agreement between nomogram predicted and actual survival outcomes. **(D)** Decision curve analyses of the nomogram based on OS outcomes.

Figure 2), implying that risk grouping was positively correlated with the clinical stage. These findings prove that the constructed GRGPI model is clinically valuable.

3.7 The tumor mutation burden

Mutation data for HNSCC were downloaded from the cBioPortal database. Somatic mutation types for the 457 patients were evaluated, and SNP was found to be the most dominant mutation type (Figures 7A, C). About 95.18% of samples in the high-risk group had SNPs, compared to 96.07% in the low-risk group (Figures 7B, D).

Given that SNP was the most dominant mutation type in HNSCC, 16,360 SNP-mediating genes were identified in the 457 samples using MusigCV. Using q<0.05 as the cut-off, the top ten genes were screened. Mutations types of the 10 genes and their distributions in high-risk and low-risk groups were analyzed (Figure 7E). The top ten genes with the highest mutation rates in the high-risk group were TP53, TTN, FAT1, MUC16, CSMD3, CDKN2A, LRP1B, KMT2D, DNAH5, and PIK3CA (Figure 7B), while those in the low-risk group were TP53, TTN, FAT1, MUC16, CSMD3, NOTCH1, SYNE1, CDKN2A, LRP1B, and PIK3CA (Figure 7D). It was observed that the gene with the highest mutation rate was TP53 in HNSCC patients regardless of the high GRGPI group or the low GRGPI group, suggesting that the mutations of the tumor suppressor gene TP53 may have potential clinical and pathophysiological significance in HNSCC patients. In fact, in a recent study, the mutational profile of TP53 has been proved to act as an independent prognostic factor in HNSCC patients. This relationship is associated with unique site-specific biological networks, consistent with our findings (17). Correlation analyses showed that GRGPI was positively correlated with TMB (R=0.015, p=0.75). The difference in the number of HNSCC patients in the high and low TMB groups was insignificant (Supplementary Figure 3A). Moreover, the difference in TMB values between the groups was negligible (Supplementary Figure 3B). We combined GRGPI and TMB and grouped them into three; high GRGPI high mutation (HTMB+HGRGPI), high GRGPI low mutation or low GRGPI high mutation (HTMB+LGRGPI & LTMB+HGRGPI), and low GRGPI low mutation (LTMB+LGRGPI). Then, Kaplan-Meier survival curves were drawn. The survival curve showed that the LTMB +LGRGPI group had the best prognosis, while the HTMB +HGRGPI group had the worst prognosis (Figure 7F). These findings imply that high GRGPI and high TMB play a synergistic role in promoting tumor occurrence and development, and the combined effects of the two may lead to worse prognostic outcomes.

3.8 Prognostic glycolysis gene interaction network

Interactions among the five glycolysis key genes and transcription factors may elucidate on mechanisms of the

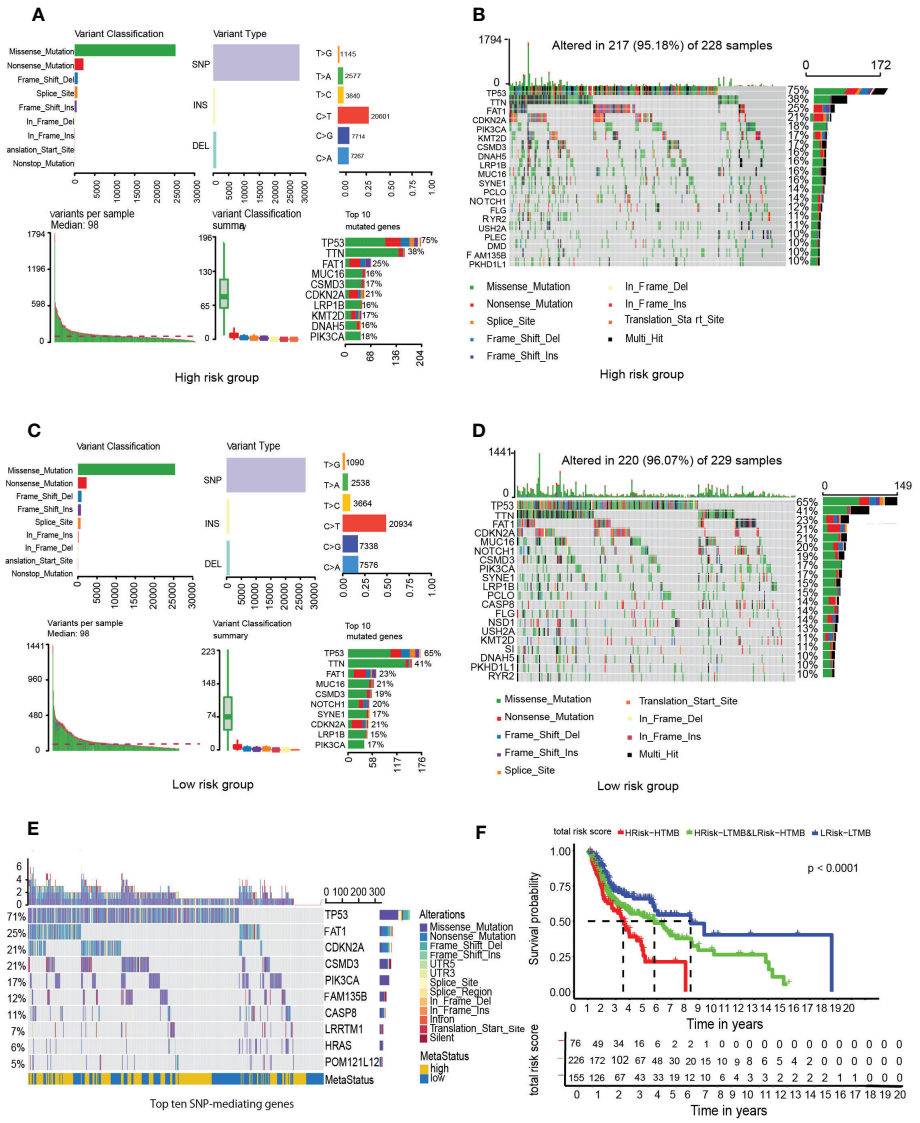

FIGURE 7
Analysis of tumor mutation burden among HNSCC patients. **(A)** High-GRGPI. **(B)** High-GRGPI group mutation types and top 20 mutated genes in the sample. **(C)** Low-GRGPI. **(D)** low-GRGPI group top 20 mutated genes. **(E)** Mutation types of the top ten SNP-driven genes and their distribution in high-GRGPI group and low-GRGPI group. **(F)** Kaplan-Meier survival curve showing OS differences among the three subgroups.

GRGPI model. Using cor Filter=0.5 and fdr Filter=0.01 as critical values, associations between AURKA, P4HA1, PL0D2 and 11 transcription factors were obtained (Supplementary Figure 4), which proved that the genes used to construct the GRGPI model were correlated with transcription factors in cancer and para cancer differentially expressed genes.

3.9 The immune microenvironment and immune status

Compared to the low-risk group, infiltrations of resting CD4 memory T cells, M0 macrophages, M2 macrophages, and activated mast cells were marked in the high-risk group, while infiltrations of CD8 T cells, follicular helper T cells, and Treg cells were to a greater extent (Figure 8A). Cell immunity-related cells, such as CD8 T cells, were highly infiltrated in the low-risk group, suggesting that immune cells may be activated in the low-risk group and suppressed in the high-risk group. Moreover, the M0 macrophages, activated mast cells, and resting CD4 memory cells were positively correlated with GRGPI scores while resting dendritic cells, CD8 T cells, follicular helper T cells, and Treg cells were negatively correlated with GRGPI scores (Figure 8B). The higher the GRGPI scores, the worse the extent of T cell infiltrations, validating that weaker antitumor immunity may be one of the reasons for poor prognostic outcomes. Therefore, the

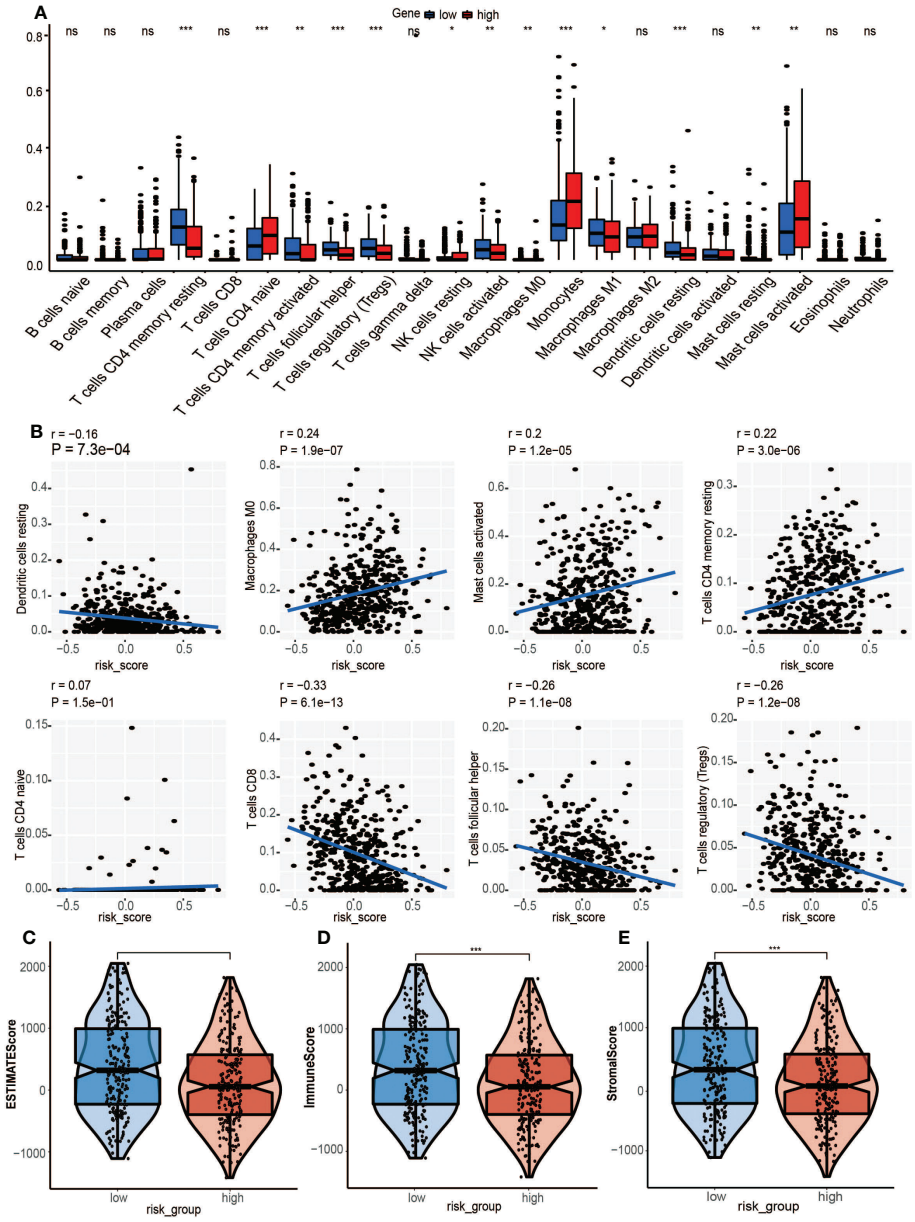

FIGURE 8
Association between tumor immunity and GRGPI scores in high and low GRGPI groups. **(A)** The 22 infiltrating immune cells are shown in boxplots. **(B)** Correlation analysis between 8 types of infiltrating immune cells and GRGPI scores. **(C–E)** Boxplots showing the correlation between GRGPI with ESTIMATE, immune, and stroma scores of HNSCC samples. (ns, not significant, *p < 0.05, **p < 0.01, ***p < 0.001).

high-risk group was defined as the low-immunity group, while the low-risk group was defined as the high-immunity group. Differences in ESTIMATE scores between the high-risk group and low-risk group were insignificant. However, the high-risk group exhibited low immune scores (p< 0.001, Figure 8D). These findings are consistent with those obtained from CIBERSORT, whereby the high-risk group exhibited worse immune status while the low-risk group exhibited better immune status. The relationship between stromal cells and GRGPI scores was further investigated (18). The high-risk group had higher stromal scores (p < 0.01, Figure 8E), implying that tumor stroma plays an important role in tumor development.

3.10 Immune checkpoints and immune pathways

ICI therapy has advanced the treatment of many solid tumors. Therefore, 11 human leukocyte antigen(HLA) class immune checkpoints were included, and their differential expressions in

high-risk and low-risk groups were determined. Four HLA class checkpoints (HLA-A, HLA-C, MICA, and MICB) were highly expressed in the high-risk group (Figure 9A), while the remaining seven were highly said in the low-risk group. Since the HLA class immune checkpoints are closely associated with immune responses, the better prognostic outcomes in the low-risk group could have been due to better immune responses. The expressions of 7 genes (CD274, CTLA4, IDO1 LAG3, PDCD1, TIGIT, and TNFRSF9) in the high-risk group and low-risk group were also analyzed (Figure 9B). Results show that five immune checkpoints cut in the high-risk group, CTLA4, IDO1, LAG3, PDCD1, and TIGIT, which are consistent with the result, once again proved that the GRGPI model and the close correlation between HLA class immune checkpoints.

GSEA was performed to assess the immune pathways, and differentially expressed immune-related pathways between the

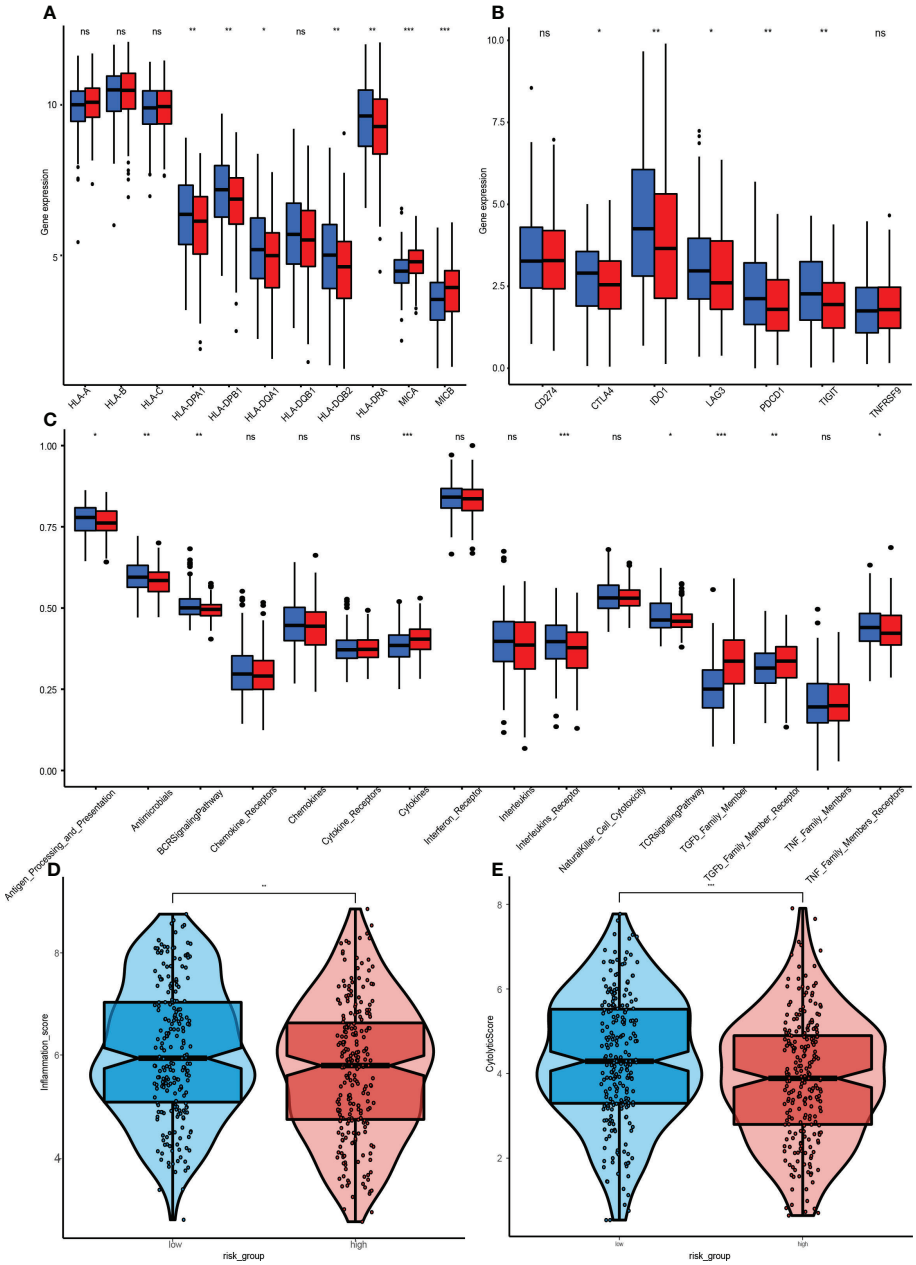

FIGURE 9
Immunization between high and low risk groups. **(A)** Differential expressions of 11 HLA class immune checkpoints. **(B)** 7 genes. CD274, CTLA4, IDO1, LAG3, PDCD1, TIGIT, and TNFRSF between the high-GRGPI group and low-GRGPI group. **(C)** Immune-related pathways. **(D, E)** Violin diagram for differences in cytolytic activities and Tumor Inflammation Signature between the high-GRGPI and low-GRGPI groups. (ns, not significant, *P<0.05, **p < 0.01, **p < 0.001).

high-risk and low-risk groups were obtained (Figure 9C). The BCR, Chemokines, Chemokine, Receptors, Interleukins Receptor, NK cell Cytotoxicity and TCR signalling pathway were found to be enriched in the high-risk group. However, enrichments of "TGFβ Family Members" and "TGFβ Family Members Receptor" were significantly high in the low-risk group, in accordance with the functions of TGF-β, which is involved in tumorigenesis and immunosuppression.

3.11 Tumor inflammation signature

The Tumor Inflammation Signature (TIS) is investigational use only (IUO) 18-gene signature that measures pre-existing but suppressed adaptive immune responses within tumors (19). The high-risk group had a low TIS score, implying that this group had weaker adaptive immune responses and worse prognostic outcomes (Figure 9D).

3.12 Cytolytic activity

The CYT score is a novel cancer immune index calculated from mRNA expressions of GZMA and PRF1 (20). The transcriptional levels of GZMA and PRF1 were determined to assess the cytolytic activities of immune lymphocytes in HNSCC. Based on previous risk grouping, the low-risk group exhibited a higher CYT score (Figure 9E), implying that immune cells in the low-risk group had stronger cytolytic activities and anti-tumor immune response, leading to a better prognosis.

3.13 GRGPI was highly predictive in ICI therapy

TIDE is a computational framework developed by Peng Jiang et al. to identify two tumor immune escape mechanisms (21). A higher TIDE score means a greater likelihood of immune evasion, indicating that a patient is less likely to benefit from ICI therapy and may have worse prognostic outcomes. The TIDE website was used to process 457 HNSCC samples with complete somatic mutation data in the training cohort, of which 131 responded to immunotherapy while the remaining 326 did not. Then, the GRGPIs of responding and non-responding samples were evaluated, which revealed that responding samples had lower GRGPIs (Figure 10A). This confirms our findings in a previous study. Since the low-risk group had better performance in immune gene expressions, immune cell infiltrations, and activation of immune pathways, the higher degree of immune cell infiltrations enables it to achieve better results in immunotherapy, proving that our definition of the low-risk group as the high-immunity group in terms of immunotherapeutic effects is correct. Then, TMB values of response and non-response samples were determined, which did not reveal significant differences in TMB values (Figure 10B). The GRGPI established in this paper is superior to TMB in predicting immunotherapeutic effects. To validate the effects of immunotherapy in IMvigor210, differences in GRGPIs between response and non-response samples were investigated and found to be insignificant (Figure 10C). Differences between the two groups of TMB values were analyzed, and the response group was found to have higher TMB values (Figure 10D).

Therefore, the proportion of response and non-response samples in the three subgroups was identified after combining GRGPI and TMB (Figure 10E). The HTMB+HGRGPI group had the most significant proportion of responding models, followed by HTMB+LGRGPI& LTMB+HGRGPI, and LTMB+LGRGPI, suggesting that immunotherapy had better effects in the HTMB +HGRGPI group. To determine the prognostic performance of the established three subgroup models, we compared the AUC values of the three predictive models of GRGPI, TMB, and GRGPI combined with TMB (Figure 10F), which were 0.534, 0.647, and 0.646. The TMB and GRGPI combined with TMB exhibited better predictive performance. Finally, the prognostic value of the predictive model in melanoma was assessed using the GSE78220 cohort for external validation. Differences in GRGPIs between response and non-response groups were insignificant (Supplementary Figure 5).

3.14 Drug sensitivity

Although ICI therapy has shown great promise for the treatment of HNSCC, given its high costs and limited therapeutic effects (326/457 showed no responses to ICI therapy in this study), chemotherapy is a clinically meaningful treatment. However, HNSCC is associated with significant resistance to chemotherapeutic drugs during clinical treatment. To assess the application effects in the clinical chemotherapy process of the established model, IC50 was used to express the sensitivity of the high-risk and low-risk groups to several common chemotherapeutic drugs. Cisplatin, paclitaxel, and docetaxel were recommended by the Chinese Society of Clinical Oncology (CSCO) Guidelines of 2021 as first-line therapeutic drugs for HNSCC. Therefore, IC50 values in a high-risk group and low-risk group of the three drugs were calculated (Figures 10G–I). Patients in the high-risk group were more sensitive to cisplatin (p=1.4e-05) and docetaxel (p=5.5e-12). In contrast, those in the low-risk group were more sensitive to paclitaxel (p=9.9e-01), implying that the established model indicates chemotherapeutic sensitivity.

3.15 RT-qPCR analysis

To verify the accuracy of GRGPI in HNSCC patients, we collected HNSCC tissues and adjacent non-tumorous tissues from 10 HNSCC patients. RT-qPCR was implemented to

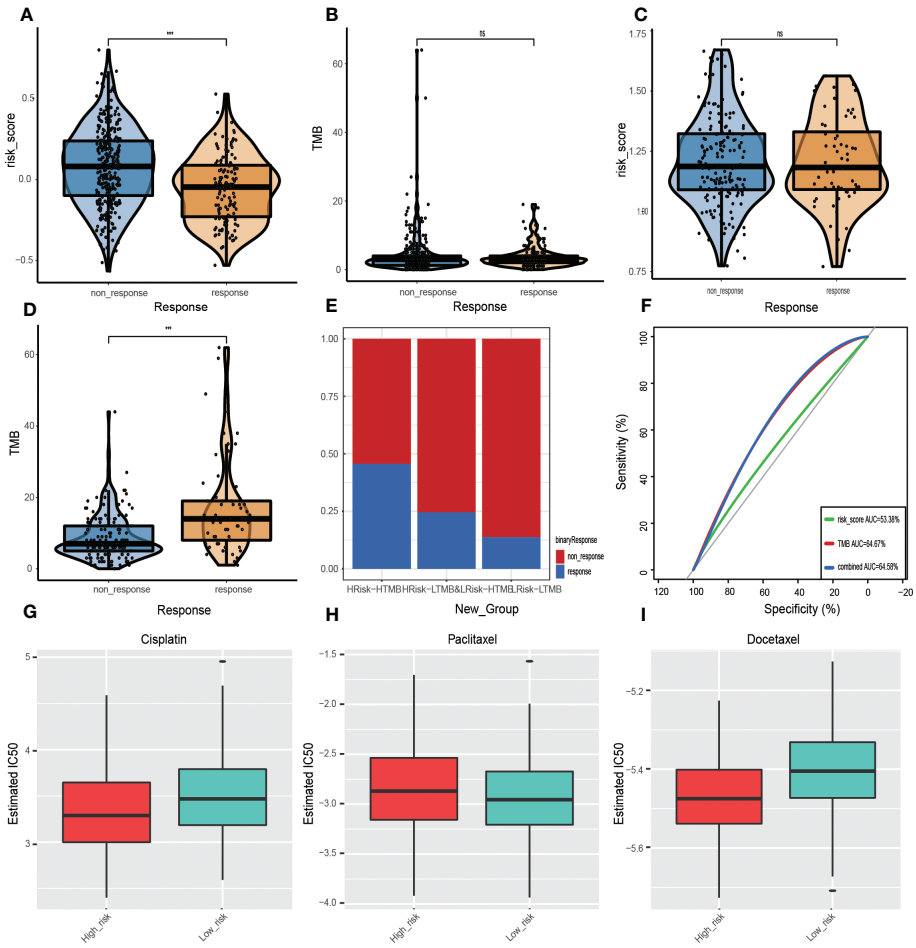

FIGURE 10
Prognostic value of ICI therapy. **(A, B)** Sizes of training cohort responses, non-response sample GRGPIs, and TMB values. **(C, D)** Differences in GRGPIs and TMB between responsive and non-responsive samples from IMvigor210. **(E)** Proportions of immunotherapy-responsive and non-responsive samples in the three subgroups from the IMvigor210 cohort. **(F)** ROC curves of GRGPI, TMB, and GRGPI combined with TMB in the IMvigor210 cohort. Analysis of drug sensitivity. Differences in IC50 values of **(G)** Gefitinib, **(H)** Erlotinib, and **(I)** Cisplatin in the high-GRGPI group and low-GRGPI group.

analyze the expressions of five prognostic glycolysis-related genes in the GRGPI. We found that compared with adjacent non-tumorous tissues, the terms of five genes were significantly up-regulated in HNSCC tissues (Figures 11A–E).

4 Discussion

Conversion of the primary energy source from oxidative phosphorylation (OXPHOS) to aerobic glycolysis is an emerging hallmark of cancer cells (22). Although the amount of ATP produced by glycolysis is low, several advantages inherent to aerobic glycolysis can explain this metabolic switch in cancer cells. Glycolysis produces ATP 100 times faster than OXPHOS (23), which can provide sufficient energy for cell survival. Second, glycolytic intermediates can be transferred to various biosynthetic pathways to provide materials for the synthesis of biomolecules and organelles (24, 25). In addition, glutathione is key in protecting cancer cells from oxidative damage and antitumor drugs. In contrast, intermediates accumulated by cancer cells during glycolysis promote the pentose phosphate pathway and can ensure their growth in an environment with reduced glutathione levels (26, 27). Finally, the formation of an acidic microenvironment associated with lactate accumulation due to increased glycolysis provides a tissue environment for tumor recurren tumor metastasis (28). These factors increase the dependence of tumor cells on glycolysis and provide a biochemical basis for the preferential killing of cancer cells by using glycolysis as a therapeutic target, possibly resulting in improved therapeutic efficacies (29).

Studies are evaluating the molecular mechanisms of glycolysis in tumorigenesis, proliferation, and invasion. For instance,

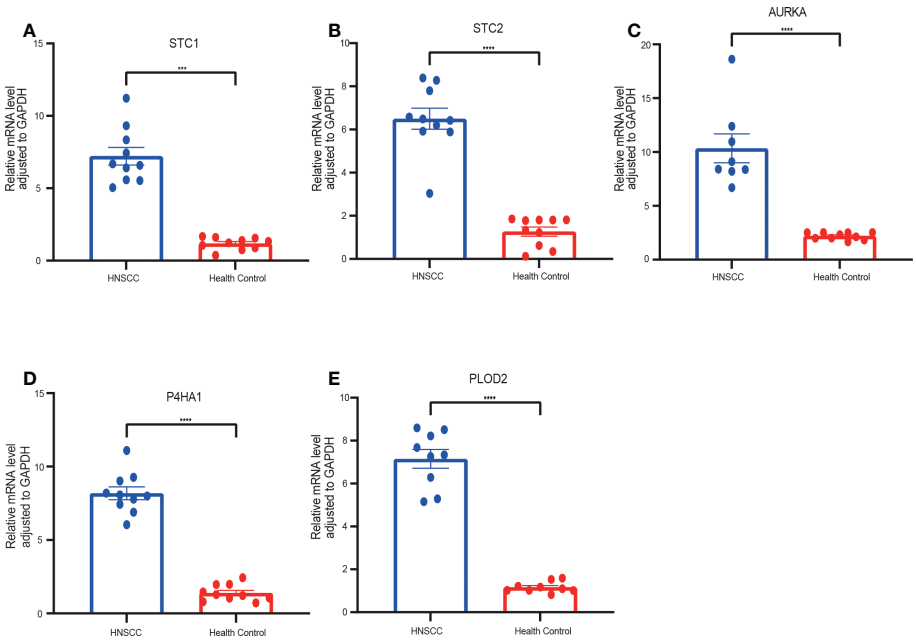

FIGURE 11
RT-qPCR analyses of five hub genes between HNSCC and Healthy control tissues. Relative mRNA expressions of **(A)** STC1, **(B)** STC2, **(C)** AURKA, **(D)** P4HA1, **(E)** PLOD2. (***p < 0.001,****p < 0.0001).

PLOD2 induces epithelial-mesenchymal transition (EMT) *via* the PI3K/AKT signaling pathway. It is involved in regulating outer stromal collagen and tumor metastasis through EMT, TGF-β, and hypoxic signaling. PLOD2 levels are significantly associated with advanced cancer staging. The presence of regional STC1 uncouples the oxidative phosphorylation process by increasing the expressions of mitochondrial UCP2, which is a valuable biomarker for the diagnosis of malignant glioma for the assessment of postoperative prognosis. Elevated STC2 levels selectiveprotectcts HeLa cells from endoplasmic reticulum stress-induced cell death and are also associated with larger tumor formation, tumor invasion, lymph node metastasis, and poor prognostic outcomes. P4HA1 is a hypoxia-responsive gene that plays a key role in regulating collagen biosynthesis (30). HPV infections promote HNSCC by suppressing P4HA1. AURKA-mediated phosphorylation can regulate the function of AURKA-discovered substrates, some of which are filamentous regulators, tumor suppressors, or factors in cancer. There are already several small molecules targeting AURKA that have been tested in AURKA (AKI) preclinical studies (31).

Given the importance of glycolysis in HNSCC, it can be hypothesized that glycolysis-related genes are potential prognostic factors for HNSCC. In addition, computed multigene prognostic markers outperformed single biomarkers in predicting overall survival. We analyzed the mRNA expression profiles of 49 glycolysis-related genes in the TCGA head and neck squamous cell carcinoma cohort. Five genes associated with glycolysis were selected as candidate prognostic factors for HNSCC. These genes are potential molecular predictive biomarkers and may help inform individualized treatments based on patient risk. We combined the established risk scores and multiple clinical parameters to construct column line plots for predicting the 1-year, 3-year, and 5-year OS in HNSCC patients. Calibration plots based on the TCGA database showed that the expected and observed values were very close, indicating the excellent predictive performance of column line plots. The predictive efficacy was equally good when examined in the validation set. Thus, our new prognostic column line plot may be better than the original clinical factors for predicting survival status for HNSCC patients and informing specific individualized treatment.

Analysis of the new risk scoring model (GRGPI) revealed higher immune cell infiltration scores in the low-risk group. Host immunosuppression is an integral factor in HNSCC carcinogenesis (32). The immune microenvironment is characterized by the presence of infiltrating immune cells (33). We compared immune cell infiltrations between the high-risk and low-risk groups of HNSCC. We found that resting CD4 memory cells, M0-phase macrophages, M2-phase macrophages, and activated mast cells were highly infiltrated in the high-risk group. In contrast, Tregs and other cells were more in the low-risk group. Acquired immune-related cell infiltrations were lower in the high-risk group compared to the low-risk group, suggesting that the higher risk score may be associated with immunosuppression. CD8 T cells directly targeting tumor cells were more stable in the low-risk group. However, CD4 T cells in

the tumor microenvironment were unstable for a broad subpopulation with potentially different functions (34). CTLA-4, which is downregulated in the low-immune group, is the first negative regulator of T cell activation identified in the context of antitumor immunity, and its blockade using monoclonal antibodies triggers tumor regression with durable antitumor immunity in preclinical models. LAG-3 acts synergistically with other checkpoint molecules to promote T cell dysfunction. However, the molecular mechanisms and pathways associated with LAG-3 signaling have not been fully established (35). In this regard, the conserved KIEELE motif in the cytoplasmic structural domain was indispensable for LAG-3 downstream signaling and inhibition of CD4 T cell activation. MHC-II/LAG-3 triggers the activation of ITAM signaling in DCs, thereby promoting a tolerance profile (36). Thus, MHC-II/LAG-3 interactions function as a bidirectional inhibitory pathway.

Through immune pathway analyses, cytokines, TGF-β family, and TGF-β family receptors were activated in the high-risk group of the TCGA dataset. The postulate that overproduction of TGF-β promotes tumor progression was verified. While the TGF-β-related pathway plays an important role in inhibiting the proliferation of immunoreactive cells and stimulating the expressions of the extracellular matrix, activation of the TGF-β-related pathway in the high-risk group may be one of the reasons for the immunosuppression and lower stromal scores. Immune cell dysfunctions within the HNSCC-TME promote immunosuppression and may thus be associated with tumor survival and progression outcomes. Therefore, it also requires therapeutic interventions (37, 38). We found that the density of CD8 T cells, resting dendritic cells, follicular helper T cells, Treg cells, and high immune scores correlated with patient prognosis, consistent with findings from previous studies (20, 39). This underscores the fact that preexisting immune responses have antitumor effects and positively influence immunotherapeutic responses. Several seminal clinical and genomic studies have reported that HNSCC has a high degree of immune cell infiltrations. However, less than 20% of HNSCC patients respond to immunotherapy, implying that even the resistant phenotype in the tumor is not an absolute predictor of immunotherapeutic responses (40, 41). Molecular analyses of HNSCC have identified a range of cytokines, chemokines, and other TME components that determine the ability of the host to mount anti-tumor immune responses. During tumorigenesis, these molecular changes may interfere with intercellular communication between infiltrating immune cells, disrupting the balance between immune tolerance and cellular activity (42).

Higher CYT scores were associated with higher expressions of inhibitory ligands by tumor cells that predispose to immune evasion. Patients with high CYT scores showed better efficacies regarding checkpoint inhibitors such as PD-L1 than those with low CYT scores. Based on previous risk groupings, we found that the low-risk group had higher CYT scores (43), suggesting that immune cells in the low-risk group had stronger cytolytic activities and antitumor immune responses may have better prognostic outcomes. Drug sensitivity assays revealed that patients in the high-risk group were more sensitive to cisplatin and docetaxel. In contrast, patients in the low-risk group were more sensitive to paclitaxel, gefitinib, and erlotinib, suggesting that this model can be used as a potential predictor of chemotherapeutic sensitivity for screening sensitive drugs. Tumor cell chemotherapy drug sensitivity testing can provide valuable information to physicians to support their treatment decisions and provide a powerful tool for physicians and patients in their battle against cancer.

Overall, according to survival analysis, functional analysis, ICI therapy, drug sensitivity, and RT-qPCR analysis, the signature was a valuable indicator for predicting survival outcomes among HNSCC patients. But our study still has some limitations. First, it was carried out based on the TCGA database, which lacked specific data on surgery, chemotherapy, and tumor size. Besides, some patients have undergone immune or targeted therapy, which may impact the prognosis analysis. Second, a very high proportion of patients with tumors located in the oral cavity in the model could make it difficult to generalize the results of head and neck cancer. Third, the number of patients we collected was too small to validate the performance of our prognostic model.

5 Conclusion

In conclusion, a new HNSCC prognostic signature based on five glycolysis-related genes was constructed in the TCGA cohort and validated in the GEO database. The signature shows excellent performance in predicting survival outcomes among HNSCC patients, reveals the relationship between glycolysis-related genes and tumor immunity in HNSCC and provides guidance to clinical treatment decisions.

Data availability statement

The original contributions presented in the study are included in the article/Supplementary Material. Further inquiries can be directed to the corresponding authors.

Ethics statement

The studies involving human participants were reviewed and approved by Cancer Hospital Affiliated to Shanxi Medical University. The patients/participants provided their written informed consent to participate in this study.

Author contributions

Conceived and designed the study: FH, H-ZW, M-JC, P-FH, X-TY, FLi. Collected and analyzed the data: Y-TH and M-JC. Performed the experiments and verificate experiments: H-ZW and FH. Wrote the initial draft: L-ZL, SL. The corresponding authors are responsible for ensuring that the descriptions are accurate and agreed by all authors. All authors contributed to the article and approved the submitted version.

Funding

This work was supported by the National Social Science Fund of China (21BTQ050) and the Key Project of Health Commission of Shanxi Province (2022XM28 to FLi).

Acknowledgments

We sincerely thank the R package developers and the maintainers of the TCGA database, GEO database, cBioPortal, STRING, TIMER and Metascape website.

Conflict of interest

The authors declare that the research was conducted in the absence of any commercial or financial relationships that could be construed as a potential conflict of interest.

Publisher's note

Supplementary material

The Supplementary Material for this article can be found online at: https://www.frontiersin.org/articles/10.3389/fonc.2022.972215/full#supplementary-material

References

1. Gillison ML, Chaturvedi AK, Anderson WF, Fakhry C. Epidemiology of human papillomavirus-positive head and neck squamous cell carcinoma. *J Clin Oncol* (2015) 33(29):3235–42. doi: 10.1200/JCO.2015.61.6995

2. Chow LQM. Head and neck cancer. *New Engl J Med* (2020) 382(1):60–72. doi: 10.1056/NEJMra1715715

3. Vaupel P, Schmidberger H, Mayer A. The warburg effect: Essential part of metabolic reprogramming and central contributor to cancer progression. *Int J Radiat Biol* (2019) 95(7):912–9. doi: 10.1080/09553002.2019.1589653

4. Lu J, Tan M, Cai Q. The warburg effect in tumor progression: Mitochondrial oxidative metabolism as an anti-metastasis mechanism. *Cancer Lett* (2015) 356(2 Pt A):156–64. doi: 10.1016/j.canlet.2014.04.001

5. Huebbers CU, Adam AC, Preuss SF, Schiffer T, Schilder S, Guntinas-Lichius O, et al. High glucose uptake unexpectedly is accompanied by high levels of the mitochondrial s-F1-Atpase subunit in head and neck squamous cell carcinoma. *Oncotarget* (2015) 6(34):36172–84. doi: 10.18632/oncotarget.5459

6. Chen L, He X, Yi S, Liu G, Liu Y, Ling Y. Six glycolysis-related genes as prognostic risk markers can predict the prognosis of patients with head and neck squamous cell carcinoma. *BioMed Res Int* (2021) 2021:8824195. doi: 10.1155/2021/8824195

7. Yang J-G, Wang W-M, Xia H-F, Yu Z-L, Li H-M, Ren J-G, et al. Lymphotoxin-A promotes tumor angiogenesis in hnscc by modulating glycolysis in a Pfkfb3-dependent manner. *Int J Cancer* (2019) 145(5):1358–70. doi: 10.1002/ijc.32221

8. Ganapathy-Kanniappan S, Geschwind JF. Tumor glycolysis as a target for cancer therapy: Progress and prospects. *Mol Cancer* (2013) 12:152. doi: 10.1186/1476-4598-12-152

9. Akram M. Mini-review on glycolysis and cancer. *J Cancer Educ* (2013) 28 (3):454–7. doi: 10.1007/s13187-013-0486-9

10. Kumar D. Regulation of glycolysis in head and neck squamous cell carcinoma. *Postdoc J* (2017) 5(1):14–28. doi: 10.14304/surya.jpr.v5n1.4

11. Vivanco I, Sawyers CL. The phosphatidylinositol 3-kinase akt pathway in human cancer. *Nat Rev Cancer* (2002) 2(7):489–501. doi: 10.1038/nrc839

12. Elstrom RL, Bauer DE, Buzzai M, Karnauskas R, Harris MH, Plas DR, et al. Akt stimulates aerobic glycolysis in cancer cells. *Cancer Res* (2004) 64(11):3892–9. doi: 10.1158/0008-5472.Can-03-2904

13. Schreiber RD, Old LJ, Smyth MJ. Cancer immunoediting: Integrating immunity's roles in cancer suppression and promotion. *Science* (2011) 331 (6024):1565–70. doi: 10.1126/science.1203486

14. Dunn GP, Old LJ, Schreiber RD. The immunobiology of cancer immunosurveillance and immunoediting. *Immunity* (2004) 21(2):137–48. doi: 10.1016/j.immuni.2004.07.017

15. Jie H-B, Srivastava RM, Argiris A, Bauman JE, Kane LP, Ferris RL. Increased pd-1 and Tim-3 tils during cetuximab therapy inversely correlate with response in head and neck cancer patients. *Cancer Immunol Res* (2017) 5(5):408–16. doi: 10.1158/2326-6066

16. Bell RB, Leidner RS, Crittenden MR, Curti BD, Feng Z, Montler R, et al. OX40 signaling in head and neck squamous cell carcinoma: Overcoming immunosuppression in the tumor microenvironment. *Oral Oncol* (2016) 52:1-10. doi: 10.1016/j.oraloncology.2015.11.009

17. Caponio VCA, Troiano G, Adipietro I, Zhurakivska K, Arena C, Mangieri D, et al. Computational analysis of Tp53 mutational landscape unveils key prognostic signatures and distinct pathobiological pathways in head and neck squamous cell cancer. *Br J Cancer* (2020) 123(8):1302–14. doi: 10.1038/s41416-020-0984-6

18. Ahmadzadeh M, Rosenberg SA. Tgf-beta 1 attenuates the acquisition and expression of effector function by tumor antigen-specific human memory Cd8 T cells. *J Immunol (Baltimore Md 1950)* (2005) 174(9):5215–23. doi: 10.4049/jimmunol.174.9.5215

19. Danaher P, Warren S, Lu R, Samayoa J, Sullivan A, Pekker I, et al. Pan-cancer adaptive immune resistance as defined by the tumor inflammation signature (Tis): Results from the cancer genome atlas (Tcga). *J For Immunotherapy Cancer* (2018) 6(1):63. doi: 10.1186/s40425-018-0367-1

20. Rooney MS, Shukla SA, Wu CJ, Getz G, Hacohen N. Molecular and genetic properties of tumors associated with local immune cytolytic activity. *Cell* (2015) 160(1-2):48–61. doi: 10.1016/j.cell.2014.12.033

21. Jiang P, Gu S, Pan D, Fu J, Sahu A, Hu X, et al. Signatures of T cell dysfunction and exclusion predict cancer immunotherapy response. *Nat Med* (2018) 24(10):1550–8. doi: 10.1038/s41591-018-0136-1

22. Hanahan D, Weinberg RA. Hallmarks of cancer: The next generation. *Cell* (2011) 144(5):646–74. doi: 10.1016/j.cell.2011.02.013

23. Locasale JW, Cantley LC. Altered metabolism in cancer. *BMC Biol* (2010) 8:88. doi: 10.1186/1741-7007-8-88

24. Deberardinis RJ, Sayed N, Ditsworth D, Thompson CB. Brick by brick: Metabolism and tumor cell growth. *Curr Opin In Genet Dev* (2008) 18(1):54–61. doi: 10.1016/j.gde.2008.02.003

25. Whitaker-Menezes D, Martinez-Outschoorn UE, Lin Z, Ertel A, Flomenberg N, Witkiewicz AK, et al. Evidence for a stromal-epithelial "Lactate shuttle" in human tumors: Mct4 is a marker of oxidative stress in cancer-associated fibroblasts. *Cell Cycle (Georgetown Tex)* (2011) 10(11):1772–83. doi: 10.4161/cc.10.11.15659

26. Pacini N, Borziani F. Cancer stem cell theory and the warburg effect, two sides of the same coin? *Int J Mol Sci* (2014) 15(5):8893–930. doi: 10.3390/ijms15058893

27. Traverso N, Ricciarelli R, Nitti M, Marengo B, Furfaro AL, Pronzato MA, et al. Role of glutathione in cancer progression and chemoresistance. *Oxid Med Cell Longevity* (2013) 2013:972913. doi: 10.1155/2013/972913

28. Pelicano H, Martin DS, Xu RH, Huang P. Glycolysis inhibition for anticancer treatment. *Oncogene* (2006) 25(34):4633–46. doi: 10.1038/sj.onc.1209597

29. Sacco AG, Cohen EE. Current treatment options for recurrent or metastatic head and neck squamous cell carcinoma. *J Clin Oncol Off J Am Soc Clin Oncol* (2015) 33(29):3305–13.

30. Li Q, Shen Z, Wu Z, Shen Y, Deng H, Zhou C, et al. High P4ha1 expression is an independent prognostic factor for poor overall survival and recurrent-free survival in head and neck squamous cell carcinoma. *J Clin Lab Anal* (2020) 34(3): e23107. doi: 10.1002/jcla.23107

31. Du R, Huang C, Liu K, Li X, Dong Z. Targeting aurka in cancer: Molecular mechanisms and opportunities for cancer therapy. *Mol Cancer* (2021) 20(1):15. doi: 10.1186/s12943-020-01305-3

32. Tsukamoto H, Fujieda K, Miyashita A, Fukushima S, Ikeda T, Kubo Y, et al. Combined blockade of Il6 and pd-1/Pd-L1 signaling abrogates mutual regulation of their immunosuppressive effects in the tumor microenvironment. *Cancer Res* (2018) 78(17):5011–22. doi: 10.1158/0008-5472.CAN-18-0118

33. Maggioni D, Pignataro L, Garavello W. T-Helper and T-regulatory cells modulation in head and neck squamous cell carcinoma. *Oncoimmunology* (2017) 6 (7):e1325066. doi: 10.1080/2162402X.2017.1325066

34. de Ruiter EJ, Ooft ML, Devriese LA, Willems SM. The prognostic role of tumor infiltrating T-lymphocytes in squamous cell carcinoma of the head and neck: A systematic review and meta-analysis. *Oncoimmunology* (2017) 6(11): e1356148. doi: 10.1080/2162402X.2017.1356148

35. Workman CJ, Dugger KJ, Vignali DAA. Cutting edge: Molecular analysis of the negative regulatory function of lymphocyte activation gene-3. *J Immunol (Baltimore Md 1950)* (2002) 169(10):5392–5. doi: 10.4049/jimmunol.169.10.5392

36. Liang B, Workman C, Lee J, Chew C, Dale BM, Colonna L, et al. Regulatory T cells inhibit dendritic cells by lymphocyte activation gene-3 engagement of mhc class ii. *J Immunol (Baltimore Md: 1950)* (2008) 180(9):5916–26. doi: 10.4049/jimmunol.180.9.5916

37. Czystowska M, Gooding W, Szczepanski MJ, Lopez-Abaitero A, Ferris RL, Johnson JT, et al. The immune signature of Cd8(+)Ccr7(+) T cells in the peripheral circulation associates with disease recurrence in patients with hnscc. *Clin Cancer Res an Off J Am Assoc For Cancer Res* (2013) 19(4):889–99. doi: 10.1158/1078-0432.CCR-12-2191

38. Davis RJ, Van Waes C, Allen CT. Overcoming barriers to effective immunotherapy: Mdscs, tams, and tregs as mediators of the immunosuppressive microenvironment in head and neck cancer. *Oral Oncol* (2016) 58:59–70. doi: 10.1016/j.oraloncology.2016.05.002

39. Mandal R, Şenbabaoğlu Y, Desrichard A, Havel JJ, Dalin MG, Riaz N, et al. The head and neck cancer immune landscape and its immunotherapeutic implications. *JCI Insight* (2016) 1(17):e89829. doi: 10.1172/jci

40. Seiwert TY, Burtness B, Mehra R, Weiss J, Berger R, Eder JP, et al. Safety and clinical activity of pembrolizumab for treatment of recurrent or metastatic squamous cell carcinoma of the head and neck (Keynote-012): An open-label, multicentre, phase 1b trial. *Lancet Oncol* (2016) 17(7):956–65. doi: 10.1016/S1470-2045(16)30066-3

41. Yarchoan M, Hopkins A, Jaffee EM. Tumor mutational burden and response rate to pd-1 inhibition. *New Engl J Med* (2017) 377(25):2500–1. doi: 10.1056/NEJMc1713444

42. Şenbabaoğlu Y, Gejman RS, Winer AG, Liu M, Van Allen EM, de Velasco G, et al. Tumor immune microenvironment characterization in clear cell renal cell carcinoma identifies prognostic and immunotherapeutically relevant messenger rna signatures. *Genome Biol* (2016) 17(1):231. doi: 10.1186/s13059-016-1092-z

43. Gao Z, Tao Y, Lai Y, Wang Q, Li Z, Peng S, et al. Immune cytolytic activity as an indicator of immune checkpoint inhibitors treatment for prostate cancer. *Front In Bioengineering Biotechnol* (2020) 8:930. doi: 10.3389/fbioe.2020.00930

frontiers | Frontiers in Oncology

TYPE Original Research
PUBLISHED 20 January 2023
DOI 10.3389/fonc.2022.1083440

OPEN ACCESS

EDITED BY
Lorenz Kadletz-Wanke,
Medical University of Vienna, Austria

REVIEWED BY
Jia-Ming Wu,
Wuwei Cancer Hospital of Gansu Province, China
Hans Christiansen,
Hannover Medical School, Germany

*CORRESPONDENCE
Lin Ma
malinpharm@sina.com

†These authors have contributed equally to this work

SPECIALTY SECTION
This article was submitted to Head and Neck Cancer, a section of the journal Frontiers in Oncology

RECEIVED 29 October 2022
ACCEPTED 28 December 2022
PUBLISHED 20 January 2023

CITATION
Meng L, Teng F, Liu Q, Du L, Cai B, Xie C, Gong H, Zhang X and Ma L (2023) Long-term outcomes of nasopharyngeal carcinoma treated with helical tomotherapy using simultaneous integrated boost technique: A 10-year result. *Front. Oncol.* 12:1083440. doi: 10.3389/fonc.2022.1083440

Long-term outcomes of nasopharyngeal carcinoma treated with helical tomotherapy using simultaneous integrated boost technique: A 10-year result

Lingling Meng[1,2†], Feng Teng[3†], Qiteng Liu[4†], Lei Du[5], Boning Cai[2], Chuanbin Xie[2], Hanshun Gong[2], Xinxin Zhang[6] and Lin Ma[1,2*]

[1]Medical School of the Chinese People's Liberation Army (PLA), Beijing, China, [2]Department of Radiation Oncology, First Medical Center of Chinese PLA General Hospital, Beijing, China, [3]Department of Radiation Oncology, China-Japan Friendship Hospital, Beijing, China, [4]Department of Radiation Oncology, Beijing Luhe Hospital, Affiliated to Capital Medical University, Beijing, China, [5]Department of Radiation Oncology, Hainan Hospital of the Chinese PLA General Hospital, Sanya, China, [6]Department of Otorhinolaryngology, First Medical Center of Chinese PLA General Hospital, Beijing, China

Background: To evaluate the long-term survival and treatment-related toxicities of helical tomotherapy (HT) in nasopharyngeal carcinoma (NPC) patients.

Methods: One hundred and ninety newly diagnosed non-metastatic NPC patients treated with HT from September 2007 to August 2012 were analyzed retrospectively. The dose at D95 prescribed was 70-74Gy, 60-62.7Gy and 52-56Gy delivered in 33 fractions to the primary gross tumor volume (pGTVnx) and positive lymph nodes (pGTVnd), the high risk planning target volume (PTV1), and the low risk planning target volume (PTV2), respectively, using simultaneous integrated boost technique. The statistical analyses were performed and late toxicities were evaluated and scored according to the Common Terminology Criteria for Adverse Events (version 3.0).

Results: The median follow-up time was 145 months. The 10-year local relapse-free survival (LRFS), nodal relapse-free survival (NRFS), distant metastasis-free survival (DMFS) and overall survival (OS) were 94%, 95%, 86%, and 77.8%; respectively. Fifty (26.3%) patients had treatment-related failures at the last follow-up visit. Distant metastasis, occurred in 25 patients, was the major failure pattern. Multivariate analysis showed that age and T stage were independent predictors of DMFS and OS, Concomitant chemotherapy improved overall survival, but anti-EGFR monoclonal antibody therapy failed. The most common late toxicities were mainly graded as 1 or 2.

Conclusions: Helical tomotherapy with simultaneous integrated boost technique offered excellent long-term outcomes for NPC patients, with mild late treatment-related toxicities. Age and clinical stage were independent predictors of DMFS and

OS. And, concurrent chemotherapy means better OS. Further prospective study is needed to confirm the superiority of this technology and to evaluate the roles of anti-EGFR monoclonal antibody treatment.

KEYWORDS

nasopharyngeal carcinoma, helical tomotherapy (HT), survival, chemotherapy, radiotherapy

Introduction

Nasopharyngeal carcinoma (NPC) is the most common malignant tumor of the head and neck in China, about 70% ~ 80% of patients are combined with the neck lymph node metastasis, and 10% ~ 15% combined with distant metastases at the first diagnosis (1). Radiation therapy is the only curative treatment method for non-metastatic NPC, and intensity-modulated radiation therapy (IMRT) has been accepted as the standard radiation technique (2). The addition of chemotherapy and anti-EGFR monoclonal antibody (Mab) treatment improves the local control rate (LCR) and the overall survival rate (OS) for advanced NPC patients (3, 4).

Helical tomotherapy (HT) is an emerging IMRT technique that mounts a 6-MV linear accelerator on a ring frame around the accelerator bed (5). The couch passes axially through the center of the stand as it rotates to irradiate the target area. With the capacity to deliver highly conformal dose distribution and pretreatment setup verification (6), HT has achieved better results in the treatment of head and neck cancer (7). In September 2007, our center installed the first HT device in China and the initial observation showed that 3-year local relapse-free survival, nodal relapse-free survival and distant metastasis-free survival were more than 90%, and 3-year overall survival was more than 85% for NPC patients (8). Here, we present a retrospective analysis of long-term (10-year) outcomes and late toxicities of HT in 190 patients with NPC.

Materials and methods

Patient's characteristics

One hundred and ninety NPC patients, treated with Hi Art TomoTherapy system (Accuray, America) at our center between September 2007 and August 2012, were analyzed. All patients underwent nasopharyngeal and skull base computed tomography (CT) or magnetic resonance imaging (MRI), endoscopic evaluation, complete blood count, liver and kidney function tests, neck and abdomen ultrasound, and bone scan. Positron emission tomography (PET) is optional. The clinical stage was determined according to the UICC 2002 staging system. Table 1 summarizes patient characteristics. This study was conducted in accordance with the declaration of Helsinki. This study was conducted with approval from the Ethics Committee of the Chinese PLA General Hospital. Written informed consent was obtained from all participants.

Treatment

The definition of the targets, techniques of planning and the HT delivery were described previously (2). Briefly, the planning dose at D95 was prescribed to the gross tumor volume (pGTVnx) and positive lymph nodes (pGTVnd) at 70–74Gy, the high risk planning target volume (PTV1) at 60–62.7 Gy and the low risk planning target volume (PTV2) at 52–56 Gy, respectively, in 33 fractions. The irradiation was delivered once daily, 5 days per week. MVCT imaging was performed prior to each part of HT treatment to validate patient settings during HT treatment. MVCT image-guidance is the automatic and manual registration of MVCT images and planned CT images, based on bone and tissue anatomy.

Cisplatin-based chemotherapy with or without concomitant anti-EGFR Mab treatment was given to 129 patients, concomitant anti-EGFR Mab treatment without chemotherapy was given to 30 patients, and radiotherapy alone was given to 31 patients. Neoadjuvant chemotherapy includes 1–2 cycles of DP (docetaxel 75 mg/m^2, d1, cisplatin 80 mg/m^2, d1 and every 3 weeks) or a single DDP regimen. According to clinical stages, tolerance and economic status, concurrent chemotherapy and/or anti-EGFR Mab therapy were performed in one of the four modes: 1) cisplatin 80 mg/m^2, d1, every 3 weeks; 2) docetaxel 60 mg/m^2, d1 and cisplatin 60 mg/m^2, every 3 weeks; 3)

TABLE 1 Patient's characteristics.

Characteristics	Patients	
	Number	%
Age (median)	10-81(44)	
Male	144	75.8
Female	46	24.2
ECOG performance status		
0	57	30
1	113	59.5
2	20	10.5
UICC 2002 stage		
I	16	8.4
II	64	33.7
III	71	37.4
IV	39	20.5

cetuximab 250 mg/m^2 or nimotuzumab 200 mg, d1, every week; 4) cetuximab 250 mg/m^2 or nimotuzumab 200 mg, d1, every week and cisplatin 80mg/m^2, d1, every 3 weeks. Adjuvant chemotherapy consisted of 4~6 cycles of DP program. Each patient received no more than 6 cycles of chemotherapy (including neoadjuvant, concurrent and adjuvant modes).

Follow-up and evaluation of outcomes

Acute side-effects were investigated weekly and peak toxicities were recorded and graded according to the established RTOG/EORTC criteria and the Common Terminology Criteria for Adverse Events (Version 3.0) as described previously (8). Patients' follow-up examinations were conducted 1 month after the completion of radiotherapy, and then every 3 months for the first year, every 6 months in the second year, and annually thereafter. Late toxicity were evaluated and scored according to the Common Terminology Criteria for Adverse Events version 3.0 (9) (CTCAE 3.0).

Statistical analysis

The Kaplan-Meier method was used to analyze local recurrence-free survival (LRFS), lymph node recurrence-free survival (NRFS), distant metastasis-free survival (DMFS) and overall survival (OS). Different prognostic factors were analyzed by log-rank test and multivariate analysis was performed using Cox proportional hazards model. P<0.05 was considered significant. Statistical analyzes were performed using the SPSS software package (Version 22.0, SPSS Inc., an IBM Company; Chicago, IL, USA).

Results

Treatment outcomes

Case selection, follow-up and statistical analysis were done by two different researchers to ensure the accuracy of the data. The median follow-up was 145 months, ranging from 141 to 148 months from the start of radiation therapy. The median age of the patients was 44 years (range 10-81 years), and the ratio of females (n=46) to males (n=144) was 1:3. The details were shown in Table 1.

The 10-year LRFS, NRFS, DMFS, and OS were 94.0%, 95%, 86% and 77.8%, respectively. The 10-year OS and NRFS for patients with stage T1/2 and stage T3/4 were 81% vs.67% and 99%vs. 88%, respectively (c= 3.9, p= 0.01 and c= 10, p= 0.01). The 10-year LRFS, NRFS, DMFS and OS for patients with stage I/II were better than those with stage III/IV(p< 0.05). The 10-year NRFS and DMFS for patients with N0-1 were better than those with N2-3 (p< 0.05). No significant differences were observed in OS and LRFS, between the patients with N0-1 and N2-3 (p> 0.05) (Table 2; Figure 1).

Until the last follow-up, treatment failure was observed in 50 patients. Among these patients, 12 and 8 patients developed local and nodal failure, respectively, and distant metastasis occurred in 25 patients was the major failure pattern after treatment. Lung, bone and liver were the most common metastatic organs. Among the 50 failed patients, 6 patients died of local failure or regional failure and 20 patients died of multiple organ failure. In addition, Five patients (stage T3-4) died of primary pharyngeal vessel bleeding after the completion of radiotherapy, and 6 died of massive hemorrhage 1 year after radiotherapy. One patient died of cerebral hernia 9 months after the completion of radiotherapy. Otherwise, 2 patients died of other causes, one from systemic lupus erythematosus and one from gas poisoning. (Table 3).

Prognostic factors

The potential prognostic factors for OS, LRFS, NRFS, and DMFS included gender, age, T stage, N stage, and various chemotherapy and anti-EGFR Mab treatment patterns. Univariate analysis by log-rank test showed that age and N stage were significantly associated with DMFS, age and T stage were significantly associated with OS, T stage and N stage were significantly associated with NRFS, and clinical stage was significantly associated with LRFS, NRFS, DMFS and OS. (Table 2).

Multivariate analysis by Cox proportional hazards model showed that only the T stage was an independent predictor for NRFS (HR=13.9, 95%CI 1.72–5.2, p= 0.01).The clinical stage was an independent predictor for LRFS, DMFS and OS. And, age and concurrent chemotherapy were independent predictors for OS. (Table 4; Figure 2).

Late toxicities

The acute treatment-related toxicities were described previously (8). At the last follow-up visit, 139 patients could be evaluated for the late treatment-related toxicities, with 51 patients lost or died. Grade1~2 xerostomia, subcutaneous tissue fibrosis, hearing loss, and tooth sensitivity were the most common late toxicities. Two patients had loss of tooth, and 2 others had pulpitis and treated with surgical operation. No toxicity and side effects of grade 3 or above trismus, temporal lobe necrosis, cranial nerve palsy, and eyeball injury were found. The data of late treatment-related toxicities were listed in Table 5.

Discussion

Intensity-modulated radiotherapy (IMRT) has been demonstrated to be potentially less toxic and more effective than conventional radiation techniques, even achieved a survival benefit compared with three-dimensional conformal radiotherapy 3DCRT (10). The advent of helical tomotherapy (HT) as image-guided radiotherapy (IGRT) has offered the potential of improved target conformation and sparing of critical structures (11). HT is particularly suitable for NPC due to the irregular target volume and proximity of critical structures (12). In the previous study, we observed satisfactory short-term efficacy, with 3-year loco-regional control rate and DMFS of more than 95%, and 3-year OS was more than 85% in 190 NPC patients treated with HT (13), this study with long-term follow-up showed that 10-year local and regional

10.3389/fonc.2022.1083440

TABLE 2 Characteristics of 190 patients and univariate analysis of prognostic factors.

Characteristics	No. of patients	10-y LRFS (%)	P value	10-y NRFS (%)	P value	10-y DMFS (%)	P value	10-y OS (%)	P value
Sex									
Female	46	95	0.67	95	0.97	83	0.047	75	0.128
Male	144	93		95		95		87	
Age (y)									
<30	22	91	0.56	95	0.71	80	0.056	77.3	0.001
30-65	154	95		96		83		81.2	
≥65	14	96		86		59		42.9	
T classification									
T1-2	121	96.5	0.093	99	0.001	0.89	0.146	84.2	0.004
T3-4	69	90.5		88		0.82		66.7	
N classification									
N0	39	94.9	0.867	97	0.003	92	0.021	82.1	0.394
N1	69	94.2		98		89		79.7	
N2	70	94.3		95		85		77.1	
N3	12	91.2		73		55		58.3	
Concurrent chemotherapy									
Yes	89	94	0.885	96	0.894	86	0.959	82	0.21
No	101	95		95		84		73	
Anti-EGFR Mab treatement									
Yes	81	96	0.392	96	0.7	81	0.082	86	0.756
No	109	93		95		90		82	
Clinical stage									
I-II	75	98	0.041	99	0.015	95	0.007	89	0.002
III-IV	115	92		92		80		70	

control remained at about 95% at 10 years, while DMFS reduced to 86%, and OS to 77.8%.

In a phase III trial including 408 patients with stage III/IV NPC, were treated with conventional 2-dimensional radiotherapy, the 10-year DFS, LRFS, and OS were 66.9%, 80.8% and 49.5%, respectively (8). Han et al. reported that the 10-year LRFS, DFS and disease-specific survival (DSS) for NPC patients with stage II-III, treated with IMRT technique, were 92%, 83.4% and 78.6% respectively (14). In the present study, the 10-year LRFS, NRFS, DMFS and OS were 94%, 95%, 86%, and 77.8%, respectively, which were significantly higher than those reported in the era of conventional RT. The reason of our better results may be related to the inclusion of stage I-II patients, with stage I accounting for 8%. In our study, the 10-year DMFS and OS of stage III-IV patients were 80% and 76%; respectively. The 10-year LRFS for patients with stage I-II was better than those with stage III-IV (98% vs. 92%, p= 0.04). In a phase III trial, 230 NPC patients with stage II achieved excellent results, with the 10-year DFS, PFS and OS of 94%, 76.7% and 83.6%; respectively (15). HT provides a technical platform to increase the dose in tumor target volume, and represents better local control (16). Belgioia et al. reported that 2 and 4-year loco-regional control rates were 92.9% and 88.2%, respectively, and 4-year OS was 93.9% in advanced NPC patients treated by HT with simultaneous integrated boost (SIB) technique, and with a dose of 66Gy/30F to the primary tumor (17).

In our research, although the 10-year NRFS and OS in patients with stage T3-4 were worse than those with stage T1-2 ($p< 0.05$), No statistical difference was detected in multivariate analysis ($p>0.05$). The 10-year LRFS and OS in patients with negative node were better than those with metastatic nodes, although without statistical significance ($p>0.05$). The 10-year NRFS and DMFS in patients with stage N2-3 were worse than those with stage N0-1 ($p< 0.05$), but no statistical difference was detected in multivariate analysis ($p>0.05$). A review showed, in 610 NPC patients with stage N0 undergoing definitive radiotherapy to their primary lesion and prophylactic radiation to upper neck, the 5-year and 10-year regional failure-free survival could be 95.8% and 91.8%; respectively (17). Han et al. demonstrated that omitting bilateral or contralateral lower neck radiotherapy would be safe and feasible for NPC patients with stage N0-1, with the potential to reduce late toxicities, is a direction of reducing toxicity and increasing efficiency (18).

Distant metastasis has become the most common mode of treatment failure. According to previous literature reports (14), the 10-year distant metastasis rate was 16.6% (144/865). In our study, there were 25 cases of distant metastases, and the rate of distant metastases was 13.2%, which was consistent with previous research results and even lower. An advanced N stage has been shown to be one of the risk factors to predicting the occurrence of metastasis (19). This raises the question of how to select patients at high risk of distant metastases who would benefit from individual therapy to improve their OS. The results of the this study indicated that the 10-year DMFS for patients with negative node were better than those with positive node. The factor of the clinical stage was also associated with the risk of distant metastasis. Patients with a more advanced stage, especially those with T4N+ disease with intracranial or neural invasion, have a higher risk of lymph node metastasis and distant metastasis. T and N stage factors were associated with distant metastasis, although without statistical significance ($p>0.05$) in multivariate analysis. This may mean that the difference between the treatment and the patient itself has become a confounding factor in the analysis.

In this study, 12, 8 and 25 patients had developed local failure, lymph nodal failure and distant metastasis; respectively. Lung, bone and live were the most common metastatic organs. In addition, Five patients (stage T3-4) died of primary pharyngeal vascular hemorrhage within one year after radiotherapy. Six patients still died of massive nasal and laryngopharyngeal hemorrhage in long-term follow-up after radiotherapy, and one patients died of cerebral hernia 9 months after the completion of radiotherapy, meaning that pharyngeal vessel bleeding (primary or secondary) was one of the leading cause of death. On the premise of ensuring the effect of tumor control, the radiation dose protection, nutrition, flushing and closer follow-up may reduce the occurrence of such events.

TABLE 3 Pattern of failures and cause of deaths.

Variable	No. of patients
Pattern of failure	
Distant metastasis	25
Local and/or regional failures	18
Local failure alone	10
Regional failure alone	6
Local and regional failures	2
Distant and local/regional failures	4
Total	50
Cause of death	
Distant metastasis	20
Local or regional failure	6
Radiation-related complications	11
Other malignant tumors	1
Non-cancer causes	2
Unknown causes	2
Total	42

At present, radical radiation therapy alone is recommended to stage I NPC, additional chemotherapy with neoadjuvant, concomitant or adjuvant forms is recommended to loco-regionally advanced NPC (14). Meta-analyses showed that concomitant chemo-radiotherapy improves survival in patients with loco-regionally advanced NPC, but the specific benefits of adjuvant chemotherapy

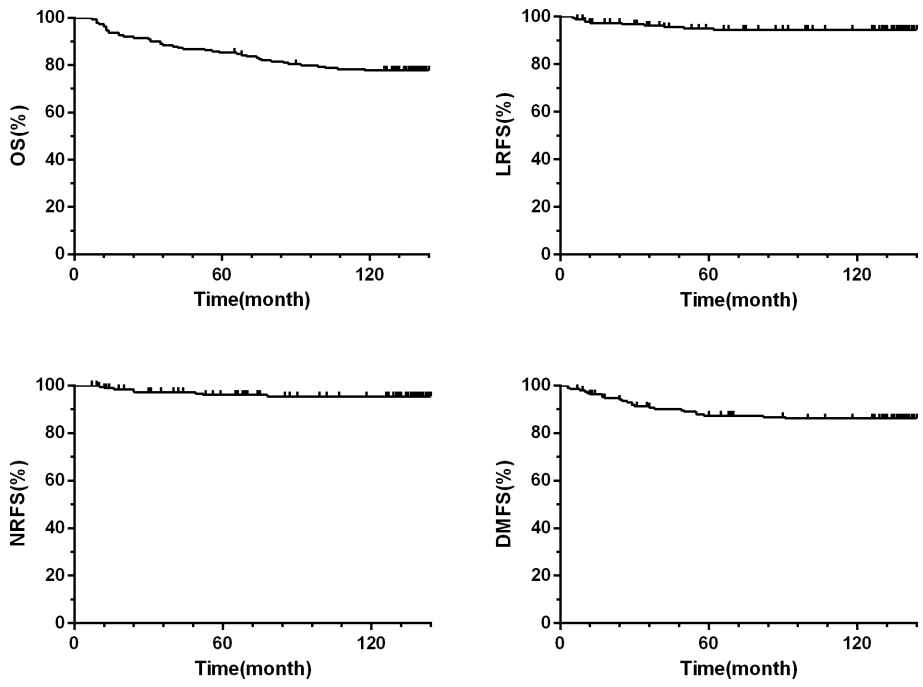

FIGURE 1
Kaplan-Meier estimate of local relapse-free survival (LRFS), nodal relapse-free survival (NRFS), distant metastases-free survival (DMFS), and overall survival (OS) rates.

10.3389/fonc.2022.1083440

TABLE 4 Multivariate analysis of prognostic factors for 190 patients.

	LRFS		NRFS		DMFS		OS	
Characteristics	HR (95%CI)	P value	HR(95%CI)	P value	HR (95%CI)	P value	HR (95%CI)	P value
Sex								
Male vs. female	1.25 (0.31 - 5.15)	0.75	1.28 (0.23 - 7.04)	0.774	0.29 (0.7 - 1.3)	0.09	0.5 (0.2-1.2)	0.121
Age (y)								
<30 vs. 30-65 vs. ≥65	8.1 (0.5 - 19.1)	0.96	0.214 (0.012 - 3.65)	0.28	0.21 (0.05 - 0.90)	0.01	3.1 (1.4-6.9)	0.005
T classification								
T1-2 vs. T3-4	0.7 (0.1 - 4.2)	0.7	13.9 (1.71 - 5.2)	0.01	0.95 (0.38 - 2.4)	0.92	1.26 (0.53-3.01)	0.59
N classification								
N0-1 vs. N2-3	0.13 (0.01 - 1.3)	0.08	3.01 (0.54 - 8.8)	0.21	0.74 (0.22 - 2.5)	0.62	0.82 (0.35-1.89)	0.63
Concurrent chemotherapy								
Yes or No	0.6 (0.14 - 2.44)	0.47	0.326 (0.06 - 1.6)	0.171	0.62 (0.26 - 1.5)	0.28	0.42 (0.21-0.82)	0.01
Anti-EGFR Mab treatement								
Yes or No	0.37 (0.08 - 1.66)	0.19	0.51 (0.10 - 2.49)	0.4	1.33 (0.57 - 3.1)	0.51	0.75 (0.4-1.41))	0.38
Clinical stage								
I+II vs. III+IV	6.4 (1.81 - 9.1)	0.02	4.8 (0.5 - 5.4)	0.96	3.9 (1.3 - 11.4)	0.01	5.5 (1.57-13.9)	0.01

after concomitant chemo-radiotherapy needs further study (20). Blanchard et al. analyzed data from 19 trials and 4806 patients and found that chemotherapy improved absolute overall survival by 6.3% over 5 years, and also improved progression-free survival, loco-regional control, distant control and reduced cancer mortality significantly (p <0.0001). The benefit of concomitant with or without adjuvant chemotherapy to radiation therapy was significantly (p=0.01), but not adjuvant chemotherapy alone or neoadjuvant chemotherapy alone. In this study, the 10-year OS in patients with concomitant chemotherapy group was better than that in the non-chemotherapy group in multivariate analysis (p<0.05).

n recent years, anti-EGFR Mabs such as cetuximab and nimotuzumab were applied as a concomitant therapy with radiation therapy for head and neck cancer (21). Bonner et al. (22)reported

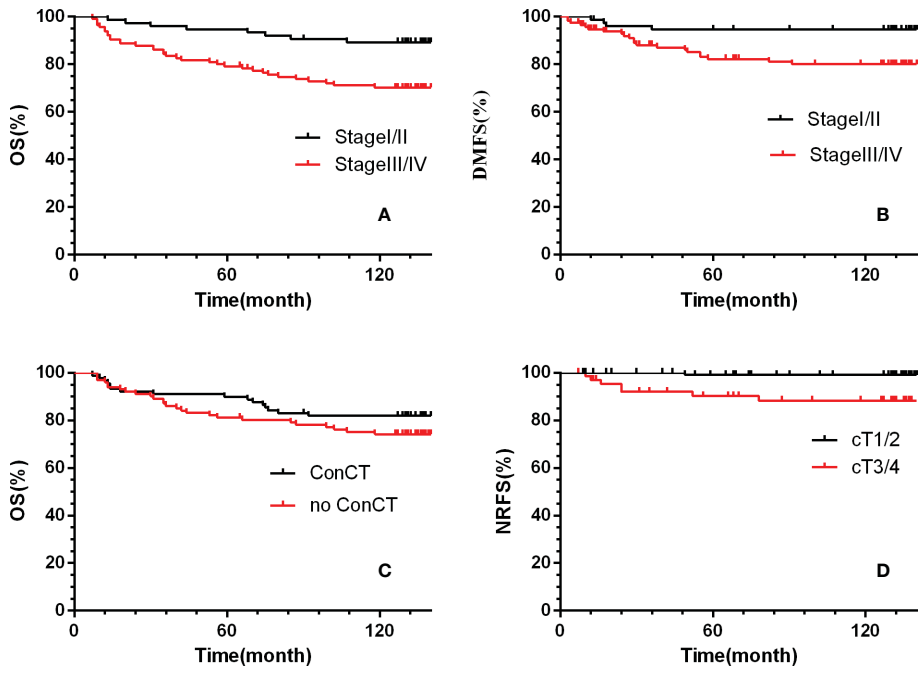

FIGURE 2
Kaplan-Meier survival curves for the two treatment groups. **(A, C)** overall survival, **(B)** distant metastasis-free survival, **(D)** nodal relapse-free survival. ConCT=concurrent chemotherapy.

TABLE 5 Late radiation related toxicities of 139 patients.

Late complications	No.of patients	
	Grade I/II	Grade III
Xerostomia	72	1
Hearing impairment	43	3
Subcutaneous fibrosis	63	10
Trismus	4	0
Temporal lobe necrosis	10	0
Cranial nerve palsies	34	0
Eyeball damage	22	0

significant improvement in survival in patients with non-NPC head and neck cancer when cetuximab was added to radiation therapy in a phase III trial. In the meta-analysis of Yuan et al. (23), anti-EGFR Mab combined with radiation therapy and/or chemotherapy improved the short-term therapeutic effect in NPC, but this benefit disappeared 1 year later. In this study, 81 patients (42.6%) had anti-EGFR Mab with HT and 30 (15.8%) with HT and chemotherapy, Unfortunately, only benefit in DMFS was detected, and without statistical significance ($p>0.05$). So the effect of anti-EGFR Mab combined with chemo-radiotherapy in NPC needs further investigations.

Huang et al. (24) reported that age and N stage were independent prognostic factors for OS, radiation dose was an independent prognostic factor for loco-regional control, and N stage was an independent prognostic factor for distant metastasis. In our update, age, concurrent chemotherapy and stage were independent prognostic factors for OS, which was consistent with the report.

Since the era of IMRT, the incidence of late grade 3 to 4 toxicities of xerostomia and neck fibrosis after radiotherapy was reduced to 16.7% and 8.3% (24). HT is a unique IMRT modality that can provide better conformity index, steeper dose gradient, shorter treatment time, and better protection of many organs at risk (OARs) especially for parotids (25).The acute treatment-related toxicities of HT in NPC treatment, which were relatively mild, In addition, the incidence of acute grade- 2 xerostomia was only 7.3% were described in our previous report (8). Belgioia et al. reported that the most significant acute toxicities were grade 2 or 3 mucositis (43%); grade 2 xerostomia was reported in 11 patients after 6 months from the end of treatment and downgrade to level 1 in 55% (6/11) patients within 12 months (6). At the last follow-up visit in our study, 139 out of 190 patients could be evaluated for the late treatment-related toxicities, xerostomia, subcutaneous tissue fibrosis, hearing loss, and tooth sensitivity were the most common late toxicities which were mainly scored as grade1 or 2. Two patients had tooth looseness, and 2 others pulpitis which needed surgical operation. It is worth noting that although the response to radiotherapy and chemotherapy is not significant, the incidence of massive bleeding complications of nasopharyngeal carcinoma in the follow-up study was 5.8%. Five cases occurred within one year after radiotherapy, and six cases occurred in long-term follow-up after radiotherapy. It suggests that the risk of major bleeding is still high for patients with late T stage and neck metastatic lymph node fusion surrounding blood vessels. During follow-up, attention should be paid to nasal cavity flushing and prevention.

There are several limitations of this study. First, the retrospective study affect the outcomes; second, patient distributions in our cohort were complex, I-IV, T1-4, N0-3 stages, which could affect the outcomes with confounding factors; third, synchronous and/or adjuvant chemotherapy, the nonuniformity pattern of combined chemotherapy could affect the outcomes of the study.

Conclusions

Helical tomotherapy with simultaneous integrated boost technique offered excellent long-term outcomes for NPC patients, with mild late treatment-related toxicities. Age and clinical stage was independent predictor of DMFS and OS. Further prospective study is needed to confirm the superiority of this technology and to evaluate the roles of anti-EGFR monoclonal antibody treatment.

Data availability statement

The original contributions presented in the study are included in the article/supplementary material. Further inquiries can be directed to the corresponding author.

Ethics statement

This study was conducted with approval from the Ethics Committee of the Chinese PLA General Hospital. Written informed consent was obtained from all participants.

Author contributions

LMe, FT, and QL made equal contributions to this work, participated in the design of the research, carried out research, made statistical analysis and drafted the manuscript. LMa conceived and designed the study and reviewed the manuscript. All authors read and approved the final manuscript.

Acknowledgments

The authors thank the staff of this study and all patients associated with this study.

Conflict of interest

The authors declare that the research was conducted in the absence of any commercial or financial relationships that could be construed as a potential conflict of interest.

Publisher's note

References

1. Liu Z, Xu C, Jiang R, Liu G, Liu Q, Zhou J, et al. Treatment of locally advanced nasopharyngeal carcinoma by helical tomotherapy: An observational, prospective analysis. *Transl Oncol* (2019) 12(5):757–63. doi: 10.1016/j.tranon.2019.02.011

2. Chen JL, Huang YS, Kuo SH, Hong RL, Ko JY, Lou PJ, et al. Intensity-modulated radiation therapy achieves better local control compared to three-dimensional conformal radiation therapy for T4-stage nasopharyngeal carcinoma. *Oncotarget* (2017) 8(8):14068–77. doi: 10.18632/oncotarget.12736

3. Blanchard P, Lee A, Marguet S, Leclercq J, Ng WT, Ma J, et al. Chemotherapy and radiotherapy in nasopharyngeal carcinoma: an update of the MAC-NPC meta-analysis. *Lancet Oncol* (2015) 16(6):645–55. doi: 10.1016/S1470-2045(15)70126-9

4. Liang R, Yang L, Zhu X. Nimotuzumab, an anti-EGFR monoclonal antibody, in the treatment of nasopharyngeal carcinoma. *Cancer Control* (2021) 28:1073274821989301. doi: 10.1177/1073274821989301

5. Van Gestel D, Van den Weyngaert D, De Kerf G, De Ost B, Vanderveken O, Van Laer C, et al. Helical tomotherapy in head and neck cancer: a European single-center experience. *Oncologist* (2015) 20(3):279–90. doi: 10.1634/theoncologist.2014-0337

6. Lee FK, Yip CW, Cheung FC, Leung AK, Chau RM, Ngan RK. Dosimetric difference amongst 3 techniques: TomoTherapy, sliding-window intensity-modulated radiotherapy (IMRT), and RapidArc radiotherapy in the treatment of late-stage nasopharyngeal carcinoma (NPC). *Med Dosim* (2014) 39(1):44–9. doi: 10.1016/j.meddos.2013.09.004

7. Thariat J, Bolle S, Demizu Y, Marcy PY, Hu Y, Santini J, et al. New techniques in radiation therapy for head and neck cancer: IMRT, CyberKnife, protons, and carbon ions. improved effectiveness and safety? impact on survival? *Anticancer Drugs* (2011) 22 (7):596–606. doi: 10.1097/CAD.0b013e328340fd2b

8. Du L, Zhang XX, Ma L, Feng LC, Li F, Zhou GX, et al. Clinical study of nasopharyngeal carcinoma treated by helical tomotherapy in China: 5-year outcomes. *BioMed Res Int* (2014) 2014:980767. doi: 10.1155/2014/980767

9. Trotti A, Colevas AD, Setser A, Rusch V, Jaques D, Budach V, et al. CTCAE v3.0: development of a comprehensive grading system for the adverse effects of cancer treatment. *Semin Radiat Oncol* (2003) 13(3):176–81. doi: 10.1016/s1053-4296(03)00031-6

10. Peng G, Wang T, Yang KY, Zhang S, Zhang T, Li Q, et al. A prospective, randomized study comparing outcomes and toxicities of intensity-modulated radiotherapy vs. conventional two-dimensional radiotherapy for the treatment of nasopharyngeal carcinoma. *Radiother Oncol* (2012) 104(3):286–93. doi: 10.1016/j.radonc.2012.08.013

11. Puebla F, Lopez Guerra JL, Garcia Ramirez JM, Matute R, Marrone I, Miguez C, et al. Effectiveness and toxicity of helical tomotherapy for patients with locally recurrent nasopharyngeal carcinoma. *Clin Transl Oncol* (2015) 17(11):925–31. doi: 10.1007/s12094-015-1328-5

12. Jeong S, Yoo EJ, Kim JY, Han CW, Kim KJ, Kay CS. Re-irradiation of unresectable recurrent head and neck cancer: using helical tomotherapy as image-guided intensity-modulated radiotherapy. *Radiat Oncol J* (2013) 31(4):206–15. doi: 10.3857/roj.2013.31.4.206

13. Huang PY, Zeng Q, Cao KJ, Guo X, Guo L, Mo HY, et al. Ten-year outcomes of a randomised trial for locoregionally advanced nasopharyngeal carcinoma: A single-institution experience from an endemic area. *Eur J Cancer* (2015) 51(13):1760–70. doi: 10.1016/j.ejca.2015.05.025

14. Tian Y-M, Liu M-Z, Zeng L, Bai L, Lin C-G, Huang S-M, et al. Long-term outcome and pattern of failure for patients with nasopharyngeal carcinoma treated with intensity-modulated radiotherapy. *Head neck.* (2019) 41(5):1246–52. doi: 10.1002/hed.25545

15. Li XY, Chen QY, Sun XS, Liu SL, Yan JJ, Guo SS, et al. Ten-year outcomes of survival and toxicity for a phase III randomised trial of concurrent chemoradiotherapy versus radiotherapy alone in stage II nasopharyngeal carcinoma. *Eur J Cancer* (2019) 110:24–31. doi: 10.1016/j.ejca.2018.10.020

16. Belgioia L, Bacigalupo A, Vecchio S, Marcenaro M, Pupillo F, Agostinelli S, et al. Excellent survival regardless of disease stage in patients with advanced nasopharyngeal cancer. *Tumori* (2016) 102(4):381–6. doi: 10.5301/tj.5000483

17. Sun J-D, Chen C-Z, Chen J-Z, Li D-S, Chen Z-J, Zhou M-Z, et al. Long term outcomes and prognostic factors of n0 stage nasopharyngeal carcinoma: a single institutional experience with 610 patients. *Asian Pacific J Cancer Prev APJCP.* (2012) 13(5):2101–7. doi: 10.7314/APJCP.2012.13.5.2101

18. Sun Z, Wang J, Huang R, Wang X, Chen C, Deng M, et al. Contralateral lower neck sparing radiotherapy in stage N1 nasopharyngeal carcinoma: Long-term survival outcomes and late toxicities. *Front Oncol* (2021) 11:628919. doi: 10.3389/fonc.2021.628919

19. Jiang C, Gao H, Zhang L, Li H, Zhang T, Ma J, et al. Distribution pattern and prognosis of metastatic lymph nodes in cervical posterior to level V in nasopharyngeal carcinoma patients. *BMC Cancer.* (2020) 20(1):667. doi: 10.1186/s12885-020-07146-z

20. Baujat B, Audry H, Bourhis J, Chan AT, Onat H, Chua DT, et al. Chemotherapy in locally advanced nasopharyngeal carcinoma: an individual patient data meta-analysis of eight randomized trials and 1753 patients. *Int J Radiat Oncol Biol Phys* (2006) 64(1):47–56. doi: 10.1016/j.ijrobp.2005.06.037

21. Hsu HW, Wall NR, Hsueh CT, Kim S, Ferris RL, Chen CS, et al. Combination antiangiogenic therapy and radiation in head and neck cancers. *Oral Oncol* (2014) 50 (1):19–26. doi: 10.1016/j.oraloncology.2013.10.003

22. Bonner JA, Harari PM, Giralt J, Cohen RB, Jones CU, Sur RK, et al. Radiotherapy plus cetuximab for locoregionally advanced head and neck cancer: 5-year survival data from a phase 3 randomised trial, and relation between cetuximab-induced rash and survival. *Lancet Oncol* (2010) 11(1):21–8. doi: 10.1016/S1470-2045(09)70311-0

23. Yuan C, Xu XH, Chen Z. Combination treatment with antiEGFR monoclonal antibodies in advanced nasopharyngeal carcinoma : a meta-analysis. *J Buon* (2015) 20(6):1510–7.

24. Chen B-B, Lu S-Y, Peng H, Sun F-F, Zhu J, Wang J, et al. Comparison of long-term outcomes and sequelae between children and adult nasopharyngeal carcinoma treated with intensity modulated radiation therapy. *Int J Radiat Oncol Biol Physics* (2020) 106 (4):848–56. doi: 10.1016/j.ijrobp.2019.11.035

25. Ren G, Xu SP, Du L, Feng LC, Qu BL, Liu HX, et al. Actual anatomical and dosimetric changes of parotid glands in nasopharyngeal carcinoma patients during intensity modulated radiation therapy. *BioMed Res Int* (2015) 2015:670327. doi: 10.1155/2015/670327

frontiers | Frontiers in Oncology

TYPE Clinical Trial
PUBLISHED 31 January 2023
DOI 10.3389/fonc.2023.1048593

OPEN ACCESS

EDITED BY
Lorenz Kadletz-Wanke,
Medical University of Vienna, Austria

REVIEWED BY
Chia-Jung Busch,
University of Greifswald, Germany
Marshall Posner,
Icahn School of Medicine at Mount Sinai,
United States

*CORRESPONDENCE
Stefano Cavalieri
stefano.cavalieri@istitutotumori.mi.it

SPECIALTY SECTION
This article was submitted to
Head and Neck Cancer,
a section of the journal
Frontiers in Oncology

RECEIVED 19 September 2022
ACCEPTED 10 January 2023
PUBLISHED 31 January 2023

CITATION
Cavalieri S, Vener C, LeBlanc M, Lopez-Perez L, Fico G, Resteghini C, Monzani D, Marton G, Pravettoni G, Moreira-Soares M, Filippidou DE, Almeida A, Bilbao A, Mehanna H, Singer S, Thomas S, Lacerenza L, Manfuso A, Copelli C, Mercalli F, Frigessi A, Martinelli E, Licitra L and BD4QoL Consortium (2023) A multicenter randomized trial for quality of life evaluation by non-invasive intelligent tools during post-curative treatment follow-up for head and neck cancer: Clinical study protocol.
Front. Oncol. 13:1048593.
doi: 10.3389/fonc.2023.1048593

A multicenter randomized trial for quality of life evaluation by non-invasive intelligent tools during post-curative treatment follow-up for head and neck cancer: Clinical study protocol

Stefano Cavalieri[1,2]*, Claudia Vener[2], Marissa LeBlanc[3,4], Laura Lopez-Perez[5], Giuseppe Fico[5], Carlo Resteghini[1], Dario Monzani[2,6,7], Giulia Marton[2,6], Gabriella Pravettoni[2,6], Mauricio Moreira-Soares[3], Despina Elizabeth Filippidou[8], Aitor Almeida[9], Aritz Bilbao[9], Hisham Mehanna[10], Susanne Singer[11], Steve Thomas[12], Luca Lacerenza[13], Alfonso Manfuso[13], Chiara Copelli[14], Franco Mercalli[15], Arnoldo Frigessi[3,4], Elena Martinelli[2], Lisa Licitra[1,2], and BD4QoL Consortium

[1]Head and Neck Medical Oncology Department, Fondazione Istituto di Ricovero e Cura a Carattere Scientifico Istituto Nazionale dei Tumori, Milan, Italy, [2]Department of Oncology and Hemato-Oncology, University of Milan, Milan, Italy, [3]Oslo Center for Biostatistics and Epidemiology, University of Oslo, Oslo, Norway, [4]Oslo Center for Biostatistics and Epidemiology, Oslo University Hospital, Oslo, Norway, [5]Universidad Politécnica de Madrid-Life Supporting Technologies Research Group, ETSIT, Madrid, Spain, [6]Applied Research Division for Cognitive and Psychological Science, IEO, European Institute of Oncology IRCCS, Milan, Italy, [7]Department of Psychology, Educational Science and Human Movement (SPPEFF), University of Palermo, Palermo, Italy, [8]Information Technology Programme Management Office, DOTSOFT, Thessaloniki, Greece, [9]DeustoTech, Faculty of Engineering, Universidad de Deusto, Bilbao, Spain, [10]Institute of head and neck studies and Education, University of Birmingham, Birmingham, United Kingdom, [11]Division of Epidemiology and Health Care Research, JGU - Johannes Gutenberg University, Mainz, Germany, [12]Division of Oral and Maxillofacial Surgery - Bristol Dental Hospital, University of Bristol - Bristol Medical School, Bristol, United Kingdom, [13]Maxillo-Facial Surgery, Fondazione IRCCS Casa Sollievo della Sofferenza, San Giovanni Rotondo, Italy, [14]Maxillo-Facial Surgery, Interdisciplinary Department of Medicine, University of Bari "Aldo Moro", Bari, Italy, [15]MultiMed Engineers srls, Parma, Italy

Patients surviving head and neck cancer (HNC) suffer from high physical, psychological, and socioeconomic burdens. Achieving cancer-free survival with an optimal quality of life (QoL) is the primary goal for HNC patient management. So, maintaining lifelong surveillance is critical. An ambitious goal would be to carry this out through the advanced analysis of environmental, emotional, and behavioral data unobtrusively collected from mobile devices. The aim of this clinical trial is to reduce, with non-invasive tools (i.e., patients' mobile devices), the proportion of HNC survivors (i.e., having completed their curative treatment from 3 months to 10 years) experiencing a clinically relevant reduction in QoL during follow-up. The Big Data for Quality of Life (BD4QoL) study is an international, multicenter, randomized (2:1), open-label trial. The primary endpoint is a clinically relevant global health-related EORTC QLQ-C30 QoL deterioration (decrease ≥10 points) at any point during 24 months post-

treatment follow-up. The target sample size is 420 patients. Patients will be randomized to be followed up using the BD4QoL platform or per standard clinical practice. The BD4QoL platform includes a set of services to allow patients monitoring and empowerment through two main tools: a mobile application installed on participants' smartphones, that includes a chatbot for e-coaching, and the Point of Care dashboard, to let the investigators manage patients data. In both arms, participants will be asked to complete QoL questionnaires at study entry and once every 6 months, and will undergo post-treatment follow up as per clinical practice. Patients randomized to the intervention arm (n=280) will receive access to the BD4QoL platform, those in the control arm (n=140) will not. Eligibility criteria include completing curative treatments for non-metastatic HNC and the use of an Android-based smartphone. Patients undergoing active treatments or with synchronous cancers are excluded.

Clinical Trial Registration: ClinicalTrials.gov, identifier (NCT05315570).

KEYWORDS

mHealth, android, head and neck cancer, QOL, BD4QoL, survivorship, unobtrusive

1 Introduction

Depending on disease stage, head and neck cancer (HNC) can be cured either with single modality or with multimodal treatments, consisting of various combinations of surgery, radiotherapy and chemotherapy. Despite treatment with curative intent, loco-regional recurrences and/or distant relapses are frequent. Moreover, these therapeutic approaches result in significant acute toxicities and late sequelae. Therefore, quality of life (QoL) is often impaired in these survivors. It is known that QoL is a prognostic factor because it is related to overall survival in cancer patients (1) and to loco-regional control in HNC patients (2). Published studies suggest that even though people having undergone treatment for HNC usually recover their global QoL by 12 months after treatment, persistent late sequelae are observed, notably poor physical functioning, fatigue, xerostomia and sticky saliva (3).

Three main validated QoL questionnaires will be used: EORTC QLQ-C30 for all types of malignancies (4), EORTC HN43 [an updated version of the formerly used H&N35 questionnaire (5)] for HNC patients only (6), EQ-5D-5L (7) which is a patient-reported measurement focused on five domains (mobility, self-care, usual activities, pain/discomfort, and anxiety/depression), that can be used for assessment of health status and also for health technology assessment (HTA) (8). Interestingly, in some subsets like nasopharyngeal carcinoma, differences in QoL are independent predictors of prognosis (9). In the context of patient-reported outcome measurements (PROMs), the cancer behavior inventory (CBI) (10) and its brief version (CBI-B) (11) are validated instruments aimed at measuring self-efficacy strategies for coping with cancer. Specifically, self-efficacy for coping with cancer is a psychosocial construct referring to people's beliefs about their capabilities of effectively executing behaviors that occur in the course of dealing with a cancer diagnosis, cancer treatments, and transitioning to survivorship (12). The results of a recent meta-analysis attest that cancer patients with higher coping self-efficacy report a higher quality of life (12). In the clinical and research contexts, the CBI-B represents a useful adjunct to other PROMs because it allows detection of cognitive changes in personal, control, and psychosocial adjustment and identification of patients who need further psychosocial services (11).

In order to minimize the risk of data misinterpretation and to maximize the precision and the accuracy in measuring QoL variations effectively, clinically meaningful differences in QoL scales have been suggested. In particular, when considering an overall indicator such as global health status according to EORTC QLQ-C30 a deterioration is considered clinically relevant if there is a reduction in at least 10 points of the score (13, 14).

Predictive factors for identifying which HNC patients are at higher risk of suffering long-term poor QoL have not yet been identified. To date, the only way we can work out if someone has poor long-term QoL is to administer repeated QoL questionnaires during follow-up. Avoiding QoL deterioration, even if temporary, is a critical clinical need. An ambitious goal would be to detect early variations in QoL (or in other measures potentially predicting later QoL deterioration) that translate into a tangible benefit (e.g., early diagnosis of incoming and evolving health status) that improves long-term QoL in HNC survivors. The combination of big-data analysis techniques and innovative use of information technology (IT) tools (e.g., smartphones) may allow targeted interventions to improve QoL. The results of a pilot study conducted on patients treated with palliative intent for gynecological cancers illustrated the potential benefits of such an approach (15). A mobile health intervention collecting both PROMs and activity data as a measure of health status was shown to be feasible and acceptable. Moreover, this was perceived to be effective in improving symptom management in patients with advanced gynecologic cancers. Most of the evidence on eHealth solutions in HNC patients is made of pilot or feasibility studies. The results of a non-blinded randomized controlled trial evaluating

Oncokompas, an eHealth application aimed at supporting self-management of symptoms and health-related quality of life in cancer survivors, including HNC, were published in 2020 (16). Oncokompas did not improve knowledge, skills, and confidence in self-management in cancer survivors. However, the median follow-up of patients included in this study was only 6 months (after treatment conclusion), thus possibly preventing the observation of late QoL declines in most subjects. The study included 185 HNC patients (99 in the intervention arm, 86 in control one) enrolled across 14 Dutch hospitals in 19 months. This means an average of 9 patients recruited per year per center. Only 68 out of the 99 (68%) HNC patients in the intervention arm, and only 64 out of the 86 patients (74%) in the control arm returned a second questionnaire after 6 months. Therefore, only 132 of the 185 HNC patients (71%) remained in the study. This means that a 30% drop-out was observed over a six-month period.

The main aim of the present study is to anticipate and reduce, with the use of the non-invasive Big Data for Quality of Life (BD4QoL) platform (described below), the proportion of HNC survivors experiencing a clinically relevant reduction in QoL. If the participants report or are identified as having a significant finding during monitoring, a specific set of interventions will be applied if symptoms and findings on monitoring indicate their application. This clinical trial was designed and set up in the framework of the BD4QoL research project (full project title "Big Data Models and Intelligent tools for Quality of Life monitoring and participatory empowerment of head and neck cancer survivors"), that lasts 5 years and is funded by the European Commission (further details are specified in Section 7) (17). The BD4QoL Consortium is an interdisciplinary partnership made of several partners from seven European Countries, combining the complementary competences, skills, structural and infrastructural capabilities.

The adoption of mobile technologies of everyday use (i.e., embedded into standard mobile phones) for behavior reconstruction and linkage of behavior modifications to quality of life indicators, and the realization of predictive models for quality of life modifications will allow seamless and unobtrusive data capture over time, making the execution of clinical investigations more precise and less burdensome as compared to standard (manual) data capture. Artificial intelligence (AI) algorithms, including Machine Learning, Transfer Learning, Deep Learning-Based Models, Knowledge-Based Activity Models (Expert Activity Models – EAM) for behavior patterns recognition, IBM Watson technologies for affective computing such as Tone Analyzer, Natural Language Classifier, Natural Language Understanding, will be used.

2 Methods and analysis

2.1 Study objectives and endpoints

The overall aim of this study is to assess if QoL deterioration can be anticipated and prevented by the addition of the BD4QoL platform to standard of care (SoC) versus SoC alone, in HNC survivors post-treatment with up to 24-month follow-up. Primary and secondary objectives and endpoints are specified in Table 1, exploratory ones in Table 2.

2.2 Study design

This is a multicenter, international, two-arm, randomized (2:1 ratio), open-label, superiority trial, designed to evaluate the proportion of HNC survivors experiencing a clinically meaningful QoL deterioration [reduction of at least 10 points in EORTC QLQ-C30 global health status (13, 14)] between at least 2 visits during post-treatment follow-up (up to 24 months from randomization) with the use of the BD4QoL platform through the web-forms tool for QoL questionnaires answers and through continuous monitoring by a mobile application (App) installed on the study subject's mobile phone in comparison to those

TABLE 1 Study objectives and endpoints.

	Objective	Endpoint
Primary	To reduce the proportion of HNC subjects experiencing a clinically meaningful deterioration of QoL between at least 2 visits during post-treatment follow-up.	The proportion of HNC survivors experiencing a clinically relevant deterioration in the global health scale of the EORTC QLQ-C30 [decrease ≥10 points, as defined in (13,14)] within the study observation (up to 24 months) period during post-treatment follow-up.
Secondary	To delay the time to the first clinically meaningful deterioration of QoL between at least 2 visits during post-treatment follow-up.	The time to first clinically relevant deterioration of EORTC QLQ-C30 global score [decrease ≥10 points, as defined in(13,14)] measured within the study observation (up to 24 months) period during post-treatment follow-up.
	To reduce the proportion of HNC subjects experiencing a clinically relevant deterioration in pre-specified QoL domains between at least 2 visits during post-treatment follow-up.	The proportion of HNC survivors experiencing a clinically meaningful deterioration [as defined in (13,14)] of pre-specified EORTC QLQ-C30 scales (emotional functioning, role functioning, sleep) within the study observation (up to 24 months) period during post-treatment follow-up.
	To reduce the proportion of HNC subjects experiencing a clinically meaningful deterioration in pre-specified head and neck cancer specific QoL domains between at least 2 visits during post-treatment follow-up.	The proportion of HNC survivors experiencing a clinically relevant deterioration of pre-specified EORTC QLQ-HN43 scales (swallowing, problems with teeth, problems opening mouth, speech, social eating, fear of progression, emotional functioning, fatigue) within the study observation (up to 24 months) period during post-treatment follow-up.
	To reduce the proportion of HNC subjects experiencing a clinically meaningful deterioration in health status between at least 2 visits during post-treatment follow-up.	The proportion of HNC survivors experiencing a clinically meaningful deterioration [as defined in (7)] of EQ-5D-5L domains (mobility, self-care, usual activities, pain/discomfort, anxiety/depression) within the study observation (up to 24 months) period during post-treatment follow-up

TABLE 2 Exploratory objectives and endpoints.

Exploratory objective	Exploratory endpoint
To assess the association of clinically relevant variations in QoL [EORTC QLQ-C30 and HN43 global scores (13, 14)] with disease recurrence and survival in HNC survivors within the study observation (up to 24 months) period during post-treatment follow-up.	Association of disease-free survival (DFS), event-free survival (EFS) and overall survival (OS) with clinically relevant variations (either increase or decrease, as appropriate according to scales) of EORTC QLQ-C30 and HN43 questionnaires, as defined in (13, 14).
To To analyze time-dependent variations of QoL (EORTC QLQ-C30 and HN43 scores) within the study observation (up to 24 months) period during post-treatment follow-up in HNC survivors assessing their association with recurrence and survival.	Association of disease-free survival (DFS), event-free survival (EFS) and overall survival (OS) with time-dependent clinically relevant variations (either increase or decrease, as appropriate according to scales) of EORTC QLQ-C30 and HN43 questionnaires, as defined in (13, 14).
To To analyze QoL scores (EORTC QLQ-C30 and HN43 scores) within the study observation (up to 24 months) period during post-treatment follow-up in nasopharyngeal cancer patients assessing their association with recurrence and survival.	Association of disease-free survival (DFS), event-free survival (EFS) and overall survival (OS) with clinically relevant variations (either increase or decrease, as appropriate according to scales) of EORTC QLQ-C30 and HN43 questionnaires, as defined in (13, 14), in nasopharyngeal carcinoma patients.
To reduce the proportion of HNC subjects experiencing a clinically meaningful deterioration in pre-specified EORTC QLQ-HN43 scales (not included in secondary endpoints) between at least 2 visits during post-treatment follow-up.	The proportion of HNC survivors experiencing a clinically meaningful deterioration [as defined in (13, 14)] of pre-specified EORTC QLQ-HN43 scales (pain in the mouth, problems with senses, body image, dry mouth and sticky saliva, coughing, social contact, neurological problems, sexuality, problems with shoulder, skin problems) within the study observation (up to 24 months) period during post-treatment follow-up.
For HNC survivors randomized in the BD4QoL platform group, using artificial intelligence techniques to build models to predict a QoL deterioration [EORTC QLQ-C30 and HN43 scores, EQ-5D-5L as defined in (7, 13, 14)] between at least 2 visits during within the study observation (up to 24 months) period during post-treatment follow-up.	The association of all the health-related data recorded by the BD4QoL platform Supplementary Material registered continuously within the study observation (up to 24 months) period during post-treatment follow-up with clinically relevant variations (either increase or decrease, as appropriate according to scales) of EORTC QLQ-C30 and HN43 questionnaires, as defined in (7, 13, 14)
To assess the association of clinically relevant variations of QoL [EORTC QLQ-C30 and HN43 global scores (13, 14)] with self-efficacy for coping with cancer in HNC survivors within the study observation (up to 24 months) period during post-treatment follow-up.	Association of clinically relevant variations (either increase or decrease, as appropriate according to scales) of EORTC QLQ-C30 and HN43 questionnaires, as defined in (13, 14), and self-efficacy for coping with cancer, defined as mean of the item scores at the CBI-B (11).
To reduce the proportion of HNC subjects experiencing a clinically meaningful deterioration of QoL between at least 2 visits during post-treatment follow-up, stratifying according to patients completing treatment within 12 months versus after 12 months.	The proportion of HNC survivors experiencing a clinically meaningful global health-related EORTC QLQ-C30 QoL deterioration [decrease ≥10 points, as defined in (13, 14)] within the study observation (up to 24 months) period during post-treatment follow-up. Stratification according to timing after study completion (less than 12 months versus more than 12 months)
To assess the economic impact on HNC survivor care and the viability, usability, and trust of using the BD4QoL platform (Health Technology Assessment, HTA).	Incremental Cost-Effectiveness Ratio measured in €/QALY. Measures of viability, usability, and trust.

without the BD4QoL platform (SoC). If a clinically relevant deterioration in global health, measured with the EORTC QLQ-C30 global health scale [decrease ≥10 points, as defined in (13, 14)] is detected during the study period, the subject participation in the study will be interrupted (because the aforementioned decrease would imply that the primary endpoint is not met for a specific participant).

Patients will be followed up as per clinical practice (18, 19):

a. All subjects will be asked to complete validated questionnaires [EORTC QLQ-C30 (4), QLQ-HN43 (6), and EQ-5D-5L (7), CBI-B (11)] and PREM on up to 5 occasions over a 2-year period, at randomization (0-month of follow-up), then once every 6 months ± 2 months (after 6, 12, 18, 24 months from randomization).

b. Participants in both arms will be offered routine SoC and asked to complete validated QoL questionnaires at regular intervals (described above). In addition, those in the intervention arm will be offered the device-generated data collection platform (BD4QoL device *plus* QoL validated questionnaires *plus* counseling and physician contact triggered by the data generated by the platform [early intervention] *plus* a possible psychological effect of the whole activities in the interventional arm). A 2:1 randomization will be used (2/3 of subjects with BD4QoL platform versus 1/3 of subjects without). Participants randomized to the control arm will not receive the above-mentioned platform; they will fill in the same validated questionnaires on web-based instruments and will be followed up as per usual clinical practice.

The study design is summarized in Figure 1. The choice of unequal randomization in randomized controlled trials is rarely resorted to. The main reasons for its justification have been reviewed by Dibao-Dina et al. (20): obtaining more safety data, exposing fewer patients to the potentially inferior group, increasing patients acceptability, reducing costs.

In this scenario, the 2:1 ratio was chosen for the following reasons: i) the study devices are deemed to be safe and able to provide timely monitoring of participants health status, thus 1) possibly improving their condition as compared to the control group and 2) minimizing the number of patients not exposed to this potential benefit; ii) the platform acts unobtrusively, and it favors contact with healthcare professional which is normally very well accepted and pursued by patients; moreover it is designed to allow for patients' empowerment; iii) we anticipate that costs associated with SoC not supported with the BD4QoL platform will be superior because subjects randomized in the intervention arm are deemed to experience less adverse events than controls. In this context, a cost-effectiveness analysis is planned as an exploratory endpoint (Table 2).

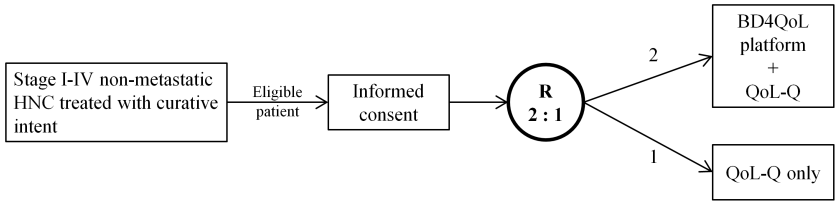

FIGURE 1
Study design of the randomized controlled trial.

As stated by Palmer et al., favoring the experimental therapy is warranted in trials of potentially significant public health benefit (21). Unequal allocation schemes can improve recruitment and partially satisfy the individual ethics criterion (the study participants have a higher probability of being randomized in the intervention arm than in control one). They can also be useful if widespread knowledge about the control therapy already exists and if more understanding is desired about the new treatment.

The randomization procedure will be web-based, centralized, computerized (software-generated randomization list using RedCap web-based platform) (22, 23). Local research teams will be blinded to the randomization list (local people designated to the randomization procedure will not know the randomization list, but clinical investigators will not be blinded to the outcome of the randomization). The biostatistician doing the analysis of the trial will be blinded to the list as well until the statistical analysis plan, previously defined, is signed.

The EORTC QLQ-C30 (4), EORTC QLQ-HN43 (6), EQ-5D-5L (8), and CBI-B (11) evaluations will be performed at 0-, 6-, 12-, 18-, 24-month from randomization. The time zero is considered to be the date of randomization. The scores of the EORTC QLQ instruments [as defined in (13, 14)] will be compared to the respective scores of the previous study time-point.

2.3 Study population

Each participating Center (recruiting patients in Italy and the United Kingdom) will enroll consecutive patients according to the eligibility criteria listed below.

2.3.1 Inclusion criteria

1. Effectively cured histologically defined head and neck squamous cell carcinoma (HNSCC) from one of these subsites: oral cavity, nasopharynx, hypopharynx, larynx, Human Papillomavirus (HPV)-positive or negative oropharynx, nasal cavity, paranasal sinuses. Non-metastatic salivary gland cancer (SGC) of any histological type can be included only if curative or postoperative radiotherapy included the neck:
    a. For p16-negative or p16-unknown HNSCC (including nasal cavity and paranasal sinuses), stage I, II, III, IVa or IVb (no IVc) according to UICC/AJCC 8th edition. Regional neck metastases from squamous cell carcinoma from unknown primary head and neck sites are allowed.
    b. For nasopharyngeal cancer (NPC), stage I, II, III, IVa (no IVb) according to UICC/AJCC 8th edition. Regional neck metastases from EBV-positive carcinoma from unknown primary head and neck sites are allowed.
    c. For SGCs, stage III, IVa or IVb according to UICC/AJCC 8th edition treated with radiotherapy that included the neck (either post-operative radiation or radical treatment in case of unresectable disease).
    d. For p16-positive oropharyngeal squamous cell carcinoma, stage I, II or III according to UICC/AJCC 8th edition. Regional neck metastases from p16-positive and/or HPV-positive squamous cell carcinoma from unknown primary head and neck sites are allowed.
2. Patients having completed treatment with curative intent (including any single modality or multimodal approach) within 10 years at the time of accrual.
3. Patients being disease-free at the time of accrual. Patients will be deemed in complete remission if the clinical examination is negative for recurrence; clinical examination should be preferably, but not mandatorily, integrated with unequivocal radiological imaging that shows the absence of disease (in case of doubt, further radiological imaging should be performed or integrated with cyto/histological samples of the area with suspected disease persistence and the exams will have to be consistently negative) after at least three months following treatment completion.
4. Ability to fill in questionnaires as per protocol.
5. Geographical accessibility and willingness to be followed-up for up to 2 years with information-technology (IT) devices in addition to questionnaires.
6. Age ≥ 18 years.
7. Signed informed consent.
8. Willingness to use their smartphone and their Internet access for the study.
9. Smartphone having the following minimum characteristics:
    1. RAM: Minimum of 2 GB
    2. Storage: Minimum of 512 MB free storage
    3. Operating system: Android version 7 (Nougat) or upper.

2.3.2 Exclusion criteria

1. Distant metastases (the following populations are excluded: stage IVc HPV-negative HNSCC and SGC, stage IV p16-

positive oropharyngeal squamous cell carcinoma, stage IVb NPC).
2. Thyroid cancers, non-melanoma skin cancers (e.g. squamous cell carcinoma of the skin, skin basal cell carcinoma, skin adnexal carcinoma), and non-carcinoma HNC (e.g. melanoma, sarcoma, etc.) are excluded.
3. Subjects with previous malignancies (except localized non-melanoma skin cancers, and the following *in situ* cancers: bladder, gastric, colon, esophageal, endometrial, cervical/dysplasia, melanoma, or breast) unless a complete remission was achieved at least 5 years prior to study entry AND no additional therapy is required during the study period. Premalignant lesions (e.g., leukoplakia, erythroplakia, lichen etc.) are allowed.
4. Participation in clinical trials with other experimental agents within 30 days of study entry or concomitant treatment with experimental drugs.
5. Patients unable to comply with the protocol, in the opinion of the investigator.
6. Any known or underlying medical conditions that, in the opinion of the investigator, could adversely affect the ability of the participating subject to comply with the study.
7. Having a smartphone operating system other than Android.

2.4 Instruments

2.4.1 Questionnaires

The EORTC QLQ-C30 is composed of both multi-item scales, including functional scales, symptom scales, a global health status/QoL scale, and single-item measures. Each of the multi-item scales includes a different set of items. Each item is represented once in each scale, meaning that no item occurs in more than one scale (24).

All scales and single-item measures range in score from 0 to 100. A high scale score represents a higher response level. Thus, a high score for a functional scale represents a high/healthy level of functioning, a high score for the global health status/QoL represents a high QoL, but a high score for a symptom scale/item represents a high level of symptoms/problems.

The principle for scales scoring is the same:

1. Estimate the average of the items that contribute to the scale (raw score).
2. Use a linear transformation to standardize the raw score (ranging from 0 to 100); a higher score in the function scales represents a higher ("better") level of functioning, or a higher score in the symptom scales a higher ("worse") level of symptoms.

The EORTC QLQ-HN43 (an update of QLQ-H&N35) is meant for use in head and neck cancer patient populations varying in disease stage and treatment modality (i.e. surgery, chemotherapy and radiotherapy). It should always be complemented by the EORTC QLQ-C30. As described for EORTC QLQ-C30, all scales and single-item measures of EORTC QLQ-HN43 range in score from 0 to 100.

The EQ-5D-5L is a standardized measure of health status developed by the EuroQol Group in order to provide a simple, generic measure of health for clinical and economic appraisal (25).

The EQ-5D-5L consists of the EQ-5D-5L descriptive system and the EQ Visual Analogue Scale (EQ VAS). The descriptive system comprises five dimensions (mobility, self-care, usual activities, pain/discomfort, anxiety/depression). Each dimension has five levels: no problems, slight problems, moderate problems, severe problems, and extreme problems. The respondent is asked to indicate his/her health state by ticking (or placing a cross) in the box against the most appropriate statement in each of the five dimensions. This decision results in a 1-digit number expressing the level selected for that dimension. The digits for 5 dimensions can be combined in a 5-digit number describing the respondent's health state. It should be noted that the numerals 1-5 have no arithmetic properties and should not be used as an ordinal score. The EQ VAS records the respondent's self-rated health on a 20 cm vertical visual analog scale with endpoints labeled 'the best health you can imagine' and 'the worst health you can imagine'. This information can be used as a quantitative measure of health as judged by the individual respondents (26).

The Cancer Behavior Inventory - Brief (CBI-B) was developed as a measure of self-efficacy strategies for coping with cancer, based on self-regulation and self-efficacy theories (11). It consists of 12 items (rated 1 = not at all confident to 7 = totally confident) and was derived from the longer version of the Cancer Behavior Inventory (CBI) (10, 27). The CBI-B represents a comprehensive and valid brief measure of self-efficacy for coping with cancer that could be easily used as a PROM. It has a consistent factor structure across several types of cancer and established good psychometric qualities (28). The CBI-B total score can be computed by averaging single item scores through arithmetic mean and, thus, ranges in value from 1 to 7.

2.4.2 BD4QoL platform

In the BD4QoL project, the opportunities linked to mobile-health (mHealth) and digital phenotyping (29) will be used to continuously monitor QoL trajectories in HNC patients and to detect early related events that need further attention from patients, clinicians, or both.

The BD4QoL platform consists of a set of services to allow patient monitoring and empowerment through two main tools: a Point of Care (PoC) web application to manage all patients' data and follow-up by clinical investigators, and a mobile application (App) installed on participating subject's smartphone. Also, a web-form tool is delivered to allow the QoL questionnaire completion.

A preliminary feasibility and users acceptability assessment has been performed at the Istituto Nazionale dei Tumori in Milan, Italy (unpublished, data not shown). This preliminary survey has outlined the preferences of users in terms of mobile technologies to be adopted (mobile phones preferred as compared to home and wearable sensors/devices). Moreover, a pilot study was performed on healthy volunteers to measure the accuracy, precision, and uniformity of data collected by the different mobile phones used by the study participants. The acceptability and usability of the platform were assessed as well within the same preliminary pilot study (data not shown).

To achieve the study objectives, the BD4QoL platform will collect the following data which will be used to identify behavioral and affective traits associated with study outcomes.

Sensors in mobile phones will provide the following readings (further details in Supplementary Material):

- Accelerometer (x,y,z measurements).

- Global Positioning System - GPS (Lat, Long).
- Ambient light (measurement of light in the room/area where the mobile device is located).
- Screen (Status ON or OFF for smartphone device screen).
- Activity (type of activity with which the person engages, which can be one of these: Still, Walking, Running, On_Bicycle, In_Vehicle)
- Daily connections to wifi networks (naming of wifi connections as well as corresponding duration).

The following data are detected from the mobile device's operating system:

- Phone usage logs (total count and timestamps of three types of events – incoming, outgoing and missed calls – with encrypted [that is hashed] collection of associated personal identifiable information, as well as total count and timestamps of incoming and outgoing/replied text messages).
- Phone applications usage (identification and seconds or minutes of total and detailed usage of any smartphone applications the study participant is using; for certain specific social media network or communication mobile apps, more specific information, that is as duration of app usage per day, is collected based on participant's permissions; these social applications include Facebook, Messenger, Whatsapp, Telegram, Viber, Zoom, Instagram; no information about the people with whom communication is made nor the content of the communication is collected).

The following data are collected from external datasets:

- Steps (daily and per hour number of steps completed through connection to external dataset from Google Fit cloud).
- Identification of places (Points of Interest) visited, based on participant's permissions, through the correlation of one's GPS signal (per day and minute) with external datasets from Foursquare and OpenStreet maps.

The above data will be used to infer activities and behaviors which have a high likelihood of being meaningfully related to participants' QoL trajectories. A list of such activities and behaviors, with an indication of the technical methods to be used for reconstruction as well as an assessment of reliability, is presented in Supplementary Material.

The BD4QoL App, available for Android (Figure 2), as listed above, will be able to collect and store information about the following domains: mobility, physical activity, activities of daily living, instrumental activities of daily living, socialization, cognitive function, health-related activities as well as personal affective data (further details in Supplementary Material). A summary of the findings and the supporting data will be available to the patient and clinical investigators (e.g., physicians, nurses), through a dashboard available on mobile devices for patients and through the PoC web application for clinical investigators. The data collected by the mobile App will not be available to the technology manufacturer and will be transferred in quasi-real-time (i.e., as soon as a connection for data transfer is available) to the central BD4QoL repository.

In the interval between visits, study participants, allocated in the intervention arm, will be able to interact electronically with a chatbot (implementation based on IBM Watson technology), which will be part of the BD4QoL App. The chatbot is an application based on a conversational user interface (30) to empower patients to manage their QoL and health under the supervision of clinical investigators. The chatbot will have a series of electronic coaching (e-coaching) functions that include: (i) dialogue management that allows the patient to be counseled by chatting electronically in a structured and effective way; (ii) management of two-way communications with healthcare professionals [e.g., for the patient to request specific support in case of special needs, or for the chatbot to invite the patient for a visit in case of an early detection of health-related QoL (HRQoL) deterioration or health issues; identified people will have to be listed on the delegation log by the Principal

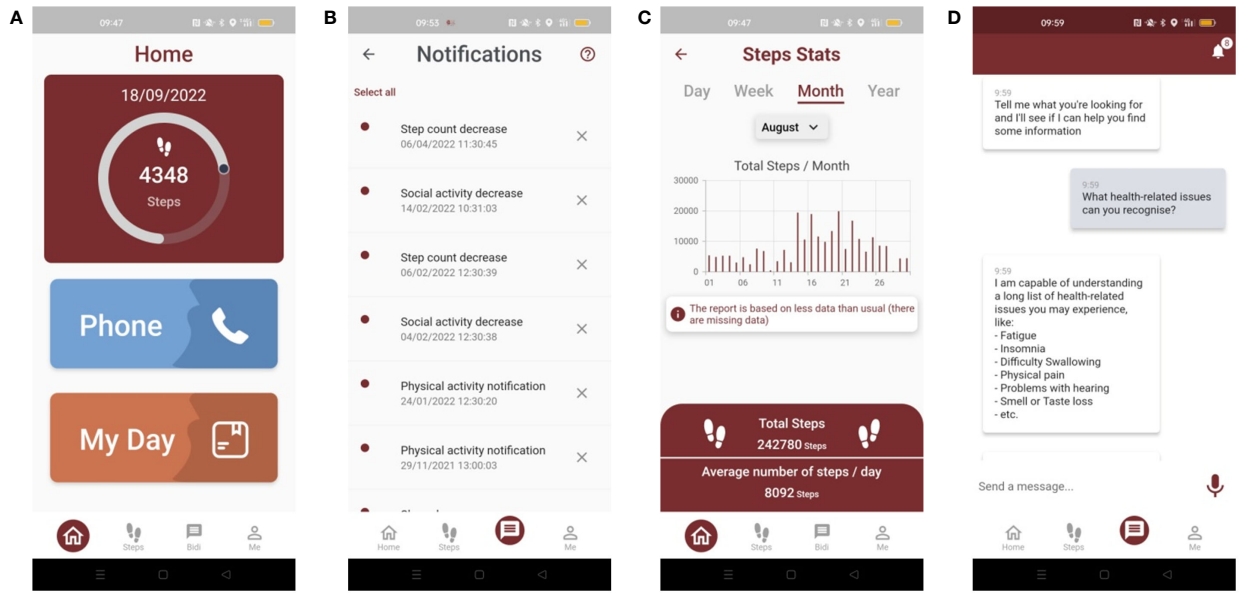

FIGURE 2
Screenshot of the BD4QoL study mobile app: **(A)** homepage, **(B)** notification dashboard, **(C)** monthly statistics of step count, **(D)** example of BiDi chatbot conversation.

Investigator (PI)]; (iii) detection of affective traits embodied in the e-coach/patient dialogue, through sentiment analysis and emotion analysis technologies to infer information about the participant mood (details about data privacy are reported in the specific section of this protocol). The latter element can be used to both re-adapt the chatbot counseling strategy as well as to provide additional information on the subject's mood to clinical investigators. The adverse events that the chatbot will be able to recognize will be the following: fatigue, malaise, fever, excessive sleepiness, difficulty sleeping, depression, change in social circumstances, neck swelling, facial pain, difficulty breathing, nose bleeds, difficulty speaking, dry mouth, tooth loss, muscle weakness, ear pain, difficulty hearing, tinnitus, vertigo, nausea, diarrhea, constipation, difficulty seeing, dry eye, eye pain, nervous eyelid, eye floaters, swollen eye, bleeding eyes, eye-watering, sexuality issues, weight loss, difficulty swallowing, mouth sores, appetite loss, difficulty opening mouth, difficulty eating, increased sensitivity to smells, no taste. Further details about adverse events and potential chatbot responses are reported in Supplementary Table 2.

The platform will provide the investigators with real-time data on device usage (e.g., number and type of alerts and chatbot interactions by pts), and it will integrate the electronic case report forms (eCRF) as a study monitoring dashboard through the PoC web application.

The BD4QoL platform used in this trial is not to be considered a medical device and is used for experimental assessment only. No drugs will be suggested by the automated chatbot responses. Tips provided by the chatbot regarding detected symptoms are also not to be considered clinical advice by any means and should not be a substitute for conversations with a member of trained medical personnel. A relevant disclaimer in this sense is also clearly shown by the chatbot itself to the study participant.

2.5 Sample size calculation and statistical plan

2.5.1 Sample size

The primary endpoint is the proportion of HNC survivors experiencing a clinically relevant deterioration in global health-related QoL as previously defined.

In the European BD2Decide project (31), funded by the Horizon 2020 program and concluded in November 2019, the analysis of QoL questionnaires was performed on over 450 stage III-IV HNSCC patients (recruited from Italy, Germany, and the Netherlands; data cut-off date 23rd September 2019): at least two consecutive EORTC QLQ-C30 questionnaires filled in after at least 6 months of follow-up were available for 117 patients; among them, a clinically meaningful deterioration of QoL (reduction of at least 10 points) was observed in 22 (19%) cases during post-curative treatment follow-up.

The second historical cohort comprised 65 patients from Mainz (Germany) having EORTC QLQ-C30 questionnaires completed 24 and 36 months after curative surgery (32). In this population, the percentage of subjects experiencing a deterioration ≥ 10 points in EORTC QLQ-C30 global health status from the 24th to the 36th months after treatments was 23%.

In the Head and Neck 5000 project (UK) (33) repeated global health scores at 12 and 36 months after treatment were available for 1241 people with HNC. A clinically meaningful deterioration of QoL (reduction of at least 10 points) was observed in 18% of these subjects.

In these three existing studies, the average percentage (arithmetic mean) of HNC patients experiencing a clinically meaningful deterioration of EORTC QLQ-C30 global score (reduction of at least 10 points) during follow-up was 20% (19% BD2Decide, 23% Mainz, 18% HN5000). These findings are preliminary and will be explored further as part of the European Union (EU) program supporting this study.

The primary endpoint of this study is the proportion of patients showing a reduction of at least 10 points in EORTC QLQ-C30 global health status score in HNC survivors. Therefore, considering the null hypothesis (H_0) of no difference for the primary endpoint, the proportion of HNC survivors showing a reduction of at least 10 points in EORTC QLQ-C30 global health status during 24-month FU in the control group is 20% (μ_0), as derived from the historical benchmark data.

Considering the alternative hypothesis (H_1), the desired proportion of HNC survivors showing a reduction of at least 10 points in EORTC QLQ-C30 global health status during FU in the intervention group is 10% (μ_1).

The minimal clinically relevant difference (δ) [superiority randomized controlled trials (RCTs)] between the null hypothesis (H_0) of no difference and the alternative hypothesis (H_1) is 10%. We fixed the significance level ($\alpha = 0.05$, one-tailed) and the power ($1\text{-}\beta = 0.80$, at least). It has been calculated a group sample sizes of 112 subjects (the control group) and 224 subjects (the intervention group) will result in 80% power ($1\text{-}\beta$) to detect a difference of 10% between the null hypothesis (H_0) that both group proportions are 20% and the alternative hypothesis (H_1) that the proportion in group under study is 10%, using a one-sided chi-squared test (χ^2 test) (Mantel-Haenszel test) and with a significance level of 0.05 (α, one-tailed) (PASS Sample Size 2020 statistical software).

With a supposed drop-out of 20%, it has been calculated a group sample size of 140 subjects (the control group) and 280 subjects (the intervention group), for a total cohort of 420 participants.

The data will be published in clinicaltrials.gov and will be reported to study PIs and to the Funding Authority. The protocol writing committee will have the final decision regarding study termination.

2.5.2 Evaluable cases for primary endpoint

For the purposes of analysis, the study populations are defined in Table 3.

2.5.3 Questionnaires (both intervention and control arms)

For the primary endpoint, a randomized patient will be considered evaluable given that at least two QoL questionnaires have been completed with the following timing: timing between 2 questionnaires ≥ 6 months as long as the study participant is disease-free.

2.5.4 BD4QoL platform (intervention arm only)

The primary endpoint will be analyzed based on intention to treat. In addition to the criteria described in point 6.2.1, a study subject randomized in the intervention arm will be considered for the per-protocol analysis, if the BD4QoL platform is turned on for at least 70% of daily hours (non-sleep activity, as defined in Supplementary Table 1).

TABLE 3 Populations for analysis.

Population	Description
All screened	All participants who sign the informed consent form.
Intent-to-treat (ITT)	All randomized participants whether or not the randomized intervention was administered. This population will be based on the study intervention to which the participant was randomized and will be the primary population for the analysis of efficacy data.
Per-protocol	All randomized participants completing at least two QoL questionnaires 6 months apart, as long as the study participant is disease-free. Participants will be analyzed according to the intervention they actually received.

2.5.5 Data collection

At study entry, the following data will be collected and recorded in the electronic case report form (eCRF): date of signed informed consent, gender, marital status, education, date of primary tumor diagnosis, comorbidity (ACE27), baseline body mass index (BMI), age at primary tumor diagnosis, primary tumor site (International Classification of Diseases for Oncology, ICD-O code), HPV and/or p16 status (mandatory if primary tumor site = oropharynx), serum plasma Epstein-Barr Virus (EBV)-DNA (optional if primary tumor site = nasopharynx), EBER (EBV Encoded small RNAs) on tumor specimen (optional if primary tumor site = nasopharynx), Baseline (pre-treatment) cTNM staging[19] (AJCC/UICC VIII edition), details about surgery, radiotherapy, systemic therapy, date of treatment completion.

At each follow-up, the following data will be collected and recorded in the eCRF: date of consultation, timing after treatment completion (first follow-up; +6 months; +12 months; +18 months; +24 months; other), BMI, disease status (recurrence; date of recurrence; site of recurrence: loco-regional and/or distant and/or second primary tumor), new non-cancer-related medical events [Medical Dictionary for Regulatory Activities (MedDRA)], grade of non-cancer-related medical events according to CTCAE (Common Terminology Criteria for Adverse Events) version 5.0, date of onset and resolution of non-cancer-related medical events, intervention for non-cancer-related medical events (no intervention; surgery; rehabilitation; medical intervention, if yes, to be specified according to Anatomical Therapeutic Chemical Classification System [ATC]; Psychological intervention; other).

2.5.6 Statistical plan

A comprehensive statistical plan will be prepared, discussed, and consented with the study team after data collection is completed and before the data analysis starts. The current plan is as follows: descriptive statistics will be generated for all clinical characteristics and outcome measures as appropriate (for continuous variables: sample size [n], mean, standard deviation, median, minimum, maximum, kurtosis, skewness; for categorical variables: frequency, percentage). All the analyzes will be performed using the ITT population and per-protocol. Missing data will be considered as lack of data. An analysis of missingness will be performed to understand whether there is relevant selection bias and appropriate methods to handle missing data will be applied according to the plausibility of the missingness mechanisms in the data.

The full sample size is expected to be accrued in an 18-month period. An interim analysis (only for checking patient number) will be performed after 12 months from the study start. If at least 50% of the planned population (≥210 subjects) have been randomized within the first 12 months of recruitment, the trial will continue with no modifications. Otherwise (randomized patients ≤ 209 patients in the first 12 months of study conduction), the BD4QoL Consortium will discuss, plan and agree strategies to foster patient recruitment, and eventually ask the funding Institution for a project extension. In case of any change in the clinical study protocol, a major amendment to the protocol will be submitted to the Ethical Committees of the participating sites.

All the analyzes, summaries, listings will be carried out using SAS statistical software (SAS version 9.4 of the SAS System, SAS Institute Inc., Cary, NC, USA). All statistical models will be fitted with SAS statistical software (SAS version 9.4 of the SAS System, SAS Institute Inc., Cary, NC, USA).

Sample size calculation was performed with PASS statistical software (PASS Sample Size 2020 - NCSS, LLC).

2.6 Study procedures

2.6.1 Consent and accrual

The study will be conducted once approval is granted by Local Ethical Committees, which will include consent to re-use administrative healthcare system data (in the informed consent patients will be asked whether in addition to the collection of clinical data from notes and other clinical sources they agree with the use of national registries (applicable for Italian Region of Lombardy), to collect further information in case they are lost to follow up) and access to data collected from mobile devices, sensors and other existing datasets for future research. Patients will be asked to sign an informed consent form that will allow them to accept or decline to participate and to use the developed monitoring tools. The informed consent will also include the possibility to share de-identified data according to *General Data Protection Regulation (*GDPR) and the results of their QoL questionnaire, which will be anonymized and made freely available on a public repository after study conclusion (e.g., Elixir network).

In this research study, the data that will be collected will be the minimum data set necessary to address the study endpoints, optimizing data quality, and participant privacy.

2.6.2 Healthy volunteers

Before starting the study recruitment, at least 20 healthy volunteers (either researchers or collaborators) will have been enrolled for beta-testing of the app outside this clinical study.

2.6.3 Quality of life data and follow up information

Quality of life information related to enrolled participants will be collected through validated questionnaires: EORTC QLQ-C30 and EORTC QLQ-HN43. Health status will be measured using the EQ-5D-5L, coping behavior using the CBI-B, and one PREM. Specifically, the PREM will be a study-specific question, asking patients "Are you satisfied about the care you have received during the follow-up?" (the possible answers will be "Absolutely disagree (I am not satisfied at all)", "Moderately disagree", "Neither agree nor disagree", "Moderately agree", "Absolutely agree (I am very satisfied)"). Questionnaires will be collected at study entry and after 6-, 12-, 18-, 24-month from randomization.

Patients' follow-up information will be collected after treatment termination and will be updated at each evaluation. Data related to the disease outcome (overall survival, OS; disease-free survival, DFS) will be collected up to 24 months from randomization (Table 4).

2.6.4 Timing of QoL questionnaires completion, PROMs and PREM

Upon informed consent signature, at study entry, participants will complete baseline QoL questionnaires and will be randomized to receive the study BD4QoL platform or not. During their follow-up, which will be conducted according to international guidelines [e.g., ESMO (18, 19)], participants will complete further QoL questionnaires as scheduled in the study flowchart reported in Table 4: at randomization; +6 months ± 2 weeks from randomization; +12 months ± 2 weeks from randomization; +18 months ± 2 weeks from randomization; +24 months ± 2 weeks from randomization.

2.6.5 QoL questionnaire data entry and data retrieval

The completion of study questionnaires will be performed the same day of the outpatient consultation ± 2 weeks, using web-based forms available at participating Centers or remotely, e.g., through tablets or personal computers (PC). QoL data will be accessible to clinical investigators, and to patients whenever asked.

If the subject does not go to the clinical institution for an outpatient visit or is not being seen every 6 months (± 2 weeks), the investigators will contact the patient by phone asking to fill in the requested questionnaires through the same web-based forms. The PoC dashboard will notify the investigators with an alert 2 weeks after the "due date" if any questionnaire has been initialized but has not been completed.

2.6.6 Electronic alerts and subsequent interventions

As anticipated in the introduction, if the participants report or are identified as having a significant finding during monitoring, a specific set of interventions will be applied. This is particularly important since this study is not simply identifying potential problems which would lead to decrement in quality of life it is also about intervening in an earlier stage before the quality of life decrement takes place and thus maintaining quality of life. Among the data collected by the BD4QoL App (Supplementary Materials), physical activity (measured through step count), non-sleep activity (through sensor-based data), and social activities (measured as phone usage and movements as recorded by smartphone GPS) will be analyzed on a daily basis, and their variations will be used to activate alerts that will be sent to the study participant through the chatbot integrated into the mobile application, and to the PoC web application (Supplementary Materials). Based on the activated alerts, specific interventions will follow:

- Based on the behavior alteration: after the first behavior alteration is identified, the chatbot is activated and the alert is recorded in the PoC, without any notification to the clinical investigator. If the same alteration occurs again and the patient has a health issue, the alert is generated and notified in the PoC. If the same alteration occurs by the third time, the alert will be generated and notified in the PoC, independently of whether the patient has answered or not to the chatbot.
- Based on symptom identification: after the first symptom is reported, the chatbot is activated. If the symptom has low priority, the alert will be recorded at PoC without notifying the clinical investigator; if the same symptom occurs once more, the chatbot is activated again, and it will ask the patient whether they would like their healthcare provider to be notified; after the third iteration of the symptom, a notification to the PoC will be sent.

TABLE 4 Study flowchart.

Procedure/evaluation	Randomization	Continuous (up to 24 months from study entry)	Months +6, +12, +18, +24 (± 2 weeks)
Informed consent	✓		
Baseline evaluation	✓		
Randomization	✓		
Demographics	✓		
Concomitant medications and medical events review	✓		✓
Clinical data retrieval (stage, pathology, HPV status)	✓		
Physical/emotional/social monitoring apps	✓	✓*	✓
QoL questionnaires	✓		✓

*for intervention arm only.

The iteration count is advanced only for consecutive events linked to the same domain and symptom.

2.6.7 Study interruption and withdrawal

Participation in the study will be interrupted in case of any of the following conditions apply: death; disease recurrence; diagnosis of second primary malignancy; referred to another center; unable to perform follow-up visits (e.g., due to comorbidities); the participant asked to exit the trial, but allowed the research team to keep patients' data that they already have collected to be used for research analysis; the participant withdrew his/her consent to the whole study, and wants his/her data to be deleted forever for any future analysis; the participant withdrew his/her consent to the whole study, and wants his/her data to not be used for any future analysis.

Moreover, the participant will discontinue the study when a decrease ≥10 points of global health-related EORTC QLQ-C30 QoL [clinically meaningful deterioration, as defined in (13, 14)] is detected between two questionnaires completed 6 months apart. This will be considered an event for the primary endpoint.

2.6.8 Data management workflow

Within the BD4QoL platform, the data collection process is done at different levels:

- Clinical data. CRF data from REDCap.
  - Data collected at study entry, after every 6 months (+/- 2 weeks) and also at unplanned visits that may occur during the trial.
  - CRF data formats are also included in Supplementary Materials.
  - Data is transferred at the moment of data entry from REDCap to the central BD4QoL repository.
  - Data managers will be provided with credentials to access the REDCap tool for data entry. Different roles will be assigned depending on the person's access (e.g., possibility to edit a patient, to lock a form, etc.). User accounts are managed directly through REDCap.
- PoC management: alerts generated, actions performed for alerts, patient enrollment and follow-up details, clinical visits report
  - Data collected during the trial, when a new patient comes, and once an event occurs.
  - PoC data-related formats are included in Supplementary Materials.
  - No data transfer is needed as data is directly stored in the central BD4QoL repository.
  - Healthcare professionals will be provided with credentials to access the PoC tool. User accounts are managed through the authentication server allocated in the BD4QoL platform. Different roles can also be assigned.
- QoL questionnaires. Study questionnaires are delivered through web-form.
  - Data collected at study entry, after each 6 months (+/- 2 weeks) and also at unplanned visits that may occur during the trial.
  - Answers of this questionnaire will be stored in the central BD4QoL repository as raw data, and the scoring of the questionnaires will also be stored in the same location.
  - No data transfer is needed as data is directly managed in the central BD4QoL repository.
  - User access for patients is based on the same credentials for the user accounts created at PoC. Only patients with authorized accounts are able to fill in the web form questionnaires. Physicians (with their PoC accounts) will also be able to fill answers on their patients' behalf, to deal with exceptional circumstances such as the patient has filled in the questionnaire on paper for some reason (i.e., internet breakdown not letting the completion of the web-based forms).
  - Healthcare professionals will assist patients if needed in the process of filling in the web forms.
- Patients' physical, social and non-sleep domains through mobile App (further details are reported in Supplementary Tables).
  - Data collected every day or every minute, depending on data category.
  - Data formats for each domain are in Supplementary Materials.
  - No data transfer is needed as data is directly stored in the central BD4QoL repository.
  - The patients will install two applications, the foreground application for continuous passive data collection and the main BD4QoL mobile application, using the credentials from their user accounts, as set at PoC. Only authorized accounts stored in the central BD4QoL repository will be able to login and fill in the mobile app.

2.6.9 Data monitoring and data quality assurance

Data quality procedures have been devised to ensure data verification and data validation. Data verification activities are used to monitor whether the mobile technology under study actually measures the data it claims to measure (i.e., steps, activities, light, phone usage information, and such). Data validation assures that the collected and subsequently processed data are "right": they need to be suitable for the objective for which they are being collected.

During the CRF definition, data quality procedures for clinical data have been defined to ensure dependencies between variables and coherence during the data collection process through REDCap. In REDCap, all data dependency and consistency rules will be implemented. A complete data collection report with all the rules implemented and the issues found (if any) will be amended by clinical center data managers and updated in REDCap forms. The implementation of these validated rules will ensure the integrity of

the data collection. Data will be transferred to the central BD4QoL repository once entered in the REDCap server. The central BD4QoL repository undergoes a periodical backup process to safeguard its content.

2.6.10 Data security

The Data will be safely transferred and stored in the central BD4QoL repository hosted by Partner INETUM (Murcia, Spain). The central BD4QoL repository consists of a Data Hub managing the various databases needed to ensure the functioning of the BD4QoL platform. The Data Hub features processes that allow integrating, enriching, analyzing, and subsequently disseminating information based on the needs of different actors (details in Supplementary Materials):

- In the acquisition layer there are different tools that guarantee the incorporation of the data, regardless of their origin, volume, digital format, in a standardized format. This acquisition layer will provide mechanisms capable of making massive loads of datasets required by the project.
- A central set of databases, as well as their data management mechanisms inherent in each solution, make up the storage layer of the system. This set of databases is governed by the applications processes providing a set of algorithms, rule engines and analytics.
- The security of the system is provided as an additional layer, transverse to the system, which exposes the information and operations only and exclusively after it has validated an authorized access.
- The communications used for the exchange of messages between the system's applications are done using the Hypertext Transfer Protocol Secure (HTTPS) protocol over the Transmission Control Protocol (TCP). The TCP protocol natively includes features such as error checking and acknowledgement interchange between peers, which means that if data is corrupted or not received, it is resent by the sender to ensure that it is received correctly. The BD4QoL Data Hub is deployed in the datacenter that INETUM has located in Murcia, Spain. This datacenter has tier IV certification, meaning that it includes capabilities to ensure data safety and availability. The characteristics of this datacenter at different levels are detailed in Supplementary Materials.
- For the cloud, specific backup and disaster-recovery policies are foreseen in case of corruption or detection of errors.
- For the mobile App, it is possible to identify if some data are missing at the stage of data collection. If this happens, it would be impossible to reconstruct the past in a digital form. If data are collected but the transmission to the cloud shows anomalies, such as data not transmitted when needed, but after a delay, specific scripts are foreseen to allocate the data in a way close to reality.

The above-mentioned technical measures ensure the integrity of the data collected in the BD4QOL platform, assuring that neither any corruption nor any data loss will occur. INETUM will not use patients' data for purposes outside this research study.

Daily backups of the BD4QoL databases will ensure data reconstruction. The mobile apps have a data log (timestamp) for data collected and transmitted to the Data Hub. The main challenges faced here involve the following two challenges:

1. Data from the mobile device not fully collected due to failure of the process: the mobile app can perform a procedure to detect when data collection has stopped. This can happen in various situations, such as the device being offline, orwith insufficient memory space to locally store the collected data, or that the stream listeners for the sensors have unexpectedly stopped, or that connection to a 3rd party physical activity data collection app (e.g., Google fit) is stopped. Although "backend" procedures can detect after a certain period of time that data collection has been stopped, it is not possible to "reconstruct" past behaviors and thus all collected data from the past.
2. Data from the mobile app not adequately transmitted to the Data Hub: The mobile app involves a procedure to detect whether data from the mobile device are adequately transmitted to the Data Hub.

    a. If no data is transmitted, this may be due to failure to connect to the Internet. When the mobile device is connected to the Internet, then the transmission will be restored.
    b. In case of connection availability but data is not transmitted to the Internet, then these may be transmitted "all at once", due to several issues specific to the mobile device itself. In this case, a "micro service" has been included to "allocate" the collected data to the estimated "right timestamps".

2.7 Study management

2.7.1 Patients' data protection and privacy

All data within BD4QoL shall be handled using tools and processes with 'privacy by design' as the mindset. In general, the security principles of "need to know" and "least privilege" will be applied while determining access rights and privileges. The project will share data, with applied internal encryption, with the subject's local identifier recorded in a hashed ID code. The list matching patient personal data and study ID will be stored offline in the clinical center which collects the data, which will manage it in compliance with relevant local legislation (e.g., some UK centers will store this document on a restricted access drive on their hospital NHS IT system). The personal data will remain at the recruiting center and will not be sent to the BD4QoL project team.

Participating hospitals are responsible for maintaining the anonymity of participants' data collected from the medical notes and for safely storing and preventing unnecessary access to any information which may disclose the patient's identity. The provisions of the above-mentioned GDPR will be adopted or – if more restrictive – national regulations in matters of personal data protection and privacy. Sensitive data (e.g., date of birth, date of diagnosis, date of follow-up visits, date of recurrence, date of death) will be used to track health-related data and will not be registered or used for the analysis

Data that leaves the participant's phone will be: activity, non-sleep, telephone usage.

For those who provide a specific consent, the following data will be added to the list of data leaving the phone: visiting places related with sports, eating/drinking, nutrition, shopping, medication, traveling, finances, culture, religion, self-care, spirituality, education, sentiment, depression, or heath.

Details about how these data will be recorded by the BD4QoL platform are provided in Supplementary Materials.

A specific data protection impact assessment (DPIA) was provided by PI and the Data Protection Office (DPO) of the Study Sponsor (INT, Milan, Italy) on the 25th June 2021, before the Ethical Committee approval.

2.7.2 Access to data and database protection

Clinical investigators (the local PI and the delegated sub-investigators) will be allowed through an authorization list to access clinical and study-generated data from patients recruited at their own Center. Access to patient's data, both anonymized and for clinical use (identifiable, as per current clinical practice), will only be granted according to each hospital regulations and restrictions (i.e., only authorized personnel that has been granted access by the patient or healthcare operators in charge of emergency interventions), and then local hospital regulations will be applied. Nonclinical study investigators will be able to access only pseudonymized data (both clinical and device-generated). Upon request, the investigators might access raw and processed unidentifiable data in the framework of the exploratory analyses mentioned above.

2.7.3 Source data and patient's files

For the eCRF completion, the source documents will be the medical records where the available demographic and medical information of a patient has to be documented. It should be possible to verify the inclusion and exclusion criteria for the study from the available data in this file. It must be possible to identify each patient by using this patient file. Additionally, any other documents with source data, especially original printouts of data that were generated by technical equipment, have to be filed. All these documents have to bear at least patient identification and the printing date to indicate to which patient and to which study procedure the document belongs. The medical evaluation of such records should be documented as necessary and signed/dated by the investigator.

2.7.4 Investigator site file and archiving

The investigator will be provided with an Investigator Site File (ISF) at the start of the study.

This file contains all relevant documents necessary for the conduct of the study. This file must be safely archived after the termination of the study.

It is the responsibility of the investigator to ensure that the patient-identification sheets are stored for 10 years beyond the end of the clinical study (defined as last patient out). All original patient files must be stored for the longest possible time permitted by the regulations at the hospital, research institute, or practice in question. If archiving can no longer be maintained at the site, the investigator will notify the Sponsor/Representative of the Sponsor.

2.7.5 Data management after study end

The investigator must retain all study records and source documents for the maximum period required by applicable regulations and guidelines or institution procedures, whichever is longer (minimum 5 years). The investigator must contact the coordinator Center prior to destroying any records associated with the study. If an Investigator of a participating Center withdraws from the study (e.g., relocation, retirement), the records shall be transferred to a mutually agreed upon designee (e.g., another investigator, IRB). Such transfer shall be reported in writing and notified to the Coordinating Center and to each Ethical Committee of the participating Centers.

Trial participants assure that the key design elements of this protocol will be posted in a publicly accessible database such as clinicaltrials.gov. In addition, upon study completion and finalization of the study report, the results of this study will be either submitted for publication and/or posted in a publicly accessible database of clinical study results. Patients will be informed of this option during the informed consent procedure.

2.7.6 Quality assurance and safety

This study is to be conducted in accordance with the ICH Note for Guidance on Good Clinical Practice (ICH, Topic E6, 1995) dated July 17, 1996.

The representatives of the Clinical Quality Assurance Team of the sponsor are permitted to inspect the study documents (study protocol, case report forms, study medication, original medical records/files), as well as representatives of national regulatory authorities. All patient data shall be treated confidentially. In line with ICH GCP guidelines, monitoring will be the responsibility of the study sponsor, and it will include the verification of data entered in the eCRFs against original patient records. This verification will be performed by direct access to the original patient records and the monitoring staff guarantees that patient confidentiality will be respected at all times. The study protocol, each step of the data-recording procedure, and the handling of the data, as well as the study report, shall be subject to monitoring activities. Audits can be conducted to assure the validity of the study data.

Each participating site will maintain appropriate medical and research records for this trial, in compliance with Section 4.9 of the ICH E6 GCP, and regulatory and institutional requirements for the protection of confidentiality of subjects.

The Principal Investigator is responsible for ensuring that all staff involved in the study are familiar with the content of the protocol and trained regarding study procedures. Moreover, all the investigators involved in the trial are responsible for patient safety, and all events potentially related to patients' safety must be reported in a timely, accurate, and complete manner.

3 Discussion

HNC survivors face many difficulties in implementing self-management in their daily life (34) (e.g. grappling with having to self-manage, interpreting self-management) and must fight personal, health-related and structural barriers (e.g. access to appropriate health services). They exhibit highly individualized approaches to self-management that often fail to meet their own specific needs. This has obvious impacts on

their health, anxiety and QoL and even more on healthcare and social costs. GPs and welfare services are not fully included into HNC post-treatment management nor have direct and coordinated links with the specialists engaged in survivors' follow-up at the cancer center. Physicians have limited insight on patients' perceptions of QoL, based on few data collected during follow-up visits from patients' interviews and – depending on hospital workflow – through structured Patient Reported Outcomes/Patient Reported Experience Measurement questionnaires (PROM/PREM) that measure body functions and health and psychological symptoms In this context, PoC specialists can only intervene when a late effect is reported or clinically diagnosed. So far, individual QoL trajectories have not been studied. Physicians are therefore applying standardized follow-ups which may delay recognition of late effects, and thus effective treatment.

The BD4QoL study is aimed at avoiding the deterioration of all HNC survivors, independently of the site of origin of their disease. Although the range of recommendations included in the chatbot is the same for all patients, we anticipate that the conversations will differ based on primary tumor site. However, the primary endpoint is the same for all HNC patients: preventing a clinically meaningful deterioration in subjectively-recorded global health status. This is still an unmet need for all HNC patients, and with this project we did not want to miss the opportunity to reach this ambitious goal avoiding a fraction of HNC survivors due to their primary tumor site. To reduce the heterogeneity of the patient cohort, we decided not to include patients with mucosal melanoma (also for their very high risk of recurrence), sarcoma, lymphoma, and thyroid cancers.

Understanding and addressing individual survivor's needs, interpreting signs and symptoms of survivors' health and psychological status is paramount in head and neck cancer where timely interventions can make the difference in individual patient's QoL (35). However, despite instruments and tools for QoL monitoring, such as e-PROMs/e-PREMs (36), have demonstrated effectiveness for QoL improvement, difficulties and barriers hinder their practical use.

In the context of patient counseling, unsolved problems are the following:

- Healthcare professionals do not have the time that would be needed to counsel patients properly. Slots for outpatient visits are pre-specified and usually their duration is insufficient to efficiently capture the global survivors' status. The standard oncological follow-up visit should mainly be focused on recognizing disease recurrence and/or major treatment-related late toxicities Indeed counselling is delivered within this scenario. All non-cancer and/or treatment related issues are referred to general practitioners.
- They do not have easily at hand the information that would be needed to counsel patients properly. The variety and the severity of reported signs and symptoms are so wide that they exceed the oncologists' knowledge to effectively counsel patients, except for the classical and expected outcomes.
- They are not able to provide patients counselling with the necessary continuity. Between visits, patients are referred to general practitioners and specialists from other disciplines. Given this type of health care organization there is a substantial interest in creating and implementing cancer survivorship care as the one that can be offered in survivor's clinics.
- Lack of information technology literacy may constitute a significant barrier for patient communication, self-management and coping strategies.

In this project, we aim to address survivors' and physicians' needs and to overcome the cultural, psychological organizational and technological barriers to systematic and coordinated monitoring of HNC survivors' QoL.

Big data analysis might pave the way to new innovation-technology (IT) tools that leverage artificial intelligence (AI) techniques (e.g. machine learning) to infer more meaningful information from patients' follow-up after treatment.

In this context, the writing of this protocol followed the EQUATOR (Enhancing the QUAlity and Transparency Of health Research) guidelines for clinical trial protocols for interventions involving artificial intelligence (the Standard Protocol Items: Recommendations for Interventional Trials – Artificial Intelligence, SPIRIT-AI Extension) (37) and according to the Clinical Trials Transformation Initiative (CTTI checklist) (38).

4 Ethics and dissemination

4.1 Protection of individuals/patients enrolled in the trial

The responsible Principal Investigator will ensure that this study is conducted in compliance with the protocol, following the instructions and procedures described in it, adhering to the principles of Good Clinical Practice and with current local legislation, and in accordance with: General Data Protection Regulation (GDPR), ICH (International Council for Harmonisation) Harmonized Tripartite Guidelines for Good Clinical Practice, Directive 2001/20/EEC of the European Parliament and of the Council, Declaration of Helsinki concerning medical research in humans (Helsinki 1964, amended Tokyo 1975, Venice 1983, Hong Kong 1989, Somerset West 1996 and Edinburgh).

4.2 Ethics and regulatory review

This trial will be initiated only after all required legal documentation has been reviewed and approved by the responsible independent ethical committee (EC) of the center according to all applying national and international regulations. Prior to patient participation in the trial, written informed consent must be obtained from each patient according to ICH GCP and to the regulatory and legal requirements of the participating country. Each signature must be personally dated by each signatory, and the informed consent and any additional patient information form retained by the investigator as part of the trial records. A signed copy of the informed consent and any additional patient information must be given to each patient or the patient's legally accepted representative. This clinical study protocol was approved by the Sponsor's Ethical Committee on 07/02/2022 (local study identifier INT267-21; PI dr. Carlo Resteghini) and at CSS on 09/03/2022 (local study identifier Prot N 20/CE; PI dr. Alfonso Manfuso)

4.3 Dissemination

The abstract of this protocol was submitted to ESMO (European Society for Medical Oncology) 2022 Conference. The final results of this clinical study will be published in impacted scientific journals and presented at international meetings.

The BD4QoL consortium

Erlend I. F. Fossen[1], Katherine Taylor[2], Paul Nankivell[3], Mriganke De[3], Ahmad Abou-Foul[3], Estefania Estevez-Priego[4], Maria Fernanda Cabrera-Umpierrez[4], Itziar Alonso[4], Sergio Copelli[5], Andy Ness[6], Miranda Pring[6] and Katrina Hurley[6]

[1]Oslo Center for Biostatistics and Epidemiology, University of Oslo, Oslo, Norway

[2]Division of Epidemiology and Health Care Research, JGU – Johannes Gutenberg University, Mainz, Germany

[3]Institute of Head and Neck Studies and Education, University of Birmingham, Birmingham, United Kingdom

[4]Oslo Center for Biostatistics and Epidemiology, Oslo University Hospital, Oslo, Norway

[6]Division of Oral and Maxillofacial Surgery - Bristol Dental Hospital, University of Bristol - Bristol Medical School, Bristol, United Kingdom

Data availability statement

Further material about the study protocol are included in the article/Supplementary Material. Further inquiries can be directed to the corresponding author.

Ethics statement

The studies involving human participants were reviewed and approved by Ethical Committee of the Fondazione IRCCS Istituto Nazionale dei Tumori, Milan, Italy and by the Ethical Committees of the clinical institutions enrolling patients. The patients/participants provided their written informed consent to participate in this study.

Author contributions

SC, CV, ML, MM-S, AF performed the statistical analyses. SC wrote the first draft of the manuscript. All authors contributed to conception and design of the study, wrote sections of the manuscript, contributed to manuscript revision, read, and approved the submitted version.

Funding

This is an investigator-initiated trial (IIT). The study is sponsored by Fondazione IRCCS Istituto Nazionale dei Tumori di Milano (INT), Italy. The BD4QoL project, in the frame of which this work is being conducted, has received funding from the European Union's Horizon 2020 research and innovation program under grant agreement No 875192.

Conflict of interest

MB discloses the following conflicts of interest: honoraria from MSD, outside of this study. DF is employed by DOTSOFT, Greece. SS discloses the following conflicts of interest: honoraria from Lilly and Eisai, outside of this study. FM is employed by MultiMed Engineers, Italy. LLi discloses the following conflicts of interest: research funds donated directly to the institute for clinical trials in which I participated from: Astrazeneca, BMS, Boehringer Ingelheim, Celgene International, Eisai, Exelixis, Debiopharm International SA, Hoffmann-La Roche ltd, IRX Therapeutics, Medpace, Merck-Serono, MSD, Novartis, Pfizer, Roche, Buran; occasional fees for participation as a speaker at conferences/congresses or as a scientific consultant for advisory boards from: Astrazeneca, Bayer, MSD, Merck-Serono, AccMed, Neutron Therapeutics, Inc.

The remaining authors declare that the research was conducted in the absence of any commercial or financial relationships that could be construed as a potential conflict of interest.

Publisher's note

Supplementary material

The Supplementary Material for this article can be found online at: https://www.frontiersin.org/articles/10.3389/fonc.2023.1048593/full#supplementary-material

References

1. Gotay CC, Kawamoto CT, Bottomley A, Efficace F. The prognostic significance of patient-reported outcomes in cancer clinical trials. *J Clin Oncol* (2008) 26:1355–63. doi: 10.1200/jco.2007.13.3439

2. Siddiqui F, Pajak TF, Watkins-Bruner D, Konski AA, Coyne JC, Gwede CK, et al. Pretreatment quality of life predicts for locoregional control in head and neck cancer patients: A radiation therapy oncology group analysis. *Int J Radiat Oncol Biol Phys* (2008) 70:353–60. doi: 10.1016/j.ijrobp.2007.06.024

3. So WKW, Chan RJ, Chan DNS, Hughes BGM, Chair SY, Choi KC, et al. Quality-of-life among head and neck cancer survivors at one year after treatment - a systematic review. *Eur J Cancer* (2012) 48:2391–408. doi: 10.1016/j.ejca.2012.04.005

4. Aaronson NK, Ahmedzai S, Bergman B, Bullinger M, Cull A, Duez NJ, et al. The European organization for research and treatment of cancer QLQ-C30: A quality-of-life instrument for use in international clinical trials in oncology. *J Natl Cancer Inst* (1993) 85:365–76. doi: 10.1093/jnci/85.5.365

5. Bjordal K, Hammerlid E, Ahlner-Elmqvist M, De Graeff A, Boysen M, Evensen JF, et al. Quality of life in head and neck cancer patients: Validation of the European organization for research and treatment of cancer quality of life questionnaire-h and N35. *J Clin Oncol* (1999) 17:1008–19. doi: 10.1200/jco.1999.17.3.1008

6. Singer S, Amdal CD, Hammerlid E, Tomaszewska IM, Castro Silva J, Mehanna H, et al. International validation of the revised European organisation for research and treatment of cancer head and neck cancer module, the EORTC QLQ-HN43: Phase IV. *Head Neck* (2019) 41:1725–37. doi: 10.1002/hed.25609

7. Simon AS, Neary MP, Cella D. Estimation of minimally important differences in EQ-5D utility and VAS scores in cancer. *Health Qual Life Outcomes* (2007) 5. doi: 10.1186/1477-7525-5-70

8. Wisløff T, Hagen G, Hamidi V, Movik E, Klemp M, Olsen JA. Estimating qaly gains in applied studies: A review of cost-utility analyses published in 2010. *Pharmacoeconomics* (2014) 32:367–75. doi: 10.1007/s40273-014-0136-z

9. Tsai WL, Chien CY, Huang HY, Liao KC, Fang FM. Prognostic value of quality of life measured after treatment on subsequent survival in patients with nasopharyngeal carcinoma. *Qual Life Res* (2013) 22:715–23. doi: 10.1007/s11136-012-0213-8

10. Merluzzi TV, Philip EJ, Heitzmann Ruhf CA, Liu H, Yang M, Conley CC. Self-efficacy for coping with cancer: Revision of the cancer behavior inventory (version 3.0). *Psychol Assess* (2018) 30:486–99. doi: 10.1037/pas0000483

11. Heitzmann CA, Merluzzi TV, Jean-Pierre P, Roscoe JA, Kirsh KL, Passik SD. Assessing self-efficacy for coping with cancer: Development and psychometric analysis of the brief version of the cancer behavior inventory (CBI-b). *Psychooncology* (2011) 20:302–12. doi: 10.1002/pon.1735

12. Chirico A, Lucidi F, Merluzzi T, Alivernini F, De Laurentiis M, Botti G, et al. A meta-analytic review of the relationship of cancer coping selfefficacy with distress and quality of life. *Oncotarget* (2017) 8:36800–11. doi: 10.18632/oncotarget.15758

13. Osoba D, Rodrigues G, Myles J, Zee B, Pater J. Interpreting the significance of changes in health-related quality-of- life scores. *J Clin Oncol* (1998) 16:139–44. doi: 10.1200/JCO.1998.16.1.139

14. Cocks K, King MT, Velikova G, De Castro G, Martyn St-James M, Fayers PM, et al. Evidence-based guidelines for interpreting change scores for the European organisation for the research and treatment of cancer quality of life questionnaire core 30. *Eur J Cancer* (2012) 48:1713–21. doi: 10.1016/j.ejca.2012.02.059

15. Wright AA, Raman N, Staples P, Schonholz S, Cronin A, Carlson K, et al. The HOPE pilot study: Harnessing patient-reported outcomes and biometric data to enhance cancer care. *JCO Clin Cancer Inf* (2018) 2:1–12. doi: 10.1200/cci.17.00149

16. van der Hout A, van Uden-Kraan CF, Holtmaat K, Jansen F, Lissenberg-Witte BI, Nieuwenhuijzen GAP, et al. Role of eHealth application oncokompas in supporting self-management of symptoms and health-related quality of life in cancer survivors: a randomised, controlled trial. *Lancet Oncol* (2020) 21:80–94. doi: 10.1016/S1470-2045(19)30675-8

17. *BIG DATA FOR QUALITY OF LIFE* . Available at: https://www.bd4qol.eu/wps/portal/site/big-data-for-quality-of-life (Accessed September 12, 2022).

18. Machiels JP, Leemans CR, Golusinski W, Grau C, Licitra L, Gregoire V. Squamous cell carcinoma of the oral cavity, larynx, oropharynx and hypopharynx: EHNS–ESMO–ESTRO clinical practice guidelines for diagnosis, treatment and follow-up†. *Ann Oncol* (2020) 31:1462–75. doi: 10.1016/j.annonc.2020.07.011

19. Bossi P, Chan AT, Licitra L, Trama A, Orlandi E, Hui EP, et al. Nasopharyngeal carcinoma: ESMO-EURACAN clinical practice guidelines for diagnosis, treatment and follow-up†. *Ann Oncol* (2020) 32(4):452–65. doi: 10.1016/j.annonc.2020.12.007

20. Dibao-Dina C, Caille A, Sautenet B, Chazelle E, Giraudeau B. Rationale for unequal randomization in clinical trials is rarely reported: A systematic review. *J Clin Epidemiol* (2014) 67:1070–5. doi: 10.1016/j.jclinepi.2014.05.015

21. Palmer CR, Rosenberger WF. Ethics and practice: Alternative designs for phase III randomized clinical trials. *Control Clin Trials* (1999) 20:172–86. doi: 10.1016/S0197-2456(98)00056-7

22. Harris PA, Taylor R, Thielke R, Payne J, Gonzalez N, Conde JG. Research electronic data capture (REDCap)–a metadata-driven methodology and workflow process for providing translational research informatics support. *J BioMed Inform* (2009) 42:377–81. doi: 10.1016/J.JBI.2008.08.010

23. Harris PA, Taylor R, Minor BL, Elliott V, Fernandez M, O'Neal L, et al. The REDCap consortium: Building an international community of software platform partners. *J BioMed Inform* (2019) 95:103208. doi: 10.1016/J.JBI.2019.103208

24. Fayers P, Aaronson NK, Bjordal K, Groenvold M, Curran D, Bottomley A. EORTC QLQ-C30 scoring manual. *Eur Organisation Res Treat Cancer* (2001).

25. EuroQol - a new facility for the measurement of health-related quality of life. *Health Policy (New York)* (1990) 16:199–208. doi: 10.1016/0168-8510(90)90421-9

26. Herdman M, Gudex C, Lloyd A, Janssen M, Kind P, Parkin D, et al. Development and preliminary testing of the new five-level version of EQ-5D (EQ-5D-5L). *Qual Life Res* (2011) 20:1727–36. doi: 10.1007/s11136-011-9903-x

27. Merluzzi TV, Nairn RC, Hegde K, Sanchez MAM, Dunn L. Self-efficacy for coping with cancer: Revision of the cancer behavior inventory (version 2.0). *Psychooncology* (2001) 10:206–17. doi: 10.1002/pon.511

28. Serpentini S, Del Bianco P, Chirico A, Merluzzi TV, Martino R, Lucidi F, et al. Self-efficacy for coping: utility of the cancer behavior inventory (Italian) for use in palliative care. *BMC Palliat Care* (2019) 18. doi: 10.1186/s12904-019-0420-y

29. Onnela JP, Rauch SL. Harnessing smartphone-based digital phenotyping to enhance behavioral and mental health. *Neuropsychopharmacol 2016 417* (2016) 41:1691–6. doi: 10.1038/npp.2016.7

30. Car LT, Dhinagaran DA, Kyaw BM, Kowatsch T, Joty S, Theng YL, et al. Conversational agents in health care: Scoping review and conceptual analysis. *J Med Internet Res* (2020) 22. doi: 10.2196/17158

31. Cavalieri S, De Cecco L, Brakenhoff RH, Serafini MS, Canevari S, Rossi S, et al. Development of a multiomics database for personalized prognostic forecasting in head and neck cancer: The big data to decide EU project. *Head Neck* (2020) 43(2):601–12. doi: 10.1002/hed.26515

32. Singer S, Danker H, Guntinas-Lichius O, Oeken J, Pabst F, Schock J, et al. Quality of life before and after total laryngectomy: Results of a multicenter prospective cohort study. *Head Neck* (2014) 36:359–68. doi: 10.1002/HED.23305

33. Ness AR, Waylen A, Hurley K, Jeffreys M, Penfold C, Pring M, et al. Establishing a large prospective clinical cohort in people with head and neck cancer as a biomedical resource: Head and neck 5000. *BMC Cancer* (2014) 14. doi: 10.1186/1471-2407-14-973

34. Dunne S, Coffey L, Sharp L, Desmond D, Gooberman-Hill R, O'Sullivan E, et al. Integrating self-management into daily life following primary treatment: head and neck cancer survivors' perspectives. *J Cancer Surviv* (2019) 13:43–55. doi: 10.1007/S11764-018-0726-4

35. Peterson SK, Garden AS, Shinn EH, Shete S, Martch SL, Camero M, et al. Using mobile and sensor technology to identify early dehydration risk in head and neck cancer patients undergoing radiation treatment: Impact on symptoms. *J Clin Oncol* (2018) 36:6063–3. doi: 10.1200/JCO.2018.36.15_SUPPL.6063

36. Rogers SN, Lowe D, Lowies C, Yeo ST, Allmark C, Mcavery D, et al. Improving quality of life through the routine use of the patient concerns inventory for head and neck cancer patients: A cluster preference randomized controlled trial. *BMC Cancer* (2018) 18:1–10. doi: 10.1186/S12885-018-4355-0/FIGURES/2

37. Cruz Rivera S, Liu X, Chan A, AK D, MJ C. Guidelines for clinical trial protocols for interventions involving artificial intelligence: the SPIRIT-AI extension. *Nat Med* (2020) 26:1351–63. doi: 10.1038/S41591-020-1037-7

38. Digital Health Technologies. *Clinical trials transformation initiative* . Available at: https://www.ctti-clinicaltrials.org/projects/digital-health-technologies (Accessed July 28, 2021).

frontiers | Frontiers in Oncology

TYPE Original Research
PUBLISHED 03 February 2023
DOI 10.3389/fonc.2023.1060674

OPEN ACCESS

EDITED BY
Lorenz Kadletz-Wanke,
Medical University of Vienna, Austria

REVIEWED BY
Serena Monti,
National Research Council (CNR), Italy
Rachel Ger,
Johns Hopkins Medicine, Johns Hopkins University, United States

*CORRESPONDENCE
Lili Guo
guolili163@163.com

SPECIALTY SECTION
This article was submitted to Head and Neck Cancer, a section of the journal Frontiers in Oncology

RECEIVED 03 October 2022
ACCEPTED 20 January 2023
PUBLISHED 03 February 2023

CITATION
Kong D, Shan W, Zhu Y, Xu Q, Duan S and Guo L (2023) Preliminary study on CT contrast-enhanced radiomics for predicting central cervical lymph node status in patients with thyroid nodules. *Front. Oncol.* 13:1060674. doi: 10.3389/fonc.2023.1060674

Preliminary study on CT contrast-enhanced radiomics for predicting central cervical lymph node status in patients with thyroid nodules

Dan Kong[1], Wenli Shan[1], Yan Zhu[1], Qingqing Xu[1], Shaofeng Duan[2] and Lili Guo[1]*

[1]Department of Imaging, The Affiliated Huaian No. 1 People's Hospital of Nanjing Medical University, Huaian, Jiangsu, China, [2]Institute of precision medicine, GE Healthcare, Shanghai, China

Objective: To explore the feasibility of using a contrast-enhanced CT image-based radiomics model to predict central cervical lymph node status in patients with thyroid nodules.

Methods: Pretreatment clinical and CT imaging data from 271 patients with surgically diagnosed and treated thyroid nodules were retrospectively analyzed. According to the pathological features of the thyroid nodules and central lymph nodes, the patients were divided into three groups: group 1: papillary thyroid carcinoma (PTC) metastatic lymph node group; group 2: PTC nonmetastatic lymph node group; and group 3: benign thyroid nodule reactive lymph node group. Radiomics models were constructed to compare the three groups by pairwise classification (model 1: group 1 vs group 3; model 2: group 1 vs group 2; model 3: group 2 vs group 3; and model 4: group 1 vs groups (2 + 3)). The feature parameters with good generalizability and clinical risk factors were screened. A nomogram was constructed by combining the radiomics features and clinical risk factors. Receiver operating characteristic (ROC) curve, calibration curve and decision curve analysis (DCA) were performed to assess the diagnostic and clinical value of the nomogram.

Results: For radiomics models 1, 2, and 3, the areas under the curve (AUCs) in the training group were 0.97, 0.96, and 0.93, respectively. The following independent clinical risk factors were identified: model 1, arterial phase CT values; model 2, sex and arterial phase CT values; model 3: none. The AUCs for the nomograms of models 1 and 2 in the training group were 0.98 and 0.97, respectively, and those in the test group were 0.95 and 0.87, respectively. The AUCs of the model 4 nomogram in the training and test groups were 0.96 and 0.94, respectively. Calibration curve analysis and DCA revealed the high clinical value of the nomograms of models 1, 2 and 4.

Conclusion: The nomograms based on contrast-enhanced CT images had good predictive efficacy in classifying benign and malignant central cervical lymph nodes of thyroid nodule patients.

KEYWORDS

thyroid, cancer, lymph node, radiomics, x-ray computed tomography, contrast enhancement

1 Introduction

Thyroid nodules are a common disease that appear in the neck, the most common of which are papillary carcinoma (PTC) and adenoma, which are often associated with enlarged lymph nodes in the neck. Patients with PTC have a relatively good prognosis, with a mortality rate of less than 10% (1, 2). However, approximately 40-70% of patients with PTC develop cervical lymph node metastases, which are associated with recurrence and poor prognosis (3). Lymph node metastasis occurs mainly in the central region, which contains the sentinel lymph nodes of thyroid cancer, while the lymph nodes of adenoma are mostly reactive hyperplasias. Some patients present with enlarged lymph nodes in the neck, and therefore, the nature of the lymph nodes often needs to be determined in the absence of a clear etiology. Currently, the analysis of lymph nodes mainly relies on morphology, but enlarged lymph nodes may be attributable to inflammatory reactive hyperplasia, while normal-sized lymph nodes may also have tumor infiltration; therefore, the accuracy in assessing benign and malignant lymph nodes based solely on morphological features (e.g., size) is not high (4), with an overall misclassification rate of approximately 15%-20% (5). Radiomics can help identify features that are difficult to observe with the naked eye in images and can be used to quantitatively assess the heterogeneity of lesions (6). Recent studies have found that radiomics can be used to describe tumor phenotypes, distinguish benign and malignant tumors, and predict lymph node metastasis and outcomes (7). Radiomics models have been shown to predict lymph node metastasis in PTC (8, 9), and CT-based radiomics models are also valuable in the differentiation of benign and malignant lymph nodes in the head and neck (10). Few studies have examined the differentiation of metastatic and nonmetastatic lymph nodes among patients with PTC and the classification of reactive hyperplastic lymph nodes among patients with benign thyroid lesions. The purpose of this study was to determine the efficacy of using a CT-based radiomics model to classify lymph nodes in the central neck regions of patients with thyroid nodules.

2 Materials and methods

2.1 General information

This retrospective study was approved by a hospital ethics committee, and informed consent was waived. We retrospectively collected data from patients with surgically and pathologically confirmed thyroid nodules from May 2020 to December 2021. Clinical data and contrast-enhanced CT images of lymph nodes in the central cervical region were collected. The inclusion criteria were as follows: 1. A single thyroid lesion, diagnosed as PTC or thyroid adenoma by postoperative pathology; 2. intraoperative lymph node dissection in the central neck region revealing a PTC pathology (for patients with PTC) or no lymph node pathology (for patients with thyroid adenoma); no history of malignant tumors or blood disorders; and normal tumor-related indicators on preoperative routine examination; 3. lymph node diameter in the central region of the neck ≥5 mm (11); 4. contrast-enhanced CT examination performed within two weeks before surgery and treatment consistent with the diagnosis and postprocessing; and 5. no radiotherapy or chemotherapy before surgery. To avoid experimental deviation, lymph nodes larger than 20 mm were excluded from this study.

For the final lymph node pathological findings, the all-or-none principle was used (12). When all lymph nodes within the central zone of PTC patients had metastatic pathological findings, the lymph nodes seen on images within the zone were labeled metastatic lymph nodes; when all lymph nodes within the zone had nonmetastatic pathological findings, the lymph nodes seen on images within the zone were labeled nonmetastatic lymph nodes; and when the lymph node pathological results were both metastatic and nonmetastatic, they were not included. One large and clearly displayed lymph node in the central region was selected as the target lesion for each patient.

A total of 271 patients were included in this study, including 41 males and 230 females, with ages ranging from 22-78 years (average 46.5 ± 17.4 years). The flowchart of inclusion and exclusion is shown in Figure 1. A total of 178 patients had PTC (71 patients in the lymph node metastasis group and 107 patients in the nonmetastasis group). Ninety-three patients were pathologically diagnosed with thyroid adenoma, and their lymph nodes were classified into the benign reactive lymph node group. Based on the pathologic findings of thyroid nodules and central lymph nodes, we divided the patients into three groups: the PTC metastatic lymph node (MLN) group; the PTC nonmetastatic lymph node (non-MLN) group; and the hyperplastic lymph node (HLN)/thyroid adenoma group. Four classification models were constructed, as shown in Figure 2.

First, three models were constructed:

Model 1: MLN 71 patients, HLN 93 patients;
Model 2: MLN 71 patients, non-MLN 107 patients;
Model 3: non-MLN 107 patients, HLN 93 patients.

Second, model 4 was constructed, including 71 patients in the MLN group and 200 patients in the HLN and non-MLN groups.

2.2 CT examination method

A Siemens definition 64-slice CT scanner from Germany was used to perform routine noncontrast scans and 2-phase enhanced scans. The tube voltages were 120 kV, and CARE Dose 4D was used. The slice thickness was 2 mm, and the pitch was 0.8. A volume of 60-70 ml of the contrast agent ioversol (containing 320 mg/ml iodine) was injected into the median elbow vein at an injection rate of 3.0 ml/s, followed by injection of 15 ml of normal saline. The aortic arch was monitored by the contrast agent bolus tracking method, with a trigger threshold of 100 HU, an arterial phase delay time of 10 s, and a venous phase delay of 25 s. Before the scan, the patients were instructed to breathe and then hold their breath with the arms placed at the sides of the body. During the scan, the patients were asked to maintain a supine position with the neck leaning backward and maximally lowered shoulders, and swallowing was prohibited. The scanning range extended from the mandible to the base of the neck. If the thyroid extended behind the sternum, the scanning range was expanded to cover the entire thyroid.

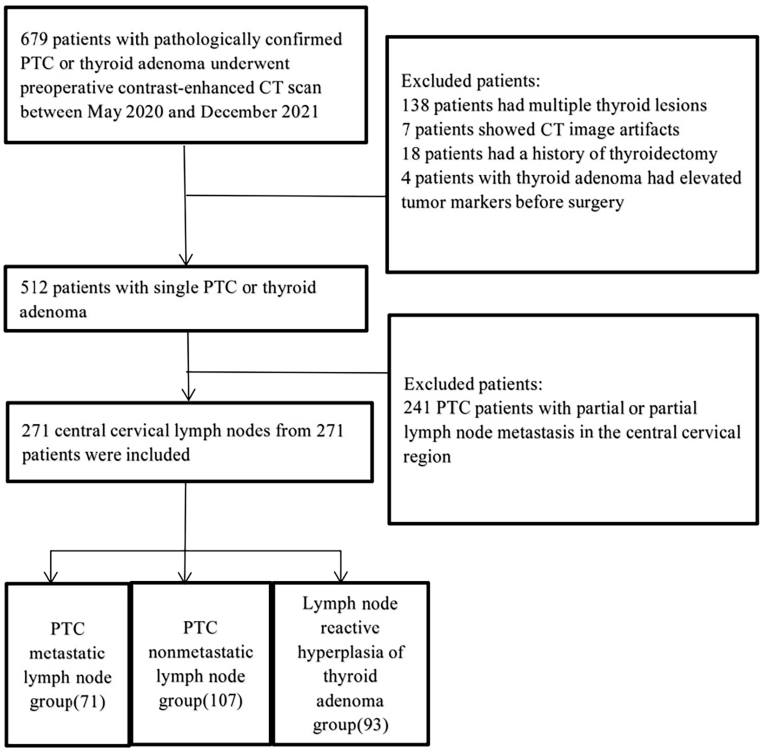

FIGURE 1
Patient enrollment process.

2.3 CT image analysis

The clinical and imaging data of all patients were analyzed by two experienced radiologists to determine lymph node status, including age, sex, the short and long diameters of the lymph nodes in the transverse axis on the slice showing the largest area, the shape of the lymph nodes, the CT value during the arterial and venous phases, and the difference in the CT value between the venous phase and arterial phase. The CT value is a measurement unit that can reflect the density of the lymph nodes. Two experienced radiologists measured the corresponding CT values three times and took the average value. During the measurement, the radiologists ensured that the solid area was as wide as possible, and cystic necrosis and calcification was avoided as much as possible. Any obvious differences between the radiologists' evaluations were resolved by consensus.

2.4 Region of interest segmentation and feature extraction

2.4.1 ROI segmentation

Two experienced radiologists (Doctor A and B) used ITK-SNAP (www.itksnap.org) software to delineate the lymph node edges layer by layer on the arterial- and venous-phase CT images to synthesize a 3-dimensional (3D) ROI. Doctor A performed two delineations, 1-2 weeks apart; Doctor B performed one.

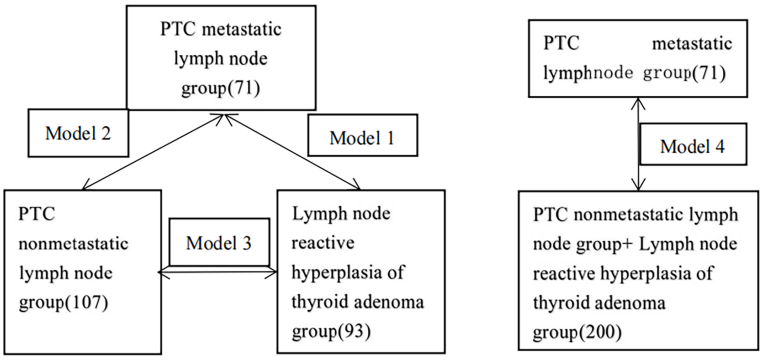

FIGURE 2
Schematic diagram of model construction.

2.4.2 Radiomics feature screening and establishment of the radiomics model

The arterial- and venous-phase images were standardized using A.K software (version: 3.2.0.r, Artificial Intelligence Ki, GE Healthcare), and then, the radiomics features were extracted from the 3D ROIs using PyRadiomics. We used R software (http://www.Rproject.org, version 3.4.4) to analyze the data. After lymph node segmentation, the software automatically obtained 14 shape features, 18 first-order features, and 68 texture features. We first performed consistency tests within and between the observer datasets; that is, we calculated the intraclass correlation coefficient (ICC) between the features extracted from the two ROIs constructed by Radiologist A as well as the ICC between the features extracted from the first ROI constructed by Radiologist A and that constructed by Radiologist B. Features with an ICC>0.75 in both calculations were retained, and the features extracted from the first ROI constructed by Radiologist A were used for subsequent analysis.

We used the stratified random sampling method to divide patients into training and test groups at a 7:3 ratio. The training group data were used for feature screening and model construction. First, maximum relevance and minimum redundancy (mRMR) were used to remove redundant and irrelevant features, ultimately retaining 30 features, which were then imported into the least absolute shrinkage and selection operator (LASSO) regression model. Ten-fold cross-validation was used to identify the hyperparameter λ of the LASSO regression model; the value corresponding to the minimum model error was selected to retain features with nonzero coefficients (Figures 3, 4). Regression and dimensionality reduction were used to further select features with good generalizability, which were then used to establish a prediction model. Each lymph node was scored according to the weights of the screening features. A diagnostic model was established by machine learning using the subset of the data screened by the feature variables, and the validity and reliability of the diagnostic model were evaluated by using the area under the receiver operating characteristic (ROC) curve (AUC). The characteristics of good repeatability and stability were used to build the radiomics model. Linear fusion of the selected features was performed to calculate the radiomics score.

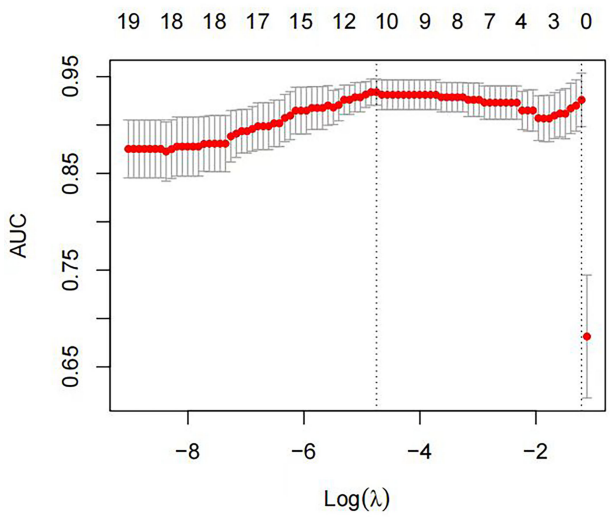

FIGURE 3
The optimal tuning parameter (λ) was selected using ten-fold cross-validation with the LASSO regression model. The horizontal axis represents the log value of the best λ, and the vertical axis represents the corresponding binomial deviation value. The red dots represent the average deviation of a given λ value, the corresponding vertical line represents the upper and lower limits, and the dotted lines represent the selected optimal log(λ) values.

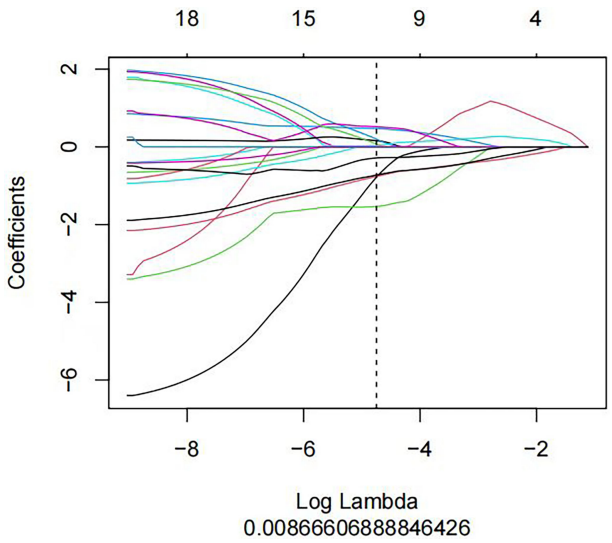

FIGURE 4
A LASSO regression model was used to screen out the profile of radiomics feature coefficients in each model. The horizontal axis represents log(λ), and the vertical axis represents the selected characteristic coefficients. Each line represents the trend for each feature.

2.5 Construction and evaluation of the radiomics nomogram

In the training group, the clinical risk factors were screened by one-way ANOVA and then were further analyzed by multivariate logistic regression analysis to finally determine the independent clinical risk factors ($P< 0.05$), which were then used to construct the clinical models. A nomogram was established by combining the radiomics signature and the clinical risk factors.

The predictive efficacy of the nomogram was assessed using ROC and calibration curve analysis. The DeLong test was used to compare the AUCs between different variables. The calibration curve reflects the agreement of the predicted probability of the nomogram with the pathological diagnosis; the closer the calibration curve is to the diagonal line, the closer the predicted value of the model is to the true value, and thus the better the calibration is. Decision curve analysis (DCA) was used to evaluate the potential net clinical benefit and utility of the prediction model and to validate it in the test group.

2.6 Statistical analysis

All data were statistically analyzed using SPSS 24.0 and R3.4.4 software (https://www.Rproject.org). Single-factor ANOVA was used to compare patient age between the 3 groups, the LSD method was

used for two-way comparisons, and the χ^2 test was used to compare differences in sex distributions. Otherwise, the Mann-Whitney U test was used for variable comparison. A two-sided *P* value<0.05 was considered significant.

3 Results

3.1 Feature extraction and model construction of Models 1-3

3.1.1 General patient information

The difference in age between the 3 groups was statistically significant, and two-by-two ANOVA showed that the average age of the MLN group [(41.8 ± 12.2)] was significantly lower than that of the HLN group [(49.9 ± 11.7)] and non-MLN group [(46.9 ± 11.2)] (*P*=0.003, *P*<0.001). The difference in the age between the HLN and non-MLN groups was not statistically significant (*P*=0.064). There was a statistically significant difference in the sex distribution among all 3 groups (χ^2=19.838, *P*<0.001), a statistically significant difference in the sex distribution between the MLN and HLN groups (χ^2=15.635, *P*=0.015), and no statistically significant difference in the sex distribution between the HLN and non-MLN groups (χ^2=8.634, *P*= 0.064). In this study, lymph nodes were included with a short diameter of 5.0 mm to 16.3 mm and a long diameter of 5.2 mm to 19.3 mm.

We used the stratified random sampling method to divide patients into training and test groups at a 7:3 ratio. In model 1, there were 115 patients in the training group (MLN group: 48 patients; HLN group: 67 patients) and 49 patients in the test group (MLN group: 23 patients; HLN group: 26 patients). In model 2, there were 125 patients in the training group (48 patients in the MLN group and 77 patients in the non-MLN group) and 53 patients in the test group (23 patients in the MLN group and 30 patients in the non-MLN group). In model 3, there were 140 patients in the training group (72 patients in the non-MLN group and 68 patients in the HLN group) and 60 patients in the test group (35 patients in the non-MLN group and 25 patients in the HLN group).

In the training group, there were statistically significant differences in age, CT value of the arterial phase and CT value difference between the venous phase and arterial phase in model 1. In model 2, there were statistically significant differences in age, sex distribution, short and long diameter of the lymph nodes, CT value of the arterial phase, CT value of the venous phase, CT value difference between venous phase and arterial phase and lymph node shape. In model 3, there were statistically significant differences in the long diameter of the lymph node, CT value of the venous phase, CT value difference between the venous phase and arterial phase and lymph node shape, as shown in Table 1.

3.1.2 Radiomics feature extraction and selection and radiomics model establishment

Eight optimal features were selected from model 1, all of which were from the arterial phase. There were 3 first-order statistical features, 2 gray level cooccurrence matrix (GLCM) features and 3 gray level dependence matrix (GLDM) features. Eleven features were screened from model 2, among which 9 were from the arterial phase and 2 were from the venous phase. There were 3 first-order statistical features, 5 gray level size zone matrix (GLSZM) features and 3 GLCM features. Sixteen features were screened from model 3, of which 9 were from the arterial phase and 7 were from the venous phase (Figure 5). There was 1 first-order statistical feature, 3 GLCM

TABLE 1 Comparison of clinical characteristics of the three models in the training group.

Variable	Model 1			Model 2			Model 3		
	MLN (n=48)	HLN (n=67)	*P* value	MLN (n=48)	non-MLN (n=77)	*P* value	non-MLN (n=72)	HLN (n=68)	*P* value
Age(mean±SD)	41.3±11.9	49.2±12.	<0.001	40.9±12.7	46.6±11.0	0.008	47.2±10.6	49.2±12.2	0.196
Sex(n, %)			0.065			0.016			0.693
Male	14 (29.2)	9(13.4)		13(27.1)	7(9.1)		6(8.3)	8(11.8)	
Female	34 (70.8)	58(86.6)		35(72.9)	70(90.9)		66(91.7)	60(88.2)	
Short diameter of lymph node(mm)	6.4 ± 2.3	5.8 ± 1.1	0.051	6.4 ± 2.3	5.8 ± 1.1	0.036	5.5 ± 0.6	5.7 ± 1.1	0.109
Long diameter of lymph node(mm)	9.0 ± 4.1	8.4 ± 2.1	0.366	9.0 ± 4.1	7.8 ± 2.1	0.029	7.4 ± 1.7	8.3 ± 2.1	0.004
CT value of arterial phase	118.2 ± 49.7	84.5 ± 16.3	<0.001	119.0 ± 52.7	81.0 ± 18.9	<0.001	81.3 ± 18.5	86.6 ± 16.9	0.079
CT value of venous phase	122.7 ± 36.8	114.7 ± 22.2	0.147	123.8 ± 37.6	101.8 ± 20.4	<0.001	102.9 ± 19.9	116.4 ± 21.9	<0.001
CT difference between venous phase and arterial phase	4.5 ± 30.5	30.2 ± 17.7	<0.001	4.9 ± 31.7	20.8 ± 14.7	<0.001	21.6 ± 14.1	29.8 ± 17.5	0.002
Shape			0.594			0.033			0.009
Regular	36(75.0)	46(68.7)		37(77.1)	71(92.2)		66(91.7)	50(73.5)	
Irregular	12(25.0)	21(31.3)		11(22.9)	6(7.8)		6(8.3)	18(26.5)	

10.3389/fonc.2023.1060674

features, 4 GLSZM features, 2 GLDM features and 6 gray level run length matrix (GLRLM) features. Based on these features and their corresponding regression coefficients, the radiomics model was constructed, and the Radscore was formulated as follows:

$$\text{Radscore} = \sum_{n}^{1} feature_i * \text{coefficient}_i + \text{Compensation coefficient}$$

Model 1: Radscore=0.839*log_sigma_4_0_mm_3D_firstorder _10Percentile. A+ -0.031*log_sigma_4_0_mm_3D_gldm_Small DependenceEmphasis.A+0.393*original_firstorder_Uniformity.A +-0.1*log_ sigma_3_0_mm_ 3D_glcm_Imc2. A+ 0.163*log_sigma _1_0_mm_3D_gldm_LargeDependenceLowGrayLevelEmphasis.A +0.028*log_sigma_5_0_mm_3D_firstorder_Median.A+0.265*log _sigma_3_0_mm_3D_gldm_LargeDependenceLowGray LevelEmphasis.A+-0.142*log_sigma_2_0_ mm_ 3D_glcm_ Imc2.A+0.443

Model 2: Radscore=-0.78*wavelet_HHH_glszm_SizeZoneNon Uniformity. A+ 0.472*log_sigma_3_0_mm_3D_firstorder _Minimum.A+0.158*wavelet_HHH_glszm_ZoneEntropy.A +-1.531*original_firstorder_RobustMeanAbsoluteDeviation. A+ 0.201*wavelet_HHH_glszm_GrayLevelNonUniformity.A +0.039*log_sigma_3_0_mm_3D_firstorder_Minimum.A +-0.763*log_ sigma_4_0_mm_3D_ firstorder_ Variance. V +0.518*original_glcm_MaximumProbability.A+-0.727*log_ sigma_5_0_ mm_3D_glszm_SizeZoneNonUniformity.A +0.072*wavelet_HHH_glszm_ZoneEntropy.V+-0.284* original_glcm_SumEntropy.A+1.013

Model 3: Radscore=-0.822*wavelet_LLL_glszm_SmallArea LowGrayLevel -Emphasis.A+0.718*wavelet_HHH_glszm _GrayLevelVariance.A+0.443*wavelet_LLL_glcm_ClusterShade.A +-0.73*original_glrlm_ LongRunLowGrayLevelEmphasis. A+-1.132*

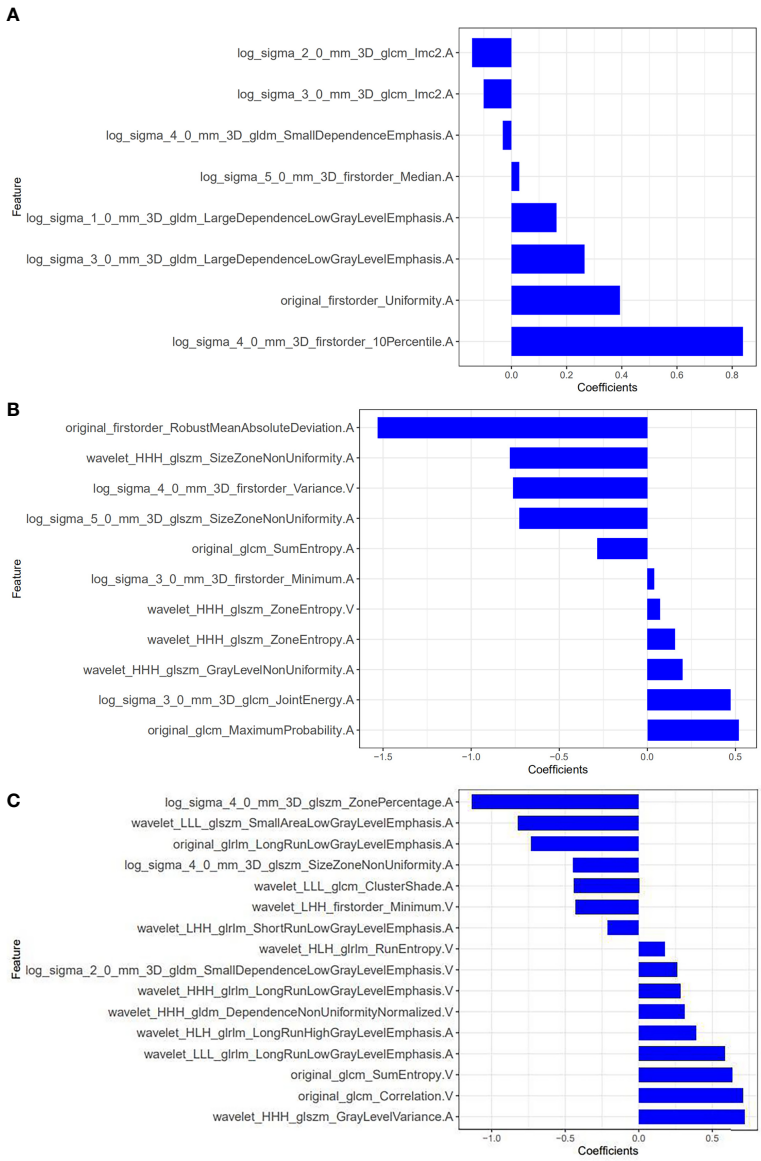

FIGURE 5
Radiomic features screened by models 1-3 and their weights. **(A)** model 1; **(B)** model 2; **(C)** model 3 (The letters A and V in the feature names indicate that the feature was extracted from the arterial phase and the venous phase, respectively).

log_sigma_ 4_0_mm_3D_glszm_ ZonePercentage. A+0.388*wavelet_ HLH_glrlm_LongRunHighGrayLevelEmphasis.A+0.31*wavelet_HHH_gldm_DependenceNonUniformity Normalized.V+-0.209* wavelet_LHH_glrlm_ ShortRunLow GrayLevelEmphasis.A+0.176*wavelet_HLH_glrlm_RunEntropy.V+0.705*original_glcm_Correlation.V+-0.444*log_sigma_4_0_mm_3D_glszm_ SizeZoneNon Uniformity.A+0.585*wavelet_LLL_glrlm_LongRunLowGrayLevelEmphasis.A+-0.43*wavelet_LHH_firstorder_Minimum.V+0.28*wavelet_HHH_glrlm_LongRunLowGrayLevelEmphasis.V+0.634*original_glcm_SumEntropy.V+-0.465

The diagnostic efficacy of radiomics models 1-3 is shown in Table 2.

3.1.3 Clinical feature screening and nomogram construction

Multivariate logistic regression analysis showed that the CT value in the arterial phase (OR=1.05, 95% CI: 1.02~1.09) was an independent clinical risk factor for model 1. Sex (OR=0.1, 95% CI: 0.01-0.67) and CT value in the arterial phase (OR=0.96, 95% CI 0.94-0.98) were independent clinical risk factors for model 2. Combining the clinical risk factors and radiomics labels, a nomogram was established, and the corresponding scores of each predictive index were obtained, which were then summed and finally reflected by the total score. The constructed nomogram is shown in Figure 6. There were no statistically significant clinically relevant risk factors in model 3, so no nomogram was constructed.

3.2 Feature extraction and model construction of model 4

In the training group, after feature extraction with mRMR and LASSO, 5 radiomics features with strong correlations were ultimately identified (Figure 7). Four features were from the arterial phase, and one was from the venous phase. Based on these features and their corresponding regression coefficients, a radiomics model was constructed. There were 3 first-order statistical features, 1 GLSZM

TABLE 2 Diagnostic efficacy of the radiomics models of models 1-4.

Evaluation indicators	Model 1		Model 2		Model 3		Model 4	
	Training group	Test group	Training group	Test group	Training group	Test group	Training group	Test group
AUC	0.97	97.92	0.97	0.85	0.93	0.74	0.94	0.93
Accuracy (%)	0.93	91.30	88.00	67.92	88.57	71.67	89.47	87.65
Sensitivity (%)	93.91	98.39	80.52	70.00	92.65	76.00	89.78	90.48
Specificity (%)	89.79	92.00	93.75	86.96	84.72	68.57	88.68	77.78
Positive predictive value (%)	91.04	88.68	100.00	84.21	85.14	63.33	95.35	93.44
Negative predictive value (%)	88.46	87.50	76.19	58.82	92.42	80.00	77.05	70.00

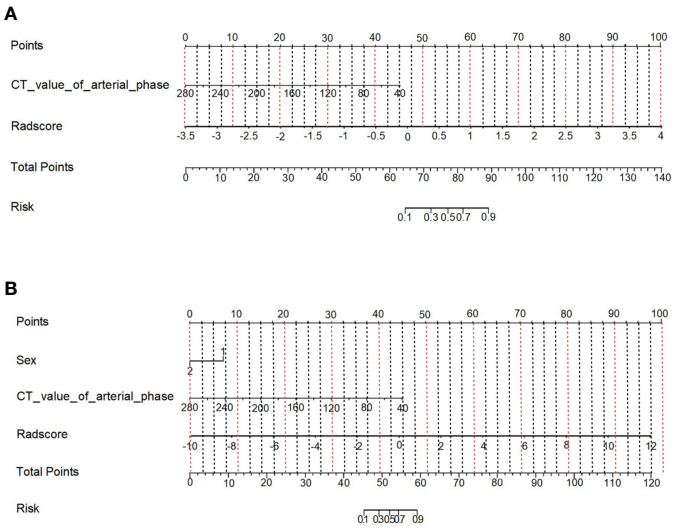

FIGURE 6
Nomogram of the prediction model combining clinical risk factors and CT radiomics features. **(A)** Model 1; **(B)** Model 2.

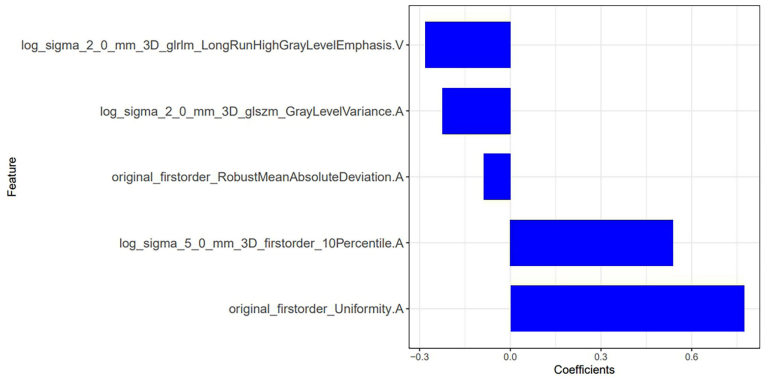

FIGURE 7
Radiomic features screen by model 4 and their weights.

feature and 1 GLRLM feature. The box diagram shows that in the training group and the test group, the difference in the radiomics score between patients in the MLN group and in the non-MLN + HLN) was statistically significant (Figure 8).

Model 4: Radscore=0.773*original_firstorder_Uniformity.A +0.539*log_sigma_ 5_0_mm_3D_firstorder_10Percentile.A +-0.226*log_ sigma_2_0_mm_3D_ glszm_ GrayLevelVariance.A +-0.089*original_ firstorder_ RobustMeanAbsolute Deviation. A +-0.282*log_ sigma_2_0_mm_ 3D_glrlm_Long RunHighGrayLevel Emphasis. V+ 1.279

The diagnostic efficacy of radiomics model 4 is shown in Table 2.

Multivariate logistic regression analysis revealed that sex (OR=0.21, 95% CI: 0.05-0.93), CT value in the arterial phase (OR=0.96, 95% CI: 0.93-0.99) and CT value in the venous phase (OR=1.03, 95% CI of 1.00-1.05) were independent clinical risk factors for discriminating between the MLN and (HLN+ non-MLN) groups. A nomogram was established combining the clinical risk factors and radiomic features (Figure 9).

3.3 ROC curve analysis, calibration curve analysis and DCA for evaluating the efficacy and value of the nomograms

ROC curve analysis was used to assess the diagnostic efficacy of the three models (Figure 10). In the training group, the AUC values of the nomogram model were higher than those of the radiomics model and clinical model. DeLong's test showed that there were no significant differences in the AUC values between the nomogram model and the radiomics model for models 1, 2, and 4 (model 1: Z=2.1482, *P*=0.062; model 2: Z=1.637, *P*=0.102; model 4: Z=7.463, *P*=0.132). The differences between the nomogram model and clinical model were statistically significant (model 1: Z=4.491, *P*< 0.001; model 2: Z=10.376, *P*<0.001; model 4: Z=3.140, *P*=0.002). In the test group, the diagnostic efficacy of the nomogram model was higher than that of the radiomics model and clinical model. DeLong's test showed that there were no significant differences between the nomogram and radiomics model for model 1, model 2, and model

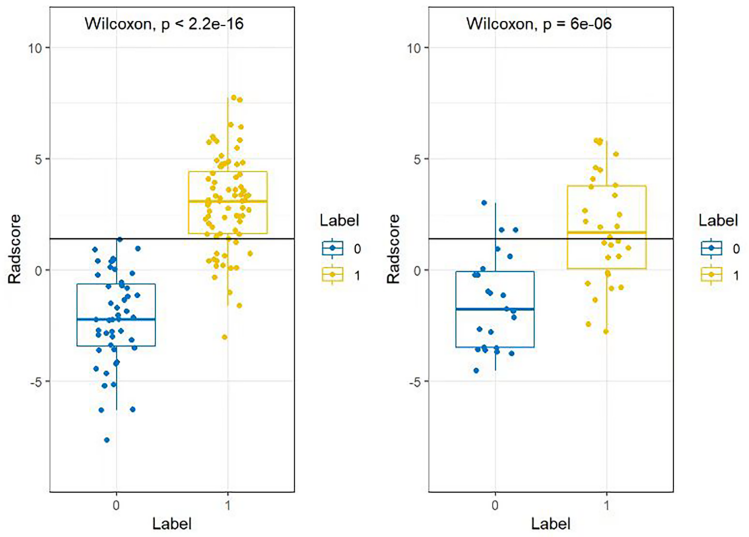

FIGURE 8
Box plot of the radiomics scores of the training group and the test group in model 4. Blue (Label 0) represents the MLN group, and yellow (Label 1) represents the HLN and non-MLN group. The difference between the two groups was statistically significant (*P*< 2.2^{e-16}).

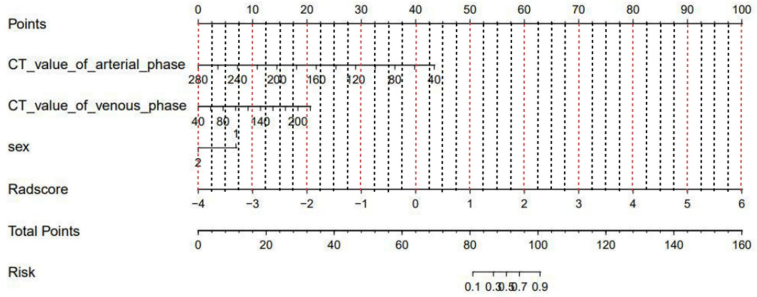

FIGURE 9
Nomogram of model 4 constructed by combining clinical risk factors and CT radiomics features.

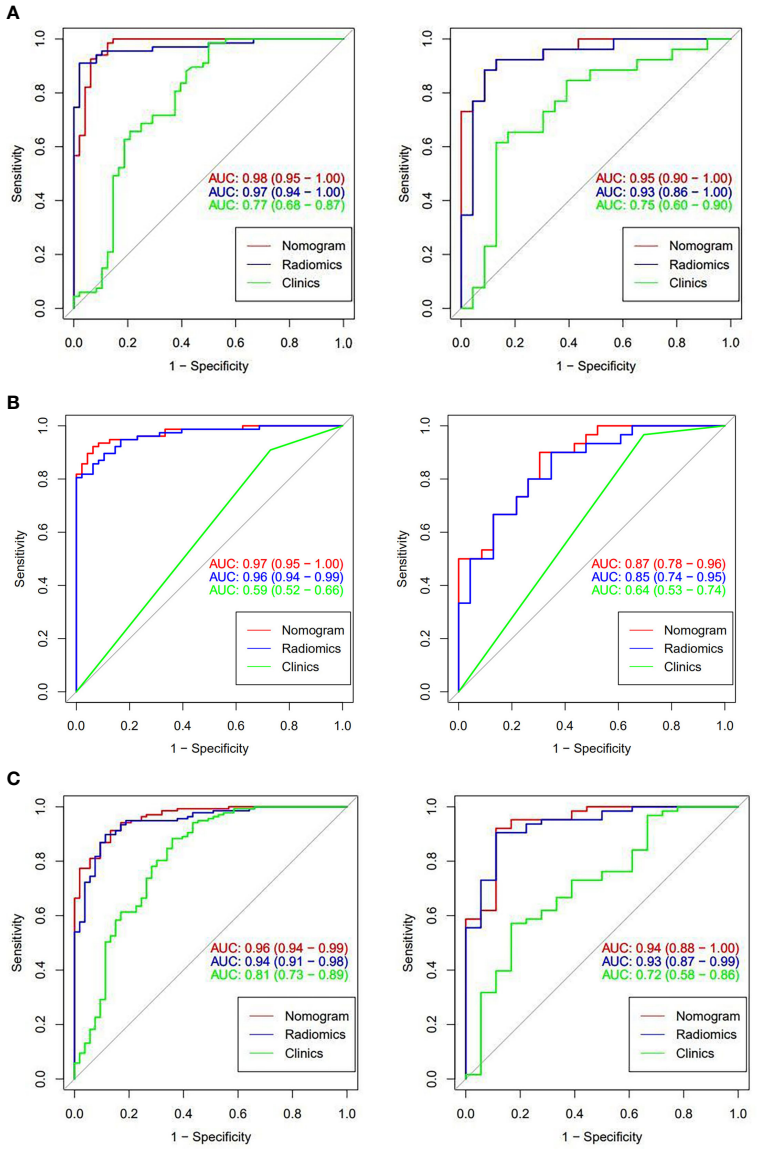

FIGURE 10
ROC curves of models 1, 2, and 4 for the corresponding classification efficacy of the radiomics models, clinical features, and nomogram models in the training group and test group. (**A** are the training group and test group of model 1, respectively; **B** are the training group and test group of model 2; and **C** are the training group and test group of model 4).

4 (model 1: Z=2.945, *P*=0.179; model 2: Z=3.599, *P*=0.086; model 4: Z= 8.051, *P*=0.142), and the differences between the nomogram and clinical model were statistically significant (model 1: Z=1.448, *P*=0.033; model 2: Z=1.345, *P*=0.019; model 4: Z=3.943, *P*< 0.001). The diagnostic efficacy of the radiomics model, clinical model and nomogram model for models 1, 2 and 4 are shown in Table 3.

The calibration curves of nomogram prediction models 1, 2, and 4 in the training group and test group showed good predictive efficacy (Figure 11). The calibration curve of model 4 is closer and better fits to the corresponding diagonal line than that of models 1 and 2. DCA showed that the nomograms of the 3 models outperformed the clinical model across all assessed risk thresholds (Figure 12).

4 Discussion

Currently, noninvasive assessment of the nature of lymph nodes mainly relies on imaging features. Ultrasound, as the main imaging method for examining the thyroid, has important value in the diagnosis of thyroid diseases and cervical lymph nodes (13, 14). However, its diagnostic accuracy is affected by the sonographer's subjectivity and diagnostic experience. CT has advantages in the evaluation of central and superior mediastinal lymph nodes, but it is limited by the need for morphological changes in the lymph nodes to diagnose metastasis. It has been reported that both ultrasound and CT have a sensitivity below 50% in diagnosing central lymph node metastasis (15). The diffusion-weighted MR imaging sequence has certain value in judging the condition of the lymph nodes, but for smaller lymph nodes, the misdiagnosis and missed diagnosis rates are high, especially when the short diameter is less than 10 mm. In recent years, many studies have demonstrated the increasing value of radiomics in determining the condition of lymph nodes. Onoue et al. (16) showed that radiomics based on CT can distinguish metastatic lymph nodes from PTC, tuberculosis, and oropharyngeal squamous cell carcinoma with significantly higher diagnostic accuracy than two neuroradiologists. Seidler et al. (17) found that machine learning texture analysis based on dual-energy CT helped to distinguish different pathological lymph nodes (metastatic head and neck squamous cell carcinoma lymph nodes, lymphoma, inflammation) and normal lymph nodes with higher accuracy. This study investigated the stratified predictive value of a radiomics model based on CT images for metastatic lymph nodes, nonmetastatic lymph nodes, and reactive hyperplastic lymph nodes of benign lesions among patients with PTC to provide guidance for treatment.

In this study, patient age, sex, and lymph node CT signs (long diameter, short diameter, arterial phase CT value, venous phase CT value, arterial and venous phase CT difference value, and lymph node morphology) were statistically different across multiple models through one-way ANOVA, indicating that clinical features and conventional CT images are of value in the identification of lymph nodes with PTC metastasis. However, the morphological signs of early metastatic lymph nodes are often atypical, and the sensitivity in diagnosis is relatively low. The interpretation of image features depends on the clinical experience of the radiologist and is subjective, and thus there is a need to incorporate objective, quantitative indicators to assist in diagnosis. Therefore, the nomogram combines clinical features with objective radiomics features to improve diagnostic efficacy.

The best feature sets identified by the four models in this study all included first-order statistical features and texture features, the latter of which accounted for the higher proportion. The first-order features can quantitatively reflect the global voxel intensity distribution of the ROI and then evaluate the overall information of the lymph nodes. Texture features can describe the spatial distribution of pixel intensity in images and reflect the histological types and pathological properties of lesions with high sensitivity (18). The combination of the two can help comprehensively evaluate the heterogeneity of lymph nodes from different perspectives. Compared with nonmalignant lymph nodes, malignant lymph nodes have more abnormal new blood vessels, increased cell permeability and internal necrosis, which will change the roughness of lymph nodes, resulting in heterogeneity. The above changes are not easily detected by the naked eye but can be

TABLE 3 Diagnostic efficacy of radiomics model, clinical model, nomogram model of model 1, 2, 4.

model 1	Training group				Test group			
	AUC	Accuracy (%)	Sensitivity (%)	Specificity (%)	AUC	Accuracy (%)	Sensitivity (%)	Specificity (%)
radiomics model	0.97	94.91	91.04	97.92	0.93	89.8	88.46	91.3
clinical model	0.77	78.26	98.51	50	0.75	63.27	76.58	30.43
nomogram model	0.98	93.04	92.54	93.75	0.95	89.8	88.89	90.91
model 2								
radiomics model	0.97	88.00	80.52	93.75	0.85	67.92	70	86.96
clinical model	0.59	66.4	90.91	27.08	0.64	67.92	96.67	30.43
nomogram model	0.97	92	88.31	97.92	0.87	75.47	84	67.86
model 4								
radiomics model	0.94	89.47	89.78	88.68	0.93	87.65	90.48	77.78
clinical model	0.81	81.58	88.32	64.15	0.72	72.84	84.13	33.33
nomogram model	0.96	90	91.24	86.79	0.94	92.59	95.24	83.33

reflected by texture features, which are not affected by subjective factors (19).

In this study, 8, 11, 16 and 5 of the best radiomics features were selected for the 4 models by LASSO regression analysis. Among them, the all features of model 1 (PTC metastatic lymph nodes and nonmetastatic lymph nodes), nine of the features of model 2 (PTC metastatic lymph nodes and nonmetastatic lymph nodes), and four of the features of model 4 (PTC metastatic lymph nodes and nonmalignant lymph nodes) were from the arterial phase, suggesting that compared with those of the venous phase, the radiomics features of the arterial phase have higher diagnostic value in distinguishing malignant lymph nodes from nonmalignant lymph nodes of PTC. Xu et al. (20) found that radiomics features extracted from dual-energy CT arterial phase-weighted fusion images can effectively diagnose PTC cervical lymph node metastasis, and the three radiomics features screened were all from the arterial phase. Zhao et al. (21) found that the model based on texture features extracted from arterial-phase CT images was more advantageous in evaluating the lymph node metastasis in PTC, with a higher diagnostic coincidence rate (75.47%) than the model built from the features extracted from the venous phase (71.69%). Consistent with the results of this study, the reason may be that metastatic lymph nodes have a more abundant blood supply and more obvious early enhancement among patients with PTC (22). Unlike other models, 9 of the 16 features in model 3 (PTC nonmetastatic lymph nodes and reactive hyperplastic lymph nodes in benign lesions) were from the arterial phase, and 7 were from the venous phase. The reason may be that the blood supply of nonmalignant lymph nodes in the venous phase is enhanced, while the enhancement in the arterial phase is relatively weaken. Therefore, the number of venous phase features extracted for the lymph nodes in model 3 was substantially increased. Park et al. (12) confirmed that arterial phase CT scans can improve the diagnostic accuracy for PTC lymph node metastasis compared with venous phase CT, which is often used to evaluate lymph nodes of

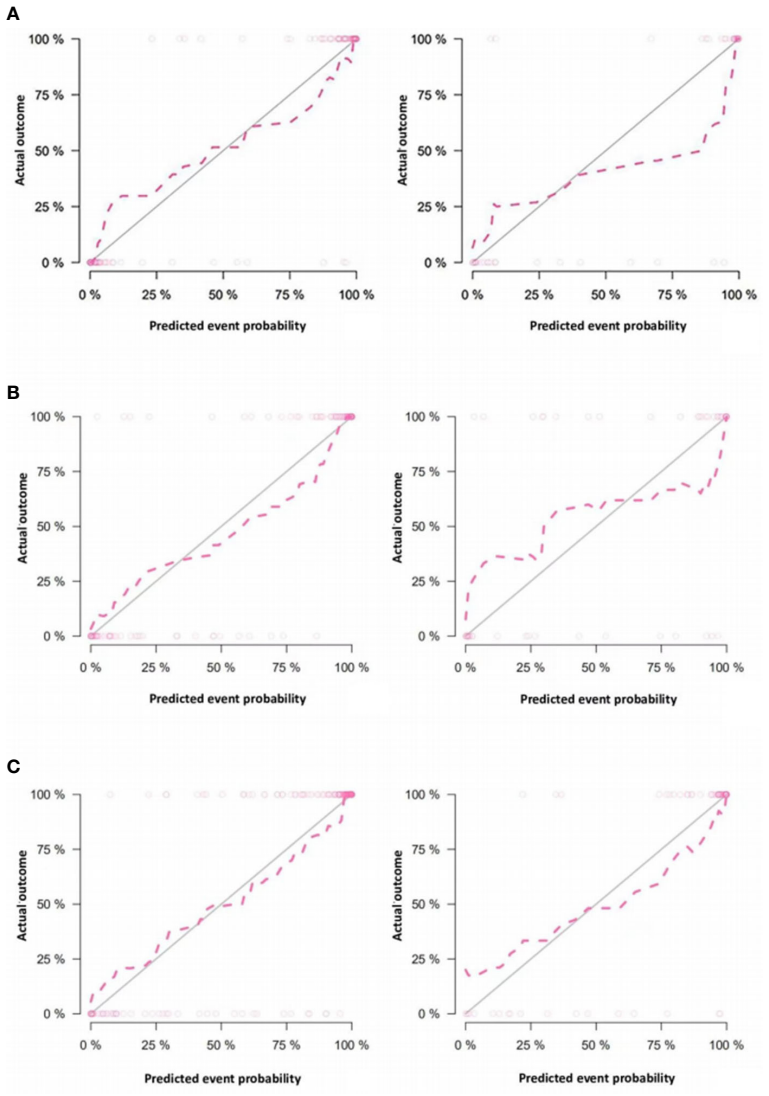

FIGURE 11
Calibration curves of the nomograms in the training group and test group of models 1, 2 and 4. (**A** are the training group and test group of model 1, respectively; **B** are the training group and test group of model 2; and **C** are the training group and test group of model 4) In the calibration curve, the horizontal axis represents the predicted model value, and the vertical axis represents the real value. The prediction efficacy is better if the red line is closer to the gray line.

other pathological types, such as squamous cell carcinoma and tuberculosis lymph nodes.

A larger short lymph node diameter and central necrosis are usually considered indications for malignant transformation, while the short diameter is proportional to the rate of metastasis. The differences between metastatic lymph nodes and nonmalignant lymph nodes and the differences between nonmetastatic lymph nodes and benign reactive lymph nodes in the models in this study were not related to the short lymph node diameter, which is consistent with the research results of Li et al. (23). Ren et al. (24) found that the difference in the short diameter between positive and negative lymph nodes in early tongue cancer pathological metastasis was statistically significant, suggesting that the short diameter of the lymph nodes has a certain reference value for the diagnosis of occult metastasis. In this study, the short lymph node diameter was statistically significant in one-way ANOVA but not in multivariate logistic regression analysis. This suggests that the short diameter of the lymph nodes may be valuable in distinguishing metastatic and nonmetastatic lymph nodes, but not to a significant degree; the reason may be that the nonmalignant lymph node group in our study included nonmetastatic lymph nodes and reactive hyperplastic lymph nodes. Reactive hyperplastic lymph nodes may be significantly enlarged, which reduces the difference in lymph node diameter between the nonmalignant and metastatic groups.

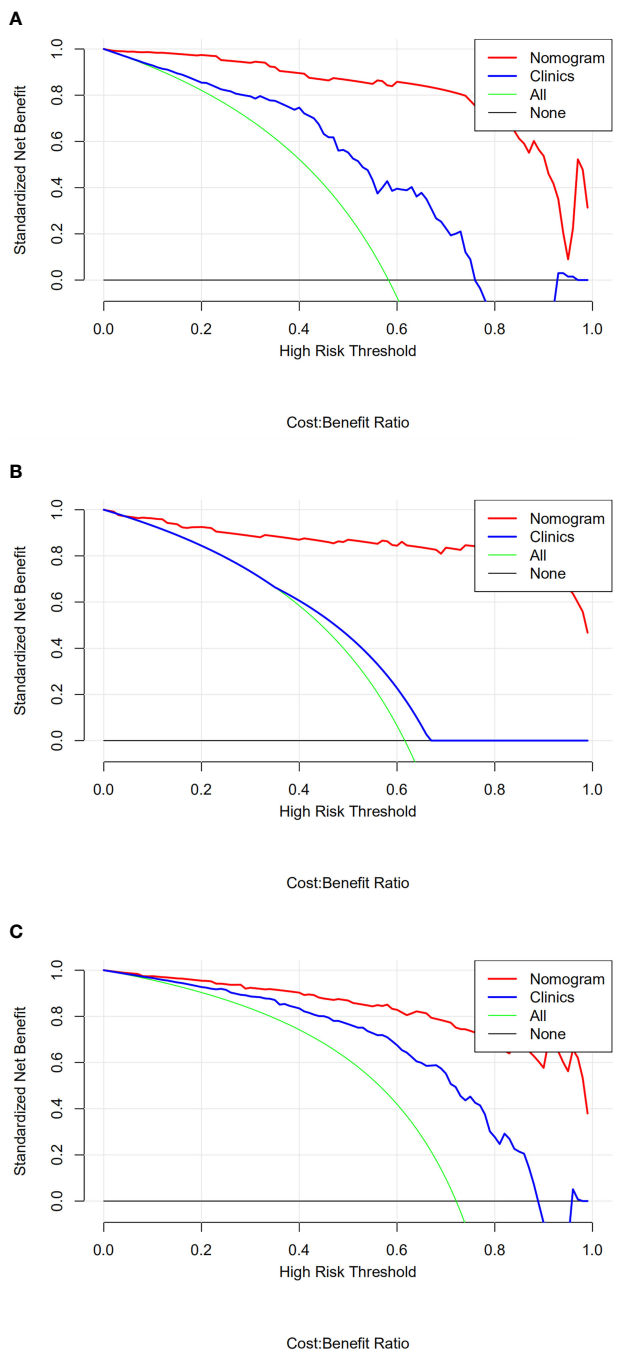

FIGURE 12
(A-C) are the decision curves of nomogram models 1, 2, and 4 for the corresponding lymph node classification in the test group, respectively. The red line in the figure represents the diagnostic nomogram model built from the imaging features, and the blue line represents the diagnostic nomogram model built from the clinical features. The green line represents the hypothesis that all patients had lymph node metastasis; the black lines running across the bottom are assuming that none of the patients had lymph node metastasis. The potential clinical benefits of the radiomics-based models are consistently higher than those of the other three models.

The nomogram in this study was established based on radiomics features and clinical data. Nomograms can more intuitively and individually evaluate the nature of lymph nodes than their corresponding models. Verification of the effectiveness of the models in this study revealed a number of findings. In the first part, the nomograms of models 1 and 2 show high diagnostic performance in both the training and test groups, higher than the performance of the models built from radiomics labels or CT imaging features alone. Our study showed that the nomograms had high predictive efficacy and encompassed the advantages of integrating CT image features and radiomics. In this study, the arterial phase CT enhancement values of models 1 and 2 were independent clinical risk factors for judging the nature of lymph nodes, suggesting that there are certain differences in early enhancement between metastatic lymph nodes, nonmetastatic lymph nodes, and reactive hyperplastic lymph nodes. The degree of enhancement in the arterial phase has a certain value in differentiating the groups. Radiomics model 3 also showed high diagnostic performance in the training group and test group. After univariate and multivariate analyses, there were no clinically relevant risk factors between the two groups of lymph nodes in model 3, suggesting that there may be some heterogeneity in the internal radiomics characteristics of the two groups; however, this heterogeneity is low and cannot be detected with clinical and routine imaging examinations. The second part of this study summarized PTC nonmetastatic lymph nodes and benign reactive hyperplastic lymph nodes and built a predictive model for differentiating the two groups. The predictive model showed high discriminative ability, similar to the diagnostic value between separate groups. This indicates that there is no significant difference between the nonmetastatic lymph nodes of PTC and reactive hyperplastic lymph nodes, and simple binary classification can also achieve high diagnostic performance. In model 4, the CT value in the arterial phase was also an independent clinical risk factor, consistent with the results of models 1 and 2, suggesting that early lymph node enhancement plays an important role in distinguishing benign and malignant lymph nodes. As in models 1 and 2, the CT value in the venous phase was also an independent risk factor in model 4. The reason may be that the proportion of blood supply in the venous phase of

nonmalignant lymph nodes is higher than that in the arterial phase. In this model, the proportion of nonmalignant lymph nodes increased, so the weight of the venous phase in the identification of the two groups increased.

ROC curve and calibration curve analyses reflect the diagnostic value of the model, and DCA reflects its clinical value (25). In this study, DCA was used to evaluate the clinical effectiveness of the model, which increased its credibility. Models 1, 2 and 4 provided a clear net benefit over the entire risk threshold range, suggesting that the models have certain clinical value.

The limitations of this study are as follows. (1) In this study, the ROIs were manually outlined by doctors with high accuracy, but due to subjectivity, the repeatability of these segmentations could be poor. Although we used a high ICC as a criterion for improving the consistency of the features, this low repeatability inevitably impacted the results. To make the model more robust and more suitable for clinical application, we will attempt to solve this problem by using semiautomatic or fully automatic segmentation using consensus contours in subsequent studies. (2) The sample size was small and drawn from a single center. The sample size will be expanded, and multicenter research and external validation research will be carried out in the future to improve the efficacy of the model. (3) In this study, only solitary thyroid nodules with a pathological result of PTC or adenoma were included. The pathological types were relatively singular; subsequent studies on the lymph nodes of lesions with different pathological types are needed to expand the scope of adaptation. Since we could not accurately judge the status of each lymph node before surgery, we adopted an all-or-nothing approach to select target lymph nodes according to postoperative pathological results. This method of lymph node selection is accurate, but due to the strict inclusion criteria, the sample size of the included lymph nodes is reduced.

In conclusion, the CT-enhanced nomogram performed well in predicting metastatic lymph nodes in the central cervical region and nonmalignant lymph nodes in patients with thyroid nodules and can provide guidance for clinical decision-making. The radiomics model showed high diagnostic efficacy in distinguishing nonmetastatic lymph nodes from benign lymph nodes, but there was no significant difference in the clinical features between the groups. There may be some heterogeneity between the two groups of lesions, but its degree was insufficient to produce significant differences on the basis of radiomics. Further experimental studies are needed.

Data availability statement

The original contributions presented in the study are included in the article/supplementary material. Further inquiries can be directed to the corresponding author.

Ethics statement

Ethical review and approval was not required for the study on human participants in accordance with the local legislation and institutional requirements. The patients/participants provided their written informed consent to participate in this study.

Author contributions

Author 1(first author): Case collection, data collection and analysis, writing – first draft; Author 2: Data collection, writing - first draft; Author 3: Delineation of the region of interest; Author 4: Data analysis, writing, editing Author 5: Software, validation Author 6:(Corresponding author): Design, supervision, writing-review and editing of experimental methods. All authors contributed to the article and approved the submitted version

Conflict of interest

Author SD was employed by GE Healthcare.

The remaining authors declare that the research was conducted in the absence of any commercial or financial relationships that could be construed as a potential conflict of interest.

Publisher's note

References

1. Man YP, Ma LB, Wu CM, Zhou PT, Wei Q. The differential value of ADC and quantitative parameters of DCE-MRI at 3.0T in1q diagnosing benign and malignant cervical lymph nodes. *RadiolPractice* (2019) 34(6):619–23. doi: 10.13609/j.cnki.1000-0313.2019.06.005

2. Peltenburg B, de Keizer B, Dankbaar JW, de Boer M, Willems SM, Philippens MEP, et al. Prediction of ultrasound guided fine needle aspiration cytology results by FDG PET-CT for lymph node metastases in head and neck squamous cell carcinoma patients. *Acta Oncol* (2018) 57(12):1687–1692. doi: 10.1080/0284186X.2018.1529426

3. Hall CM, Snyder SK, Lairmore TC. Central lymph node dissection improves lymph node clearance in papillary thyroid cancer patients with lateral neck metastases, even after prior total thyroidectomy. *Am Surg* (2018) 84(4):531–536. doi: 10.1177/000313481808400426

4. Osarogiagbon RU, Ramirez RA, Wang CG, Miller LE, McHugh L, Adair CA, et al. Size and histologic characteristics of lymph node material retrieved from tissue discarded after routine pathologic examination of lung cancer resection specimens. *Ann Diagn Pathol* (2014) 18(3):136–9. doi: 10.1016/j.anndiagpath.2014.02.004

5. Forghani R, Yu E, Levental M, Som PM, Curtin HD. Imaging evaluation of lymphadenopathy and patterns of lymph node spread in head and neck cancer. *Expert Rev Anticancer Ther* (2015) 15(2):207–24. doi: 10.1586/14737140.2015.978862

6. Luo T, Xu K, Zhang Z, Zhang L, Wu S. Radiomic features from computed tomography to differentiate invasive pulmonary adenocarcinomas from non-invasive pulmonary adenocarcinomas appearing as part-solid ground-glass nodules. *Chin J Cancer Res* (2019) 31(2):329–38. doi: 10.21147/jissn.1000-9604.2019.02.07

7. Lambin P, Leijenaar RTH, Deist TM, Peerlings J, de Jong EEC, van Timmeren J, et al. Radiomics: The bridge between medical imaging and personalized medicine. *Nat Rev Clin Oncol* (2017) 14(12):749–62. doi: 10.1038/nrclinonc.2017.141

8. Li J, Wu X, Mao N, Zheng G, Zhang H, Mou Y, et al. Computed tomography-based radiomics model to predict central cervical lymph node metastases in papillary thyroid carcinoma: A multicenter study. *Front Endocrinol (Lausanne)* (2021) 12:741698. doi: 10.3389/fendo.2021.741698

9. Liu N, Xie YL, Huang ZF, Wang X. Preliminary study on radiomics based on CT contrast-enhanced images in predicting cervical lymph node metastasis in patients with papillary thyroid carcinoma. *Radiol Pract* (2021) 36(8):971–5. doi: 10.13609/j.cnki.1000-0313.2021.08.005

10. Hu DT, Xia CH, Li L, Gao B. Differentiation of benign and malignant lymph nodes in the head and neck based on CT radiomics model. *Radiol Pract* (2021) 36(8):965–70. doi: 10.13609/j.cnki.1000-0313.2021.08.004

11. Yip SS, Aerts HJ. Applications and limitations of radiomics. *Phys Med Biol* (2016) 61(13):R150–66. doi: 10.1088/0031-9155/61/13/R150

12. Park JE, Lee JH, Ryu KH, Park HS, Chung MS, Kim HW, et al. Improved diagnostic accuracy using arterial phase CT for lateral cervical lymph node metastasis from papillary thyroid cancer. *AJNR Am J Neuroradiol* (2017) 38(4):782788. doi: 10.3174/ajnr.A5054

13. Yuan WL, Wang YM, Wang Y, Wang Y, Deng W. Diagnostic method of ultrasonic and pathology for thyroid Carcinoma: A comparative study. *Chin J Oper Proc Gen Surg (ELectronic Edition)* (2018) 12(3):234–7. doi: 10.3877/cma.j.issn.1674-3946.2018.03.017

14. Liu J, Li XP, Su L, Sang JF, Yao YZ. Clinical analysis of cervical lymph node metastasis in 206 patients with papillary thyroid carcinoma. *J Southeast Univ (Med Sci Edi* (2020) 39(1):70–3. doi: 10.3969/j.issn.1671-6264.2020.01.015

15. Zhou Y, Su GY, Hu H, Ge YQ, Si Y, Shen MP, et al. Radiomics analysis of dual-energy CT-derived iodine maps for diagnosing metastatic cervical lymph nodes in patients with papillary thyroid cancer. *Eur Radiol* (2020) 30(11):6251–62. doi: 10.1007/s0033002006866x

16. Onoue K, Fujima N, Andreu-Arasa VC, Setty BN, Sakai O. Cystic cervical lymph nodes of papillary thyroid carcinoma, tuberculosis and human papillomavirus positive oropharyngeal squamous cell carcinoma: Utility of deep learning in their differentiation on CT[J]. *Am J Otolaryngol* (2021) 42(5):103026. doi: 10.1016/j.amjoto.2021.103026

17. Seidler M, Forghani B, Reinhold C, Pérez-Lara A, Romero-Sanchez G, Muthukrishnan N, et al. Dual-energy CT texture analysis with machine learning for the evaluation and characterization of cervical Lymphadenopathy[J]. *Comput Struct Biotechnol J* (2019) 17:1009–15. doi: 10.1016/j.csbj.2019.07.004

18. Liu Y, Xu X, Yin L, Zhang X, Li L, Lu H, et al. Relationship between glioblastoma heterogeneity and survival time: An MR imaging texture analysis. *AJNR Am J Neuroradiol* (2017) 38(9):16951701. doi: 10.3174/ajnr.A5279

19. Zhang L, Fang M, Yi Z, Zhu YB, Dong D, Liu X, et al. Development and application of radiomics. *Chin J Radiol* (2017) 51(1):75–7. doi: 10.3760/cma.j.issn.1005-1201.2017.01.017

20. Xu XQ, Zhou Y, Su GY, Hu H, Ge YQ, Si Y, et al. Integrating CT image features and quantitative dual-energy CT parameters for diagnosing metastatic lymph nodes from papillary thyroid carcinoma. *Chin J Radiol* (2021) 55(2):137–42. doi: 10.3760/cma.j.cn112149-20200222-00226

21. Zhao HB, Yin YL, Liu C, Zhu QQ, Shi BW, Liu LL, et al. Prediction of lymph node metastasis in patients with papillary thyroid carcinoma: A radiomics method based on dual phase contrast enhanced CT. *Radiol Pract* (2021) 36(4):458–63. doi: 10.13609/j.cnki.1000-0313.2021.04.008

22. Onoue K, Fujima N, Andreu-Arasa VC, Setty B, Qureshi MM, Sakai O, et al. Cystic cervical lymph nodes of papillary thyroid carcinoma, tuberculosis and human papillomavirus positive oropharyngeal squamous cell carcinoma: Comparative CT analysis for their differentiation. *Eur J Radiol* (2020) 132:1093–10. doi: 10.1016/j.ejrad.2020.1093-10

23. Li L, Hu DT, Xia CH, Li HX. Prediction of lymph node metastasis of head and neck malignant tumor based on CT radiomics nomogram. *J Pract Med* (2021) 37(14):1872–7. doi: 10.3969/j.issn.1006-5725.2021.14.020

24. Ren JL, Song QB, Yuan Y, Tao XF. Value of MRI radiomics for predicting occult cervical lymph nodes metastases in early-stage oral tongue squamous cell carcinoma. *Chin J Radiol* (2022) 56(1):30–5. doi: 10.3760/cma.j.cn112149-20211010-00906

25. Rousson V, Zumbrunn T. Decision curve analysis revisited: Overall net benefit, relationships to ROC curve analysis, and application to case-control studies. *BMC Med Inform Decis Mak* (2011) 11:45. doi: 10.1186/1472-6947-11-45

frontiers | Frontiers in Oncology

TYPE Original Research
PUBLISHED 07 February 2023
DOI 10.3389/fonc.2023.1030014

OPEN ACCESS

EDITED BY
Lorenz Kadletz-Wanke,
Medical University of Vienna, Austria

REVIEWED BY
Nobuhisa Matsuhashi,
Gifu University, Japan
Shilpi Sharma,
Aarvy Healthcare Superspeciality Hospital, India

*CORRESPONDENCE
Zhen Zhang
zhen2017zhang@163.com

†First author

SPECIALTY SECTION
This article was submitted to Head and Neck Cancer, a section of the journal Frontiers in Oncology

RECEIVED 28 August 2022
ACCEPTED 20 January 2023
PUBLISHED 07 February 2023

CITATION
Bai Z, Wang X and Zhang Z (2023) Pharyngoesophageal diverticulum mimicking thyroid nodules: Some interesting ultrasonographic signs. *Front. Oncol.* 13:1030014. doi: 10.3389/fonc.2023.1030014

Pharyngoesophageal diverticulum mimicking thyroid nodules: Some interesting ultrasonographic signs

Zhiqun Bai†, Xuemei Wang and Zhen Zhang*

Department of Ultrasonic Diagnosis, The First Hospital of China Medical University, Shenyang, Liaoning, China

Objective: To analyze the ultrasonographic features of pharyngoesophageal diverticulum (PED) mimicking thyroid nodules and to explore the clinical value of ultrasonography in the diagnosis of PED.

Method: The sonographic findings of 68 patients with PED were retrospectively reviewed. According to the diverticulum echo intensity characteristics, the lesions were divided into solid nodular diverticulum, gas-containing nodular diverticulum, liquid-containing nodular diverticulum, and atypical diverticular changes; and the ultrasonographic manifestations were compared among the four groups.

Results: 30/68 were solid nodular diverticula. The diverticulum cavity was oval or elliptic with a clear border, and the diverticulum wall suggested exhibited a typical hyper-hypo-hyper-echogenic pattern. The diverticulum wall and esophageal wall were seen to be continuous if multiple sections were scanned, and hypoechoic walls showed punctate blood flow. 29/68 diagnosed with air-containing nodular diverticulum, lesions appeared with gas-like hyper-echogenicity internally, with some amount of gas and change in the tail pattern during swallowing. 6/68 patients were diagnosed with liquid-containing nodular diverticulum, and the main ultrasonic manifestations were an anechoic internal diverticulum cavity that was clearly bounded from the thyroid but continuous with the esophageal wall, with a typical hyper-hypo-echoless pattern from the outside to the inside. Another 3/68 were found to have atypical diverticular changes, regional convexities of the esophageal wall with unfashioned nodules. The convex segment was continuous with the hyper-hypo-echogenic esophageal wall and could be seen on slitting scanning.

Conclusion: Overall, PEDs mimicking thyroid nodules have specific ultrasonographic features. Familiarity with them can avoid missed diagnoses and misdiagnoses.

KEYWORDS

pharyngoesophageal diverticulum, Zenker's diverticulum, Killian–Jamieson diverticulum, thyroid nodules, ultrasonographic features

Abbreviations: PED, pharyngoesophageal diverticulum; ZD, Zenker's diverticulum; FNA, fine needle aspiration; TI-RADS, Thyroid image reporting and data system; IPTH, Immunoreactive parathyroid hormone.

Introduction

Pharyngoesophageal diverticulum (PED) is a rare benign disease of the esophagus in and is always on the left side. However, it can sometimes mimic thyroid disease, leading to misdiagnosis (1, 2). Zenker's diverticulum (ZD) is the most common type of PED and was first described by Friedrich Albert von Zenker, a German pathologist, in 1867 (3). ZD occurs in the posterior wall of the esophagus due to a defect between the ring pharynx and stenosis of the pharyngeal muscles, which causes the esophagus to burst behind the mucous membranes (3). Killian–Jamieson diverticulum is a rare esophageal diverticulum that occurs at a ratio of 1:4 to ZD, with a prevalence rate between 0.0025% and 0.025%; it is characterized by an evagination of a muscular gap in the anterolateral of the wall of the esophagus (4). Both types of PED can simulate thyroid nodules, and physical examination, ultrasonography, and computed tomography may lead to clinicians unaware of PED's specific imaging features to mistake PED for thyroid nodules (5),resulting in unnecessary ultrasound-guided fine needle aspiration (FNA) or surgical treatment (6).

However, while PED is a benign disease of the esophagus, esophagofiberscopes and transesophageal echocardiography probes may mistakenly enter the diverticulum cavity, especially during ultrasound-guided FNA, which can penetrate the thin diverticulum wall, leading to subsequent inflammation, infection, and other clinical symptoms (7). Therefore, it is important to differentiate between PED and thyroid nodules. We collected and collated 68 patients with PED to analyze images of the lesion and identify sonographic diagnostic features.

Materials and methods

Research subjects

Retrospective analyses were performed on 68 patients who were suspected to have PED at the First Affiliated Hospital of China Medical University from June 2011 to June 2021. Among them, 63 patients were confirmed to have PED following a barium swallow test. Ultrasonographic findings in 5 patients had typical signs of air, and there was movement relative to the thyroid during swallowing. Diverticulum and esophageal wall that were continuous when multiple sections were scanned on at least two follow-ups were considered separate PEDs. The patients' ages ranged 18–82 years (mean, 41.7 ± 3.1 years), and 44 were women. 61 cases were misdiagnosed as thyroid nodules or parathyroid nodules, and the remaining seven cases were detected incidentally during thyroid sonography.

There were no special clinical symptoms in 62 patients; 4 patients inadvertently touched the front-neck block and moved it during swallowing, and 2 patients clinically showed swelling in the front of the neck and had difficulty swallowing.

The inclusion criteria were as follows: 1) PED with a well-established ultrasound examination and confirmed using barium meal examination or ultrasound follow-up; and 2) a "nodule" with a close relationship to the thyroid gland that may be misdiagnosed as a thyroid nodule.

The exclusion criteria were as follows: 1) PED located outside the anatomical location of the thyroid gland; and 2) patients with suspected PED on ultrasonography only but refused further examination to confirm the diagnosis.

All methods were performed in accordance with the guidelines set forth in the Declaration of Helsinki. All patients provided oral or written informed consent to participate in the study before biopsy.

Inspection methods

Ultrasonography

The diagnostic instruments used were a Preirus® (linear array probe = 5-12 MHz; Hitachi, Tokyo, Japan), AixPlorer® (linear array probe = 4-15 MHz; Supersonic, France), and IU22® (linear array probe = 5-12 MHz; Philips, Amsterdam, Netherlands).

With patients in the supine position, thyroid ultrasonography was performed routinely to determine the internal echo, with or without thyroid nodules. Thyroid image reporting and data system (TI-RADS) grading was performed (8). When cervical nodules were detected at the level of the thyroid, the size, echogenicity, shape, border, blood flow, and location of the lesion were recorded and stored for future review.

To determine whether the lesion was connected to the adjacent esophageal wall, changes in the lesion shape, echogenicity, and movement relative to the thyroid were observed during the patient's ingestion of water. To consider if a barium meal examination was appropriate, gastroscopy or follow-up observation was recommended.

Thyroid function tests, such as thyroglobulin level, antithyroid autoantibody to thyroglobulin ratio, and thyroid microsomal antigen level, were performed using a Losi cobas e601 immunoassay analyzer (Roche Diagnostics Indiana, USA).

X-ray barium meal examination

An Aquillion radiographic image enhancement system (Toshiba, Tokyo, Japan) with an IBS system was used. Standard X-ray barium meal examination was performed at the Department of Radiology of the First Affiliated Hospital of China Medical Hospital. After 4 h of fasting, the patients received resuspended barium sulfate. The patients were assessed in a standard posture. Images were obtained in the right front oblique position, left front oblique position, and positive position. The movement of the barium sulfate suspension in the esophagus was examined to identify whether there was bag-like extrusion or its limitations increased in size.

Classification of the PED

According to the internal echo, there were four types of ultrasonic features of PED in our study:

(1) Solid nodular diverticulum: The lesion was an oval-shaped mixed nodule, with outpouching of the esophageal wall and almost located on the left lobe of the thyroid gland. Compared to the echogenicity of the thyroid gland, this type is divided into solid hypoechoic nodular diverticula, solid isoechoic nodular diverticula, and solid high-low echogenic intermixed nodular diverticula (Figures 1A–C).

The nodules may project into the thyroid parenchyma, thus making it more difficult to distinguish from a thyroid nodule, or they can be located behind the tegument at the posterior margin of the thyroid. The diverticulum is typically full of

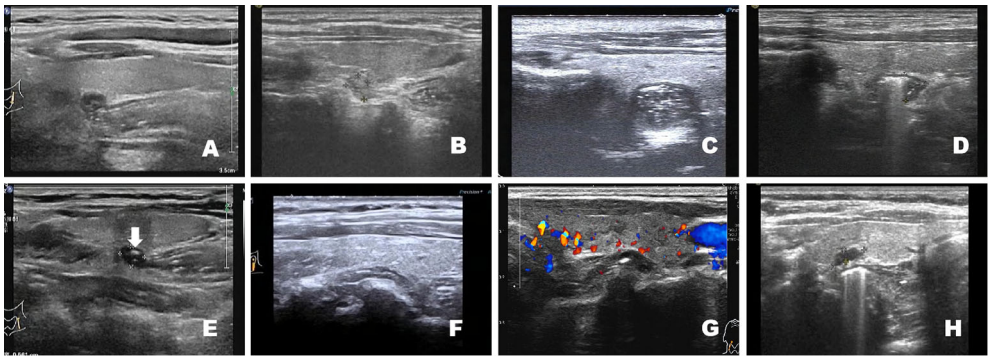

FIGURE 1
Compared with the echogenicity of the thyroid gland, solid nodular diverticula are classified as solid hypoechoic nodular diverticula **(A)**, image from a 29-year-old woman), solid isoechoic nodular diverticula **(B)**, image from a 56-year-old man), and solid high-low echogenic intermixed nodular diverticula **(C)**, image from a 34-year-old woman). Air-containing nodular diverticulum. The lesion contains a central strongly echogenic area associated with a comet-tail artifact. The presence of gas can be seen, and the tail pattern changed during swallowing **(D)**, image from a 32-year-old man). Liquid-containing nodular diverticulum with echoless interior **(E)**, white arrow, image from a 46-year-old man). Atypical diverticular changes: Regional convexities of the esophageal wall with no obvious nodules **(F)**, image from a 64-year-old man; **(G)**, image from a 51-year-old man; **(H)**, image from a 53-year-old woman).

food debris or esophageal mucosal folds, with few or no air echoes.

(2) Air-containing nodular diverticulum: The lesion contained a central strong echogenic area associated with a comet-tail artifact, and the amount of gas and the tail pattern changed during swallowing (Figure 1D).

(3) Liquid-containing nodular diverticulum: The lesion was echoless on internal dynamic scanning or after drinking water; the internal echoless parts were visible on flow sensing. There was movement relative to the thyroid during swallowing actions (Figure 1E).

(4) Atypical diverticular changes: Regional convexities of the esophageal wall with no obvious nodules (Figures 1F–H).

Statistical analysis

We used SPSS v23.0 (IBM, Armonk, NY, USA). Measurement data are presented as the mean ± SD. Student's t-test was used to compare the maximum diameter of the "T" and "V" acoustic tails in the air-containing nodular diverticulum group. Statistical significance was set at $p<0.05$.

Results

Clinical and pathology results

A total of 68 patients were included in the study. In two patients, the diverticulum was located behind the right lobe of the thyroid gland, while in 66 it was located behind the left lobe. Eight patients had Hashimoto's thyroiditis, four had autoimmune thyroiditis, three had hyperthyroidism, and 50 had combined thyroid nodules (TI-RADS 3, n=32; TI-RADS 4a, n=15; TI-RADS 4b, n=2; TI-RADS 4c, n=1) (Figure 2A), as well as three cases after thyroidectomy (Figure 2B). Immunoreactive parathyroid hormone (IPTH) and serum calcium and phosphorus levels were within the normal range in all patients. The sonographic findings and diagnostic features of PED are presented in Table 1.

Ultrasonographic findings

Solid nodular diverticulum

Thirty patients were diagnosed with solid nodular diverticulum; the long diameter of all PEDs measured using sonography ranged from 9.1 mm to 58 mm (average 17.7 ± 12.1 mm). The diverticulum wall had a typical hyper-hypo-hyper-echogenic pattern (Figure 3).

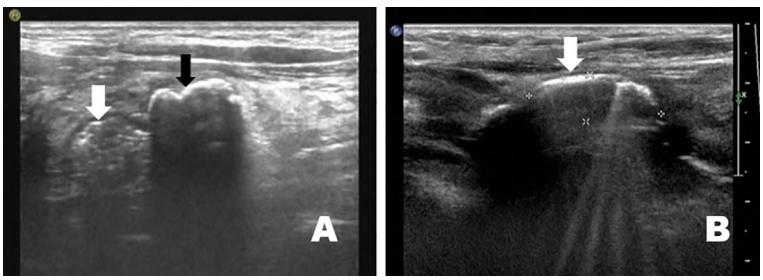

FIGURE 2
PED was found in combination with thyroid nodules in 73.5% (50/68) of cases **(A)**, image from a 56-year-old man). After thyroidectomy, a PED appeared in the thyroid region **(B)**, image from a 42-year-old man).

10.3389/fonc.2023.1030014

TABLE 1 Physical and laboratory examinations.

	Solid nodular diverticulum	Air-contained nodular diverticulum	Liquid-containing nodular diverticulum	Atypical diverticular alters
Age (years)				
≥45	21	18	2	2
<45	9	11	4	1
Sex				
Male	12	11	1	1
Female	18	18	5	2
Long diameter (mm)	17.7 ± 12.1	11.2 ± 5.3	12.1 ± 4.7	16.4 ± 11
Location				
The right	6	4	1	0
The left	24	25	5	3
With thyroid nodules				
Yes	26	20	2	2
No	4	9	4	1
Serum calcium				
Normal	27	27	3	3
Abnormal	3	2	3	0
thyroid hormone and related antibody				
Normal	24	27	2	2
Abnormal	6	2	4	1
Diagnostic method				
Barium meal test	27	26	6	3
Follow-up	3	3	0	0

More people (n=24) exhibited "nodules" that protruded into the essence of the thyroid gland and were located behind the tegument at the thyroid posterior margin than did not (n=6). The high-low echogenic pattern intermixed with solid nodular diverticulum suggested striped strong internal echoes, with no acoustic tail or acoustic shadow. It could also be seen that the diverticulum wall and esophageal wall were continuous if multiple sections were visualized, such as with a crosscut and then cut-scanned (Figure 4). Punctate blood flow could be seen as a hypoechoic middle layer of the diverticulum wall (Figure 5).

Air-containing nodular diverticulum

Twenty-nine patients were diagnosed with air-containing nodular diverticulum; the long diameter of the PED measured using sonography ranged from 4.2 mm to 48 mm (average 11.2 ± 5.3 mm). Specific ultrasonographic features included gas-like strong internal echoes with acoustic tails. According to the amount of air inside, the diverticula were divided into the "rich-in" air-type and "single" air-type. The former was seen as a gas-like hyperechogenic signal inside the diverticulum, sometimes followed by a typical "V" tail sign (Figure 6A). The latter had a hyperechoic linear appearance in the diverticulum and was sometimes followed by a typical "T" tail sign (Figure 6B). The maximum diameters of the "T" and "V" acoustic tails were 1.2–2.2 cm and 2.5–4.8 cm respectively. The difference was statistically significant ($p < 0.001$).

Liquid-containing nodular diverticulum

Six patients were diagnosed with liquid-containing nodular diverticulum; the long diameter of all PEDs measured using sonography ranged from 4.5 mm to 32 mm (average 12.1 ± 4.7 mm). The main ultrasonic manifestations were characterized by a typical hyper-hypo-echoless sign from the outside to the inside, such that the diverticulum was echoless internally. Using dynamic scanning or after drinking water, the echoless cavity was visible on flow sense imaging; however, there was no obvious change in diverticulum size. The diverticulum wall and the esophageal wall were seen as continuous if cut scanned, and there was no blood flow visualized inside.

Atypical diverticular changes: Three patients had atypical diverticular changes. The long diameter of all PEDs measured using sonography ranged from 9.6 mm to 45 mm (average 16.4 ± 11 mm). There were regional convex parts outside the esophageal wall, with no

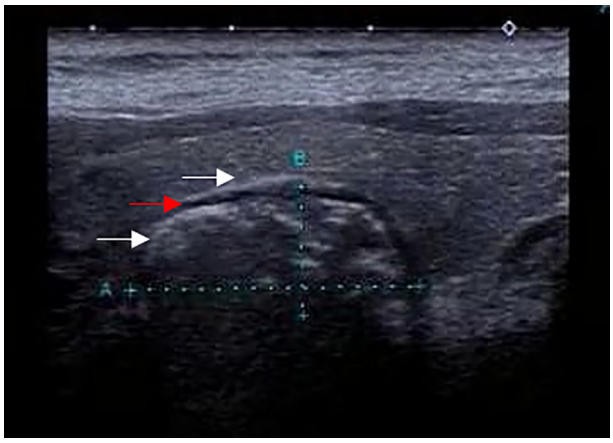

FIGURE 3
The solid nodular diverticulum wall has a typical hyper-hypo-hyper echogenic pattern (image from a 37-year-old woman).

obvious nodules. The convex segment continued with the esophageal wall and could be seen on slitting scanning. The inner diameter of the esophagus in the corresponding area increased.

Discussion

ZD, the most common form of PED, results from herniation of the Killian triangle, which is an area of muscular weakness between the transverse cricopharyngeal fibers and oblique fibers of the thyropharyngeal muscle (9). Killian–Jamieson diverticulum is an uncommon condition, resulting from herniation of the Laimer membrane leading to a defect of the esophagus in the gullet (8). Common clinical presentations include dysphagia, regurgitation, choking, chronic cough, aspiration pneumonitis, globus, weight loss and, less commonly, dysphonia (10). For decades, the mainstay of treatment for ZD was an open surgical approach through a neck incision with performance of myotomy of the UES and removal or suspen-alternative and often preferable incisionless transoral approaches have been developed (11). With the development of minimally invasive endoscopic approaches for the esophagus in recent years, peroral endoscopic myotomy (POEM) in the treatment of esophageal diverticulum has been described recently in some reports due to its successful outcomes (12).

Most PEDs were located behind the left lobe of the thyroid gland. Due to the proximity of the thyroid gland, PED can occasionally mimic thyroid nodules and can be misdiagnosed as a thyroid mass (13). Currently, there are few reports on the sonographic findings of PEDs. In previous reports (7, 14–16), many researchers have misdiagnosed PED as thyroid nodules and performed FNA or surgical treatment.

We analyzed the ultrasonographic features in 68 cases of PED mimicking thyroid nodules and classified them into four types, aiming to improve the accuracy of preoperative diagnosis and to avoid misdiagnosis and inappropriate invasive treatment. Among them, solid nodular diverticulum was the most common type and can easily confused with thyroid nodules. The main reason for this is the absence of typical gas-like strong echogenicity, which is replaced by esophageal mucosa or food debris. Sometimes it is associated with a central hyperechoic area, which can be easily confused with thyroid nodules with microcalcifications. It is useful to diagnose and prevent patients from undergoing invasive procedures, such as aspiration and unnecessary surgery.

Nevertheless, based on the ultrasound features summarized in this study, the following characteristics of solid nodular diverticula can be used to distinguish them from true thyroid nodules if examined carefully. First, the diverticulum wall has a typical hyper (esophageal mucosa and debris)-hypo (esophageal myometrium)-hyper (esophageal serosa and posterior capsule of thyroid)-echogenic pattern. Second, the PED was found to be connected to the adjacent esophageal wall if multiple sections were scanned. Moreover, when the patient swallowed, the thyroid and diverticulum moved relative to each other. Eventually, real-time

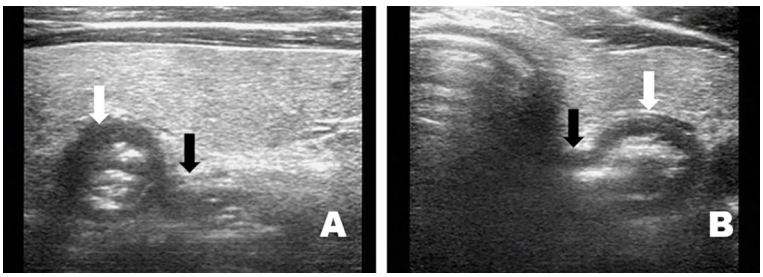

FIGURE 4
The solid nodular diverticulum wall and esophageal wall are continuous if viewed with multiple sections such as crosscut and then cut scanned **(A)**, image from a 21-year-old man: **(B)**, image from a 39-year-old man).

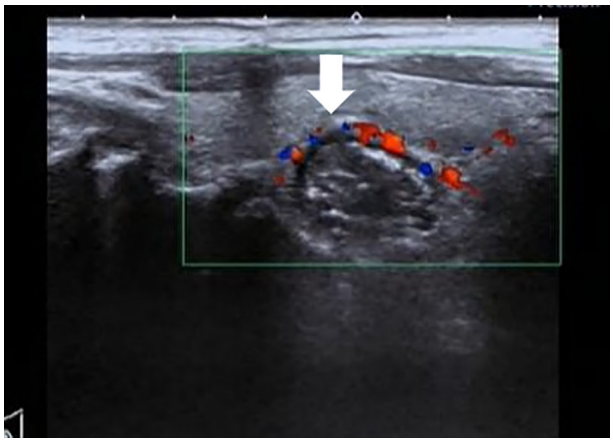

FIGURE 5
Punctate blood flow can be seen in the middle hypoechoic layer of the solid nodular diverticular (image from a 42-year-old woman).

sonography was performed during the patient's ingestion of water and demonstrated transient changes: an increase in the size of the lesion, a reduction in the definition of the margins, and heterogeneous echogenicity of the lesion's contents. No apparent blood flow signal was observed in the lesions. However, thyroid nodules have marked hypoechogenicity with regular/irregular margins and extrathyroidal growth. Punctate blood flow can also be seen. It moves in the same direction as the thyroid during swallowing, but there was no significant change in the appearance of the lesion.

It is not difficult to diagnose air-containing nodular diverticula because there are obvious gas-like strong echoes. However, there are some atypical strong echoes, and acoustic tails need to be distinguished. Based on these changes, the diverticula were divided into "rich-in" gas-type followed by a typical "V" tail sign and "single" gas-type with a typical "T" tail sign. Because of the appearance of the acoustic tail, it is difficult to view the echo of the posterior structure of the diverticulum and its relationship with the esophageal wall. The instability of the gas causes the shape of the acoustic tail to easily change with movement, so that changes were more obvious with swallowing. Twenty-six patients were diagnosed with air-containing nodular diverticulum following X-ray barium meal examination, and three patients were diagnosed after a 3-year follow-up interview.

Therefore, PED should be considered if a nodular echo intensity is found behind the thyroid, accompanied by a gas-like stronger echo and an unstable acoustic tail. At this time, the patient should be asked to swallow to observe the relative movement between the lesion and thyroid gland or the patient should drink some water for real-time dynamic scanning to increase the accuracy of diagnosis.

The amount of liquid-containing nodular diverticula was relatively low in this study. The main ultrasonic manifestation was that the diverticulum cavity was echoless. We speculate that the cysts (fluid components) are related to the caudal direction of the diverticulum. If the caudal direction is directed to the centripetal end, the liquid or residue is easily deposited and difficult to remove. The echoless area may then be formed from the mucus secreted by the esophageal mucosa or the accumulation of liquid after drinking water. If the caudal directed to the head end, gases tend to accumulate more easily. The echoless area in the diverticulum can be scanned more clearly because the thyroid gland is a sound transmission window. However, this often puzzles ultrasonographers, leading to liquid-containing nodular diverticula to be diagnosed as lesions of parathyroid origin. PEDs with anechoic changes are very rare. Nine patients were considered to have PED, but the remaining three patients were considered to have parathyroid or lymphadenopathy. Six patients were finally diagnosed with PED following X-ray barium meal examination.

We reviewed the sonograms of these six patients and found that on real-time dynamic scanning, a slight floating could be visualized in the anechoic mass in the diverticulum cavity. Therefore, real-time dynamic scanning is necessary. In the case of ambiguous potential

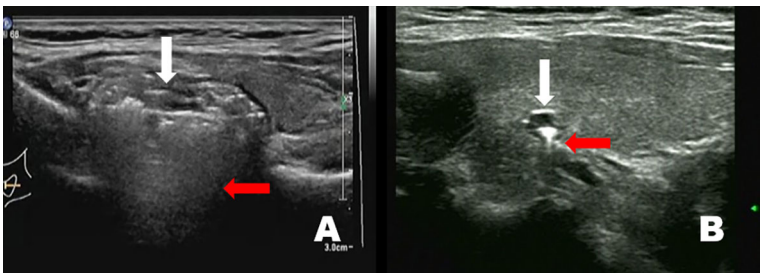

FIGURE 6
Some air-containing nodular diverticula are full of gas-like hyperechoicity internally and have a typical "V" tail sign **(A)**, image from a 35 year-old woman). Some have a hyperechoic linear appearance and sometimes have a typical "T" tail sign **(B)**, image from a 63-year-old woman).

diverticula, it is suggested to use X-ray barium meal examination to aid diagnosis.

Atypical diverticular changes in this study refer to regional convex parts outside the esophageal wall with unfashioned nodules. The formation of PED is not only due to the weakness of the esophageal wall itself, but also due to an increase in pressure in the esophageal cavity. Strictly speaking, external traction can also lead the esophageal wall to form a diverticulum (15). Three patients showed atypical diverticulum changes in this study, and one patient had Hashimoto's thyroiditis and a medical history of chronic bronchitis. Therefore, the diverticular changes may have been due to increased intraesophageal pressure. Meanwhile, inflammation can also pull the esophageal wall outward, resulting in segmental protrusion of the esophageal wall.

Conclusion

PED mimicking thyroid nodules can occasionally be encountered in daily diagnostic work. Real-time dynamic and multi-slice scanning are essential to identifying solid nodular diverticula. Identifying the typical hyper-hypo-hyper echogenic pattern of the diverticulum wall is very important in the diagnosis. It is easier to diagnose when there is gas in the diverticulum; however, familiarity with the characteristic "V" and "T" tail can increase the confidence in diagnosis. The key to diagnosing liquid-containing nodular diverticulum is echogenicity in the diverticulum. Real-time sonography performed during the patient's ingestion of water helps differentiate a PED from thyroid disease without the need for imaging with a contrast agent. For atypical diverticular changes, familiarity with the normal course of the esophageal wall is necessary to identify the disease. Awareness of changeable internal echoes and not mistaking strong echogenic foci caused by air for calcifications are the most important factors for making differentiating PEDs from thyroid nodules.

Data availability statement

The original contributions presented in the study are included in the article/supplementary material. Further inquiries can be directed to the corresponding author.

Ethics statement

The studies involving human participants were reviewed and approved by The First Hospital of China Medical University. Written informed consent for participation was not required for this study in accordance with the national legislation and the institutional requirements.

Author contributions

ZB designed the study and wrote the manuscript; XW contributed to manuscript preparation and produce metadata; ZZ revised the work and approved the version to be published. All authors contributed to the article and approved the submitted version.

Funding

This research was supported by the Natural Science Foundation of Liaoning Province, China (2019-ZD-0772), and the National Natural Science Foundation of China (Grant Nos. 81471809 and 81971639).

Conflict of interest

The authors declare that the research was conducted in the absence of any commercial or financial relationships that could be construed as a potential conflict of interest.

Publisher's note

References

1. Marcy PY, Benisvy D, Poissonnet G, Sadoul JL, Thariat J. Zenker's diverticulum: The diagnostic power of ultrasound. *Thyroid* (2010) 20:1317–8. doi: 10.1089/thy.2010.0140

2. Gray SL, O'Neill G, McGarry G. The predictive value of structured ultrasonographic staging for thyroid nodules. *J Laryngol Otol* (2014) 128:914–21. doi: 10.1017/S0022215114002072

3. Walts AE, Braunstein G. Fine-needle aspiration of a paraesophageal diverticulum masquerading as a thyroid nodule. *Diagn Cytopathol* (2006) 34:843–5. doi: 10.1002/dc.20570

4. Ota K, Onoe M, Oka M, Ota K, Taniguchi K, Sakaue M, et al. Killian-jamieson diverticulum mimicking a thyroid nodule: A case report. *J Gen Fam Med* (2019) 20:62–4. doi: 10.1002/jgf2.222

5. Kwak JY, Kim EK. Sonographic findings of zenker diverticula. *J Ultrasound Med* (2006) 25:639–42. doi: 10.7863/jum.2006.25.5.639

6. Nauschuetz KK, Ogden LL, Starling CE, Saleh MJ, Golding AC, Traweek ST. Pharyngoesophageal diverticula simulating thyroid nodules: An unusual occurrence with unique features. *Diagn Cytopathol* (2018) 46:193–7. doi: 10.1002/dc.23817

7. Chen HC, Chang KM, Su WK. Incidental pharyngoesophageal diverticulum mistaken for a thyroid nodule: Report of two cases. *Diagn Cytopathol* (2019) 47:503–6. doi: 10.1002/dc.24144

8. Abrams J. Sonographic differential diagnosis of thyroid nodule. pharyngoesophageal diverticulum. *HNO* (2011) 59:1215–8. doi: 10.1007/s00106-011-2314-z

9. Siddiq MA, Sood S, Strachan D. Pharyngeal pouch (Zenker's diverticulum). *Postgrad Med J* (2001) 77:506–11. doi: 10.1136/pmj.77.910.506

10. Martinez Paredes JF, Alfakir R, Kasperbauer JL, Rutt A. Zen. zenker diverticulum: Does size correlate with preoperative symptoms? *Int Arch Otorhinolaryngol* (2021) 26: e334-8. doi: 10.1055/s-0041-1730457

11. Castaneda D, Azar FF, Hussain I, Lara LF, Pimentel RR, Alemar G, et al. A cooperative approach for treatment of zenker's diverticulum. *Surg Endosc* (2022) 6:36. doi: 10.1007/s00464-021-08736-z

12. Zeng X, Bai S, Zhang Y, Ye L, Yuan X, Hu B. Peroral endoscopic myotomy for the treatment of esophageal diverticulum: An experience in China. *Surg Endosc* (2021) 35:1076–89. doi: 10.1007/s00464-020-07593-6

13. Haddad N, Agarwal P, Levi JR, Tracy JC, Tracy LF. Presentation and management of killian jamieson diverticulum: A comprehensive literature review. *Ann Otol Rhinol Laryngol* (2020) 129:394–400. doi: 10.1177/0003489419887403

14. Little RE, Bock JM. Pharyngoesophageal diverticuli: Diagnosis, incidence and management. *Curr Opin Otolaryngol Head Neck Surg* (2016) 24:500–4. doi: 10.1097/MOO.0000000000000309

15. Shanker BA, Davidov T, Young J, Chang EI, Trooskin SZ. Zenker's diverticulum presenting as a thyroid nodule. *Thyroid* (2010) 20:439–40. doi: 10.1089/thy.2009.0177

16. Oertel YC, Khedmati F, Bernanke AD. Esophageal diverticulum presenting as a thyroid nodule and diagnosed on fine-needle aspiration. *Thyroid* (2009) 19:1121–3. doi: 10.1089/thy.2009.0136

frontiers | Frontiers in Oncology

TYPE Original Research
PUBLISHED 09 March 2023
DOI 10.3389/fonc.2023.1048205

OPEN ACCESS

EDITED BY
Lorenz Kadletz-Wanke,
Medical University of Vienna, Austria

REVIEWED BY
Jianhua Zhou,
Sun Yat-sen University Cancer Center (SYSUCC), China
Lun Li,
Fudan University, China

*CORRESPONDENCE
Pintong Huang
huangpintong@zju.edu.cn

†These authors have contributed equally to this work

SPECIALTY SECTION
This article was submitted to Head and Neck Cancer, a section of the journal Frontiers in Oncology

RECEIVED 19 September 2022
ACCEPTED 24 February 2023
PUBLISHED 09 March 2023

CITATION
Luo J, Jin P, Chen J, Chen Y, Qiu F, Wang T, Zhang Y, Pan H, Hong Y and Huang P (2023) Clinical features combined with ultrasound-based radiomics nomogram for discrimination between benign and malignant lesions in ultrasound suspected supraclavicular lymphadenectasis.
Front. Oncol. 13:1048205.
doi: 10.3389/fonc.2023.1048205

Clinical features combined with ultrasound-based radiomics nomogram for discrimination between benign and malignant lesions in ultrasound suspected supraclavicular lymphadenectasis

Jieli Luo[1,2†], Peile Jin[1,2†], Jifan Chen[1,2], Yajun Chen[1,2], Fuqiang Qiu[1,2], Tingting Wang[1,2], Ying Zhang[1,2], Huili Pan[1,2], Yurong Hong[1,2] and Pintong Huang[1,2,3*]

[1]Department of Ultrasound in Medicine, Zhejiang University School of Medicine Second Affiliated Hospital, Zhejiang University, Hangzhou, China, [2]Research Center of Ultrasound in Medicine and Biomedical Engineering, Zhejiang University School of Medicine Second Affiliated Hospital, Zhejiang University, Hangzhou, China, [3]Research Center for Life Science and Human Health, Binjiang Institute of Zhejiang University, Hangzhou, China

Background: Conventional ultrasound (CUS) is the first choice for discrimination benign and malignant lymphadenectasis in supraclavicular lymph nodes (SCLNs), which is important for the further treatment. Radiomics provide more comprehensive and richer information than radiographic images, which are imperceptible to human eyes.

Objective: This study aimed to explore the clinical value of CUS-based radiomics analysis in preoperative differentiation of malignant from benign lymphadenectasis in CUS suspected SCLNs.

Methods: The characteristics of CUS images of 189 SCLNs were retrospectively analyzed, including 139 pathologically confirmed benign SCLNs and 50 malignant SCLNs. The data were randomly divided (7:3) into a training set (n=131) and a validation set (n=58). A total of 744 radiomics features were extracted from CUS images, radiomics score (Rad-score) built were using least absolute shrinkage and selection operator (LASSO) logistic regression. Rad-score model, CUS model, radiomics-CUS (Rad-score + CUS) model, clinic-radiomics (Clin + Rad-score) model, and combined CUS-clinic-radiomics (Clin + CUS + Rad-score) model were built using logistic regression. Diagnostic accuracy was assessed by receiver operating characteristic (ROC) curve analysis.

Results: A total of 20 radiomics features were selected from 744 radiomics features and calculated to construct Rad-score. The AUCs of Rad-score model, CUS model, Clin + Rad-score model, Rad-score + CUS model, and Clin + CUS + Rad-score model were 0.80, 0.72, 0.85, 0.83, 0.86 in the training set and 0.77, 0.80, 0.82, 0.81, 0.85 in the validation set. There was no statistical significance among the AUC of all models in the training and validation set. The calibration curve also indicated the good predictive performance of the proposed nomogram.

Conclusions: The Rad-score model, derived from supraclavicular ultrasound images, showed good predictive effect in differentiating benign from malignant lesions in patients with suspected supraclavicular lymphadenectasis.

KEYWORDS

supraclavicular lymph node, radiomics, ultrasound, nomogram, lymphadenectasis

1 Introduction

Supraclavicular lymphadenectasis has been frequently observed in patients with benign diseases such as reactive hyperplasia, tuberculosis, granulomatous inflammation, etc., and malignant diseases such as lung cancer metastasis, breast cancer metastasis, esophageal cancer metastasis, etc (1). Thus, it is important to distinguish between benign and malignant supraclavicular lymph nodes (SCLNs) for the further treatment of patients (2, 3). Computerized tomography (CT) examination is based on the density of lymph nodes and surrounding soft tissue to distinguish, the enlarged supraclavicular lymph nodes are often indistinguishable from the surrounding tissues and muscles on plain CT scan (4). Due to the fixed and superficial location of the supraclavicular region and clear supraclavicular anatomical structure, high frequency conventional ultrasound (CUS) has its unique advantages for SCLNs examination. CUS is preferred as the first choice for SCLNs with high resolution, low cost and no radiation. However, there is overlap between benign and malignant images for atypical CUS features.

Radiomics, a process of converting radiographic images into quantifiable information, can provide more comprehensive and richer information than radiographic images, which are imperceptible to human eyes (5, 6). Imaging examination is one of the routine steps in routine clinical diagnosis, so radiomics research based on images has certain feasibility. Some studies showed that radiomics analysis on CUS images can effectively predict malignant parotid gland lesions (7). Some studies have shown that image feature-based radiomics extraction has objective characteristics and great value in predicting central lymph node metastasis in papillary thyroid carcinoma patients with Hashimoto's thyroiditis (8). However, the clinical value of CUS-based radiomics analysis to differentiate of benign and malignant SCLNs was unknown.

Therefore, the purpose of this investigation was to extract the radiomics parameters from supraclavicular CUS images and to establish predictive a nomogram radiomics score (Rad-score) model to noninvasively identify benign and malignant SCLNs.

2 Materials and methods

2.1 Patients

Between January 2021 and July 2022, a total of 189 patients participated in the retrospective study, including pathologically confirmed 50 benign lesions and 139 malignant lesions. The inclusion criteria were as follows: (1) patients with CUS suspected SCLNs; (2) patients who underwent pathological examination within 2 weeks after a SCLNs CUS examination; (3) patients who had high-quality ultrasound image; (4) patients who had definite pathological findings. The exclusion criteria were as follows: (1) patients who underwent previous SCLN treatment (resection biopsy, radiotherapy, chemotherapy); (2) patients who had poor ultrasound image quality; (3) patients who had incomplete clinical data. (4) patients who missed histopathological results. (5) lesion larger than 5 cm in diameter due to the limited width of the US probe.

2.2 Ultrasound examination and pathological examination

The CUS examination was performed using GE LOGIQ E9, Esaote Mylab 90, Toshiba Aplio 500, Mindray Resona 7, and Philips iU22 with corresponding high-frequency linear array probes. Each patient was placed in the supine position while lying on the examination bed. Then, the neck was fully extended, and the patient was told to breathe calmly. The SCLNs were examined by 3-year experience radiologist in superficial CUS. If there were multiple lesions, then the most suspicious would be first recommended for further pathological examination. If the most suspicious one is not suitable for biopsy, the largest one (short diameter) would be second recommended for further pathological examination. The boundary (clear and unclear), shape (long/short diameter < 2, long/short diameter ≥ 2), calcification (with calcification, without calcification), hilus (present or absent), margin (well-defined and ill-defined), structure (cystic or hyperechoic nodule, no cystic and hyperechoic nodule) of the SCLNs were observed and recorded. The most suspected supraclavicular lymphadenectasis were included in the study. CUS suspected SCLN was submitted to ultrasound guided biopsy at ultrasound department. The pathological section was read by a pathologist with more than 5 years of experience. For the pathological benign SCLN, we followed up at least for 6 months. No benign SCLN had progression on ultrasound image.

2.3 Region of interest (ROI) segmentation and feature extraction

Firstly, the patients were randomly divided into the training and validation groups in a 7:3 ratio. The jpg format ultrasound images were exported from the imaging system and imported into PyCharm software (Community edition 2022.2). All images were

resampled and normalized before feature extraction (7). Then, the ROI was manually segmented by an experienced radiologist and confirmed by another one by using Labelme (3.16.7) software package. Both were blinded to the pathological results before performing image annotation, and consensus was reached by discussion in cases of disagreement. Finally, the radiomics data was extracted by python package pyradiomics (V3.0.1) (https://pyradiomics.readthedocs.io/en/latest/features.html) and 744 radiomics features from SCLNs were extracted in this study.

2.4 Radiomics feature selection

Radiomics features were extracted from lesions after image processing with different filters by using the open-source Pyradiomics package V3.0.1 and were divided into the following classes: (a) first-order statistics; (b) shape-based features; (c) high-order features, including gray-level co-occurrence matrix (GLCM), gray-level size zone matrix (GLSZM), gray-level run length matrix (GLRLM), gray-level dependence matrix (GLDM), and neighboring gray tone difference matrix (NGTDM). Firstly, independent *t*-test was used to select significant features with statistically significant difference ($P < 0.05$). Then, the least absolute shrinkage and selection operator (LASSO) was used to select nonzero coefficients by 10-fold cross validation. Finally, Rad-score was calculated based on the selected features.

2.5 Models construction

The clinical and CUS data were analyzed by multivariate analysis firstly to select the statistically significant predictors of distinguishing between benign and malignant lesions and follow by logistic regression analysis. The Rad-score model, CUS model, radiomics-CUS (Rad-score + CUS) model, clinic-radiomics (Clin + Rad-score) model, and combined CUS-clinic-radiomics (Clin + CUS + Rad-score) model were established both in training and validation sets. The calibration curve was used to evaluate the calibration ability. The prediction accuracy of the models was represented by the receiver operating characteristic (ROC) curve and was quantified by the area under the ROC curve (AUC) in both the training and test sets.

2.6 Statistical analysis

Statistical analyzes were performed using statistical software for Windows version 23.0 (SPSS Inc., Chicago, IL, USA) and R software version 4.2.1 (R project for statistical computing). Quantitative data with abnormal distribution was expressed as median (interquartile range 25^{th}, 75^{th} percentile). Quantitative data with normal distribution was expressed as mean ± standard deviation. Wilcox test was conducted to compare the data displaying an abnormal distribution. Statistical analysis was by chi-squared test when comparing categorical variables. The LASSO method constructed a penalty function by adding constraint conditions, and a prediction model was constructed by performing a 10-fold cross-validation. The models were built using logistic regression and the diagnostic performance for differentiating between benign and malignant lesions was using ROC. DeLong's test was used to evaluate different ROC curves. Calibration curves were constructed to assess the predictive value of different models. A *P* value of less than 0.05 was considered statistically significant.

3 Results

3.1 Basic information of patients with SCLNs lymphadenectasis

A total of 189 patients were recruited (Figures 1, 2), including 50 pathologically confirmed benign (16 males and 34 females; age 59.5 (44.5-67.75) years) and 139 malignant (73 males and 66 females; age 65 (53.5-70) years). The specific pathological findings of 50 benign and 139 malignant SCLNs lymphadenectasis was showing (Supplemental Table 1). The median follow-up after biopsy for benign SCLNs lymphadenectasis was 10 (range, 6-20) months. No benign SCLN had progression on ultrasound image. The SCLNs malignant rates of the training set and the validation set were 70.23% and 81.03%, respectively. There were no significant differences in patient age, sex, location, pathology, diameter, tumor history, boundary, margin, calcification, shape, hilus, structure, and rad-score between the training set and the validation set ($P>0.05$), as shown in Table 1.

3.2 Univariate analysis of clinical features, CUS features, and Rad-score for malignant lesions

Benign lesions were more likely to be found with no tumor history ($P<0.05$, Table 2) in the training set. The validation set also

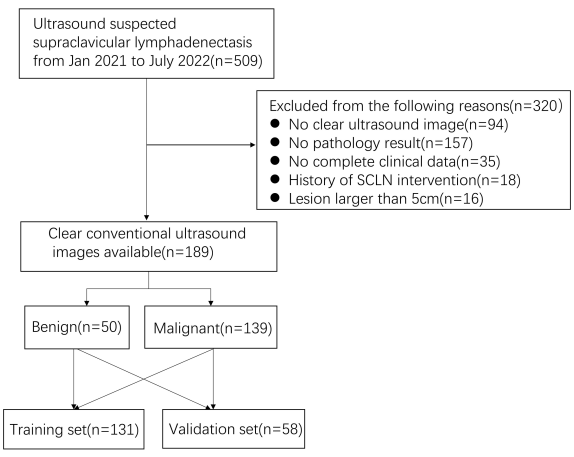

FIGURE 1
The flowchart of patient selection for dividing into the training set and validation set.

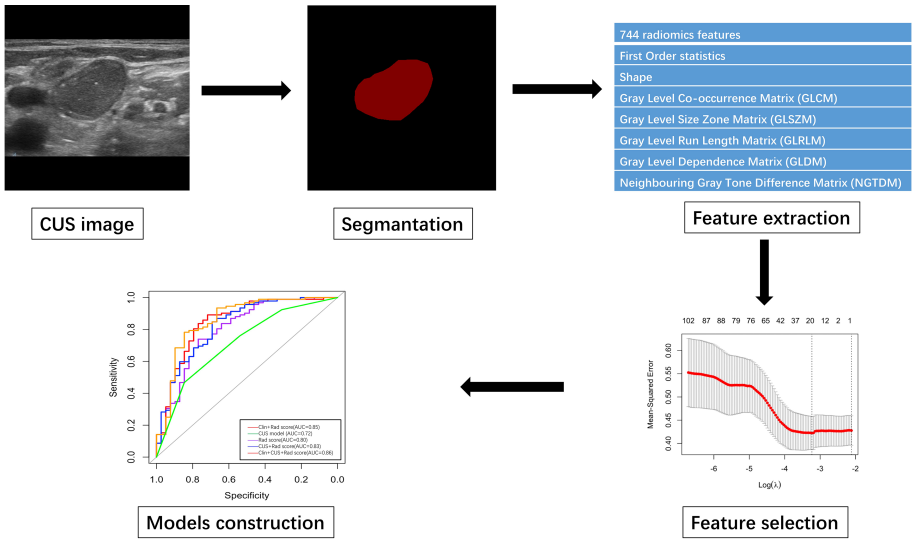

FIGURE 2
The flowchart of CUS segmentation, feature extraction, feature selection and models construction.

found the same findings. For CUS features, well-defined margin, clear boundary, and long/short diameter≥2 shape were commonly observed in benign lesions (all $P<0.05$) in the training set. The same results were also found in the validation set.

Seven hundred and forty-four radiomic features were extracted from each ROI, and a total of 20 radiomic features (Supplemental Table 2) with non-zero coefficients were screened out based on t test and LASSO (Figure 3). The Rad-score was calculated between benign and malignant lesions (Supplemental Table 3). The results showed that patients with benign lesions had lower Rad-score than patients with malignant lesions, which was statistically significant in both training (0.64(0.16, 0.9) vs. 1.08 (0.87, 1.26), $P < 0.05$) and validation sets (0.63(0.13, 0.89) vs. 0.98 (0.81, 1.24), $P < 0.05$).

TABLE 1 Clinic-CUS characteristics of suspected supraclavicular lymphadenectasis between training and validation set.

Characteristic	Training set	Validation set	*P* value
Age(year)	65 (51,70)	62 (52.25,68.75)	0.73
Diameter (cm)	2.11 (1.28,2.77)	2.19 (1.7,2.9)	
Sex (%)			0.80
Male	63 (48%)	26 (45%)	
Female	68 (52%)	32 (55%)	
Location (%)			0.06
Left	74 (56%)	42 (72%)	
Right	57 (44%)	16 (28%)	
Tumor history			0.56
No	82 (63%)	33 (57%)	
Yes	49 (37%)	25 (43%)	
Pathology			0.17
Benign	39 (30%)	11 (19%)	
Malignant	92 (70%)	47 (81%)	
Boundary			0.12
Clear	85 (65%)	37 (64%)	

(Continued)

TABLE 1 Continued

Characteristic	Training set	Validation set	*P* value
Unclear	46 (35%)	21 (36%)	
Margin			0.19
Well-defined	58 (44%)	19 (33%)	
Ill-defined	73 (56%)	39 (67%)	
Calcification			0.99
No calcification	97 (74%)	43 (74%)	
Calcification	34 (26%)	15 (26%)	
Shape			0.61
Long/short diameter≥2	43 (33%)	22 (38%)	
Long/short diameter<2	88 (67%)	36 (62%)	
Hilus			0.71
Present	14 (11%)	8 (14%)	
Absent	117 (89%)	50 (86%)	
Structure			0.11
No cystic and hyperechoic nodule	125 (95%)	51 (88%)	
Cystic or hyperechoic nodule	6 (5%)	7 (12%)	
Rad-score	0.98 (0.71,1.19)	0.95 (0.77,1.15)	0.86

CUS, conventional ultrasound.

3.3 Multivariate analysis of variables for predicting malignant lesions

In the multivariate analysis of clinical information, CUS features and Rad-score characteristics, tumor history (OR=4.88, 95%CI 1.65-17.24), long/short diameter < 2 shape (OR=2.69, 95% CI 1.04-7.14), Rad-score (OR=15.57, 95%CI 5.20-64.49) were significantly correlated with pathological results ($P<0.05$). However, sex, boundary, and the margin were not independent signatures for predicting malignant lesions (Supplemental Table 4).

TABLE 2 Univariate analysis of clinical information, CUS features, and Rad-score for distinguishing benign from malignant lesions in the training set.

	Benign	Malignant	*P* value
Clinical information			
Age (year)	57 (45, 67.5)	65.5 (54.75, 70)	0.093
Male/Female	13/26	50/42	0.044
Diameter (cm)	2.11 (1.28, 2.77)	2.1 (1.35, 3.04)	0.678
Tumor history (N/Y)	33/6	49/43	0.001
CUS feature			
Boundary (clear/unclear)	31/8	54/38	0.038
Margin (well-defined/ill-defined)	24/15	34/58	0.016
Calcification (no calcification/calcification)	27/12	70/22	0.548
Shape (long/short diameter ≥ 2/< 2)	21/18	22/70	0.002
Hilus (present/absent)	4/35	10/82	1.000
Structure (no cystic and hyperechoic nodule/cystic or hyperechoic nodule)	38/1	87/5	0.669
CUS-radiomics			
Rad-score	0.64 (0.16,0.9)	1.08 (0.87,1.26)	<0.001

CUS, conventional ultrasound.

10.3389/fonc.2023.1048205

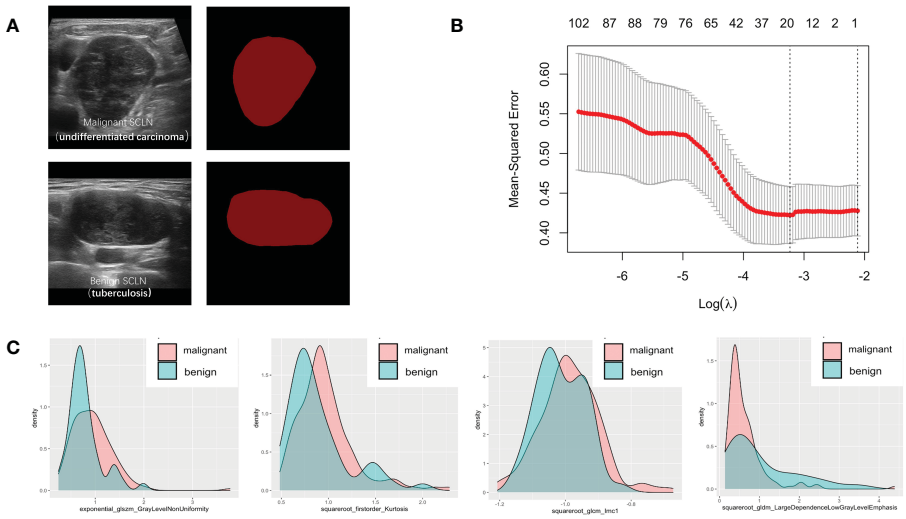

FIGURE 3
Variables extracted from benign and malignant supraclavicular lymph node. **(A)** The ROI of benign and malignant supraclavicular lymph node. **(B)** The Mean-square error plot of LASSO regression in supraclavicular lymph node. **(C)** The density plots between extracted radiomics variables in benign and malignant supraclavicular lymph node.

3.4 Performance, construction and validation of nomogram

The Rad-score model, Clin + Rad-score model, Rad-score + CUS model, and Clin + CUS + Rad-score model were constructed based on clinical information, CUS features and Rad-score (Figure 4). The AUC of CUS model, Rad-score model, Clin + Rad-score model, Rad-score + CUS model, and Clin + CUS + Rad-score model were 0.72, 0.80, 0.85, 0.83 and 0.86 in the training set, respectively (Figure 5; Table 3). The AUC of CUS model, Rad-score model, Clin + Rad-score model, Rad-score + CUS model, and Clin + CUS + Rad-score model were 0.80, 0.77, 0.82, 0.81 and 0.85 in the validation set. By the Delong test, there was no significant difference in the AUC of the Rad-score between the training set and the validation set (p=0.70). There were no significant differences among all models in terms of AUC. A nomogram that contains Rad-score, shape and tumor history variables describing SCLNs to predict the malignant lesion with CUS suspected supraclavicular lymphadenectasis.

4 Discussion

SCLN metastasis is of great significance for treatment decision-making and prognostic evaluation (9–11). Among all imaging methods, CUS is considered the most convenient method for assessing the characteristics of SCLN. However, the diagnostic value of CUS in assessing lymph nodes is controversial. Zheng et al.'s study reported that the diagnostic performance of axillary CUS was poor with an AUC of 0.585-0.719 (12). In our study, several clinical and ultrasound imaging features were associated with the differential diagnosis of benign and malignant lesions. Benign SCLNs were more likely to have no tumor history, which was consistent with previous research (13). For CUS features, well-defined margin, clear boundary, and long/short diameter ≥ 2 shape were commonly observed in benign lesions, but also occasionally seen in malignant lesions (14). The overlapping of CUS features and clinic data brings some difficulties in the diagnosis of benign and malignant lymph nodes.

CUS-based radiomics could provide a large number of quantitative image features from ultrasonic images, which tend to be hard for the naked eyes to recognize (7). Seven hundred and forty-four radiomics features were selected from SCLN. These included first-order statistics and high-order features with various filters (NGTDM, GLRLM, GLSZM, GLCM, and GLDM). First-order statistics, also known as grayscale histogram features, are mainly used to perform statistical calculations on the entire image or the ROI within the image, and are used to describe the grayscale of the image. Second-order statistics refer to the spatial relationship between the intensities of each voxel. Higher-order statistics are used for feature extraction and image preprocessing such as wavelet decomposition, Fourier transform and other filtering (15). The software automatically extracts radiomics features to compensate for errors introduced by manual and subjective measurements. In our results, the AUCs of Rad-score model, Clin + Rad-score model, Rad-score + CUS model, and Clin + CUS + Rad-score model were 0.80, 0.85, 0.83, 0.86 in the training set and 0.77, 0.82, 0.81, 0.85 in

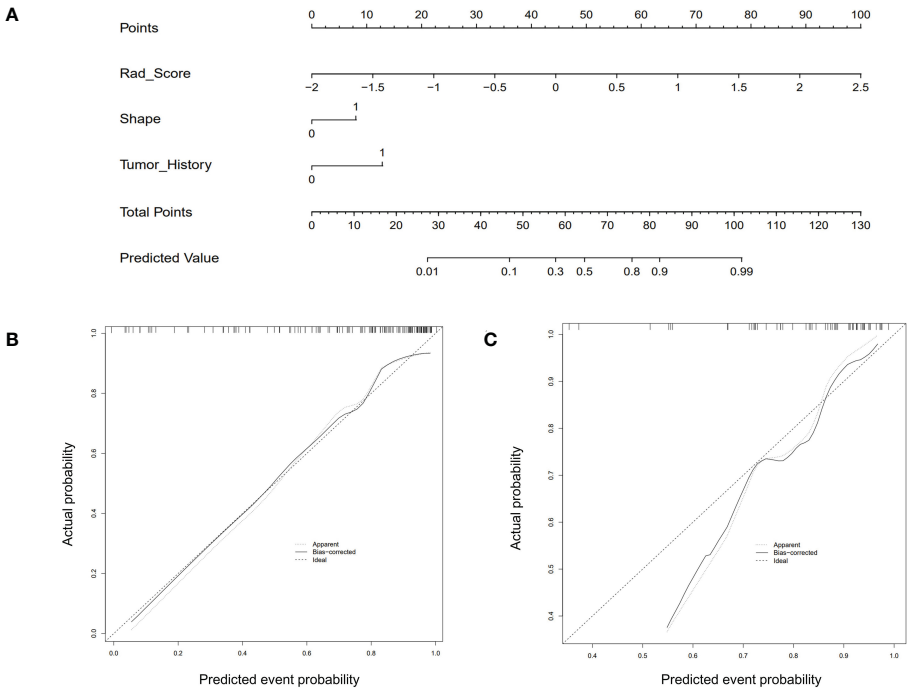

FIGURE 4
The CUS-based radiomics nomogram and calibration curves of the nomogram. **(A)** Integrating Rad-score, shape, and tumor history, the CUS-based nomogram was established. Calibration curves of the nomogram in the training **(B)** and testing **(C)** set.

the validation set. There were no significant differences among all models in terms of AUC. Zhou et al. (16) developed an ultrasound radiomics nomogram to identify central lymph node metastasis in patient papillary thyroid cancer, the AUCs for the training set, internal validation set, and external validation set were 0.816 and 0.858, respectively. Radiomics based on analysis of CUS images showed good performances as other routine methods. Through the Rad-score model, we could distinguish benign and malignant lesions when supraclavicular lymphadenopathy is suspected on ultrasonography.

This study has some limitations. First, the overall sample size is small. The sample size should be expanded in future studies. Second, this was a single-center retrospective study with good predictive power, which may indicate the need for an external validation set to validate this predictive model. Third, the study included several different ultrasound machines that could have

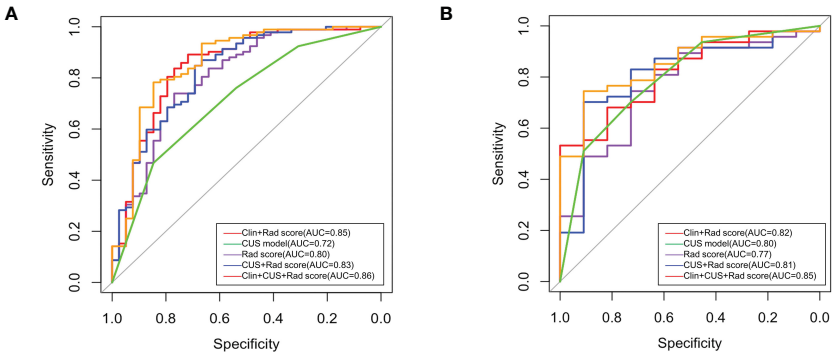

FIGURE 5
Receiver operating characteristic (ROC) curves of all models in training set **(A)** and validation set **(B)**.

TABLE 3 The ROC, accuracy, sensitivity, and specificity of five models in the training set and validation set.

Group	Model	AUC (95%CI)	Accuracy	Sensitivity	Specificity
Training set	Rad-score	0.80 (0.71-0.89)	0.75	0.74	0.77
	CUS	0.72 (0.62-0.81)	0.58	0.47	0.85
	Clin + Rad-score	0.85(0.77-0.93)	0.84	0.89	0.72
	CUS + Rad-score	0.83(0.75-0.91)	0.80	0.85	0.69
	Clin + CUS + Rad-score	0.86(0.78-0.94)	0.80	0.78	0.85
Validation set	Rad-score	0.77(0.61-0.92)	0.74	0.75	0.73
	CUS	0.80 (0.65-0.94)	0.71	0.70	0.73
	Clin + Rad-score	0.82(0.69-0.94)	0.62	0.53	1.00
	CUS + Rad-score	0.81(0.66-0.96)	0.74	0.70	0.91
	Clin + CUS + Rad-score	0.85(0.74-0.96)	0.78	0.75	0.91

AUC, area under the curve; CI, confidence interval; Rad-score, radiomics score; Clin, Clinical; CUS, common ultrasound.

affected the findings. Fourth, the biopsy specimen had a possibility of false negative. In the future, large, multi-center clinical studies, more subgroups and enhanced ultrasound images are needed to further confirm the findings of this study.

5 Conclusion

In conclusion, the radiomics nomogram, derived from CUS, showed favorable prediction efficacy for differentiating benign from malignant in patients with suspected supraclavicular lymphadenectasis. The Rad-score model improves the differentiation of the benign lesion from malignant lesion.

Data availability statement

The raw data supporting the conclusions of this article will be made available by the authors, without undue reservation.

Ethics statement

The retrospective study was approved by the ethics consultant committee of Zhejiang University School of Medicine Second Affiliated Hospital. Written informed consent for participation was not required for this study in accordance with the national legislation and the institutional requirements.

Author contributions

JL and PJ contributed equally to this study. JL and PJ were responsible for the conception and design of this study. JL and JC contributed to the data analysis and writing of the manuscript. YC, FQ, and TW contributed to data collection. YH, YZ, HP, and PJ contributed to data analysis and manuscript preparation. PH contributed to writing-reviewing. All authors contributed to the article and approved the submitted version.

Funding

This study was funded by the National Natural Science Foundation of China (Grants No. 81420108018), Natural Science Foundation nonprofit research projects of Zhejiang Province of China (Grants No.LGF19H180020) and China ultrasound physician technology star program (Grants No.KJXX2018003).

Acknowledgments

We thank the National Natural Science Foundation of China, Natural Science Foundation nonprofit research projects of Zhejiang Province of China, China ultrasound physician technology star program for support.

Conflict of interest

The authors declare that the research was conducted in the absence of any commercial or financial relationships that could be construed as a potential conflict of interest.

Publisher's note

Supplementary material

The Supplementary Material for this article can be found online at: https://www.frontiersin.org/articles/10.3389/fonc.2023.1048205/full#supplementary-material

References

1. Zhang W, Peng J, Zhao S, Wu W, Yang J, Ye J, et al. Deep learning combined with radiomics for the classification of enlarged cervical lymph nodes. *J Cancer Res Clin Oncol* (2022), 148(10):2773-2780. doi: 10.1007/s00432-022-04047-5

2. Yu J, Deng Y, Liu T, Zhou J, Jia X, Xiao T, et al. Lymph node metastasis prediction of papillary thyroid carcinoma based on transfer learning radiomics. *Nat Commun* (2020) 11(1):4807. doi: 10.1038/s41467-020-18497-3

3. Coopey SB. Supraclavicular and contralateral axillary lymph node involvement in breast cancer patients. *Ann Surg Oncol* (2022), 29(10):6100-6105. doi: 10.1245/s10434-022-12134-7

4. Morawitz J, Bruckmann NM, Dietzel F, Ullrich T, Bittner AK, Hoffmann O, et al. Comparison of nodal staging between CT, MRI, and [(18)F]-FDG PET/MRI in patients with newly diagnosed breast cancer. *Eur J Nucl Med Mol Imag.* (2022) 49(3):992–1001. doi: 10.1007/s00259-021-05502-0

5. Xv Y, Lv F, Guo H, Liu Z, Luo D, Liu J, et al. A CT-based radiomics nomogram integrated with clinic-radiological features for preoperatively predicting WHO/ISUP grade of clear cell renal cell carcinoma. *Front Oncol* (2021) 11:712554. doi: 10.3389/fonc.2021.712554

6. Bernatowicz K, Grussu F, Ligero M, Garcia A, Delgado E, Perez-Lopez R. Robust imaging habitat computation using voxel-wise radiomics features. *Sci Rep* (2021) 11 (1):20133. doi: 10.1038/s41598-021-99701-2

7. Li Q, Jiang T, Zhang C, Zhang Y, Huang Z, Zhou H, et al. A nomogram based on clinical information, conventional ultrasound and radiomics improves prediction of malignant parotid gland lesions. *Cancer Lett* (2022) 527:107–14. doi: 10.1016/j.canlet.2021.12.015

8. Jin P, Chen J, Dong Y, Zhang C, Chen Y, Zhang C, et al. Ultrasound-based radiomics nomogram combined with clinical features for the prediction of central lymph node metastasis in papillary thyroid carcinoma patients with hashimoto's thyroiditis. *Front Endocrinol (Lausanne).* (2022) 13:993564. doi: 10.3389/fendo.2022.993564

9. Chen SC, Shen SC, Yu CC, Huang TS, Lo YF, Chang HK, et al. Long-term outcomes of breast cancer patients who underwent selective neck dissection for metachronous isolated supraclavicular nodal metastasis. *Cancers (Basel)* (2021) 14 (1):164. doi: 10.3390/cancers14010164

10. Diao K, Andring LM, Barcenas CH, Singh P, Carisa Le-Petross H, Reed VK, et al. Contemporary outcomes after multimodality therapy in patients with breast cancer presenting with ipsilateral supraclavicular node involvement. *Int J Radiat Oncol Biol Phys* (2022) 112(1):66–74. doi: 10.1016/j.ijrobp.2021.08.026

11. Li Y, Wang T, Fu YF, Shi YB, Wang JY. Computed tomography-guided biopsy for sub-centimetre lung nodules: Technical success and diagnostic accuracy. *Clin Respir J* (2020) 14(7):605–10. doi: 10.1111/crj.13172

12. Zheng X, Yao Z, Huang Y, Yu Y, Wang Y, Liu Y, et al. Deep learning radiomics can predict axillary lymph node status in early-stage breast cancer. *Nat Commun* (2020) 11(1):1236. doi: 10.1038/s41467-020-15027-z

13. Gronkiewicz JJ, Vade A. Cervical lymph node fine needle aspiration in patients with no history of malignancy. *Ultrasound Q* (2013) 29(4):323–6. doi: 10.1097/RUQ.0b013e3182a44eff

14. Ye F, Gong Y, Tang K, Xu Y, Zhang R, Chen S, et al. Contrast-enhanced ultrasound characteristics of preoperative central cervical lymph node metastasis in papillary thyroid carcinoma. *Front Endocrinol (Lausanne).* (2022) 13:941905. doi: 10.3389/fendo.2022.941905

15. Linsalata S, Borgheresi R, Marfisi D, Barca P, Sainato A, Paiar F, et al. Radiomics of patients with locally advanced rectal cancer: Effect of preprocessing on features estimation from computed tomography imaging. *BioMed Res Int* (2022) 2022:2003286. doi: 10.1155/2022/2003286

16. Zhou SC, Liu TT, Zhou J, Huang YX, Guo Y, Yu JH, et al. An ultrasound radiomics nomogram for preoperative prediction of central neck lymph node metastasis in papillary thyroid carcinoma. *Front Oncol* (2020) 10:159. doi: 10.3389/fonc.2020.01591

frontiers | Frontiers in Oncology

TYPE Case Report
PUBLISHED 18 May 2023
DOI 10.3389/fonc.2023.1078814

OPEN ACCESS

EDITED BY
Thomas Gander,
University Hospital Zürich, Switzerland

REVIEWED BY
Zhaohui Shi,
Institute of ENT and Shenzhen Key Laboratory of ENT, China
Wei Gao,
Longgang Otolaryngology Hospital, China
Changyuan Wei,
Affiliated Tumor Hospital of Guangxi Medical University, China

*CORRESPONDENCE
Jieshan Guan
guanjieshan1785@gzucm.edu.cn

†These authors have contributed equally to this work

RECEIVED 24 October 2022
ACCEPTED 25 April 2023
PUBLISHED 18 May 2023

CITATION
Zhang J, Dai Z, Liao P and Guan J (2023) Partial response to niraparib in combination with tislelizumab in a patient with metastatic undifferentiated tonsillar carcinoma: a case report and literature review.
Front. Oncol. 13:1078814.
doi: 10.3389/fonc.2023.1078814

Partial response to niraparib in combination with tislelizumab in a patient with metastatic undifferentiated tonsillar carcinoma: a case report and literature review

Jing Zhang[1,2†], Zi Dai[1,2†], Pei Liao[1,2†] and Jieshan Guan[1*]

[1]Department of Oncology, The First Affiliated Hospital of Guangzhou University of Traditional Chinese Medicine, Guangzhou, China, [2]First Clinical Medical College, Guangzhou University of Traditional Chinese, Guangzhou, China

Undifferentiated tonsillar carcinoma is an extremely rare head and neck cancer. The treatment options are challenging due to insensitivity to chemotherapy and easy development of drug resistance. In this study, we reported a case of advanced undifferentiated tonsillar carcinoma with multiple mediastinal lymph node metastases that failed to respond to chemotherapy. Next-generation sequencing (NGS) revealed germline BReast CAncer gene (BRCA) 1 mutation and a high tumor mutational burden. Poly (adenosine diphosphate [ADP]-ribose) polymerase (PARP) inhibitors have demonstrated efficacy in solid tumors with BRCA1/2 mutations. Immune checkpoint inhibitors (ICIs) provide a treatment option for unresectable head and neck cancer. After local control treatment by embolization, niraparib and tislelizumab were administered to this patient. A partial response (PR) was achieved, and progression-free survival (PFS) and overall survival (OS) were 12 months and 19 months, respectively. This case reveals molecular profiling as an important therapeutic strategy for rare malignancies with no standard of care. Moreover, the underlying synergistic antitumor activity of PARPi and PD-L1 blockade was reviewed.

KEYWORDS

metastatic undifferentiated tonsillar carcinoma, niraparib, PARP inhibitor, immune checkpoint inhibitors, next-generation sequencing, case report

Introduction

Over the past 20 years, the incidence of primary tonsillar malignancies has increased at an annual rate of 0.35% (1). Squamous cell carcinoma with human papillomavirus (HPV) is the most common type with a good prognosis due to its sensitivity to radiation and chemotherapy (2–4). In contrast, HPV-negative undifferentiated tonsillar carcinoma is a

rare malignancy, which is insensitive to chemotherapy. There is no available standard treatment for patients with inoperable or metastatic disease at diagnosis, and prognosis is poor. Programmed cell death 1 (PD-1) checkpoint inhibitors have been used in platinum-resistant recurrent/metastatic (R/M) head and neck squamous cell carcinoma (HNSCC), with an overall response rate of 14% in patients with PD-L1-positive/HPV-negative disease (5). Niraparib is an oral, highly selective poly (adenosine diphosphate [ADP]-ribose) polymerase (PARP)1 and PARP2 inhibitor with antitumor efficacy in BRCA1/2-mutated solid tumors (6). We present the first case of metastatic HPV-negative undifferentiated tonsillar carcinoma with germline BRCA1 mutation and high tumor mutational burden (TMB). The patient was administered niraparib and tislelizumab after failed chemotherapy and achieved a partial response (PR). With improvement in quality of life, the patient had a progression-free survival (PFS) of 12 months and an overall survival (OS) of 19 months. Moreover, we also systematically reviewed the literature and explored the potential mechanism of the synergy of PARP inhibitors and immunotherapy. The following case is presented in accordance with the CARE reporting checklist.

Case presentation

A 50-year-old man with pharyngalgia and right neck mass presented to the hospital in December 2020. The patient had previously been diagnosed with hepatitis B infection and diabetes, had long-term work experience with chemical drugs and had no history of smoking, alcohol consumption and history of cancers. Physical examination showed an exophytic yellow-white cauliflower-like mass on the surface of the right tonsil, partially extending beyond the midline, but not invading other tissues around the oropharynx (Figure 1A). Several swollen lymph nodes were palpable on both sides of the neck. Head and neck magnetic resonance imaging (MRI) (December 20, 2020) showed a mass of 32 mm × 16 mm in the right tonsil and multiple enlarged lymph nodes around the bilateral carotid arteries. The largest lymph nodes were 40 mm × 23 mm (right) and 36 mm × 31 mm (left). Whole-body Positron Emission Tomography-Computed Tomography (PET/CT) (December 22, 2020) showed multiple enlarged lymph nodes in the mediastinum and hilum, with a maximum of 21 × 18 mm (Figure 1A). Biopsy of cervical lymph nodes and the tonsil mass revealed diffuse growth of medium to large lymphocyte tumor cells,

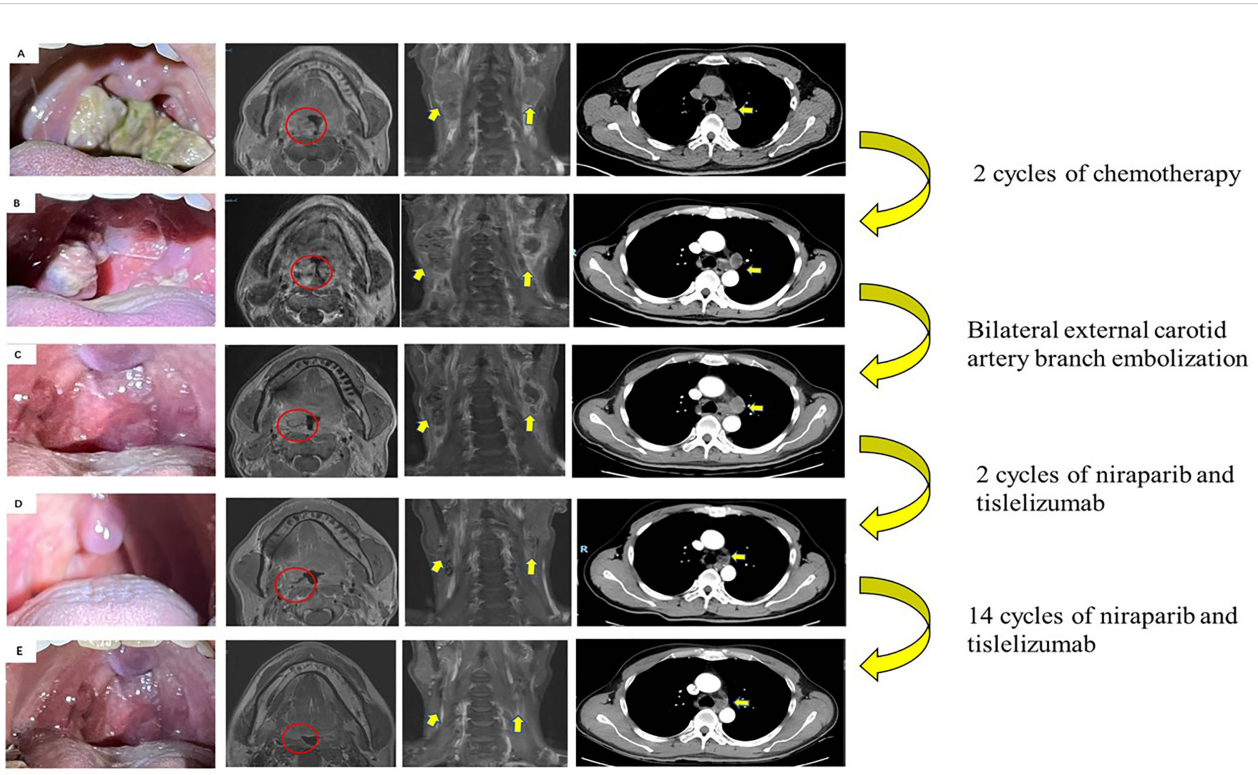

FIGURE 1
Images of primary tumor and metastatic lymph nodes during therapy. **(A)** Initial scans showed a mass in the right tonsil (red circle). Enlarged lymph nodes in the neck and mediastinum (yellow arrows) (December 2020). **(B)** Disease progression after 2 cycles of chemotherapy by RECIST criterion (February 2021). **(C)** After bilateral external carotid artery branch embolization (March 2021). **(D)** Partial response after 2 cycles of niraparib and tislelizumab by RECIST criterion (May 2021). **(E)** Re-examination of MRI and CT revealed no evidence of progression to the tonsils, cervical lymph nodes, and mediastinal and hilar lymph nodes (May 31, 2022).

indicating lymphoma and requiring further assessment. The biopsy specimens were delivered to the central laboratory for analysis (Guangzhou, China). Due to severe pharyngalgia, dysphagia and wheezing, the patient was administered two cycles of chemotherapy (doxorubicin liposomal at 40 mg on d1, vincristine at 2 mg on d1 and prednisone at 100 mg on d1-d5) from December 31, 2020. However, head and neck MRI (February 19, 2021) showed a 36 × 25 mm mass in the right tonsil, and the largest cervical lymph nodes were 45 × 37 mm (right) and 36 × 39 mm (left). Chest CT showed multiple enlarged lymph nodes in the mediastinum and hilus, with a maximum of 29 mm × 23 mm (Figure 1B). According to Response Evaluation Criteria in Solid Tumors (RECIST) version 1.1, the efficacy was evaluated as progressive disease (PD). The pathological results of the central laboratory were confirmed on March 5, 2021.

Tonsil mass was demonstrated as malignancy by hematoxylin-eosin (H&E) staining which showed small foci of heterotypic tumor cells, some cells with light stained and obvious large nucleoli cell (Figure 2A). Immunohistochemistry (IHC) revealed that the tumor cells were positive for Ki-67 (95%), CD138 and Vimentin, PD-L1 (90%) (Figure 2B–E), and negative for CK, p16, CD20, CD3, CD30, CD4, CD8, LCA, CD5, CD7, ALK, CD56, CD31, ERG, CD21, CD23, CD38, CAM5.2, CD117, EMA, S-100, SOX-10 and Mum-1, κ, λ. Epstein-Barr encoding region (EBER) *in situ* hybridization was negative. The final diagnosis of this patient was based on a thorough review of gene rearrangements analysis, histopathology and IHC analysis. Lymphoma was excluded by the gene rearrangement assay (lymphoma biomarkers IGH, IGK and IGL were negative, S1). According to the H&E staining, IHC and

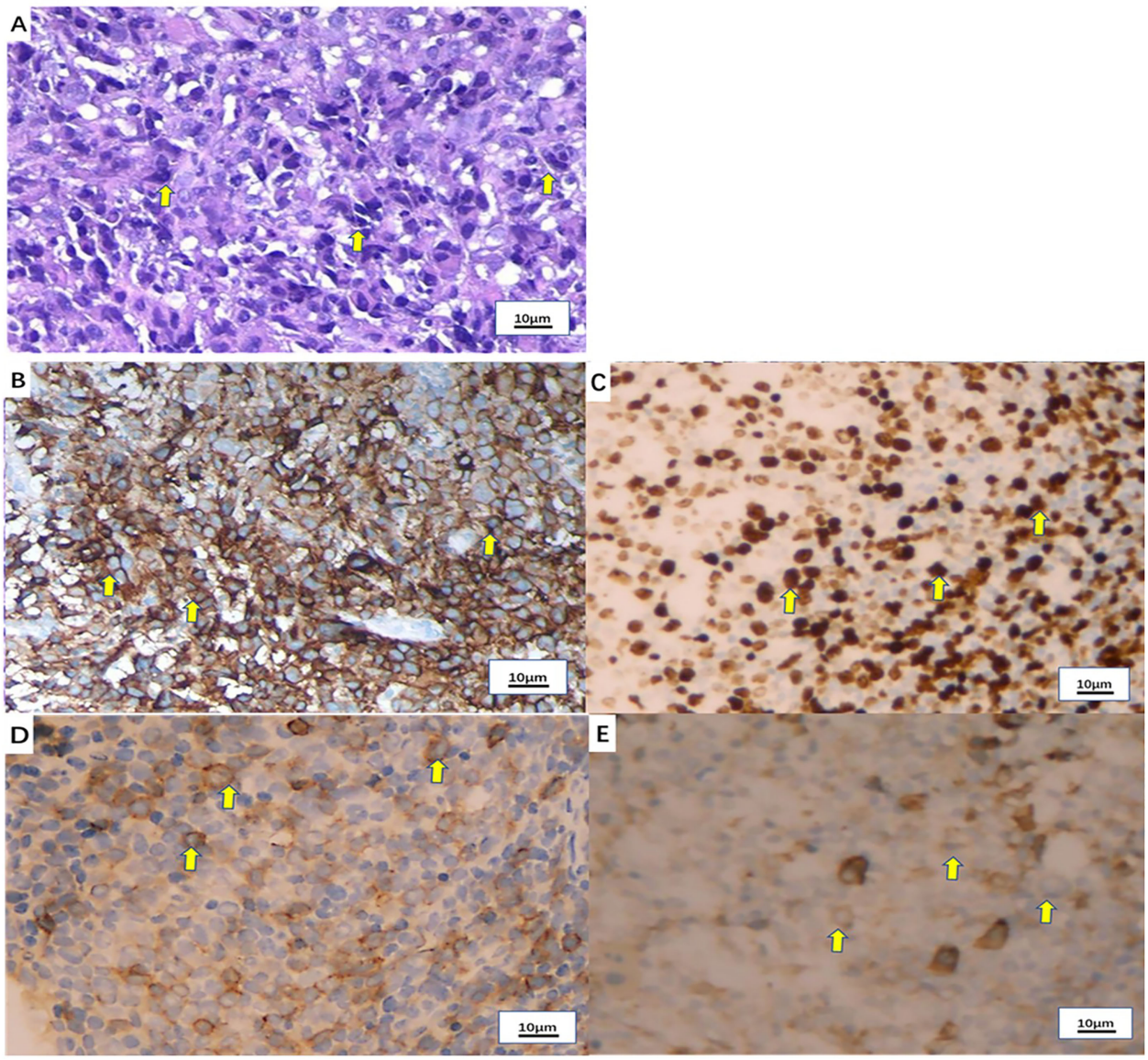

FIGURE 2
Pathological examination of the tonsil mass. **(A)** Hematoxylin-eosin (H&E) staining of the tonsil mass (x100). **(B)** PD-L1 expression by immunohistochemistry (90%+). **(C)** Ki-67 expression by immunohistochemistry (80%+). **(D)** CD138 expression by immunohistochemistry (partial +). **(E)** Vimentin expression by immunohistochemistry (+).

PET/CT results, the patient was finally diagnosed with undifferentiated tonsillar carcinoma with multiple cervical and mediastinal lymph nodes metastases [cT2N2M1, stage IVC, American Joint Committee on Cancer (AJCC) 8th edition]. Next generation sequencing (NGS, Geneseeq Technology Inc) identified germline BRCA1 gene P.S1374Rfs * 3 exon 12 frameshift mutation and a high TMB of 30.7 mutations/MB in the tumor tissue. Considering the high risk of operative hemorrhage and asphyxia, surgical oncologist believed that the risks of surgery outweigh the benefits. After carefully evaluating the patient's performance status, treatment tolerance, tumor imaging and the feasibility of intravascular interventional therapy, the multidisciplinary team developed a focused treatment plan individualized to the patient. The patient received bilateral external carotid artery branch embolization on March 15, 2021 and March 18, 2021 because of the obvious enlargement of the tonsil mass and the high risk of airway obstruction. Intravascular interventional therapy was less invasive and had a low risk of surgical complications. After locoregional operation, the patient had only mild pain around the neck, the tonsil mass was reduced to 20×15 mm, and the largest cervical lymph nodes were 32 × 20 mm (right) and 27 × 17 mm (left) (March 25, 2021) (Figure 1C). According to the germline BRCA1 mutation, high TMB and the PD-L1 positive status, the patient was administered 300 mg niraparib QD and 200 mg tislelizumab Q3W from March 25, 2021. Follow-up MRI and CT (May 12, 2021) revealed a striking decrease in tumor burden after the second treatment cycle. The tonsil mass basically disappeared, and the largest cervical lymph nodes shrank to 21 × 18 mm (right) and 18 × 13 mm (left). The hilar lymph node was reduced to 20 × 14 mm (Figure 1D). The patient achieved a PR under treatment of niraparib combined with tislelizumab according to the RESISIT 1.1 criteria. Surveillance imaging showed continuous partial remission for 12 months (Figure 3). The patient developed mild fatigue, leukopenia (2.26×10^9/L) and anemia (HGB 83g/L) in the first month of niraparib administration. These adverse events were rated as levels 1-2 (CTCAE 5.0) and resolved after niraparib was reduced to 200 mg QD. The patient resumed normal work with a high quality of life. In March 2022, the patient was admitted to the hospital with hematochezia and anemia (HGB 67 g/L). Colonoscopy revealed a mass in the ascending colon, accounting for about 2/3 of the intestinal lumen, with superficial fragility and hemorrhage (Figure 4A). Whole-body CT and barium meal examination of the digestive tract showed a mass of 43mm x 22mm in the proximal ascending colon, with no signs of new lesions elsewhere (April 25, 2022). The patient underwent ascending colectomy with lymph node dissection on April 28, 2022. Postoperative pathology showed that the colonic mass was metastatic undifferentiated tonsillar carcinoma, with no lymph node metastasis (Figure 4B). Re-examination of MRI and CT revealed no evidence of progression to the tonsils, cervical lymph nodes, and mediastinal and hilar lymph nodes (May 31, 2022) (Figure 1E). However, owing to the worse performance status after intestinal surgery, the patient declined any further treatment, except palliative care. Eventually, he died of multiple organ failure in July 2022. The patient's PFS and OS were 12 months and 19 months, respectively, after treatment with niraparib and tislelizumab. The timeline of the relevant information is shown in Figure 3.

Discussion

Malignant tumors of the tonsil account for about 1.3-5.0% of all malignant tumors in the whole body (2). The subtype of undifferentiated carcinoma is relatively rare and lacks data reports, especially HPV-negative tumors. A small sample size case series reported 16 cases of oropharyngeal undifferentiated carcinoma (7). Only one case was HPV-negative undifferentiated carcinoma, and the prognosis was much worse than that of HPV-positive patients. Moreover, patients with metastatic oropharynx carcinoma have a poor prognosis. Median PFS and OS in R/M HNSCC patients are about 5 months and 10 months, respectively (8). The HPV status and PD-L1 expression determine the treatment strategy. According to the WHO classification of head and neck tumors (2017), HPV-negative tumors are more genetically diverse and show a worse prognosis compared with HPV-positive tumors (9). The preferred therapeutics for R/M non-nasopharyngeal cancers are the PD-1 inhibitors including pembrolizumab and nivolumab (10–12). Unfortunately, current clinical trials were designed to recruit most common squamous-cell carcinoma cases, without including undifferentiated carcinoma. Moreover, immunotherapy acts selectively in the patient population, and only a minority of patients benefit from a monotherapeutic

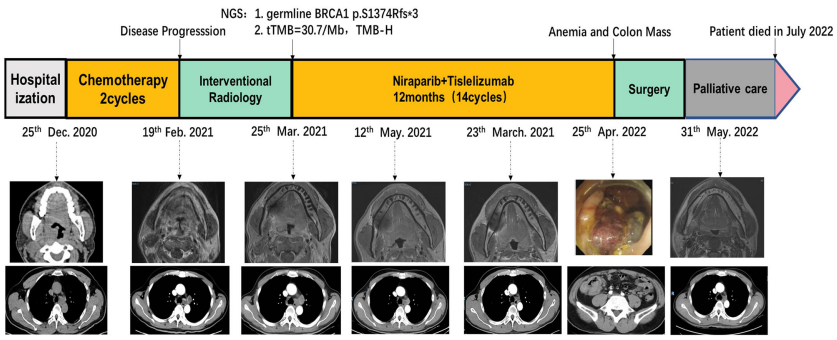

FIGURE 3
Treatment timeline.

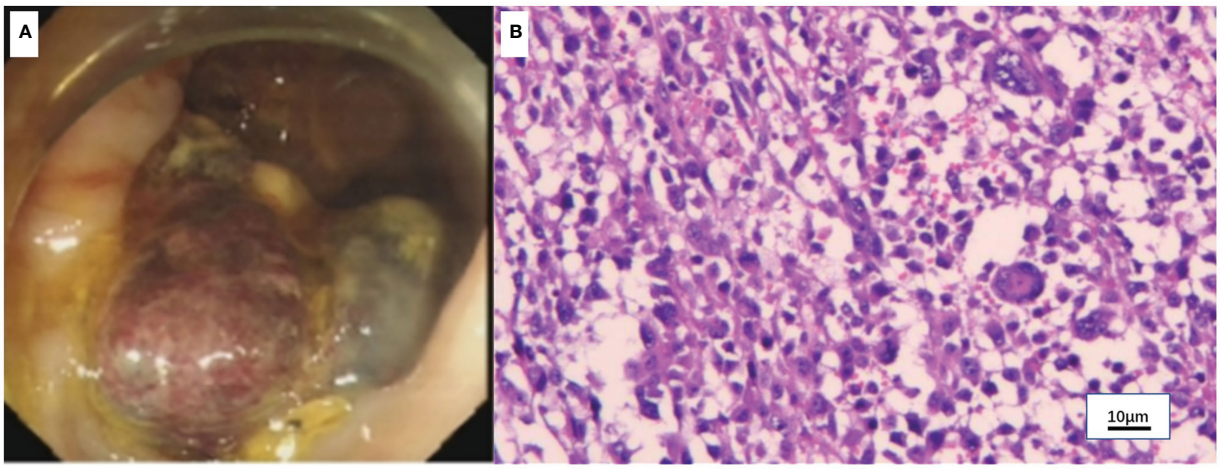

FIGURE 4
Colonoscopy and pathology of the colon mass. **(A)** Colonoscopy showed a mass in the ascending colon. **(B)** Hematoxylin-eosin (H&E) staining of the colon mass (x100).

approach. The overall response rate remains quite low and disappointing. Only a 14% response rate was detected in PD-L1-positive/HPV-negative HNSCC (5). An estimated 85% of patients have no response to PD-1 inhibitors or have a response that is followed by disease progression and death. The final diagnosis of this patient was HPV-negative metastatic undifferentiated carcinoma of the tonsil. There are limited data from randomized, prospective studies to guide decisions regarding this rare type of head and neck cancer. The choice of therapy should be individualized based on patient characteristics. The search for new therapeutic strategies is of utmost importance in this case.

Through molecular profiling, targeted alteration was identified, and precision therapy was implemented. Given that the patient harbors a germline BRCA1 mutation, PARPi therapy could be considered. PARP1 and PARP2 are key enzymes detecting and repairing single strand DNA breaks (SSBs). PARP1/2 inhibition lead to an accumulation of SSBs and stalled replication forks, which subsequently lead to double strand breaks (DSBs) requiring homologous recombination repair (HRR). HRR function relies on proteins such as BRCA1 and 2. Since BRCA1/2 mutated cells are inefficient in HR, DSBs are repaired in an error-prone manner by nonhomologous end joining (NHEJ), inducing genomic instability that causes cell death (13, 14). Niraparib is a highly selective PARP1/2 inhibitor approved for maintenance therapy of advanced ovarian cancer (15). PD-1 inhibitor tislelizumab was also added to the treatment regimen due to high PD-L1 expression (90%) in the tumor tissue. PD-1 inhibitors have shown efficacy in head and neck cancer, especially in PD-L1-positive tumors (16). As a result, the patient had a long survival time with the combination of niraparib and tislelizumab after failed chemotherapy. The combination had an acceptable safety profile and favorable quality of life.

Using a literature review, we sought to summarize the rationale for the synergistic antitumor effects of PARPi and PD-L1 blockade. Evidence showed PARPi-induced genomic instability modulates the tumor microenvironment (TME) (17). PARPi promotes the accumulation of cytosolic DNA and increases TMB, then activates the cGAS-STING pathway, enhances T cell infiltration, and stimulates type I interferon expression, thereby priming the TME (18–20). In addition, DNA fragments within the cytoplasm induces the production and expression of neo-antigens on the cell surface, thereby increasing immune activation and the odds of ICI response (21). PARPi enhances immunosuppression by upregulating PD-L1 expression through the inactivation of GSK3β (22). Increased amounts of tumor infiltrating lymphocytes, neoantigen release, and PD-L1 upregulation driven by PARPi suggest an increase of immunogenicity and present a potential role for ICIs. The synergistic antitumor effects of PARP and PD-L1 blockade have been observed in different types of solid tumors (23). The TOPACIO study reported the efficacy of niraparib combined with pembrolizumab in BRCA-mutated recurrent ovarian and advanced triple-negative breast cancer (TNBC). In the intention to treat patients, an ORR of 25% and a DCR of 68% were recorded, while in BRCA-mutated tumors, the ORR and DCR were elevated to 45% and 73%, respectively (24). The JASPER study was the first to investigate the efficacy of niraparib plus pembrolizumab as a first-line treatment option for metastatic or locally advanced non-small cell lung cancer (NSCLC), and the antitumor activity of this combination regimen was confirmed in NSCLC. Patients with high PD-L1 expression (TPS ≥ 50%) achieved a favorable ORR of 56.3%, versus 44.8% for pembrolizumab monotherapy in KEYNOTE-024 (25). The MEDIOLA trial reported the efficacy of olaparib combined with durvalumab for advanced solid cancers, including TNBC, ovarian, cervical and uterine cancers. For patients with germline BRCA1/2 mutations, ORR and DCR at 12 weeks were 63% and 81%, respectively (26). In these trials, the most common toxicities included anemia, fatigue and thrombocytopenia, and immune-related toxicities were comparable with single agent PD-1 inhibitor therapy. These data are encouraging and suggest high efficacy and good tolerability for PARPi and PD-1 inhibitor in combination. Treatment-emergent hematologic events are most common in PARPi treatments. In our

case, low-grade leukopenia and anemia were observed in the first month of niraparib administration. The dose of niraparib was modified from 300mg QD to 200mg QD to reduce hematologic toxicity. Immune-related toxicity was not observed in this case. Overall, niraparib combined with tislelizumab was well tolerated and complications were manageable. This combination regimen may benefit a broader population than monotherapy. This combination may be useful in other head and neck tumors with BRCA 1/2 mutations and needs to be validated by further studies.

Conclusion

This study highlights the importance of molecular-matched therapy for rare malignancies with no standard of care. Targeted therapy based on genetic alterations detected by NGS may improve survival and the quality of life in these patients. The combination of PARPi with PD-1 inhibitor was effective and well-tolerated for the current patient because of BRCA mutation and high PD-L1 expression. Personalized therapy based on broad molecular profiling needs to be further explored.

Data availability statement

The original contributions presented in the study are included in the article/supplementary material. Further inquiries can be directed to the corresponding author.

Ethics statement

The studies involving human participants were reviewed and approved by Ethics Committee of the First Affiliated Hospital of Guangzhou University of Traditional Chinese Medicine. The patients/participants provided their written informed consent to participate in this study. Written informed consent was obtained from the individual(s) for the publication of any potentially identifiable images or data included in this article.

Author contributions

JZ, ZD and PL collected the clinical, diagnostic and therapeutic information of the patient. JZ wrote and submitted the manuscript. JG revised the manuscript and identified the case. JZ, ZD and PL contributed equally to this work. All authors contributed to the article and approved the submitted version.

Funding

This work was supported by the Science and Technology Project of Guangzhou (Grant No.201707010299), and Science and Technology Project of Guangdong Province (Grant No.2016B090918059).

Conflict of interest

The authors declare that the research was conducted in the absence of any commercial or financial relationships that could be construed as a potential conflict of interest.

Publisher's note

Supplementary material

The Supplementary Material for this article can be found online at: https://www.frontiersin.org/articles/10.3389/fonc.2023.1078814/full#supplementary-material

References

1. Weatherspoon DJ, Chattopadhyay A, Boroumand S, Garcia I. Oral cavity and oropharyngeal cancer incidence trends and disparities in the united states: 2000-2010. *Cancer Epidemiol* (2015) 39(4):497–504. doi: 10.1016/j.canep.2015.04.007

2. Wright JM, Vered M. Update from the 4th edition of the world health organization classification of head and neck tumours: odontogenic and maxillofacial bone tumors. *Head Neck Pathol* (2017) 11(1):68–77. doi: 10.1007/s12105-017-0794-1

3. Mehanna H, Evans M, Beasley M, Chatterjee S, Dilkes M, Homer J, et al. Oropharyngeal cancer: united kingdom national multidisciplinary guidelines. *J Laryngol Otol* (2016) 130(S2):S90–s6. doi: 10.1017/s0022215116000505

4. Ang KK, Harris J, Wheeler R, Weber R, Rosenthal DI, Nguyen-Tân PF, et al. Human papillomavirus and survival of patients with oropharyngeal cancer. *N Engl J Med* (2010) 363(1):24–35. doi: 10.1056/NEJMoa0912217

5. Seiwert TY, Burtness B, Mehra R, Weiss J, Berger R, Eder JP, et al. Safety and clinical activity of pembrolizumab for treatment of recurrent or metastatic squamous cell carcinoma of the head and neck (Keynote-012): an open-label, multicentre, phase 1b trial. *Lancet Oncol* (2016) 17(7):956–65. doi: 10.1016/s1470-2045(16)30066-3

6. Sandhu SK, Schelman WR, Wilding G, Moreno V, Baird RD, Miranda S, et al. The Poly(Adp-ribose) polymerase inhibitor niraparib (Mk4827) in brca mutation carriers and patients with sporadic cancer: a phase 1 dose-escalation trial. *Lancet Oncol* (2013) 14(9):882–92. doi: 10.1016/s1470-2045(13)70240-7

7. Carpenter DH, El-Mofty SK, Lewis JS. Undifferentiated carcinoma of the oropharynx: a human papillomavirus-associated tumor with a favorable prognosis. *Mod Pathol* (2011) 24(10):1306–12. doi: 10.1038/modpathol.2011.87

8. Vermorken JB, Mesia R, Rivera F, Remenar E, Kawecki A, Rottey S, et al. Platinum-based chemotherapy plus cetuximab in head and neck cancer. *N Engl J Med* (2008) 359(11):1116–27. doi: 10.1056/NEJMoa0802656

9. D'Souza G, Westra WH, Wang SJ, van Zante A, Wentz A, Kluz N, et al. Differences in the prevalence of human papillomavirus (Hpv) in head and neck

squamous cell cancers by sex, race, anatomic tumor site, and hpv detection method. *JAMA Oncol* (2017) 3(2):169–77. doi: 10.1001/jamaoncol.2016.3067

10. Qiao XW, Jiang J, Pang X, Huang MC, Tang YJ, Liang XH, et al. The evolving landscape of pd-1/Pd-L1 pathway in head and neck cancer. *Front Immunol* (2020) 11:1721. doi: 10.3389/fimmu.2020.01721

11. Theodoraki MN, Laban S, Hoffmann TK. [Immunotherapy of head and neck cancer: highlights of the asco and esmo annual meetings 2021]. *Hno* (2022) 70(4):271–7. doi: 10.1007/s00106-021-01142-w

12. Harrington KJ, Ferris RL, Blumenschein GJr., Colevas AD, Fayette J, Licitra L, et al. Nivolumab versus standard, single-agent therapy of investigator's choice in recurrent or metastatic squamous cell carcinoma of the head and neck (Checkmate 141): health-related quality-of-Life results from a randomised, phase 3 trial. *Lancet Oncol* (2017) 18(8):1104–15. doi: 10.1016/s1470-2045(17)30421-7

13. De Vos M, Schreiber V, Dantzer F. The diverse roles and clinical relevance of parps in DNA damage repair: current state of the art. *Biochem Pharmacol* (2012) 84 (2):137–46. doi: 10.1016/j.bcp.2012.03.018

14. Konstantinopoulos PA, Matulonis UA. Parp inhibitors in ovarian cancer: a trailblazing and transformative journey. *Clin Cancer Res* (2018) 24(17):4062–5. doi: 10.1158/1078-0432.Ccr-18-1314

15. González-Martín A, Pothuri B, Vergote I, DePont Christensen R, Graybill W, Mirza MR, et al. Niraparib in patients with newly diagnosed advanced ovarian cancer. *N Engl J Med* (2019) 381(25):2391–402. doi: 10.1056/NEJMoa1910962

16. Burtness B, Harrington KJ, Greil R, Soulières D, Tahara M, de Castro GJr., et al. Pembrolizumab alone or with chemotherapy versus cetuximab with chemotherapy for recurrent or metastatic squamous cell carcinoma of the head and neck (Keynote-048): a randomised, open-label, phase 3 study. *Lancet* (2019) 394(10212):1915–28. doi: 10.1016/s0140-6736(19)32591-7

17. Pantelidou C, Sonzogni O, De Oliveria Taveira M, Mehta AK, Kothari A, Wang D, et al. Parp inhibitor efficacy depends on Cd8(+) T-cell recruitment Via intratumoral sting pathway activation in brca-deficient models of triple-negative breast cancer. *Cancer Discovery* (2019) 9(6):722–37. doi: 10.1158/2159-8290.Cd-18-1218

18. Sen T, Rodriguez BL, Chen L, Corte CMD, Morikawa N, Fujimoto J, et al. Targeting DNA damage response promotes antitumor immunity through sting-mediated T-cell activation in small cell lung cancer. *Cancer Discovery* (2019) 9 (5):646–61. doi: 10.1158/2159-8290.Cd-18-1020

19. Maio M, Covre A, Fratta E, Di Giacomo AM, Taverna P, Natali PG, et al. Molecular pathways: At the crossroads of cancer epigenetics and immunotherapy. *Clin Cancer Res* (2015) 21(18):4040–7. doi: 10.1158/1078-0432.Ccr-14-2914

20. Chabanon RM, Rouanne M, Lord CJ, Soria JC, Pasero P, Postel-Vinay S. Targeting the DNA damage response in immuno-oncology: developments and opportunities. *Nat Rev Cancer* (2021) 21(11):701–17. doi: 10.1038/s41568-021-00386-6

21. Vikas P, Borcherding N, Chennamadhavuni A, Garje R. Therapeutic potential of combining parp inhibitor and immunotherapy in solid tumors. *Front Oncol* (2020) 10:570. doi: 10.3389/fonc.2020.00570

22. Jiao S, Xia W, Yamaguchi H, Wei Y, Chen MK, Hsu JM, et al. Parp inhibitor upregulates pd-L1 expression and enhances cancer-associated immunosuppression. *Clin Cancer Res* (2017) 23(14):3711–20. doi: 10.1158/1078-0432.Ccr-16-3215

23. Moutafi M, Economopoulou P, Rimm D, Psyrri A. Parp inhibitors in head and neck cancer: molecular mechanisms, preclinical and clinical data. *Oral Oncol* (2021) 117:105292. doi: 10.1016/j.oraloncology.2021.105292

24. Konstantinopoulos PA, Waggoner S, Vidal GA, Mita M, Moroney JW, Holloway R, et al. Single-arm phases 1 and 2 trial of niraparib in combination with pembrolizumab in patients with recurrent platinum-resistant ovarian carcinoma. *JAMA Oncol* (2019) 5(8):1141–9. doi: 10.1001/jamaoncol.2019.1048

25. Ramalingam SS, Thara E, Awad MM, Dowlati A, Haque B, Stinchcombe TE, et al. Jasper: phase 2 trial of first-line niraparib plus pembrolizumab in patients with advanced non-small cell lung cancer. *Cancer* (2022) 128(1):65–74. doi: 10.1002/cncr.33885

26. Domchek SM, Postel-Vinay S, Im SA, Park YH, Delord JP, Italiano A, et al. Olaparib and durvalumab in patients with germline brca-mutated metastatic breast cancer (Mediola): an open-label, multicentre, phase 1/2, basket study. *Lancet Oncol* (2020) 21(9):1155–64. doi: 10.1016/s1470-2045(20)30324-7

frontiers | Frontiers in Oncology

TYPE Original Research
PUBLISHED 19 July 2023
DOI 10.3389/fonc.2023.1055717

OPEN ACCESS

EDITED BY
Yasumasa Kato,
Ohu University, Japan

REVIEWED BY
Zhiwei He,
Shenzhen University, China
Jian Zhang,
Shanghai Jiao Tong University, China
Jia-nan Gong,
Chinese Academy of Medical Sciences and Peking Union Medical College, China

*CORRESPONDENCE
Wei Gao
gaoweisxent@sxent.org
Yongyan Wu
wuyongyan@sxent.org
Xianhai Zeng
zxhklwx@163.com

†These authors have contributed equally to this work

RECEIVED 28 September 2022
ACCEPTED 29 June 2023
PUBLISHED 19 July 2023

CITATION
Zheng X, Zheng D, Zhang C, Guo H, Zhang Y, Xue X, Shi Z, Zhang X, Zeng X, Wu Y and Gao W (2023) A cuproptosis-related lncRNA signature predicts the prognosis and immune cell status in head and neck squamous cell carcinoma. *Front. Oncol.* 13:1055717. doi: 10.3389/fonc.2023.1055717

A cuproptosis-related lncRNA signature predicts the prognosis and immune cell status in head and neck squamous cell carcinoma

Xiwang Zheng[1,2†], Defei Zheng[3†], Chunming Zhang[1,2,4†], Huina Guo[1,2], Yuliang Zhang[1,2], Xuting Xue[1,2], Zhaohui Shi[5,6], Xiangmin Zhang[5,6], Xianhai Zeng[5,6*], Yongyan Wu[5,6*] and Wei Gao[5,6*]

[1]Shanxi Key Laboratory of Otorhinolaryngology Head and Neck Cancer, First Hospital of Shanxi Medical University, Taiyuan, Shanxi, China, [2]Shanxi Province Clinical Medical Research Center for Precision Medicine of Head and Neck Cancer, First Hospital of Shanxi Medical University, Taiyuan, Shanxi, China, [3]Department of Hematology/Oncology, Children's Hospital of Soochow University, Suzhou, Jiangsu, China, [4]Department of Otolaryngology Head & Neck Surgery, First Hospital of Shanxi Medical University, Taiyuan, Shanxi, China, [5]Department of Otolaryngology Head & Neck Surgery, Longgang Otolaryngology Hospital, Shenzhen, Guangdong, China, [6]Shenzhen Institute of Otolaryngology & Key Laboratory of Otolaryngology, Longgang Otolaryngology Hospital, Shenzhen, Guangdong, China

Introduction: The incidence of head and neck squamous cell carcinoma (HNSCC), one of the most prevalent tumors, is increasing rapidly worldwide. Cuproptosis, as a new copper-dependent cell death form, was proposed recently. However, the prognosis value and immune effects of cuproptosis-related lncRNAs (CRLs) have not yet been elucidated in HNSCC.

Methods: In the current study, the expression pattern, differential profile, clinical correlation, DNA methylation, functional enrichment, univariate prognosis factor, and the immune effects of CRLs were analyzed. A four-CRL signature was constructed using the least absolute shrinkage and selection operator (LASSO) algorithm.

Results: Results showed that 20 CRLs had significant effects on the stage progression of HNSCC. Sixteen CRLs were tightly correlated with the overall survival (OS) of HNSCC patients. Particularly, lnc-FGF3-4 as a single risk factor was upregulated in HNSCC tissues and negatively impacted the prognosis of HNSCC. DNA methylation probes of cg02278768 (MIR9-3HG), cg07312099 (ASAH1-AS1), and cg16867777 (TIAM1-AS1) were also correlated with the prognosis of HNSCC. The four-CRL signature that included MAP4K3-DT, lnc-TCEA3-1, MIR9-3HG, and CDKN2A-DT had a significantly negative effect on the activation of T cells follicular helper and OS probability of HNSCC. Functional analysis revealed that cell cycle, DNA replication, and p53 signal pathways were enriched.

Discussion: A novel CRL-related signature has the potential of prognosis prediction in HNSCC. Targeting CRLs may be a promising therapeutic strategy for HNSCC.

KEYWORDS

copper, cuproptosis, lncRNAs, cell death, head and neck squamous cell carcinoma, prognosis

Introduction

Copper is a crucial cofactor for all organisms, and the dysregulation of copper ions can induce oxidative stress and cytotoxicity (1). A new copper-dependent cell death form was proposed and termed "cuproptosis" by Tsvetkov et al. in a recent study (2). The researchers demonstrated that copper ions can directly bind to lipoylated components in the tricarboxylic acid cycle and result in the aggregation of lipoylated protein and subsequent iron-sulfur cluster protein loss. The above events finally lead to proteotoxic stress and cell death (1, 2). Cuproptosis-related genes (CRGs) and cuproptosis-related lncRNAs (CRLs) have begun to be investigated in cancer and have exhibited promising potential in the diagnosis and prognosis prediction of cancer (3–5). However, the clinical application of CRGs in head and neck squamous cell carcinoma (HNSCC) remains unclear.

HNSCC is the sixth-most common neoplasm in the world and has 890,000 new cases reported and estimated deaths of ~450,000 in 2018. More importantly, the incidence of HNSCC is increasing rapidly and is expected to increase by 30% by 2030 (6). The molecular markers can contribute to the diagnosis and prognosis prediction in cancer clinic settings (7). Long non-coding RNAs (lncRNAs) are non-coding RNAs with longer than 200 nucleotides and lack protein-coding potential. lncRNAs play an essential role in most cellular processes and are well known as suppressed factors or oncogenes (8). Although proteins play a pivotal role in cancer diagnosis and therapy, lncRNAs also have showed the promising potential in serving as the new signature or target in early diagnosis, prognosis prediction, and treatment of many cancers (9–11). To our knowledge, there is currently no report about CRLs as signatures or targets in the diagnosis, prognosis prediction, or treatment of HNSCC.

In the current study, we primarily focused on the potentiality of CRLs as the diagnosis and prognosis prediction signature in HNSCC. A total of 501 HNSCC and 43 adjacent normal samples were analyzed in this study. The expression pattern, differential profile, clinical correlation, DNA methylation, functional enrichment, univariate prognosis factor, and immune status were analyzed. DNA methylation changes of cg02278768 (MIR9-3HG), cg07312099 (ASAH1-AS1), and cg16867777 (TIAM1-AS1) sites were correlated with HNSCC prognosis. lnc-FGF3-4 as a single risk factor was upregulated in HNSCC tissues and negatively impacted the prognosis of HNSCC. A four-CRL signature that included MAP4K3-DT, lnc-TCEA3-1, MIR9-3HG, and CDKN2A-DT was also constructed using LASSO algorithm. The four-CRL signature was found to have significantly negative effects on the immune status and prognosis of HNSC. Finally, a nomogram consisting of the four-CRL signature and clinical features was constructed for overall survival (OS) prediction of HNSCC in clinical utilization.

Materials and methods

Data collection

The transcriptome sequencing data of 501 HNSCC and 43 adjacent normal tissue samples were obtained from the Cancer Genome Atlas database (TCGA, https://portal.gdc.cancer.gov/). All HNSCC patients were randomly divided into the training cohort (TCGA-A) and the validation cohort (TCGA-B) in a 3:2 ratio (12). The corresponding clinical characteristics of the above patients were acquired from UCSC Xena database (https://xenabrowser.net/), and a summary of clinical characteristics is listed in Supplemental Table S1. Moreover, epigenomics data of HNSCC DNA methylation were also obtained from the TCGA database. Ten CRGs were manually collected from published studies (2), and the top 10 correlated lncRNAs of each CRG served as CRLs for analysis in the current study (Supplemental Table S2). In this study, if the information of an lncRNA was available in the NCBI (https://www.ncbi.nlm.nih.gov/gene/) or

Abbreviations: HNSCC, Head and neck squamous cell carcinoma; CRLs, Cuproptosis-related lncRNAs; LASSO, Least absolute shrinkage and selection operator; OS, Overall survival; TCGA, The Cancer Genome Atlas; deCRLs, Differentially expressed CRLs; DMPs, Differentially methylated probes; pcRNAs, Protein-coding RNAs; MF, Molecular function; CC, Cellular component; BP, Biological process; GO, Gene ontology; KEGG, Kyoto encyclopedia of genes and genomes; ROC, Receiver operating characteristic; LM22, Leukocyte signature matrix; DSS, Disease-specific survival; PFI, Progression-free interval; AUC, Area under the curve.

HGNC (https://www.genenames.org/) database, the official symbol was used as the name for that lncRNA. If some lncRNAs were not included into the NCBI or HGNC database but were included into the LNCipedia (https://lncipedia.org/) database, the name of these lncRNAs in the LNCipedia was used as the name for lncRNAs. If the information of a lncRNA was not available in all above three database, the ID of that lncRNA in ensembl (https://ensembl.org/) database was used as the name for lncRNA in this study.

Cell culture of HNSCC and quantitative real-time PCR

Human embryonic kidney cells HEK293T (obtained from the China Center for Type Culture Collection, Wuhan, China) and HNSCC cell lines CAL-27, FaDu, AMC-HN-8 and WSU-HN30 (obtained from the Cell Bank of Chinese Academy of Sciences, Shanghai, China) were cultured for analysis of CRLs expression in the study. HEK293T and HNSCC cell lines were cultured in Dulbecco's Modified Eagle's Medium (DMEM; Life Technologies, USA) with 10% fetal bovine serum (FBS). All cell lines were maintained in a humidified atmosphere containing 5% CO2 at 37° C. 18S rRNA were used as internal controls and it's primer sequences were sense: 5'-3' CCTGGATACCGCAGCTAGGA and antisense:5'-3' GCGGCGCAATACGAATGCCCC. The primer sequences of lnc-FGF3-4 were sense: 5'-3' GTTTCCCACGCTCCCTATGA and antisense:5'-3' TCGACAGATGAAATGAAGGCA.

Validation of CRLs expression in laryngeal squamous cell carcinoma tissues

It were used for further validation of CRLs expression that RNA-Seq data that were consisted of 107 paired laryngeal squamous cell carcinoma (LSCC, one of the most common HNSCC) and matched adjacent normal mucosa (ANM) tissues. The samples processing, sequencing procedure and analysis methods were introduced in previous studies (13, 14).

Analysis of expression patterns

A chord diagram of correlations among CRGs was implemented using *circlize* (v0.4.15) package in R (v4.1.0). The network of correlations amongst CRLs was plotted using the *corrr* (v0.4.3) package in R. The expression patterns of CRLs were analyzed and visualized using the hierarchical clustering method and the *pheatmap* (v1.0.12) package in R. *DESeq2* (v1.32.0) in R was employed to screen the differentially expressed CRLs (deCRLs) between HNSCC and normal tissues. The cutoff of $p \leq 0.05$ and $|\log_2\text{Fold change}| > 0$ was threshold for significant deCRLs. The volcano plot of deCRLs was plotted using the *ggplot2* (v3.3.6) package in R. Student's *t*-test was used to statistically analyze the correlations between expression levels and clinical features, and $p \leq 0.05$ was used as the significantly differential cutoff.

DNA methylation analysis

DNA methylation status of CRLs was analyzed using *ChAMP* (v2.22.0) package in R according to the recommended methylation chip analysis pipeline (15). The globe methylation visualization of HNSCC was implemented using *circlize* and *pheatmap*. The cutoff of $p \leq 0.05$ and $|\log_2\text{Fold change}| > 0$ were used to screen the significantly differentially methylated probes (DMPs). Moreover, the effects of DMPs on survival prognosis were analyzed using univariate Cox analysis and Kaplan–Meier method. Forest plots of Cox analysis results and Kaplan–Meier curves were visualized using *forestplot* (v2.0.1) and *survival* (v3.3-1) packages in R, respectively.

Construction of network and functional enrichment analysis

In CRL–protein-coding RNAs (pcRNAs) interaction network, the cutoff values of $|Pearson's\ r| \geq 0.6$ and $p \leq 0.05$ were used as the threshold of correlation. The pcRNAs were used to analyze the biological functions in HNSCC, and the enrichment analysis was performed using *clusterProfiler* (v4.0.5) package in R (16), the analysis content of which included molecular function (MF), cellular component (CC), and biological process (BP) terms of gene ontology (GO) and Kyoto encyclopedia of genes and genomes (KEGG).

Survival analysis and construction of prediction model for prognosis

The deCRLs were analyzed using univariate Cox regression to screen the survival-related risk factors. Kaplan–Meier curves were used to validate the analysis results of Cox regression. To estimate the integrated effects of CRLs on the prognosis of HNSCC patients, LASSO algorithm was used to construct the prognostically predicted model for HNSCC patients. LASSO was implemented using the *glmnet* (v4.1-4) package in R. A formula for the risk score of CRL-related signature model was constructed, and the risk score for each patient was calculated as follows: $\text{risk score} = \sum_{i=1}^{n}(coe_{CRLsi} \times exp_{CRLsi})$, where exp_{CRLsi} is the expression level of the risk factor *CRLsi*; coe_{CRLsi} is the coefficient of *CRLsi*; and n is the quantity of CRLs in CRL-related signature. Time-dependent receiver operating characteristic (ROC) analysis was employed to estimate the ability of CRL-related signature for prognosis prediction and was performed using *timeROC* (v0.4) package in R. Furthermore, the synergistic ability of CRL-related signature model and clinical features on prognostic prediction in clinical utilization was analyzed, and a nomogram was also established. Nomogram was plotted using *rms* (v6.3-0) package in R. The calibrate curves and decision curves were used to assess the performance and reliability of the nomogram and were implemented using *rms* package and *rmda* (v1.6) package in R, respectively.

Immune cell infiltration analysis

CIBERSORT algorithm was utilized to analyze the effects of CRL-related signature on immune cell infiltration in HNSCC. Analysis pipeline of CIBERSORT algorithm in R and leukocyte signature matrix (LM22, including 22 immune-related cells) were manually collected from published literature (17). Boxplot with jitter points of CIBERSORT analysis results was plotted using *ggpubr* (v0.4.0) package in R. $p \leq 0.05$ was the significantly differential cutoff.

Results

Signification of CRLs on HNSCC progression in clinic

To investigate the effects of CRLs on HNSCC, We comprehensively analyzed the underlying regulatory mechanisms of CRLs in HNSCC based on bioinformatic method and cell experiments (Figure 1). Ten CRGs including FDX1, LIAS, LIPT1, DLD, DLAT, PDHA1, PDHB, MTF1, GLS, and CDKN2A were manually curated for analysis in the current study (Figure 2A, Supplemental Figure S1A). The expression patterns of MTF1, GLS, and CDKN2A, especially MTF1, were opposite of those of remaining CRGs, results of which were consistent with a previous study (2). Correlation analysis was performed to identify the lncRNAs correlated with CRGs, and 99 CRLs were finally selected (Figure 2B, Supplemental Figure S1B, Supplemental Table S2). The heatmap in Figure 2C and Supplemental Figure S1C shows that the expression pattern between HNSCC and normal tissue was different. Differential analysis was also performed to screen the deCRLs in HNSCC tissues. There were some deCRLs in HNSCC tissues compared to normal tissues (Figure 2D, Supplemental Figure S1D). A total of 39 deCRLs respectively served as univariate factors in subsequent clinical correlation analysis. Figures 2E, F show that the expressions of EIF3J-DT, lnc-IAH1-2, and lnc-ENDOU-7 were upregulated in the advanced pathologic stage (stage III–IV) in HNSCC patients. EIF3J-DT, PDCD4-AS1,

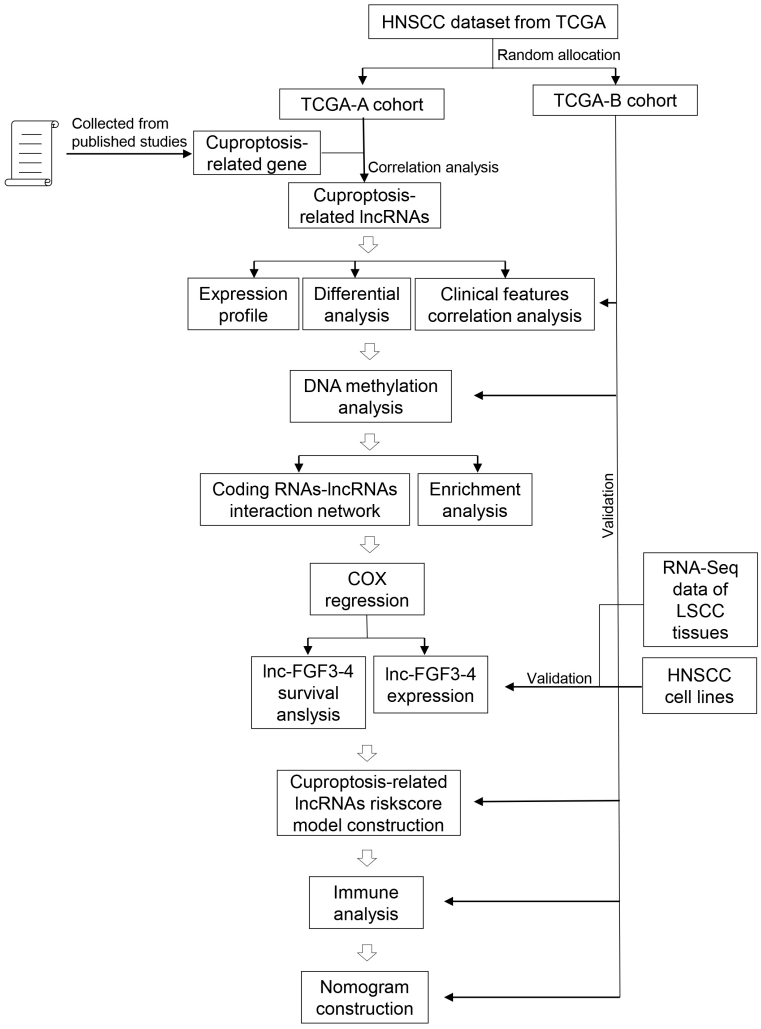

FIGURE 1
Schematic diagram of the study design.

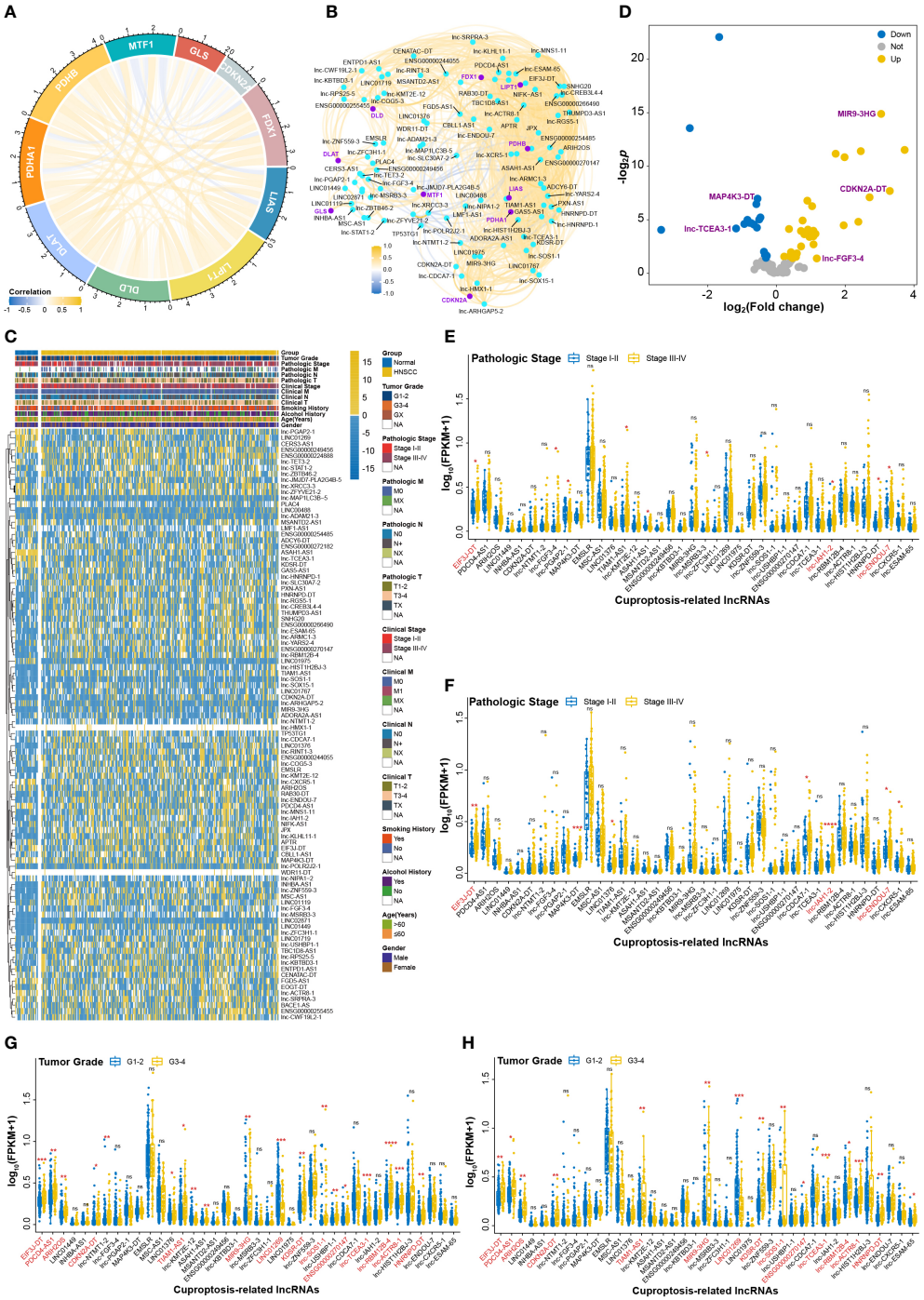

FIGURE 2
The effects of CRLs on developing and progressing HNSCC. **(A)** Correlation analysis among CRGs. **(B)** CRLs identified by correlation analysis. **(C)** The heatmap of CRLs expression between HNSCC and normal tissues. **(D)** Volcano plot of differential analysis of CRLs. **(E, F)** The effects of deCRLs on pathologic stage of HNSCC in training cohort **(E)** and in validation cohort **(F)**. **(G, H)** The effects of deCRLs on tumor grade of HNSCC in training cohort **(G)** and in validation cohort **(H)**. *$p < 0.05$; **$p < 0.01$; ***$p < 0.001$; ****$p < 0.0001$; ns, not significant.

ARIH2OS, CDKN2A-DT, TIAM1-AS1, MIR9-3HG, LINC01269, KDSR-DT, lnc-SOS1-1, ENSG00000270147, lnc-TCEA3-1, lnc-RBM12B-4, lnc-ACTR8-1, and HNRNPD-DT had a tight correlation with the development of tumor grade in HNSCC (Figures 2G, H). lnc-KMT2E-12 had a higher expression level in clinical stage III–IV than that in clinical stage I–II (Supplemental Figures S1E, F). Moreover, EMSLR, lnc-KMT2E-12 and lnc-SOS1-1, CDKN2A-DT and lnc-SOS1-1, MIR9-3HG, EIF3J-DT, TIAM1-AS1, MIR9-3HG, lnc-USHBP1-1, ENSG00000270147, lnc-CDCA7-1, lnc-TCEA3-1, and HNRNPD-DT had a close correlation with clinical N stage, clinical T stage, age, and gender, respectively (Supplemental Figures S2A–H). In summary, correlation analysis

10.3389/fonc.2023.1055717

between clinical features and CRLs revealed that CRLs have a potential influence on the initiation and progression of HNSCC in clinical application.

DNA methylation status of CRLs in HNSCC

DNA methylation plays an essential role in gene expression and tissue differentiation and can act as the signature for the evaluation of immune response and prognosis of cancers (18). To assess DNA methylation status of CRLs in HNSCC tissue, K450 Illumina DNA methylation arrays data of HNSCC obtained from TCGA database were analyzed. Figure 3A shows that DNA methylation changes were widespread on chromosomes of HNSCC tissues. Furthermore, DNA methylation arrays showed that DNA region of CRLs had different methylated levels between HNSCC and normal tissues (Figure 3B). Differential analysis was also performed and indicated some methylated sites that showed significantly methylated changes in CRLs DNA region (Figure 3C). In

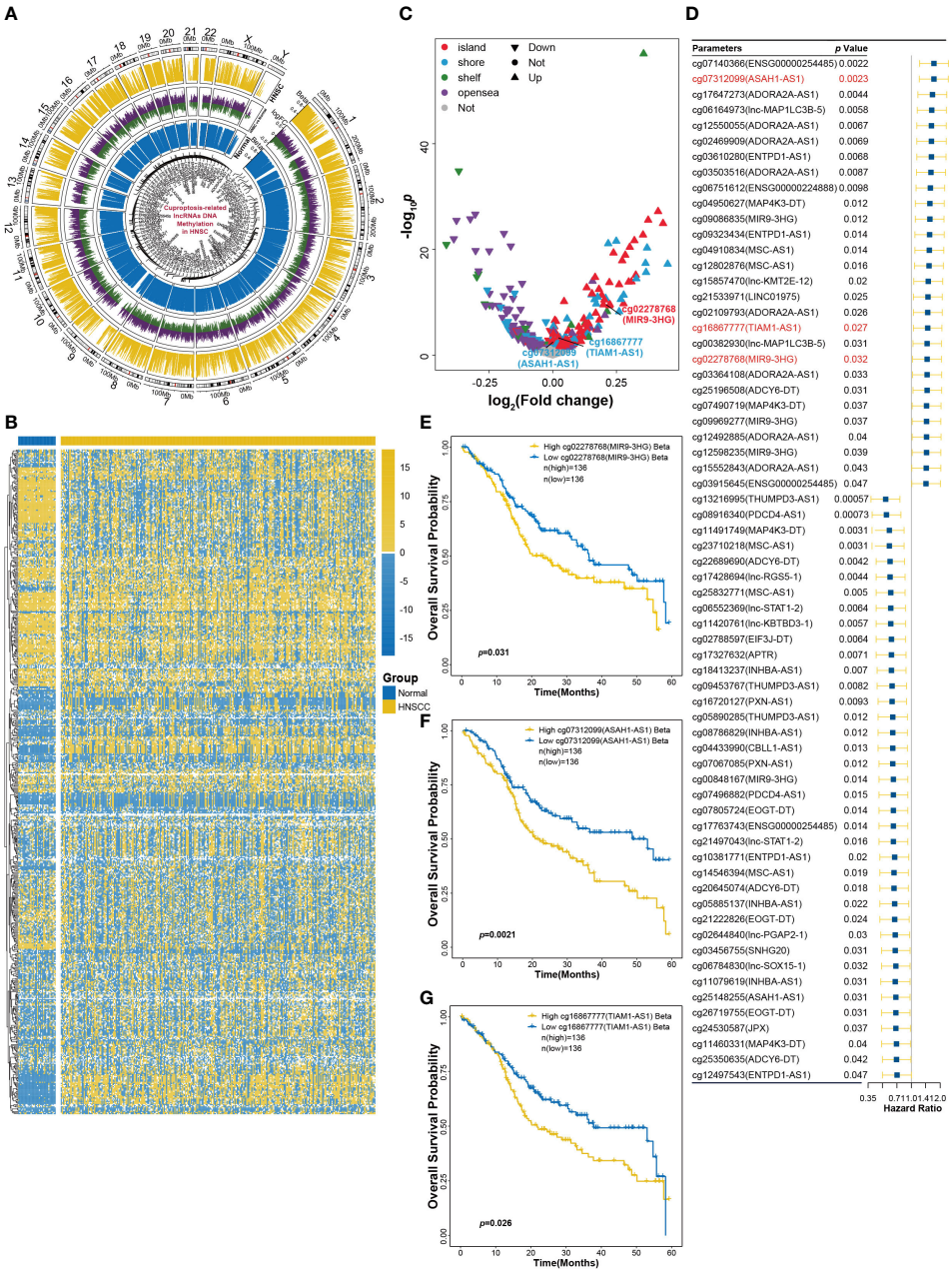

FIGURE 3
DNA methylation analysis of CRLs in HNSCC. **(A)** Methylation changes in all chromosomes of HNSCC tissues. **(B)** The heatmap of CRLs DNA methylation levels between HNSCC and normal tissues. **(C)** Volcano plot of differential analysis of CRLs DNA methylation. **(D)** Univariant Cox regression analysis for CRLs DNA methylation as an independent prognostic factor. **(E–G)** Kaplan–Meier OS curves for patients with HNSCC based on cg02278768 (MIR9-3HG) **(E)**, cg07312099 (ASAH1-AS1) **(F)** and cg16867777 (TIAM1-AS1) **(G)** in training cohort.

addition, effects of CRL DNA methylation on survival prognosis of HNSCC patients were analyzed using univariate Cox regression method. Results showed that 66 methylated sites correlated with the prognosis of HNSCC patients (Figure 3D). The OS probability of HNSCC patients in 5-year survival was also analyzed to validate the results of univariate Cox regression. Kaplan–Meier curves showed that the methylation of cg02278768 (MIR9-3HG), cg07312099 (ASAH1-AS1), and cg16867777 (TIAM1-AS1) sites had significant effects on survival probability in the training cohort (Figures 3E–G) and the validation cohort (Supplemental Figures S3A–C).

Construction of CRL–pcRNAs interaction network and enrichment analysis

The biological functions of lncRNAs can be fulfilled through the regulation of targeted genes (19). To investigate the functional pathway of CRLs, correlation analysis was performed to screen CRL-related pcRNAs and construct the CRL–pcRNA interaction network. Based on the cutoff of $|Pearson's\ r| \geq 0.6$ and $p \leq 0.05$, 1475 CRL-related pcRNAs were selected (Supplemental Table S3), and a CRL–pcRNA interaction network was also finally established (Figure 4A). CRL-related pcRNAs were subsequently analyzed for

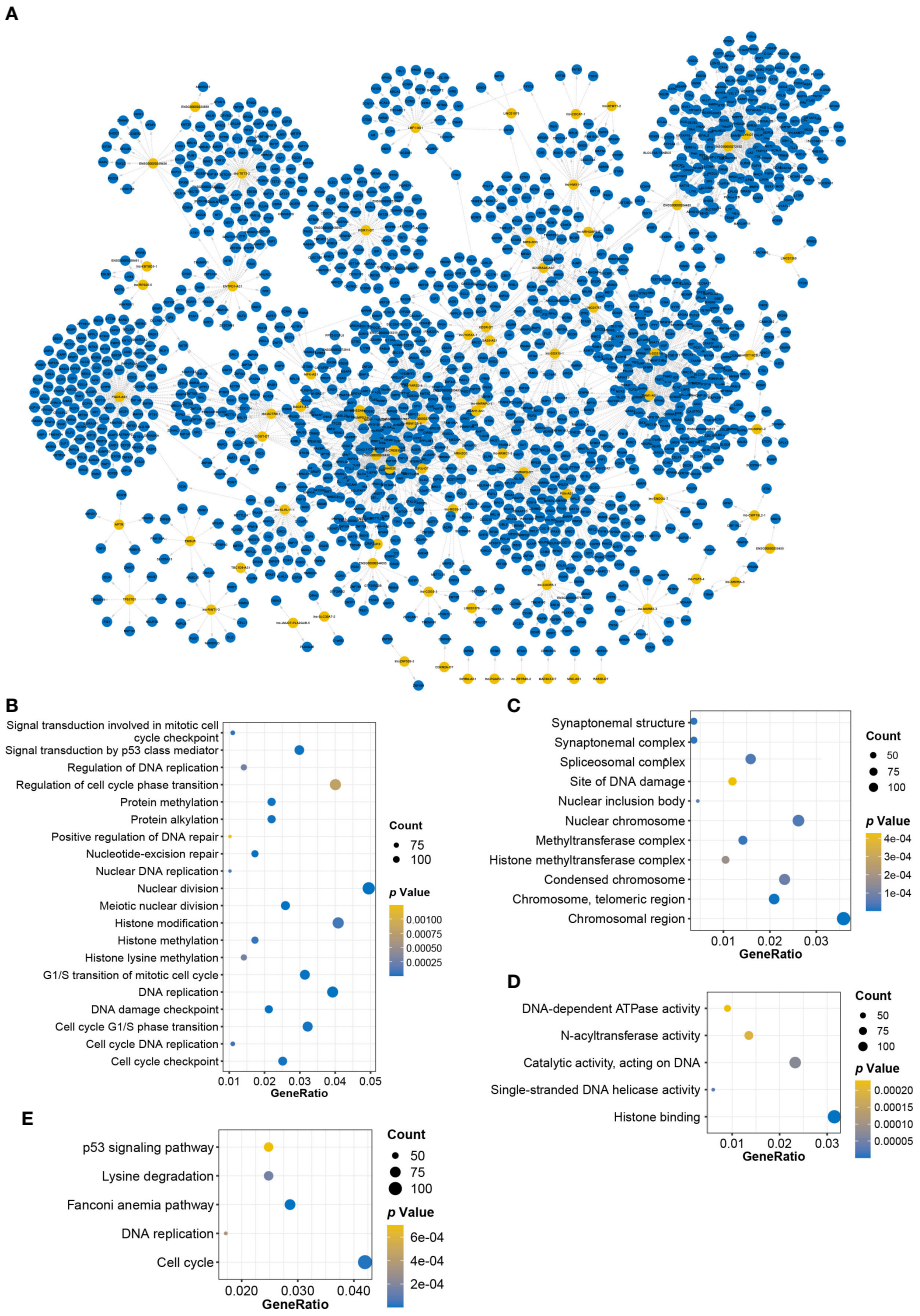

FIGURE 4
Constructing CRLs–pcRNAs interaction network and enrichment analysis. **(A)** Constructing CRLs–pcRNAs interaction network. Yellow: CRLs, blue: pcRNAs. **(B–D)** BP **(B)**, CC **(C)** and MF **(D)** terms of GO enrichment analysis. **(E)** The dotplot of KEGG enrichment analysis.

functional enrichment. Results of GO enrichment analysis, including MF, CC, and BP terms, showed that pcRNAs regulated by CRLs mainly enriched in cell cycle, DNA replication, histone modification, nuclear division, and p53 signal pathway (Figures 4B–D). Furthermore, KEGG analysis validated the results that pcRNAs mainly enriched in cell cycle, DNA replication, and p53 signal pathway obtained from GO analysis (Figure 4E).

lnc-FGF3-4 was upregulated and affected survival prognosis of HNSCC patients

To evaluate the effects of each deCRL on HNSCC prognosis, univariate Cox regression was performed to analyze the correlation between survival prognosis and continuous changes of deCRL expression. Cox analysis showed that a total of 16 CRLs that included MIR9-3HG, BACE1-AS, lnc-FGF3-4, LINC01767, APLC4, lnc-RPS25-5, lnc-TCEA3-1, lnc-COG5-3, MSC-AS1, MAP4K3-DT, lnc-SOS1-1, LMF1-AS1, lnc-ACTR8-1, lnc-YARS2-4, SNHG20, and GAS5-AS1 were correlated with HNSCC prognosis (Figure 5A). Especially, lnc-FGF3-4 as a high-risk factor for HNSCC was upregulated in HNSCC tissues (Figures 5B, C). It also were confirmed that the upregulated expression of lnc-FGF3-4 in HNSCC cell lines, which included CAL-27, FaDu, AMC-HN-8 and WSU-HN30 cells (Figure 5D). Furthermore, the RNA-Seq data of 107 paired LSCC and matched ANM tissues showed the high expression of lnc-FGF3-4 in LSCC tissues (Figure 5E). Subsequently, Kaplan–Meier curves were used to validate the analysis results of Cox regression. Figure 5F shows that OS probability of HNSCC patients in high-lnc-FGF3-4-expression group was lower than those in low-lnc-FGF3-4-expression group. The upregulation of lnc-FGF3-4 was also observed to have a negative effect on OS probability of HNSCC patients in TCGA-B cohort (Figure 5G). The elevated expression of lnc-FGF3-4 also exhibited the adverse impacts on disease-specific survival (DSS) and progression-free interval (PFI) of HNSCC patients in the validation cohort (Figures 5H, I). Furthermore, lnc-FGF3-4 showed the significant correlations with SHANK2 in expression levels in both TCGA-A and TCGA-B cohort (Figures 5J, K).

Construction and validation of CRL-related signature for OS prediction of HNSCC patients

The performance of multi-gene model for prognosis prediction is better than the single-gene model (20). To evaluate the integrated effects of CRLs on OS probability of HNSCC, CRLs were used to establish a predicted model based on the LASSO algorithm. A four-CRL signature, with MAP4K3-DT, lnc-TCEA3-1, MIR9-3HG, and CDKN2A-DT, was finally constructed, and the risk score of HNSCC patients was expressed as follows: risk scores = $(0.0079 \times exp_{MAP4K3\text{-}DT}) + (-0.0108 \times exp_{lnc\text{-}TCEA3\text{-}1}) + (-0.1030 \times exp_{MIR9\text{-}3HG}) + (-0.1181 \times exp_{CDKN2A\text{-}DT})$ (Figure 6A). High-risk-score group of the four-CRL signature exhibited a significantly negative effect on OS probability of HNSCC patients in the 5-year survival (Figure 6B). ROC curves were used to assess the sensitivity and specificity of the four-CRL signature in different lengths of survival prognosis. The area under the curve (AUC) of ROC curve was 64.65%, 66.12%, and 89.48% in 2-, 3-, and 5-year OS prediction, respectively (Figure 6C). The four-CRL signature also had a poor impact on the probability of DSS, and the AUC of ROC for DSS prediction was 62.25%, 65.95%, and 80.99% in 2-, 3-, and 5-year survival, respectively (Figures 6D, E). Although the effect of the four-CRL signature on PFI was not statistically significant in Kaplan–Meier estimate, it was highly significant that the four-CRL signature as a risk factor had an adverse impact on PFI probability in univariate analysis (p(HR) = 0.0024, Figure 6F). In addition, the AUC of ROC for PFI prediction was 63.65%, 61.70%, and 92.67% in 2-, 3-, and 5-year survival, respectively (Figure 6G). Finally, the adverse effect of the four-CRL signature on OS probability was validated in the validation cohort (Figure 6H).

High-risk scores of the four-CRL signature suppressed the immune status of HNSCC

In the initiation and development of cancer, the peripheral immune system is often weak (21). To assess the effects of the four-CRL signature on the immune status of HNSCC, CIBERSORT method was used to analyze the correlation between the four-CRL signature and immune cell abundance. Figure 7A displays the different proportions of 22 immune-related cells in HNSCC tissues. The distributed trends of 22 immune-related cells in TCGA-B cohort have confirmed the analysis results in the training cohort (Figure 7B). T cells follicular helper is a specific subgroup of $CD4^+$ T cells that help B cells produce antibodies against foreign antigens (22). The proportion of T cells follicular helper was significantly suppressed in high-risk score of the four-CRL signature (Figure 7C). In addition, trends of T cells follicular helper weakened by the four-CRL signature were confirmed in the validation cohort (Figure 7D).

Construction of a CRL-related nomogram for clinical application

Combining biomarkers and clinical features can improve the efficiency of disease diagnosis or prognosis prediction compared with that obtained using a single indicator (23). To screen the clinical features correlated with HNSCC prognosis, univariate Cox regression was employed for risk factor analysis. Results revealed that pathologic T and pathologic N stages were significantly correlated with the prognosis of HNSCC (Supplemental Figure S4). In this study, a nomogram consisting of the four-CRL signature and pathologic T and pathologic N stages was constructed for survival prognosis prediction in clinical use (Figure 8A). The calibrate curves were used to evaluate the prediction ability of the nomogram model, and the nomogram exhibited a great prognostic predictive validity of OS in 2-, 3-, and 5-year survival (Figure 8B). Moreover, decision curves showed the net benefit of the four-CRL signature and nomogram model in OS prediction (Figure 8C). Figure 8D shows the high-risk group in the nomogram model had significantly negative effects on OS probability in 5-year survival.

10.3389/fonc.2023.1055717

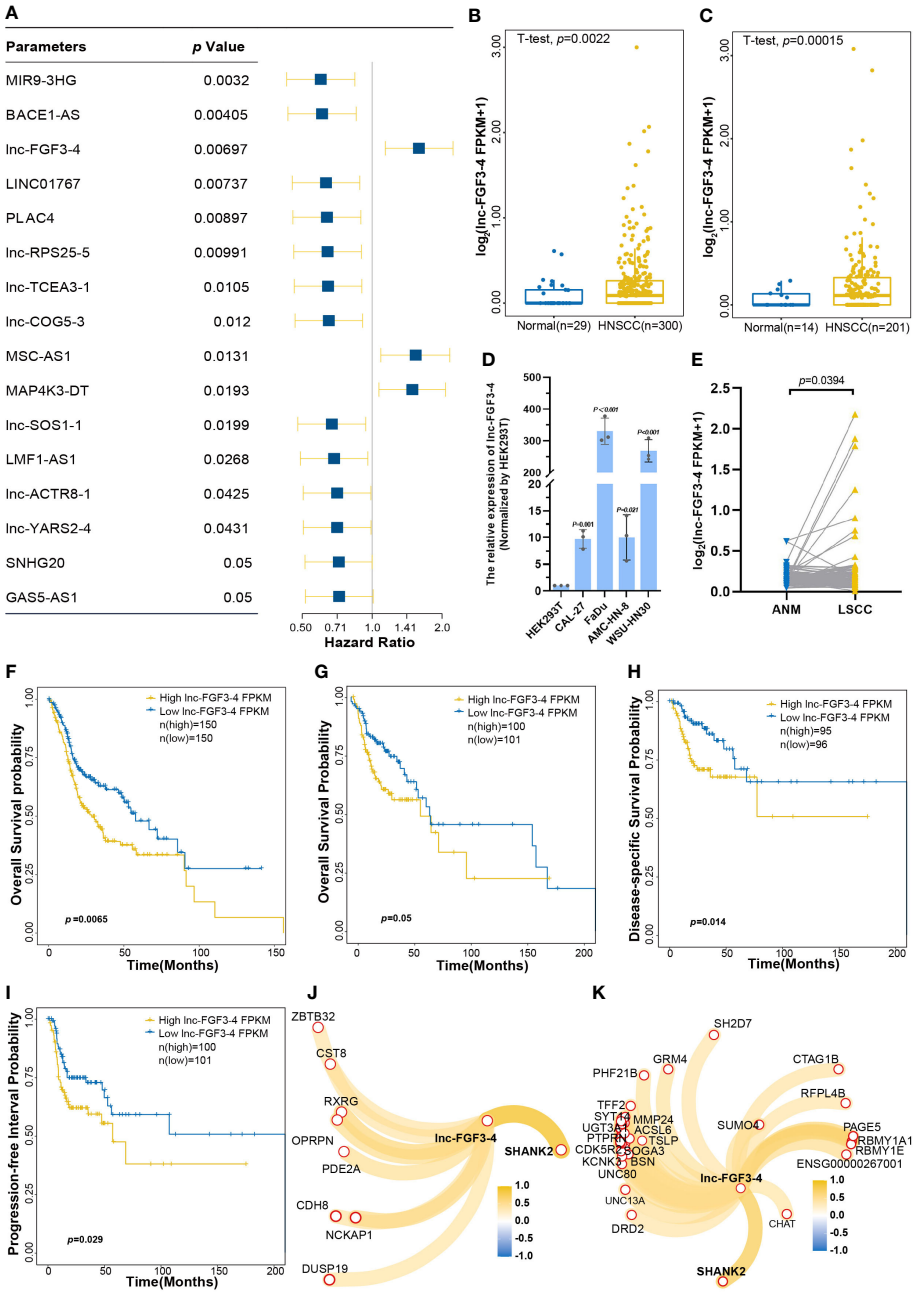

FIGURE 5
The effects of lnc-FGF3-4 on prognosis of HNSCC. **(A)** Univariant Cox regression analysis for CRLs as the independent prognosis risk factor. **(B, C)** Boxplot of lnc-FGF3-4 expression levels between HNSCC and normal tissues in training cohort **(B)** and in validation cohort **(C)**. **(D)** The expression leves of lnc-FGF3-4 in HNSCC cell lines. **(E)** The expression leves of lnc-FGF3-4 in 107 paired LSCC and matched ANM tissues. **(F)** Kaplan–Meier curves for OS of HNSCC based on lnc-FGF3-4 expression in TGCA-A cohort. **(G–I)** Kaplan-Meier curves of OS **(G)**, DSS **(H)** and PFI **(I)** of HNSCC based on lnc-FGF3-4 expression in TGCA-B cohort. **(J, K)** Protein-coding RNAs correlated with lnc-FGF3-4 expression in TGCA-A **(J)** and TGCA-B **(K)** cohort, |*Pearson's r*| ≥ 0.5 and $p \leq 0.05$.

TCGA-B cohort validated the performance of the nomogram model in OS prediction in the training cohort (Figure 8E).

Discussion

In this study, 99 CRLs were analyzed in 501 HNSCC and 43 normal tissue samples. The expression pattern, differential profile, clinical correlation, DNA methylation, functional enrichment, univariate prognosis factor, and the immune status were analyzed. A four-CRL signature for OS probability prediction was constructed using LASSO algorithm. Furthermore, a nomogram consisting of the four-CRL signature and clinical features was established for clinical utilization of HNSCC.

lncRNAs play a crucial role in the regulation of most cellular processes at various levels, such as epigenetic modification, and the

10.3389/fonc.2023.1055717

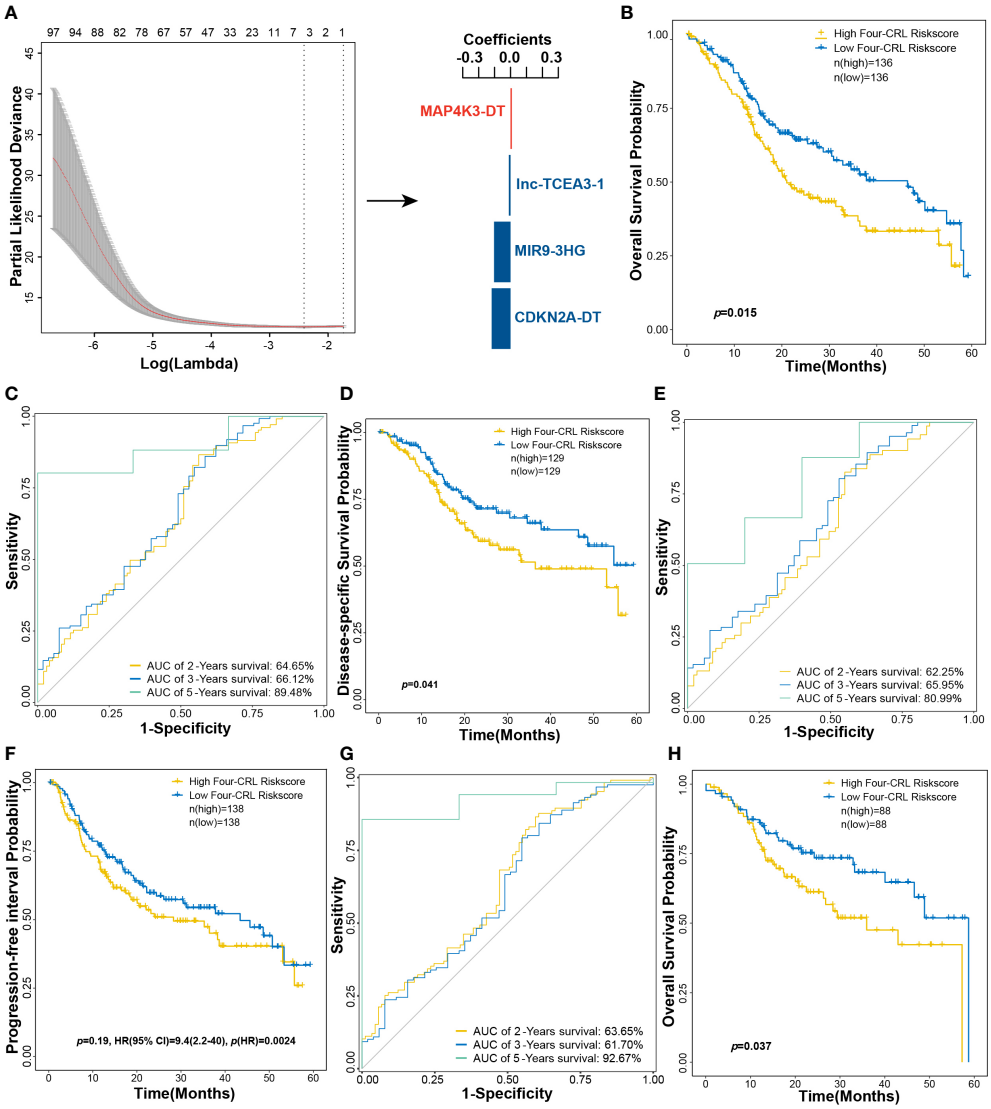

FIGURE 6
A four-CRL signature was constructed based on LASSO method. **(A)** constructing multi-CRL signature for OS of HNSCC. **(B)** Kaplan–Meier OS curves for HNSCC patients based on the four-CRL signature in training cohort. **(C)** ROC curves of 2-, 3-, 5-year OS survival according to the four-CRL signature. **(D)** Kaplan–Meier DSS curves for HNSCC patients based on the four-CRLs signature in training cohort. **(E)** ROC curves of 2-, 3-, 5-year DSS survival according to the four-CRL signature. **(F)** Kaplan–Meier PFI curves for HNSCC patients based on the four-CRL signature in training cohort. **(G)** ROC curves of 2-, 3-, 5-year PFI survival according to the four-CRL signature. **(H)** Kaplan-Meier OS curves for HNSCC patients based on the four-CRL signature in validation cohort.

regulation of transcription, post-transcription, translation, and post-translation. lncRNAs also regulate the initiation and progression in cancers of diverse tissues through various molecular mechanisms (9). Certain deCRLs, namely, EIF3J-DT, lnc-IAH1-2, lnc-ENDOU-7, PDCD4-AS1, ARIH2OS, CDKN2A-DT, TIAM1-AS1, MIR9-3HG, LINC01269, KDSR-DT, lnc-SOS1-1, ENSG00000270147, lnc-TCEA3-1, lnc-RBM12B-4, lnc-ACTR8-1, HNRNPD-DT, lnc-KMT2E-12, EMSLR, lnc-USHBP1-1, and lnc-CDCA7-1 were significantly correlated with clinical features in the current study. In the lncRNAs above, EIF3J-DT, PDCD4-AS1, CDKN2A-DT, MIR9-3HG, LINC01269, and EMSLR have been reported to play a critical role in the regulation of cancers (24–29). In particular, a previous study revealed that LINC01269 could be a tumor inhibitor as it triggered therapeutic efficacy in HNSCC (28), which validated the analysis result that LINC01269 was significantly correlated with the progression of HNSCC tumor grade in the current study. These results fully demonstrated that CRLs have potential effects on the initiation and progression of HNSCC in clinical applications and can be used to construct the progression or prognosis prediction model.

DNA methylation, as one of the epigenetic modifications, regulates gene expression without changing the DNA sequence and is actively involved in the progression of cancers (30). DNA methylation has also been reported to impact the stage progression of HNSCC (31). In the current study, many methylation probes that targeted DNA sequence of CRLs brought significant changes in HNSCC tissues. More particularly, it was identified that DNA methylation changes of cg02278768 (MIR9-3HG), cg07312099

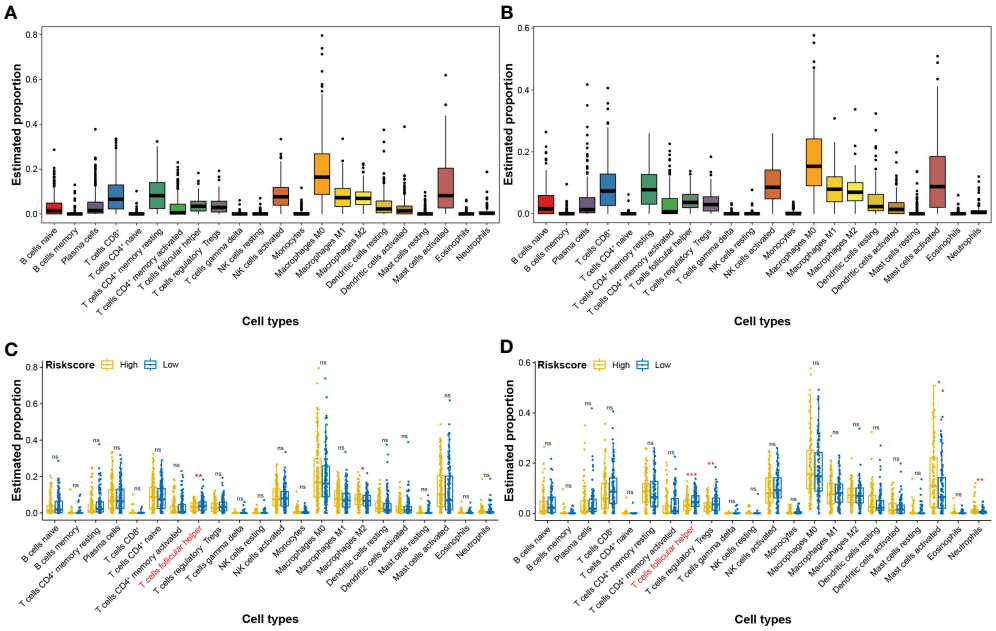

FIGURE 7
Effects of the four-CRL signature on immune cells status in HNSCC tissues. **(A, B)** The proportion of 22 immune cells in HNSCC tissues in training cohort **(A)** and in validation cohort **(B)**. **(C, D)** The proportional difference of 22 immune cells between high and low four-CRL signature risk-score in training cohort **(C)** and in validation cohort **(D)**. *$p < 0.05$; **$p < 0.01$; ***$p < 0.001$; ns, not significant.

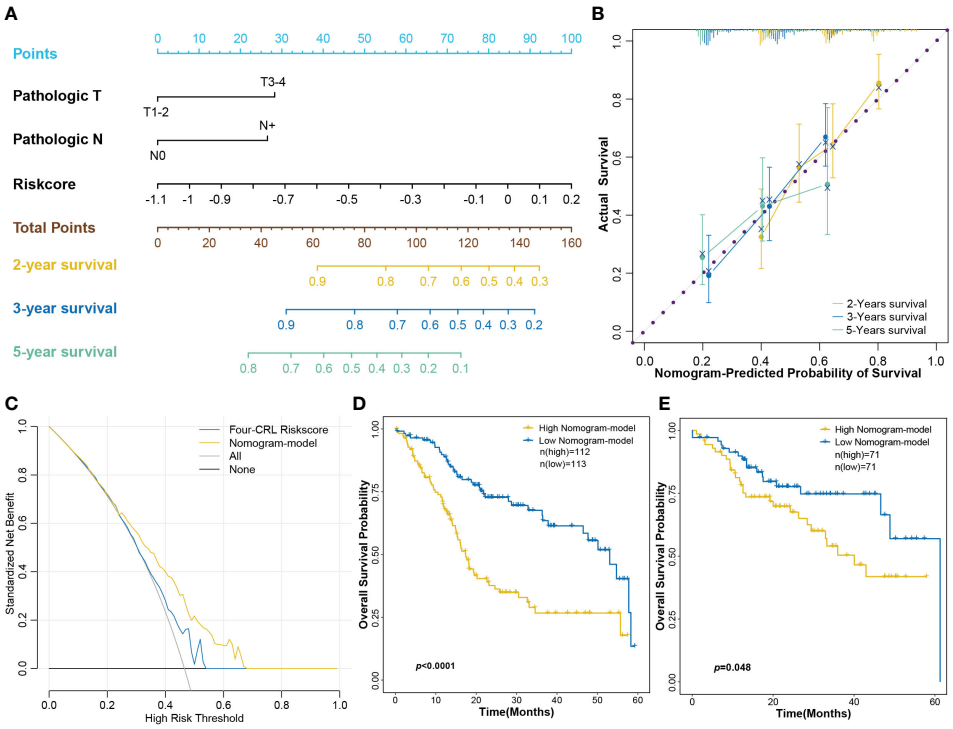

FIGURE 8
Constructing a nomogram consisted of the four-CRL signature and clinical characters. **(A)** The nomogram for OS survival prediction of HNSCC patients. **(B)** The calibrate curves evaluated the prediction ability of nomogram model. **(C)** The decision curves for evaluating the four-CRL signature and nomogram model in OS prediction. **(D, E)** Kaplan–Meier curves for OS based on the nomogram model in training cohort **(D)** and in validation cohort **(E)**.

(ASAH1-AS1), and cg16867777 (TIAM1-AS1) sites were correlated with the prognosis of HNSCC. Based on the published literature, the expression of MIR9-3HG was regulated by its DNA methylation changes in prostate cancer (32). MIR9-3HG was hypomethylated in DNA sequence and upregulated in the transcriptome level in this study. The results of DNA methylation analysis revealed that DNA methylation levels of CRLs might regulate their expression levels. Particularly, DNA hypomethylation elevated the expression of MIR9-3HG, and the change of methylated site in MIR9-3HG DNA sequence even affected the OS of HNSCC patients.

Certain CRLs have already been used to analyze the effects on the progression of cancers and predict the prognosis of patients (5, 33, 34). However, the regulatory mechanisms of CRLs in HNSCC are still unclear until now. In our study, 99 CRLs were utilized for functional enrichment analysis. Results of GO and KEGG analysis showed that CRLs mainly enriched in histone modification, nuclear division, cell cycle, DNA replication, and p53 signal pathway. The dysregulation of histone modification can generate the inappropriate activation of oncogenes or tumor suppressors (35). Abnormal nuclear division is an important event in the development of cancers and can be used to assess the initiation of cancers (36, 37). DNA replication stress is one of the hallmarks of cancers, induced by tumor driver genes to result in a rapid proliferation of tumor cells (38). It is well known that disturbed regulation of the cell cycle is one of the main causes of tumorigenesis (39). P53 signal pathway has preeminent importance in regulating cell proliferation, and its mutation directly promotes the initiation of cancers (40). These results suggest that CRLs play an essential role in the regulation of cancers and have the potential as biomarkers or targets in the prediction and therapy of cancers.

In our study, independent risk factors were identified using univariate Cox proportional hazards models. A total of 16 CRLs, which included MIR9-3HG, BACE1-AS, lnc-FGF3-4, LINC01767, APLC4, lnc-RPS25-5, lnc-TCEA3-1, lnc-COG5-3, MSC-AS1, MAP4K3-DT, lnc-SOS1-1, LMF1-AS1, lnc-ACTR8-1, lnc-YARS2-4, SNHG20, and GAS5-AS1 had significant effects on OS probability of HNSCC patients. The overexpression of BACE1-AS promoted the invasive and metastatic capacity of hepatocellular carcinoma (41). MSC-AS1 enhances the proliferation and glycolysis of gastric cancer (42). MAP4K3-DT was positively correlated with the VEGF-C/VEGFR3-induced lymph node metastasis of bladder cancer (43). SNHG20 is an aberrant expression in various cancers and promotes the development and progression of tumors, such as hepatocellular carcinoma, ovarian cancer, colorectal cancer, and bladder cancer (44). Downregulation of GAS5-AS1 can suppress the development and metastasis of cervical cancer (45). Particularly, a novel lncRNA lnc-FGF3-4 as a single risk factor was upregulated in HNSCC tissues and had a significantly negative impact on the patient's prognosis. Deletion of GLS confer sensitivity to copper-induced cell death in cuproptosis mechanism (2). Because lnc-FGF3-4 is a significantly expression-associated lncRNA with GLS, lnc-FGF3-4 may maintain the cells survival by elevating the expression of GKL to suppress the copper-induced cell death. Moreover, lnc-FGF3-4 also show a significant positive correlation with SHANK2 in expression levels. SHANK2 is upregulation in cancer cells and can suppress the Hippo signaling pathway (46). lnc-FGF3-4 may promote tumor cell proliferation by upregulating SHANK2 to inhibit the Hippo signaling pathway. The above results reveal that CRLs could affect the OS probability of HNSCC patients and exhibit promising potential in the prognosis prediction of HNSCC.

The multi-gene model for prognosis prediction performs better than the single-gene model (20). We have constructed a four-CRL signature that included MAP4K3-DT, lnc-TCEA3-1, MIR9-3HG, and CDKN2A-DT using the LASSO algorithm. In the 2-, 3-, and 5-year survival prediction, the AUC values of the four-CRL risk score for OS were 64.65%, 66.12%, and 89.48%, for DSS were 62.25%, 65.95%, and 80.99%, and for PFI were 63.65%, 61.70%, and 92.67%, respectively. MAP4K3-DT, MIR9-3HG, and CDKN2A-DT have been reported to have the predictive ability of cancer prognosis and regulate the development and progression of cancers (26, 27, 43). The knockout of FDX1 resulted in cancer cells becoming sensitive to the copper ion concentration, conversely, the knockout of CDKN2A improved the tolerance of cancer cells to copper ion (2). As the expression-correlated lncRNAs of FDX1, MAP4K3-DT is significantly downregulated in HNSCC, and perhaps suppresses the death of HNSCC cells through attenuating the expression of FDX1 that a core gene in cuproptosis. Moreover, MIR9-3HG and CDKN2A-DT, the expression-correlated lncRNAs of CDKN2A, are upregulated in HNSCC and may be improve the resistance of HNSCC cells to copper-induced cell death through regulating expression of CDKN2A.

Immunoevasion and immunosuppression are ubiquitous in malignant cancer and serve as emerging hallmarks (40). HNSCC has an immunosuppressive tumor microenvironment that is accompanied by low tumor-infiltrating lymphocytes (47). In our study, the proportion of T cells follicular helper was significantly suppressed in high-risk score of the four-CRL signature. T cells follicular helper is a specific subgroup of $CD4^+$ T cells that helps B cells produce antibodies against foreign antigens (22). Some recent studies indicated that the mediatory effect of follicular helper T cells on diverse cancers. For instance, a functional analysis in non-small cell lung carcinoma revealed that follicular helper T cells were capable of promoting the differentiation of regulatory B cells and $CD14^+$ human leukocyte antigen (HLA) - DR - cells. Furthermore, a analysis in the same study uncovered a negative association between follicular helper T cells and disease-free survival in patients with non-small cell lung carcinoma (48). One study uncovered that the infiltration of follicular helper T cells in HPV^+ HNSCC patients was higher than who in HPV^- HNSCC patients cohort (49). Moreover, a investigation based on HNSCC patients showed genes expression signature related with $CD4^+$T follicular helper cells could affect the progression-free survival of HNSCC patients (50). These results suggest that follicular helper T cells may play an important role in the initiation and development of HNSCC. Therefore, the effect of the four-CRL on follicular helper T cells may be one of its regulatory pathways in HNSCC. Combining molecular biomarkers and clinical characteristics can improve the efficiency of disease diagnosis or prognosis prediction compared with that obtained using a single indicator (23). We also established a nomogram consisting of a four-CRL signature and clinical characteristics for clinical application. The calibrate curves and decision curves have validated the prediction ability of the nomogram model in HNSCC. The above results fully demonstrate that the four-CRL

signature has promising potential in the prognosis prediction of HNSCC and as the treatment targets in clinical therapy.

Notwithstanding its novel findings, the current study has a few limitations. First, the cohorts of HNSCC patients analyzed in our study were retrospective data based on the public database. Our prospective multi-center clinical data will be used to further verified the prognostically predictive model in the future. Second, it is inevitable that relying on only a limited number of genes to build a prognostic model has the inherent weaknesses. As the public data grows, more CRLs will also be incorporated in future studies. Finally, it must be emphasized here that the correlation between the four-CRL signature and promotion of HNSCC has not yet been experimentally addressed. The experimental investigation of CRLs in HNSCC will act as a new object for further exploration.

Conclusion

In this study, the expression pattern, differential profile, clinical correlation, DNA methylation, functional enrichment, univariate prognosis factor, and immune status were analyzed. DNA methylation changes of cg02278768 (MIR9-3HG), cg07312099 (ASAH1-AS1), and cg16867777 (TIAM1-AS1) sites were correlated with the prognosis of HNSCC. lnc-FGF3-4, as a single risk factor, was upregulated in HNSCC tissues and negatively impacted the prognosis of HNSCC. A four-CRL signature that included MAP4K3-DT, lnc-TCEA3-1, MIR9-3HG, and CDKN2A-DT was constructed. This four-CRL signature has exhibited significantly negative effects on the immune status and survival prognosis of HNSCC. Finally, a nomogram consisting of the four-CRL signature and clinical features was also established for clinical applications. CRLs have exhibited promising potential in the prognosis prediction of HNSCC and as the treatment targets in immunotherapy.

Data availability statement

Publicly available datasets were analyzed in this study. TCGA data can be found here: https://portal.gdc.cancer.gov/, https://xenabrowser.net/. RNA-seq data of 107 paired LSCC can be found at GEO (https://www.ncbi.nlm.nih.gov/geo/) with accession number GSE127165 and GSE130605.

Author contributions

XWZ obtained data, calculated data, plotted figure and drafted the manuscript. DZ and CZ performed the statistical analysis, drafted and revised the manuscript. HG, YZ, XX, ZS, and XMZ calculated data, cultured cells, quantitated RNAs, and plotted figures. XHZ, YW, and WG designed the study, administrated the project, and revised the manuscript. All authors reviewed and approved the final manuscript. All authors contributed to the article and approved the submitted version.

Funding

This work was supported by the National Natural Science Foundation of China (No. 82073101), Shenzhen Science and Technology Program (No. RCJC20210706091950028, JCYJ20220531102815036, JCYJ20190813154405551), Basic and Applied Basic Research Foundation of Guangdong Province (No. 2023A1515010342), Fundamental Research Program of Shanxi Province (No. 20210302124088), the Research Project of Shanxi Province Health and Family Planning Commission (No. 2019033), Shanxi Scholarship Council of China (No. 2020165), the Fund for the Scientific Activities of Selected Return Overseas Professionals in Shanxi Province (No. 20200034), and the Research Funds for China Central Government guided Development of Local Science and Technology (No. 2020-165-19).

Conflict of interest

The authors declare that the research was conducted in the absence of any commercial or financial relationships that could be construed as a potential conflict of interest.

Publisher's note

Supplementary material

The Supplementary Material for this article can be found online at: https://www.frontiersin.org/articles/10.3389/fonc.2023.1055717/full#supplementary-material

SUPPLEMENTARY FIGURE 1
The validation of CRLs's role in developing and progressing HNSCC. **(A)** Correlation analysis of among CRGs in validation cohort. **(B)** Correlation analysis among CRLs in validation cohort. **(C)** The heatmap of CRLs expression between HNSCC and normal tissues in validation cohort. **(D)** Volcano plot of differential analysis of CRLs in validation cohort. **(E, F)** The effects of deCRLs on clinical stage of HNSCC in training cohort **(E)** and in validation cohort **(F)**. *$p < 0.05$; **$p < 0.01$; ***$p < 0.001$; ****$p < 0.0001$; ns, not significant.

SUPPLEMENTARY FIGURE 2
The effects of CRLs on clinical features of HNSCC patients. **(A, B)** The effects of deCRLs on clinical T stage of HNSCC in training cohort **(A)** and validation cohort **(B)**. **(C, D)** The effects of deCRLs on clinical N stage of HNSCC in training cohort **(C)** and validation cohort **(D)**. **(E, F)** The correlation between deCRLs and age of HNSCC patients in training cohort **(E)** and validation cohort **(F)**. **(G, H)** The correlation between deCRLs and gender of HNSCC patients in training cohort **(G)** and validation cohort **(H)**. *$p < 0.05$; **$p < 0.01$; ***$p < 0.001$; ****$p < 0.0001$; ns, not significant.

SUPPLEMENTARY FIGURE 3
DNA methylation analysis validation of CRLs in HNSCC in validation cohort. **(A–C)** Kaplan–Meier OS curves for HNSCC patients based on cg02278768 (MIR9-3HG) **(A)**, cg07312099 (ASAH1-AS1) **(B)** and cg16867777 (TIAM1-AS1) **(C)** methylation levels in validation cohort.

SUPPLEMENTARY FIGURE 4
Univariant Cox regression analysis of OS based on clinical features.

SUPPLEMENTARY TABLE 1
Clinical characters of HNSCC patients in the current study.

SUPPLEMENTARY TABLE 2
A list of cuproptosis-related lncRNAs.

SUPPLEMENTARY TABLE 3
A list of protein conding RNAs correlated with CRLs.

References

1. Li S, Bu L, Cai L. Cuproptosis: lipoylated TCA cycle proteins-mediated novel cell death pathway. *Signal Transduct Target Ther* (2022) 7:158. doi: 10.1038/s41392-022-01014-x

2. Tsvetkov P, Coy S, Petrova B, Dreishpoon M, Verma A, Abdusamad M, et al. Copper induces cell death by targeting lipoylated TCA cycle proteins. *Science* (2022) 375:1254–61. doi: 10.1126/science.abf0529

3. Mo X, Hu D, Yang P, Li Y, Bashir S, Nai A, et al. A novel cuproptosis-related prognostic lncRNA signature and lncRNA MIR31HG/miR-193a-3p/TNFRSF21 regulatory axis in lung adenocarcinoma. *Front Oncol* (2022) 12:927706. doi: 10.3389/fonc.2022.927706

4. Zhang Z, Zeng X, Wu Y, Liu Y, Zhang X, Song Z. Cuproptosis-related risk score predicts prognosis and characterizes the tumor microenvironment in hepatocellular carcinoma. *Front Immunol* (2022) 13:925618. doi: 10.3389/fimmu.2022.925618

5. Shen J, Wang L, Bi J. Bioinformatics analysis and experimental validation of cuproptosis-related lncRNA LINC02154 in clear cell renal cell carcinoma. *BMC Cancer* (2023) 23:160. doi: 10.1186/s12885-023-10639-2

6. Johnson DE, Burtness B, Leemans CR, Lui VWY, Bauman JE, Grandis JR. Head and neck squamous cell carcinoma. *Nat Rev Dis Primers* (2020) 6:92. doi: 10.1038/s41572-020-00224-3

7. Li W, Liu J, Hou L, Yu F, Zhang J, Wu W, et al. Liquid biopsy in lung cancer: significance in diagnostics, prediction, and treatment monitoring. *Mol Cancer* (2022) 21:25. doi: 10.1186/s12943-022-01505-z

8. Dai F, Dai L, Zheng X, Guo Y, Zhang Y, Niu M, et al. Non-coding RNAs in drug resistance of head and neck cancers: a review. *BioMed Pharmacother* (2020) 127:110231. doi: 10.1016/j.biopha.2020.110231

9. Nandwani A, Rathore S, Datta M. LncRNAs in cancer: regulatory and therapeutic implications. *Cancer Lett* (2021) 501:162–71. doi: 10.1016/j.canlet.2020.11.048

10. Li S, Zhang J, Lu S, Huang W, Geng L, Shen Q, et al. The mechanism of allosteric inhibition of protein tyrosine phosphatase 1B. *PloS One* (2014) 9:e97668. doi: 10.1371/journal.pone.0097668

11. Lu S, Qiu Y, Ni D, He X, Pu J, Zhang J. Emergence of allosteric drug-resistance mutations: new challenges for allosteric drug discovery. *Drug Discovery Today* (2020) 25:177–84. doi: 10.1016/j.drudis.2019.10.006

12. Wang Y, Wong GL, He F, Sun J, Chan AW, Yang J, et al. Quantifying and monitoring fibrosis in nonalcoholic fatty liver disease using dual-photon microscopy. *Gut* (2020) 69:1116–26. doi: 10.1136/gutjnl-2019-318841

13. Zheng X, Gao W, Zhang Z, Xue X, Mijiti M, Guo Q, et al. Identification of a seven-lncRNAs panel that serves as a prognosis predictor and contributes to the malignant progression of laryngeal squamous cell carcinoma. *Front Oncol* (2023) 13:1106249. doi: 10.3389/fonc.2023.1106249

14. Gao W, Guo H, Niu M, Zheng X, Zhang Y, Xue X, et al. circPARD3 drives malignant progression and chemoresistance of laryngeal squamous cell carcinoma by inhibiting autophagy through the PRKCI-Akt-mTOR pathway. *Mol Cancer* (2020) 19:166. doi: 10.1186/s12943-020-01279-2

15. Tian Y, Morris TJ, Webster AP, Yang Z, Beck S, Feber A, et al. ChAMP: updated methylation analysis pipeline for illumina BeadChips. *Bioinformatics* (2017) 33:3982–4. doi: 10.1093/bioinformatics/btx513

16. Wu T, Hu E, Xu S, Chen M, Guo P, Dai Z, et al. clusterProfiler 4.0: a universal enrichment tool for interpreting omics data. *Innovation (Camb)* (2021) 2:100141. doi: 10.1016/j.xinn.2021.100141

17. Newman AM, Liu CL, Green MR, Gentles AJ, Feng W, Xu Y, et al. Robust enumeration of cell subsets from tissue expression profiles. *Nat Methods* (2015) 12:453–7. doi: 10.1038/nmeth.3337

18. Zou Q, Wang X, Ren D, Hu B, Tang G, Zhang Y, et al. DNA Methylation-based signature of CD8+ tumor-infiltrating lymphocytes enables evaluation of immune response and prognosis in colorectal cancer. *J Immunother Cancer* (2021) 9:e002671. doi: 10.1136/jitc-2021-002671

19. Liu T, Feng H, Yousuf S, Xie L, Miao X. Differential regulation of mRNAs and lncRNAs related to lipid metabolism in duolang and small tail han sheep. *Sci Rep* (2022) 12:11157. doi: 10.1038/s41598-022-15318-z

20. He L, Chen J, Xu F, Li J, Li J. Prognostic implication of a metabolism-associated gene signature in lung adenocarcinoma. *Mol Ther Oncolytics* (2020) 19:265–77. doi: 10.1016/j.omto.2020.09.011

21. Shi Y, Lammers T. Combining nanomedicine and immunotherapy. *Acc Chem Res* (2019) 52:1543–54. doi: 10.1021/acs.accounts.9b00148

22. Cui C, Wang J, Fagerberg E, Chen P, Connolly KA, Damo M, et al. Neoantigen-driven b cell and CD4 T follicular helper cell collaboration promotes anti-tumor CD8 T cell responses. *Cell* (2021) 184:6101–18.e13. doi: 10.1016/j.cell.2021.11.007

23. Sun Y, Goodison S, Li J, Liu L, Farmerie W. Improved breast cancer prognosis through the combination of clinical and genetic markers. *Bioinformatics* (2007) 23:30–7. doi: 10.1093/bioinformatics/btl543

24. Luo Y, Zheng S, Wu Q, Wu J, Zhou R, Wang C, et al. (lncRNA) EIF3J-DT induces chemoresistance of gastric cancer via autophagy activation. *Autophagy* (2021) 17:4083–101. doi: 10.1080/15548627.2021.1901204

25. Wang D, Wang Z, Zhang L, Sun S. LncRNA PDCD4-AS1 alleviates triple negative breast cancer by increasing expression of IQGAP2 via miR-10b-5p. *Transl Oncol* (2021) 14:100958. doi: 10.1016/j.tranon.2020.100958

26. Zhao Q, Dong D, Chu H, Man L, Huang X, Yin L, et al. lncRNA CDKN2A-AS1 facilitates tumorigenesis and progression of epithelial ovarian cancer via modulating the SOSTDC1-mediated BMP-SMAD signaling pathway. *Cell Cycle* (2021) 20:1147–62. doi: 10.1080/15384101.2021.1924947

27. Li F, Liang Y, Ying P. Knockdown of MIR9–3HG inhibits proliferation and promotes apoptosis of cervical cancer cells by miR–498 via EP300. *Mol Med Rep* (2021) 24:748. doi: 10.3892/mmr.2021.12388

28. Zhao Y, Huang X, Zhang Z, Li H, Zan T. The long noncoding transcript HNSCAT1 activates KRT80 and triggers therapeutic efficacy in head and neck squamous cell carcinoma. *Oxid Med Cell Longev* (2022) 2022:4156966. doi: 10.1155/2022/4156966

29. Priyanka P, Sharma M, Das S, Saxena S. E2F1-induced lncRNA, EMSLR regulates lncRNA LncPRESS1. *Sci Rep* (2022) 12:2548. doi: 10.1038/s41598-022-06154-2

30. Zhu C, Zhang S, Liu D, Wang Q, Yang N, Zheng Z, et al. A novel gene prognostic signature based on differential DNA methylation in breast cancer. *Front Genet* (2021) 12:742578. doi: 10.3389/fgene.2021.742578

31. Ghafarpour V, Khansari M, Banaei-Moghaddam AM, Najafi A, Masoudi-Nejad A. DNA Methylation association with stage progression of head and neck squamous cell carcinoma. *Comput Biol Med* (2021) 134:104473. doi: 10.1016/j.compbiomed.2021.104473

32. Tonmoy MIQ, Fariha A, Hami I, Kar K, Reza HA, Bahadur NM, et al. Computational epigenetic landscape analysis reveals association of CACNA1G-AS1, F11-AS1, NNT-AS1, and MSC-AS1 lncRNAs in prostate cancer progression through aberrant methylation. *Sci Rep* (2022) 12:10260. doi: 10.1038/s41598-022-13381-0

33. Yang M, Zheng H, Xu K, Yuan Q, Aihaiti Y, Cai Y, et al. A novel signature to guide osteosarcoma prognosis and immune microenvironment: cuproptosis-related lncRNA. *Front Immunol* (2022) 13:919231. doi: 10.3389/fimmu.2022.919231

34. Huang J, Xu Z, Teh BM, Zhou C, Yuan Z, Shi Y, et al. Construction of a necroptosis-related lncRNA signature to predict the prognosis and immune microenvironment of head and neck squamous cell carcinoma. *J Clin Lab Anal* (2022) 36:e24480. doi: 10.1002/jcla.24480

35. Audia JE, Campbell RM. Histone modifications and cancer. *Cold Spring Harb Perspect Biol* (2016) 8:a019521. doi: 10.1101/cshperspect.a019521

36. Lee S, Ahn Y, Kim J, Cho Y, Park J. Downregulation of NOP53 ribosome biogenesis factor leads to abnormal nuclear division and chromosomal instability in human cervical cancer cells. *Pathol Oncol Res* (2020) 26:453–9. doi: 10.1007/s12253-018-0531-4

37. Ionescu ME, Ciocirlan M, Becheanu G, Nicolaie T, Ditescu C, Teiusanu AG, et al. Nuclear division index may predict neoplastic colorectal lesions. *Maedica (Bucur)* (2011) 6:173–8.

38. Macheret M, Halazonetis TD. DNA Replication stress as a hallmark of cancer. *Annu Rev Pathol* (2015) 10:425–48. doi: 10.1146/annurev-pathol-012414-040424

39. Kolb S, Fritsch R, Saur D, Reichert M, Schmid RM, Schneider G. HMGA1 controls transcription of insulin receptor to regulate cyclin D1 translation in pancreatic cancer cells. *Cancer Res* (2007) 67:4679–86. doi: 10.1158/0008-5472.CAN-06-3308

40. Hanahan D, Robert AW. Hallmarks of cancer: the next generation. *Cell* (2011) 144:646–74. doi: 10.1016/j.cell.2011.02.013

41. Liu C, Wang H, Tang L, Huang H, Xu M, Lin Y, et al. LncRNA BACE1-AS enhances the invasive and metastatic capacity of hepatocellular carcinoma cells through mediating miR-377-3p/CELF1 axis. *Life Sci* (2021) 275:119288. doi: 10.1016/j.lfs.2021.119288

42. Jin X, Qiao L, Fan H, Liao C, Zheng J, Wang W, et al. Long non-coding RNA MSC-AS1 facilitates the proliferation and glycolysis of gastric cancer cells by regulating PFKFB3 expression. *Int J Med Sci* (2021) 18:546–54. doi: 10.7150/ijms.51947

43. Zheng H, Chen C, Luo Y, Yu M, He W, An M, et al. Tumor-derived exosomal BCYRN1 activates WNT5A/VEGF-C/VEGFR3 feedforward loop to drive lymphatic metastasis of bladder cancer. *Clin Transl Med* (2021) 11:e497. doi: 10.1002/ctm2.497

44. Zhao W, Ma X, Liu L, Chen Q, Liu Z, Zhang Z, et al. SNHG20: a vital lncRNA in multiple human cancers. *J Cell Physiol* (2019) 234:14519–25. doi: 10.1002/jcp.281432

45. Wang X, Zhang J, Wang Y. Long noncoding RNA GAS5-AS1 suppresses growth and metastasis of cervical cancer by increasing GAS5 stability. *Am J Transl Res* (2019) 11:4909–21.

46. Xu L, Li P, Hao X, Lu Y, Liu M, Song W, et al. SHANK2 is a frequently amplified oncogene with evolutionarily conserved roles in regulating hippo signaling. *Protein Cell* (2021) 12:174–93. doi: 10.1007/s13238-020-00742-6

47. Jia L, Wang Y, Wang C. circFAT1 promotes cancer stemness and immune evasion by promoting STAT3 activation. *Adv Sci (Weinh)* (2021) 8:2003376. doi: 10.1002/advs.202003376

48. Qiu L, Yu Q, Zhou Y, Zheng S, Tao J, Jiang Q, et al. Functionally impaired follicular helper T cells induce regulatory b cells and CD14+ human leukocyte antigen-DR- cell differentiation in non-small cell lung cancer. *Cancer Sci* (2018) 109:3751–61. doi: 10.1111/cas.13836

49. Xu L, Jin Y, Qin X. Comprehensive analysis of significant genes and immune cell infiltration in HPV-related head and neck squamous cell carcinoma. *Int Immunopharmacol* (2020) 87:106844. doi: 10.1016/j.intimp.2020.106844

50. Cillo AR, Kürten CHL, Tabib T, Qi Z, Onkar S, Wang T, et al. Immune landscape of viral- and carcinogen-driven head and neck cancer. *Immunity* (2020) 52:183–99.e9. doi: 10.1016/j.immuni.2019.11.014

frontiers | Frontiers in Oncology

TYPE Original Research
PUBLISHED 23 August 2023
DOI 10.3389/fonc.2023.1046951

OPEN ACCESS

EDITED BY
Sharon R. Pine,
University of Colorado,
United States

REVIEWED BY
Jie Ren,
Third Affiliated Hospital of Sun Yat-sen University, China
Pietro Giorgio Calo',
University of Cagliari, Italy

*CORRESPONDENCE
Shao-Dong Qiu
shaodongqiu@126.com
Fei Chen
flyly@126.com

†These authors have contributed equally to this work and share first authorship

‡These authors have contributed equally to this work

RECEIVED 17 September 2022
ACCEPTED 21 July 2023
PUBLISHED 23 August 2023

CITATION
Lu W-J, Mao L, Li J, OuYang L-Y, Chen J-Y, Chen S-Y, Lin Y-Y, Wu Y-W, Chen S-N, Qiu S-D and Chen F (2023) Three-dimensional ultrasound-based radiomics nomogram for the prediction of extrathyroidal extension features in papillary thyroid cancer.
Front. Oncol. 13:1046951.
doi: 10.3389/fonc.2023.1046951

Three-dimensional ultrasound-based radiomics nomogram for the prediction of extrathyroidal extension features in papillary thyroid cancer

Wen-Jie Lu†, Lin Mao†, Jin Li, Liang-Yan OuYang, Jia-Yao Chen, Shi-Yan Chen, Yun-Yong Lin, Yi-Wen Wu, Shao-Na Chen, Shao-Dong Qiu*‡ and Fei Chen*‡

Department of Ultrasound, The Second Affiliated Hospital of Guangzhou Medical University, Guangzhou, China

Purpose: To develop and validate a three-dimensional ultrasound (3D US) radiomics nomogram for the preoperative prediction of extrathyroidal extension (ETE) in papillary thyroid cancer (PTC).

Methods: This retrospective study included 168 patients with surgically proven PTC (non-ETE, n = 90; ETE, n = 78) who were divided into training (n = 117) and validation (n = 51) cohorts by a random stratified sampling strategy. The regions of interest (ROIs) were obtained manually from 3D US images. A larger number of radiomic features were automatically extracted. Finally, a nomogram was built, incorporating the radiomics scores and selected clinical predictors. Receiver operating characteristic (ROC) curves were performed to validate the capability of the nomogram on both the training and validation sets. The nomogram models were compared with conventional US models. The DeLong test was adopted to compare different ROC curves.

Results: The area under the receiver operating characteristic curve (AUC) of the radiologist was 0.67 [95% confidence interval (CI), 0.580–0.757] in the training cohort and 0.62 (95% CI, 0.467–0.746) in the validation cohort. Sixteen features from 3D US images were used to build the radiomics signature. The radiomics nomogram, which incorporated the radiomics signature, tumor location, and tumor size showed good calibration and discrimination in the training cohort (AUC, 0.810; 95% CI, 0.727–0.876) and the validation cohort (AUC, 0.798; 95% CI, 0.662–0.897). The result suggested that the diagnostic efficiency of the 3D US-based radiomics nomogram was better than that of the radiologist and it had a favorable discriminate performance with a higher AUC (DeLong test: $p < 0.05$).

Conclusions: The 3D US-based radiomics signature nomogram, a noninvasive preoperative prediction method that incorporates tumor

location and tumor size, presented more advantages over radiologist-reported ETE statuses for PTC.

KEYWORDS

three-dimensional ultrasound, radiomics, nomogram, extrathyroidal extension (ETE), papillary thyroid cancer (PTC)

Introduction

Papillary thyroid cancer (PTC) is the most common endocrine malignant tumor, and its incidence rate is increasing all over the world (1). The reason for this increase in incidence is partly because of the popularization of routine physical examination and the improvement of high-frequency ultrasound (US) (2). Most PTC patients have a good prognosis; more than 90% of them have survived for more than 10 years (3). Although PTC has a favorable prognosis, some cases show aggressive clinical features, such as lymph node and distance metastases, and poorer prognosis (4). Extrathyroidal extension (ETE) has long been considered to be an independent predictor of poor prognosis in PTC patients (5). Also, ETE is regarded to be an important risk factor associated with recurrence and metastasis, and it has an important impact on staging and the choice of operation (6). The recurrence and mortality after surgery will increase in an ETE patient. The 15-year survival rate among PTC patients with ETE was significantly worse than that in patients without ETE (7, 8). Traditional surgical setting includes total and subtotal thyroidectomies for PTC, according to the National Comprehensive Cancer Network (NCCN) Guidelines for Thyroid Carcinoma (Third Edition, 2018); total thyroidectomy is the best method to treat ETE patients in PTC (7). Although both surgical procedures have no significant effect on distant metastasis and cancer-specific mortality rates, subtotal thyroidectomies can retain some functionality of the thyroid gland and prevent injuries of the parathyroid and contralateral laryngeal recurrent nerve (9). Therefore, predicting ETE preoperatively is critical for clinicians to choose the surgical approach.

Currently, only pathological biopsy is the gold standard for the diagnosis of ETE (10). Imaging methods such as magnetic resonance imaging (MRI), computerized tomography (CT), single-photon emission computed tomography (SPECT), and US are commonly used for the diagnosis of ETE. MRI has a high resolution of soft tissue and spatial resolution. In a previous study, Wei et al. (11) used multiparametric MRI for preoperative assessment of ETE in 132 cases of PTC, with areas under the receiver operating characteristic curve (AUCs) of 0.96 and 0.87 in the training and testing sets, respectively. However, MRI is relatively expensive and time-consuming; it is also not suitable for patients with implants or who have claustrophobia (12). CT has a certain advantage in evaluating the relationships between the lesions and surrounding tissue, but CT has a potential risk of radiation exposure. From the SPECT examination, the anatomic location of the tumor can be shown clearly. Moreover, a study suggested that SPECT also exhibits promising advantages including higher sensitivity (50%) and specificity (100%) (13). Although several studies have suggested the value of the nuclear medicine method, it could not be widely used clinically in thyroid carcinoma for reasons of universality, radiation, and cost-effectiveness. At present, US examination has become the most frequently used imaging method in PTC patients because of a series of advantages, such as being inexpensive, being noninvasive, and using non-ionizing radiation. Kwak et al. (14) reported that the sensitivity of US examination was 65.2% and the specificity was 81.8% when more than 25% of thyroid nodules contacts with the adjacent capsule. For >50% contact between the tumor and capsule, Lee et al. (15) reported that US findings of capsule disruption had a better AUC (0.674 vs. 0.638) in predicting ETE than CT in 377 PTC patients, while CT combined with US imaging to detect ETE could get the best diagnostic accuracy, with an AUC of 0.744.

With the development of US technology, the emergence of three-dimensional (3D) US provides more possibilities in choosing the imaging method of thyroid disease. Through scanning the target organs by a single sweep of a US beam, it can easily provide the images in multiple slices and planes from the stored data. Therefore, 3D imaging can provide significantly more information about lesions than the traditional two-dimensional (2D) imaging. According to several previous research reports, 3D US examination may help to overcome the limitations of 2D US in various organs (16, 17). Kim et al. (18) reported that compared to 2D thyroid US, 3D had higher sensitivity for predicting ETE (66.7% vs. 46.4%, $p = 0.03$). Consequently, 3D US may have diagnostic potential in predicting ETE status in PTC patients.

Radiomics is an emerging and burgeoning subject in medical research, especially in oncology. Radiomics analysis was first reported by Lambin et al. (19) in 2012. By extracting and analyzing a large number of quantitative features from medical images, radiomics can improve the ability of disease diagnosis and prediction (20, 21). Studies have shown that image feature-based radiomics extraction has objective characteristics and great value in predicting clinical outcomes (19). Radiomics analysis has been applied in various diseases, such as cervical cancer, breast cancer, prostate cancer, lung cancer, rectum cancer, and musculoskeletal tumors (22–27). In the thyroid grand, Wang et al. (28) believe that 2D US radiomics can effectively evaluate whether ETE occurs in papillary thyroid carcinoma, and the AUC is 0.824. But at present, there are no reports applying 3D US radiomics to evaluate ETE in PTC.

Therefore, the purpose of this study is to construct a 3D US radiomics nomogram to predict ETE to help the doctors select the most appropriate strategy of treatment in PTC patients.

Materials and methods

Patient data

This retrospective study was approved by the institutional review board of our institution. Informed consent was obtained from participants before the examination. Between November 2020 and October 2021, a total of 168 individuals who underwent preoperative 2D and 3D thyroid US at our institute were included in this study. All patients underwent subtotal or total thyroidectomy within 1 week after US examination. PTC was confirmed by pathology postoperatively. Exclusion criteria were as follows: 1) the clinical information of the patients was incomplete; 2) the patients had been submitted to thyroidectomy; 3) the entire lesion was not covered by the scan; 4) the images had poor quality; 5) the patients only had routine preoperative 2D or 3D US examination; 6) the maximum diameter of the primary tumor was <5 mm.

US examination and US-reported ETE status

Figure 1 shows the study procedure. Before receiving total and subtotal thyroidectomies, all patients underwent 2D US with 12-5 MHz linear array transducer and 3D US with 13-5 MHz dedicated volume transducer (Philips IU Elite Ultrasound System). The patients were placed in a supine position appropriately with a pillow underneath the neck, with their neck stretched sufficiently to expose the anterior region of the neck. All images were obtained at identical instrument settings for depth, focus position, and gain setting. Clinical data, such as age, sex, and body mass index (BMI), were obtained during the US examination.

After completing the 2D thyroid examination, all subjects underwent 3D examination by two experienced radiologists who were blinded to the data sample identity (8 and 10 years of experience in thyroid US). For 3D US, a volume box size was chosen to cover the tumor lesion. The sectorial and mechanical transducer with a scanning angle of 30° was used for automatic acquisition of tilt-series and 3D images. The two radiologists received a training course consisting of 20 unregistered cases to familiarize themselves with 3D scanning before this study. During the 2D and 3D US examination, they recorded the size of the lesion, nodule position (upper pole, middle pole, or lower pole), primary site (left lobe, right lobe, or isthmus), nodule border (clear or fuzzy), internal echo pattern (nonuniform or uniform), and nodule location (unilateral or bilateral). And they independently reviewed the US imaging features of every patient and recorded a final diagnosis. In case of disagreement, additional reading sessions were used until a consensus was reached. Based on the American Joint Committee on Cancer (AJCC) guidelines (29–32), ETE can be diagnosed when one of the following criteria presents: 1) >25% of the primary tumor perimeter is in contact with the thyroid capsule; 2) the glands between the lesions and thyroid disappear; 3) the primary tumor exceeds the thyroid capsule and extends to the surrounding structures, such as the larynx, recurrent laryngeal nerve, trachea, vasculature, the strap muscles, or esophagus.

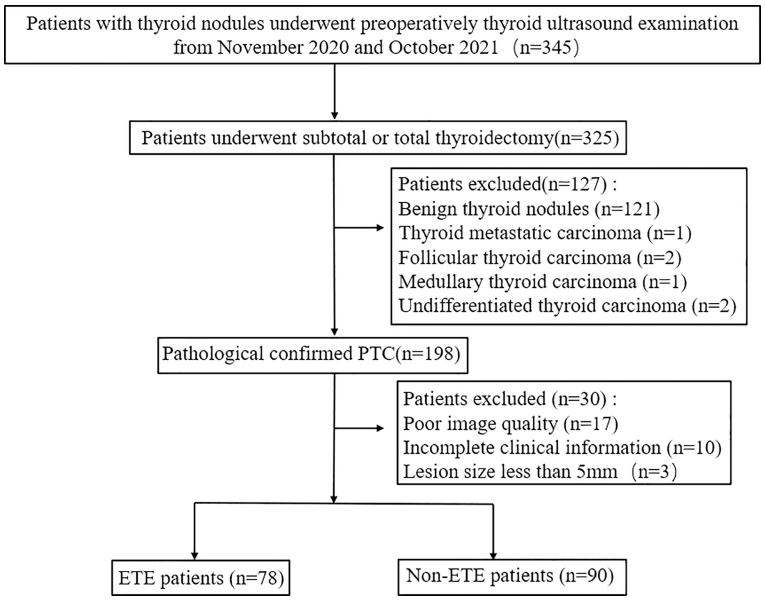

FIGURE 1
Flowchart of patient selection in this study. PTC, papillary thyroid cancer; ETE, extrathyroidal extension.

Tumor segmentation and radiomic feature extraction

The two abovementioned radiologists were informed about the tumor location confirmed by operation and were blinded to other pathologic results and clinical information. The regions of interest (ROIs) of the 3D images were drawn layer by layer manually by the radiologists using the software ITK-SNAP (version 3.8.0, http://www.itksnap.org). Lastly, all final tumor regions could be defined by the overlapping region of two ROIs independently drawn by the two radiologists. In case of disagreement, additional reading sessions were used until a consensus was reached. Figure 2 shows a typical case with 2D and 3D US images and the ROIs. Texture analysis was performed on the acquired US images of 168 patients. All feature extraction methods were performed using PyRadiomics package, which was imported from the Python programming language. Subsequently, a total of 1,693 features were extracted for each patient, including First Order Statistics (19 features), Shape-based (3D) (16 features), Shape-based (2D) (10 features), Gray-Level Co-Occurrence Matrix (24 features), Gray-Level Run Length Matrix (16 features), Gray-Level Size Zone Matrix (16 features), Neighboring Gray Tone Difference Matrix (5 features), and Gray-Level Features Matrix (14 features).

Feature selection and radiomics signature building

All data were divided into training and validation sets at a ratio of 7:3 according to random stratified sampling strategy. First, Levene tests were performed to verify variance homogeneity. For two groups, we used the independent-sample t-test or Mann–Whitney U test to acquire significant features with p-values <0.05. After that, the least absolute shrinkage and selection operator (LASSO) regression method with 10-fold cross-validation was applied to select the most useful predictive ETE status-related features from the training cohort. The LASSO is a machine learning regression analysis technique; it not only can reduce model overfitting and improve the results of prediction but also is regarded as a promising method to select significant features through regularization and variable selection (33). A formula was generated using a linear combination of selected features that were weighted by their respective LASSO coefficients, and the formula was then used to calculate a risk score (defined as the radiomics score or radiomics signature). The radiomics signature was then used to build a nomogram combining with clinical predictors.

Development of the ultrasound radiomics nomogram

The chi-square test (categorical variables) and Student's t-test (continuous variables) were adopted to identify the association between the clinical risk factors and ETE. In this study, clinical predictors including age, sex, BMI, lesion, nodule location, nodule position, nodule border, internal echo pattern, and radiological ETE diagnosis were used to conduct a multivariate logistic regression model. To find the incremental value of the radiomics signature for prediction of ETE in PTCs, the radiomics model was built by combining the radiomics signature with clinical predictors with $p < 0.05$. Next, the model was converted into a radiomics nomogram to help clinicians predict ETE visually in PTC patients. We calculated the AUC for predictive analysis. Then, the DeLong test was performed to compare the differences between the receiver operating characteristic (ROC) curves of the nomogram and the radiologists.

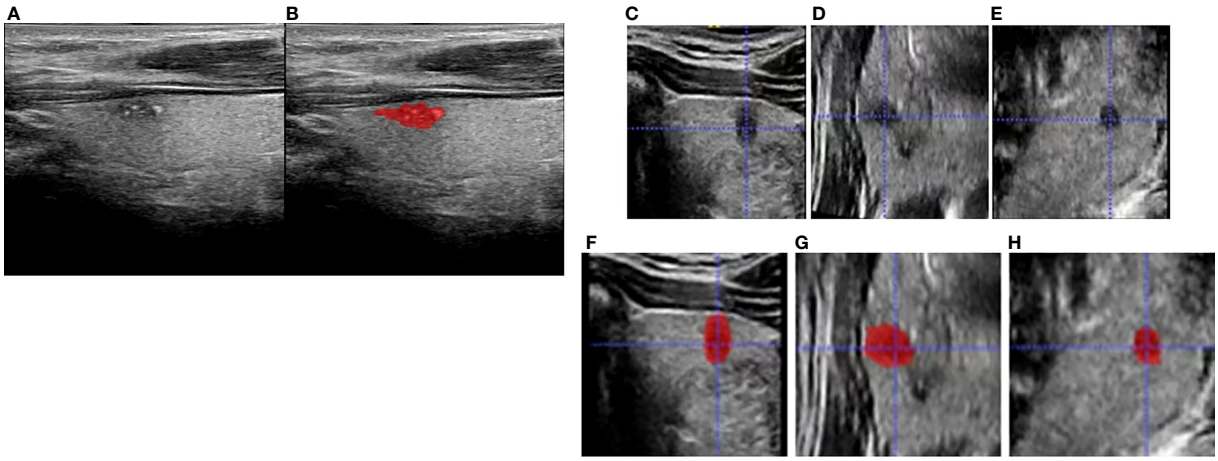

FIGURE 2
Schematic diagram for region of interest (ROI) delineation of ultrasound image: **(A)** was the original two-dimensional image during ultrasound (US) examination; **(B)** was the ROI delineated in the largest section of the tumor based on the original two-dimensional ultrasound image. **(C–E)** are transverse, coronal, and sagittal planes, respectively, and **(F–H)** are corresponding three-dimensional ROIs.

Assessment of nomogram performance

The 3D US-based radiomics nomogram incorporating selected clinical predictors was developed on the training cohort and then tested in the validation cohort. The calibration curve and Hosmer–Lemeshow (H-L) test were used to assess the calibration of the radiomics nomogram. The discriminative performance of the radiomics nomogram was evaluated by using Harrell's concordance index (C-index).

Histopathologic analysis

Two experienced pathologists with 9 and 12 years of experience, respectively, evaluated the histopathology of the tumor specimens. PTC specimens of paraffin embedding slice were followed by hematoxylin and eosin (H&E) dyeing. According to the guidelines published by the American Thyroid Association (ATA), the pathologists evaluated the ETE features (34). Then, the patients were divided into two groups: ETE and non-ETE groups.

Statistical analysis

All statistical tests in this study were conducted using R software (version 4.0.3, https://www.r-project.org). Statistical analysis of clinical data, multivariate logistic regression, and H-L test were performed using SPSS software (version 22.0, SPSS Inc.). The corresponding 95% confidence interval (CI) was used to describe the correlation results. If the measurement data satisfy normal distribution, we use mean ± standard deviation (SD) to express. Other values were reported as median and interquartile range (IQR). Independent-sample t-test was adopted for normally distributed measurement data; otherwise, Mann–Whitney U test was used for non-normally distributed measurement data. The count dates were expressed as frequency (percentage) and compared by chi-square test or Fisher exact test. The factors of ETE in PTC patients were analyzed by multivariate logistic regression (stepwise forward) method. Next, the goodness of fit for logistic regression models was assessed by the H-L test.

ROC was employed to quantify the discriminative capability of the nomogram by comparing nomogram-predicted versus the observed ETE probability. A two-sided $p < 0.05$ was considered statistically significant.

Results

Clinical characteristics

A total of 168 PTC patients aged 41.96 ± 0.881 years (range, 20–72 years) were enrolled in this research. In this study, 90 patients (41.71 ± 12.73 years old) and 78 patients (42.24 ± 11.22 years old) were assigned to the non-ETE and ETE groups, respectively, based on pathologic results. There was no significant difference in the tumor size, nodule location, nodule position, nodule border, and internal echo pattern between the ETE group and non-ETE group (all $p > 0.05$). According to the degree of the diagnostic criteria of ETE, there were 10 patients with thyroid capsule contact approximately >25% of the primary tumor perimeter, 47 patients with the glands between the lesions and thyroid disappear, 21 patients with the primary tumor that exceeds the thyroid capsule and extends to surrounding structures. The 168 patients were divided into a training group (n = 117) and a validation group (n = 51) by stratified sampling. Table 1 shows the clinical data of the 168 patients.

Radiomics score

A total of 1,693 features were extracted from the original 3D US images in the training cohort. In this study, LASSO regression with L1 regularization was further used to select the optimal radiomic features. The complexity depends on the lambda (λ). According to 10-fold cross-validation, the results indicated that when extracting 3D image features, the models had the lowest mean squared error (MSE) when λ was 0.037. After LASSO regression analysis, 691 radiomic features were reduced to 16 potential predictors. As Figure 3 shows, the 16 features were included in the radiomics score formula. Table 2 shows the 16 best radiomic features in 3D US image.

Development and performance of the prediction model

In this study, the AUC of the radiologists is 0.67 (95% CI, 0.580–0.757) in the training cohort and 0.62 (95% CI, 0.467–0.746) in the validation cohort. Then, according to the forward Logistic regression (LR) method, bilateral tumor ($p = 0.004$)and tumor size ($p = 0.005$) were identified as independent predictive factors to predictive ETE. Then, we could get a radiomics nomogram with the predictive factors (Figure 4). The prediction model was constructed as follows:

Linear predictor = -27.722 - 1.153 × X1 -1.148 × X2 + 57.033 × X3. X1 being tumor location, X2 being tumor size, X3 being radiomics signature.

In the training cohort, the radiomics nomogram showed good discrimination with an AUC 0.810 (95% CI, 0.727–0.876), which was significantly higher than that of the radiologists (DeLong test, $p = 0.0136$). In the validation set, it also shows better discrimination with an AUC of 0.798 (95% CI, 0.662–0.897; DeLong test, $p = 0.0296$). The ROC curves of the two models for both the training and validation sets are presented in Figure 5. The calibration curve and the H-L test showed good calibration in the training cohort (Figure 6A, $p = 0.828$) and the validation cohort (Figure 6B, $p = 0.071$). The C-index of the radiomics nomogram is 0.831. From the result, we could know that the above-described radiomics nomogram performed well in differentiating ETE from non-ETE and may help in the clinical decision-making process.

10.3389/fonc.2023.1046951

TABLE 1 Basic clinical data for our group.

	Training Set(n=117)			Validation Set(n=51)		
Variable	ETE(n=54)	Non-ETE (n=63)	p Value	ETE(n=24)	Non-ETE (n=27)	p Value
Age mean ± SD,years	42.50 ± 11.18	40.89 ± 11.61	0.634	42.33 ± 11.22	42.67 ± 11.34	0.914
Sex						
Women	28(51.85%)	42(66.67%)	0.103	17(70.83%)	21(77.78%)	0.570
Men	26(48.15%)	21(33.33%)		7(29.17%)	6(22.22%)	
BMI mean ± SD,kg/m^2	23.45 ± 3.92	22.79 ± 3.73	0.360	22.97 ± 3.24	22.67 ± 3.82	0.765
Radiomics score mean	0.48 ± 0.02	0.51 ± 0.02	<0.001	0.50 ± 0.01	0.50 ± 0.01	<0.001
Tumor size(cm)						
≥1	31(57.41%)	16(25.40%)	<0.001	20(83.33%)	10(37.04%)	0.001
<1	23(42.59%)	47(74.60%)		4(16.67%)	17(62.96%)	
Tumor border						
Clear	21(38.89%)	24(38.10%)	0.930	11(45.83%)	12(44.44%)	0.921
Fuzzy	33(61.11%)	39(61.90%)		13(54.17%)	15(55.56%)	
Tumor location						
Unilateral	14(25.93%)	31(49.21%)	0.010	5(20.83%)	14(51.85%)	0.020
Bilateral	40(74.07%)	32(50.79%)		19(79.17%)	13(48.15%)	
Internal echo pattern						
Uniform	21(38.89%)	30(47.62%)	0.342	12(50.00%)	12(44.44%)	0.692
Nonuniform	33(61.11%)	33(52.38%)		12(50.00%)	15(55.56%)	
Radiological ETE diagnosis						
ETE	25(46.30%)	16(25.40%)	0.018	5(20.83%)	13(25.49%)	0.042
Non- ETE	29(53.70%)	47(74.60)		19(79.17%)	14(27.45%)	
Tumor position						
Upper pole	12(22.22%)	9(14.29%)	0.148	5(20.83%)	2(7.41%)	0.104
Middle pole	22(40.74%)	37(58.73%)		10(41.67%)	19(70.37%)	
Inferior pole	20(37.04%)	17(26.98%)		9(37.50%)	6(22.22%)	
Primary site						
Left lobe	27(50.00%)	24(38.10%)	0.198	9(37.50%)	12(44.44%)	0.524
Right lobe	26(48.15%)	34(53.97%)		14(58.33%)	15(55.56%)	
Isthmus	1(1.85%)	5(7.93%)		1(41.67)	0	

ETE, extrathyroidal extension; non-ETE, without extrathyroidal extension; SD, standard deviation.

Discussion

Due to the prevalence of coronavirus disease 2019 (COVID-19), delayed investigations and treatment may further lead to an increase in the incidence and mortality of thyroid carcinoma (35). As the most common pathological type of differentiated thyroid carcinoma (DTC), PTC has a low degree of malignancy and a high cure rate if detected and treated in a timely manner. The presence of ETE is considered to be significantly important in PTC patients, and it is included in almost all prognostic scoring systems as a staging variable. Literature reported that the incidence of ETE in PTC ranges between 5% and 45%, and in our patient population, the incidence of ETE was 46% (78/168); the values did not differ much (36). Moreover, PTC patients with ETE have poor prognosis and a high risk of recurrence in the near future (37). And a study found that patients with a history of ETE display a poorer therapeutic

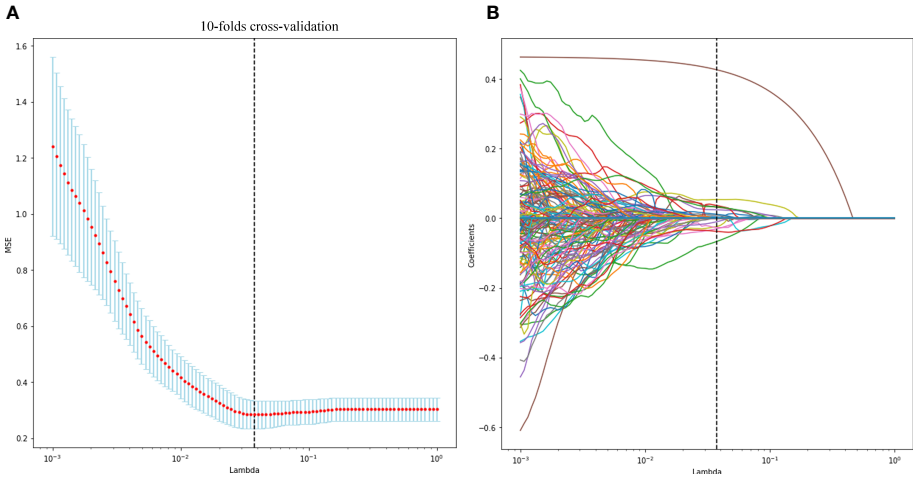

FIGURE 3
Radiomic feature selection using the least absolute shrinkage and selection operator (LASSO) regression model. The LASSO regression with 10-fold cross-validation **(A)** was used to reduce the dimension of the grouping characteristics **(B)**. Finally, 16 radiomic features with non-zero coefficients were selected.

effect following 131I ablation (38). The thyroid capsule is closely adjacent to the surrounding tissues such as recurrent laryngeal nerve, the patients who are not diagnosed correctly before surgery often need reoperation, which increases the pain and economic burden of PTC patients. Taken together, it is very important to identify the presence of ETE before thyroid surgery.

At present, only pathological diagnosis is the gold standard of ETE diagnosis. Reliable and accurate preoperative imaging examination of ETE will help in accurate diagnosis and selection of the optimum therapeutic strategy. Although fine-needle aspiration biopsy (FNAB) is the most widely used method for the assessment of thyroid nodules preoperatively, it is an invasive procedure, and its samples cannot always reach satisfying diagnostic power. Alternatively, the diagnostic capacity for ETE in PTC patients is limited (39). Noninvasive imaging examinations such as ultrasonic imaging, MRI, CT, and positron emission tomography not only play an increasingly important role in the diagnosis of ETE but also can be useful to guide treatment and patient follow-up. Among them, US is the sole fundamental imaging modality for the assessment of thyroid nodules. US examination is noninvasive, fast, and reliable and can help to enhance the early detection of pathologies (40–42). However, these traditional imaging examinations depend on the experience and subjective judgments of the radiologists, which limit the ability to make an objective decision.

TABLE 2 The 16 best radiomic features in 3D US image.

Feature variable	Coefficient
original_gldm_DependenceNonUniformityNormalized	-0.067
gradient_glrlm_ShortRunEmphasis	0.031
l lbp-2D_firstorder_InterquartileRange	-0.031
squareroot_glrlm_ShortRunLowGrayLevelEmphasis	-0.024
wavelet-LHL_firstorder_Kurtosis	0.001
wavelet-LHH_firstorder_Entropy	0.008
wavelet-LHH_firstorder_Maximum	0.054
wavelet-LHH_gldm_DependenceEntropy	-0.027
wavelet-HLL_glszm_SmallAreaHighGrayLevelEmphasis	0.024
wavelet-HLH_glcm_JointEnergy	-0.010
wavelet-HLH_glrlm_LongRunHighGrayLevelEmphasis	0.037
wavelet-HHH_glcm_MaximumProbability	0.037
wavelet-HHH_gldm_HighGrayLevelEmphasis	-0.038
wavelet-HHH_glrlm_HighGrayLevelRunEmphasis	0.003
wavelet-HHH_glrlm_LowGrayLevelRunEmphasis	-5.049
wavelet-LLL_glcm_ClusterShade	0.033

Therefore, a noninvasive sample and quantitative methods are needed to help clinically predict ETE. Radiomics is a hot topic; it allows the quantitative extraction of high-throughput features from radiographic images, with the advantage of objectivity. Numerous studies have confirmed the usefulness of 3D US in clinical settings. Based on the transverse and longitudinal views of 2D US, 3D US technology improves the visualization of target lesions by adding a new dimension, coronal view. In a study involving 85 PTC patients, Kim et al. (18) believed that 3D US not only had higher sensitivity (66.7% vs. 46.4%, $p = 0.03$) but also showed better agreement (k 0.53 vs. 0.37) than 2D for predicting ETE, and 3D thyroid US saved time for scanning compared with 2D. But at present, there are no reports applying 3D US radiomics to compare the diagnostic performance to evaluate ETE in PTC, which is the main novelty of this research paper.

Kim et al. (43) found that the tumor size ≥1 cm was considered to be a dependent prognostic factor to predict ETE in PTC. In our study, after forward LR method, we found that the PTC patients with tumor size ≥1 cm had been associated with ETEs, which was in line with the above findings. We also found that the location of the

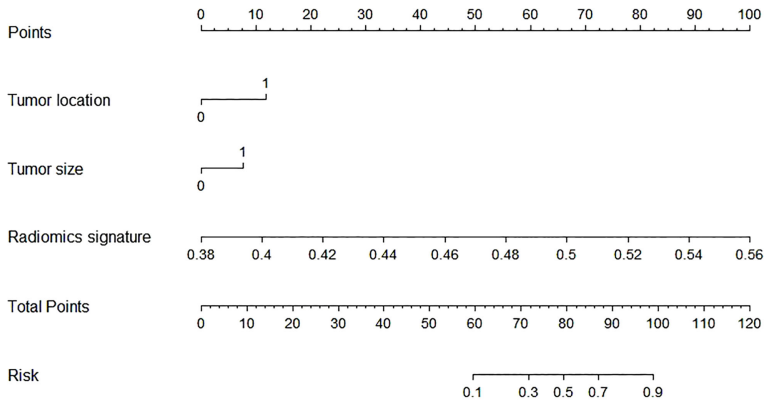

FIGURE 4
The radiomics nomogram was developed by incorporating the radiomics scores and selected clinical predictors. The radiomics nomogram incorporated tumor location (unilateral or bilateral), tumor size, and the radiomics signature.

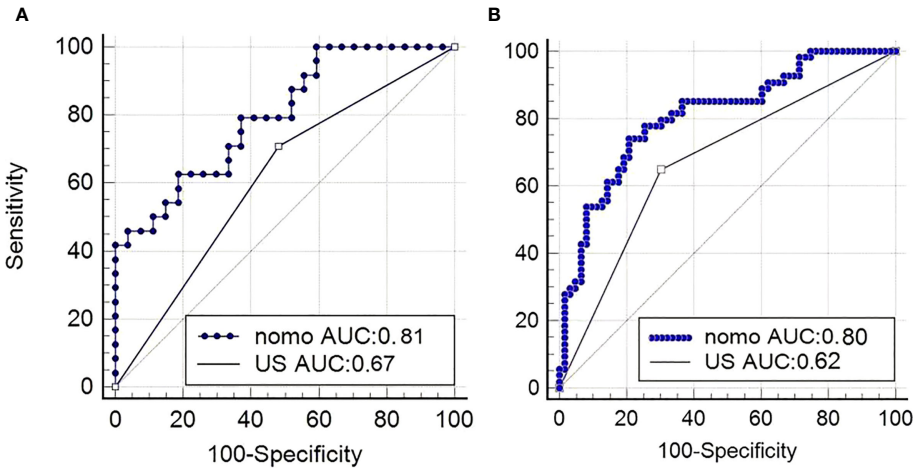

FIGURE 5
Performance of the nomogram. **(A)** ROC curves of US-reported ETE status and radiomics nomogram for predicting ETE in the validation cohort and in the primary cohort **(B)**. nomo, nomogram; US, ultrasound; ROC, receiver operating characteristic; ETE, extrathyroidal extension.

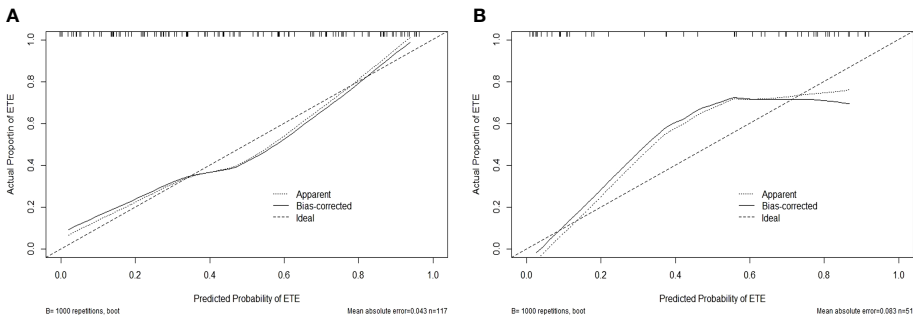

FIGURE 6
Calibration curves for the radiomics nomogram in the training **(A)** and validation **(B)** sets. The calibration curve and the Hosmer–Lemeshow test showed good calibration in the training cohort (p = 0.828) and in the validation cohort (p = 0.071).

nodules (unilateral or bilateral) was another clinical predictor. Then, we built a radiomics nomogram based on the clinical risk factors, tumor size and tumor location, to predict ETE. As the result showed, the AUC of the radiomics nomogram in diagnosing ETE was higher than that of the radiologists in both the training cohort and the validation cohort. In addition, the C-index and calibration curve also showed good consistency in the primary group and validation group. Hence, the 3D US-based radiomics signature nomogram, a noninvasive preoperative prediction method that incorporates tumor location and tumor size, presented more advantages over radiologist-reported ETE statuses for PTC, which could be a visualization tool for the clinic to choose a suitable surgical modality.

Inevitably, our present study has several limitations. First, this study was a retrospective and single-center study, lacking external validation. Therefore, these results are not necessarily suitable to all patients with PTC preoperatory; multicenter studies are warranted to further validate the results. Moreover, to improve the diagnostic capability, the algorithm and models will be further optimized to improve the accuracy of external validation. Second, in this study, the radiomic features might not be sufficient because we only used grayscale US images to perform the radiomics nomogram. In future research, we will add radiomic characteristics of multimodal US such as elastography and contrast-enhanced US images to the nomogram. Finally, the ROI segmentation was obtained manually, which might be affected by the radiologist's subjective bias. And it may be resolved by semiautomatic/automatic segmentation.

Our 3D US-based radiomics nomogram combining clinical predictors, tumor location and tumor size, shows favorable predictive accuracy for preoperative ETE in patients with PTC. This nomogram is a promising tool to improve the diagnostic accuracy.

Data availability statement

The original contributions presented in the study are included in the article/supplementary material. Further inquiries can be directed to the corresponding authors.

Ethics statement

The studies involving human participants were reviewed and approved by The Second Affiliated Hospital of Guangzhou Medical University. The patients/participants provided their written informed consent to participate in this study. Written informed consent was obtained from the individual(s) for the publication of any potentially identifiable images or data included in this article.

Author contributions

W-JL: investigation, data curation, formal analysis, conceptualization, writing–original draft, and writing–review and editing. LM: investigation, data curation, formal analysis, conceptualization, writing–original draft, and writing–review and editing. JL: data curation, writing–original draft, and writing–review and editing. Y-WW: data curation, writing–original draft, and writing–review and editing. S-NC: writing–original draft and writing–review and editing. Y-YL: writing–original draft and writing–review and editing. L-YO: writing–original draft and writing–review and editing. J-YC: writing–original draft and writing–review and editing. S-YC: writing–original draft and writing–review and editing. S-DQ: supervision, formal analysis, conceptualization, writing–original draft, and writing–review and editing. FC: supervision, formal analysis, conceptualization, writing–original draft, and writing–review and editing. All authors contributed to the article and approved the submitted version.

Funding

This study was supported by the Science and Technology Program of Guangzhou city (grant numbers: 202102010049).

Conflict of interest

The authors declare that the research was conducted in the absence of any commercial or financial relationships that could be construed as a potential conflict of interest.

Publisher's note

References

1. Lim H, Devesa SS, Sosa JA, Check D, Kitahara CM. Trends in thyroid cancer incidence and mortality in the United States, 1974-2013. *JAMA* (2017) 317:1338–48. doi: 10.1001/jama.2017.2719

2. Yu J, Deng Y, Liu T, Zhou J, Jia X, Xiao T, et al. Lymph node metastasis prediction of papillary thyroid carcinoma based on transfer learning radiomics. *Nat Commun* (2020) 11:4807. doi: 10.1038/s41467-020-18497-3

3. Pamedytyte D, Simanaviciene V, Dauksiene D, Leipute E, Zvirbliene A, Sarauskas V, et al. Association of MicroRNA expression and BRAF(V600E) mutation with recurrence of thyroid cancer. *Biomolecules* (2020) 12(7):10. doi: 10.3390/biom10040625

4. Chen F, Jin Y, Feng L, Zhang J, Tai J, Shi J, et al. RRS1 gene expression involved in the progression of papillary thyroid carcinoma. *Cancer Cell Int* (2018) 18:20. doi: 10.1186/s12935-018-0519-x

5. Yao Y, Chen X, Yang H, Chen W, Qian Y, Yan Z, et al. I_circ_0058124 promotes papillary thyroid cancer tumorigenesis and invasiveness through the NOTCH3/GATAD2A axis. *J Exp Clin Cancer Res* (2019) 38:318. doi: 10.1186/s13046-019-1321-x

6. Kamaya A, Tahvildari AM, Patel BN, Willmann JK, Jeffrey RB, Desser TS. Sonographic detection of extracapsular extension in papillary thyroid cancer. *J Ultrasound Med* (2015) 34:2225–30. doi: 10.7863/ultra.15.02006

7. Shaha AR. Implications of prognostic factors and risk groups in the management of differentiated thyroid cancer. *Laryngoscope* (2004) 114:393–402. doi: 10.1097/00005537-200403000-00001

8. Sundram F, Robinson BG, Kung A, Lim-Abrahan MA, Bay NQ, Chuan LK, et al. Well-differentiated epithelial thyroid cancer management in the Asia Pacific region: A report and clinical practice guideline. *Thyroid* (2006) 16:461–9. doi: 10.1089/thy.2006.16.461

9. Hay ID, Grant CS, Bergstralh EJ, Thompson GB, van Heerden JA, Goellner JR. Unilateral total lobectomy: Is it sufficient surgical treatment for patients with AMES low-risk papillary thyroid carcinoma? *Surgery* (1998) 124:958–64. doi: 10.1016/S0039-6060(98)70035-2

10. Miller B, Burkey S, Lindberg G, Snyder WR, Nwariaku FE. Prevalence of Malignancy within cytologically indeterminate thyroid nodules. *Am J Surg* (2004) 188:459–62. doi: 10.1016/j.amjsurg.2004.07.006

11. Wei R, Wang H, Wang L, Hu W, Sun X, Dai Z, et al. Radiomics based on multiparametric MRI for extrathyroidal extension feature prediction in papillary thyroid cancer. *BMC Med Imaging* (2021) 21:20. doi: 10.1186/s12880-021-00553-z

12. Tang CY, Wang VX, Lun MY, Mincer JS, Ng JC, Brallier JW, et al. Transient changes in white matter microstructure during general anesthesia. *PloS One* (2021) 16:e247678. doi: 10.1371/journal.pone.0247678

13. Barwick T, Murray I, Megadmi H, Drake WM, Plowman PN, Akker SA, et al. Single photon emission computed tomography (SPECT)/computed tomography using Iodine-123 in patients with differentiated thyroid cancer: Additional value over whole body planar imaging and SPECT. *Eur J Endocrinol* (2010) 162:1131–9. doi: 10.1530/EJE-09-1023

14. Kwak JY, Kim EK, Youk JH, Kim MJ, Son EJ, Choi SH, et al. Extrathyroid extension of well-differentiated papillary thyroid microcarcinoma on US. *Thyroid* (2008) 18:609–14. doi: 10.1089/thy.2007.0345

15. Lee DY, Kwon TK, Sung MW, Kim KH, Hah JH. Prediction of extrathyroidal extension using ultrasonography and computed tomography. *Int J Endocrinol* (2014) 2014:351058. doi: 10.1155/2014/351058

16. Cho N, Moon WK, Cha JH, Kim SM, Han BK, Kim EK, et al. Differentiating benign from Malignant solid breast masses: Comparison of two-dimensional and three-dimensional US. *Radiology* (2006) 240:26–32. doi: 10.1148/radiol.2401050743

17. Li QY, Tang J, He EH, Li YM, Zhou Y, Zhang X, et al. Clinical utility of three-dimensional contrast-enhanced ultrasound in the differentiation between noninvasive and invasive neoplasms of urinary bladder. *Eur J Radiol* (2012) 81:2936–42. doi: 10.1016/j.ejrad.2011.12.024

18. Kim SC, Kim JH, Choi SH, Yun TJ, Wi JY, Kim SA, et al. Off-site evaluation of three-dimensional ultrasound for the diagnosis of thyroid nodules: Comparison with two-dimensional ultrasound. *Eur Radiol* (2016) 26:3353–60. doi: 10.1007/s00330-015-4193-2

19. Lambin P, Rios-Velazquez E, Leijenaar R, Carvalho S, van Stiphout RG, Granton P, et al. Radiomics: Extracting more information from medical images using advanced feature analysis. *Eur J Cancer* (2012) 48:441–6. doi: 10.1016/j.ejca.2011.11.036

20. Gillies RJ, Kinahan PE, Hricak H. Radiomics: Images are more than pictures, they are data. *Radiology* (2016) 278:563–77. doi: 10.1148/radiol.2015151169

21. Yip SS, Aerts HJ. Applications and limitations of radiomics. *Phys Med Biol* (2016) 61:R150–66. doi: 10.1088/0031-9155/61/13/R150

22. Park SH, Lim H, Bae BK, Hahm MH, Chong GO, Jeong SY, et al. Robustness of magnetic resonance radiomic features to pixel size resampling and interpolation in patients with cervical cancer. *Cancer Imaging* (2021) 21:19. doi: 10.1186/s40644-021-00388-5

23. Conti A, Duggento A, Indovina I, Guerrisi M, Toschi N. Radiomics in breast cancer classification and prediction. *Semin Cancer Biol* (2021) 72:238–50. doi: 10.1016/j.semcancer.2020.04.002

24. Avanzo M, Stancanello J, Pirrone G, Sartor G. Radiomics and deep learning in lung cancer. *Strahlenther Onkol* (2020) 196:879–87. doi: 10.1007/s00066-020-01625-9

25. Huang YQ, Liang CH, He L, Tian J, Liang CS, Chen X, et al. Development and validation of a radiomics nomogram for preoperative prediction of lymph node metastasis in colorectal cancer. *J Clin Oncol* (2016) 34:2157–64. doi: 10.1200/JCO.2015.65.9128

26. Chianca V, Albano D, Messina C, Vincenzo G, Rizzo S, Del GF, et al. An update in musculoskeletal tumors: From quantitative imaging to radiomics. *Radiol Med* (2021) 126(8)1095-105. doi: 10.1007/s11547-021-01368-2

27. Woźnicki P, Westhoff N, Huber T, Riffel P, Froelich MF, Gresser E, et al. Multiparametric MRI for prostate cancer characterization: Combined use of radiomics model with PI-RADS and clinical parameters. *Cancers (Basel)* (2020) 18(1):145. doi: 10.3390/cancers12071767

28. Wang X, Agyekum EA, Ren Y, Zhang J, Zhang Q, Sun H, et al. A radiomic nomogram for the Ultrasound-Based evaluation of extrathyroidal extension in papillary thyroid carcinoma. *Front Oncol* (2021) 11:625646. doi: 10.3389/fonc.2021.625646

29. Hay ID, Johnson TR, Thompson GB, Sebo TJ, Reinalda MS. Minimal extrathyroid extension in papillary thyroid carcinoma does not result in increased rates of either cause-specific mortality or postoperative tumor recurrence. *Surgery* (2016) 159:11–9. doi: 10.1016/j.surg.2015.05.046

30. Chen W, Zheng R, Baade PD, Zhang S, Zeng H, Bray F, et al. Cancer statistics in China, 2015. *CA Cancer J Clin* (2016) 66:115–32. doi: 10.3322/caac.21338

31. Cooper DS, Doherty GM, Haugen BR, Kloos RT, Lee SL, Mandel SJ, et al. Revised American Thyroid Association management guidelines for patients with thyroid nodules and differentiated thyroid cancer. *Thyroid* (2009) 19:1167–214. doi: 10.1089/thy.2009.0110

32. Lee CY, Kim SJ, Ko KR, Chung KW, Lee JH. Predictive factors for extrathyroidal extension of papillary thyroid carcinoma based on preoperative sonography. *J Ultrasound Med* (2014) 33:231–8. doi: 10.7863/ultra.33.2.231

33. Bien J, Taylor J, TibshIrani R. A lasso for hierarchical interactions. *Ann Stat* (2013) 41:1111–41. doi: 10.1214/13-AOS1096

34. Haugen BR. 2015 American Thyroid Association Management Guidelines for Adult Patients with Thyroid Nodules and Differentiated Thyroid Cancer: What is new and what has changed? *Cancer-Am Cancer Soc* (2017) 123:372–81. doi: 10.1002/cncr.30360

35. Liang W, Guan W, Chen R, Wang W, Li J, Xu K, et al. Cancer patients in SARS-CoV-2 infection: A nationwide analysis in China. *Lancet Oncol* (2020) 21:335–7. doi: 10.1016/S1470-2045(20)30096-6

36. Hu S, Zhang H, Wang X, Sun Z, Ge Y, Li J, et al. Can Diffusion-Weighted MR imaging be used as a tool to predict extrathyroidal extension in papillary thyroid carcinoma? *Acad Radiol* (2021) 28:467–74. doi: 10.1016/j.acra.2020.03.005

37. Chreau N, Buffet C, Trsallet C, Tissier F, Golmard JL, Leenhardt L, et al. Does extracapsular extension impact the prognosis of papillary thyroid microcarcinoma? *Ann Surg Oncol* (2014) 21:1659–64. doi: 10.1245/s10434-013-3447-y

38. Li C, Zhang J, Wang H. Predictive value of LN metastasis detected by (18)F-FDG PET/CT in patients with papillary thyroid cancer receiving iodine-131 radiotherapy. *Oncol Lett* (2019) 18:1641–8. doi: 10.3892/ol.2019.10500

39. Lu Y, Moreira AL, Hatzoglou V, Stambuk HE, Gonen M, Mazaheri Y, et al. Using diffusion-weighted MRI to predict aggressive histological features in papillary thyroid carcinoma: A novel tool for pre-operative risk stratification in thyroid cancer. *Thyroid* (2015) 25:672–80. doi: 10.1089/thy.2014.0419

40. Intenzo CM, Dam HQ, Manzone TA, Kim SM. Imaging of the thyroid in benign and Malignant disease. *Semin Nucl Med* (2012) 42:49–61. doi: 10.1053/j.semnuclmed.2011.07.004

41. Wang J, He X, Ma L, Li M, Sun L, Jiang J, et al. Multimode ultrasonic technique is recommended for the differential diagnosis of thyroid cancer. *Peerj* (2020) 8:e9112. doi: 10.7717/peerj.9112

42. Merz E. Three-dimensional transvaginal ultrasound in gynecological diagnosis. *Ultrasound Obstet Gynecol* (1999) 14:81–6. doi: 10.1046/j.1469-0705.1999.14020081.x

43. Kim SS, Lee BJ, Lee JC, Kim SJ, Lee SH, Jeon YK, et al. Preoperative ultrasonographic tumor characteristics as a predictive factor of tumor stage in papillary thyroid carcinoma. *Head Neck* (2011) 33:1719–26. doi: 10.1002/hed.21658

frontiers | Frontiers in Oncology

TYPE Original Research
PUBLISHED 10 October 2023
DOI 10.3389/fonc.2023.1046014

OPEN ACCESS

EDITED BY
Sharon R. Pine,
University of Colorado Anschutz Medical Campus, United States

REVIEWED BY
Yasemin Giles Senyürek,
Istanbul University, Türkiye
Flavio Hojaij,
University of São Paulo, Brazil

*CORRESPONDENCE
Lei Xie
xielsrrsh@zju.edu.cn

RECEIVED 16 September 2022
ACCEPTED 25 September 2023
PUBLISHED 10 October 2023

CITATION
Shi L, Le K, Qi H, Feng Y, Zhou L, Wang J and Xie L (2023) The safety and efficacy of delayed surgery by simulating clinical progression of observable papillary thyroid microcarcinoma: a retrospective analysis of 524 patients from a single medical center. *Front. Oncol.* 13:1046014.
doi: 10.3389/fonc.2023.1046014

The safety and efficacy of delayed surgery by simulating clinical progression of observable papillary thyroid microcarcinoma: a retrospective analysis of 524 patients from a single medical center

Liuhong Shi[1], Kehao Le[1], Haiou Qi[2], Yibing Feng[3], Liang Zhou[1], Jianbiao Wang[1] and Lei Xie[1*]

[1]Department of Head and Neck Surgery, Affiliated to Sir Run Run Shaw Hospital, Zhejiang University School of Medicine, Hangzhou, Zhejiang, China, [2]Department of Nursing, Affiliated to Sir Run Run Shaw Hospital, Zhejiang University School of Medicine, Hangzhou, Zhejiang, China, [3]Department of Second Surgery, Longyou County People's Hospital, Sir Run Run Shaw Hospital, Quzhou, Zhejiang, China

Objective: When active surveillance (AS) is developed in the patients with low-risk papillary thyroid microcarcinoma (PTMC), a medical center needs to ensure the delayed operation that is caused by PTMC clinical progression to have the same prognosis as that of immediate operation. The objective of this study was to investigate the efficacy of delayed surgery by simulating clinical progression (tumor size enlargement and appearance of lymph node metastasis) of PTMCs with AS in a single medical center.

Methods: We retrospectively analyzed the response to therapy in 317 papillary thyroid carcinoma patients treated with total thyroidectomy and post-operative radioactive iodine ablation. They were classified into three groups according to tumor size (group A ≤0.5 cm; group B >0.5 cm and ≤1 cm; group C >1 cm and ≤1.5 cm) or two groups according to the presence (cN1) or absence (cN0) of the clinical lymph node (LN) metastasis. Groups C and cN1 were regarded as simulated clinical progression of observational PTMC and the operation for them was assumed to be "delayed surgery". However, Groups A, B and cN0 were regarded as no clinical progression and the operation for them was considered as immediate surgery.

Results: There were no significantly differences in excellent response to therapy and recurrence-free survival not only among the group A, B and C, but also between the group cN0 and cN1. In other words, these insignificant differences were found between immediate and simulated "delayed" surgeries.

Conclusion: For the PTMC patients suitable for AS, the oncological outcomes were also excellent even if surgery was delayed until after the presence of clinical progression, according to our clinical simulation. Furthermore, we consider that it was feasible for medical centers to assess the ability to implement AS for PTMC

patients by retrospectively analyzing their own previous clinical data using the described simulation.

KEYWORDS

papillary thyroid carcinoma, microcarcinoma, active surveillance, lymph node, response to therapy

Introduction

Papillary thyroid carcinoma (PTC) is the most common endocrine malignancy, and it usually has an indolent biological nature. When the cancer measures ≤10 mm in its largest diameter, it is called a papillary thyroid microcarcinoma (PTMC). A rapid increase in the incidence of PTC has been reported in the past several decades in many countries, and approximately 50% of PTCs are PTMCs (1). However, a majority of PTMCs are occult and detected because of overscreening in the healthy population. On this basis, in 1993, Professor Miyauchi of Kuma Hospital in Japan proposed that low-risk PTMC patients could be followed with active surveillance (AS) rather than immediately undergo surgery; their later study showed that the incidence rates of size enlargement, novel appearance of node metastasis, and progression to clinical disease in 1,235 PTMC patients were 8.0%, 3.8%, and 6.8% over a 10-year observation period, respectively (2). Therefore, presently AS is the first-line management of low-risk PTMC patients at Kuma Hospital (3).

Although AS is an option for PTMC patients, as stated in the 2015 guidelines of the American Thyroid Association (ATA) (4), questions remain as to how to identify low-risk patients, how to deal with 30%~40% subclinical metastasis in central neck lymph nodes (LNs), and how to relieve the anxiety of patients and their families during the observation period. The major concerns are, for PTMC patients under AS, whether the prognosis of immediate operation is the same as that of delayed surgery due to clinical progression, whether the medical center has an ability to reach, and how to assess this ability. However, few studies in this area have been published.

The recurrence risk estimate is one of the most important ways of evaluating prognosis in PTC patients; therefore, a response to therapy system was proposed in the 2015 ATA guidelines (4). According to the clinical data obtained from imaging examinations and biochemical and cytopathological findings, the postoperative clinical responses of PTC patients to therapy are described as follows: an excellent response, a biochemical incomplete response, a structural incomplete response, and an indeterminate response. In this study, we retrospectively analyzed the response to therapy in PTMC patients initially eligible for AS, with different size tumors and with or without LN metastasis, to investigate the efficacy of delayed surgery by simulating clinical progression (tumor size enlargement and appearance of LN metastasis) in a single medical center.

Materials and methods

Patients

Between January 2013 and December 2015, 562 PTC patients underwent unilateral lobectomy or total thyroidectomy (TT) and central neck dissection (CND), with or without lateral neck dissection (LND), as an initial surgical treatment at our hospital (Figure 1). Among them, 524 patients with a primary tumor size ≤1.5 cm and who had undergone thyroidectomy were enrolled in this study. Exclusion criteria were as follows: no PTC diagnosis, aggressive histology (e.g. tall cell, hobnail variant, columnar cell carcinoma), distant metastasis, extrathyroidal extension to nearby organs (e.g. trachea or esophagus), a poorly differentiated PTC (diagnostic criteria were on the basis of the Turin consensus proposal) (5), a coexisting malignancy, a thyroid lobectomy, a tumor size >1.5 cm, and no radioactive iodine (RAI) ablation. Finally, 317 patients met the selection criteria and included 286 cN0 and 31 cN1 patients. The current definition of "clinically apparent" LN metastasis (cN1 disease) includes any metastatic LN identified by palpation or imaging either before initial surgery or intraoperatively (6). When a suspicious LN appeared at level VI or II-IV, it was defined as cN1a or cN1b, respectively. Accordingly, patients without cN1 disease were defined as cN0. Therefore, 286 cN0 and seven cN1a patients underwent TT+CND, and 24 cN1b patients underwent TT+CND +LND. These 286 cN0 patients were enrolled to analyze the clinicopathologic characteristics associated with the size of their primary tumors and to compare them with 31 cN1 patients to analyze the clinicopathologic differences caused by clinically involved neck LN metastasis. After surgery, a histological diagnosis was confirmed by two experienced pathologists from the Department of Pathology. The study was approved by the Ethics Committee of the Affiliated Sir Run Run Shaw Hospital, Zhejiang University School of Medicine, and all enrolled patients provided informed consent.

Treatment protocol

The indication of TT was strictly in accordance with the 2009 ATA guidelines (7). Shi L et al. described the indications of CND and modified LND (8). RAI remnant ablation was performed postoperatively in all patients with TT according to the 2009 ATA guidelines (7).

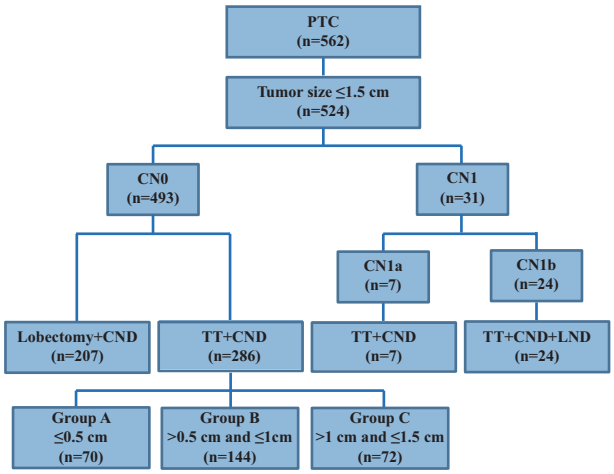

FIGURE 1
Flow diagram of included papillary thyroid carcinoma patients.

Assessment of treatment response

The response to the therapy re-staging system has been designed for the follow-up of PTC patients in the 2015 ATA guidelines. According to biochemical, imaging, and cytopathologic findings, for patients treated with TT and RAI remnant ablation, there were four response-to-therapy categories, including excellent, biochemical incomplete, structural incomplete, and indeterminate responses (4). In this study, we rearranged them into two categories consisting of excellent response and non-excellent response. The latter included biochemical incomplete, structural incomplete, and indeterminate responses. According to the ATA guidelines, the recurrence rate for the excellent response group is 1%–4%, which is much lower compared with that for other groups (biochemical incomplete response: 20% develop structural disease, structural incomplete response: 50%–85% continue to have persistent disease despite additional therapy, and indeterminate response: 15%–20% will have structural disease) (4).

All PTC patients were followed after completion of RAI remnant ablation. Routine neck ultrasound examinations and measurement of serum thyroglobulin (Tg) and anti-Tg antibodies were performed in a state of thyroid-stimulating hormone suppression every 3 months in the first year and every 6–12 months thereafter. When biochemical or structural incomplete responses occurred, more frequent follow-up was recommended, and additional examinations (e.g. computed tomography scan and fine needle aspiration) were proposed. Postoperative follow-up periods for the 317 patients ranged from 35–75 months (median follow-up time, 57 months), and the assessment of response to therapy was on the basis of the latest examination results. Serum Tg (normal range, 1.15–35.00 ng/mL) and Tg antibodies (normal range, 0–4.11 IU/mL) were measured using an electrochemiluminescence immunoassay in an Abbott Aeroset® automated instrument analyzer (Toshiba Medical Systems, Tochigi, Japan) (9–11). When TgAb exceeded the upper limit of its normal value, the value of TgAb was considered as positive.

Study design

The patients were classified into three groups according to tumor size (group A ≤0.5 cm; group B >0.5 cm and ≤1 cm; group C >1 cm and ≤1.5 cm) or two groups according to the presence (cN1) or absence (cN0) of clinical LN metastasis. Groups C and cN1 were regarded as simulated clinical progression of observable PTMC and the operation for them was assumed to be "delayed surgery", whereas Groups A, B and cN0 were regarded as no clinical progression and the operation for them was considered as immediate surgery. The response-to-therapy and recurrence-free survival (RFS) were analyzed among these groups in order to compare the safety and effectiveness between immediate and simulated "delayed" surgeries.

Statistical analysis

Continuous variables and categorical variables were determined using the Mann–Whitney U and chi-squared tests (including Fisher's exact probability tests, if needed), respectively. The results were presented as medians with range and numbers with percentages. Univariate logistic regression analyses were performed on gender, age, tumor size, tumor multifocality, ETE, chronic lymphocytic thyroiditis (CLT), and N stage. The variables exhibiting $p<0.05$ in univariate analysis were then selected and analyzed using multivariate logistic regression analysis. The results are represented as odds ratios (ORs) with 95% confidence intervals (CIs). For all analyses, two-sided tests were employed, and differences with $p<0.05$ were regarded as statistically significant.

Statistical analyses were performed using SPSS software (version 23.0, Inc., Chicago, IL, USA).

Results

Characteristics of PTC patients who underwent TT

It is shown in Figure 1 that 524 PTC patients with tumor sizes ≤1.5 cm were enrolled, but 207 cN0-PTC patients who underwent lobectomy and CND were excluded from our study. The remaining 317 PTC patients who underwent TT and CND or together with LND were enrolled and included 286 cN0 and 31 cN1 cases.

The clinicopathological characteristics of the 317 PTC patients are summarized in Table 1; Figure 1. The median age of the cohort was 43 years (range, 13–72 years). Most patients were women (77.6%), and most were less than 55 years old (82.6%). Patients were grouped according to tumor size: ≤0.5 cm (22.7%), >0.5 cm and ≤1 cm (51.1%), >1 cm and ≤1.5 cm (26.2%). Multifocality, CLT, and ETE were found in 58.0% (184/317), 26.5% (84/317), and 30.3% (96/317) of patients, respectively. The clinical N stage included 286 cN0 (90.2%), seven cN1a (2.2%), and 24 cN1b (7.6%) patients, whereas the pathological N stage included 155 pN0 (48.9%), 138 pN1a (43.5%), and 24 pN1b (7.6%) patients. An excellent response to primary therapy was observed in 249 patients (78.6%). According to ATA risk stratification, there were 155 (48.9%), 82 (25.9%), and 80 (25.2%) patients in the low, intermediate, and high-risk categories, respectively.

Patient clinicopathologic features associated with the primary tumor size of cN0-PTC

There were 286 cN0-PTC patients who were divided into three groups according to their primary tumor size: group A ≤0.5 cm (n=70), group B >0.5 cm and ≤1 cm (n=144), and group C >1 cm and ≤1.5 cm (n=72). As shown in Table 2, P1 represents the statistical difference between group A and group B, and P2 represents the statistical difference between group B and group C. Because group B was used in the statistical analysis twice, we subsequently used Bonferroni correction and defined P<0.025 (P<0.05/2) as statistically different.

Comparison of the postoperative pathologic results revealed that most clinicopathologic factors were not statistically different (P>0.025) between group A and group B (P1) or group B and group C (P2). These factors were gender, age, multifocality, ETE, CLT, temporary vocal cord paralysis (VCP), temporary hypoparathyroidism (hypoPT), and response to therapy. To describe the features of the mLNs, a statistical analysis was performed for the presence and number of central mLNs (CmLNs). We found that these two factors were significantly different between group A and group B (P1<0.001, both) but not different between group B and group C (P2 = 0.083, P2 = 0.105, respectively). According to the 2015 ATA guidelines, patients with

TABLE 1 Characteristics of 317 PTC patients with total thyroidectomy.

Characteristics	Total (n=317)
Gender	
Male (22.4%)	71
Female (77.6%)	246
Age of diagnosis (years)	
Median (range), year	43 (13-72)
<55 years (82.6%)	262
≥55 years (17.4%)	55
Primary tumor size (cm)	
≤0.5 (22.7%)	72
>0.5 and ≤1 (51.1%)	162
>1 and ≤1.5 (26.2%)	83
Multifocality	
Absent (42.0%)	133
Present (58.0%)	184
CLT	
Absent (73.5%)	233
Present (26.5%)	84
ETE	
Absent (69.7%)	221
Present (30.3%)	96
Postoperative complications	
Absent (86.7%)	275
Temporary VCP (1.6%)	5
Permanent VCP (0.0%)	0
Temporary Hypo-PT (11.7%)	37
Permanent Hypo-PT (0.0%)	0
Clinical Node stage [a]	
cN0 (90.2%)	286
cN1a (2.2%)	7
cN1b (7.6%)	24
Pathological Node stage [a]	
pN0 (48.9%)	155
pN1a (43.5%)	138
pN1b (7.6%)	24
ATA response-to-therapy categories [b]	
Excellent Response (78.6%)	249
Biochemical Incomplete Response (0.3%)	1
Structural Incomplete Response (2.5%)	8[d]

(Continued)

TABLE 1 Continued

Characteristics	Total (n=317)
Indeterminate Response (18.6%)	59
ATA Risk stratification [c]	
Low Risk (48.9%)	155
Intermediate Risk (25.9%)	82
High Risk (25.2%)	80

[a]Tumor, node, metastasis (TNM) classification system established by the American Joint Commission on Cancer (AJCC; 2010, 7th edition).
[b]Response to therapy according to the 2015 American Thyroid Association (ATA) management guidelines for differentiated thyroid cancer patients treated with total thyroidectomy and RAI remnant ablation.
[c]Risk stratification system according to the 2015 American Thyroid Association (ATA) management guidelines for adult patients with thyroid nodules and differentiated thyroid cancer. CLT, chronic lymphocytic thyroiditis; ETE, extra-thyroidal extension.
[d]Among these eight patients, recurrence was confirmed by reoperation in four patients, while in other four patients, recurrence was highly suspicious by ultrasound examination but was not proven by surgery or biopsy. In our study, recurrence was diagnosed if the lesion recurred after 12 months of no evidence of disease, according to the guidelines of the Chinese Society of Clinical Oncology (12).

mLNs ≤5 belong to the low-risk category. Therefore, we regarded mLNs ≤5 as an index, and we found no difference among these three groups (P1 = 0.273, P2 = 0.423). Furthermore, no significant difference was presented in staging of the response to therapy among these three groups. Therefore, it could be seen that the incidence and the number of mLNs in the central area were increasing when the tumor increased in size, especially from 0.5–1 cm, and that the incidence of excellent response was the same in three groups with different size primary tumors ranging from 0–1.5 cm.

A comparison of clinicopathologic features between cN0-PTC and cN1-PTC patients with tumors ≤1.5 cm

We divided 317 patients with primary lesions ≤1.5 cm into two groups according to whether their neck LN was clinically metastatic: cN0-PTC (n=286) and cN1-PTC (n=31). A comparison of the clinicopathologic features between the two groups is shown in Table 3.

The results showed that cN1-PTC patients comprised significantly more males (48.4% vs. 19.6%, P<0.001), younger ages (37 vs. 43, p=0.004), and larger sized tumors (1.0 cm vs. 0.7 cm, P=0.002) than cN0 patients. There was no statistical difference between the two groups regarding multifocality, ETE, CLT, temporary VCP, temporary hypoPT, or response to therapy (P>0.05, all). Therefore, cN1 was associated with larger tumor size, but was unassociated with other aggressive characteristics, and the incidence of excellent response was the same whether PTMC patients had clinical metastasis or not.

Risk factors for non-excellent response to therapy in PTC patients with TT

Risk factors for non-excellent response to therapy was analyzed in 317 PTC patients (286 cN0 and 31 cN1). As shown in Table 4, univariate analysis indicated that CLT (<0.001) and >5 pathological CmLNs (p=0.002) significantly increased the risk of classification into the non-excellent response to therapy category. Furthermore, these two factors were independent variables for response to therapy in multivariate analysis (p<0.001). Therefore, we determined that CLT (absent vs. present) and the number of pathological CmLNs (≤5 vs. >5) represented independent risk factors for predicting clinical outcome, rather than tumor size or cN1.

Recurrence-free survival according to tumor size and clinical N stage

Four cases of disease recurrence were identified during the median follow-up period of 57 months (range 35–75 months) across all PTC patients. The mean time of recurrence was 29.5 months. The RFS were not significantly different among the three groups of 1~1.5cm, 0.5~1cm and ≤0.5 cm (97.2% vs. 98.6% vs. 100%, log-rank P>0.05) (Figure 2A) and between cN1 and cN0 groups (100% vs. 98.6%, log-rank P=0.528) (Figure 2B).

Discussion

At Kuma Hospital, the indications for surgery in low-risk PTMC patients under AS are tumor enlargement ≥3 mm, tumors that are 1.2 cm in diameter, or LN metastasis (called clinical progression) (13). Therefore, we used our data to simulate clinical progression and designed this study in two parts. Part one involved dividing the cN0 patients into three groups according to tumor size (≤0.5 cm, 0.5~1 cm and 1~1.5 cm) to simulate tumor size increase. We found the incidence and the number of mLNs in the central area were increasing when the tumor increased in size, especially from 0.5–1 cm, but there was no significant difference in the incidences of excellent response and RFS among these three groups. Part two involved setting up two groups: cN0 and cN1 to simulate metastatic LN appearance. We found cN1 was associated with larger tumor size, but was unassociated with other aggressive characteristics, and the incidences of excellent response and RFS were the same whether PTMC patients had clinical metastasis or not. Additionally, we determined that CLT (absent vs. present) and the number of pathological CmLNs (≤5 vs. >5) represented independent risk factors for predicting clinical outcomes, rather than tumor size or clinical lymph node metastasis. If we set tumors with 1~1.5cm in size or cN1 as clinical progression of observable PTMC, then their corresponding surgeries can be considered as simulated “delayed surgery”. Our results suggested, therefore, that the oncologic outcome of “delayed surgery” for PTMC with AS showing clinical progression was as good as that of immediate operation.

Woolner and his colleagues from the Mayo Clinic were the first scientists to coin the term occult papillary carcinoma for PTCs ≤1.5 cm in size in 1960 (14). Their study showed that occult papillary carcinoma patients had a good prognosis on the basis of 30 years of follow-up of 140 cases. In 1989, the World Health Organization introduced the term papillary microcarcinoma to replace the term

TABLE 2 Characteristics of pN1a and pN0 patients according to primary tumor size.

Characteristics	Primary tumor size (cm) (n=286)			*P1*	*P2*
	Group A ≤0.5 (n=70)	Group B >0.5 and ≤1 (n=144)	Group C >1 and ≤1.5 (n=72)		
Gender					
Male	11 (15.7%)	26 (18.1%)	19 (26.4%)	0.671	0.155
Female	59 (84.3%)	118 (81.9%)	53 (73.6%)		
Age of diagnosis (years)					
Median (range), year	43 (23-69)	43 (23-72)	45 (13-66)	0.836	0.389
<55 years	55 (78.6%)	119 (82.6%)	59 (81.9%)	0.474	0.899
≥55 years	15 (21.4%)	25 (17.4%)	13 (18.1%)		
Multifocality					
Absent	27 (38.6%)	47 (32.6%)	48 (66.7%)	0.393	<0.001
Present	43 (61.4%)	97 (67.4%)	24 (33.3%)		
Extrathyroidal extension					
Absent	58 (82.9%)	101 (70.1%)	44 (61.1%)	0.046	0.183
Present	12 (17.1%)	43 (29.9%)	28 (38.9%)		
CLT					
Absent	47 (67.1%)	106 (73.6%)	55 (76.4%)	0.325	0.659
Present	23 (32.9%)	38 (26.4%)	17 (23.6%)		
Central lymph node metastasis					
Absent (N0)	54 (77.1%)	74 (51.4%)	28 (38.9%)	< 0.001	0.083
Present (N1a)	16 (22.9%)	70 (48.6%)	44 (61.1%)		
Number of CmLN					
Median (range)	0 (0-5)	0 (0-18)	1 (0-8)	< 0.001	0.105
≤5	70 (100%)	139 (96.5%)	67 (93.1%)	0.273 [#]	0.423[#]
>5	0 (0%)	5 (3.5%)	5 (6.9%)		
Temporary VCP [a]					
Absent	70 (100%)	142 (98.6%)	70 (97.2%)	1.000*	0.858[#]
Present	0 (0%)	2 (1.4%)	2 (2.8%)		
Temporary Hypo-PT [b]					
Absent	59 (84.3%)	127 (88.2%)	63 (87.5%)	0.426	0.882
Present	11 (15.7%)	17 (11.8%)	9 (12.5%)		
Response-to-therapy [c]					
Excellent Response	54 (77.1%)	118 (81.9%)	55 (76.4%)	0.407	0.335
Non- Excellent Response	16 (22.9%)	26 (18.1%)	17 (23.6%)		

P1: P value of statistical analysis between group A and group B.
P2: P value of statistical analysis between group B and group C.
[a]No permanent VCP was found in any cases.
[b]No permanent hypoPT was found in any cases.
[c]Response to therapy on the basis of the 2015 American Thyroid Association (ATA) management guidelines for differentiated thyroid cancer patients treated with total thyroidectomy and RAI remnant ablation.
[#]Continuity correction[b].
*Fisher's exact test.
According to the Bonferroni correction test, P<0.025 (0.05/2) is defined as statistically different.

TABLE 3 Characteristics of PTC patients with tumors ≤1.5 cm according to cN0 and cN1.

Characteristics	cN0 (n=286)	cN1 (n=31)	*P*
Gender			
Male	56 (19.6%)	15 (48.4%)	<0.001
Female	230 (80.4%)	16 (51.6%)	
Age of diagnosis (years)			
Median (range), year	43 (13-72)	37 (20-58)	0.004
<55 years	233 (81.5%)	29 (93.5%)	0.092
≥55 years	53 (18.5%)	2 (6.5%)	
Tumor size (cm)	0.7 (0.2-1.5)	1.0 (0.5-1.5)	0.002
≤0.5	70 (24.5%)	2 (6.5%)	<0.001
>0.5 and ≤1	144 (50.3%)	18 (58.1%)	
>1 and ≤1.5	72 (25.2%)	11 (35.4%)	
Multifocality			
Absent	122 (42.7%)	11 (35.5%)	0.442
Present	164 (57.3%)	20 (64.5%)	
Extrathyroidal extension			
Absent	203 (71.0%)	18 (58.1%)	0.137
Present	83 (29.0%)	13 (41.9%)	
CLT			
Absent	208 (72.7%)	25 (80.6%)	0.343
Present	78 (27.3%)	6 (19.4%)	
Temporary VCP [a]			
Absent	282 (98.6%)	30 (96.8%)	0.404
Present	4 (1.4%)	1 (3.2%)	
Temporary Hypo-PT [b]			
Absent	249 (87.1%)	31 (100%)	0.066
Present	37 (12.9%)	0 (0%)	
Response-to-therapy [c]			
Excellent Response	227 (79.4%)	22 (71.0%)	0.279
Non- Excellent Response	59 (20.6%)	9 (29.0%)	

[a]No permanent VCP was found in any cases.
[b]No permanent hypoPT was found in any cases.
[c]Response to therapy based on the 2015 American Thyroid Association (ATA) management guidelines for differentiated thyroid cancer patients treated with total thyroidectomy and RAI remnant ablation.

occult papillary carcinoma, and they defined papillary microcarcinomas as being PTCs ≤1 cm in diameter (15). PTMC was regarded as an important variant of PTC because of its low malignancy and exceptionally rare distant metastasis: 6%~35% frequency as incidental findings in autopsy studies, and increasing frequency in life by modern methods of investigation. Hence the size of low-risk PTMCs suitable for observation generally range between 1 cm and 1.5 cm. However, the Chinese Association of Thyroid Oncology (CATO) suggests that the size of observed low-risk PTMCs should be not greater than 0.5 cm (16). CATO's view is on the basis of a contrastive study of two screening criteria for AS in 1,001 low-risk PTMC patients. Compared with that in the Kuma low-risk PTMC group (≤1 cm), Qian et al. found a lower incidence of multifocal lesions, ETEs, central LN metastasis, progression rates, and prolonged DFS in the CATO low-risk PTMC group (≤0.5 cm). Therefore, in our study on PTMC, the PTC patients with primary tumors ≤1.5 cm were chosen and were divided into three groups according to tumor size, and the tumors sized 1 to 1.5 cm were assumed to be clinical progression of observable PTMC.

The emergence of "delayed surgery" is accompanied by AS practiced for PTMC, so it has been well-known. However, in fact, there are few relative articles found and the long-term clinical outcomes after delayed surgery remain unclear (17). Korean scholars did an interesting study. A total of 2863 PTMC patients were assigned into three groups due to a delay period of ≤6 months, 6–12 months, and >12 months. They found that there were no significant differences in the development of structural recurrent/persistent disease and disease-free survival among the groups (18). Actually, they simulated a situation that patients with PTMC could be observed for a period of time before operation. The reason of their delayed operations was not clinical progression of PTMC, so it had nothing to do with "delayed operation" for the PTMCs with simulation clinical progression in our article. In addition, "delayed surgery" was really mentioned in some articles, but it was often taken in one stroke (19, 20).

Miyauchi and his colleagues found that rapid or slow growth happened in approximately one quarter of PTMCs (21), which will be likely switched to delayed surgery. Therefore, another issue facing surgeons is whether delaying surgery will increase surgical complications or not. In the study of Oda et al., they analyzed the incidence of unfavorable events in PTMC patients between AS and immediate surgery groups, and they showed that the oncological outcomes of the immediate surgery and AS groups were similarly excellent, but the incidence of unfavorable events were higher in the immediate surgery group (20). However, by further analyzing their data on surgical complications in all patients who were operated on, we found that the incidences of temporary VCP and hypoPT in the delayed surgery group were actually higher than in the immediate surgery group, although the incidences of permanent ones were similar between the two groups. This result from their data is logical, because larger or more lesions must also increase surgical difficulty. As for our study, there were no significant differences in the incidence of surgical complications among the groups (see Table 2). However, we also emphasized that certain PTMCs that occur in anatomically sensitive sites should be identified and treated surgically, such as those located in the area adjacent to the entrance of the recurrent laryngeal nerve to the larynx, the so-called "danger triangle" (22).

Although still controversial, more and more endocrinologists and some thyroid surgeons and medical teams are beginning to use AS in low-risk PTMC patients. Therefore, the choice of AS is a very serious issue not only for the patients and their families, but also for doctors, especially in China (23, 24). Prescribing AS is a decision that involves considering three aspects, namely inherent tumor characteristics, patient characteristics, and medical team

TABLE 4 Relationships between clinicopathologic variables and non-excellent response to therapy in PTC patients with total thyroidectomy.

Characteristics	Univariate		Multivariate	
	OR (95% CI)	*p*	OR (95% CI)	*p*
Gender (Male vs Female)	1.882 (0.906-3.907)	0.090		
Age of diagnosis (years) (<55 vs ≥55)	0.573 (0.257-1.279)	0.174		
Primary tumor size (cm) (≤1 vs >1)	1.348 (0.748-2.429)	0.321		
Multifocality (Absent vs Present)	1.317 (0.758-2.290)	0.329		
ETE (Absent vs Present)	0.587 (0.312-1.104)	0.098		
CLT (Absent vs Present)	5.130 (2.892-9.099)	<0.001	6.179 (3.365-11.343)	<0.001
Clinical N stage (cN0 vs cN1)	1.574 (0.689-3.598)	0.282		
Pathological N stage (pN0 vs pN1)	1.400 (0.815-2.405)	0.223		
Number of pathological CmLN (≤5 vs >5)	3.582 (1.571-8.167)	0.002	5.617 (2.292-13.768)	<0.001

CLT, chronic lymphocytic thyroiditis; ETE, extra-thyroidal extension; CmLN, central neck metastatic lymph node.

characteristics. Among these three aspects, we think that an experienced medical group is a vital factor in performing AS smoothly. It should not only include multidisciplinary cooperation, an excellent sonographer, and an active management of patients and their data, but also the ability to retrospectively analyze the medical group's own patients previously surgically treated, like in this study, to answer the question "whether the therapeutic result of delayed surgery is the same as that of immediate surgery in my medical center". We would suggest that only if the result of its data analysis is acceptable should the medical team propose AS for low-risk PTMC patients.

This study had several limitations. First, there were not many relapsed cases in our consecutive patients from 2013–2015, and therefore we had to choose the index of response to therapy to evaluate the therapeutic effect. Because this assessment system is usually performed in PTC patients treated with TT and RAI ablation in a majority of published studies (25–27). Therefore, in our study we just enrolled the PTMC patients treated with TT and RAI ablation, and we excluded those with thyroid lobectomy. Second, the treatment for our PTC patients from 2013–2015 was performed according to the 2009 ATA guidelines. If we refer to the 2015 ATA guidelines, our disease management at that time must be regarded as over-treatment, and thyroid lobectomy should have been enough for the majority of them. Presently, we cannot use our data to answer the question of whether thyroid lobectomy performed after the presence of clinical progression is also feasible. Third, generally speaking, the evolution of papillary thyroid carcinoma is a very slow process and a patient with the same tumor size may not have the same tumor evolution process. However, a tumor with 1cm in size must have grown from a tumor

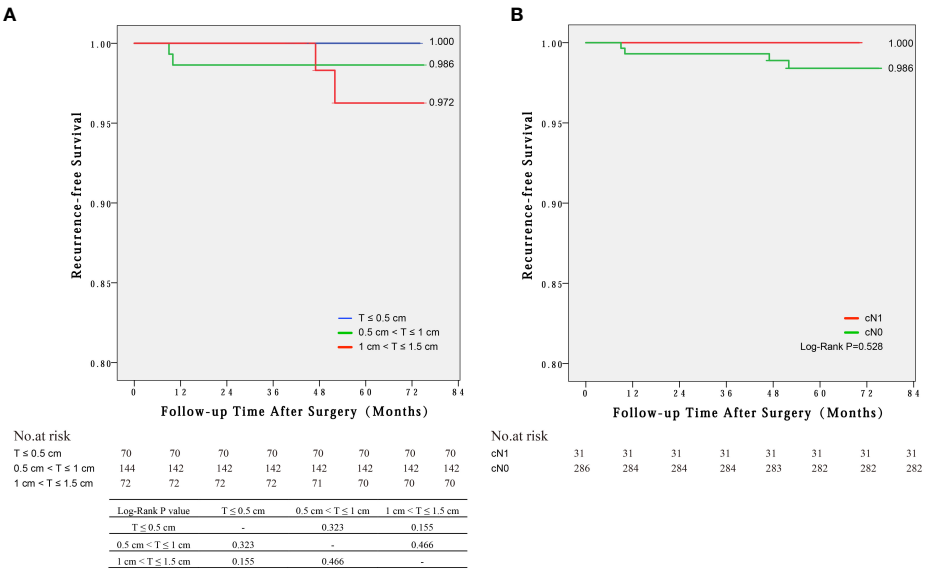

FIGURE 2
Recurrence-free survival by Kaplan-Meier curves for different groups: **(A)** Tumor sizes of 1~1.5cm, 0.5~1cm and ≤0.5 cm, **(B)** cN1 and cN0 groups.

with 0.5cm in size, and a tumor with lymphatic metastasis must have developed from no metastasis. Therefore, this study was done by simulating clinical progression of PTMCs with AS. Groups C and cN1 were regarded as simulated clinical progression of observable PTMC and the operation for them was assumed to be "delayed surgery", whereas, Groups A, B and cN0 were regarded as no clinical progression and the operation for them was considered as immediate surgery. Forth, there were only 317 consecutive patients enrolled from 2013-2015 with a relatively short follow-up period. Therefore, additional studies with longer follow-up and multicenter data are needed.

To some extent, this study reflected that the oncological outcomes were also excellent even if surgery was delayed until after the presence of clinical progression (tumor size enlargement and appearance of LN metastasis), according to our clinical simulation. Furthermore, we considered that it was feasible for medical centers to assess the ability to implement AS in PTMC patients by retrospectively analyzing their own previous clinical data in the described simulation.

Data availability statement

The raw data supporting the conclusions of this article will be made available by the authors, without undue reservation.

Ethics statement

The study was approved by the Ethics Committee of the Affiliated Sir Run Run Shaw Hospital, Zhejiang University School of Medicine, and all enrolled patients provided informed consent.

Author contributions

LS and LX designed the study and confirm the authenticity and legitimacy of all raw data. LZ, JW and KL performed the data collection and analysis. LS interpreted the results. HQ and YF performed the follow-up plan and collected the data from patients. LX supervised the project. All authors read and approved the final manuscript.

Funding

This research was supported by Medicine and Health Technology project from the Zhejiang Health Commission (grant no. 2019ZD030) and The Special Project for Modernization of Traditional Chinese Medicine of Zhejiang Province (grant no. 2022ZQ058).

Acknowledgments

We thank Mark Abramovitz, PhD, from Liwen Bianji (Edanz) (www.liwenbianji.cn) for editing the language of a draft of this manuscript.

Conflict of interest

The authors declare that the research was conducted in the absence of any commercial or financial relationships that could be construed as a potential conflict of interest.

Publisher's note

References

1. McGuire S. World Cancer Report 2014. Geneva, Switzerland: World Health Organization, International Agency for Research on Cancer, Who Press, 2015. *Adv Nutr* (2016) 7(2):418–9. doi: 10.3945/an.116.012211

2. Miyauchi A. Clinical trials of active surveillance of papillary microcarcinoma of the thyroid. *World J Surg* (2016) 40(3):516–22. doi: 10.1007/s00268-015-3392-y

3. Ito Y, Miyauchi A. Active surveillance of low-risk papillary thyroid microcarcinomas in Japan and other countries: A review. *Expert Rev Endocrinol Metab* (2020) 15(1):5–12. doi: 10.1080/17446651.2020.1707078

4. Haugen BR, Alexander EK, Bible KC, Doherty GM, Mandel SJ, Nikiforov YE, et al. American thyroid association management guidelines for adult patients with thyroid nodules and differentiated thyroid cancer: the American thyroid association guidelines task force on thyroid nodules and differentiated thyroid cancer. *Thyroid* (2015) 26(1):1–133. doi: 10.1089/thy.2015.0020

5. Volante M, Collini P, Nikiforov YE, Sakamoto A, Kakudo K, Katoh R, et al. Poorly differentiated thyroid carcinoma: the turin proposal for the use of uniform diagnostic criteria and an algorithmic diagnostic approach. *Am J Surg Pathol* (2007) 31(8):1256–64. doi: 10.1097/PAS.0b013e3180309e6a

6. Randolph GW, Duh QY, Heller KS, LiVolsi VA, Mandel SJ, Steward DL, et al. The prognostic significance of nodal metastases from papillary thyroid carcinoma can be stratified based on the size and number of metastatic lymph nodes, as well as the presence of extranodal extension. *Thyroid* (2012) 22(11):1144–52. doi: 10.1089/thy.2012.0043

7. Cooper DS, Doherty GM, Haugen BR, Kloos RT, Lee SL, Mandel SJ, et al. American Thyroid Association Guidelines Taskforce on Thyroid N, Differentiated Thyroid C. Revised American thyroid association management guidelines for patients with thyroid nodules and differentiated thyroid cancer. *Thyroid* (2009) 19(11):1167–214. doi: 10.1089/thy.2009.0110

8. Shi L, Zhou L, Wang J, Jin L, Lei Y, Xia L, et al. The effect of the area proportion of the metastatic lesion within the central metastatic lymph node on response to therapy in papillary thyroid carcinoma. *Oncol Lett* (2021) 21(4):284. doi: 10.3892/ol.2021.12545

9. Spencer CA. Clinical review: clinical utility of thyroglobulin antibody (Tgab) measurements for patients with differentiated thyroid cancers (Dtc). *J Clin Endocrinol Metab* (2011) 96(12):3615–27. doi: 10.1210/jc.2011-1740

10. Segurado OG, Volmer W, Dowell B. Psa standardization: A review of nccls, stanford and abbott efforts. *Anticancer Res* (1997) 17(4B):2919–20.

11. Feldt-Rasmussen U, Rasmussen AK. Serum thyroglobulin (Tg) in presence of thyroglobulin autoantibodies (Tgab). Clinical and methodological relevance of the interaction between tg and tgab in vitro and in vivo. *J Endocrinol Invest* (1985) 8 (6):571–6. doi: 10.1007/BF03348564

12. Chinese society of clinical oncology (Csco) diagnosis and treatment guidelines for persistent/recurrent and metastatic differentiated thyroid cancer 2018 (English version). *Chin J Cancer Res* (2019) 31(1):99–116. doi: 10.21147/j.issn.1000-9604.2019.01.06

13. Ito Y, Miyauchi A, Kihara M, Higashiyama T, Kobayashi K, Miya A. Patient age is significantly related to the progression of papillary microcarcinoma of the thyroid under observation. *Thyroid* (2014) 24(1):27–34. doi: 10.1089/thy.2013.0367

14. Woolner LB, Lemmon ML, Beahrs OH, Black BM, Keating FR Jr. Occult papillary carcinoma of the thyroid gland: A study of 140 cases observed in a 30-year period. *J Clin Endocrinol Metab* (1960) 20:89–105. doi: 10.1210/jcem-20-1-89

15. Hedinger C, Williams ED, Sobin LH. The who histological classification of thyroid tumors: A commentary on the second edition. *Cancer* (1989) 63(5):908–11. doi: 10.1002/1097-0142(19890301)63:5<908::aid-cncr2820630520>3.0.co;2-i

16. Gao M, Ge M, Ji Q, Cheng R, Lu H, Guan H, et al. Chinese expert consensus and guidelines for the diagnosis and treatment of papillary thyroid microcarcinoma. *Cancer Biol Med* (2016) 14(3):203–11. doi: 10.20892/j.issn.2095-3941.2017.0051

17. Aygun N, Isgor A, Uludag M. Can active surveillance be an alternative to surgery in papillary thyroid microcarcinoma?: the current situation worldwide. *Sisli Etfal Hastan Tip Bul* (2018) 52(4):233–43. doi: 10.14744/SEMB.2018.15428

18. Jeon MJ, Kim WG, Kwon H, Kim M, Park S, Oh HS, et al. Clinical outcomes after delayed thyroid surgery in patients with papillary thyroid microcarcinoma. *Eur J Endocrinol* (2017) 177(1):25–31. doi: 10.1530/EJE-17-0160

19. Sakai T, Sugitani I, Ebina A, Fukuoka O, Toda K, Mitani H, et al. Active surveillance for T1bn0m0 papillary thyroid carcinoma. *Thyroid* (2019) 29(1):59–63. doi: 10.1089/thy.2018.0462

20. Oda H, Miyauchi A, Ito Y, Yoshioka K, Nakayama A, Sasai H, et al. Incidences of unfavorable events in the management of low-risk papillary microcarcinoma of the thyroid by active surveillance versus immediate surgery. *Thyroid* (2016) 26(1):150–5. doi: 10.1089/thy.2015.0313

21. Miyauchi A, Kudo T, Ito Y, Oda H, Yamamoto M, Sasai H, et al. Natural history of papillary thyroid microcarcinoma: kinetic analyses on tumor volume during active surveillance and before presentation. *Surgery* (2019) 165(1):25–30. doi: 10.1016/j.surg.2018.07.045

22. Shin JH, Baek JH, Ha EJ, Lee JH. Radiofrequency ablation of thyroid nodules: basic principles and clinical application. *Int J Endocrinol* (2012) 2012:919650. doi: 10.1155/2012/919650

23. Kondro W. Doctor-patient confidentiality eroded in Canada. *Lancet* (1996) 347 (9018):1827. doi: 10.1016/s0140-6736(96)91644-x

24. Ma S, Xu X, Trigo V, Ramalho NJ. Doctor-patient relationships (Dpr) in China. *J Health Organ Manag* (2017) 31(1):110–24. doi: 10.1108/JHOM-09-2016-0165

25. Wei L, Bai L, Zhao L, Yu T, Ma Q, Ji B. High-dose rai therapy justified by pathological N1a disease revealed by prophylactic central neck dissection for cn0 papillary thyroid cancer patients: is it superior to low-dose rai therapy? *World J Surg* (2019) 43(5):1256–63. doi: 10.1007/s00268-019-04924-0

26. Vaisman F, Momesso D, Bulzico DA, Pessoa CH, Dias F, Corbo R, et al. Spontaneous remission in thyroid cancer patients after biochemical incomplete response to initial therapy. *Clin Endocrinol (Oxf)* (2012) 77(1):132–8. doi: 10.1111/j.1365-2265.2012.04342.x

27. Llamas-Olier AE, Cuellar DI, Buitrago G. Intermediate-risk papillary thyroid cancer: risk factors for early recurrence in patients with excellent response to initial therapy. *Thyroid* (2018) 28(10):1311–7. doi: 10.1089/thy.2017.0578

frontiers | Frontiers in Oncology

TYPE Original Research
PUBLISHED 28 November 2023
DOI 10.3389/fonc.2023.1073614

OPEN ACCESS

EDITED BY
Sharon R. Pine,
University of Colorado Anschutz Medical Campus, United States

REVIEWED BY
Daisuke Sano,
Yokohama City University, Japan
Luzeng Chen,
Peking University, China

*CORRESPONDENCE
Gaoyi Yang
yanggaoyi8@163.com

RECEIVED 18 October 2022
ACCEPTED 27 October 2023
PUBLISHED 28 November 2023

CITATION
Tong J, Lin T, Wen B, Chen P, Wang Y, Yu Y, Chen M and Yang G (2023) The value of multimodal ultrasound in diagnosis of cervical lymphadenopathy: can real-time elastography help identify benign and malignant lymph nodes?
Front. Oncol. 13:1073614.
doi: 10.3389/fonc.2023.1073614

The value of multimodal ultrasound in diagnosis of cervical lymphadenopathy: can real-time elastography help identify benign and malignant lymph nodes?

Jiahui Tong[1,2], Ting Lin[1], Boping Wen[3], Peijun Chen[3], Ying Wang[4], Yuehui Yu[4], Menghan Chen[4] and Gaoyi Yang[2,3]*

[1]The Fourth Clinical Medical College, Zhejiang Chinese Medicine University, Hangzhou, China, [2]Department of Ultrasonography, Hangzhou First People's Hospital, Hangzhou, China, [3]Department of Ultrasonography, Hangzhou Red Cross Hospital, Hangzhou, China, [4]Hangzhou Normal University, Hangzhou, China

Aim: To investigate the multimodal ultrasound(MMUS) features of cervical lymphadenopathy and to assess its value in the differential diagnosis of benign and malignant cervical lymph nodes.

Methods: A retrospective analysis of 169 patients with cervical lymph node enlargement who attended Hangzhou Red Cross Hospital from March 2020 to October 2022. All patients underwent conventional ultrasound (CUS), contrast-enhanced ultrasound (CEUS), and real-time elastography (RTE), and were divided into training set and validation set. Univariate analysis was applied to screen out statistically significant parameters, and CUS model and MMUS model were constructed by multifactorial logistic regression analysis. The receiver operator characteristic (ROC) curve was established, and the area under the curve (AUC) was used to compare CUS model with MMUS model to assess the value of MMUS.

Results: Of the cervical 169 lymph nodes in 169 patients included in the study. The 169 enrolled patients were divided into a training set (132 patients) and a validation set (37 patients). In the training set, univariate analysis showed statistically significant differences in long diameter/short diameter(L/S), border, margin, hilus, dermal medulla boundary, blood flow type, enhancement mode, enhancement type, and RTE score (all $p< 0.05$). Multifactor logistic analysis showed that L/S, blood flow type, enhancement mode and enhancement type were correlates of malignant lymph nodes (all $p< 0.05$). The comparison of AUC demonstrated that the discriminative ability of the MMUS model was superior to using the CUS model, both in the training set($p = 0.004$) and validation set ($p<0.001$).

Conclusion: In this study, MMUS shows higher diagnostic efficiency than CUS. Ultrasound features such as L/S, blood flow type, mode of enhancement, type of enhancement are helpful in distinguishing benign and malignant lymphadenopathy.

The addition of CEUS can greatly improve the sensitivity and specificity of ultrasonic diagnosis of malignant cervical lymph nodes. RTE score is of limited value in the diagnosis of malignant cervical lymph nodes.

KEYWORDS

elastography, contrast-enhanced ultrasound, conventional ultrasound, cervical lymph nodes, logistic regression analysis

1 Introduction

Cervical lymphadenopathy is a common group of diseases that occur in the head and neck. Referral patterns and treatment strategies are different for different types of lymphadenopathy. Accurate identification of lesion type is important for follow-up treatment and clinical management (1). However, most cervical lymph nodes lack specific clinical manifestations, and it is difficult to distinguish benign and malignant cervical lymphadenopathy by interrogation and physical examination (2).

In the diagnosis of lymphadenopathy, ultrasound is the preferred modality of examination (3, 4). Conventional ultrasonography (CUS) allows assessment of the size, border, margin, and internal echogenicity of lymph nodes, as well as obtaining information on blood flow in the major vessels within the lymph nodes by color Doppler flow imaging. Contrast-enhanced ultrasound (CEUS) can further reveal the small vessels as well as capillaries within the diseased lymph nodes, as well as identify areas of necrosis. Real-time elastography (RTE) can assess the stiffness (elastic modulus) of the lymph nodes. However, due to the diversity and complexity of cervical lymphadenopathy, the diagnostic value of various ultrasound features for the diagnosis of benign and malignant lymph nodes remains controversial. This makes it difficult for ultrasonographers to diagnose benign and malignant lymph nodes.

Therefore, we planned to collect and integrate various ultrasound features that may be associated with malignant lymph nodes and construct a multimodal ultrasound (MMUS) model to assess cervical lymph nodes by logistic regression analysis. The value of MMUS in diagnosing the benignity and malignancy of cervical lymph node disease was determined by comparing it with CUS. The purpose of our study was to reduce the difficulty of diagnosing benign and malignant lymph nodes by ultrasonographers.

2 Materials and methods

2.1 Patients

This retrospective study was approved by the institutional review board of Hangzhou Red Cross Hospital. The requirement for the patients' informed consent was waived. All enrolled patients underwent core-needle biopsy (CNB) between March 2020 and October 2022 at the Department of Ultrasound, Chest Hospital, Zhejiang University School of Medicine. In this study, pathological or pathogenic findings in the cervical lymph nodes were used as the gold standard for diagnosis. Inclusion criteria were as follows: (1) Patients with complaints of enlarged lymph nodes in the neck. (2) All patients underwent core-needle biopsy. (3) All patients underwent CUS, RTE and CEUS within 24h before the biopsy. Exclusion criteria were as follows: (1) Patients who cannot be diagnosed by pathological or etiological findings. (2) Poor image quality or image data loss. (3) Incomplete clinical data. (4) Received radiotherapy or chemotherapy.

All enrolled patients were divided into a training set and a validation set according to the time of diagnosis. Patients enrolled from January 2021 to October 2022 are included in the training set. Patients enrolled from March 2020 to January 2021 are included in the validation set. The relevant flow chart is shown in Figure 1.

2.2 Ultrasound examination

An iU22 diagnostic ultrasound instrument (Philips Healthcare, Bothell) with L12-5 and L9-3 probes, corresponding to 5-12 MHz and 3-9 MHz, respectively, was used. patients were placed in a supine position with the neck fully exposed. The cervical lymph nodes were then scanned. Ultrasound characteristic data of the lymph nodes, such as lymph node size, borders, morphology, internal echogenicity and corticomedullary demarcation, were recorded on the largest longitudinal and transverse sections. The flow types of lymph nodes were also recorded by color Doppler flow imaging, and we classified the flow types of lymph nodes as central, avascular or spot flow, peripheral, and mixed (4–6). Where the central type is defined as vessels located mainly in the central location of the lymph node, with branching vessels disperse to the periphery. The avascular or spot flow type is defined as no blood flow signal is detected in the lymph node or a small amount of spot flow signal can be detected, the peripheral type is defined as the vascular signal of the lymph node travels along the edge of the lymph node, and the mixed type is defined as the presence of both peripheral and central blood flow.

RTE is performed by manual rhythmic compression of the lymph nodes in the vertical direction using the same equipment and

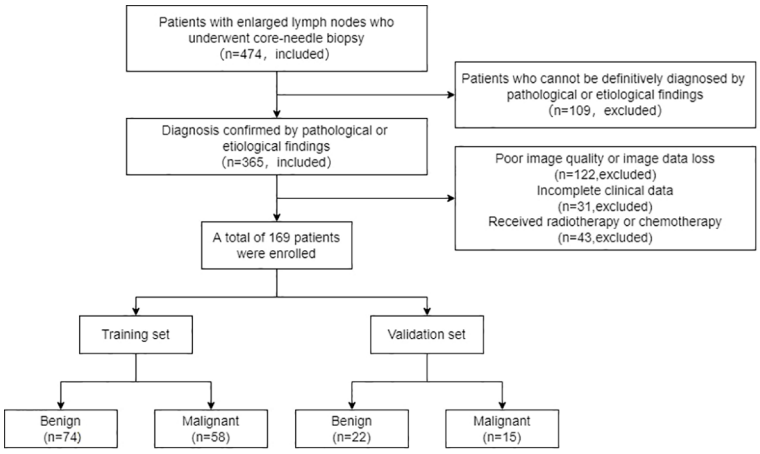

FIGURE 1
Flowchart of 169 lymph nodes included in the study.

probe. The elastogram is examined in dual mode on the screen in parallel with the real-time B-mode image. Bring the surrounding adipose tissue with lymph nodes into the region of interest (ROI). Real-time tissue elasticity was recorded with color charts. RTE assessment was performed referring to the protocol described by Tanaka et al, using a simplified quadruple scale for each lymph node to score RTE based on the proportional distribution of hard (blue areas) and soft (green areas) areas in the examined lymph nodes (7). The quadruple scale is shown in Table 1.

CEUS examination with low mechanical index (0.06) pulsed reverse harmonic imaging and the sulfur hexafluoride microbubble ultrasound contrast agent SonoVue (Bracco SpA, Milan, Italy) was used for patient examination. After intravenous injection of 2.4 ml of contrast agent, lymph node enhancement was dynamically observed and continuously observed for 2 minutes. The images were stored on the hard disk of the instrument, and the enhancement mode of each lymph node and the enhancement type at the time of peak were analyzed and recorded. We classified enhancement modality into centripetal and non-centripetal enhancement, and enhancement type at peak into homogeneous enhancement, asynchronous enhancement, beehive or divider enhancement, and rim-like enhancement (8–10). Homogeneous enhancement is defined as diffuse enhancement of the entire lymph node with uniform perfusion. Asynchronous enhancement is defined as diffuse enhancement of the entire lymph node but with heterogeneous perfusion. Beehive enhancement is defined as the presence of multiple non-enhancing areas within the lymph nodes in a foveal pattern. Divider enhancement is defined as the presence of multiple larger non-enhancing areas within the lymph node in a compartmentalized pattern. Rim-like enhancement is defined as lymph node circumferential enhancement with no central enhancement.

TABLE 1 Four subscales of real-time elastography(RTE) score.

RTE score	Degree of hardness	Elastography view
1	Soft	Mostly green areas and less than 10% blue areas
2	Mostly soft	Mostly green areas and less than 45% blue areas
3	Mostly hard	Mostly blue areas and less than 45% green areas
4	Hard	Mostly blue areas and less than 10% green areas

2.3 Core-needle biopsy

The puncture procedure was strictly adhered to the puncture protocol. After routine disinfection and spreading of the towel, local anesthesia was administered subcutaneously with 2% lidocaine at the puncture site. A Bard automatic puncture biopsy gun (Carvington, USA), 18G, with a sampling length of 2.0 cm, was used for real-time ultrasound-guided puncture biopsy. The tissue strips obtained by puncture were fixed with 10% formaldehyde and sent to the pathology department for examination. Generally, 1 to 3 stitches were punctured, and the pathologist was on site to observe whether the material was taken satisfactorily. Tissue strip samples are shown in Figure 2. To prevent puncture complications, all patients were observed for 30 min after puncture was completed.

2.4 Data processing

The information of patients' age, gender, clinical diagnosis, and ultrasound reports were removed, and only the corresponding ultrasound imaging data (including CUS, CEUS, and RTE) were retained. The data were then randomly numbered, and two sonographers (JH T and PJ C) observed the data and recorded the ultrasound imaging characteristics of each data separately. After completing the above operation, the observation results of both of them were compared, and the imaging data with inconsistent observation results were given to a senior (more than 20 years of experience) sonographer (BP W) to review and give the final results.

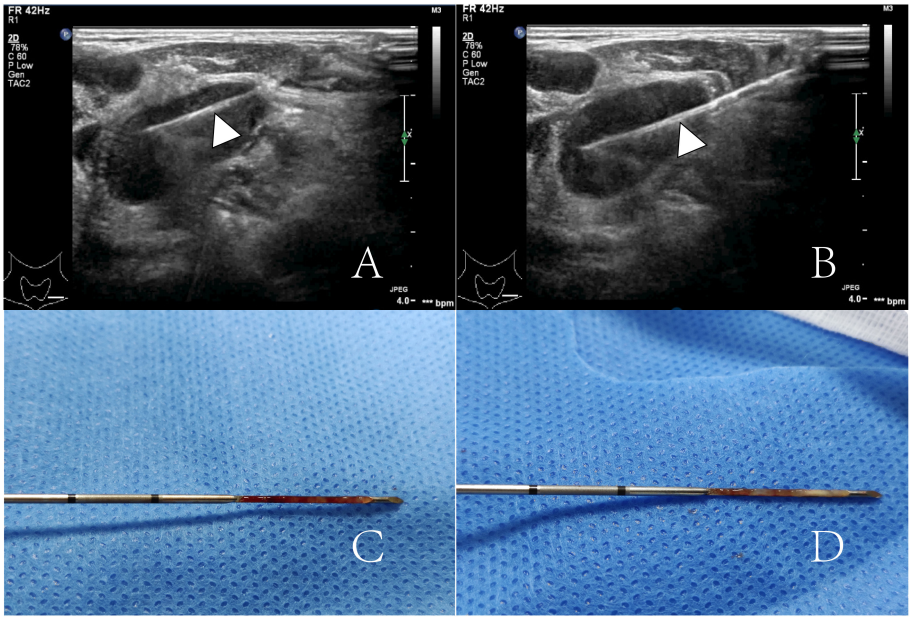

FIGURE 2
(A, B) show a lymph node was punctured twice by an 18G core-needle (arrowheads). **(C, D)** show two punctured tissue strips.

2.5 Statistical analysis

Continuous data were expressed as mean ± standard deviation. Percentages and composition ratios were used to represent categorical parameters. Parametric data were compared using t-tests. Univariate analyses of categorical variables were compared using the chi-square test and Fisher's exact test. A multivariate logistic regression analysis incorporating all the parameters in the training cohort was performed to establish the MMUS prediction model. At the same time, The CUS model was developed to compare the value of the MMUS model. The ability of the MMUS and CUS models to identify malignant lymph nodes was assessed using the area under the receiver operating characteristic curves (ROC). The method of DeLong et al. was used to compare the area under curve (AUC). The Youden index was applied to determine the optimal cut-off point for the logistic regression model. All statistical analysis was performed using R 3.4.3 software package. $p<0.05$ was considered to be statistically significant.

3 Results

After applying the following inclusion and exclusion criteria, 169 enrolled patients were divided into a training set (132 patients) and a validation set (37 patients). The ultrasound characteristics of all patients in the training set were shown in Tables 2, 3. Of the 132 patients, 74 patients (male to female ratio 30:44; Mean age 42.7 ± 18.7 years) had benign lymph node lesions, 58 cases (male to female ratio 43:15; Mean age 59.5 ± 16.3 years) with malignant lymphadenopathy. There were significant differences in age and gender between the two groups ($p< 0.001$).

In univariate analysis, the following imaging characteristics showed significant associations with malignancy compared with benign lymphadenopathy: Length to short diameter ratio(L/S) ($p<0.001$), border($p=0.011$), margin($p=0.022$), hilus($p=0.002$), demarcation of the cortex and medulla ($p<0.001$), blood flow type ($p<0.001$), enhancement mode($p<0.001$), enhancement type ($p<0.001$), and RTE score ($p=0.024$).

In the multivariate logistic regression analysis performed on the training set, four variables remained as the independent predictors in the MMUS model: L/S(OR = 0.140; 95% CI, 0.047-0.423; $p<0.001$), mixed blood flow(OR = 20.220; 95% CI, 2.224-183.825;

TABLE 2 Pathological results of the enrolled lymph nodes.

Pathologies	Training set (n=132)	Validation set (n=37)
Benign lesions	74 (56.1%)	22(59.5%)
Reactive hyperplasia	38 (28.8%)	9(24.4%)
Tuberculosis of lymph node	24(18.2%)	8(21.6%)
Kikuchi disease	7(5.3%)	N/A
Cat scratch disease	2(1.5%)	1(2.7%)
Non-specific lymphadenitis	2(1.5%)	4(10.8%)
Sarcoidosis	1(0.7%)	N/A
Malignant lesions	58(43.9%)	15(40.5%)
Metastatic lymph node	43(32.6%)	13(35.1%)
Lymphoma	15(11.3%)	2(5.4%)

N/A, not available.

TABLE 3 Comparisons of multimodal ultrasound (MMUS) characteristic parameters of the cervical lymph nodes.

Characteristic		Diagnosis		χ2/t/Z value	P
		Benign	Malignant		
L/S		2.09 ± 0.56	1.72 ± 0.43	4.225	p<0.001
Border	Well defined	68 (91.9%)	44 (75.9%)	6.499	0.011
	Poorly defined	6 (8.1%)	14 (24.1%)		
Margin	Regular	67 (90.5%)	44 (75.9%)	5.237	0.022
	Irregular	7 (9.5%)	14 (24.1%)		
Fusion	No	60 (81.1)	45 (77.6%)	0.244	0.621
	Yes	14 (18.9%)	13 (22.4%)		
Hilus	Present	17 (23.0%)	2 (3.4%)	10.059	0.002
	Absent	57 (77.0%)	56 (96.6%)		
Demarcation of the cortex and medulla	Well defined	17 (23.0%)	1 (1.7%)	12.446	p<0.001
	Poorly defined	57 (77.0%)	57 (98.3%)		
Hyperechoic islands	Absent	71 (95.9%)	52 (89.7%)	2.025	0.155
	Present	3 (4.1%)	6 (10.3%)		
Anechoic area	Absent	69 (93.2%)	48 (82.8%)	3.549	0.06
	Present	5 (6.8%)	10 (17.2%)		
Calcification	Absent	69 (93.2%)	54 (93.1%)	5.019	0.061
	Gravel like	0 (0%)	3 (5.2%)		
	Non-gravel	5 (6.8%)	1 (1.7%)		
Blood flow type	Central	18 (24.3%)	1 (1.7%)	21.323	p<0.001
	Avascular or spot	21 (28.4%)	11 (19.0%)		
	Peripheral	14 (18.9%)	10 (17.2%)		
	Mixed	21 (28.4%)	36 (62.1%)		
Enhancement mode	Non-centrality	67 (94.3%)	33 (56.9%)	20.04	p<0.001
	Centripetal	7 (5.7%)	25 (43.1%)		
Enhancement type	Homogeneous	25 (33.8%)	8 (13.8%)	17.339	p<0.001
	Beehive or divider	19 (25.7%)	24 (41.4%)		
	Rim-like	15 (20.3%)	3 (5.2%)		
	Asynchronous	15 (20.3%)	23 (39.7%)		
RTE score (median (P25,P75))		3 (2,4)	3.5 (3,4)	2.256	0.024

p=0.008), centripetal enhancement mode (OR = 14.005; 95% CI, 3.711-52.858; p<0.001), rim-like enhancement type (OR = 0.124; 95% CI, 0.017-0.924; p = 0.042). Shown in Table 4. According to the regression coefficient, the prediction model with a statistical significance was constructed as follows:

$$\text{Logit}(p) = 0.597 - 1.963X1 + 3.007X2 + 2.693X3 - 2.086X4$$

X1 indicates L/S; X2 indicates blood flow type (other = 0; mixed =1); X3 indicates enhancement mode (other = 0; centripetal = 1); X4 indicates enhancement type (other = 0; rim-like =1).

The AUC of the MMUS model was 0.891 (95% CI: 0.835-0.947) in the training set and 0.957 (95% CI: 0.903-1) in the validation set, both demonstrating a good discrimination. By maximizing the Youden index, the optimal cut-off value of the MMUS model was identified and applied to obtain the measurements of sensitivity, specificity in the training set. 0.483 was determined as the optimal cut-off value for the MMUS model, and the sensitivity and specificity were 81.0% and 85.1%, respectively.

We also calculated the AUC of CUS model for the diagnosis of malignant lymph nodes. Regarding the CUS model, the AUC was

TABLE 4 Logistic regression analysis of relevant factor for cervical lymph nodes.

Characteristics		OR(95% CI)	p value
L/S		0.140(0.047-0.423)	p<0.001*
Blood flow type	Central		
	Avascular or spot	5.325(0.537-52.823)	0.153
	Peripheral	5.920(0.529-66.324)	0.149
	Mixed	20.220(2.224-183.825)	0.008*
Enhancement mode	Non-centrality		
	Centripetal	14.005(3.711-52.858)	p<0.001*
Enhancement type	Homogeneous		
	Beehive or divider	1.510(0.406-5.607)	0.538
	Rim-like	0.124(0.017-0.924)	0.042*
	Asynchronous	2.024(0.500-8.189)	0.323

*p<0.05.

0.763 (95% CI: 0.682-0.844) in the training set and 0.744 (95% CI: 0.582-0.905) in the validation set. The comparison of AUC demonstrated that the discriminative ability of the MMUS model was superior to using the CUS model, both in the training set($p = 0.004$) and validation set ($p<0.001$). Figures 3, 4 shows the ROC curve of the CUS model and the MMUS model in the training set and validation set.

4 Discussion

The overlap between benign and malignant lymph nodes, both in terms of clinical presentation and imaging features, makes the diagnosis of malignant lymph nodes difficult on ultrasound (4, 11). Previous studies have shown that CUS alone cannot accurately differential diagnosis benign and malignant lymph nodes, and CEUS can help improve the accuracy of ultrasound diagnosis (9). In this study, we established a MMUS model by logistic regression analysis and compared it with CUS model, which confirmed that MMUS has higher diagnostic efficacy than CUS, and also found that the addition of RTE did not help to identify the benignity and malignancy of lymph nodes.

Among characteristics of CUS, L/S and blood flow type are related factors in the diagnosis of malignant lymph nodes. In recent years, a large number of studies have proved that L/S is an ultrasound index for the diagnosis of malignant lymph nodes, and the smaller the value of L/S, the lower the possibility of malignant lymph nodes (12–15). In addition, mixed blood flow can also help to diagnose malignant lymph nodes (14, 16). Tumor cells infiltrate lymph nodes and produce tumor angiogenesis factor (TAF) inside lymph nodes, causing the proliferation of peripheral blood vessels (6, 17–19). Mixed blood flow can help diagnose malignant lymph nodes in the early stage. Since the lymphatic portal vessel are not invaded in the early stage, mixed blood flow can be seen in malignant lymph nodes, but such manifestations will disappear in the later stage due to the destruction of tumor cells (6). In this study, we did not find an association between avascular or spot flow, peripheral flow and malignant lymph nodes. The invasion of tumor cells into the internal vessels of lymph nodes can lead to increased blood flow resistance in lymph nodes (20). Because color Doppler ultrasound cannot show the tiny, slow-flowing sinusoid vessels in the lymph nodes, malignant lymph nodes may show avascular or spot blood flow (4). In addition, when the internal lymph node necrosis occurs, there will also be avascular or spot blood flow, peripheral blood flow and other manifestations.

In univariate analysis, there was no significant difference in the presentation of benign and malignant lymph nodes in terms of lymph node fusion, absence of echogenicity, hyperechoic islands, and calcification ($p > 0.05$). The presence of hyperechoic islands in

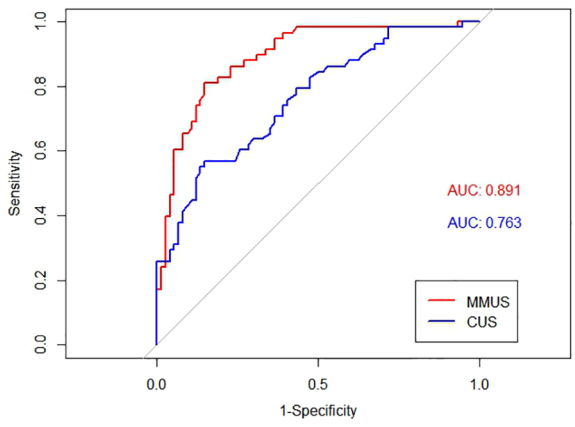

FIGURE 3
Receiver operating characteristic(ROC) curve alignment of multimodal ultrasound(MMUS) model and conventional ultrasound (CUS) model in the training set. The area under the curve(AUC) values of MMUS is 0.891, the area under the curve(AUC) values of CUS is 0.763.

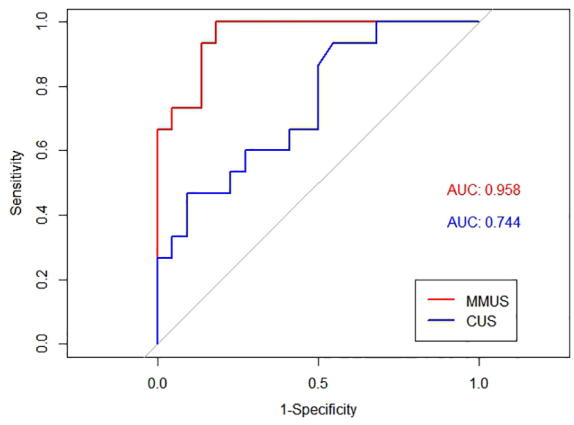

FIGURE 4
ROC curve alignment of MMUS model and CUS model in the validation set. AUC values of MMUS model is 0.958, AUC values of CUS model is 0.744.

lymph nodes has been shown to be specific for metastatic lymph nodes, with a specificity of 77.8% for differentiating lymph node metastases from benign lymph nodes (11, 16). However, hyperechoic islands are usually associated with papillary thyroid cancer metastases and their presence is uncommon in practice; only 7.2% (2/24) of metastatic lymph nodes in this study had hyperechoic islands in them (11).

CUS can help identify the benignity and malignancy of lymph nodes, but does not fully reflect the characteristics of malignant lymph nodes. Similarly, color Doppler flow imaging has limitations in detecting low-velocity blood flow and cannot fully assess the internal blood supply of lymph nodes. Compared with CUS, CEUS can detect tissue necrosis with higher sensitivity and show the internal blood perfusion of lymph nodes.

As qualitative characteristics of CEUS, both centripetal enhancement and rim-like enhancement can be used to differentially diagnose benign and malignant lymph nodes (9). Centripetal enhancement is an independent risk factor for the diagnosis of malignant lymph nodes. Pathological studies have shown that the vessels of normal lymph nodes enter by lymphatic portals and spread in all directions. In contrast, tumor cells reach the periphery of the lymph node through the afferent lymphatics, proliferate and generate new vessels (5, 6). Current studies suggest that the abnormal blood supply to malignant lymph nodes is responsible for the centripetal enhancement (16, 21). Circumferential enhancement as an independent protective factor for malignant lymph nodes is more commonly seen in benign lymph nodes. Perfusion defects are often associated with the development of necrosis within the lymph nodes, which occurs in both malignant and benign lymph nodes (9). The types of beehive, divider, and rim-like enhancement represent different stages of lymph node necrosis, and as the disease progresses the type of enhancement in the diseased lymph node changes from beehive to rim-like enhancement until the onset of rupture (22). In the present study, 62.5% (15/24) of lymph node nodules showed necrosis, which was higher than 34.8% (15/43) of metastatic lymph nodes, and no necrosis was seen in lymphomas. In addition to this, of the 18 lymph nodes with rim-like enhancement, only 3 were metastatic lymph nodes and the remaining 15 were benign lymph nodes (12 lymph node tuberculosis, 2 reactive lymph nodes and 1 cat-scratch disease). It has been shown that necrosis within benign lymphadenopathy is more pronounced than in malignant lymph nodes (23). For beehive or divider enhancement as well as asynchronous enhancement, we did not find a correlation between these signs and malignant lymph nodes in the present study ($p > 0.05$). It has been suggested that asynchronous enhancement may be associated with metastatic lymph nodes, where tumor cells reach the lymph nodes via lymphatic vessels and form confined tumor colonies causing the manifestation of heterogeneous enhancement in the lymph nodes, but related studies also found that the diagnostic sensitivity and specificity of asynchronous enhancement were unsatisfactory, 64.6% and 64.8%, respectively (16, 21). Therefore, the potential of asynchronous enhancement needs to be further evaluated.

Although the RTE scores of benign and malignant lymph nodes were significantly different in the univariate analysis, we found that the inclusion of RTE scores did not change the diagnostic efficacy of the multimodal ultrasound model. The RTE scores in diagnosing benign and malignant cervical lymph nodes was not significant (12). In our study, the mean RTE score for benign lymph nodes was 3 (median(2, 4)), which indicates that the overall stiffness of benign lymph nodes was stiff. The increased stiffness of malignant lymph nodes is thought to be the result of tumor cell infiltration and proliferation of mesenchymal cells (24). However, the hardness of lymph nodes also increases when calcification occurs in malignant lymph nodes and adhesions occur between the lesion and the surrounding tissue (25). Lymphomas tend to show low stiffness due to their homogeneous structure, which may produce false negative results (26, 27). Invasion of Mycobacterium tuberculosis into lymph nodes induces abnormal proliferation of lymphocytes, macrophages, and mesenchymal cells, forming granulomas. As the disease progresses, fibrosis, calcification, and adhesions to surrounding tissues occur, leading to increased lymph node stiffness (28, 29). Different depths of the lymph nodes also affect the stiffness values. Pressure and frequency perception of some deep lymph nodes (e.g., supraclavicular lymph nodes) will be affected due to signal attenuation (30). Therefore, RTE is not suitable for screening malignant lymph nodes in clinical practice.

This study has several limitations. First, the relatively limited sample size of this retrospective study resulted in too few positive cases for further analysis of features such as anechoic, hyperechoic, and strong echogenicity. Second, only some qualitative features in CUS, CEUS, and RTE were collected in this study. Qualitative parameters such as vascular flow velocity, vascular resistance index, peak attainment time of ultrasonography, peak intensity, and strain index in elastic ultrasound were not included in the study. Third, only patients with enlarged lymph nodes were included in this study, while patients with lymph nodes that did not exhibit enlargement did not participate in our study. Although the MMUS model has shown high accuracy in the validation set, more external studies are still needed to validate and support it. Prospective studies with larger sample sizes will be needed in the future to address the above issues.

5 Conclusion

MMUS, as an effective noninvasive adjunct in the evaluation of cervical lymphadenopathy, has high diagnostic efficacy in differentiating benign from malignant cervical lymph nodes and helps to avoid unnecessary biopsies. CEUS is extremely helpful in improving the sensitivity and specificity of ultrasound in the diagnosis of malignant lymph nodes. In contrast, RTE is of limited value in differentiating benign and malignant cervical lymph nodes.

Data availability statement

The original contributions presented in the study are included in the article/supplementary material. Further inquiries can be directed to the corresponding author.

Ethics statement

The studies involving human participants were reviewed and approved by the ethics committee of the Hangzhou Red Cross Hospital. The requirement for informed consent was therefore waived.

Author contributions

JHT was responsible for project administration, methodology, data creation, writing review, and editing. GYY, BPW, PJC, TL, YW, MHC, and YHY were responsible for case collection, data processing, and manuscript writing and revision. All authors contributed to and approved the submitted version of the manuscript.

Funding

This work was supported by Science and Technology Special Project of Hangzhou Biomedical and Health Industry Development Support (the Sixth Issue)(2022WJC046).

Acknowledgments

The authors thank the additional members of the Department of Ultrasound, Hangzhou Red Cross Hospital who helped with the enrollment and evaluation of participants. Special thanks to BPW, a senior sonographer with extensive experience, for his assistance in this study.

Conflict of interest

The authors declare that the research was conducted in the absence of any commercial or financial relationships that could be construed as a potential conflict of interest.

Publisher's note

All claims expressed in this article are solely those of the authors and do not necessarily represent those of their affiliated organizations, or those of the publisher, the editors and the reviewers. Any product that may be evaluated in this article, or claim that may be made by its manufacturer, is not guaranteed or endorsed by the publisher.

References

1. Ludwig BJ, Wang J, Nadgir RN, Saito N, Castro-Aragon I, Sakai O. Imaging of cervical lymphadenopathy in children and young adults. *AJR Am J Roentgenol* (2012) 199(5):1105–13. doi: 10.2214/AJR.12.8629

2. Pynnonen MA, Gillespie MB, Roman B, Rosenfeld RM, Tunkel DE, Bontempo L, et al. Clinical practice guideline: evaluation of the neck mass in adults. *Otolaryngol Head Neck Surg* (2017) 157(2_suppl):S1–S30. doi: 10.1177/0194599817722550

3. Junn JC, Soderlund KA, Glastonbury CM. Imaging of head and neck cancer with CT, MRI, and US. *Semin Nucl Med* (2021) 51(1):3–12. doi: 10.1053/j.semnuclmed.2020.07.005

4. Ryoo I, Suh S, You SH, Seol HY. Usefulness of microvascular ultrasonography in differentiating metastatic lymphadenopathy from tuberculous lymphadenitis. *Ultrasound Med Biol* (2016) 42(9):2189–95. doi: 10.1016/j.ultrasmedbio.2016.05.012

5. Ahuja A, Ying M. Sonographic evaluation of cervical lymphadenopathy: is power Doppler sonography routinely indicated? *Ultrasound Med Biol* (2003) 29(3):353–9. doi: 10.1016/s0301-5629(02)00759-7

6. Na DG, Lim HK, Byun HS, Kim HD, Ko YH, Baek JH. Differential diagnosis of cervical lymphadenopathy: usefulness of color Doppler sonography. *AJR Am J Roentgenol* (1997) 168(5):1311–6. doi: 10.2214/ajr.168.5.9129432

7. Onol S, Ozkaya O. Diagnostic value of real-time elastography in diagnosing lymph node metastasis of skin cancer. *Cureus* (2020) 12(10):e10997. doi: 10.7759/cureus.10997

8. Zhang Y, Yu T, Su D, Tang W, Yang G. Value of contrast-enhanced ultrasound in the ultrasound classification of cervical tuberculous lymphadenitis. *Front Med (Lausanne)* (2022) 9:898688. doi: 10.3389/fmed.2022.898688

9. Spiesecke P, Neumann K, Wakonig K, Lerchbaumer MH. Contrast-enhanced ultrasound (CEUS) in characterization of inconclusive cervical lymph nodes: a meta-analysis and systematic review. *Sci Rep* (2022) 12(1):7804. doi: 10.1038/s41598-022-11542-9

10. Zhang X, Wang L, Feng N, Ni T, Tang W. Reassessing the value of contrast-enhanced ultrasonography in differential diagnosis of cervical tuberculous lymphadenitis and lymph node metastasis of papillary thyroid carcinoma. *Front Oncol* (2021) 11:694449. doi: 10.3389/fonc.2021.694449

11. Tao L, Zhou W, Zhan W, Li W, Wang Y, Fan J. Preoperative prediction of cervical lymph node metastasis in papillary thyroid carcinoma *via* conventional and contrast-enhanced ultrasound. *J Ultrasound Med* (2020) 39(10):2071–80. doi: 10.1002/jum.15315

12. Cai D, Wu S. Efficacy of logistic regression model based on multiparametric ultrasound in assessment of cervical lymphadenopathy - a retrospective study. *Dentomaxillofac Radiol* (2022) 51(2):20210308. doi: 10.1259/dmfr.20210308

13. Dudea SM, Lenghel M, Botar-Jid C, Vasilescu D, Duma M. Ultrasonography of superficial lymph nodes: benign vs. *gnant Med Ultrason* (2012) 14(4):294–306.

14. Ahuja AT, Ying M, Ho SY, Antonio G, Lee YP, King AD, et al. Ultrasound of Malignant cervical lymph nodes. *Cancer Imag* (2008) 8(1):48–56. doi: 10.1102/1470-7330.2008.0006

15. Ryu KH, Lee KH, Ryu J, Baek HJ, Kim SJ, Jung HK, et al. Cervical lymph node imaging reporting and data system for ultrasound of cervical lymphadenopathy: A pilot study. *AJR Am J Roentgenol* (2016) 206(6):1286–91. doi: 10.2214/AJR.15.15381

16. Kim DW, Choo HJ, Lee YJ, Jung SJ, Eom JW, Ha TK. Sonographic features of cervical lymph nodes after thyroidectomy for papillary thyroid carcinoma. *J Ultrasound Med* (2013) 32(7):1173–80. doi: 10.7863/ultra.32.7.1173

17. Steinkamp HJ, Mäurer J, Cornehl M, Knöbber D, Hettwer H, Felix R. Recurrent cervical lymphadenopathy: differential diagnosis with color-duplex sonography. *Eur Arch Otorhinolaryngol* (1994) 251(7):404–9. doi: 10.1007/bf00181966

18. Ariji Y, Kimura Y, Hayashi N, Onitsuka T, Yonetsu K, Hayashi K, et al. Power Doppler sonography of cervical lymph nodes in patients with head and neck cancer. *AJNR Am J Neuroradiol* (1998) 19(2):303–7.

19. Wu CH, Chang YL, Hsu WC, Ko JY, Sheen TS, Hsieh FJ. Usefulness of Doppler spectral analysis and power Doppler sonography in the differentiation of cervical lymphadenopathies. *AJR Am J Roentgenol* (1998) 171(2):503–9. doi: 10.2214/ajr.171.2.9694484

20. Ho SS, Metreweli C, Ahuja AT. Does anybody know how we should measure Doppler parameters in lymph nodes? *Clin Radiol* (2001) 56(2):124–6. doi: 10.1053/crad.2000.0588

21. Hong YR, Luo ZY, Mo GQ, Wang P, Ye Q, Huang PT. Role of contrast-enhanced ultrasound in the pre-operative diagnosis of cervical lymph node metastasis in patients with papillary thyroid carcinoma. *Ultrasound Med Biol* (2017) 43(11):2567–75. doi: 10.1016/j.ultrasmedbio.2017.07.010

22. Schor AM, Schor SL. Tumour angiogenesis. *J Pathol* (1983) 141(3):385–413. doi: 10.1002/path.1711410315

23. Lo WC, Chang WC, Lin YC, Hsu YP, Liao LJ. Ultrasonographic differentiation between Kikuchi's disease and lymphoma in patients with cervical lymphadenopathy. *Eur J Radiol* (2012) 81(8):1817–20. doi: 10.1016/j.ejrad.2011.04.030

24. Suh CH, Choi YJ, Baek JH, Lee JH. The diagnostic performance of shear wave elastography for Malignant cervical lymph nodes: A systematic review and meta-analysis. *Eur Radiol* (2017) 27(1):222–30. doi: 10.1007/s00330-016-4378-3

25. You J, Chen J, Xiang F, Song Y, Khamis S, Lu C, et al. The value of quantitative shear wave elastography in differentiating the cervical lymph nodes in patients with thyroid nodules. *J Med Ultrason (2001)* (2018) 45(2):251–9. doi: 10.1007/s10396-017-0819-0

26. Tan R, Xiao Y, He Q. Ultrasound elastography: Its potential role in assessment of cervical lymphadenopathy. *Acad Radiol* (2010) 17(7):849–55. doi: 10.1016/j.acra.2010.03.014

27. Ahuja A, Ying M. Sonography of neck lymph nodes. Part II: abnormal lymph nodes. *Clin Radiol* (2003) 58(5):359–66. doi: 10.1016/s0009-9260(02)00585-8

28. Ganchua SKC, White AG, Klein EC, Flynn JL. Lymph nodes-The neglected battlefield in tuberculosis. *PloS Pathog* (2020) 16(8):e1008632. doi: 10.1371/journal.ppat.1008632

29. Nyman HT, O'Brien RT. The sonographic evaluation of lymph nodes. *Clin Tech Small Anim Pract* (2007) 22(3):128–37. doi: 10.1053/j.ctsap.2007.05.007

30. Ying L, Hou Y, Zheng HM, Lin X, Xie ZL, Hu YP. Real-time elastography for the differentiation of benign and Malignant superficial lymph nodes: a meta-analysis. *Eur J Radiol* (2012) 81(10):2576–84. doi: 10.1016/j.ejrad.2011.10.026

frontiers | Frontiers in Oncology

TYPE Original Research
PUBLISHED 08 February 2024
DOI 10.3389/fonc.2024.1002798

OPEN ACCESS

EDITED BY
Jan Baptist Vermorken,
University of Antwerp, Belgium

REVIEWED BY
Mojgan Alaeddini,
Tehran University of Medical Sciences, Tehran, Iran
Pierre Busson,
Centre National de la Recherche Scientifique (CNRS), France

*CORRESPONDENCE
Magdalena Stocker
ma.stocker@salk.at

†These authors have contributed equally to this work

‡These authors have contributed equally to this work and share senior authorship

RECEIVED 25 July 2022
ACCEPTED 22 January 2024
PUBLISHED 08 February 2024

CITATION
Stocker M, Blancke Soares A, Liebsch G, Meier RJ, Canis M, Gires O and Haubner F (2024) Quantification of oxygen consumption in head and neck cancer using fluorescent sensor foil technology.
Front. Oncol. 14:1002798.
doi: 10.3389/fonc.2024.1002798

Quantification of oxygen consumption in head and neck cancer using fluorescent sensor foil technology

Magdalena Stocker[1*†], Alexandra Blancke Soares[1†], Gregor Liebsch[2], Robert J. Meier[2], Martin Canis[1], Olivier Gires[1‡] and Frank Haubner[1‡]

[1]Department of Otorhinolaryngology, Head and Neck Surgery, University Hospital, Ludwig Maximilians University (LMU) Munich, Munich, Germany, [2]PreSens Precision Sensing GmbH, Imaging Solutions, Regensburg, Germany

Introduction: Head and neck squamous cell carcinoma (HNSCC) patients suffer from frequent local recurrences that negatively impact on prognosis. Hence, distinguishing tumor and normal tissue is of clinical importance as it may improve the detection of residual tumor tissue in surgical resection margins and during imaging-based surgery planning. Differences in O_2 consumption (OC) can be used to this aim, as they provide options for improved surgical, image-guided approaches.

Methods: In the present study, the potential of a fluorescent sensor foil-based technology to quantify OC in HNSCC was evaluated in an *in vitro* 3D model and in situ in patients.

Results: *In vitro* measurements of OC using hypopharyngeal and esophageal cell lines allowed a specific detection of tumor cell spheroids embedded together with cancer-associated fibroblasts in type I collagen extracellular matrix down to a diameter of 440 µm. Pre-surgery in situ measurements were conducted with a handheld recording device and sensor foils with an oxygen permeable membrane and immobilized O_2-reactive fluorescent dyes. Lateral tongue carcinoma and carcinoma of the floor of the mouth were chosen for analysis owing to their facilitated accessibility. OC was evaluated over a time span of 60 seconds and was significantly higher in tumor tissue compared to healthy mucosa in the vicinity of the tumor.

Discussion: Hence, OC quantification using fluorescent sensor foil-based technology is a relevant parameter for the differentiation of tumor tissue of the head and neck region and may support surgery planning.

KEYWORDS

tumor hypoxia, HNSCC, tumor imaging, head and neck cancer, oxygen consumption

Abbreviations: OC, oxygen consumption rate; HNSCC, head and neck squamous cell carcinoma; HIFs, hypoxia inducible factors; GATA3, GATA binding protein 3; DDB2, damaged DNA binding protein; region of interest, ROI; TME, tumor microenvironment.

1 Introduction

Standard treatment of head and neck tumors is based on surgical therapy with adjuvant radio (chemo) therapy, if necessary (1–3). The prerequisite for surgical treatment is the resectability of the tumor in the absence of distant metastases, as cases staged M1 are preferably subjected to systemic treatment. In the context of surgical resection, complete removal of tumor tissue, typically with a minimum resection margin of 5 mm, is of considerable prognostic importance (4–6). Complete removal of the tumor is currently based on intraoperative evaluation by the surgeon and histopathological assessment of frozen sections taken intraoperatively. The assessment of the extent of resection is thus dependent on the experience of the respective surgeons and pathologists. Despite an assessment as R0 in the final histological report of intraoperative frozen sections (*in sano*, no residual tumor cells detectable), minimal residual disease (MRD) must be assumed based on the frequency of local relapses (7). Even in the case of an R0 resection, 10-30% of patients will be diagnosed with a local recurrence within less than three years after treatment. Therefore, additional tools for the assessment of resection margins are in great demand, which could help identifying residual tumor cell depositions in R0-resections and potentially prevent local recurrences (8). Additionally, taking tissue samples from the correct regions for frozen section diagnosis is also dependent on the expertise of the surgeon. An objectifiable imaging method that indicates possible residual tumor tissue *in situ* intraoperatively could result in a considerable facilitation in the decision of the extent of resection and thus in optimized therapy for the patient with a presumably better prognosis. This refers to both, a sufficient tumor resection and to an avoidance of unnecessarily large resection margins with the ensuing increase in morbidity.

Several aspects of tumor biology have been assessed as sources of markers to improve resection margin recognition. These include the antibody-mediated detection of tumor-associated antigens such as the epidermal growth factor receptor EGFR and the epithelial cell adhesion molecule EpCAM in combination with near-infrared dyes (9, 10). Confocal laser endomicroscopy, second and third harmonic generation, Raman spectroscopy, and other technologies are under evaluation to address differences in morphology and collagen distribution between normal and malignant tissue (11). Endomicroscopic methods can be combined with 5-aminolevulinic acid (5-ALA)-induced protoporphyrin IX (PPIX) fluorescence, which accumulates more strongly in tumors (12). A meta-analysis of the sensitivity and specificity of various methods of non-invasive imaging methods for oral cancers has been summarized recently by Mendonca et al. (13).

Alternatively, metabolic changes in malignant cells may be harnessed to differentiate normal and tumor areas. From the 1920's on, the Warburg effect has been widely discussed as a major driving force in tumor initiation and progression. Tumor cells use aerobic glycolysis for ATP generation, despite the availability of oxygen and thus of the more efficient energy supply through mitochondrial oxidative phosphorylation (OXPHOS) (14). The Warburg effect is still to date of great interest to better understand tumor metabolism (15, 16). The description of the Warburg effect led over time to the deduction that mitochondria and OXPHOS play an inferior if any role in the energy consumption of tumor cells (17). It must however be noted that numerous malignancies with strongly proliferating cells are characterized by a high O_2 consumption (OC), including HNSCC (18–20). Reports on an association of the OXPHOS pathway with a gene signature of recurrent oral squamous cell carcinoma (OSCC) support an important function of the OC in head and neck tumor and their progression (21). Consequently, genes associated with aerobic glycolysis and OXPHOS are both found up-regulated in malignant HNSCC cells with differences between classical and human papillomavirus (HPV)-associated tumors (19, 22).

High OC and insufficient re-oxygenation via a frequently leaky and poorly structured intratumoral neo-vasculature eventually result in oxygen depletion in tumor and surrounding tissues. This process enhances hypoxia along with the induction of transcription factors such as hypoxia inducible factors (HIFs) and the activation of signaling pathways. Hypoxia-related pathways impact numerous cellular functions such as apoptosis, necrosis, angiogenesis, the metastatic cascade via induction of epithelial-to-mesenchymal transition (EMT), and others (23–26). The knowledge of hypoxia markers has been used to assess surgical resection margins. Adjacent dysplastic tissue of HNSCC has shown an overexpression of hypoxia marker carbonic anhydrase 9 (CA IX), indicating high OC and insufficient O_2 replenishment not only in the tumor tissue itself, but also in dysplastically altered surrounding tissue (27). High-grade dysplasia often occurs in peritumoral areas of HNSCC in the sense of field cancerization. Even though not yet invasively growing, these dysplasia need to be completely surgically removed due to the risk of the development of malignancy (28, 29). The fact that not only intratumoral, but also dysplastically altered peritumoral areas show signs of high OC and resulting hypoxia underlines the importance of adequate resection margins and the relevance of OC as a tool to optimize tumor margin recognition. Even though methods like immunohistology can provide relevant information on the tumor and its surroundings, *i.e.* the tumor microenvironment (TME), these methods are invasive to the tissue and require time-consuming preparations of the respective tissue. Non-invasively evaluating tissue oxygenation and OC via methods like fluorescent sensor foil technology could therefore bring further benefits to tumor diagnostics.

From the perspective of clinical management of patients with solid tumors, hypoxia resulting from high OC and poor re-oxygenation is recognized as a negative factor regarding therapeutical options. Particularly with respect to poor response to radiotherapy, hypoxia in tumor tissue has been the subject of previous and current research (30, 31). Hypoxia in tumor tissue is associated with poorer overall survival and poorer locoregional recurrence control, among others in HNSCC (32).

Similarly, the presence of a small safety margin during tumor resection, *i.e.* removal of the tumor with little surrounding healthy tissue, is associated with poorer overall survival. Such so-called "close margins" are usually defined as a resection margin of less than five millimeters (8). Ettl et al. described a 5-year overall survival in patients with head and neck tumors of 78% with a resection margin greater than five millimeters, but of only 51.7% when the resection margin was less than five millimeters (8). It is

therefore of utmost importance to be able to clearly define the boundary between tumor and healthy tissue, preferably already intraoperatively.

The aim of the present study was to establish a high-resolution measurement of OC in HNSCC patients using a fluorescent sensor foil technology. This technology has been used to assess oxygen content in chronic wounds (33). Furthermore, it has been used to monitor the perfusion of free flaps after reconstructive surgery (34). The focus of this project was a time-dependent, comparative evaluation of oxygen consumption in macroscopically normal and malignant tissue. Therefore, following a feasibility assessment in a 3D co-culture model of carcinoma cells and fibroblasts isolated from the periphery of HNSCCs, proof-of-concept measurements of OC were conducted *in situ* in six HNSCC patients.

2 Materials and methods

2.1 Cell lines and cell culture

FaDu (hypopharyngeal carcinoma) and Kyse30 cells (esophageal squamous cell carcinoma) used in this study were purchased from DSMZ (Braunschweig, Germany). Peritumoral fibroblasts (PtFs) were isolated from HNSCC patient biopsies from mucosa macroscopically free of cancer (35).

To create red fluorescent FaDu and Kyse30 cells, parental cells were transfected with the pCAG-ef1-mCherry plasmid and stable cell lines were created by drug selection with 1 µg/ml puromycin.

Cells were grown in T25 or T27 cell culture treated flasks (Sarstedt AG, Nümbrecht, Germany) in an incubator at 37°C, 5% CO_2 and 100% humidity, and passaged 1:5 to 1:20 (FaDu, Kyse30) or 1:4 (NF8) two to three times weekly. Kyse30 cells were grown in RPMI 1640 with L-Glutamine (Gibco, Dublin, Ireland) supplemented with 10% FCS and 1% Penicillin/Streptomycin (final concentration: 100 µg/ml, Gibco, Dublin, Ireland). For FaDu cells, DMEM (Gibco, Dublin, Ireland) supplemented with 10% FCS (FBS Superior, Sigma Aldrich, St.Louis, USA) and 1% Penicillin/Streptomycin (final concentration: 100 µg/ml, Gibco, Dublin, Ireland) was used. NF8 cells were grown in Fibroblast Growth Medium 2 (FGM-2) (C-23220, PromoCell, Heidelberg, Germany) supplemented with Supplement Mix 2 (C-39325, PromoCell).

2.2 3D co-culture model

Spheroids from red fluorescent FaDu and Kyse30 cells were generated by seeding 1000-20.000 cells per well into BIOFLOAT 96-well U-bottom plates (F202003, faCellitate, Mannheim, Germany) and leaving the spheroids to form over 72 hours. Next, spheroids were embedded into a type I collagen matrix. First a layer of 250 µl type I collagen (diluted to 1.5 mg/ml in imaging medium (RPMI w/o phenol-red, 10% FBS, 1% Penicillin/Streptomycin), and 0.5% 1M NaOH) was pipetted into the inner well of an ibidi 35mm glass bottom dish (81218-200, Ibidi GmbH, Gräfelfing, Germany) and allowed to form a gel at 37°C for 30 minutes. Two to five spheroids were carefully placed on top of the collagen layer and covered with 200 µl type I collagen at 1.5 mg/ml mixed with $2x10^5$ NF8 cells. After one hour at 37°C, 1.5 ml FGM was added, and the matrix-embedded co-culture was incubated over night at 37°C and 5% CO_2.

For generating z-stacks of type I matrix-embedded spheroids, 10 µg/ml fluorescein (F6377, Sigma-Aldrich, St. Louis) was added to the 1.5 mg/ml collagen I solution. Z-stacks were acquired using the z-stack function of the LASX software and a Leica SP8 confocal laser scanning microscope using a 10x objective and the 488 nm laser for excitation of fluorescein and a 540 nm laser for excitation of mCherry.

2.3 *In vitro* OC measurements

Before OC measurement, FGM was replaced with 1.5 ml of above-mentioned imaging medium. Measurements were performed using the STOp-Q method, as described previously (36), including the VisiSens TD Mic (PreSens Precision Sensing Technology GmbH, Regensburg, Germany) readout unit for microscopic O2 imaging. Ibidi dishes containing the spheroids embedded in type I collagen and NF8 cells were inserted into 6-well plates to fit into the imaging apparatus. Microscopic images over the entire area containing the spheroids and collagen/cell matrix were acquired using the tile scan function of the LASX software and a Leica DMi8 widefield fluorescence microscope (Leica, Wetzlar, Germany). Images were acquired with a 5x objective in the TXR channel (Excitation: 560/40, Emission: 639/75) and phase contrast. After a one-hour equilibration at 37°C in the incubator containing the STOp-Q device, measurements were performed in 10 second intervals for one hour using an exposure time of 150 ms (Figure 1).

2.4 Software, data analysis and statistics

Oxygen heatmaps for the *in vitro* measurements were exported from the VisiSens VS software after noise correction, which is conducted using a gaussian blur image filter with a kernel box size of 3*3 pixels on the processed delayered RGB image, and a 2*2 pixel software binning on the overall analyte image.

Microscopic images were processed by adjusting brightness/contrast, size and adding scale bars using Fiji ("FIJI Is Just ImageJ") (37). Figures were generated using Inkscape (www.inkscape.org).

2.5 *In vivo* measurements

OC was measured *in vivo* in tumors of the head and neck area and macroscopically healthy tissue of patients that were treated at the department of otorhinolaryngology of the university hospital of LMU Munich. Six patients diagnosed with tumors of the head and neck area, four males and two females, were enrolled in this proof-of-concept study. Three patients suffered from lateral tongue carcinoma and three patients from carcinoma of the floor of the mouth. For detailed clinical and demographic parameters of all patients see Table 1. All examined tumors were HPV-negative tumors with a T-status ranging from T1 to T4. As a common risk factor, all patients

10.3389/fonc.2024.1002798

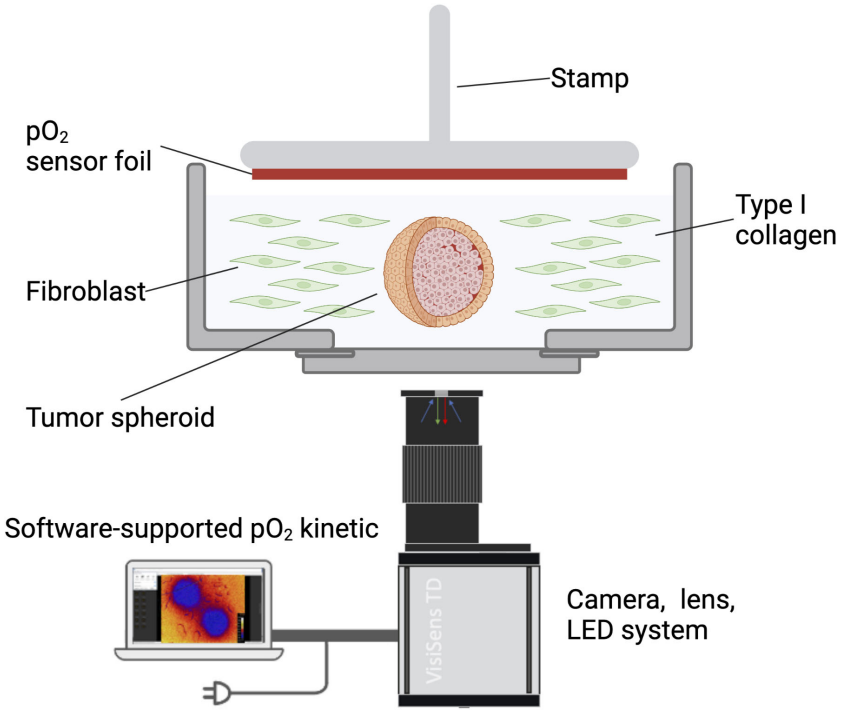

FIGURE 1
Schematic representation of the *in vitro* 3D model. Tumor cell spheroids were embedded in type I collagen containing HNSCC patient-derived fibroblasts. Oxygen consumption was measured with a sensor foil and an LED/camera system and recorded using the VisiSens software.

smoked cigarettes and four of the six included patients drank alcohol daily. Two patients suffered from secondary carcinoma and had already undergone surgical tumor resection and adjuvant radiochemotherapy several years before. The macroscopically normal mucosa that was measured in conjunction with tumor areas for each patient were located several centimeters apart from the tumor areas. With measurements of lateral tongue carcinoma for example, normal mucosa was measured from the opposite side of the

TABLE 1 Patient profiles, clinical characteristics of patients included into the study (n=6).

Patient	Age	Sex	Tumor type	TNM	Therapy	Risk factors	HPV status	Additional information
1	78	f	lateral tongue carcinoma	pT1 pN0 L0 V0 Pn0 M0 R0 G2	transoral tumor resection, ipsilateral neck dissection	nicotine	negative	
2	58	m	lateral tongue carcinoma	pT2 pN0 L0 V0 Pn1 M0 R0 G3	transoral tumor resection, ipsilateral neck dissection	alcohol, nicotine	negative	
3	65	m	floor of mouth carcinoma	cT4 cN0 M0 G3 with infiltration of mandible	systemic therapy (pembrolizumab)	alcohol, nicotine	negative	oropharyngeal carcinoma 2011, pT3 pN0 M0 G2 R0, tumor resection, bilateral neck dissection, tracheostomy, radial flap, adjuvant radiochemotherapy
4	65	f	floor of mouth carcinoma	pT1 pN0 L0 V0 Pn0 M0 R0 G2	transoral tumor resection, bilateral neck dissection, tracheostomy	alcohol, nicotine	negative	
5	56	m	floor of mouth carcinoma	pT2 pN0 L0 V0 Pn0 M0 R0 G2	transoral tumor resection, bilateral neck dissection, tracheostomy	alcohol, nicotine	negative	
6	62	m	lateral tongue carcinoma	pT3 pN0 L0 V0 Pn0 M0 R0 G2	transoral tumor resection, bilateral neck dissection, tracheostomy, radial flap	nicotine	negative	oropharyngeal carcinoma 2013, pT1 pN2b L1 V0 M0 G3 R0, tumor resection, bilateral neck dissection, adjuvant radiochemotherapy

f, female; m, male.

tongue. With measurements from the floor of the mouth, normal mucosa was measured either from a macroscopically healthy area from the floor of the mouth or – if the tumor consumed a large part of the floor of the mouth – from parts of the tongue.

Measurements were performed either in an intraoperative setting before tumor biopsy/resection or preoperatively. All measurements were performed after detailed patient information and verbal and written consent of the patients. The project was in accordance with the ethical standards of the institutional ethics committee of the Medical faculty of the LMU Munich (project 20-244) and with the 1964 Helsinki declaration and its later amendments or comparable ethical standards.

Luminescence imaging of oxygen was performed with the VisiSens 2D imaging System A1 (PreSens Precision Sensing Technology GmbH, Regensburg, Germany). The imaging setup including samples, sensor foil, and camera/lens is schematically depicted in results section. A handheld device to record the datasets and sensor foils for measuring oxygen consumption were used. The sensor foils were cut in adequate size and shape with sterile scissors (Fuhrmann GmbH, Bövingen 139, Munich, Germany), to fit on the respective regions of interest (tumor and healthy tissue). Data recording and evaluation was performed via the VisiSens AnalytiCal software (PreSens, Regensburg, Germany) provided with the systems.

3 Results

3.1 Discrimination of cancer cell spheroids and fibroblasts in a 3D *in vitro* co-culture model

In a comparison of esophageal and HNSCC cell lines comprising Kyse30, FaDu, Cal27, and Cal33, Kyse30 and FaDu showed the highest oxygen consumption rates (OCR) using the STOp-Q technology. Furthermore, high OCR for these two cell lines were confirmed using the Seahorse technology and were significantly higher than primary human nasal epithelial cells that served as normal controls (36). We opted for these two cell lines to provide optimal measurement conditions and thus allow for the highest sensitivity in the present 3D reconstruction model (Figure 1).

PtFs were used in the present model to incorporate peritumoral fibroblasts as a major cell type of non-malignant stromal cells and thereby mimic closely the situation *in vivo*. Tumor spheroids were visualized based on the constitutive expression of mCherry fluorescent protein following stable transfection (Figures 2A, B). To measure the thickness of the collagen matrix and the localization of tumor cell spheroids, the matrix was stained using fluorescein and z-stacks were acquired by confocal laser scanning microscopy. The total thickness of the matrix was approximately 2.5 mm, and the distance from the spheroid to the surface of the matrix was approximately 1.5 mm (Figure 2A, left panels).

Oxygen measurements were performed over a time period of one hour in ten second intervals and with an exposure time of 150 ms using the STOp-Q technology (36). Oxygen heatmaps depicted in Figure 2B represent the oxygen concentration after 5 minutes and 30 minutes of measurement, respectively. FaDu cell spheroids embedded in type I collagen and PtF matrix were detected down to a diameter of 440 µm within 5 minutes of measurement. Smaller spheroids were not detected even after 30 minutes of measurement (Figure 2B; Figure S1). Under identical conditions, Kyse30 cell spheroids with a minimum diameter of 630 µm were detected after five minutes of measurement (Figure 2B; Figure S2). After 30 minutes also spheroids with a diameter of 440 µm were identified based on OC measurements (Figure S2).

In summary, STOp-Q-based OC measurements allowed the spatial discrimination of tumor cell spheroids from surrounding stromal fibroblasts in ECM. Hence, 3D tumor cell depositions in the sub-millimeter range were detected based on their oxygen consumption and could be distinguished from fibroblasts in a type I collagen-based matrix.

3.2 *In situ* OC measurement of tumor tissue and healthy mucosa in HNSCC patients

Measurement of OC was performed as described in detail in the Materials and Methods section for n = 6 HNSCC patients. The sensor foil placed on the sample surface contains a red fluorescent oxygen indicator dye, a stable green reference fluorescent dye, embedded in an oxygen-permeable and transparent membrane. The red indicator fluorescence decreases with increasing oxygen content, whereas the green fluorescence remains stable regardless of changes in oxygen content and serves as reference. The red-to-green fluorescence signal ratio informs about the oxygen content of tissue and in time dependence also about the OC. The detector unit is a small handheld USB-powered camera system with incorporated excitation LEDs and fluorescence filters. The excitation LEDs illuminate the respective sensor foil with blue light and excite the luminophores that are enclosed in the sensitive layer of the foil. Optical filters separate excitation and emission light. The sensor foils emit red and green signals (indicator signal and reference signal, respectively), which are collected in the wavelength-separated red and green channels of the RGB camera detector and stored in a RGB color image (Figures 3A, B).

Sensor foils were carefully applied to the regions of interest of all six HNSCC patients without pressure to avoid tissue hypoxia due to external application of pressure onto the tissue, but firmly enough to avoid fresh air – and with that, ambient oxygen – to reach the sensor foils while measuring. With such a setup, the camera creates an airtight seal, so that only the tissue oxygen consumption is measured without any replenishment from the surrounding oxygen. Due to the uneven surface of tumor tissue with possible exulcerations, the adhesion of the sensor foils and the contact of the handheld device with the sensor foils and the tissue underneath can be more difficult than with evenly flat mucosa. This might alter the measurements due to difficulties in creating an airtight seal. Therefore, areas where proper adhesion of the sensor foils was impossible were excluded from the measurements. *In situ* measurements were performed in three second intervals with a

10.3389/fonc.2024.1002798

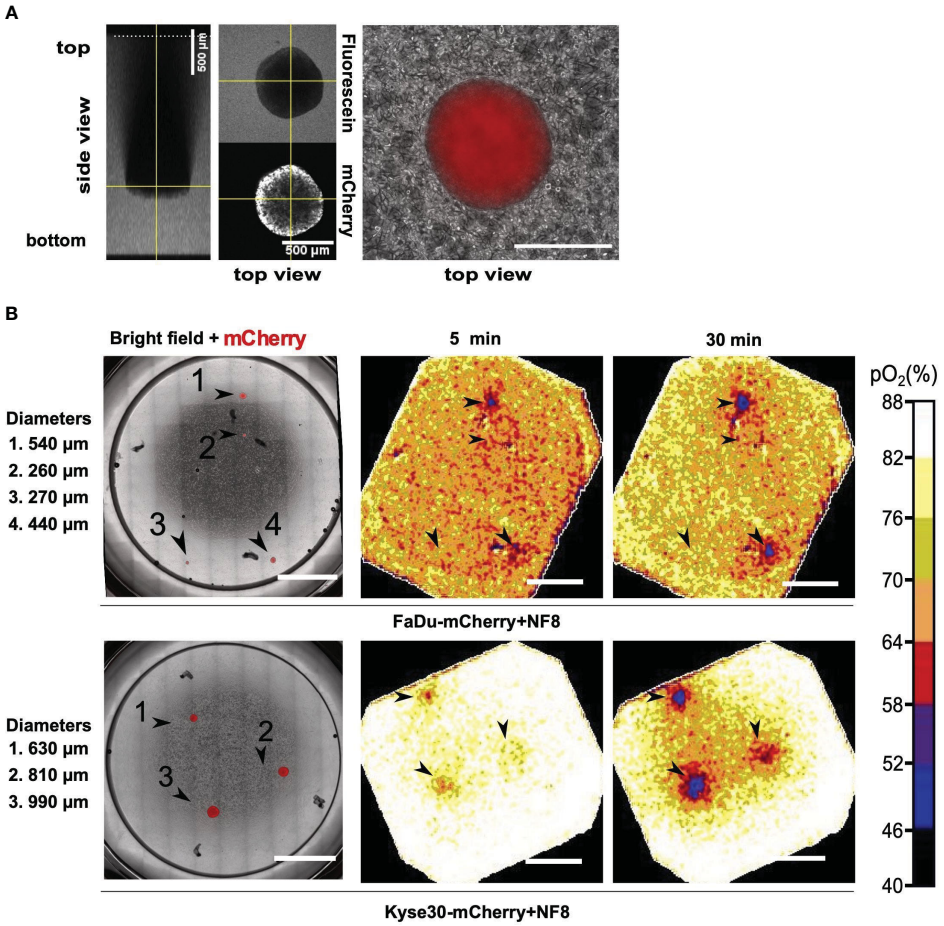

FIGURE 2
Oxygen consumption measurements in a 3D *in vitro* tumor model. **(A)** Z-stack of a FaDu mCherry expressing spheroid in a fluorescein labelled collagen I matrix. Left image represents side view, central and right images represent top view. Overlay of mCherry signal and phase contrast of a Kyse30 mCherry expressing spheroid within a collagen I and fibroblast (NF8) matrix are shown in the right panel. **(B)** Overlay of mCherry signal and phase contrast of FaDu/Kyse30 mCherry expressing spheroids within a collagen I and NF8 matrix. Spheroid diameters are indicated on the left (left panels). Oxygen heatmaps of the area shown in the microscopic images after 5 and 30 minutes of oxygen measurement (middle and right panels). Data of FaDu cells are depicted in the top row, data for Kyse30 cells in the bottom row. Arrowheads indicate the location of spheroids. Scale bars: 5 mm. Color bar indicating oxygen concentrations are shown on the right. Shown are representative images of n = 3 independent experiments performed with multiple spheroids for each cell line.

maximum measurement time of two minutes. Data recording and evaluation was performed via the VisiSens analytical software (PreSens, Regensburg, Germany) provided with the system.

The detector was placed on the O_2 sensor foil, which was applied on the area of interest (*i.e.*, normal mucosa or carcinoma areas). OC were measured in tumor and macroscopically normal mucosa of the tongue or floor of the mouth in all six patients. Figure 3D shows a representative picture of an *in situ* measurement of mucosa of the lateral tongue with the sensor foil and detecting camera. Oxygen heatmaps depicted in Figure 3C represent the oxygen consumption of healthy mucosa (upper panel) and tumor (lower panel) in one exemplary measurement of one of the six measured patients in this study. Heatmaps start with bright yellow colors, indicating a high oxygen content in the tissue. The darker the color of the heatmaps develop, the lower the oxygen content in the tissue gets over time, with deep blue colors at the end of the measurement indicating the lowest oxygen content of the measurement over time.

Quantified OC of tumor and healthy tissues were plotted against time and standardized to the initial O_2 percentage (Figure 4). Both, healthy mucosa, and tumor areas showed a measurable consumption of oxygen within the time frame of the assessment. Oxygen partial pressure levels in normal mucosa gradually decreased over time and reached values below 5% air saturation (7.46 torr) after approx. 48 seconds on average. Oxygen levels in tumor areas dropped sharply to levels below 5% air saturation within 15 seconds of measurement on average and stayed at this low level throughout the remaining measurement time. Differences of OC between healthy mucosa and tumor areas were analyzed for statistical significance with a two-sample t-test assuming different variances. With a p-value of 0,01168221 at a time point of 15 seconds into the measurement and a p-value of 0,01623259 at a time point of 30 seconds into the measurement, the differences between OC in tumor tissue versus healthy tissue were significant. 60 seconds into the measurement, most of the readings leveled off, so that a stable oxygen partial

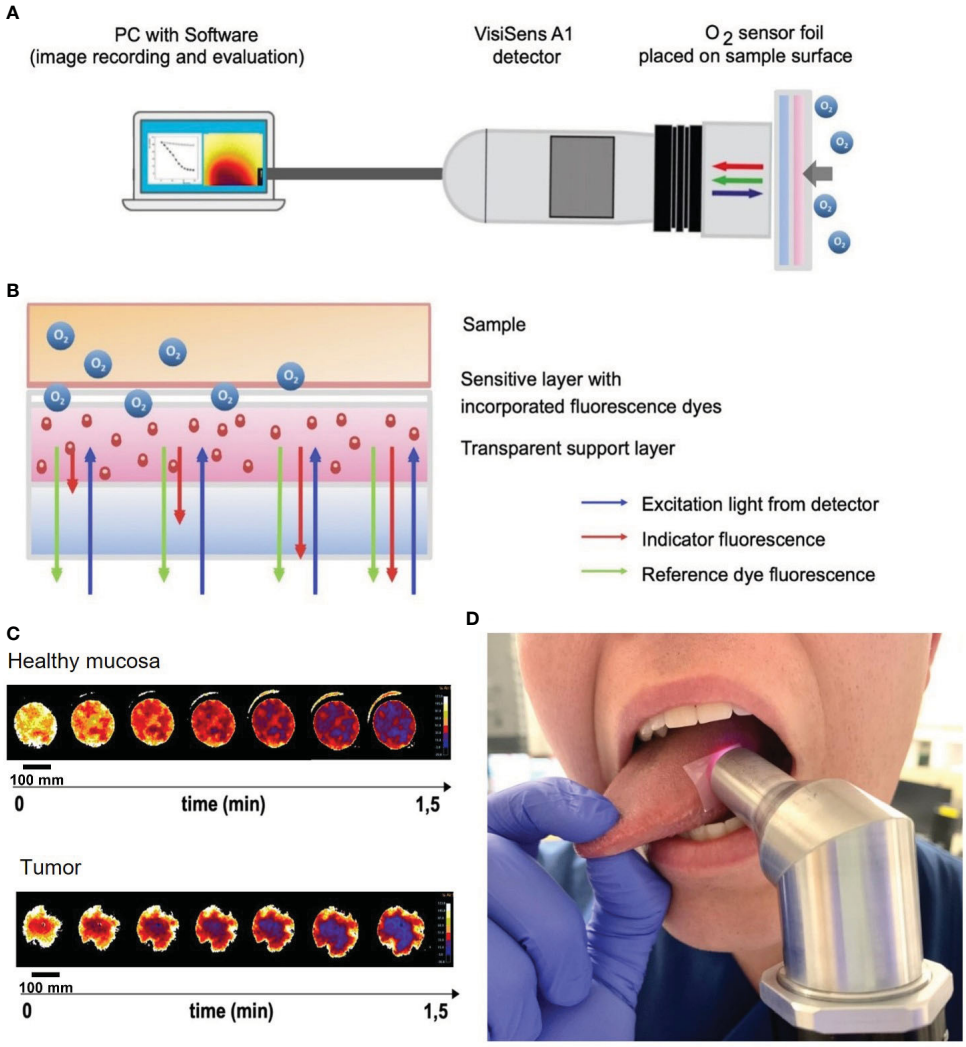

FIGURE 3
Oxygen consumption rate measurements *in situ* on HNSCC of the tongue and mouth. **(A)** Schematic of the VisiSens A1 detector camera connected to a laptop with the VisiSense software for image recording and evaluation. The handheld camera records the oxygen consumption rate measured by the sensor foil that is placed on the tissue (tumor and healthy mucosa). **(B)** Schematic of the measurement principle of the used sensor foils. The foil has two components: a sensitive layer with incorporated fluorescence dyes and a transparent support layer. The foil is placed on the tissue with the sensitive layer facing the tissue. Tissue oxygen and with it the OC are detected by a shift in the indicator fluorescence signal of the sensor foil. The reference dye fluorescence signal emits a steady signal. The excitation light derives from the detector camera. **(C)** Heatmaps of oxygen consumption of a representative patient showing measurements of healthy mucosa (upper image) and tumor (lower image). Note, that peripheral areas with continuously high O_2 values are a result of fresh oxygen at the border of the handheld camera entering via the air and have been excluded from the measurements. Scale bars: 100 mm. **(D)** Example of *in situ* measurement of mucosa of the lateral tongue with the sensor foil and detecting camera.

pressure value was reached. Interestingly, at this time point, all oxygen consumption values had reached almost 100% for carcinomas, whereas values for normal mucosa as low as < 50% were observed in patient #1 (Figure 4). Of note, measurements of the two patients that had suffered from secondary carcinoma and had undergone adjuvant radiochemotherapy several years back showed the lowest OC at t15 in tumor tissue (patients 2 and 6), but not in healthy tissue. In accordance with all other measurements of tumor though, these two measurements eventually leveled off at 100% OC after 60 seconds, too. Hence, these relevant differences can only be seen early into the measurements. Not all measurements started at 100% O_2 saturation. However, the intra-individual measurements of each patient showed repeatedly steady starting points of O_2 saturation, be it at 100% or below. In addition, the measurements of tumor and healthy tissue in each patient had similar saturation starting points. We believe that the differences in starting O_2 saturation has to do with external factors like the patients' body temperature and others. To demonstrate the temporal reproducibility of the measurements, we performed measurements of healthy mucosa in one volunteer at different time points (t=0 as first measurement, t=5 after 5 minutes, t=15 after 15 minutes and t=30 after 30 minutes in total, see Figure 5). The volunteer did not eat or drink in between the measurements, nor did they talk excessively or were otherwise physically active.

In conclusion, significant differences of OC were detected in matched pairs of normal mucosae and HNSCC *in situ*.

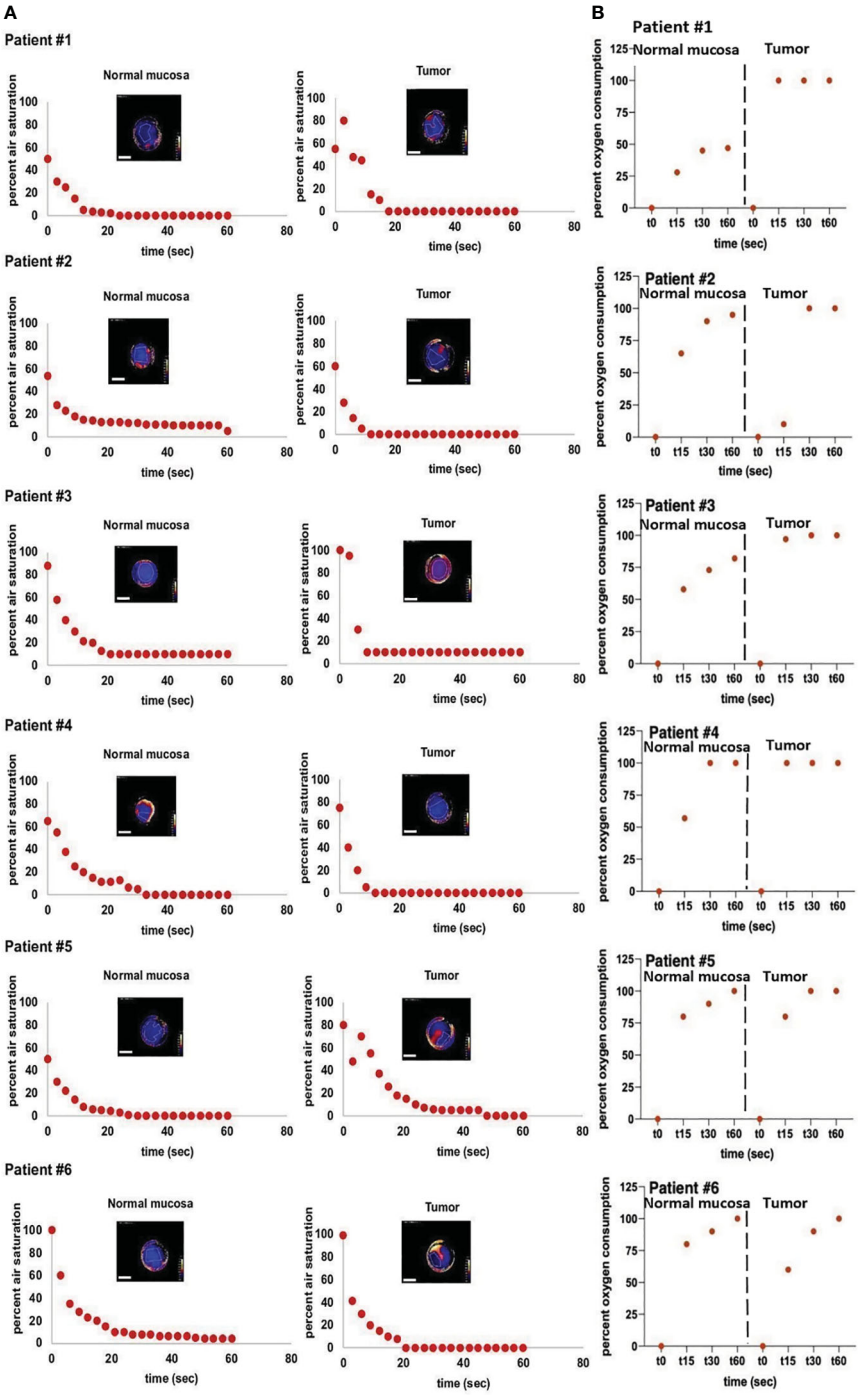

FIGURE 4
In vivo measurements of air saturation and OC-rates. Measurements of air saturation and oxygen consumption of normal mucosa und tumor tissue of six individual patients. **(A)** depicts the raw measurement points, meaning a drop in oxygen (y-axis) over a time span of 60 seconds (x-axis) of normal mucosa (left panels) and tumor (right panels). All depicted heatmaps represent the last measurement of each individual measurement. Areas with poor adhesion of the sensor foil to the tissue were excluded from the measurements. Note, that peripheral areas with continuously high O_2 values are a result of fresh oxygen at the border of the handheld camera entering via the air and have been excluded from the measurements. Scale bars: 10 mm. **(B)** depicts the oc-rate (y-axis) of the same patients (normal mucosa: left panels, tumor tissue: right panels) over a time span of 60 seconds (x-axis). The OC-rate starts at 0, indicating no consumption of oxygen at the beginning of the measurement and ends at a maximum value of 100%, indicating that all available tissue oxygen of the respective region of interest (ROI) has been consumed. For clearer separation, measurements of normal mucosa and tumor tissue are separated by dotted lines. In summary, **(B)** depicts the conversion from the raw data of **(A)** into oxygen consumption over time.

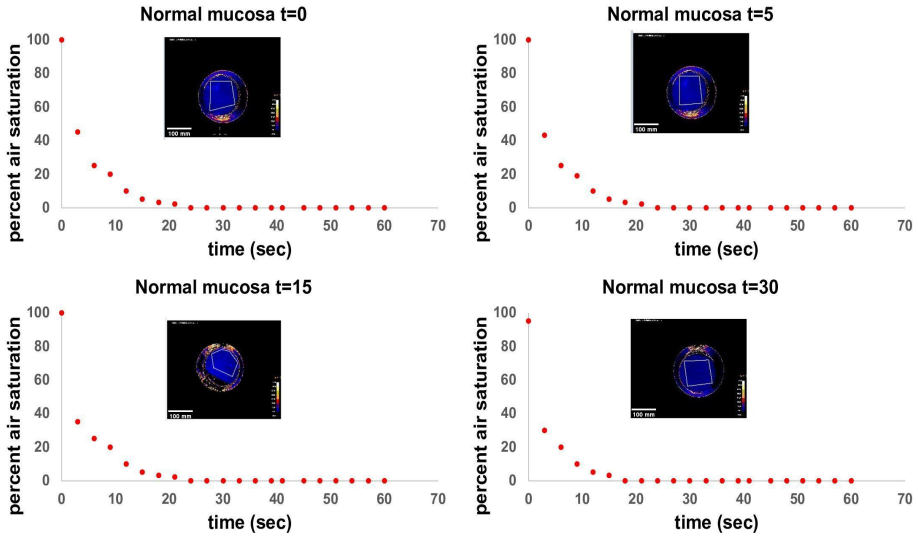

FIGURE 5
Standardized measurement of OC in healthy mucosa at different time points. T=0 as first measurement, t=5 after 5 minutes, t=15 after 15 minutes and t=30 after 30 minutes in total. Measurements were performed in a healthy volunteer in the same area of the tongue (anterior part of the lateral tongue). The volunteer did not eat or drink in between the measurements, nor did they talk excessively or were otherwise physically active. Time in seconds is shown on the x-axis, air saturation in per cent is shown on the y-axis. Every point on the diagram represents a measurement point at an interval of three seconds each. The heatmap in each diagram represents the ending point of the measurement after 60 seconds. Note, that peripheral areas with continuously high O_2 values are a result of fresh oxygen at the border of the handheld camera entering via the air and have been excluded from the measurements. Scale bars: 10 mm.

4 Discussion

Physiological homeostasis of oxygen supply and consumption assures balanced metabolic rates. In tumor tissue, however, this homeostasis frequently gets out of balance and oxygen consumption exceeds the available supply. A high OCR, thus, can result in a hypoxic TME and tissue hypoxia (20). In solid tumors, hypoxia has been recognized as a negative prognostic factor regarding therapeutical options, particularly regarding radiotherapy (30, 31). Subpopulations of tumor cells can survive in hypoxic conditions and play a major, unfavorable role in resistance to irradiation (30). Hypoxic conditions in the TME occur in several solid tumors (38–40). For HNSCC, tumor hypoxia is associated with a poorer overall survival and poorer locoregional recurrence control (41). Upregulation of the transcription factor (TF) GATA binding protein 3 (GATA3) in HNSCC leads to an inhibition of degradation of the TF HIF-1α and thereby creates hypoxic conditions in the TME (41). As a counter-regulating mechanism observed in HNSCC, hypoxic conditions induce the upregulation of a nucleotide excision repair protein, DDB2 (damaged DNA binding protein), which represses the transcription and expression of HIF-1α and other markers of hypoxia (42).

Hence, not only can hypoxia be used as a potential target in cancer therapy, but the visualization of OCR as a sign of hypoxia is of great diagnostical and therapeutic interest. This notion is further supported by reports on the implication of OXPHOS in tumor recurrences in HNSCC (21) and as metabolic vulnerability in highly aggressive triple-negative breast cancer that fail to respond to chemotherapy (43). OXPHOS also represents an attractive target for therapeutic strategies targeting cancer stem cells, which may preferentially rely on this energy source, for example in ovarian cancers, therapy-resistant metastatic breast cancer, and others (44). However, to reliably distinguish malignant from healthy tissue using pO_2, it is mandatory to perform measurements *in situ* with high spatiotemporal resolution. In contrast to systems based on electrodes or soluble sensors, immobilized O_2-sensitive fluorophores - as used in this research project – are deemed more suitable for such application (45). Main advantages of a setup with sensor foils in combination with a handheld camera are (a) that no preparation or treatment of the tissue is required, (b) measurements can be performed *in situ* in a time frame of a few minutes, and (c) topological assessment with high resolution is obtained. Sensor foils with immobilized fluorophores can be safely used on skin and mucosa without the harm of possible toxicity of applying soluble sensors. Another advantage is the spatiotemporal resolution in the sub-millimeter range as shown *in vitro* in the 3D co-culture tumor model presented in this study. These measurements showed promising results with a detection of tumor cell spheroids with two cell lines that had shown high OCR in previous studies via the STOp-Q method down to a diameter of 440 µm. It must be noted that FaDu (hypopharynx) and Kyse30 (esophagus) differ in their original sub-localization from the primary tumors measured *in vivo*. Although differences in the actual size limit of detection between *in vitro* and *in vivo* settings might result partly from malignant cells of varying sub-localization, the choice of upper aerodigestive tract carcinoma cell lines with higher OCR enabled us to provide detection limits under optimized conditions. It must however be noted that altered detection limits may result with additional cell lines and, even more so, *in situ*. In the latter situation, measurements may by further hindered by saliva, topology, and

accessibility. The measurement of oral cavity cancers was designed as a proof-of-concept study with easily accessible malignancies under non-surgical conditions. Future aims comprise the transfer of this technology to intraoperative measurements of residual tumor cells to provide optimized tools for R0 resections.

For the case of disseminated tumor cells in lymph nodes, isolated tumor cells (ITCs), micrometastases, and (macro)metastases are distinguished according to size. ITCs are regarded as metastatic lesions of less than 0.2 mm and are staged pN0. Micrometastases are 0.2-2.0 mm in size and are staged pN1mi, whereas macrometastases, also termed metastases, are larger than 2.0 mm. Assimilating these criteria for residual tumor cells in the vicinity of primary cancers, OC measurements using sensor foils would potentially allow the detection of micro-/and macrometastases and could therefore help eradicate these malignant clusters during surgical procedures (46).

In situ measurements on a small cohort of HNSCC patients corroborated our *in vitro* results and allowed a distinction of matched normal epithelia from cancer tissue via OC measurements over a time frame of few seconds (*i.e.*, 15 s). To our knowledge, this is the first implementation of measurements of OC over a defined timeline of HNSCC *in situ*. Since pO_2 is a metabolic parameter of high clinical and prognostic value, devices that allow standardized and easy measurement of this parameter could represent a significant benefit for patients. Based on the proof-of-concept described in the present study, tissue imaging via sensor foils with immobilized fluorophores qualifies as a potential diagnostic imaging tool due to its high spatiotemporal resolution of tumor aggregates at the micrometastasis size range. Such measurements can be easily integrated in an intraoperative workflow as a non-invasive, rapid procedure to facilitate decisions concerning surgical margins intraoperatively. This could result in a higher treatment safety for the individual patient in terms of sufficient resection margins. Further projecting into the future, OCR measurements might be used as planning tools to detect optimal surgical margins prior to surgery. If a spatial resolution in the micrometer range could be reliably reached *in vivo*, the surgeon might have support in resecting the respective tumor oncologically as safe as possible and functionally as beneficial as possible.

Limitations to this study are the small cohort size and heterogeneity of the tumor stages within the cohort. Larger cohorts of patient samples with different tumor stages (T1-T4 after TNM classification) could give more information on tumor stage-specific OC and could strengthen the theory of higher OC in tumor tissue with higher statistical impact. Another limitation to the application is the handling and adherence of the sensor foils. The foils are placed onto the tissue manually; after placing the sensor foil onto the tissue, the handheld camera is placed onto the sensor foil. An incorporation of the foil into the handheld camera would simplify the measurement process. Additionally, measuring oropharyngeal tissue is always accompanied by the possibility of saliva, mucus or blood being trapped between tissue and sensor foil and influencing the measurements. The areas of interest were tapped dry before applying the sensor foils, but this remains a possible source of error. Furthermore, it must be mentioned that the measurements of different patients showed different starting values of O_2. This must be critically evaluated. Different tissue temperature or moisture may alter the onset of the measurement. The standardized measurement of healthy mucosa at different time intervals in a volunteer as depicted in Figure 5 also shows a minimal change in the starting value of O_2 in the last measurement at 30 minutes (90% at t=30 vs 100% at earlier time points). This might indicate a possible influence of a slight alteration in temperature of the tissue over time on pO_2 measurement. In further experiments, possible factors that could alter the measurements need to be thoroughly evaluated and considered. Since this was a proof-of-concept study, further experiments will also focus on improvements in the execution of the experiments *in situ*.

Two of the six patients included in this study had undergone radiochemotherapy several years back for the treatment of oropharyngeal carcinoma. These two patients showed the lowest OC in tumor tissue of all patients at early time points of measurement. This is in line with previous studies that described differences in oxygenation of irradiated compared to non-irradiated skin. Auerswald et al. showed significantly decreased oxygen levels of chronic wounds of irradiated human skin *in vivo* compared to intact, non-irradiated skin (33). Therefore, a time-dependent measurement of oxygen consumption may provide information on the behavior of not only tumor tissue but generally on tissue that has undergone extensive treatment like radiotherapy.

5 Conclusion

In this project, we present an approach to distinguish tumor tissue of the head and neck area from healthy tissue via measurements of the oxygen consumption (OC). In an *in vitro* model, we performed a detection of tumor cell spheroids in a type I collagen matrix containing stromal cells down to a diameter of 440 µm with the STOp-Q-method, showing the high spatiotemporal resolution of this method. An *in vivo* proof-of-concept study concentrated on the distinction between matched healthy and tumor tissue of the head and neck area in oral cancers that were easily accessible in a pre- and intraoperative setting. We found a significantly higher OC in tumor tissue compared to macroscopically normal tissue. This approach harbors great clinical potential regarding an *in vivo* differentiation of normal and malignant tissue, especially with respect to resection margins.

Data availability statement

The original contributions presented in the study are included in the article/Supplementary Material. Further inquiries can be directed to the corresponding author.

Ethics statement

The studies involving humans were approved by the medical faculty of the LMU Munich (Ludwig-Maximilians-University

Munich) (project 20-244). The studies were conducted in accordance with the local legislation and institutional requirements. The participants provided their written informed consent to participate in this study.

Author contributions

MS performed *in situ* measurement, generated figures, and wrote the manuscript; AS performed *in vitro* measurement, generated figures, and wrote the manuscript; GL and RM provided foils and measurement devices, and support in data analysis; MW, MC, and FH enrolled patients; MC helped writing the manuscript; OG and FH coordinated the study, wrote the manuscript, and acquired funding. All authors contributed to the article and approved the submitted version.

Funding

The author(s) declare financial support was received for the research, authorship, and/or publication of this article. Part of the work was funded by the "Bayerisches Staatsministerium für Wirtschaft, Energie und Technologie", Bio- und Gentechnologie - Forschung, project name TuWuMox, Grant number: BIO-1803-0003.

Conflict of interest

Co-authors RM and GL are employees of PreSens Precision Sensing GmbH, Regensburg, Germany.

The remaining authors declare that the research was conducted in the absence of any commercial or financial relationships that could be construed as a potential conflict of interest.

Publisher's note

Supplementary material

The Supplementary Material for this article can be found online at: https://www.frontiersin.org/articles/10.3389/fonc.2024.1002798/full#supplementary-material

SUPPLEMENTARY FIGURE 1
Oxygen measurements in a 3D *in vitro* tumor model with FaDu spheroids. Overlay of mCherry signal and phase contrast of FaDu mCherry expressing spheroids within a collagen I and NF8 matrix. Spheroid diameters are indicated on the left (left panels). Oxygen heatmaps of the area shown in the microscopic images after 5, 20 and 30 minutes of oxygen measurement (middle panels). Arrowheads indicate the location of spheroids. Scale bars: 5 mm. Color bar indicating oxygen concentrations on the right.

SUPPLEMENTARY FIGURE 2
Oxygen measurements in a 3D *in vitro* tumor model with Kyse30 spheroids. Overlay of mCherry signal and phase contrast of Kyse30 mCherry expressing spheroids within a collagen I and NF8 matrix. Spheroid diameters are indicated on the left (left panels). Oxygen heatmaps of the area shown in the microscopic images after 5, 20 and 30 minutes of oxygen measurement (middle panels). Arrowheads indicate the location of spheroids. Scale bars: 5 mm. Color bar indicating oxygen concentrations on the right.

References

1. Katada C, Muto M, Fujii S, Yokoyama T, Yano T, Watanabe A, et al. Transoral surgery for superficial head and neck cancer: National Multi-Center Survey in Japan. *Cancer Med* (2021) 10:3848–61. doi: 10.1002/cam4.3927

2. Seiwert TY, Cohen EEW. State-of-the-art management of locally advanced head and neck cancer. *Br J Cancer* (2005) 92:1341–8. doi: 10.1038/sj.bjc.6602510

3. Hoffman HT, Karnell LH, Shah JP, Ariyan S, Brown GS, Fee WE, et al. Hypopharyngeal cancer patient care evaluation. *Laryngoscope* (1997) 107:1005–17. doi: 10.1097/00005537-199708000-00001

4. Meier JD, Oliver DA, Varvares MA. Surgical margin determination in head and neck oncology: Current clinical practice. The results of an International American Head and Neck Society Member Survey. *Head Neck* (2005) 27:952–8. doi: 10.1002/hed.20269

5. Loree TR, Strong EW. Significance of positive margins in oral cavity squamous carcinoma. *Am J Surg* (1990) 160:410–4. doi: 10.1016/s0002-9610(05)80555-0

6. Chen TY, Emrich LJ, Driscoll DL. The clinical significance of pathological findings in surgically resected margins of the primary tumor in head and neck carcinoma. *Int J Radiat Oncol Biol Phys* (1987) 13:833–7. doi: 10.1016/0360-3016(87)90095-2

7. Ionna F, Bossi P, Guida A, Alberti A, Muto P, Salzano G, et al. Recurrent/metastatic squamous cell carcinoma of the head and neck: A big and intriguing challenge which may be resolved by integrated treatments combining locoregional and systemic therapies. *Cancers (Basel)* (2021) 13(10):2371. doi: 10.3390/cancers13102371

8. Ettl T, El-Gindi A, Hautmann M, Gosau M, Weber F, Rohrmeier C, et al. Positive frozen section margins predict local recurrence in R0-resected squamous cell carcinoma of the head and neck. *Oral Oncol* (2016) 55:17–23. doi: 10.1016/j.oraloncology.2016.02.012

9. Bhattacharyya S, Patel N, Wei L, Riffle LA, Kalen JD, Hill GC, et al. Synthesis and biological evaluation of panitumumab-IRDye800 conjugate as a fluorescence imaging probe for EGFR-expressing cancers. *Medchemcomm* (2014) 5:1337–46. doi: 10.1039/C4MD00116H

10. Englhard AS, Palaras A, Volgger V, Stepp H, Mack B, Libl D, et al. Confocal laser endomicroscopy in head and neck Malignancies using FITC-labelled EpCAM- and EGF-R-antibodies in cell lines and tumor biopsies. *J Biophotonics* (2017) 10:1365–76. doi: 10.1002/jbio.201600238

11. Volgger V, Girschick S, Ihrler S, Englhard AS, Stepp H, Betz CS. Evaluation of confocal laser endomicroscopy as an aid to differentiate primary flat lesions of the larynx: A prospective clinical study. *Head Neck* (2016) 38(Suppl 1):E1695–704. doi: 10.1002/hed.24303

12. Filip P, Lerner DK, Kominsky E, Schupper A, Liu K, Khan NM, et al. 5-aminolevulinic acid fluorescence-guided surgery in head and neck squamous cell carcinoma. *Laryngoscope* (2024) 134(2):741–8. doi: 10.1002/lary.30910

13. Mendonca P, Sunny SP, Mohan U, Birur NP, Suresh A, Kuriakose MA. Non-invasive imaging of oral potentially Malignant and Malignant lesions: A systematic review and meta-analysis. *Oral Oncol* (2022) 130:105877. doi: 10.1016/j.oraloncology.2022.105877

14. Warburg O, Wind F, Negelein E. THE METABOLISM OF TUMORS IN THE BODY. *J Gen Physiol* (1927) 8:519–30. doi: 10.1085/jgp.8.6.519

15. Gatenby RA, Gillies RJ. Why do cancers have high aerobic glycolysis? *Nat Rev Cancer* (2004) 4:891–9. doi: 10.1038/nrc1478

16. Liberti MV, Locasale JW. The Warburg effect: how does it benefit cancer cells? *Trends Biochem Sci* (2016) 41:211–8. doi: 10.1016/j.tibs.2015.12.001

17. Frederick M, Skinner HD, Kazi SA, Sikora AG, Sandulache VC. High expression of oxidative phosphorylation genes predicts improved survival in squamous cell carcinomas of the head and neck and lung. *Sci Rep* (2020) 10:6380. doi: 10.1038/s41598-020-63448-z

18. Finley LWS. What is cancer metabolism? *Cell* (2023) 186:1670–88. doi: 10.1016/j.cell.2023.01.038

19. Fleming JC, Woo J, Moutasim K, Mellone M, Frampton SJ, Mead A, et al. HPV, tumour metabolism and novel target identification in head and neck squamous cell carcinoma. *Br J Cancer* (2019) 120:356–67. doi: 10.1038/s41416-018-0364-7

20. Li JZ, Gao W, Chan JY-W, Ho W-K, Wong T-S. Hypoxia in head and neck squamous cell carcinoma. *ISRN Otolaryngol* (2012) 2012:708974. doi: 10.5402/2012/708974

21. Noh JK, Woo SR, Kong M, Lee MK, Lee JW, Lee YC, et al. Gene signature predicting recurrence in oral squamous cell carcinoma is characterized by increased oxidative phosphorylation. *Mol Oncol* (2023) 17:134–49. doi: 10.1002/1878-0261.13328

22. Ohashi T, Terazawa K, Shibata H, Inoue N, Ogawa T. Metabolic profiling analysis of head and neck squamous cell carcinoma. *Oral Dis* (2022). doi: 10.1111/odi.14432

23. Gammon L, Mackenzie IC. Roles of hypoxia, stem cells and epithelial-mesenchymal transition in the spread and treatment resistance of head and neck cancer. *J Oral Pathol Med* (2016) 45:77–82. doi: 10.1111/jop.12327

24. Brahimi-Horn C, Pouysségur J. The role of the hypoxia-inducible factor in tumor metabolism growth and invasion. *Bull Cancer* (2006) 93:E73–80.

25. Garvalov BK, Acker T. Implications of oxygen homeostasis for tumor biology and treatment. *Adv Exp Med Biol* (2016) 903:169–85. doi: 10.1007/978-1-4899-7678-9_12

26. Ryan HE, Poloni M, McNulty W, Elson D, Gassmann M, Arbeit JM, et al. Hypoxia-inducible factor-1alpha is a positive factor in solid tumor growth. *Cancer Res* (2000) 60:4010–5.

27. Pérez-Sayáns M, Suárez-Peñaranda JM, Torres-López M, Supuran CT, Gándara-Vila P, Gayoso-Diz P, et al. Expression of CA IX in dysplasia adjacent to surgical resection margins of oral squamous cell carcinoma. *Biotech Histochem* (2014) 89:91–7. doi: 10.3109/10520295.2013.818166

28. Gokavarapu S, Parvataneni N, Pavagada S, Chandrasekhara Rao LM, Raju KV, Rao TS. Mild to moderate dysplasia at surgical margin is a significant indicator of survival in patients with oral cancer. *Oral Surg Oral Med Oral Pathol Oral Radiol* (2017) 123:330–7. doi: 10.1016/j.oooo.2016.10.028

29. Mehanna HM, Rattay T, Smith J, McConkey CC. Treatment and follow-up of oral dysplasia - a systematic review and meta-analysis. *Head Neck* (2009) 31:1600–9. doi: 10.1002/hed.21131

30. Horsman MR, Overgaard J. The impact of hypoxia and its modification of the outcome of radiotherapy. *J Radiat Res* (2016) 57(Suppl 1):i90–8. doi: 10.1093/jrr/rrw007

31. Grimes DR, Warren DR, Warren S. Hypoxia imaging and radiotherapy: Bridging the resolution gap. *Br J Radiol* (2017) 90:20160939. doi: 10.1259/bjr.20160939

32. Walsh JC, Lebedev A, Aten E, Madsen K, Marciano L, Kolb HC. The clinical importance of assessing tumor hypoxia: Relationship of tumor hypoxia to prognosis and therapeutic opportunities. *Antioxid Redox Signal* (2014) 21:1516–54. doi: 10.1089/ars.2013.5378

33. Auerswald S, Schreml S, Meier R, Blancke Soares A, Niyazi M, Marschner S, et al. Wound monitoring of pH and oxygen in patients after radiation therapy. *Radiat Oncol* (2019) 14:199. doi: 10.1186/s13014-019-1413-y

34. Meier JK, Prantl L, Müller S, Moralis A, Liebsch G, Gosau M. Simple, fast and reliable perfusion monitoring of microvascular flaps. *Clin Hemorheol Microcirc* (2012) 50:13–24. doi: 10.3233/CH-2011-1439

35. Zhou J, Schwenk-Zieger S, Kranz G, Walz C, Klauschen F, Dhawan S, et al. Isolation and characterization of head and neck cancer-derived peritumoral and cancer-associated fibroblasts. *Front Oncol* (2022) 12:984138. doi: 10.3389/fonc.2022.984138

36. Blancke Soares A, Meier R, Liebsch G, Schwenk-Zieger S, Kirmaier ME, Theurich S, et al. High-resolution spatiotemporal pHe and pO2 imaging in head and neck and oesophageal carcinoma cells. *Cancer Metab* (2021) 9:21. doi: 10.1186/s40170-021-00257-6

37. Schindelin J, Arganda-Carreras I, Frise E, Kaynig V, Longair M, Pietzsch T, et al. Fiji: An open-source platform for biological-image analysis. *Nat Methods* (2012) 9:676–82. doi: 10.1038/nmeth.2019

38. Axelson H, Fredlund E, Ovenberger M, Landberg G, Påhlman S. Hypoxia-induced dedifferentiation of tumor cells–a mechanism behind heterogeneity and aggressiveness of solid tumors. *Semin Cell Dev Biol* (2005) 16:554–63. doi: 10.1016/j.semcdb.2005.03.007

39. Harris AL. Hypoxia–a key regulatory factor in tumour growth. *Nat Rev Cancer* (2002) 2:38–47. doi: 10.1038/nrc704

40. Brahimi-Horn MC, Chiche J, Pouysségur J. Hypoxia and cancer. *J Mol Med (Berl)* (2007) 85:1301–7. doi: 10.1007/s00109-007-0281-3

41. Lin M-C, Lin J-J, Hsu C-L, Juan H-F, Lou P-J, Huang M-C. GATA3 interacts with and stabilizes HIF-1α to enhance cancer cell invasiveness. *Oncogene* (2017) 36:4243–52. doi: 10.1038/onc.2017.8

42. Bommi PV, Chand V, Mukhopadhyay NK, Raychaudhuri P, Bagchi S. NER-factor DDB2 regulates HIF1α and hypoxia-response genes in HNSCC. *Oncogene* (2020) 39:1784–96. doi: 10.1038/s41388-019-1105-y

43. Evans KW, Yuca E, Scott SS, Zhao M, Paez Arango N, Cruz Pico CX, et al. Oxidative phosphorylation is a metabolic vulnerability in chemotherapy-resistant triple-negative breast cancer. *Cancer Res* (2021) 81:5572–81. doi: 10.1158/0008-5472.CAN-20-3242

44. Nayak AP, Kapur A, Barroilhet L, Patankar MS. Oxidative phosphorylation: A target for novel therapeutic strategies against ovarian cancer. *Cancers (Basel)* (2018) 10 (9):337. doi: 10.3390/cancers10090337

45. Schreml S, Meier RJ, Kirschbaum M, Kong SC, Gehmert S, Felthaus O, et al. Luminescent dual sensors reveal extracellular pH-gradients and hypoxia on chronic wounds that disrupt epidermal repair. *Theranostics* (2014) 4:721–35. doi: 10.7150/thno.9052

46. Majumdar KS, Rao VUS, Prasad R, Ramaswamy V, Sinha P, Subash A. Incidence of micrometastasis and isolated tumour cells in clinicopathologically node-negative head and neck squamous cell carcinoma. *J Maxillofac Oral Surg* (2020) 19:131–5. doi: 10.1007/s12663-019-01239-4

Frontiers in Oncology

Advances knowledge of carcinogenesis and tumor progression for better treatment and management

The third most-cited oncology journal, which highlights research in carcinogenesis and tumor progression, bridging the gap between basic research and applications to imrpove diagnosis, therapeutics and management strategies.

Discover the latest Research Topics

See more →

Frontiers

Avenue du Tribunal-Fédéral 34
1005 Lausanne, Switzerland
frontiersin.org

Contact us

+41 (0)21 510 17 00
frontiersin.org/about/contact